

AD-A148 635

PROCEEDINGS OF THE INTERNATIONAL CONFERENCE ON THE
PERFORMANCE OF OFF-ROAD... (U) INTERNATIONAL SOCIETY FOR
TERRAIN-VEHICLE SYSTEMS M J DWYER AUG 84

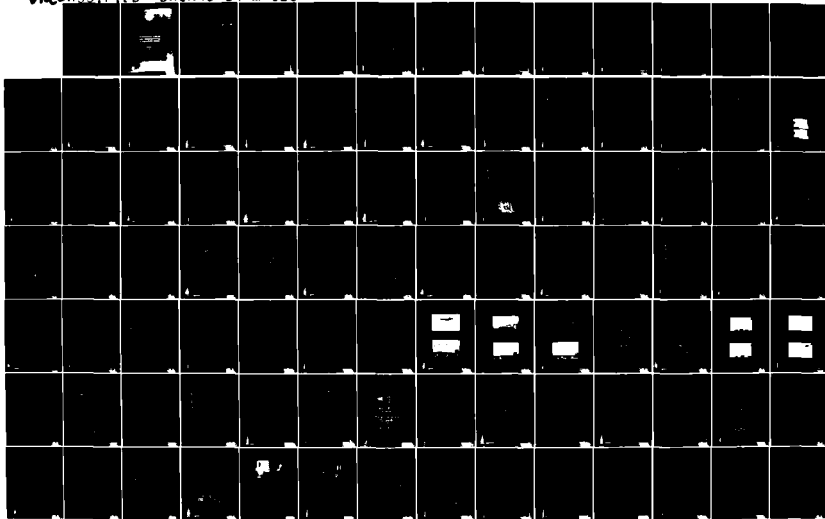
1/5

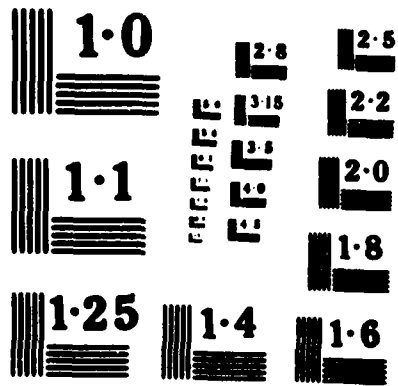
UNCLASSIFIED

DAJA45-84-M-0251

F/G 13/6

NL





AD-A148 635

International Energy Research Institute

8th International Conference

8th International Conference

8th International Conference

APPROVED FOR PUBLIC RELEASE: DISTRIBUTION
UNLIMITED

FILE COPY

COMPONENT PART NOTICE

THIS PAPER IS A COMPONENT PART OF THE FOLLOWING COMPILATION REPORT:

(TITLE): Proceedings of the International Conference on the Performance of
Off-Road Vehicles and Machines (8th) Volume 2 Held at Cambridge,
England on August 5-11, 1983

(SOURCE): International Society for Terrain-Vehicle Systems

DTIC

DEC 27 1984

TO ORDER THE COMPLETE COMPILATION REPORT USE AD-A148 615 .

A

THE COMPONENT PART IS PROVIDED HERE TO ALLOW USERS ACCESS TO INDIVIDUALLY AUTHORED SECTIONS OF PROCEEDINGS, ANNUALS, SYMPOSIA, ETC. HOWEVER, THE COMPONENT SHOULD BE CONSIDERED WITHIN THE CONTEXT OF THE OVERALL COMPILATION REPORT AND NOT AS A STAND-ALONE TECHNICAL REPORT.

THE FOLLOWING COMPONENT PART NUMBERS COMPRISE THE COMPILATION REPORT:

ADN:	TITLE:
POOL 283	The reasearch of the driving wheel with movable lugs of the paddy field floating tractor
POOL 284	An investigation of the driving wheel thrust of paddy field tractors
POOL 285	Mobility of the small combine (track type) on soft ground - Relationship between the position of the center of gravity and the mobility
POOL 286	The stress-strain- time graph of rheological soils and its application
POOL 287	Behaviour of soil under a lugged wheel
POOL 288	Prediction accuracy of the torques for rotary tillage by an analog tool
POOL 289	The analysis on the dynamic performance of a single lug
POOL 290	Study of the motion of agricultural vehicles on steep grass-covered slopes
Pool 291	Some stability and control problems with trailed farm tankers on slopes
POOL 292	Control of tractors on sloping ground
POOL 293	Stability indicators for front end loaders
POOL 294	Pressure tests in soil below tires of agricultural vehicles
POOL 295	Quality control in soil compaction by behaviour of exciter
POOL 296	Smoother terrain machine
POOL 297	Compaction of sand using ordinary off-road vehicles
POOL 298	A simple perdictior model for soil compaction under various wheel loads and geometries as an aid to vehicle design
POOL 299	Flotation tires and subsurface compaction
POOL 300	Tractor power selection with compaction constraints
POOL 301	The guidelines to design the lever turning gears in articulated vehicles
POOL 302	Study on controllability and stability of high speed tracked vehicles
POOL 303	Forces on undriven, angled wheels
POOL 304	Turning behaviour of articulated frame steering tractor

COMPONENT PART NOTICE (CON'T)

<p>ADW: POOL 305 POOL 306 POOL 307 POOL 308</p>	<p>TITLE: A tracked vehicle test plant for the simulation of dynamic operation Proffleinfluss auf Widerstands-und lenkkraft frei rollender reifen (The influence of the tyre tread on the rolling resistance and steering forces on undriven wheels) (including English translation) Basic study on the turning resistance of track Study on steerability of articulated tracked vehicles</p>
---	---

Accession For	
NTIS GRA&I	<input checked="" type="checkbox"/>
DTIC TAB	<input type="checkbox"/>
Unannounced Justification	
By	
Distribution/.	
Availability Codes	
Dist	Avail and/or Special
A-1	

This document has been approved for public release and sale; its distribution is unlimited.

Unclassified

SECURITY CLASSIFICATION OF THIS PAGE (When Data Entered)

REPORT DOCUMENTATION PAGE		READ INSTRUCTIONS BEFORE COMPLETING FORM	
1. REPORT NUMBER	2. GOVT ACCESSION NO.	3. RECIPIENT'S CATALOG NUMBER	
	AD-A148635		
4. TITLE (and Subtitle) PROCEEDINGS: 8th INTERNATIONAL CONFERENCE INT. SOC. FOR TERRAIN VEHICLE SYSTEMS		5. TYPE OF REPORT & PERIOD COVERED FINAL MAY - AUG 1984	
7. AUTHOR(s) ED: MICHAEL J. DMYER		8. CONTRACT OR GRANT NUMBER(s) DAJA45-84-M-0251	
9. PERFORMING ORGANIZATION NAME AND ADDRESS INT. SOC. FOR TERRAIN VEHICLE SYSTEMS NIAE, WREST PARK, SILSOE BEDFORD MK45 4HS, U.K.		10. PROGRAM ELEMENT PROJECT TASK AREA & WORK UNIT NUMBER 61102A-It161102-BH57-01	
11. CONTROLLING OFFICE NAME AND ADDRESS USARDCG-UK PO Box 65 FPO NY, NY 09510-1000		12. REPORT DATE AUG 84	
14. MONITORING AGENCY NAME & ADDRESS (if different from Controlling Office)		13. NUMBER OF PAGES: 1304 (3 vols)	
		15. SECURITY CLASS (of this report): Unclassified	
		15a. DECLASSIFICATION/DOWNGRADING SCHEDULE	
16. DISTRIBUTION STATEMENT (of this Report) Approved for public release; distribution unlimited.			
17. DISTRIBUTION STATEMENT (of the abstract entered in Block 20, if different from Report)			
18. SUPPLEMENTARY NOTES			
19. KEY WORDS (Continue on reverse side if necessary and identify by block number) MOBILITY; CROSS-COUNTRY MOBILITY; OFF-ROAD MOBILITY; SOIL-VEHICLE INTERACTION; VEHICLE DYNAMICS.			
20. ABSTRACT (Continue on reverse side if necessary and identify by block number) The three volumes consist of a collection of all significant papers presented at the 8th International Conference. Subjects include; Tyre-soil interaction; theoretical aspects of ride dynamics; track-soil interaction; practical aspects of ride dynamics; operation in paddy fields; operation on steep slopes; soil compaction; steering; computer modelling; vehicle component design; measurement of soil and snow properties and soil bin facilities; and vehicle design.			

DD FORM 1306 1 JAN 73 1073 EDITION OF 1 NOV 65 IS OBSOLETE

Unclassified

SECURITY CLASSIFICATION OF THIS PAGE (When Data Entered)

H 148 635

INTERNATIONAL SOCIETY FOR TERRAIN VEHICLE SYSTEMS

USACRREL, 72 Lyme Road, Hanover, New Hampshire,
03755, USA

SFM/FOA 2, Box 27322, S-102 54, Stockholm, Sweden



8th International Conference

The Performance of Off-Road Vehicles
and Machines

August 5-11, 1984

Churchill College, Cambridge University, England

Proceedings

Volume II of III

Accession For	
NTIS GRA&I	<input checked="" type="checkbox"/>
DTIC TAB	<input type="checkbox"/>
Unannounced	<input type="checkbox"/>
Justification	
By _____	
Distribution/ _____	
Availability Codes	
Dist	Avail and/or Special
A-1	

VOLUME II

	Page
TOPIC 5 OPERATION IN PADDY FIELDS	493
Chairman: Dr. A.R. Reece, Soil Machine Dynamics Ltd., England	
Rapporteur: Prof. T. Tanaka, Kyoto University, Japan	
 The research of the driving wheel with movable lugs of the paddy field floating tractor	
Prof. Chen Bing Cong and Chao Yu Fan, Jilin University of Technology, China	495 ✓
 An investigation of the driving wheel thrust of paddy field tractors	
Deng Zhuorong and Youg Shuchang, Luoyang Tractor Research Institute, China	507 ✓
 Mobility of the small combine (track type) on soft ground - Relationship between the position of the center of gravity and the mobility	
Dr. Prof. H. Esaki, Tsukuba University, Japan	521 ✓
 The stress-strain-time graph of rheological soils and its application	
Prof. Pan Jun Zhang, Jiangsu Institute of Technology, China	539 ✓
 Behaviour of soil under a lugged wheel	
S.X. Wu, J.H. Hu and Prof. J.Y. Wong, Carleton University, Canada	545 ✓
 Prediction accuracy of the torque for rotary tillage by an analog tool	
Minoru Yamazaki and Prof. Takashi Tanaka, Kyoto University, Japan	561 ✓
 The analysis on the dynamic performance of a single lug	
Zhang T.L. and Prof. J.Y. Shao, South China Agricultural College	575 ✓

	Page
TOPIC 6 OPERATION ON STEEP SLOPES	593
Chairman: Dr. R. Rarlas, Helsinki University, Finland	
Rapporteur: Dr. A. Grecenko, Agricultural Machinery Research Institute, Czechoslovakia	
 Study of the motion of agricultural vehicles on steep grass- covered slopes	
Dr. A. Grecenko, Agrost-Research Institute of Agricultural Machinery, Czechoslovakia	595
 Some stability and control problems with trailed farm tankers on slopes	
A.G.M. Hunter, Scottish Institute of Agricultural Engineering	615
 Control of tractors on sloping ground	
H.B. Spencer, Scottish Institute of Agricultural Engineering, and Dr. D.A. Crolla, Leeds University, England	635
 Stability indicators for front end loaders	
G. Mray and J. Nazalawicz, Stevens Institute of Technology, USA, and A.J. Rwitowski, US Bureau of Mines	655

	Page
TOPIC 7 SOIL COMPACTION	673
Chairman: Prof. W. Soehne, Munich University, Germany	
Rapporteur: Dr. J.H. Taylor, National Tillage Machinery Laboratory, USA	
 Pressure tests in soil below tires of agricultural vehicles Dipl.-Ing. I. Bolling, München Technische Universität, Germany	675 ✓
 Quality control in soil compaction by behaviour of exciter S. Hata and K. Tateyama, Kyoto University, Japan	691 ✓
 Smoother terrain machine B. Marklund, Swedish University of Agricultural Sciences	707
 Compaction of sand using ordinary off-road vehicles Col. Dr. S. Shaaban, Military Technical College, Egypt	725 ✓
 A simple prediction model for soil compaction under various wheel loads and geometries as an aid to vehicle design D.L.O. Smith, Scottish Institute of Agricultural Engineering	737 ✓
 Flotation tires and subsurface compaction Dr. J.H. Taylor and Dr. E.C. Burt, National Tillage Machinery Laboratory, USA	751 ✓
 Tractor power selection with compaction constraints Dr. B.D. Witney, E.B. Elbarra, and K. Ezzat Oskoui, North of Scotland College of Agriculture.	761 ✓

	Page
TOPIC 8 STEERING	775
Chairman: Prof. A.J. Soltynski, Warsaw University, Poland	
Reporteur: Dr. P. Dudzinski, Wroclaw University, Poland	
 The guidelines to design the lever turning gears in articulated vehicles	
Dr. P. Dudzinski and Prof. Dr. H. Hawrylak, Technical University of Wroclaw, Poland	777
 Study on controllability and stability of high speed tracked vehicles	
F. Eiyō and Prof. M. Kitano, The National Defence Academy, Japan	789
 Forces on undriven, angled wheels	
M. McAllister, National Institute of Agricultural Engineering, England	803
 Turning behaviour of articulated frame steering tractor	
Dr. A. Oida, Kyoto University, Japan	821
 A tracked vehicle test plant for the simulation of dynamic operation	
Prof. Dr.-Ing. I. Schmid, University of German Armed Forces	835
 Profileinflüsse auf Widerstands- und Lenkkräfte frei rollender reifen (The influence of the tyre tread on the rolling resistance and steering forces on undriven wheels) (including English translation)	
Dr. H. Schwanhart and K. Rott, Technische Universität München, Germany	855
 Basic study on the turning resistance of track	
Dr. M. Sugiyama and H. Kondo, Tokai University, Japan	889
 Study on steerability of articulated tracked vehicles	
K. Natanabe and Prof. M. Kitano, The National Defence Academy, Japan	901

TOPIC 5
OPERATION IN PADDY FIELDS

↙

The Research of Driving Wheel with Movable Lugs of the Paddy Field Floating Tractor

Dr. Li Jin-song, Chen Ya-san

Jilin University of Technology, Changchun, Jilin, P.R.C.

ABSTRACT

This paper discussed the kinematics and dynamics of the paddy wheel with movable lugs penetrating into and coming out from soil perpendicularly. The calculation of the electric computer shows that for the requirement of a certain tractive force the wheel should have a certain sinkage so that it has the optimal tractive efficiency. The experiment on the specific test bench designed by the author shows that this type of wheel has a less rolling resistance and a higher tractive efficiency.

The rigid lugged wheel is the driven wheel adopted widely by the paddy tractors in China. Because the adhesive performance of this wheel is not good, and the rolling resistance is larger, the efficiency of the wheel is much lower. The appearance of the paddy field boat tractor makes the machine possess less moving resistance. The reason is that the boat has a large bottom area which greatly decreases the ground pressure and causes a small sinkage. At the same time due to the lubrication of water, the friction coefficient of sliding between the bottom of boat and the surface layer of the paddy field is also small. But its driving gear---lugged wheel itself still has the problem that the rolling resistance is large. For example, the boat tractor---Hubei-12 weighs 811 kg, the weight distributed only on bottom is 540 kg, and on the wheels is 271 kg. But the sliding resistance of boat is only 73 kg and the rolling resistance of the wheels reach even 307 kg. The rolling resistance is so large that wheels are not able to offer enough tractive force and the efficiency is very low. This means a waste of oil and non-economics of the production.

Up to now, the research of this rigid wheel is made mainly by the method of selecting the geometric shape of the lug, which keeps soil from being dug up and decreases the rolling resistance. The lugs fixed on the wheel move in different trochoids, which decides that the lugs have to connect the soil no matter whatever geometric shape and lug angle are adopted. The great majority holds that the connection of the soil by wheel is just the main reason causing rolling resistance.

This paper studies the wheel with movable lugs which pene-

AD-P004 283

trate into and come out from soil perpendicular to its plane in Fig. 1.

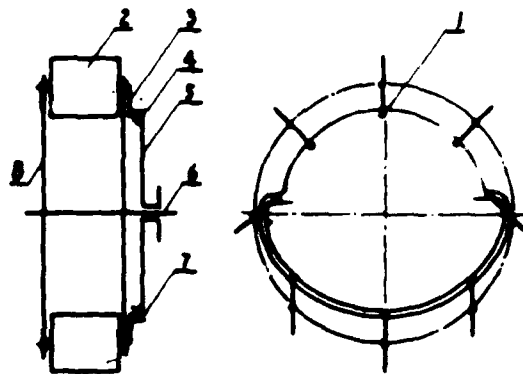


Fig. 1-1 Rigid wheel with movable lugs
 1. roller on the connecting rod of lug 2. lug
 3. connecting rod of lug 4. sliding groove
 5. fixing chute plate 6. driven axle
 7. chute 9. rib plate of lug

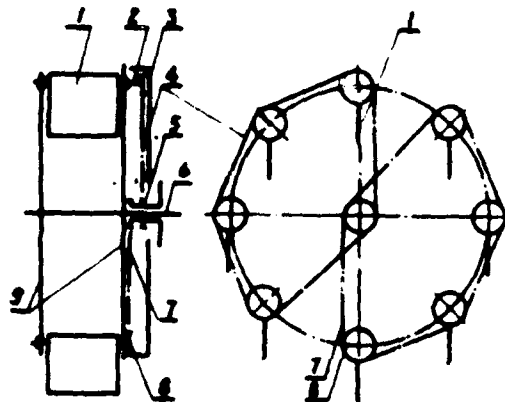


Fig. 1-2 Rigid wheel with movable lugs
 1. lug 2. lug axle 3. case 4. chain
 5. fixed sprocket 6. driven axle 7. chute
 8. sprocket 9. rib plate of lug
 Because the lugs penetrate into soil perpendicularly the loss of power of compaction to soil is greatly decreased, and the total weight of the tractor is supported only by the bottom of the boat.

1. The operation of the wheel and the shape of the puncher

Note.

The kinematics locus of the axle centre of the lugs of this wheel is trochoids. The loci of all points on the lug in soil are parallel to it. Then the lug moves perpendicularly in soil. The kinematics equation of any point M on the lug is

$$\begin{aligned} X_M &= r(1 - \delta) \theta - R \sin \theta \\ Y_M &= r(1 - \delta) - R \cos \theta + h_M \end{aligned} \quad (1)$$

where h_M is the distance from point M to the apex of the lug, R is the radius of the wheel, i.e. the distance from the wheel centre to the axle centre of the lug. θ is the angle turning from the lowest position of the wheel lug: it is positive when the lug penetrates into soil, and negative when out from soil.

According to different slips the motion of lug in soil may be divided into three cases: it bulldozes the soil twice, once, or it does not bulldoze the soil as shown in Fig. 2

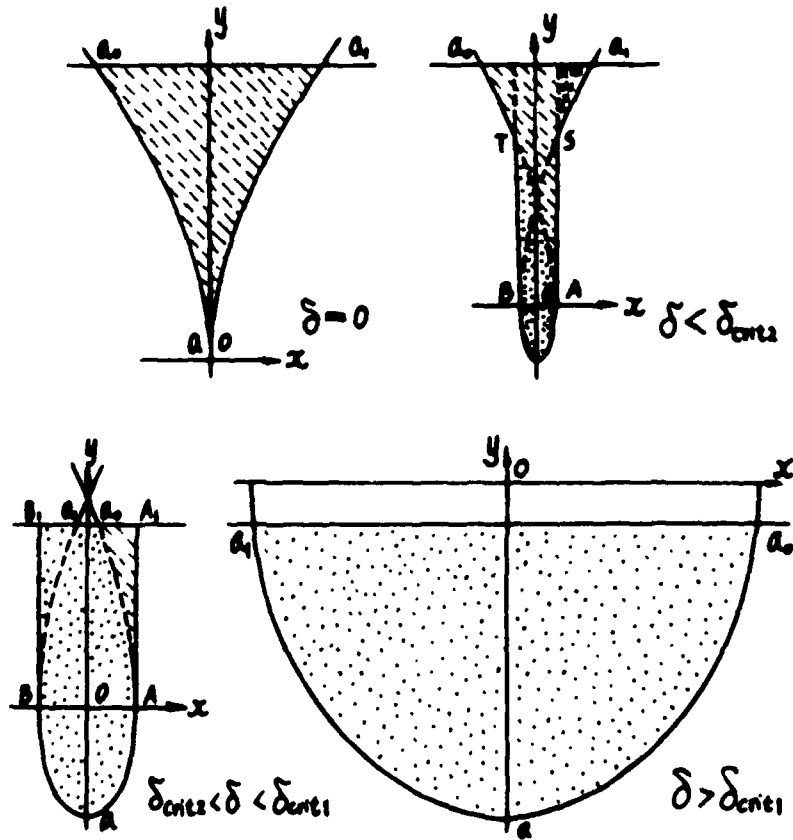


Fig. 2 The lug hole of the soil at different slips

Where the dotted lines represent the bulldozed soil on the first time, . represents the soil sheared and pressed backward, x represents the soil bulldozed on the second time.

Obviously, there must be a certain critical slip δ_{crit1} . When the wheel rolls with a slightly smaller slip than it, the lug bulldozes soil twice, and the lug bulldozes soil only once with a slightly larger slip than it. δ_{crit1} can be determined by the following equation. It is more complicated and can be solved by the electric computer.

$$(1-\delta)\left\{\cos^{-1}(1-\delta)+\cos^{-1}\left(\frac{R-H}{R}\right)-\sqrt{2\delta-\delta^2}-\sqrt{\frac{2RH-H^2}{R}}\right\}=0 \quad (2)$$

There also exists a certain critical slip δ_{crit2} . The lug bulldozes soil once with a slightly smaller slip than it, and does not bulldoze soil with a slightly larger slip than it. δ_{crit2} can be determined by

$$\delta_{crit2}=H/R \quad (3)$$

2. The dynamics performance of the wheel with movable lugs

1) The derivation of the drawbar pull of the wheel with movable lugs

The horizontal forward thrust of the soil against a single lug can be calculated by

$$P_k = \frac{1}{2} \gamma b h^2 N(\phi) + 2cbh \sqrt{N(\phi)} \quad (4)$$

where γ is the specific weight of soil, ϕ is the angle of friction, C is the coefficient of cohesion, b is the width of lug, h is the depth of the sinkage of lug, $N(\phi)$ is the flow value and equal to $\tan^2(\pi/4 + \phi/2)$.

To keep the penetrating lugs from interfering each other when they act on soil, the slip should be confined within the necessary limit

$$\delta < 1 - \frac{H \sqrt{N(\phi)}}{2R \sin(\pi/N)} \quad (5)$$

where H is the sinkage of the wheel, N is the number of the movable lugs of the wheel.

We can calculate the average tractive force \bar{P}_k of a single lug, then the tractive force P_k of the wheel is

$$P_k = N \bar{P}_k \quad (6)$$

The result of calculation by the electric computer shows that the maximum-drawbar pull and the optimal tractive efficiency of the wheel exist only when the slip is between δ_{crit2} and δ_{crit1} . Hence here we only introduce the formula in which the slip is between δ_{crit2} and δ_{crit1} . Through derivation we obtain the equation as follows

$$P_k = \frac{DN \sqrt{N(\phi)}}{4} \left\{ (R^2 - 2HR + \frac{1}{2}R^2) \left[3\cos^{-1}(1-\delta) - \cos^{-1}\left(\frac{R-H}{R}\right) \right] - 3\sqrt{2\delta-\delta^2} \left(\frac{\delta}{2}\right)^2 - 2HR + \frac{3}{2}R^2 + \frac{3}{2}(R-H)\sqrt{2RH-H^2} \right\} + \frac{DCN \sqrt{N(\phi)}}{2} \left\{ (1-\delta) \left[3\cos^{-1}(1-\delta) - \cos^{-1}\left(\frac{R-H}{R}\right) \right] + 3R\sqrt{2\delta-\delta^2} - \sqrt{2RH-H^2} \right\} \quad (7)$$

The rolling resistance P_{ext} of soil to the wheel is mainly from the three respects, i.e. the bulldozing resistance P_{f1} , the resistance P_{f2} of the friction and adhere of soil, the resistance of P_{f3} of the compaction of soil due to the thickness of the lugs. Hence

$$P_{\text{ext}} = P_{f1} + P_{f2} + P_{f3} \quad (8)$$

$$\text{where } P_{f1} = \frac{bN}{4\pi} N(\Phi) \left\{ \left[\cos^{-1} \left(\frac{R-H}{R} \right) - \cos^{-1} (1-\delta) \right] (H^2 - 2HR + \frac{3}{2}R^2) + \frac{3}{2}(H-R) \sqrt{2HR - H^2} - R \sqrt{2\delta - \delta^2} (2H - \delta R - \frac{3}{2}R) \right\} + \frac{bCN}{\pi} \sqrt{N(\Phi)} \left\{ \left[\cos^{-1} \left(\frac{R-H}{R} \right) - \cos^{-1} (1-\delta) \right] (H-R) + \sqrt{2HR - H^2} - \sqrt{2\delta - \delta^2} R \right\}$$

$$P_{f2} = \frac{bN\delta\mu_f}{2\pi(1-\delta)} (2H - R\delta)$$

$$P_{f3} = \frac{btNKH^{n+1}}{2(n+1)\pi R(1-\delta)}$$

where μ_f is the friction coefficient of soil, K is the bearing coefficient, t is the thickness of the lug.

2) The maximum-drawbar pull $P_{K\text{max}}$ of the wheel with movable lugs

The drawbar pull of the wheel $P_{K\text{max}}$ is equal to the difference of P_K from P_{ext} . It is easy to obtain the maximum-drawbar pull of the wheel in different depth of the sinkage by means of the electric computer. Fig. 3 shows $H-P_{K\text{max}}-\delta$ curves with three different structure-parameters.

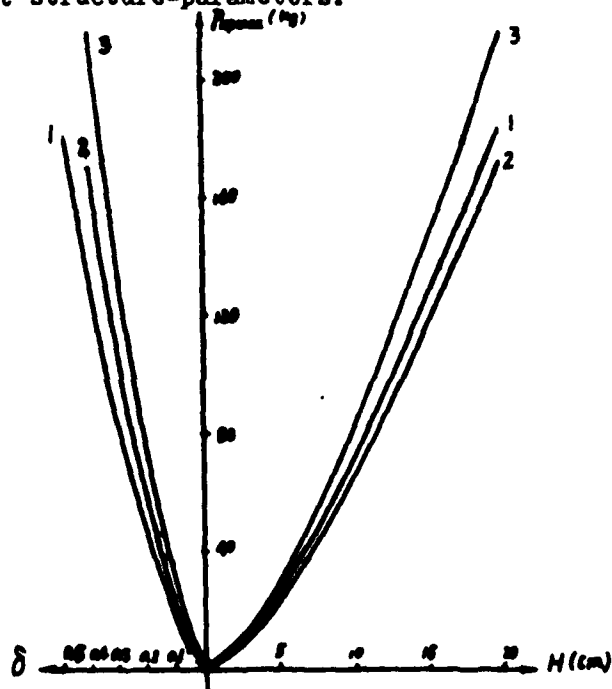


Fig. 3 $P_{\text{max}} - \delta$ curves of various configurations
parameter of the wheel
curve 1. $R = 37\text{cm}$ $N = 8$
curve 2. $R = 47\text{cm}$ $N = 8$
curve 3. $R = 47\text{cm}$ $N = 10$

The curves show that the maximum-drawbar pulls are different with the different sinkage and correspondent slip. The larger the sinkage, the larger the maximum-drawbar pull, and the larger the slip is. If other conditions are the same and the number of the lug is fixed while the radius of the wheel increases, the maximum-drawbar pull decreases. The result is contrary to that of the tire wheel. The distance between two near punching holes is $S_k = 2R(1-\delta)\sin\frac{\pi}{N}$. If N is not changed and δ gets larger and then the relevant slip gets smaller, S_k certainly gets larger. This means the area decreases on which the wheel acts per unit length of soil. And then the obtained thrust from the soil is smaller. If R and N become larger at the same time, the distance between two near lugs keeps approximately constant, and the change of S_k is not very large, then P_{max} increases with δ .

3) The optimal tractive efficiency of the wheel with movable lugs

The formula for calculating the tractive efficiency of this wheel is

$$\eta_{\text{tr}} = \eta_{\text{int}} \eta_{\text{ext}} \eta_{\text{s}} = \eta_{\text{s}} \eta_{\text{e}} \quad (9)$$

The external rolling efficiency of the wheel can be obtained by $\eta_{\text{ext}} = P_{\text{tr}}/P_k$. The internal rolling efficiency of the wheel can be represented by $\eta_{\text{int}} = \frac{M_k - M_{\text{int}}}{M_k}$. And the slipping efficiency is $\eta_{\text{s}} = 1 - \delta$.

There are two ways to seek the maximum-tractive efficiency. First, to a given sink, changing the slip of the wheel, we can seek the slip with which the wheel has the maximum-tractive efficiency, and the relevant drawbar pull can be also obtained. Where η_{tr} is the function of slip δ . Second, to a given requirement of drawbar pull, changing the depth of the sinkage and slip with which the wheel has the maximum-tractive efficiency. Where η_{tr} is the function of the sinkage H and the slip δ .

Some discussions belong to the first. It is obvious that the ranges to seek the optimum by these two ways are different. In practice, the paddy field floating tractor should determine the optimal sinkage of the wheel according to required drawbar pull. Fig. 4 gives the curves $H - \delta - \eta_{\text{tr}} - P_{\text{tr}}$ calculated by the electric computer in those two ways mentioned above with some given soil-parameters. For instance, by the first way, if $H = 14\text{cm}$, $\delta = 0.2000$, we obtain $\eta_{\text{tr}} = 0.5830$, $P_{\text{tr}} = 28.45\text{kg}$. By the second way, if $P_{\text{tr}} = 28.45\text{kg}$, we obtain $H = 12.22\text{cm}$, $\delta = 0.2230$ and $\eta_{\text{tr}} = 0.5932$. The meaning of curve 2, therefore, is that to a given drawbar pull the curve shows the optimal depth of the sinkage of the wheel i.e. to this requirement of the drawbar pull, the wheel has the optimal tractive efficiency

in this case.

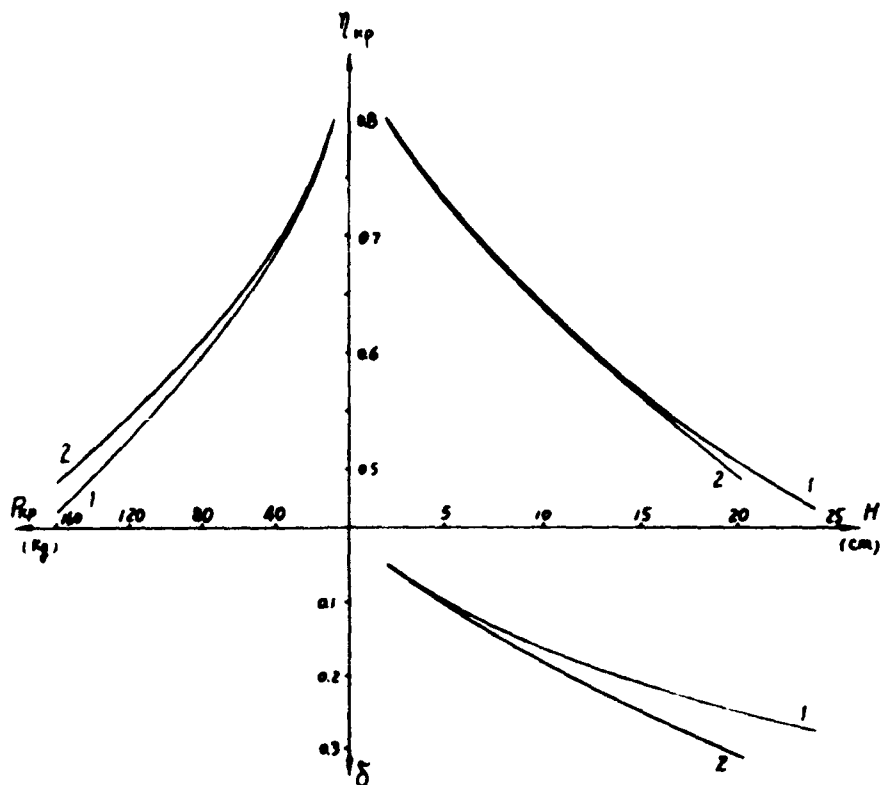


Fig. 4 curves of maximum tractive efficiency
 Curve 1. maximum tractive efficiency vs. corresponding drawbar pull, slip at a given sinkage
 Curve 2. maximum tractive efficiency vs. corresponding sinkage, slip at a given drawbar pull

3. Experiment and conclusions

A wheel was manufactured with the design principle in Fig. 1-2. The wheel was tested on the specific device shown in Fig. 5.

The device is able to 1. adjust and fix the sinkage of the tested wheel, 2. control the slip, 3. test the axle-torque of the tested wheel, 4. test the drawbar pull, 5. test the ideal force of the soil against the tested wheel.

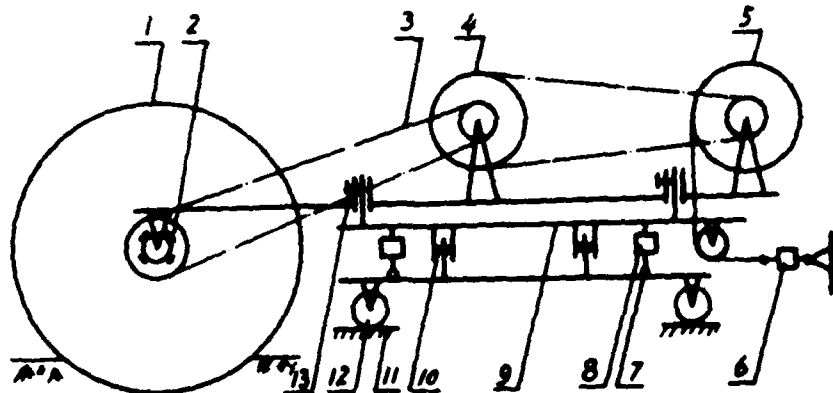


Fig. 5 test set
 1. tested wheel 2. full electric bridge for measuring the torque of the axle 3. chain 4. gear box output 5. winch for controlling slip 6. pull-compression sensor for measuring Draw-bar forces (not including resistance of the test set) 7. roller 8. pull-compression sensor for measuring the vertical reaction of the soil 9. upper chassis of the test set 10. sliding joint for transmitting horizontal forces 11. rail 12. small wheel of the test set 13. set for adjusting the sinkage of the tested wheel

The practised tractive efficiency of the tested wheel can be tested and calculated by

$$\eta_{\text{up}} = \frac{R_{\text{tr}} V}{M_{\text{tr}} \omega_{\text{tr}}} = \frac{R_{\text{tr}} \dot{\phi}}{(M_{\text{tr}} - M_{\text{tr}0}) \dot{\phi}} \cdot \frac{M_{\text{tr}} - M_{\text{tr}0}}{M_{\text{tr}}} \quad (10)$$

$$= \frac{R_{\text{tr}} L}{(M_{\text{tr}} - M_{\text{tr}0}) \theta} \cdot \eta_{\text{tr}}$$

The result of the experiment is shown in Fig. 6 and Fig. 7. The tested curves of a wheel with hyperboloid lugs are included in these figures. From which we can see:

- 1) The theoretical curves of the drawbar pull and the tractive efficiency of the wheel with movable lugs which penetrate and leave the soil perpendicularly are higher than the other tested curves and they have some "advance" simultaneously. This is because of the result by simplifying the formula of plasticity.

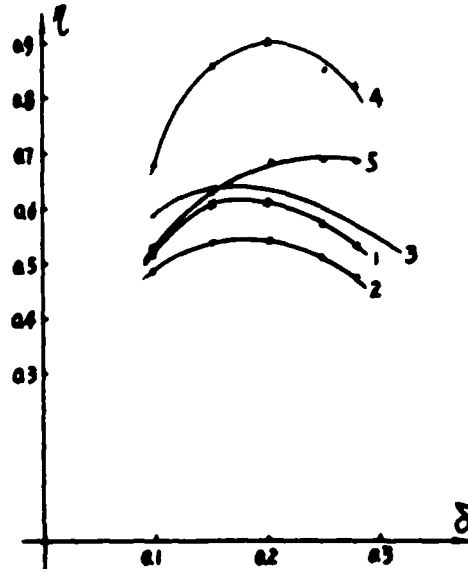


Fig.6 curves of efficiency vs. slip

1. experimental tractive efficiency of the rigid wheel with movable lugs
2. experimental tractive efficiency of the rigid wheel with hyperboloidal lugs
3. theoretical efficiency curve of the rigid wheel with movable lugs
4. experimental rolling efficiency curve of the rigid wheel with movable lugs
5. experimental rolling efficiency curve of the rigid wheel with hyperboloidal lugs

1) The rolling and tractive efficiencies of the wheel with the movable lugs are higher than that of the wheel with hyperboloidal lugs. This is obvious when the slip is 12-18%. Without the internal friction its tractive efficiency would be higher in 14-18%. Hence, it is important to decrease the internal friction of this wheel.

2) The curves (1) (4) show that the external rolling efficiency of the former is higher than that of the latter in 16-18%, which is the essential reason that the former tractive efficiency is higher.

3) With the same slip, the drawbar pull of the wheel with movable lugs is greater.

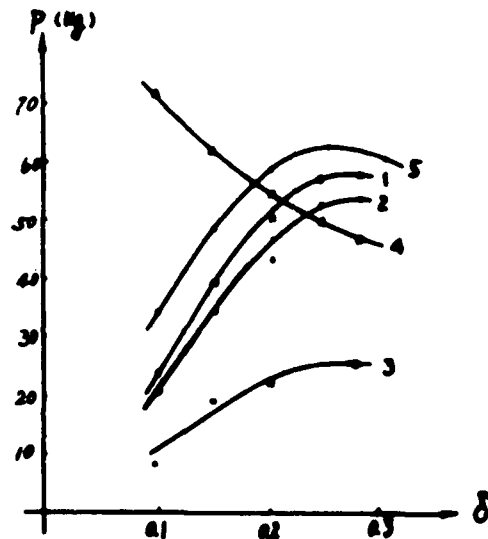


Fig.7 curves of force VS slip

1. experimental curve of drawbar pull of rigid wheel with movable lugs
2. experimental curve of drawbar pull of rigid wheel with hyperboloidal lugs
3. experimental curve of the vertical compressive force to the soil by the rigid wheel with movable lugs
4. experimental curve of the vertical compressive force to the soil by the rigid wheel with hyperboloidal lugs
5. curve of theoretical drawbar pull of the rigid wheel with movable lugs

5) The compactive force of the wheel with movable lugs to the soil is much smaller than that of the wheel with hyperboloidal lugs. The wheel has a higher external rolling and tractive efficiency just due to the small compact loss of the soil.

The End

This paper studies some problems about the large rolling resistance of the driving wheel of the paddy field floating tractor. According to the point of view that the rolling resistance comes mainly from the compaction of soil by lugs, the paper analyses the kinematics and the dynamics of the wheel with the movable lugs. Some experiment has been made.

10. The conclusions are:

1) The lugs, set at an angle and leaving soil perpendiculary can increase greatly the correction to the soil.

2) The external rolling and tractive efficiencies of the wheel with movable lugs are higher than that of the wheel with hyperboloidal lugs.

3) To a given requirement of the drawbar pull an optimal depth of the sinkage can be sought by the electric computer. With this depth, the wheel has the optimal tractive efficiency.

It should be pointed out that due to the movable lugs the structure of the wheel is more complicated. And some internal friction losses generated by the movable lugs.



AN INVESTIGATION OF THE DRIVING WHEEL THRUST OF PADDY FIELD TRACTORS

Deng Zhuorong ; Youg Shucheng

The Chinese Society of Agricultural Machinery , Beijing , China
 The Tractor Research Institute of China , Luoyan , Henan , China

ABSTRACT

In this paper, the producing process of the driving wheel thrust of paddy field tractor is analyzed through experiments made in a soil bin. In essence, it is a process in which the wheel lugs are moved against the soil so that the soil in the neighbourhood of contact surface is compressed and sheared. The methods for predicting the driving wheel thrust and the lug motion trajectory of paddy field tractor are proposed. The predicted values of the thrust are compared with those obtained through experiments. It shows that the predicted thrust agrees fairly satisfactorily with the measured results.

INTRODUCTION

One of the main problems of paddy tractor is that the driving wheel must be suitable to the condition of paddy field. Although a lot of tractors have been used in paddy field, their traction efficiency have not been satisfactory. The power loss of the driving wheels accounts for nearly 66% of the total loss. Thus, it is seen that the traction efficiency should be improved and more suitable types and parameters of the tractor wheels in design need to be provided. For this reason, a thorough study of the interaction between the paddy soil and driving wheel of paddy field tractor should be made in order to understand the producing process of thrust and rolling resistance.

This paper attempts to analyse the producing process of the driving wheel thrust of paddy tractor through observation in the soil bin and to propose accurate methods based on this analysis for calculating it in design.

THE PROPERTY OF PADDY SOIL

The property of paddy soil is different from the dry field soil as a result of planting rice for many years. Since the soil property is closely related to wheel performance, the relevant parts of mechanical property of paddy soil are roughly described as follow:

The agrotechnique of rice requires a large amount of water to be kept in the field for a long time. This causes the paddy field to have a deeper and soft soil layer. Depending on the groundwater level, the time of planting rice and the kind of soil, two cases of the soil generally existed beneath the soft soil layer. One case is that the

AD-P004 284

soil forms a hardened layer and the other does not. The strength of soft soil layer is very weak but the adhesion is great. These soil conditions and the particular requirements of cultivation in paddy field make it difficult to design high efficiency driving wheels.

The pressure-sinkage relationships of paddy soil are varied. But when plowing field, the pressure-sinkage curve is generally displayed as Fig.1.

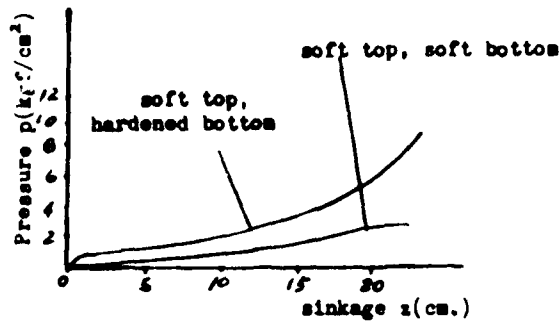


Fig. 1 Pressure-sinkage curves of a plate for a paddy soil

According to the measured data of paddy soil in the field and using the effective portion of the pressure-sinkage curves, the relationship of these two parameters could be described by the following equation based on the requirement of simple and practical application[1].

$$p = k_1 + k_2 z^2 \quad (1)$$

where p-plate pressure, (kgf/cm²)
 z-plate sinkage, (cm)
 k₁-coefficient of soil sinkage, (kgf/cm²)
 k₂-coefficient of soil sinkage, (cm⁻¹)

Due to the effect of soil consolidation, the water content and density of paddy soil are different in respective layers. It causes the cohesion, internal friction angle, adhesion etc. to be varied with soil depth. The curves of cohesion and internal friction angle vs soil depth are shown in Fig.2.

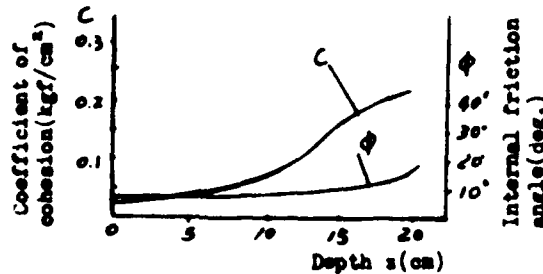


Fig.2 Coefficient of cohesion and internal friction angle vs soil depth

However, the coefficient of cohesion has a close relationship with the pressure-sinkage relation. It could be described by the following equation:

$$c = \alpha p + u \quad (2)$$

where c -coefficient of soil cohesion, (kgf/cm^2)
 α -proportion constant
 u -coefficient of soil cohesion in the surface layer, (kgf/cm^2)

OBSERVATION AND ANALYSIS OF THE BEHAVIORS OF DRIVING WHEEL IN PADDY SOIL

Since the thrust of a driving wheel of paddy tractor is mainly produced by the interaction between the soil and wheel lugs, the study of the producing process of a wheel thrust would be the study of the producing process of the lug thrust. Therefore the behavior of driving wheel lugs in soil was observed firstly.

1. OBSERVATION EQUIPMENT AND METHOD

The equipment is composed of a soil bin, a carriage and power unit. On the carriage is mounted a slip control mechanism for the driving wheel moving at a definite slippage. Some ballasts were used as the vertical load applied on the driving wheel. In one side of the soil bin there is a glass window.

The soil in the soil bin was picked from a nature paddy field whose particle size distribution is shown in Table 1.

Table 1. The soil partical distribution in the soil bin

Soil particle dia. (mm)	Distribution(%)	
	Cultivation layer	Bottom layer
> 0.05	5	5
0.01 ~ 0.05	37	44
0.005 ~ 0.01	12	11
0.001 ~ 0.005	26	21
< 0.001	20	19

The soil was laid and compacted in the soil bin layer upon layer just like real paddy field, and then water was poured into the soil bin. On the side surface of the soil against the glass window, white lattices and points were drawn.

The dimensions of the wheel used in the test are shown in Table 2. When the driving wheel moves against the glass window with a certain slippage, the lug motion and soil displacement were photographed.

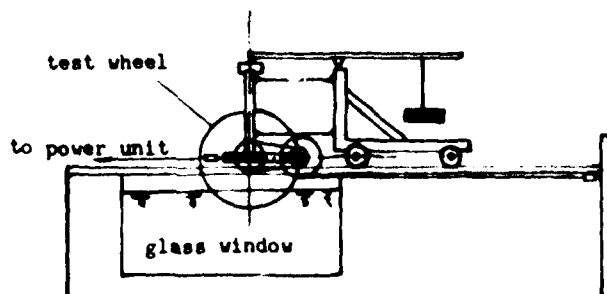


Fig. 3 Sketch of the test device

Table 2. The dimensions of the test wheel

Wheel diameter	75 (cm)	Lug driving side angle	25(deg)
Wheel width	10((cm)	Lug front side angle	10(deg)
Lug length	10 (cm)	Lug angle	90(deg)
Lug height	7.25 (cm)	Number of lugs	9
Lug top face width	2 (cm)		

2. RESULTS OF OBSERVATION AND ANALYSIS

In Fig. 4-6. is shown either a single lug or several lugs of wheel moving in paddy soil, the soil in the neighbourhood of lugs has a regular movement. The interaction between the driving wheel lug and the paddy soil is similar to that of a retaining wall. The wheel lugs are applied upon by passive pressure. But the problem is the changes of the soil slip region due to the effect of lug location and tractive force. When the lug enters into action and applies a force to the soil, the soil particles in the neighbourhood of lug are moved against each other in which local compression and shear will occur. With the force increasing the movement of soil particles is increased and then proceed to develop a continuous slip face in the direction of low resistance. When the lug force is higher than the soil bearing capacity, the soil will be failed and lugs sink again. In other words, the rotation of the wheel causes the vertical load of lugs entering into the soil to be increased and they move downwards again until reaching the equilibrium, although the traction force is very small. But at any lug location, the soil had been reached the state of plastic equilibrium which causes the slip face to be produced. It can be seen during the test.

However, the lug lying over the instantaneous rotation center moves downwards and forwards so that the soil under the driving side of lugs is compressed downwards and forms two slip regions. This is similar to the state in which the plate is applied a force at a certain angle. With the rotation of wheel, lugs lying below the instantaneous center move downwards and backwards. The soil under the driving side of lug is compressed downwards and is sheared backwards. Only one slip face exists. This is shown in Fig. 7.



Fig. 4 Movement of the paddy soil particles under the action of a single lug with slippage 25%

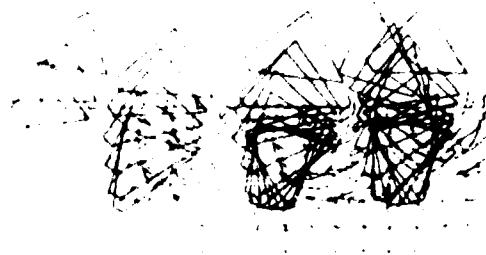


Fig. 5 Movement of the paddy soil particles under the action of driving wheel lugs with slippage 25%

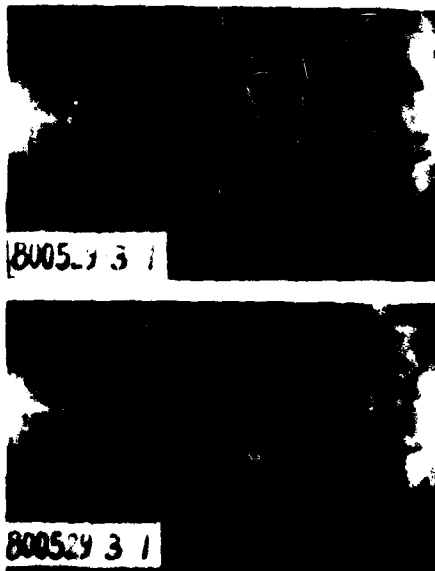


Fig. 6 Photographs of the driving wheel lug moved in paddy soil with slippage 25%

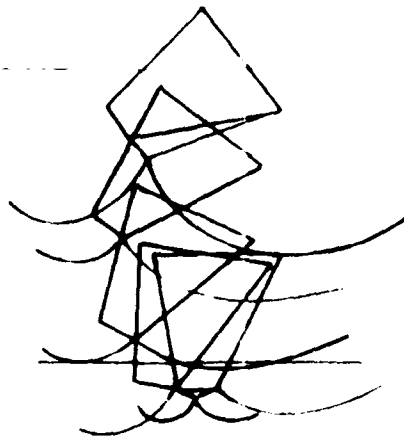


Fig. 7 Slip faces of the paddy soil under the action of driving wheel in various positions.

From observation, the shape of slip face which is developed in the paddy soil under the action of each lug is curving and approximates to a logarithmic spiral. But when the lug top face moves at the bottom of cultivation layer, the slip face is developed along the top of bottom layer. It is noteworthy that as the lug is moving in soil, the soil beside both lug lateral sides will also produce slip faces. But their curvatures are more gentle.

From above analysis, it could be seen that the thrust producing process of a paddy tractor driving wheel is a process in which the wheel lugs are moving against the soil so that the soil in the neighbourhood of contact surface is compressed and sheared. Therefore, the thrust of a driving wheel will depend on the shear characteristic of paddy soil.

THRUST CALCULATION

Empirical equations may be used to calculate the thrust. It is simple and convenient in calculation so that it should be developed continuously. However, using the principle of soil pressure to derive the models, we will be able to integrate the calculation of thrust and rolling resistance and widen the limitation of application and analyse the interaction between the driving wheel and soil. Although the principle of soil pressure used to calculate the thrust is very complex, it is still considered as a feasible method connected with the particularity of paddy soil because the digital computer has widely been used recently.

The evaluation of soil passive pressure by the logarithmic spiral method has been studied by many researchers.[2] [3][4][5][6][7]. This method assumes the slip face to be composed of a logarithmic spiral and a plane section. It approximates to the shape of slip face of the paddy soil applied by lugs, but in a given soil its pole location is different due to the lug moving. In respect to the driving side of lug, when it moves below the instantaneous rotation center the assumption of the logarithmic spiral pole locates on the radius of lug top face approximates fairly to the real situation according to our experiments as Fig.8. Thus, this assumption could be used in calculating the lug force.

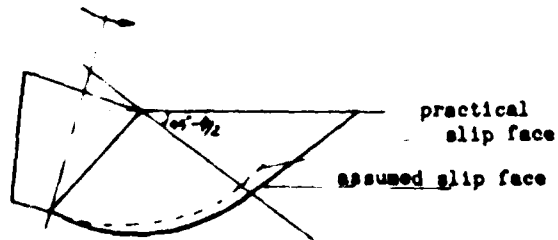


Fig. 8 The practical and assumed slip face of paddy soil.

It must be pointed out that the soil characteristics will be a main factor when calculating. In our tests it is found that the deviation of calculated value, neglecting the variations of soil parameters, is larger than that of the slip face shape assumed in calculation which deviates from the real shape slightly. Therefore, to evaluate accurately the thrust of paddy field driving wheel using the logarithmic spiral method, we must consider the variation of soil parameters.

From the above reason, lugs location must be decided first in calculating their forces. It is worth noticing that the motion trajectory of wheel lugs may be a cycloid or not. It will depend on the soil characteristics and construction. In respect of a driving wheel of paddy tractor with high lugs and wide pitch, its instantaneous rotation center lies on the lowest lug first. When front lugs are moving at the depth where the vertical soil reaction forces α equalize the wheel load, the instantaneous rotation center moves onto the front adjacent lug. But this lug also sinks since the wheel rotation causes its vertical load to be increased. Thus, the moving trajectory of lugs is neither a cycloid nor a circle. Since the strength of paddy soil differs in different layer, the sinkage of the front adjacent lug onto which the instantaneous rotation center begin to move is different. It is shown that the moving trajectory of lugs is correlated with the soil characteristics.

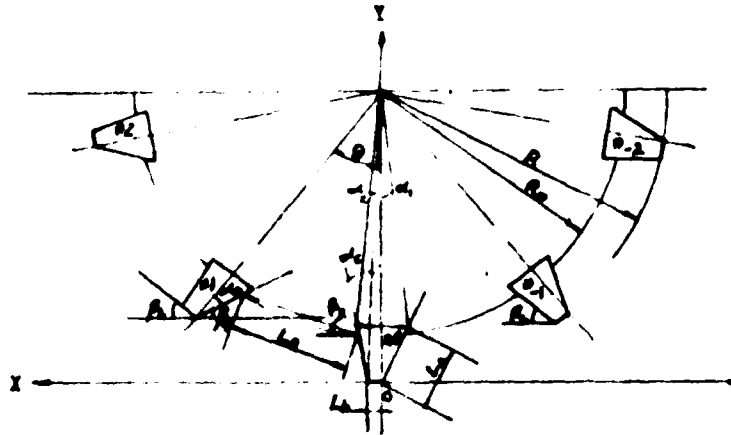


Fig. 9 Schematic diagram of test wheel

Assuming that the location of lowest lug lies on the origin of coordinate, Fig. 9, the moving trajectory of lugs may be expressed as follows:

$$\begin{aligned} X &= X_0 + r \sin(i\theta - \psi - \theta') \\ Y &= Y_0 - r \cos(i\theta - \psi - \theta') \end{aligned} \quad (3)$$

where

$$\begin{aligned} X_0 &= 0.0175 R \psi (1 - \delta) \\ Y_0 &= R \cos[(N-1)\theta - \psi] \end{aligned} \quad (4)$$

when $(N-1)\theta \leq \psi \leq (N-1)\theta + \psi_0$

and

$$\begin{aligned} X_0 &= 0.0175 R \psi (1 - \delta) \\ Y_0 &= Z_0 - Z_{\psi, i} + R \cos(N\theta - \psi) \end{aligned} \quad (5)$$

when $(N-1)\theta + \psi_0 \leq \psi \leq N\theta$

- ψ -- Rotation angle of wheel (deg)
 δ -- Average slippage based on the outside diameter of wheel
 θ -- Center angle between two adjacent lugs (deg)
 r -- Radius of a point on wheel lug (cm)
 X_0, Y_0 -- Wheel center location in the coordinate (cm)
 R -- Wheel outside radius (cm)
 θ' -- Angle between the radiuses of a point and the lug top face (deg)
 i -- Ordinal number of lugs as shown in Fig. 9
 N -- Ordinal number of wheel rotation period, i.e.
 $-2\theta \leq \psi \leq -\theta, N=-1$;
 $-\theta \leq \psi \leq 0, N=0$;
 $0 \leq \psi \leq \theta, N=1$;
 and so forth.
 Z_0 -- Max. wheel sinkage (cm)
 $Z_{\psi, i}$ -- Sinkage of the i th lug at the rotation angle ψ (cm)
 ψ_0 -- Wheel rotation angle when the front adjacent lugs move to the location where the sum of the vertical components of soil reaction forces applied on θ lug sides equals zero. It may be calculated approximately by the following equation;

$$B \left\{ L [mk_1 (e^{k_2(Z_0-d_0)} + 1) + 2u] [\sin(\alpha_a - \psi_0) - \tan \gamma \cos(\alpha_a - \psi_0)] (1 - e^{-j_0/K}) - l_a C_a \cos(\alpha_a - \psi_0) \right\} \sin \omega = 0 \quad (6)$$

where

- B -- Lug length (cm)
 γ -- Friction angle of the paddy soil and the lug side (deg)
 C_a -- Soil adhesion (kgf/cm²)
 ω -- Lug angle (deg)
 l_a -- The contact height of a lug side and soil (cm)
 L -- Length of shearing face, may be taken $L = 2R(1-\delta)\sin(\theta/2)$ (cm)
 K -- Slip coefficient of shear-displacement curves (cm)
 j_0 -- Lug slip displacement, may be taken

$$j_0 = R \left\{ \sin \left[\theta - \tan^{-1} \frac{(1-\delta) - \cos \theta}{\sin \theta} \right] + \sin \psi_0 - 0.0175(1-\delta) \left[\psi_0 + \theta - \tan^{-1} \frac{(1-\delta) - \cos \theta}{\sin \theta} \right] \right\} (\text{cm})$$

$\tan^{-1} \frac{(1-\delta)\cos\theta}{\sin\theta}$ -- Wheel rotation angle when #1 lug moves to the location where its slip displacement equals zero. (deg)

$d_0 = 0.5B \sin(2 \sin^{-1} \frac{R(\rho\omega - \psi_0)}{2R} \cos\omega)$ -- Height of the #1 lug top face middle point, when $\varphi = \psi_0$ (cm)

When the number of lug, radius of rim and lug angle increase, ψ_0 would have a tendency towards zero and the motion trajectory of lug would have a tendency towards a cycloid.

Z_0 and Z_{ψ_0} could be calculated by the method based on the equilibrium of the wheel load G and the vertical component of soil forces P_v , i.e.

$$G = \sum P_{v,i}$$

It should be pointed out that the lug location in soil are different. Some lugs are over the instantaneous rotation center of wheel and some lugs below it. In the former case, the lug driving side applies the vertical load to the soil and the lug top face applies both vertical load and horizontal force to the soil. But in the latter case, they are reverse.

According to the observation, it may be found that the soil slip face is developed backwards and downwards since the lug driving side applies vertical load to the soil. However, if horizontal force is applied to soil additionally, the location of slip face would be higher than former, as Fig.10.

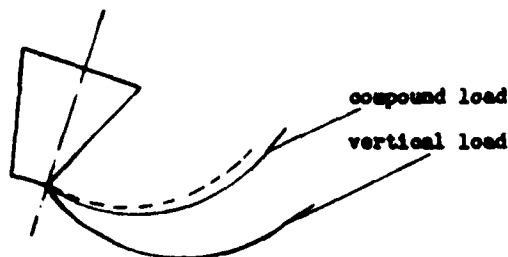


Fig. 10 Slip faces of the paddy soil under the action of driving wheel.

This causes the soil bearing capacity to be reduced even though in the same depth and leads to the lug sinking again until the vertical component of soil passive pressure can equal the load on the lug driving side. This is the main factor causing the wheel slip sinkage. For this reason, its effect should be considered in calculating lug force, i.e. when lugs are below the instantaneous rotation center of wheel, the soil passive pressure should be used to calculate their driving side force and the pressure-sinkage relationship might be used to calculate the force of their top face. Otherwise, they should be reversed.

It will be seen that the thrust P_q of the paddy tractor driving wheels is the sum of effective horizontal components of forces applied on the lugs inside the soil.

$$P_q = \sum P_{q,i}$$

The average thrust of paddy driving wheel approximates the thrust when one lug locates at the place, where it is in front of the lowest position about $\theta/8$ wheel rotation angle. Calculating the average thrust, the following equation might be used.

Since $\sum_{i=1}^n (\varphi - 7\theta/8) \approx Z_0$,

$$\begin{aligned} P_{q,av.} = & \sum_{i=0}^n \left\{ [n(k_1 e^{k_2(Z_0-S-d)} + 1) + 2u] \left[B L_1 \sin \beta_a \sin \omega + 0.5 A_n \cos(45^\circ - \varphi/2) \right] \right. \\ & (1 - e^{-j/K}) \left. + \sum_{i=1}^n 2b L_R k_1 e^{k_2(Z_0-T)} \left(1 - \frac{k_2 L_R}{2l} \sin \beta_R \right) \right. \\ & + \frac{(k_2 L_R \sin \beta_R)^2}{3l} (1 - e^{-j/K}) \cos \beta_R \tan \phi \sin \beta_a \\ & + \sum_{i=1}^n B L_b k_1 e^{k_2(Z_0-S-d)} \left(1 - \frac{k_2 L_b \sin \beta_b}{2l} + \frac{(k_2 L_b \sin \beta_b)^2}{3l} \right) \\ & \left. \tan \gamma \cos \beta_b \sin \omega + \sum_{i=1}^n B C_n L_b \cos \beta_b \sin \omega \right\} \quad (7) \end{aligned}$$

where

$$\begin{aligned} \beta_a & \text{--- Rake angle of the lug driving side,} \\ & \quad -90 - [(1-7/8)\theta + \alpha_a] \quad (\text{deg}) \\ \beta_b & \text{--- Rake angle of the lug top face,} \\ & \quad -(1-7/8)\theta \quad (\text{deg}) \\ \beta_R & \text{--- Rake angle of the rim chord between adjacent lugs,} \\ & \quad -(1-11\theta/8) + \alpha_2/2 \quad (\text{deg}) \\ S & = R \{ \cos(\theta/8) - \cos[(1-7/8)\theta] \} \quad (\text{cm}) \\ T & = R \cos(\theta/8) - R_0 \cos(1\theta - \alpha_1) \quad (\text{cm}) \\ d & = 0.5 B \sin[(1-7/8)\theta + 2 \sin^{-1}(\frac{R \cos \omega}{2R})] \cos \omega \quad (\text{cm}) \\ A_n & = 0.5 n' l L_1 \sin \beta_a \quad (\text{cm}^2) \\ L_R & = R_0 [\sin(\theta/2 - \alpha_1) + \sin(\theta/2 - \alpha_2)] \quad (\text{cm}) \\ L_b & \text{--- Width of the lug top face} \quad (\text{cm}) \\ R_0 & \text{--- Rim radius} \quad (\text{cm}) \\ n' & \text{--- Number of the lateral shearing faces of each lug, may be} \\ & \quad \text{taken the value of 2 (for single lugs wheel) or 1.5 (for} \\ & \quad \text{dual lugs wheel)} \\ n & \text{--- The ordinal number of front lugs} \\ j & = R \left\{ \sin \left[\theta - \tan^{-1} \frac{(1-\delta) - \cos \theta}{\sin \theta} \right] - \sin(1\theta - \varphi) \right. \\ & \quad \left. - 0.0175(1-\delta) \left[\varphi - (1-1)\theta - \tan^{-1} \frac{(1-\delta) - \cos \theta}{\sin \theta} \right] \right\}, \quad (\varphi = 7\theta/8) \end{aligned}$$

$$L_{1 \sim n} = l$$

$$L_{1 \sim n} = L - j, \quad (\varphi = 0)$$

EXPERIMENTS

For the verification of above analysis, experiments had been carried out in a soil bin. The test wheel is the same as that used in observation, however, on the lugs are mounted sensors. The information of sensors are stored in a tape recorder and calculated with digital computer.

The test soil is the same as that used in observation too. The soil parameters are shown in Table 3. The wheel load is 135 kgf.

The results of experiment and calculated value are shown in Fig-11. It is found that the calculated values of thrust agrees fairly satisfactorily with the measured results.

Table 3. Soil parameters

Water content	Surface	36.8	37.2	%
	Cultivation layer	32.9	34.8	%
	Bottom layer	22.9	26.8	%
Coefficient of soil sinkage, k_1		0.3837 (kgf/cm ²)		
Coefficient of soil sinkage, k_2		0.1351 (cm ⁻¹)		
Proportion constant of soil cohesion, m		0.0963		
Soil cohesion in the surface layer, u		0.075 (kgf/cm ²)		
Soil adhesion, $C_{a,av}$		0.09 (kgf/cm ²)		
Slip coefficient of shear-displacement curve, K_{av}		0.4 (cm)		
Friction angle of paddy soil-lug side, γ_{av}		8 (deg)		
Wet density, ρ_{av}		2.23 (g/cm ³)		
Internal friction angle of soil, ϕ_{av}		17 (deg)		

CONCLUSIONS

1. The producing process of the driving wheel thrust of paddy tractor is a process in which the wheel lugs are moved against the soil so that the soil in the neighbourhood of contact surface is compressed and sheared. For a given paddy driving wheel, the thrust depends on the shear characteristics of soil.
2. The paddy field soil is nonhomogeneous, the water content, cohesion, adhesion, internal friction angle, wet density and friction angle of interface are different in respective soil layers.
3. The motion trajectory of paddy wheel lugs may be a cycloid or not. It depends on the soil characteristics, wheel structure and parameters.
4. The main factor of slip sinkage of paddy driving wheel is the soil slip face moves upwards which causes the soil bearing capacity to be

reduced.

5. When designing the driving wheel of paddy field tractor, the calculation method derived by authors may be used to obtain a better predicating wheel thrust.

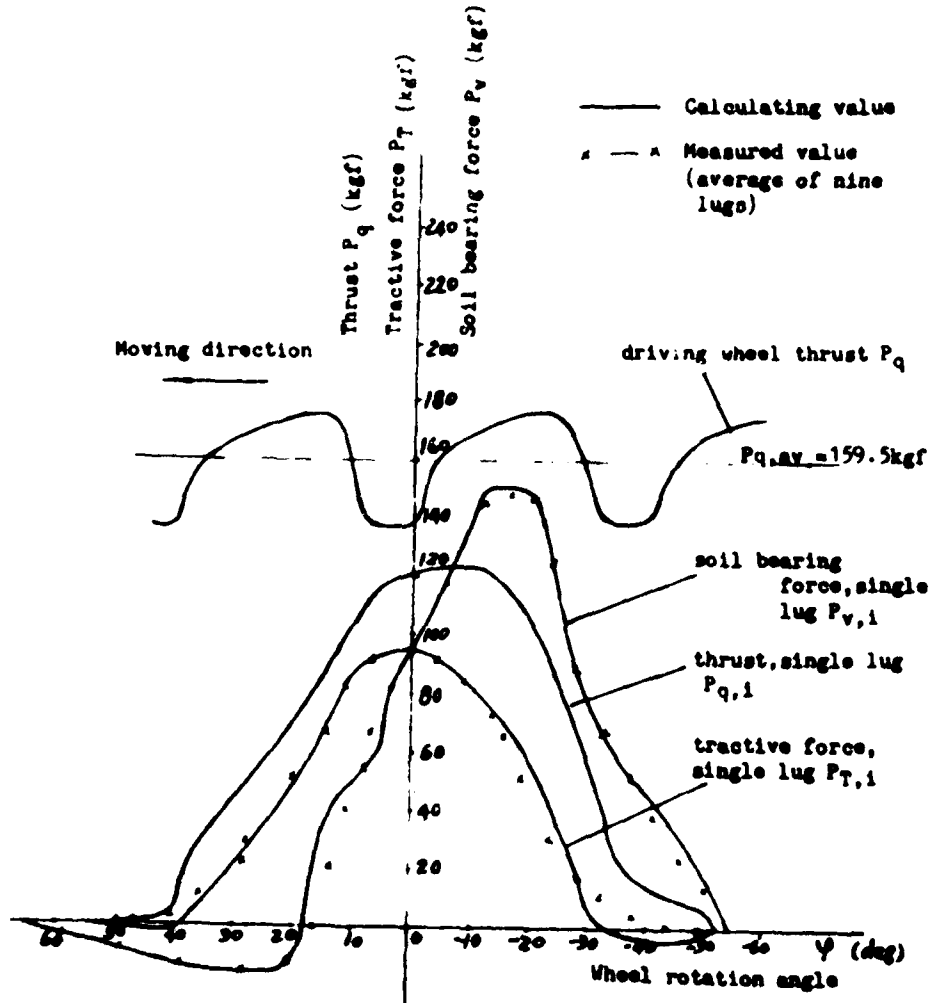


Fig. 11 Comparison of the calculating value of thrust, tractive force, soil bearing force and those of measured values

REFERENCES

- (1) 中国拖拉机试验研究(第一集) 中国农机部拖拉机和汽车 1960
- (2) C. Terraghi. "Theoretical Soil Mechanics", John Wiley and Sons, New York, N.Y. 1944.
- (3) M.G. Bekker. "Off-the-Road Locomotion", The Univ. of Michigan Press, 1960.
- (4) M.G. Bekker. "Introduction to Terrain-Vehicle Systems", The Univ. of Michigan Press, 1969.
- (5) D.R.P. Hettiaratchi, B.D. Witney, A.R. Reece, "The calculation of Passive Pressure in Two-Dimensional Soil Failure", J. Agric. Engng. Res. 1966, 11(2).
- (6) 地基极限承载力设计法 郑大同编 1974
- (7) 通用土壤力学 郑大同编 1953



MOBILITY OF THE SMALL COMBINE (TRACK TYPE) ON SOFT GROUND
-RELATIONSHIP BETWEEN THE POSITION OF THE CENTER OF GRAVITY
AND THE MOBILITY-

Haruo ESAKI
Institute of Agr.Eng., UNIVERSITY OF TSUKUBA, JAPAN

ABSTRACT

In East Asia, approximately one million small-sized rice combines have been used on paddy fields. The objective of this study is to carry out fundamental investigations on the mobility of small combines associated with changes in the position of the center of gravity. The relationship between the position of the center of gravity and the performance of the combine in straight and circular drive was analysed.

INTRODUCTION

There are approximately three million and five hundred thousand combines in the world. Two million and five hundred thousand combines of the general type have been used on upland fields in the USA, Europe, USSR and other countries. One million small rice combines with cutter bar of less than 1.5m in width have been used in East Asia, especially in Japan (Fig.1). More than eighty percent of small combines (app. 0.8 million) are two-row rice combines with a cutter bar approximately 0.7m long. The grain tank or grain platform which can carry several bags of grain is located on the right side of these combines.

These small combines (Japanese type combine, J.T.combine) are primarily used to harvest rice in paddy fields on soft ground. Therefore these machines are equipped with crawlers and are designed so that the mean ground contact pressure is as low as possible. The mean ground contact pressure of the J.T.combine ranges from 15kPa to 25kPa (0.15- 0.25kgf/cm²). To decrease the contact pressure, the ground contact area should be widened,

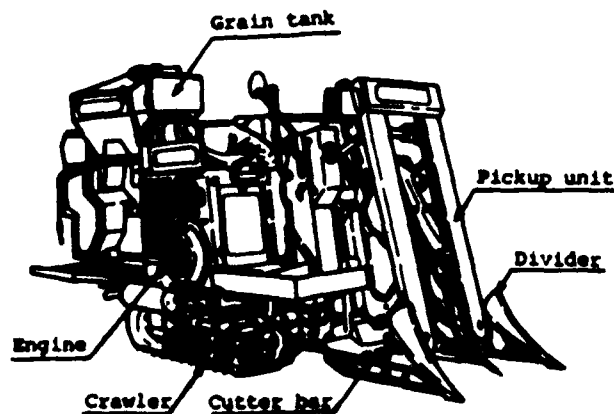


Fig.1 Japanese type combine.

AD-P004 285

but the outer area of the two crawlers should be narrower than the cutter bar length. As a result the crawlers are comparatively longer. The ratio of the length L (cm) to the width W (cm) of a crawler ranges from 3.2 to 3.5.

The weight of the J.T.combine G (kg) ranges between 400kg and 3000kg. Since the weight of the combine increases with the length of the cutter bar W (cm),

$$G = 2W - 550 \quad (1)$$

The mean weight of the two-row combine is 850kg.

The position of the static center of gravity of the J.T.combine is comparatively high with values of G_z (cm) ranging from $0.55L$ to $0.9L$, when the ground contact length of the crawler L (cm) is taken into account. This position of the static center of gravity is much higher than that of other track laying vehicles, such as bulldozers for which values of G_z ranging between $0.2L$ and $0.3L$ are recorded.

In this report, the center line of the ground contact length of the crawler is referred to as the X-X axis, the center line of the two crawlers is the Y-Y axis, the point of intersection of the two lines is the origin of the coordinate axis, and the vertical axis from the point of intersection is the Z-Z axis.

The center of gravity is usually located in front of the X-X axis with values of G_y (cm) ranging from $-0.05L$ to $0.25L$, and on the left side of the Y-Y axis with values of G_x (cm) ranging from $-0.1B$ to $0.08B$, where B (cm) is the distance between the center line of the two crawlers (Fig.2). The two-row rice J.T.combine is comparatively light, weighing 500~1200kg, and it is able to run on paddy fields with soft ground. Since the grain tank located on the right side of the vehicle is able to carry 100 to 300kg of paddy, thus the position of the dynamic center of gravity shows a much wider range of variation than the static center of gravity.

OBJECTIVE

The purpose of this study is to evaluate the mobility of the small combine (J.T.combine) on paddy fields with soft ground depending on the changes of the position of the center of gravity. In this report the performance of the vehicle will be analysed in straight and circular drive.

TRACK-LAYING VEHICLES USED IN THIS STUDY

The following three vehicles were used in the experiments.

- 1) Reconstructed vehicle based on the design of the Japanese type combine, and where the position of the center of gravity can be easily changed by adjusting the weight on the main frame.
- 2) Model I scaled down to $0.44L$ and $0.27W$ from the ground contact length L and width W of the original combine, respectively.
- 3) Model II scaled down to $(0.26\sim0.43)L$ and $(0.30\sim0.41)W$ from those of the original combines (Table 1).

Table 1. Main specifications of tested track of vehicles.

Combine and Models		Two-row combine	Model I	Model II
Cutterbar width	m	0.75	-	-
Weight	kg	640	33	22
Width of track, W	m	0.27	0.073	0.08-0.11
Length of track, L	m	0.81	0.36	0.21-0.35
Ground contact pressure	kPa	15	9	5
Pitch of lug, P	mm	75	18	24
Distance between the center of the crawlers, B	cm	72	30	24

ROAD BED

The first vehicle was tested on a hard surface (concrete road bed) as a standard road, as well as on upland fields and paddy fields where the field conditions are controlled by the plowing depth, number of packerrings and moisture content. Model vehicles were tested in a soilbin filled uniformly with soil, which was tilled and hardened for every test.

The shearing stress τ , coefficient of cohesion C, angle of friction ϕ and soil hardness (kPa), moisture content, liquid limit and plastic limit of soil were determined (Table 2).

Table 2. Characteristics of road bed

Year of test	1979		1980		1981		1982		1983		1984	
	Tested vehicles		Combine	Model I	Model I	Combine	Combine	Combine	Model I	Combine	Combine	Combine
Moisture ratio	Wb	87	47	45	101	73	88	-	73	47	-	-
Coefficient of cohesion, C	kPa	19	42	17	14	4	20	42	4	5	-	-
Angle of friction, ϕ deg		35	26	38	44	35	35	26	15	25	-	-
Shearing stress	kPa	29	49	-	27	18	29	45	18	12	-	-
Liquid limit	Wb	76	82	87	99	76	95	82	76	-	-	-
Plastic limit	Wb	71	62	69	74	73	76	62	73	-	-	-
Soil hardness	kPa	340-	30	-	100-	940-	270-	-	10-	120-	-	-
		390			255	990	430		190	360		

P.F.: Paddy field, S.B.: Soil Bin, U.F.: Upland field

THE CENTER OF GRAVITY OF THE VEHICLES

The determination of the C.G. ratio (ξ_x , ξ_y and ξ_z) which is defined in the next equations enables to compare the position of the center of gravity of the various vehicles and the values obtained are based on the calculation of the ground contact length L and width W of the crawler.

$$\xi_x = \frac{G_x}{B} \times 100 (\%), \quad \xi_y = \frac{G_y}{L} \times 100 (\%), \quad \xi_z = \frac{G_z}{L} \times 100 (\%) \quad (2)$$

where ξ_x ranges from -25% to 25%, ξ_y ranges from -30% to 30% and ξ_z ranges from 55% to 90% (Table 3, Fig. 2).

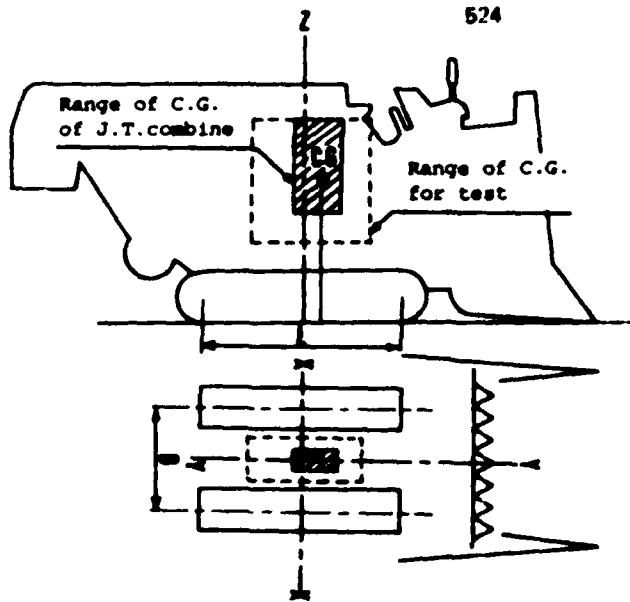


Fig.2 The position of the center of gravity.

Table 3. Center of gravity of tested vehicles

C.G. RATIO TEST VEHICLE	$\xi_x = G_x/B \times 100\%$	$\xi_y = G_y/L \times 100\%$	$\xi_z = G_z/L \times 100\%$
J.T. combine	-10-0	-1-22	55-90
Combine (1979)	$\pm 2.5 \pm 5 \pm 21$ 827	-3 -4 13 22 28	69
Model I (1980)	0 ± 22 ± 44	0 ± 28	42 53 67
Model II (1981)	0 ± 12.5	0 ± 10 ± 21	89
Combine (1981)	± 1 ± 12.5	0 ± 11 ± 13 ± 28 ± 29	55
Combine (1982)	0 ± 10 ± 20	0 ± 12.5 ± 25	68
Model II (1982)	0	0	56 60 83
Combine (1982)	0 ± 13 ± 23	0 ± 11 .29	55
Combine (1983)	0 ± 10 ± 20	0 ± 12.5 ± 25	59

VEHICLE PERFORMANCE IN STRAIGHT DRIVE

When the combine is unable to move in a straight line, the operator must steer several times the vehicle to cut the crops in rows, even if the machine is equipped with automatic control units. Such operation is associated with considerable mental and physical stress.

The relationship between the C.G. ratio and the performance of the vehicle in straight drive was analysed. When the tested vehicle runs without requiring any steering over a certain distance, sometimes there is a left or right turn with a radius R (m) depending on the position of the C.G. and the conditions of the road bed (Fig.3). The value of the curve radius

ratio ρ is defined in the next equation, based on the distance between the center lines of the two crawlers B (cm). When the tested vehicle runs in a straight line, the value of ρ is 0 and when the absolute value of ρ is larger than 0, straight drive performance is not satisfactory.

$$\rho = \frac{B}{R} \times 100 (\%) \quad (3)$$

Forward slippage of the crawler was observed in straight run and the cause of this phenomenon, as well as the relationship between the slippage and the position of the C.G. or the value of ρ is discussed in the following section.

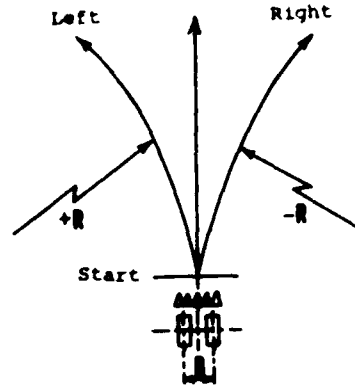


Fig.3 Radius of curve in straight drive.

Curve of vehicle in relation to the position of C.G.

When the center of gravity is situated on the Y-Y axis, the vehicle runs straight, even on paddy fields or on a hard road bed. This also applies when the C.G. is situated in front or in rear of X-X axis.

When the absolute value of ξ_x exceeds 10%, implying that the C.G. is situated on the right or left hand side of the Y-Y axis, straight drive performance is impaired.

For instance, when the vehicle runs on a hard road, concrete road or hard upland fields, where the soil hardness is 980kPa (10kgf/cm²), and the value of ξ_x of the vehicle is above 10%, the value of ξ_y ranges from -15% to 15%, and the vehicle tends to make a curve to the left, although the C.G. is on the right hand side of the vehicle. When the value of ξ_y is above 20%, namely implying that the C.G. is situated forward remarkably, the vehicle tends to make a curve to the right, toward the side where the crawler is overloaded.

When the vehicle runs on soft paddy fields, where the soil hardness ranges from 100kPa to 300kPa (1-3kgf/cm²), the vehicle tends to make a curve toward the side where the crawler is overloaded, although the C.G. is situated forward or backward (Fig.4).

Forward slippage and straight drive

The crawler of the J.T. combine consists of an endless rubber track with inner steel plates and steel wires. The rubber track bends due to the pressure from the track wheels. At the level of the first track wheel, the rubber track bends along the arc of circle drawn by the track wheel, and then the head of the

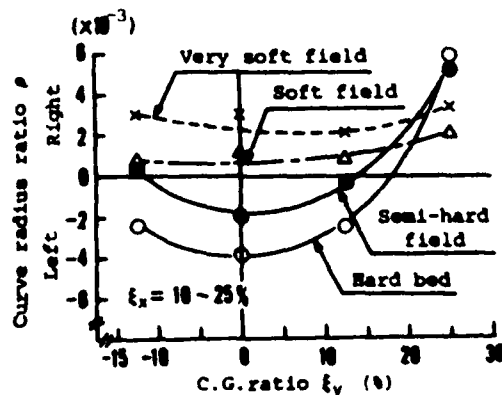


Fig.4 Relation between C.G. ratio ξ_y and curve radius ratio ρ (straight drive).

lugs of the track is widened and comes in contact with the road bed over a wider distance $P + \Delta P$ (cm) than the pitch of the lug P (cm), and the distance between the other lugs under the track wheel may become wider due to the pressure of the track wheel (Fig.5).

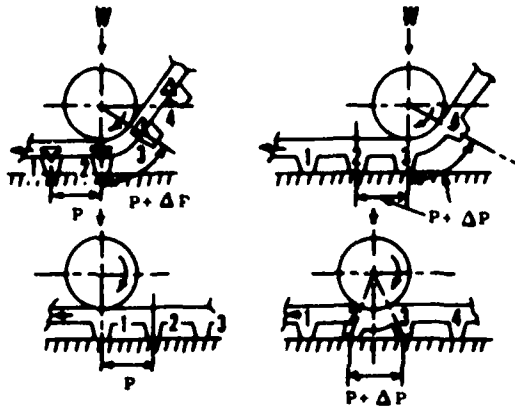


Fig.5 Forward slippage.

When the vehicle runs on a hard surface, deformation of surface due to the lugs is minimum, and the increase in the distance between the lugs may lead to forward slippage. However when the vehicle runs on a soft field, the traction of the track exerts a pressure on the soil, and backward slippage may occur, and the distance between the lugs may decrease. Backward slippage has not been observed in the straight drive test even on paddy fields with soft ground. The distance of forward slippage on a hard surface was longer than that of slippage on soft ground. The value of the slippage ratio ν_f (%) is defined in the next equation,

$$\nu_f = \frac{+ \Sigma \Delta P}{\Sigma P} \times 100 \quad (4)$$

where ΣP (cm) is the theoretical running distance and $\Sigma P \pm \Delta P$ (m) is the distance actually measured.

When the position of the center of gravity moves forward and backward, the slippage ratio shows minor variations on fields with soft ground such as paddy fields, but when the C.G. is situated far from the X-X axis, the value of ν_f become larger on a hard surface (Fig.6).

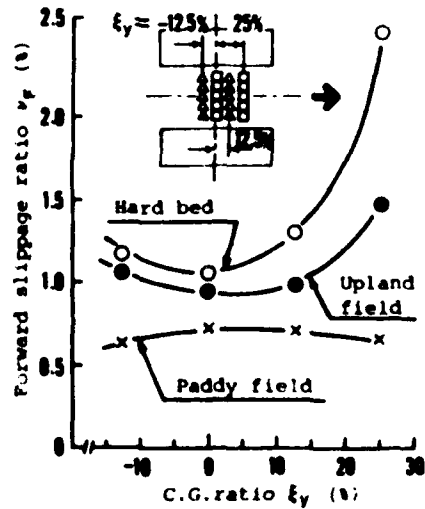


Fig.6 Forward slippage ratio in relation to ξ_y .

When the position of the C.G. shifts to the left and right, there are few variations in v_f on soft ground, but when the weight of the load on the right crawler is reduced, the slippage of the right crawler increases (Fig.7).

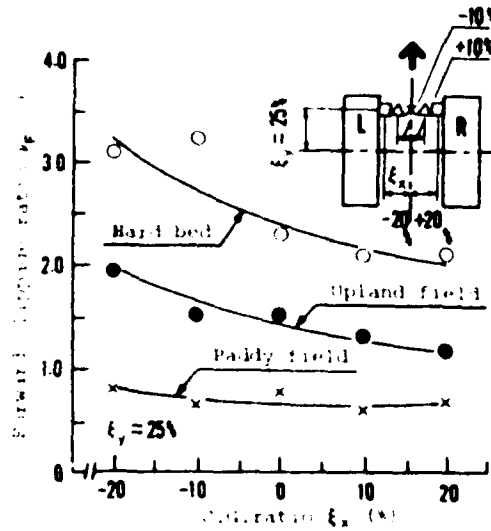


Fig.7 Forward slippage ratio of right (R) track in relation to ξ_x .

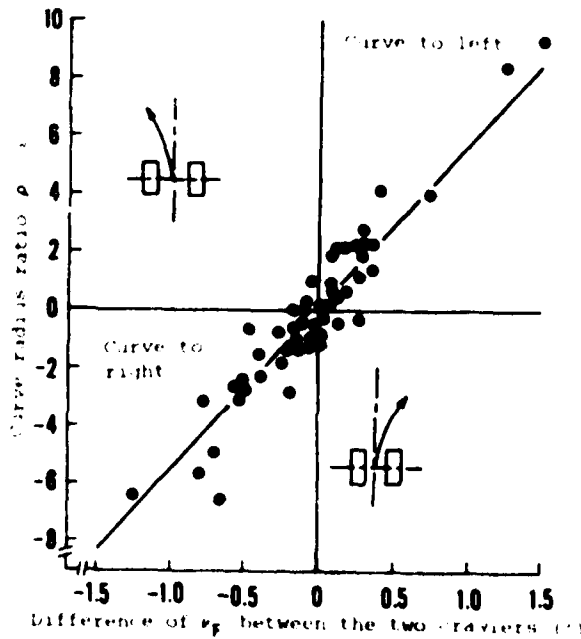


Fig.8 Curve radius ratio ρ in relation to the difference of v_f between the two crawlers (v_f of right crawler - v_f of left crawler).

Due to differences in the value of v_f between the right and left crawlers, the vehicle makes a left or right curve. When the value of v_f of the right crawler is larger than that of the left crawler, the vehicle turns to the left (Fig.8).

The forward slippage of the crawler is affected by the performance of the vehicle on the road bed including the shearing stress τ kPa (kgf/cm²) which may be determined by the next equation.

$$\tau = C + \delta \tan \phi \quad (5)$$

where C is the coefficient of cohesion of soil kPa (kgf/cm²), ϕ is the angle of friction of soil and δ is the ground contact pressure of the vehicle, the average value being 15kPa (0.15kgf/cm²). The smaller the value of τ , the larger the forward slippage when the performance on soil is compared (Fig.9).

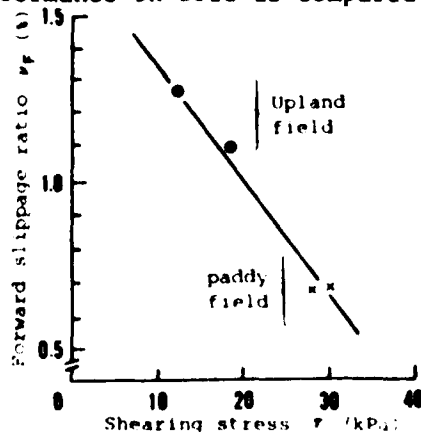


Fig.9 Relationship between mean forward slippage ratio v_f and shearing stress τ of soil.

Power requirement in straight drive

The power requirement of the tested vehicle (J.T.combine: weight, 640kg) varies depending on the coefficient of running resistance μ of the crawler. For example the value of μ was

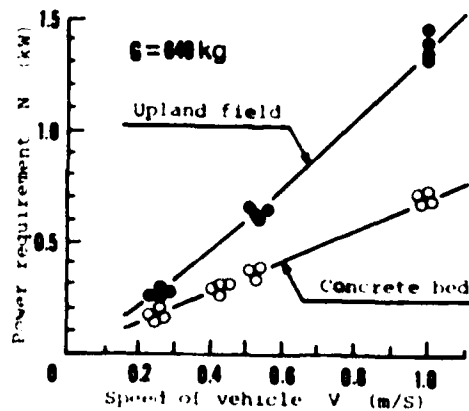


Fig.10 Power requirement of J.T.combine in straight drive.

equal to 0.11×10^4 on a hard road bed, while μ was equal to 0.21×10^4 on upland fields. This value can be calculated by the following equation (Fig.10).

$$N = \mu \cdot g \cdot G \cdot V \quad (6)$$

where N (kW) is the power requirement of the crawlers, g is equal to 9.8 m/s , G (kg) is the weight of the vehicles and V (m/s) is the speed in straight drive.

The power requirement on a concrete road N_1 (kW) and on upland fields N_2 (kW) is shown in the equation.

$$N_1 = 0.69V, \quad N_2 = 1.32V \quad (7)$$

The power requirement of the right crawler increases, while that of the left crawler decreases, when the position of the C.G. shifts to the right (Fig.11).

When the position of the C.G. shifts forward or backward, the power requirement increases slightly more than when the C.G. is located at the origin of the coordinate axis (Fig.12).

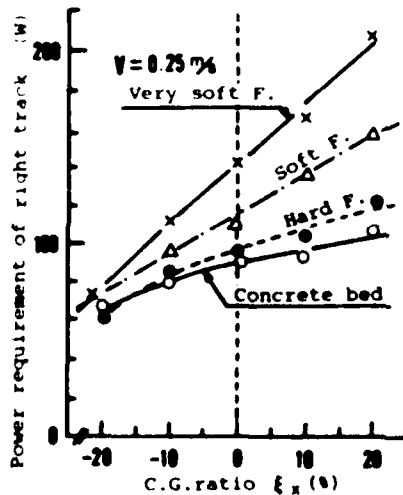


Fig.11 Power requirement of right track in relation to the changes in the position of the center of gravity.

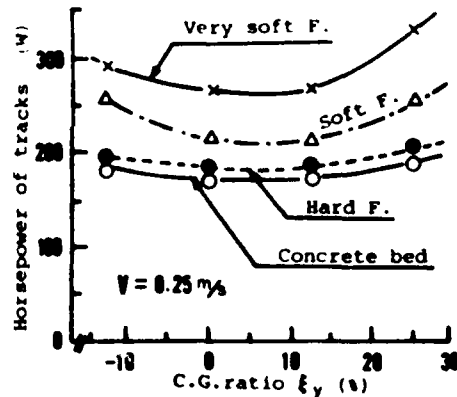


Fig.12 Horsepower of crawlers in straight drive in relation to the position of the center of gravity.

VEHICLE PERFORMANCE IN CIRCULAR DRIVE

Small combines must turn frequently to harvest rice in small-sized paddy fields as those in Japan. For example the two-row Japanese type combine turns approximately seventy times to harvest rice on paddy fields, 0.1 ha ($50 \text{ m} \times 20 \text{ m}$) in size, which tend to prevail in Japan. Since the Japanese type combine has to turn in the corner of paddy fields with the smallest turning radius, one of the crawlers is completely braked in the circular drive.

The effect of the position of the center of gravity on the turning radius, slippage of track and the power requirement in circular drive was analysed in this report.

The position of the center of turning C.T. (T_x, T_y) on the X-Y plane indicates the value of the turning radius of the vehicle.

The value of the C.T. ratio (γ_x, γ_y) is defined in the following equations to compare it with the C.G. ratio (Fig.13).

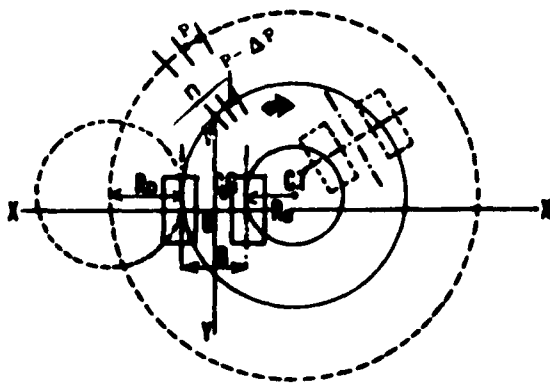


Fig.13 Circular drive of vehicle.

Relation between the position of the C.G. and C.T.

The ideal position of the center of turning is that corresponding to the center of the braked track when the vehicle turns with one of the crawlers being braked completely.

Actually the position of the center of turning corresponds to the distance from the center of the braked track depending on the position of the C.G. and the condition of the fields (Fig.14).

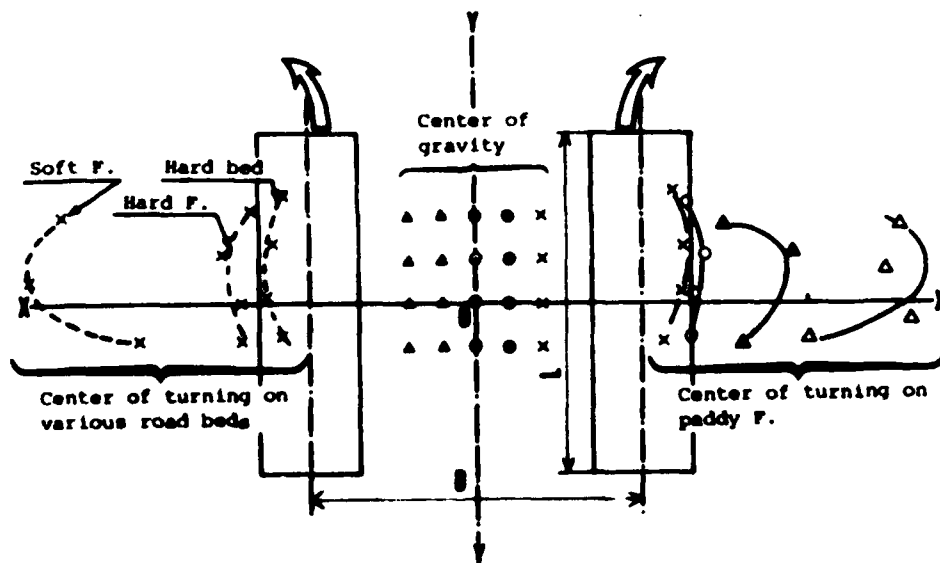


Fig.14 Relationship between the position of the center of gravity and the center of turning.

Shift of the center of the gravity in front or behind the X-X axis (Relation between ξ_y and η_y)

When the center of gravity is situated in front or behind the X-X axis, the center of turning is also situated in front or behind the X-X axis respectively, regardless of the conditions of the road bed. The relationship between the value of ξ_y and η_y is shown in the next equation (Fig. 15).

$$\eta_y = \xi_y + 2.5 \quad (8)$$

When the center of gravity shifts forward and backward, the center of turning shifts to the right or the left, along with shifting forward or backward. The value of η_x increases when the value of soil hardness decreases.

The value of η_x is maximum when that of ξ_y ranges from 0 to 10%. When the center of gravity is situated near the center of the crawlers, the center of turning may be at a distance from the Y-Y axis. But when the center of gravity is distant from the X-X axis, the center of turning comes close to the Y-Y axis (Fig. 16).

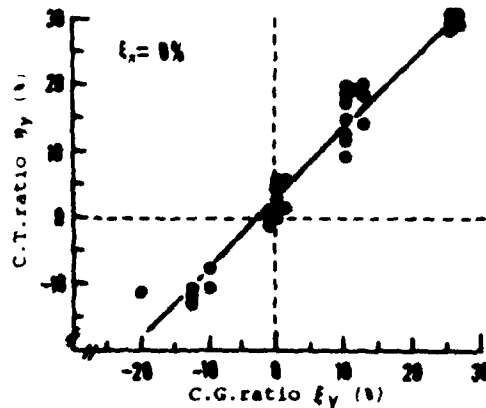


Fig. 15 Center of turning ratio η_y in relation to the center of gravity ratio ξ_y .

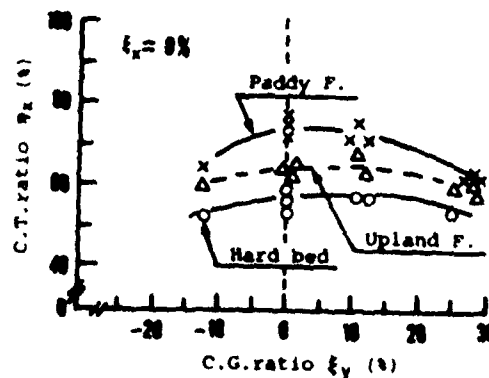


Fig. 16 Center of turning ratio η_x in relation to the center of gravity ratio ξ_y .

Lateral displacement of the center of gravity to the right or left (Relation between ξ_x and η)

When the center of gravity moves horizontally, the position of the center of turning changes considerably depending on the conditions of the soil or road bed. The center of turning becomes distant from the Y-Y axis, when the vehicle runs on soft ground, where slippage is likely to occur. The value of η_x becomes larger in proportion to the shift of the center of gravity from the center of the braked crawler, particularly when the vehicle runs on paddy fields (Fig.17). The value of η_y is not appreciably large, ranging from -10% to 10%, and the values of ξ_x and η_y may change independently (Fig.18).

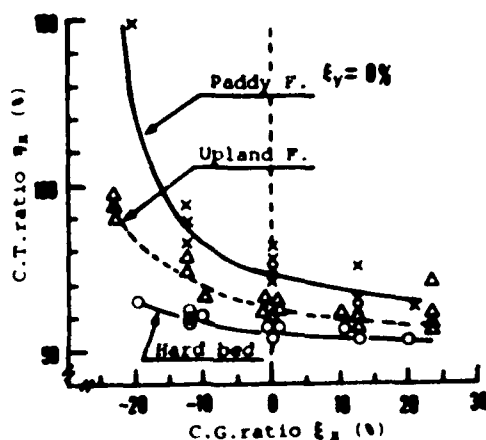


Fig.17 Center of turning ratio η_x in relation to the center of gravity ratio ξ_x .

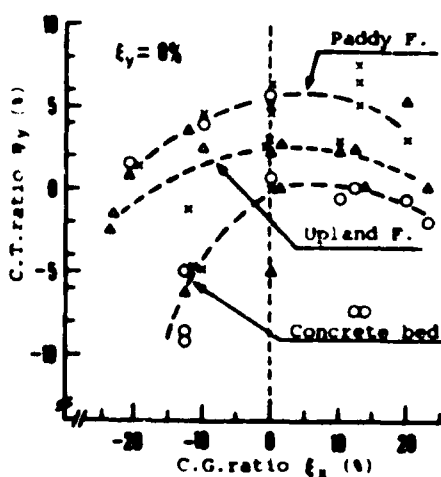


Fig.18 Center of turning ratio η_y in relation to the center of gravity ratio ξ_x .

The slippage of the track

The changes in the position of the center of turning were analysed to develop a method to enable to evaluate the mobility or the turning performance of the track, and relationships between the changes of the position of the center of gravity and of the center of turning could be demonstrated. However the turning performance of a vehicle does not depend solely upon the position of the center of turning.

As shown in Fig.13, both the driving crawler and the braked crawler are describing circles when slipping on the soil.

The turning radius R_b (m) of the braked crawler is defined by the length of a perpendicular line joining the center of turning to the center line of the braked crawler, and the turning radius R_D (m) of the driving crawler may be expressed as $R_b + B$ (m). The number of lug-marks (n) of the driving crawler in one circle multiplied by the pitch of the lug P (m) is the theoretical turning circle of the driving crawler as defined in the equation.

$$n \cdot P = 2\pi(R_b + B) + S_D \quad (9)$$

where S_D (m) is the amount of slippage of the driving crawler in a circle.

The amount of slippage of the braked crawler S_b (m) and of the driving crawler S_D (m) in a circle may be determined and expressed in the next equations:

$$S_b = 2\pi R_b, \quad S_D = 2\pi R_D \quad (10)$$

where R_D (m) is the assumed slippage radius of the driving crawler.

The slippage ratio of the driving crawler ν_D and of the braked crawler ν_b may be defined in the next equations:

$$\nu_D = \frac{S_D}{n \cdot P} = \frac{2\pi R_D}{n \cdot P} \quad (11)$$

$$\nu_b = \frac{S_b}{n \cdot P} = \frac{2\pi R_b}{n \cdot P}$$

Relation between the position of the center of gravity and the slippage of the crawler

Slippage increases with the softness of the field ground or road bed. The slippage of the crawler is particularly significant, when the center of gravity shows a lateral displacement to the right or left from the center line of the two crawlers, hence the slippage of the unloaded crawler is larger than that of the loaded crawler. For example, the value of the slippage ratio of the braked crawler ν_b is equal to 10% and ν_D is 25% for a C.G. ratio ξ_x

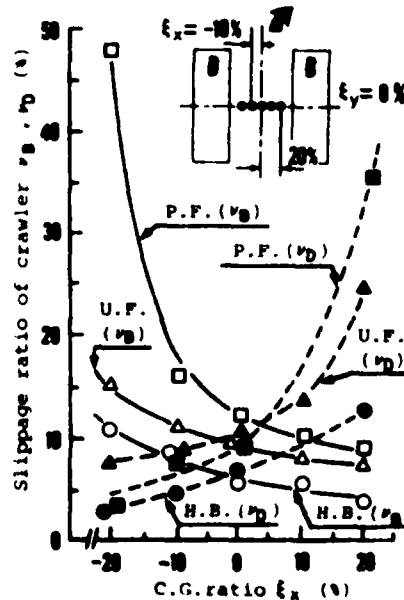


Fig.19 Slippage ratio of crawlers in circular drive.
P.F.: paddy field, U.F.: upland field
and H.B.: concrete bed, B: braked crawler
and D: driving crawler.

of 15%. When the center of gravity shifts to the opposite side and $\xi_x = -15\%$, the value of the slippage ratio of the braked crawler becomes as large as $\nu_0 = 50\%$, in spite of the negligible amount of slippage of the driving crawler and ν_0 is approximately equal to 5% when the vehicle runs on paddy fields (Fig.19).

Forward and backward shifts of the center of gravity do not affect appreciably the value of the slippage ratio (Fig.20).

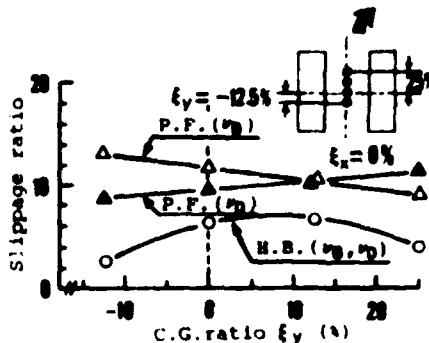


Fig.20 Slippage ratio of crawlers in circular drive.

Power requirement in circular drive

The shaft torque is measured by placing a strain gauge on the final drive shaft of the track. The driving torque was measured in the driving crawler shaft, and the resistance of the track was measured in the braked crawler shaft.

The conditions of the road bed affected appreciably the power requirement in general, although there were few differences between paddy fields (soil hardness: 0.25MPa) and upland fields (soil hardness: 1.1MPa) in the tests of the J.T.combine.

The power requirement increased with the increase in the weight of the load of the driving crawler (Fig.21). The maximum values of the turning torque were recorded when the center of gravity was located near the center of the X-X axis, that is to say, when ξ_x ranged between 0 and 10% (Fig.22).

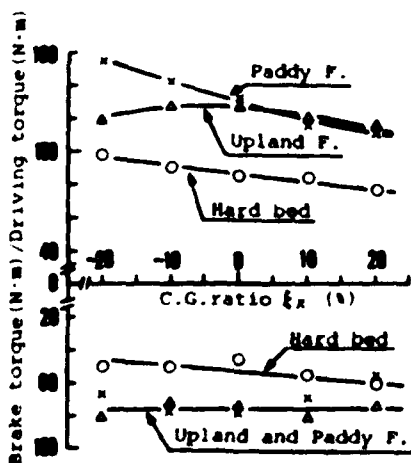


Fig.21 Driving torque in relation to the center of gravity ratio ξ_x .

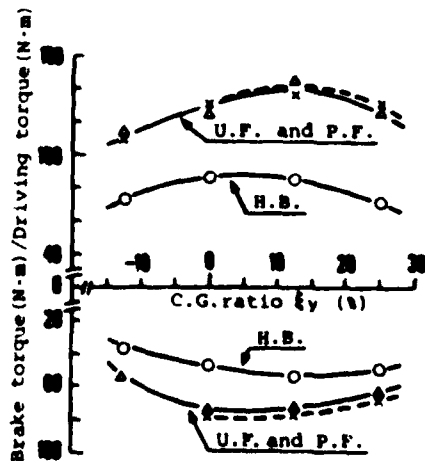


Fig.22 Driving torque in relation to the center of gravity ratio ξ_y .

Track slippage and tractive power

The values of the driving torque of the track are closely related to the slippage of the track. The vehicle can make a circular drive with low driving power on a hard road bed, where slippage of the track is negligible. But on a soft and slippery ground such as that of paddy fields, the vehicle is often unable to turn smoothly, due to the lack of adequate turning torque associated with the slippage. When the vehicle turns to the right, the left crawler is the driving crawler, and in this case, if the center of gravity shifts to the right, the slippage is considerable. As a result the value of the driving torque does not increase, and the vehicle can not turn properly (Fig.23).

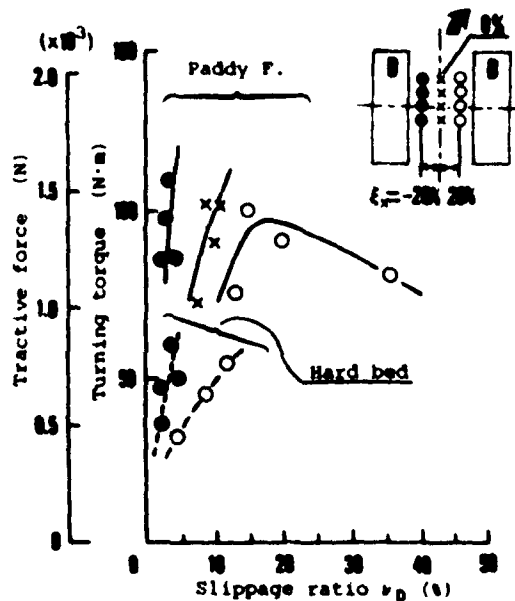


Fig.23 Relationship between the slippage ratio of the driving track and the turning torque, and tractive force.

CONCLUSION

The position of the center of gravity of the track-laying small combine shows a wide range of variation when the vehicle runs on paddy fields for harvesting rice. Therefore the relationship between the position of the center of gravity and the mobility of the track was analysed and the following results were obtained:

Shift of the center of gravity to the right or left:

1. When the center of gravity is situated on the Y-Y axis, the vehicle may run in a straight line.

2. When the absolute value of ξ_x exceeds 10%, straight drive performance becomes difficult and the vehicle tends to make a curve to the side where the crawler is overloaded on paddy fields. On a hard surface, the vehicle makes a curve to the side where the crawler is unloaded, when the value of ξ_y ranges from -15% to 15%, and the vehicle makes a curve to the left when the value of ξ_y exceeds 20%.
3. Forward slippage of the track was observed in straight drive, when the center of gravity shifted to the left and right. The difference in slippage between the two crawlers, was responsible for the lateral displacement of the vehicle in straight drive.
4. When the center of gravity is located on the right side, the power requirement of the right crawler may increase, while that of the left crawler decreases.
5. The position of the center of turning becomes distant from the Y-Y axis, when the center of gravity becomes distant from the braked crawler.
6. The amount of slippage of the unloaded crawler is larger than that of the loaded crawler.
7. The power required for turning increases with the weight of the load on the driving crawler.
8. When the center of gravity is situated near the braked crawler, slippage of the vehicle is likely to occur and the vehicle may not be able to turn properly.

Shift of the center of gravity forward or backward:

1. Forward slippage of the track of the vehicle occurs on a hard surface, when the center of gravity shifts forward.
2. In straight drive, when the center of gravity is situated forward or backward, horsepower of the vehicle is a little larger than when the center of gravity is situated in the center of the track.
3. The center of turning may shift forward or backward along with the position of the center of gravity.
4. The center of turning may shift toward the Y-Y axis when the center of gravity moves forward and backward. The distance of the center of turning from the Y-Y axis is maximum, when the center of gravity is situated on the X-X axis.
5. There is little difference in the backward slippage between the two crawlers even if the center of gravity shifts forward or backward.
6. Maximum values of the turning torque are observed when the center of gravity is situated slightly in front of the X-X axis.

NOMENCLATURE

- A = Ground contact area of track, cm^2
 B = Distance between the center line of the two crawlers, cm
 C = Coefficient of cohesion, kPa
 G = Weight of tested vehicle, kg
 G_x = Distance between the center of gravity and the Y-Y axis, cm
 G_y = Distance between the center of gravity and the X-X axis, cm
 G_z = Position of the center of gravity, cm
 L = Ground contact length of track, cm
 N = Horsepower, kW

n = Number of track lugs in one circle,
 P = Pitch of lugs, cm
 ΔP = Slippage of lug-pitch, cm
 R = Radius of curve in straight drive, m
 R_B = Turning radius of braked crawler, m
 R_0 = Assumed slippage radius of driving crawler, m
 S_B = Length of slip of braked crawler in one circle, m
 S_0 = Length of slip of driving crawler in one circle, m
 T_x = Distance between the center of turning and the Y-Y axis, cm
 T_y = Distance between the center of turning and the X-X axis, cm
 V = Speed of vehicle, m/s
 W = Width of track, cm
 δ = Ground bearing contact pressure, kPa
 η_x, η_y = Center of turning ratio, %
 μ = Coefficient of running resistance,
 ν_B = Slippage ratio of braked crawler, %
 ν_0 = Slippage ratio of driving crawler, %
 ν_F = Forward slippage ratio, %
 ξ_x, ξ_y, ξ_z = Center of gravity ratio, %
 ρ = Curve radius ratio, %
 τ = Shearing stress, kPa
 ϕ = Angle of friction, °



THE STRESS-STRAIN-TIME GRAPH OF RHEOLOGICAL SOILS AND
ITS APPLICATION

PAN JUN-ZHENG*

CHINESE SOCIETY OF AGRICULTURAL MACHINERY, BEIJING, CHINA

The Burgers model (Fig.1) and its modified form have generally been considered as the rheological model of clayey soils since 1950's through tests and analyses (1-11). The corresponding rheological equation is

$$\gamma = \tau \left[\frac{1}{G_0} + \frac{1}{G} (1 - e^{-\tau/T}) + \frac{t}{\eta} \right]$$

where γ - strain

τ - stress

G_0, G - moduli of elasticity

η, η_0 - coefficients of viscosity

T - retardation time of Voigt body, $T = \eta/G$

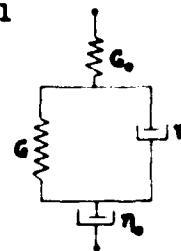


Fig. 1

Six samples of paddy soils from four provinces in South China have been collected and tested. The Burgers model is accepted as the general model of these clayey soils. By means of orthogonal tests and variance analyses, it is found that the effect of soil conditions (mechanical composition, water content, bulk density) on rheological parameters $G_0, G, \eta,$ and η_0 is particularly significant, while that of load conditions (load value, shape and size of bearing surface) is not significant (8-11). The rheological parameters, therefore, are constants for the same soil conditions. Based on the recorded rheological curves (Fig. 2) of the soil and the calculated values of rheological parameters, sufficient data are obtained for predicting the sinkage of vehicles or the resistance against soil-cutting elements and improving their performance.

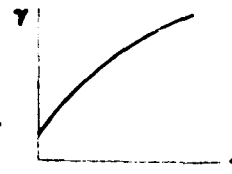


Fig. 2

According to the above statement, the stress-strain-time graph (Fig. 3) of the rheological soil characterized by the clayey paddy soils in South China with definite soil conditions will be established as follows:

When the stress is constant, the rheological curve of the soil mentioned above is shown as in Fig. 2.

When the stress is kept within a certain limit, such as from τ_1 to τ_2 , a rheological surface (Fig. 3) is generated

*Professor, Department of Agricultural Mechanization, Jiangsu Institute of Technology, Zhenjiang, Jiangsu, People's Republic of China.

AD-P004 286

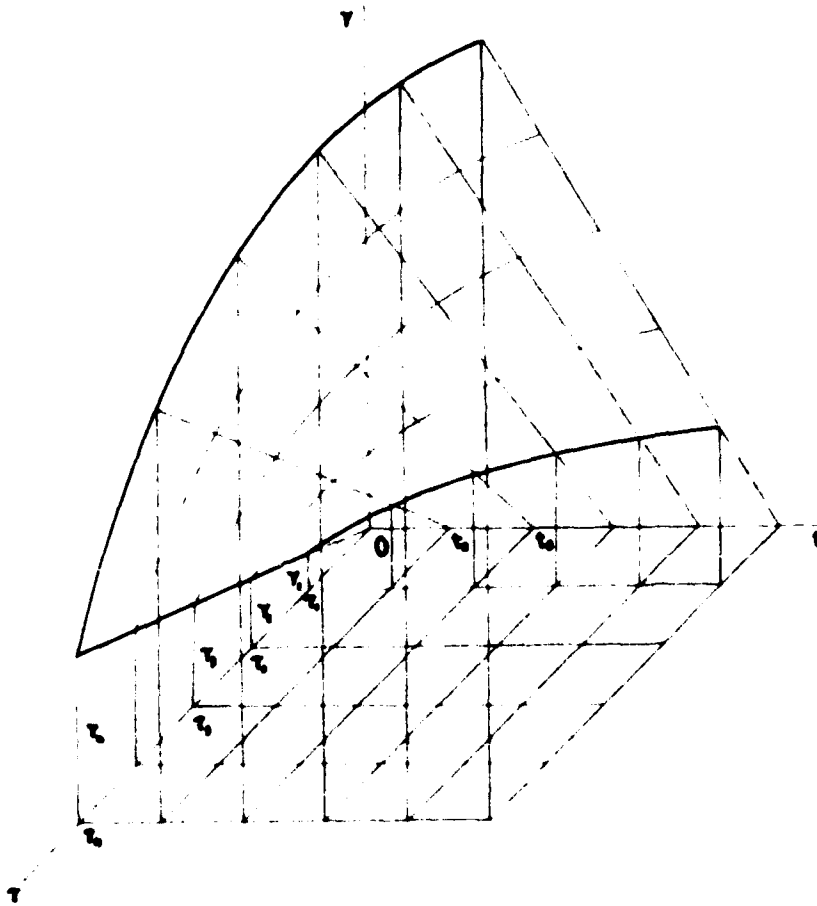


Fig. 3

by the rheological curves in a three-dimensional stress-strain-time space. All the stress-strain-time relations that may happen can be defined on this surface.

Thus, the author proposes that this graph be named the stress-strain-time graph of the rheological soils.

Fig.3 shows:

(1) When the time t is constant and is equal to $t_1, t_2, t_3, \dots, t_n$ successively, the projections of the lines of intersection of the rheological surface with the corresponding planes parallel to the coordinate plane $\gamma-\tau$ on this plane form a family of radiating straight lines with the origin at O (Fig.4). These straight lines are suggested to be named as iso-time lines. At the same instant t_j , the $\gamma-\tau$ relationship is linear. The larger is the value of t_j ($j=1,2,3,\dots,n$), the greater is the slope of the straight line.

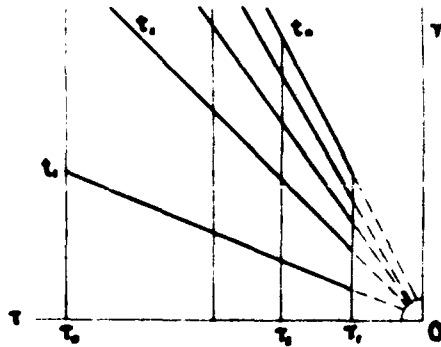


Fig.4

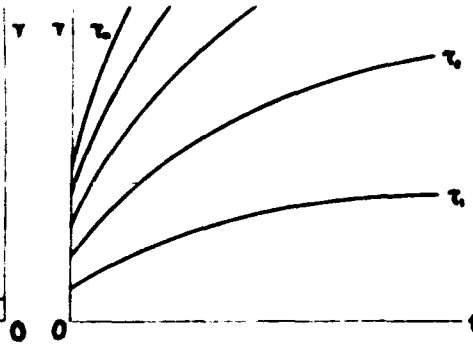


Fig.5

(2) When the stress τ is constant and is equal to $\tau_1, \tau_2, \tau_3, \dots, \tau_n$ successively, the projections of the lines of intersection of the rheological surface with the corresponding planes parallel to the coordinate plane $t-\gamma$ on this plane form a family of curved lines (Fig.5). These curved lines, generally known as creep curves, are suggested to be named as iso-stress lines. For any constant stress, the strain increases with time.

(3) When the strain γ is constant and is equal to $\gamma_1, \gamma_2, \gamma_3, \dots, \gamma_n$ successively, the projections of the lines of intersection of rheological surface with the corresponding

planes parallel to the coordinate plane $t-\tau$ on this plane form a family of curved lines (Fig.6). These curved lines, generally known as stress relaxation curves, are suggested to be named as iso-strain lines. For the same strain, the stress decreases as time increases.

Consequently, it is postulated:

(1) The angle $\arctan (\gamma_{ij} / \tau_i)$ ($i=1,2,3,\dots,n$) increases as the time t_j ($j=1,2,3,\dots,n$) increases (Fig.4). Therefore, when vehicles are being driven on rheological soils, the effect of load (stress) on sinkage (strain) increases with time.

Since the resistance increases with sinkage, or even it would belly out vehicles, the time of loading should be kept short in order to diminish sinkage, that is to say, high speed should be kept.

However, the increasing rate of the angle $\arctan (\gamma_{ij} / \tau_i)$ decreases with the time t_j . Therefore, the effect of raising vehicle speed is significant for the purpose of diminishing sinkage for a high-speed vehicle (a small value of t_j), while for a low-speed vehicle (a large value of t_j) it is not so significant.

(2) When the strain γ has a comparatively high value, the slope of tangent lines at the point on the iso-strain curve varies drastically. In the beginning, the stress τ_i drops rapidly as the time t_j increases. After the time t_j reaches a certain value corresponding to point C in Fig.6, the stress τ decreases steadily. In order to attain a definite strain γ ($K=1,2,3,\dots,n$) within a definite time, all values of t_j corresponding to point C's are recommended if the time limitation is not too strict. This may be of some use for the determination of the speed of the plow, harrow or bulldozer, on account of the fact that the resistance drops greatly as compared with high-speed implements while the speed can still be kept at a reasonable value for the time being.

From this point of view, if an obvious resistance drop, and therefore an obvious economy of energy resources, is needed, the speed of high-speed plows should not exceed too much those values corresponding to point C's.

When the strain γ has a small value (such as γ in Fig.6),

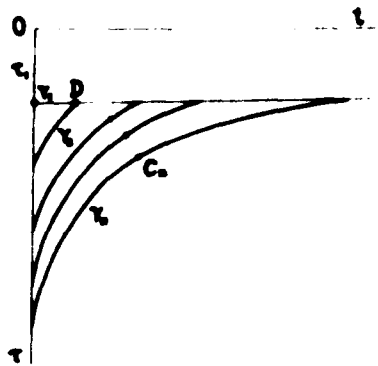


Fig.6

for instance, as a bulldozer is pushing hard soils, the resistance drops greatly with the decreasing speed. But there is a limit. When the speed drops to a point corresponding to point D (Fig.6), a further drop in speed will give no help to the resistance drop. τ is the stress corresponding to the least resistance.

The author sincerely hopes that this graph would be useful to reveal something that is interesting in tillage and traction. Any comments and suggestions will be deeply appreciated.

REFERENCES

- (1) E. C. W. A. Geuse and Tan Tjong-Kie: The mechanical behavior of clays, Proc. 2nd International Conference on Rheology, Oxford, 1953
- (2) C. P. Gupta and A. C. Pandya: Rheological Behavior of soil under static loading, Trans. ASAE, 9 (5), 1966
- (3) R. B. Ram, C. P. Gupta: Relationship between rheological coefficients and soil parameters in compression test, Trans. ASAE, 15 (6) 1972
- (4) S. Sudo, R. Yasutomi and P. Yamasaki: The mechanical behaviour of soil and its state of stress, J. Soc. Material Science, Japan, 17 (175), 1968
- (5) Isao Yoshida: Experimental study of the trafficability of agricultural vehicles (1), J. Soc. Agricultural Machinery, Japan, 32 (1), 1970
- (6) Isao Yoshida: Experimental study of the trafficability of agricultural vehicles (4), J. Soc. Agricultural Machinery, Japan, 34 (3), 1972
- (7) R. L. Schiffman: Analysis of the displacements of the ground surface due to a moving vehicle, Proc. 1st International Conference on the Mechanics of Soil-Vehicle Systems, 1961
- (8) Pan Jun-sheng: Preliminary study on rheological model of paddy field soil in China, J. Zhenjiang Institute of Agricultural Machinery, 1981 (2)
- (9) Lu Ze-jian, Qian Yan-qiao, Pan Jun-sheng: Rheological characteristics of paddy-field soils in China (1), Trans. Chinese Soc. Agri. Machinery, 1982 (2)
- (10) Qian Yan-qiao, Lu Ze-jian, Pan Jun-sheng: Rheological characteristics of paddy-field soils in China (2), Trans. Chinese Soc. Agri. Machinery, 1982 (3)
- (11) Pan Jun-sheng et al.: Rheological characteristics of paddy-field soils in China (4), Trans. Chinese Soc. Agri. Machinery, 1983 (3)



AD-P004 287

BEHAVIOUR OF SOIL UNDER A LUGGED WHEEL

S.X. WU, J.H. HU, and J.Y. WONG

TRANSPORT TECHNOLOGY RESEARCH LABORATORY,
CARLETON UNIVERSITY, OTTAWA, CANADA

INTRODUCTION

Wheels with a narrow rim and large lugs are widely used in Southeast Asia on tractors for paddy fields. The lugs of these wheels perform one or both of the following two functions: developing tractive effort and supporting vehicle weight. A great deal of field data on the performance of these wheels have been accumulated over the years. The mechanics of this type of wheel, however, has not yet been fully elucidated. To reach a better understanding of the physical nature of the problem, an investigation into the interaction between the lugs of the wheel and the soil was carried out.

Experiments were conducted in a glass-sided box in which model wheels, with different number of lugs at various angles to the wheel radius, were driven at varying slips close up against a glass plate. The nature of soil flow and deformation under the action of the lugs were then photographed through the glass.

The characteristics of the flow patterns and deformation of a dry sand and a clay under the action of the lugs of the model wheels are presented. The boundaries of the failure zones in the soil and the trajectories of soil particles are identified. It is believed that the results of this investigation will provide a basis upon which an improved method for predicting the performance of this type of wheel can be developed.

APPARATUS AND EXPERIMENTAL METHODS

Several techniques, including the photographic and x-ray techniques, may be used to investigate the soil flow and deformation under the action of the lugs of a wheel. The photographic technique has been successfully used in examining soil behaviour beneath rigid wheels [1], and is therefore employed in this study.

Experiments were conducted in a glass-sided box in which the model wheel was driven at varying slips close up against a glass plate, as shown in Fig. 1. The flow patterns and deformation of the soil were then photographed through the glass. The wheel was pulled along the box by means of a cable connected to a hydraulic ram. Various slips were obtained by anchoring one end of a cable wrapped around two pulleys with appropriate diameters fixed on either side of the model wheel. The radius of the pulley determined the rolling radius of the wheel and thus controlled its slip. The wheel was operated at constant sinkage using a horizontal guide for the wheel axle. The experimental method employed in this study is essentially the same as that described in reference [1].

The model wheel rim had a diameter of 27 cm and a width of 4 cm. Various numbers of lugs, of 9.6 cm wide and 4.5 cm long, were fitted to the rim

at different angles to the wheel radius (Fig. 1).

In the experiments for determining the flow patterns of soil under the action of the lugs, the box was held stationary and the wheel moved. The lugs of the moving wheel caused soil movements within certain zones. In sand, these movements can be clearly observed in a photograph taken by a fixed camera. In the resulting film, the stationary soil mass not affected by the lugs shows up as individual grains with sharp images while the grains influenced by the lugs move and appear as streaks. The boundaries of the flow zones can, therefore, easily be identified and the streaks give a clear picture of the movements of the sand under the action of the lugs.

In clay, the particle size is too small to be identified. Therefore, a number of white round dots, 1.2 mm in diameter, were marked on the vertical face of the clay before fitting the glass plate on to the soil box. These were made by blowing white powder through holes in a plastic plate on to the clay surface. The distance between the dots was 5 mm in both directions. When the wheel was moving in a steady-state condition, photographs were taken with a fixed camera. In the resulting film, the movements of clay particles can be identified from the streaks made by the white dots.

The sand used in the experiments was dry, round particle, Ottawa sand. It was in a dense condition (1.52 g/cm^3) for which the angle of internal shearing resistance was 29° and the angle of interface friction between the sand and the steel used for the lugs was 10° . The clay used had a density of 1.84 g/cm^3 , a moisture content of 37.5%, and a cohesion of 1.96 kPa. The angle of internal shearing resistance was about 4° and the angle of interface friction with the steel used for the lugs was approximately 1.5° .

FLOW PATTERNS IN SAND

The flow patterns in sand under lugged wheels with 1, 9, and 12 lugs are shown in Figs. 2, 3, and 4, respectively. The wheels were driven at the same slip of 28%, and the angle between the lugs and wheel radius (usually referred to as "lug angle") was set at 30° . It should be pointed out that when the wheel moves, the lugs on the wheel, such as OA, are rotating about an instantaneous centre located on a vertical line passing through the wheel centre.

The flow pattern beneath a wheel with a single lug, shown in Fig. 2, appears to be similar to that in front of a soil cutting blade with the appropriate rake angle translating in the horizontal direction, as reported by Hettiaratchi and Reece [2][3]. The failure zone appears to consist of an interface zone, a transition zone, and a Rankine passive zone. The lower boundary of the failure zone is identified by the dotted line shown in Fig. 2.

The flow pattern under a wheel with multiple lugs, shown in Figs. 3 and 4, is, however, quite different from that under a wheel with a single lug shown in Fig. 2. Since part of the soil mass has been excavated by the preceding lug, a cavity is formed between BC and the lug. As a result, the free soil surface OCB is no longer horizontal. The failure pattern appears to consist of an interface zone adjacent to the lug and a transition zone. The Rankine passive zone does not appear in the flow pattern under a wheel with multiple lugs. Based on these observations, it appears that the interaction between a lug on a wheel with multiple lugs and soil is different from that between a soil cutting blade and a semi-infinite soil mass with a horizontal free surface. This also indicates that the results of the analysis of passive soil resistance

obtained for a structure translating in a semi-infinite soil mass, such as those presented in reference [2], may not be directly applicable to the calculation of the interacting forces between a wheel with multiple lugs and soil, and that a new method has to be specifically developed for this purpose.

Fig. 5 shows a comparison of the soil mass affected by wheels with 1, 9, and 12 lugs for a given slip. It is shown that other conditions being equal, the amount of soil mass interacting with a lug decreases with the increase of the number of lugs on a wheel. Consequently, it can be expected that the magnitude of the forces acting on each lug decreases with the increase of the number of lugs on a wheel.

Fig. 6 shows the flow pattern under a wheel with 9 lugs and 30° lug angle at a wheel slip of 68%. In comparison with the flow pattern at a wheel slip of 28% shown in Fig. 3, it can be seen that as the wheel slip increases, the soil mass excavated by the preceding lug and hence the size of the cavity increase. Consequently, the amount of soil mass interacting with each lug decreases with the increase of wheel slip. This indicates that the magnitude of the forces acting on each lug may decrease with the increase of wheel slip. Fig. 7 shows a comparison of the failure zones of a wheel with 9 lugs and 30° lug angle at three different slips of 28%, 52% and 68%. The decrease in the size of the failure zone with the increase in wheel slip may explain why the total tractive effort of a lugged wheel does not increase continuously with the increase of wheel slip, rather it decreases beyond a certain wheel slip. This phenomenon has been frequently observed in field testing of lugged wheels.

Fig. 8 shows a comparison of the flow patterns beneath wheels having 9 lugs with lug angles of 15° and 30° . It can be seen that the lug angle has some influence on the flow patterns and hence the performance of a lugged wheel.

Fig. 9 shows the flow patterns of sand under a lug at different angular positions. The variation of the flow pattern with the angular position of the lug indicates that the forces acting on the lug are expected to fluctuate as the wheel rotates. This implies that the torque input, tractive effort, lift force, and motion resistance of a lugged wheel will vary periodically as the wheel moves forward. This is also consistent with field observations.

FLOW PATTERNS IN CLAY

The flow patterns in clay beneath wheels with 1 and 9 lugs are shown in Figs. 10 and 11, respectively. The wheels were driven at the same slip of 28%, and lug angle was set at 30° . The existence of a soil wedge adjacent to the lug in both cases can be noted from Figs. 12 and 13. The trajectories of clay particles immediately under the lug and those at a distance away from the lug for wheels with 1 and 9 lugs are shown in Figs. 14 and 15, respectively. From these figures, it can be seen that for a wheel with a single lug, the flow pattern seems to consist of an interface zone (soil wedge), a transition zone bounded by a section of a circle and a Rankine passive zone. For a wheel with multiple lugs, however, part of the soil mass has been excavated by the preceding lug and a cavity is formed. As a result, the free soil surface is no longer horizontal. The Rankine passive zone does not appear in the failure pattern under a wheel with multiple lugs.

The flow patterns under a wheel with 9 lugs and lug angle of 30° at various angular positions are shown in Fig. 16. This indicates that the failure

patterns in clay also vary with the angular position of the lug, similar to those in sand shown in Fig. 9. Fig. 17 shows how the deformation of the clay develops under the lug as the wheel rotates.

It should be pointed out that the shape and size of the cavity, formed as a result of the excavation of a certain amount of soil mass by the lug, are of interest, as they affect the amount of soil mass interacting with the following lug, hence the interacting forces. In the past, the shape and size of the cavity were predicted based on the assumption that the kinematics of lug - soil interaction is analogous to that of a rack and pinion, neglecting the actual behaviour of the soil and the influence on soil deformation by adjacent lugs. Figs. 18 and 19 show the actual size and shape of the cavity as compared with those predicted by kinematic analysis in sand and clay, respectively. It can be seen that there is a noticeable difference between them, particularly the shape of the leading part of the cavity, CD. This is because CD is affected by the deformation and movement of the soil mass under the action of the adjacent lug.

It has been reported in the literature that under a thick lug there is a noticeable forward flow zone. In this study, it has been observed, however, that the soil beneath a thin lug normally flows in the same direction of wheel rotation; except for a short period of time immediately after the lug tip comes into contact with the soil surface, during which the soil mass within a small zone in front of the lug flows forward.

CONCLUSIONS

1. The interaction between a lug on a wheel with multiple lugs and soil is shown to be different from that between a cutting blade (or a retaining wall) and a semi-infinite soil mass with a horizontal free surface. The soil excavated by the preceding lug creates a cavity. As a result the soil mass interacting with the following lug no longer has a horizontal free soil surface. Consequently, the results of the analysis of passive soil resistance obtained for a structure translating in a semi-infinite soil mass may not be directly applicable to the calculation of the interacting forces between the lugs of a wheel and soil. It appears that a new method has to be specifically developed for this purpose.

2. It is shown that the failure patterns in soil under the action of a lugged wheel vary with the number of lugs, lug angle, and wheel slip. It appears that there is a close relationship between the failure patterns of soil under the lugs of a wheel and its performance. A number of field observations of the performance of the lugged wheel can be directly related to the characteristics of soil flow and deformation described in this study. This indicates that an improved method for predicting the performance of a lugged wheel should be developed based on the knowledge of soil failure beneath it.

ACKNOWLEDGEMENTS

The work described in this paper was supported in part by a research grant (No. A5590) awarded to Professor J.Y. Wong by the Natural Sciences and Engineering Research Council of Canada. Messers. Wu and Hu are Visiting Scholars at the Transport Technology Research Laboratory, Carleton University.

REFERENCES

1. J.Y. Wong, Behaviour of Soil Beneath Rigid Wheels, Journal of Agricultural Engineering Research, Vol. 12, No. 2, pp. 257-269, 1967.
2. D.R.P. Hettiaratchi and A.R. Reece, The Calculation of Passive Soil Resistance, Geotechnique, Vol. 24, No. 3, pp. 289-310, 1974.
3. D.R.P. Hettiaratchi and A.R. Reece, Boundary Wedges in Two-Dimensional Passive Soil Failure, Geotechnique, Vol. 25, No. 2, pp. 197-220, 1975.

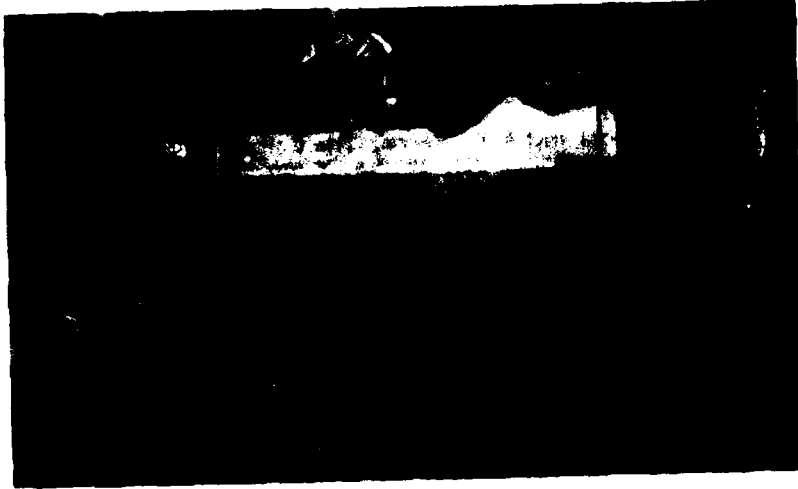


Fig. 1 Apparatus used for investigating soil behaviour beneath lugged wheels



Fig. 2 Flow pattern in sand beneath a wheel with a single lug and 30° lug angle at 28% slip



Fig. 3 Flow pattern in sand beneath a wheel with 9 lugs and 30° lug angle at 28% slip

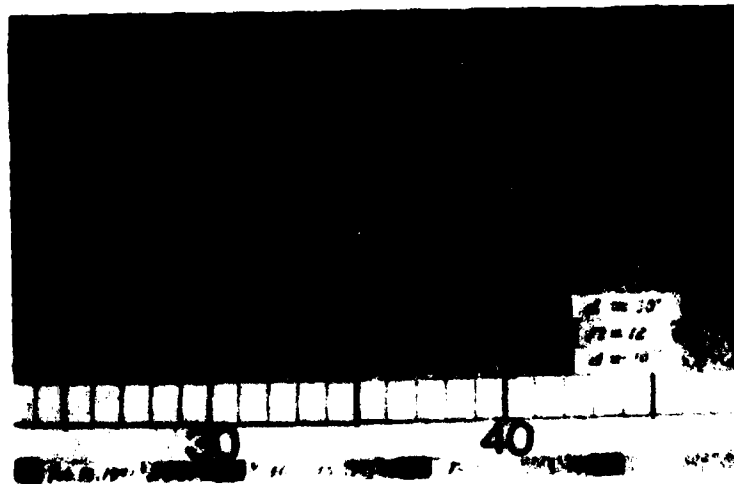


Fig. 4 Flow pattern in sand beneath a wheel with 12 lugs and 30° lug angle at 28% slip

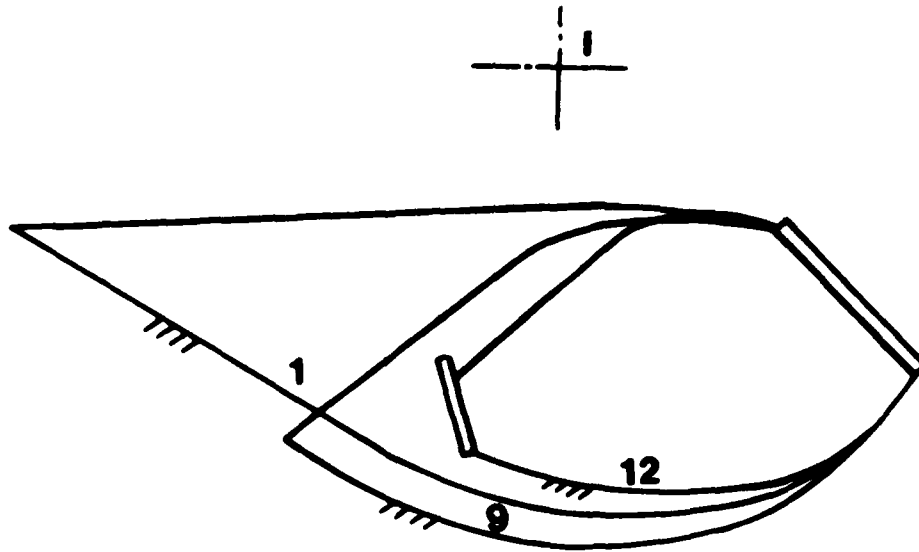


Fig. 5 Comparison of flow zones in sand beneath wheels with 1, 9, and 12 lugs having 30° lug angle at 28% slip

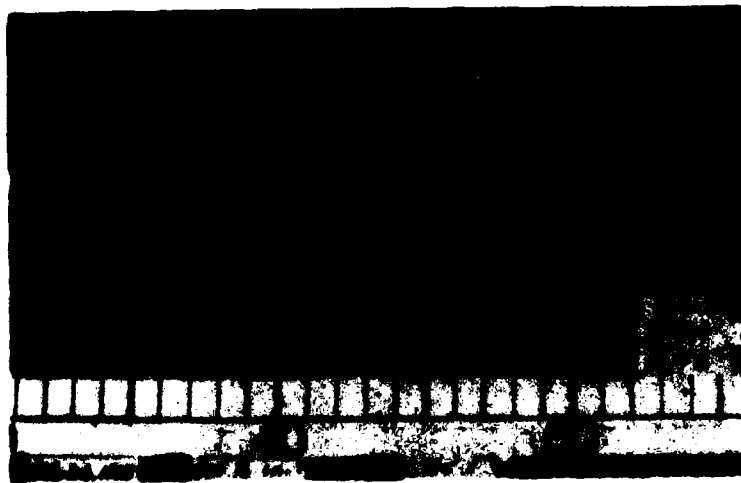


Fig. 6 Flow pattern in sand beneath a wheel with 9 lugs and 30° lug angle at 68% slip

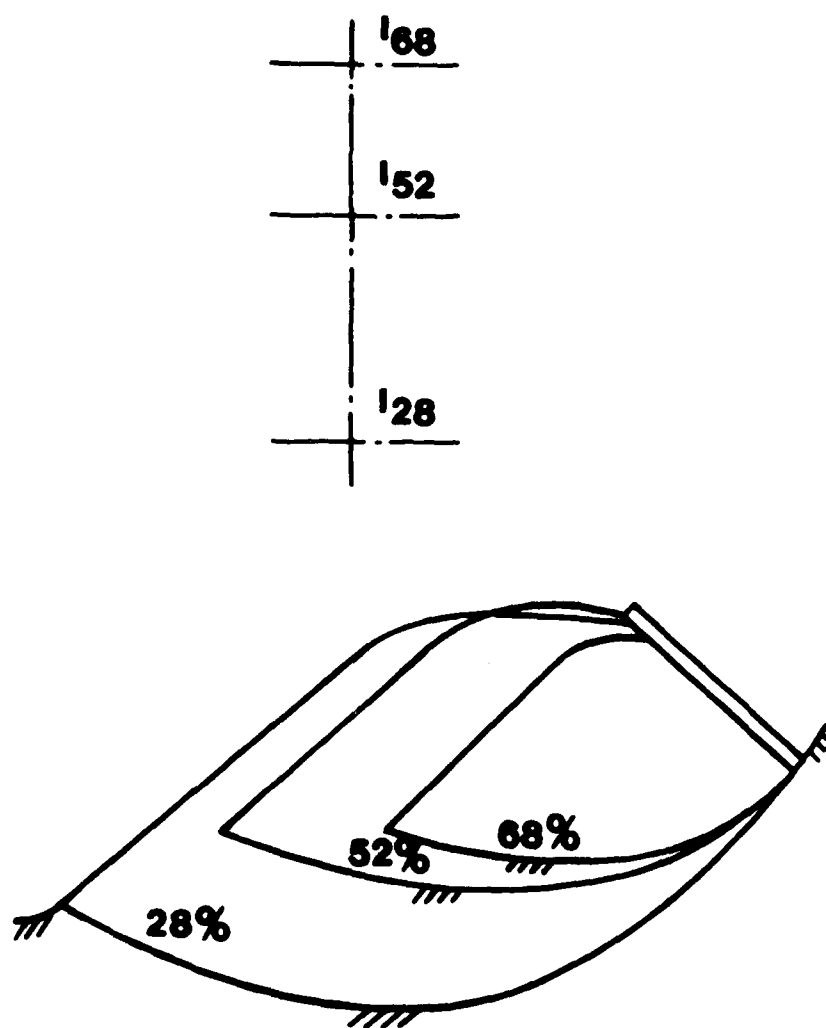


Fig. 7 Comparison of flow zones in sand beneath a wheel with 9 lugs and 30° lug angle at slips of 28%, 52% and 68%

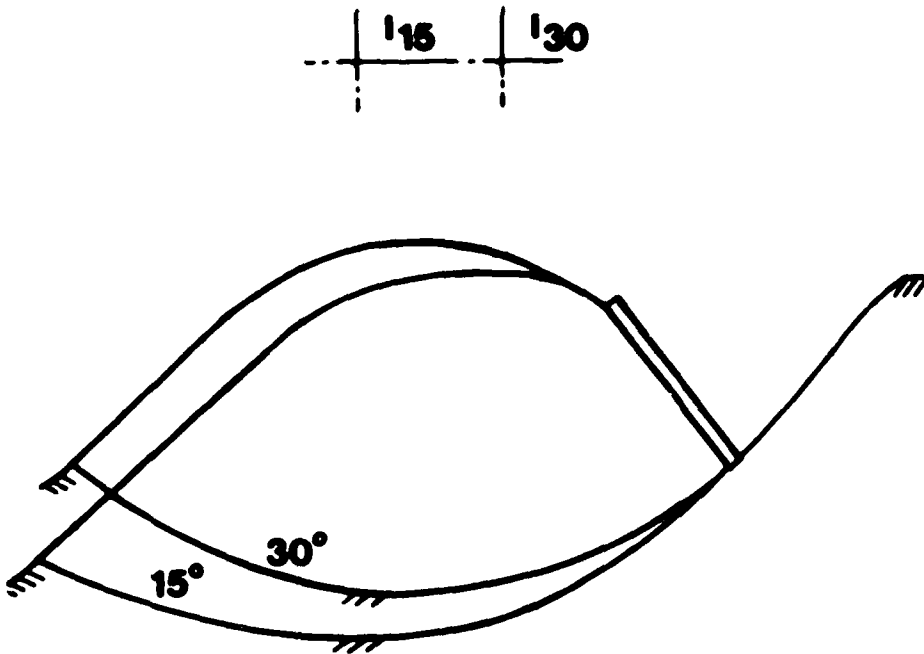


Fig. 8 Comparison of flow zones in sand beneath wheels having 9 lugs with lug angles of 15° and 30° at 28% slip

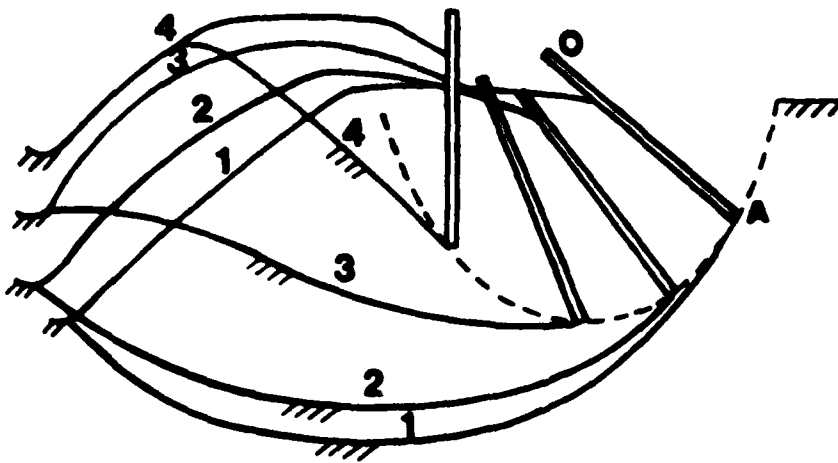


Fig. 9 Comparison of flow zones in sand beneath a wheel with 9 lugs and 30° lug angle at various angular positions at 28% slip

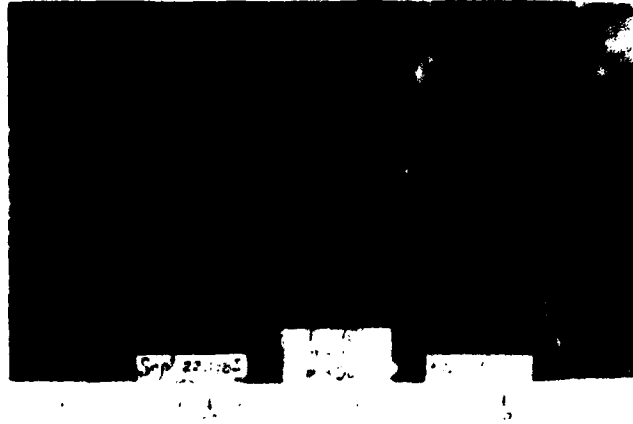


Fig. 10 Flow pattern in clay beneath a wheel with a single lug and 30° lug angle at 28% slip

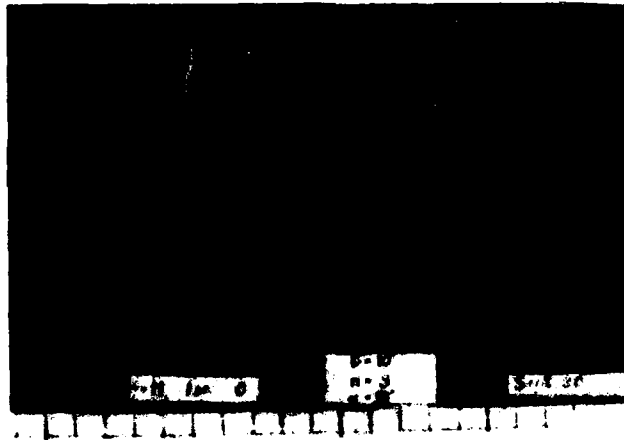


Fig. 11 Flow pattern in clay beneath a wheel with 9 lugs and 30° lug angle at 28% slip

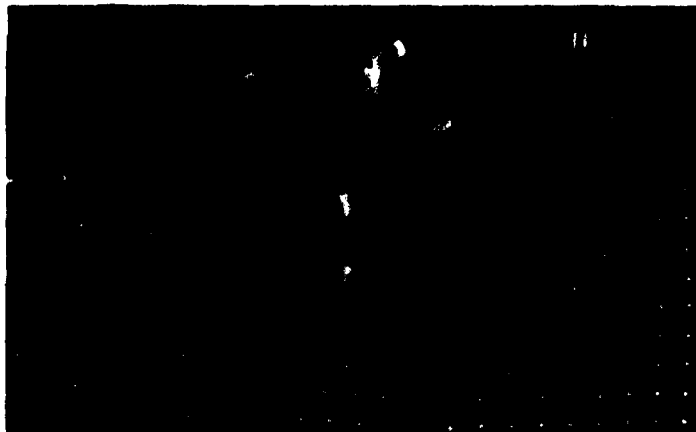


Fig. 12 Soil wedge formed adjacent to the lug of a wheel with a single lug and 30° lug angle at 28% slip in clay

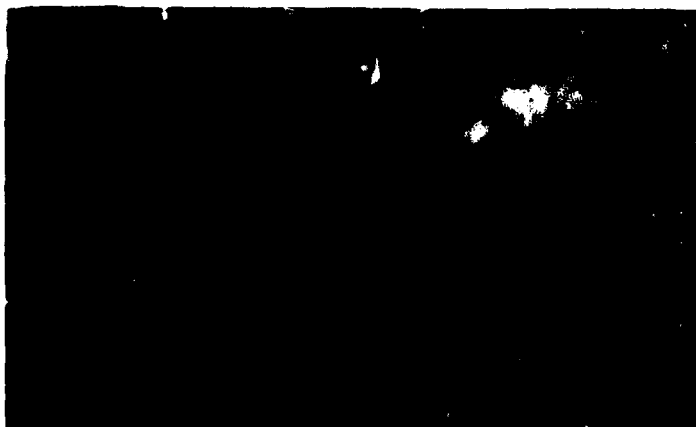


Fig. 13 Soil wedge formed adjacent to the lug of a wheel with 9 lugs and 30° lug angle at 28% slip in clay

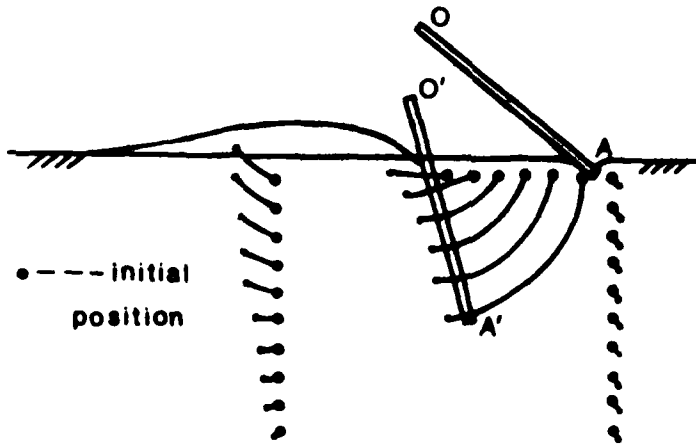


Fig. 14 Trajectories of clay particles beneath a wheel with a single lug and 30° lug angle at 28% slip

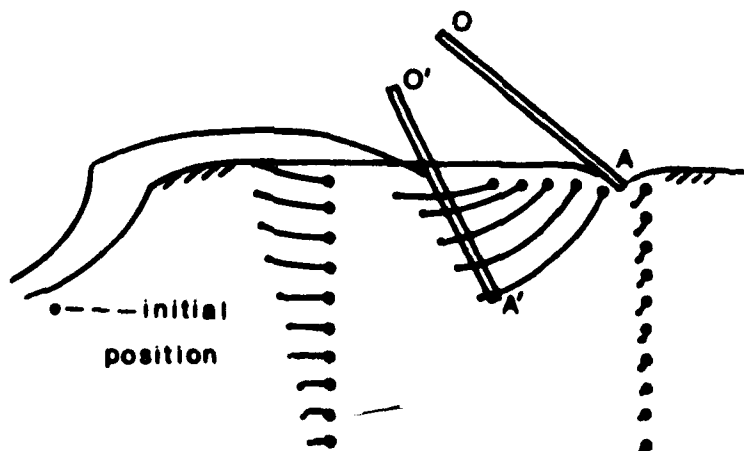


Fig. 15 Trajectories of clay particles beneath a wheel with 9 lugs and 30° lug angle at 28% slip

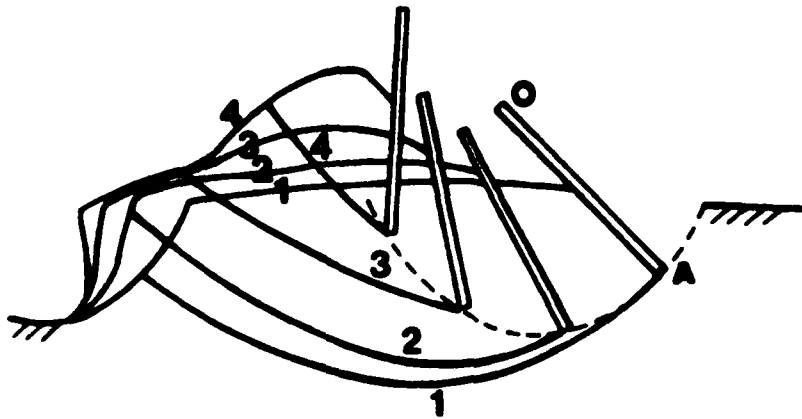


Fig. 16 Comparison of flow zones in clay beneath a wheel with 9 lugs and 30° lug angle at various angular positions at 28% slip

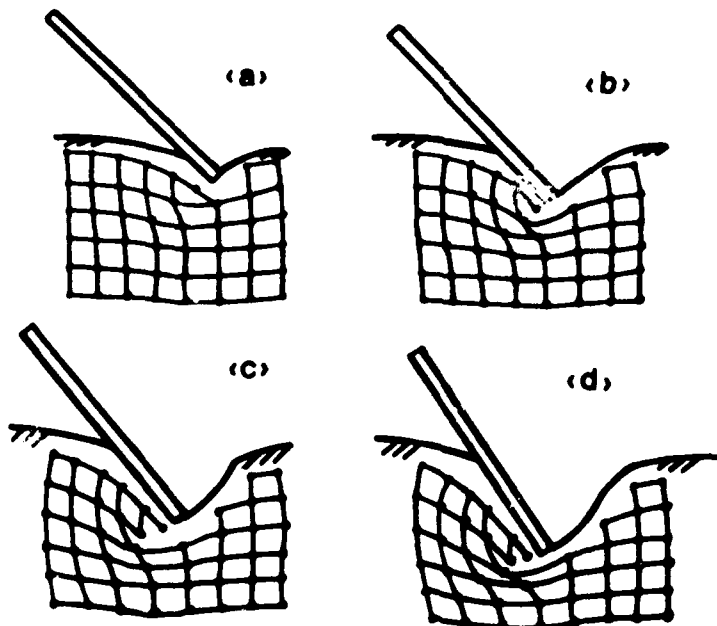


Fig. 17 Deformation of the clay beneath the lug of a wheel with 9 lugs and 30° lug angle at various angular positions at 28% slip

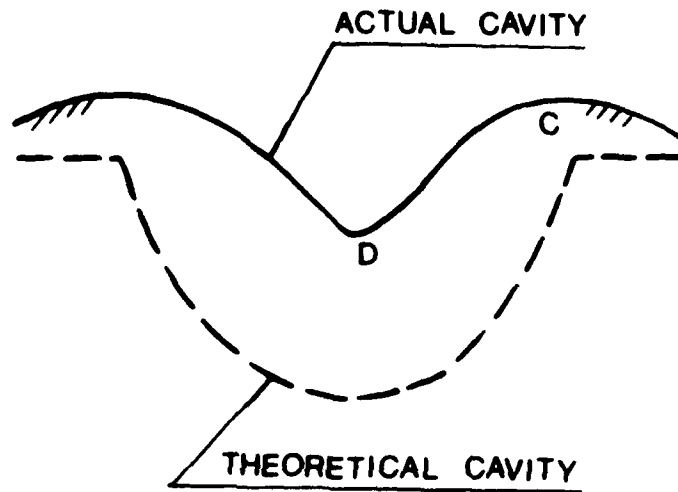


Fig. 18 Comparison of the theoretical and actual shapes of the cavity formed by the lug of a wheel in sand

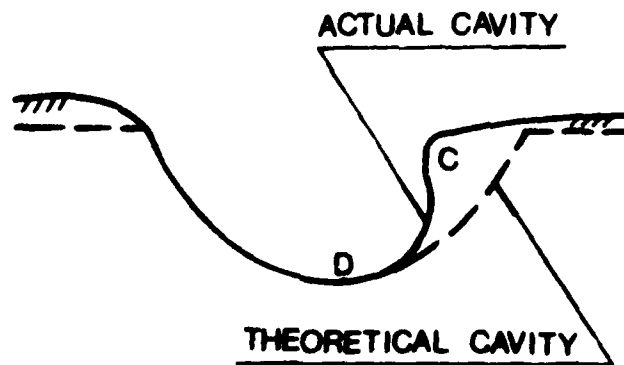


Fig. 19 Comparison of the theoretical and actual shapes of the cavity formed by the lug of a wheel in clay



AD-P004 288

PREDICTION ACCURACY OF THE TORQUES
FOR ROTARY TILLAGE BY AN ANALOG TOOL

Minoru Yamazaki and Takashi Tanaka

Faculty of Agriculture, Kyoto University, Kyoto, Japan

ABSTRACT

The analog prediction system developed and investigated by R. L. Schafer and C. A. Reaves was used for predicting torque on rotary blade. Three sizes of rotary blades with a similar configuration and cones as an analog tool were chosen to be in ratios of 1 : 1, 1 : 1.25 and 1 : 1.61 relative to the smallest size. The largest blade that is on the market and two other blades were called prototype, M-1 blade and M-2 blade respectively.

Tests were run in silt soil at three moisture levels; MC1(21.3%), MC2 (28.8%) and MC3(33.8%). The tillage test was designed to run in three levels of depth and in one level of forward speed and peripheral speed of blade. A movable soil bin with stationary rotary tillage device was used. Soil fitting procedure was conducted mainly by hand with a scoop, a leveler and a patting tool before each test. The cones were penetrated vertically downward into the soil at a speed of 5.5 mm/s by means of a hydraulic cylinder. Torque on rotary blade, cone penetration force, depth etc. were measured and the average torque from three repetition tests and the average penetration force from soil surface to each corresponding scaled depth were calculated.

Through the data analysis, the following results were obtained. The average prediction errors in the absolute value were 13.49 % for M-1 blade and 24.57 % for M-2 blade. There was a tendency that the prediction accuracy decreased in the shallow zone. The adoption of the average cone penetration force was effective in the prediction.

INTRODUCTION

Performances of prototype in soil-machine systems have been investigated and predicted by scale model data using similitude theory. However, a satisfactory prediction is not attained especially in common soil conditions where distortions occur, since present knowledge of soil-machine interactions is meager.

The objective of this study is to investigate the usefulness or feasibility of an analog for predicting torques on rotary blades which bring about a considerable high speed interaction. An analog prediction technique developed by Schafer et al. was used. The technique is based on the equation (1).

$$\delta = R / R_m = n^s \dots\dots\dots (1)$$

where R and R_m are the forces on the prototype and model respectively, n is length scale and s is an exponent for a particular soil-machine system.

ANALYSIS OF THE PREDICTION SYSTEM

The following equations were assumed as to the force-size relations when a series of rotary blades and cones with geometrically similar configurations are operated in the same soil.

$$F = f \cdot n^{sf} \dots\dots\dots(2)$$

$$P = p \cdot n^{sp} \dots\dots\dots(3)$$

where,

F = force to prototype blade
 f = force to model blade
 P = force to the largest cone
 p = force to other cones
 n = length scale and
 sf, sp = exponents for both systems

In this study, as torques are to be predicted,

$$T/L = (t/l) n^{sf} \dots\dots\dots(4)$$

where,

T = torque on prototype
 t = torque on model
 L = a representative length of prototype
 l = a representative length of model

Equation (4) can be written as,

$$T = t \cdot n^{sf+l} \dots\dots\dots(5)$$

or

$$T = t \cdot n^{st} \dots\dots\dots(6)$$

where, $st = sf + l$.

For equal values of n, equations (6) and (3) can be combined to get

$$T = t \cdot p^{-st \cdot sp^{-1}} \cdot p^{st \cdot sp^{-1}} \dots\dots\dots(7)$$

or,

$$T = A \cdot p^{stp} \dots\dots\dots(8)$$

where,

$$A = t \cdot p^{-st \cdot sp^{-1}}$$

$$stp = st \cdot sp^{-1} \quad \text{or} \quad st = stp \cdot sp$$

Then, the prediction equation would be

$$T = t \cdot n^{stp \cdot sp} = t \cdot n^{st} \dots\dots\dots(9)$$

EXPERIMENTAL DESIGN AND PROCEDURERotary Blade

The curved blades for rotary tillage on the market which are widely used in Japanese paddy field were chosen as a prototype and the geometrically similar models with scales of 62 % and 80 % were manufactured (Figure 1).

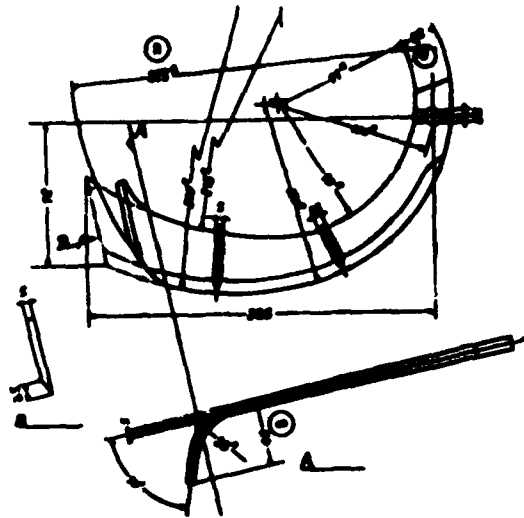


Figure 1. Rotary blade tested (P blade)

Table 1 shows their main dimensions. The distance R from the center of rotation to the tip of blade was determined as a representative length. Six blades were installed on a rotary shaft as shown in Figure 2. Therefore, three sets of rotary shaft with blades of different kinds were prepared.

Cones

Three circular cones with an apex angle of 60 deg. were used as an analog device. The diameters of their base are determined to have the same length scale in proportion to the ratios of three rotary blades (Figure 3).

Table 1. Dimensions of rotary blades tested.

symbol of blade	radius of rotation	width of cut	angle of bend	radius of curvature	thickness of blade tip	scale	length scale
	R (mm)	B (mm)	(deg)	(mm)	(mm)		n
P	225	40	70	35	6	1.00	1.00
M-1	180	32	70	28	4	0.80	1.25
M-2	140	25	70	25	3	0.62	1.61

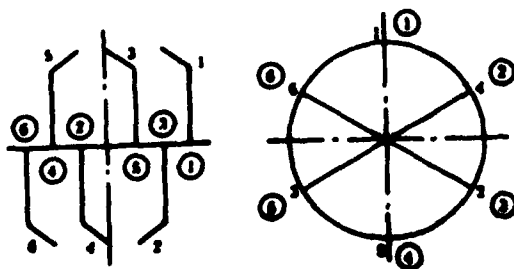
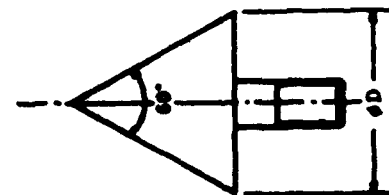


Figure 2. Arrangement of rotary blades.
(Numbers in circles denote the order of dig.)



φDcm	φ45	φ36	φ28
n	1.000	1.250	1.607

Figure 3. Cones as an analog device.

Experimental Devices and Measuring Points

A facility of a straight, movable soil bin with stationary tool was designed and constructed as shown in Figure 4.

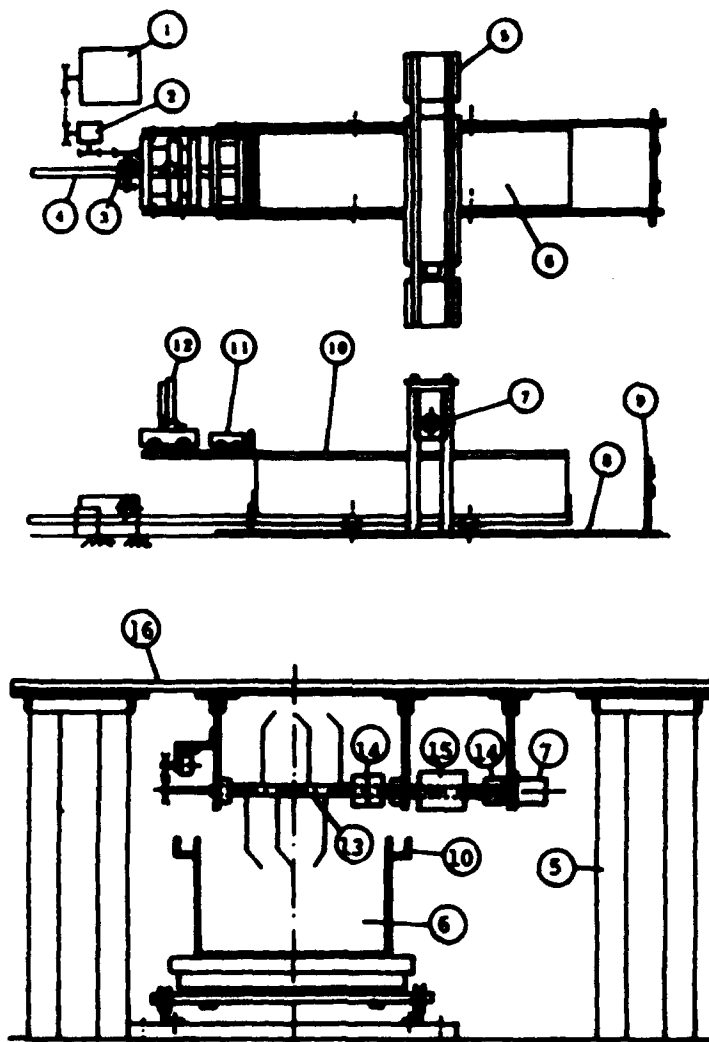


Figure 4. Soil bin facility

1. Variable speed motor
2. Reduction gears
3. Drive sprocket
4. Thrust steel rod with chains
5. Supporting stand
6. Soil box (46 x 200 x 30 cm)
7. Hydraulic motor
8. Rails for soil box
9. Fence
10. Rails on both upper sides of soil box
11. Carriage with leveling plate
12. Carriage with cone penetrometer
13. Rotary shaft
14. Coupling
15. Slip ring
16. Beams for detecting force components to blades.

Adjustment of tilling depth was conducted as follows. Firstly, soil box 6 was jacked up and spacing blocks were inserted between the bin and a truck which runs on the rails 8. Then, the bin was lowered on the spacers, and with this, an approximate adjustment of depth was attained. Secondly, a precise depth adjustment was done by regulating the height of a leveling plate which is set up on a carriage 11 on the rails 10 located on both upper sides of the bin.

The drive system of the soil box consists of a variable speed, electric motor 7, a reduction gears 2, driving sprockets 3 and a thrust steel rod 4 on which chains are installed. By this system, a comparative steady speed in the range 0 - 30 cm/s was obtained.

A hydraulic power unit composed of a piston pump, flow control valves and electromagnetic valves was adopted to drive the rotary shaft and cone penetrometer. An orbit motor 7 was used to drive rotary shaft. After a set of rotary shaft was tested, it was changed for another set.

A scoop, a compacting board with a handle and a leveler were prepared for soil preparation.

The measuring points and the instrument used were as follows.

1. Torque on rotary shaft: strain gages and slip ring 15.
2. Components of both vertical and longitudinal forces on rotary blades: strain gages 16.
3. Velocity of soil box (tilling speed): an electric pulse generator.
4. Rotational speed of the shaft: a tachometer generator.

All data were recorded by a data recorder.

Cone penetrometer

The cone was screwed on the tip of penetration rod which is connected with a hydraulic cylinder through the intermediation of a force transducer. The penetration speed was 5.5 mm/s. Penetration resistance was measured by means of the force transducer of strain gage type and depth was detected by use of a differential linear transformer.

Soil and its Preparation

The soil used was silt consisting of 9.8 % clay, 41.4 % silt and 48.8 % sand. After being dried, smashed, sifted and bagged, it is on the market in Kyoto. Plastic limit and liquid limit were found to be 29.2 % and 52.9 %. We determined three levels of soil moisture content as shown in Table 2, considering that the soils tested should have the moisture contents as seen in common paddy fields.

Each soil was processed by adding predetermined amount of water little by little by a water pot and mixed by a scoop in a box. Then, the soil was filled up into the soil box and was covered a sheet of vinyl film for a week to equalize moisture. Before every tillage test, the following soil preparation was carried out. The soil was loosened to the bottom by a scoop and the surface soil was leveled and compacted. These manual works were carefully conducted by a definite way. Finally, the adjustment of tilling depth was done.

Table 2. Symbols of the soils and their moisture contents

symbols	MC 1	MC 2	MC 3
moisture content (%)	21.30	28.79	33.76

Test Conditions

The design and operating conditions shown in the equations (10) - (14) should be held between the prototype and the models. The terms on soil properties are not included.

$$l / R = L_m / R_m \dots\dots\dots (10)$$

$$\alpha = \alpha_m \dots\dots\dots (11)$$

$$Z / R = Z_m / R_m \dots\dots\dots (12)$$

$$V^2/g \cdot R = V_m^2 / g_m \cdot R_m \dots\dots\dots (13)$$

$$N/\sqrt{R/g} = N_m/\sqrt{R_m/g_m} \dots\dots\dots (14)$$

where, R = the maximum rotational radius of blade
 l = other lengths of blade (width of cut etc.)
 α = angles of blade (angle of bend etc.)
 Z = tilling depth
 V = tilling forward speed
 N = rotational speed of rotary shaft
 g = acceleration of gravity and
 m denotes model.

The equations (10) and (11) were realized among the blades. Therefore, three levels of Z, V and N were determined respectively for P blade in the first place. And, Z_m , V_m and N_m for blades M-1 and M-2 were set up. But, in this report, the results are shown about the case presented in Table 3. Three repetition tests were carried out.

Table 3 Tillage conditions

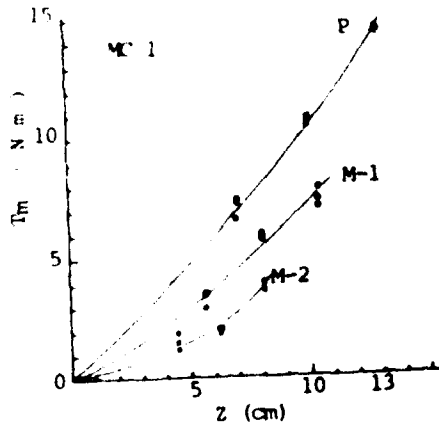
blades	Z1 cm	Z2 cm	Z3 cm	V cm/s	N rpm
P	7.0	10.0	13.0	24.0	205
M-1	5.6	8.0	10.4	21.5	229
M-2	4.4	6.2	8.1	18.9	260

RESULTS

Torques, Penetration Forces vs. Size

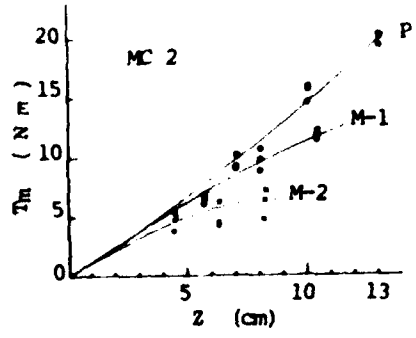
The torques obtained in the three repetition tests at three scaled depths for each rotary blade are shown in Figure 5 (a), (b) and (c). As is seen in the figures, the dispersion of each three points was notable at higher moisture levels, at shallower scaled depths and in smaller blades. This was thought to be consequent upon the nonuniformity and the variations of the strength of soils which were prepared for every tillage run. Especially, at MC2 and MC3, small-sized soil balls were formed as the tests advanced. The soil balls disturbed the precise adjustment for the scaled depths designed, though we made an effort to break them. Hereafter, the mean of torques T_m by three replications was used. As for the cones, the averaged values of penetration forces from soil surface to the scaled depths were adopted. For example, the averaged values of penetration forces from soil surface to the depths of 7, 10 and 13 cm were used.

The relations of torques - blade sizes and penetration forces - cone sizes are presented in Figures 6 and 7 in logarithical form. Judging from the results that the relationships were drawn as the straight lines, we considered that the fundamental equations (2) and (3) were satisfied.

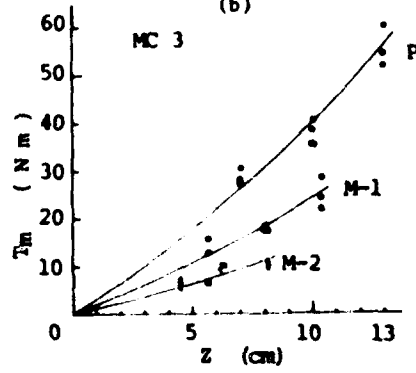


(a)

Figure 5. Torques at the scaled depths



(b)



(c)

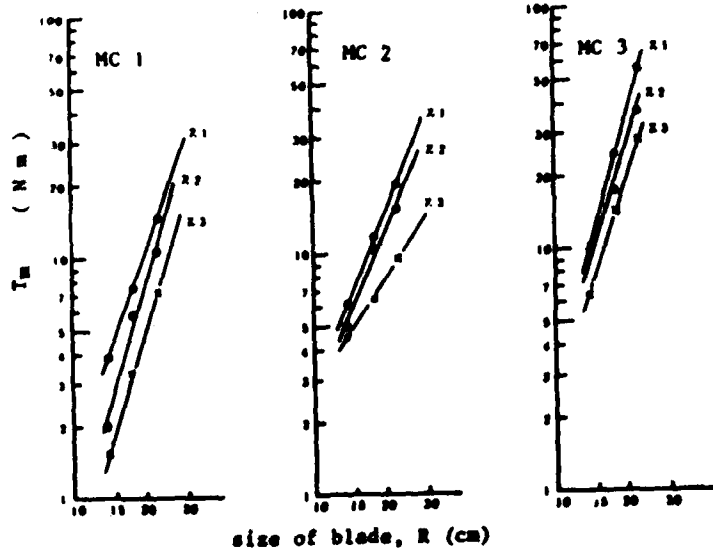


Figure 6. Torques vs. blade sizes

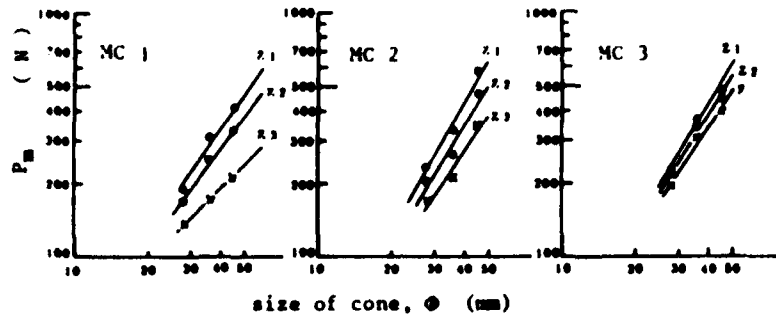


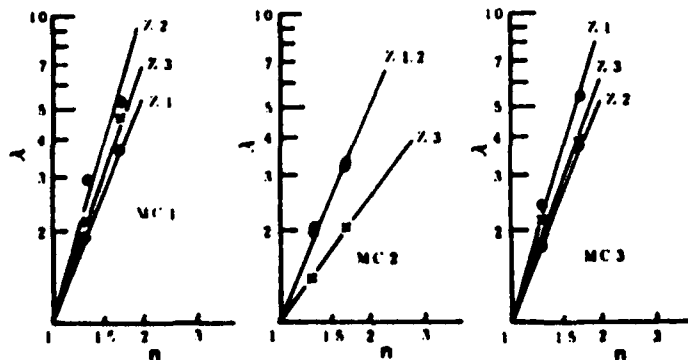
Figure 7. Penetration forces vs. cone sizes

Exponents S_t , S_p and S_{tp}

To predict and examine torques on P blade according to the analog prediction theory, it is necessary to get the exponents S_t , S_p and S_{tp} from all the regression lines regardless of soil moisture and depth levels. Therefore, normalization was done as to torques and penetration forces in order to eliminate the effects of soil conditions and the depth on the exponents. Normalization was conducted in such a way that the torques were divided by the torque on the smallest M-2 blade for each moisture and depth level combination, and the ratio was named λ . As to the penetration forces, the same way was applied and the ratio was named μ .

Figures 8, 9 and 10 show the relationships λ vs. n , μ vs. n and λ vs. μ in each moisture level. Properly speaking, these figures should not be presented separately by moisture levels, but they will tell us that the considerable dispersion of dots and differences of the slopes in some combination of MC and Z level. This fact means that an ideal result, in which the exponent S_{tp} is always definite, was not obtained and that the prediction accuracy was decreased in some measure.

The exponents based on all the data and based on each MC level for reference were calculated by means of regression analysis. The estimated values of S_t which will be written by the symbol \hat{S}_t hereafter, the values of S_t due to the observed value and their ratios are shown in Table 4. As most of \hat{S}_t values are smaller than those of S_t , it is expected that the predicted torques will be less than the measured in general.

Figure 8. Torque ratio λ vs. length scale n

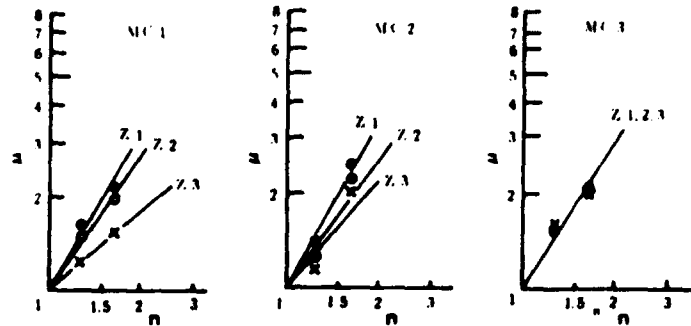
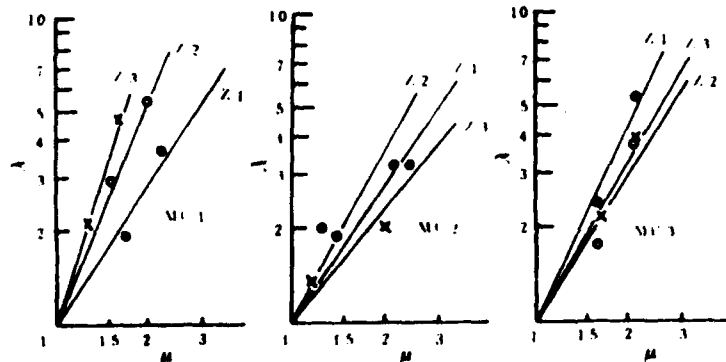
Figure 9. Cone force ratio μ vs. n Figure 10. λ vs. μ

Table 4. The exponents obtained from all the data and each soil moisture level.

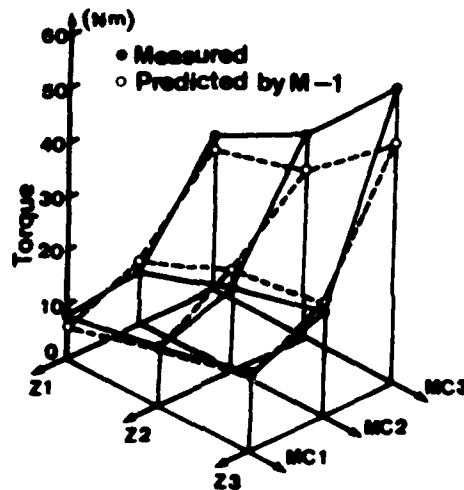
	S_c	S_p	S_{tp}	\hat{S}_c	$\frac{\hat{S}_c - S_c}{S_c}$
all data	2.8633	1.5361	1.7525	2.6921	-0.171
MC1 level	3.2841	1.4066	2.0538	2.8889	-0.120
MC2 level	2.1965	1.5732	1.3515	2.1262	-0.032
MC3 level	3.1104	1.6292	1.8864	3.0733	-0.012

Prediction of Torques on P Blade

Figure 11 shows the measured torques and the predicted values based on all data from M-1 and M-2 blades in relation to MC and Z levels. A better concurrence was noticed in lower moisture levels and larger model blade. Then, the prediction error (A) derived from all the data was defined by the equation (15) and the results are presented in Tables 5 and 6.

$$\text{Prediction Error (A)} = \frac{(\text{Predicted} - \text{Observed})}{\text{Observed}} \times 100 \dots (15)$$

As for the prediction error (A) derived from all the data, the largest error was brought on at MC2 level with two model blades. There is a distinct inclination that over prediction occurred only at MC2, but the cause is inexplicable. The average of all the errors was very small as the result of offset account and accordingly their standard deviations were considerably large (Table 5). On the contrary, the prediction error (A) based on the data from each MC level were smaller (Table 6). Now, it may be effective or useful to adopt an absolute value of the prediction error (A), we call it "the prediction error (B)", when we refer to the average error. As with the prediction error (B), the averages from M-1 and M-2 blades became larger and were 13.5 % and 24.6 %, but the standard deviations decreased to 7.61 % and 20.4 % respectively. The average errors for each Z level, on the whole, suggests that the non-uniformity of soil strength on the torques exists especially in the shallower zone.



(a) Prediction by M - 1 blade

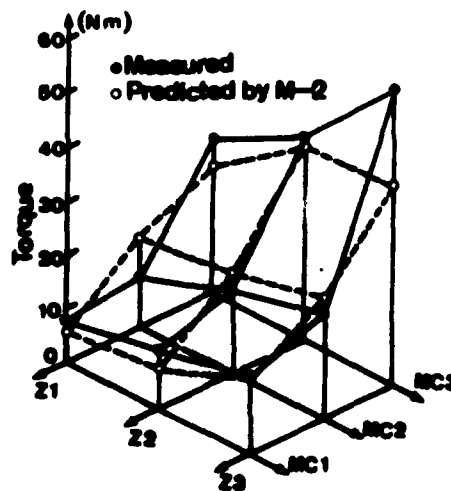


Figure 11. Prediction of torques on P blade based on all the data

Table 5. Prediction errors based on all the data

MC level	Z level	measured torque P blade	M - 1 blade		M - 2 blade	
			predicted torque	error(A)	predicted torque	error(A)
MC 1	Z 1	7.02 ^{Nm}	5.91 ^{Nm}	-15.84 ^Z	5.38 ^{Nm}	-23.38 ^Z
	Z 2	10.45	10.39	- 0.54	6.99	-33.08
	Z 3	14.09	13.33	- 5.40	13.52	- 4.05
MC 2	Z 1	9.32	11.47	23.06	16.28	74.68
	Z 2	15.11	18.73	23.94	17.61	16.53
	Z 3	19.36	21.06	8.79	21.66	11.88
MC 3	Z 1	27.89	25.42	- 8.86	22.77	-18.35
	Z 2	36.69	30.93	-15.71	34.86	- 5.00
	Z 3	54.42	43.95	-19.25	35.82	-34.17

Average error	M-1 blade	M-2 blade
MC1 (A)	- 7.26 ^Z	-20.17 ^Z
(B)	7.26	20.17
MC2 (A)	18.60	34.36
(B)	18.60	34.36
MC3 (A)	- 14.16	-19.17
(B)	14.16	19.17
Z 1 (B)	15.92	38.85
Z 2 (B)	13.40	18.20
Z 3 (B)	11.15	16.70
All data (A)	- 1.09	- 1.66
Stand. devi.	15.45	31.89
All data (B)	13.49	24.57
Stand. devi.	7.61	20.40

Table 6. Prediction errors based on the data from each MC level.

MC level	Z level	measured torque P blade	M - 1 blade		M - 2 blade	
			predicted torque	error(A)	predicted torque	error(A)
MC 1	Z 1	7.02 ^{Nm}	6.17 ^{Nm}	-12.11 ^Z	5.91 ^{Nm}	-15.81 ^Z
	Z 2	10.45	10.86	3.92	7.68	-26.51
	Z 3	14.09	13.93	- 1.14	14.84	5.32
MC 2	Z 1	9.32	10.11	8.48	12.45	33.58
	Z 2	15.11	16.51	9.27	13.46	-10.92
	Z 3	19.36	18.56	- 4.13	16.56	-14.46
MC 3	Z 1	27.89	27.68	- 0.75	27.28	- 2.19
	Z 2	36.69	33.67	- 8.23	27.28	13.85
	Z 3	54.42	47.85	-12.07	42.93	-21.11

Average error	M-1 blade	M-2 blade
MC1 (A)	- 3.11 ^x	-12.33 ^x
(B)	5.72	15.88
MC2 (A)	4.54	- 2.73
(B)	7.29	19.65
MC3 (A)	- 7.02	- 3.15
(B)	7.02	12.38
Z 1 (B)	7.11	17.19
Z 2 (B)	7.14	17.09
Z 3 (B)	5.78	13.63
All data (A)	- 1.86	- 4.25
Stand. devi.	7.61	18.00
All data (B)	6.68	15.97
Stand. devi.	4.09	9.33

DISCUSSION

A general similitude technique for soil-machine systems is not established under the present condition though many researches have been conducted. The method using an analog device is considered to have the possibility to predict the performance of a prototype from models. We paid more attention to the prediction accuracy setting aside an appropriateness of cone as an analog tool.

Various appraisals could be possible as to the prediction errors obtained in this experiment. If a tentative target of the prediction error is settled to be 10 % as Schafer et al. proposed, the number of errors over 10 % amounted more than twice the number of errors below 10 %. Also, it was found that the standard deviation of the prediction errors (A) and (B) were too large for a practical prediction system. But, considering that a high speed soil-machine interaction occurs in rotary tillage, one might say that the results obtained exceeded expectation. The reason would be as follows. One is due to the minute soil preparation which was possible because of the small-scale soil box. The other is attributable to adopt the average penetration force.

Then, the investigation was made on the large variations of prediction errors which were expressed by standard deviations. Another cone penetration was conducted to examine the uniformity of soil strengths using a cone with 60 deg. apex angle and 25 mm diameter before every tillage run. The result is shown about the case of MC 3, where the soil preparation was most difficult. At MC 3, twenty seven penetration tests were conducted before every tillage run. The cone was penetrated at the center of the soil box and twenty seven depth-force diagrams were obtained. From them, the average penetration forces from soil surface to the four depths (3, 5, 10 and 13 cm) and the standard deviation were obtained. Table 7 shows the result that the coefficient of variation was about 10 %. This means that the immanent nonuniformity of soil strength is one of the reasons for the large prediction errors.

The analysis of variance concerning with the prediction error (A) was also conducted. Through the analysis, it was found that only MC was significant at 5 % critical rate and the other factors or the interactions proved to be judged insignificant. It comes to a conclusion that a series of cones as an analog could not function so as to correspond with the change

of soil conditions. Naturally, the prediction based on the exponents gained from each MC level lacks universal validity for practical use. In conclusion, an analysis of prediction errors will be necessary along with the development of better analogs. To put it concretely, it is important to decrease and measure the effects of test facility and method on prediction errors in order to throw light upon true validity of an analog device.

Table 7. Variations of the strength of soil prepared.

depth (cm)	3	5	10	13
average cone force (N)	123.8	165.8	183.9	181.9
standard deviation (N)	13.8	16.9	17.3	21.8
coefficient of variation (%)	11.1	10.2	9.4	12.0

REFERENCES

- 1) R. L. Schafer et al. : An Interpretation of Distortion in the Similitude of Certain Soil-Machine Systems. Trans. of the ASAE, 12(1), 145-149, 1969
- 2) R. L. Schafer and C. A. Reaves : Distorted Model Predictions Using an Analog Device. Trans. of the ASAE, 19(6), 1008-1014, 1976
- 3) C. E. Johnson et al. : Some Soil-Tool Analogs. Trans. of the ASAE, 23(1), 9-13, 1980



↙ THE ANALYSIS ON THE DYNAMIC PERFORMANCE OF A SINGLE LUG

TAI LING ZHANG YAO JIAN SHAO
SOUTH CHINA AGRICULTURAL COLLEGE

AD-P004 289

SUMMARY

The lug of a rigid lugged wheel for the paddy-field tractor is the basic element to interact with soil. The lug angle has significant effect on the tractive performance of a rigid lugged wheel in rice field.

This paper analyses the interaction process between lug and soil. A calculating method of the soil reaction on a single lug based on the equation of passive pressure in two dimensional soil failure is presented. It is shown that there is a good agreement between the measured and predicted pull and lift forces developed by a single lug within the test range. Based on the law of conservation of energy, the dynamic performance of a lug is predicted according to energy distribution under lug-soil interaction, and a computer program is developed. The vertical vibration of wheel axle, the unsteadiness of speed and slip of multi-lugs wheel are studied theoretically and preliminarily.

INTRODUCTION

The lug is the basic element to interact with soil, and it has significant effect on the performance of wheeled tractor.

According to the Law of Conjugate Action between two meshing profiles and the kinematics of lug, Y.J. Shao proposed nine equations for geometrical parameters of lug with respect to slip. (1)¹Deng and Yu analyzed the flow pattern of soil beneath lug, they noted that the failure zone was nearly a logarithmic spiral and straight line, and that the equation of passive failure proposed by Hettiaratchi and Reece (3) was adoptable to predict the maximum thrust of lug at definite position in paddy field, and there was good agreement between the measured and predicted values. (2)

D. Gee-Clough (4,5,6) in his paper studied and determined the influence of various parameters on the forces of single lug. He applied Bekker's pressure-sinkage equation and Reece's equation to calculate the soil reaction on lug. His recent experiment into the effect of lug angle to performance came to conclusion that 30° lug angle wheel obtained the largest tractive power.

Besides, J.Y. Wong (7), L.L. Karafiath and E.A. Nowatzki also (8) studied and analysed the lug-soil interaction.

In this paper, experiments were conducted in soil bin to measure the soil reactions on a single lug. This paper analyses the interaction process between lug and soil. A calculating method of the soil reaction on a single lug based on the equation of passive pressure in two-dimensional soil failure is presented. Based on the Law of Conservation of Energy, the dynamic performance of a single lug is predicted and evaluated. The vertical vibration of wheel axle and the unsteadiness of speed and slip of lugged wheel under fluctuating soil reaction are studied theoretically and preliminarily.

I. APPARATUS AND EXPERIMENT METHODS

All experiments were conducted at a soil bin built in the Department of Agricultural Machinery at South China Agricultural College. The soil bin has a dimension of 20m length x 1.6m width x 1.0m depth. The soil layers in soil bin are shown in Fig. 1. The paddy field soil formed by long period cultivation of rice were taken from the College Farm. The grain sizes of soil and their distribution are shown in Fig. 2 that the various size of particles are in good composition.

In order to measure the soil reaction, an experimental flat lug model 120mm in length x 200mm in width was designed, its inclined angle was adjustable from 3° - 50° , and its radius of tip was adjustable from 350-450mm. An octagonal sensor which had good linear relationship between measured forces and deformation was set between the lug and powered shaft to measure the soil reaction R and its radial component R_n and tangential component R_t as shown in Fig. 3, 4, 5.

The lug tester had two motors, of which one motor was used to drive the shaft of lug and the other motor to control the slip and speed. All forces from soil reaction were picked up by strain amplifier and graphed by recorder. The rotational speed of the model lug was set at 6.34 rpm. The sinkage of the lug was controlled at 138mm measured from tip.

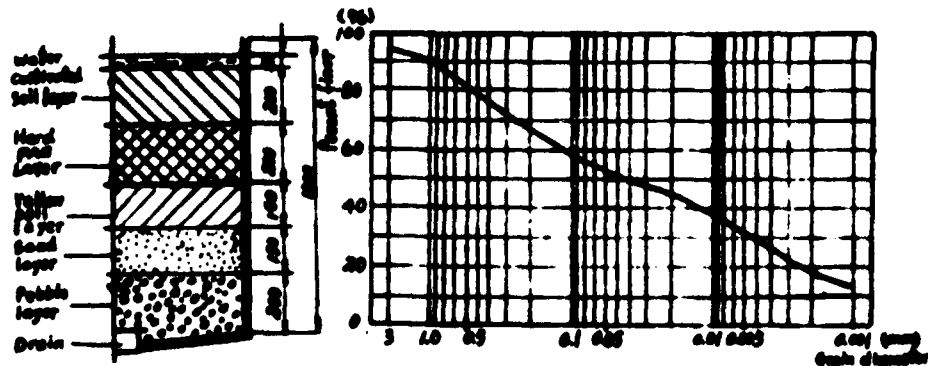


Fig.1 Soil layers in soil bin

Fig.2 Soil grain sizes and distribution

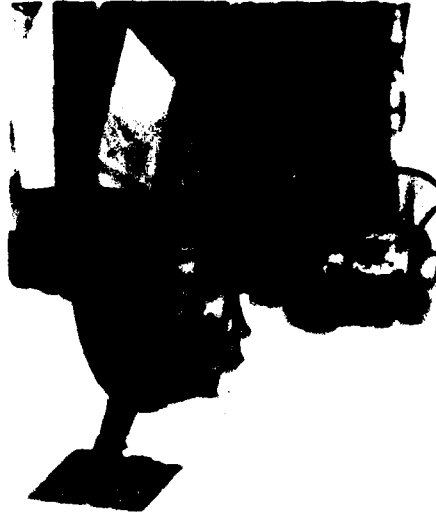


Fig.3 The model lug
with sensor



Fig.4 The lug tester

The soil reactions were measured at various slips (15%, 25%, 40%) and inclined angles (15°, 27°, 30°, 35°) of the model lug. The water content, cohesion and internal friction angle of soil at various depth (30mm, 80mm, 130mm) were tested before experiment. From the tests, the values of cohesion c increased with depth, but there were small changes in the internal friction angle.

The relationship of shear-displacement of the soil in soil bin could be expressed in Janosi Formula:

$$\tau = \tau_{max} (1 - e^{-j/k}) \quad (1 - 1)$$

In order to obtain the value of k , expression (1 - 1) was transformed into the following expression by means of a logarithmic method.

$$\ln(1 - \tau/\tau_{max}) = -j/k \quad (1 - 2)$$

The adhesion and external friction angle of the soil in soil-bin were also tested.

II. THE MEASURED SOIL REACTIONS

The recorded soil reactions from experiments were the radial component R_n and tangential component R_t as shown in Fig. 5a. Their relationship with vertical component R_z and horizontal component R_x may be expressed in the following equation:

$$\begin{Bmatrix} R_x \\ R_z \end{Bmatrix} = \begin{bmatrix} \cos(\theta + \alpha) \sin(\theta + \alpha) \\ \sin(\theta + \alpha) - \cos(\theta + \alpha) \end{bmatrix} \begin{Bmatrix} R_t \\ R_n \end{Bmatrix} \quad (2 - 1)$$

where

$$\alpha = \tan^{-1} \left[\frac{AB \sin(\beta - \angle ABC)}{r_0 - AB \cos(\beta - \angle ABC)} \right] \quad (2 - 2)$$

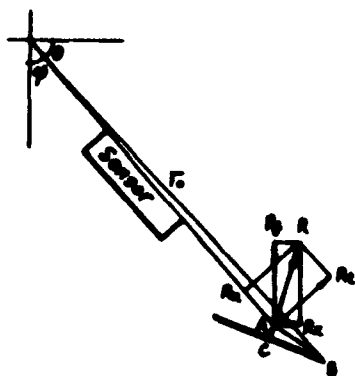
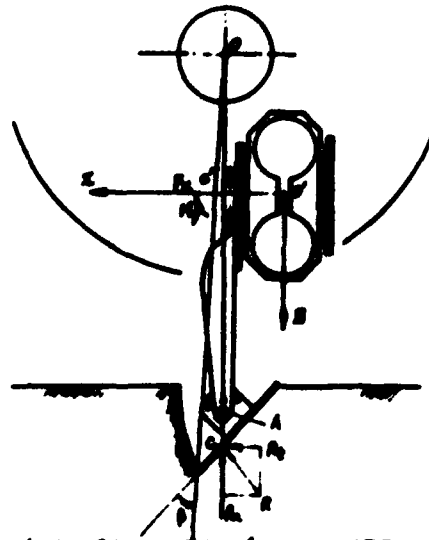


Fig. 5 The soil reactions measuring

Fig. 6 The analysis of measured force system



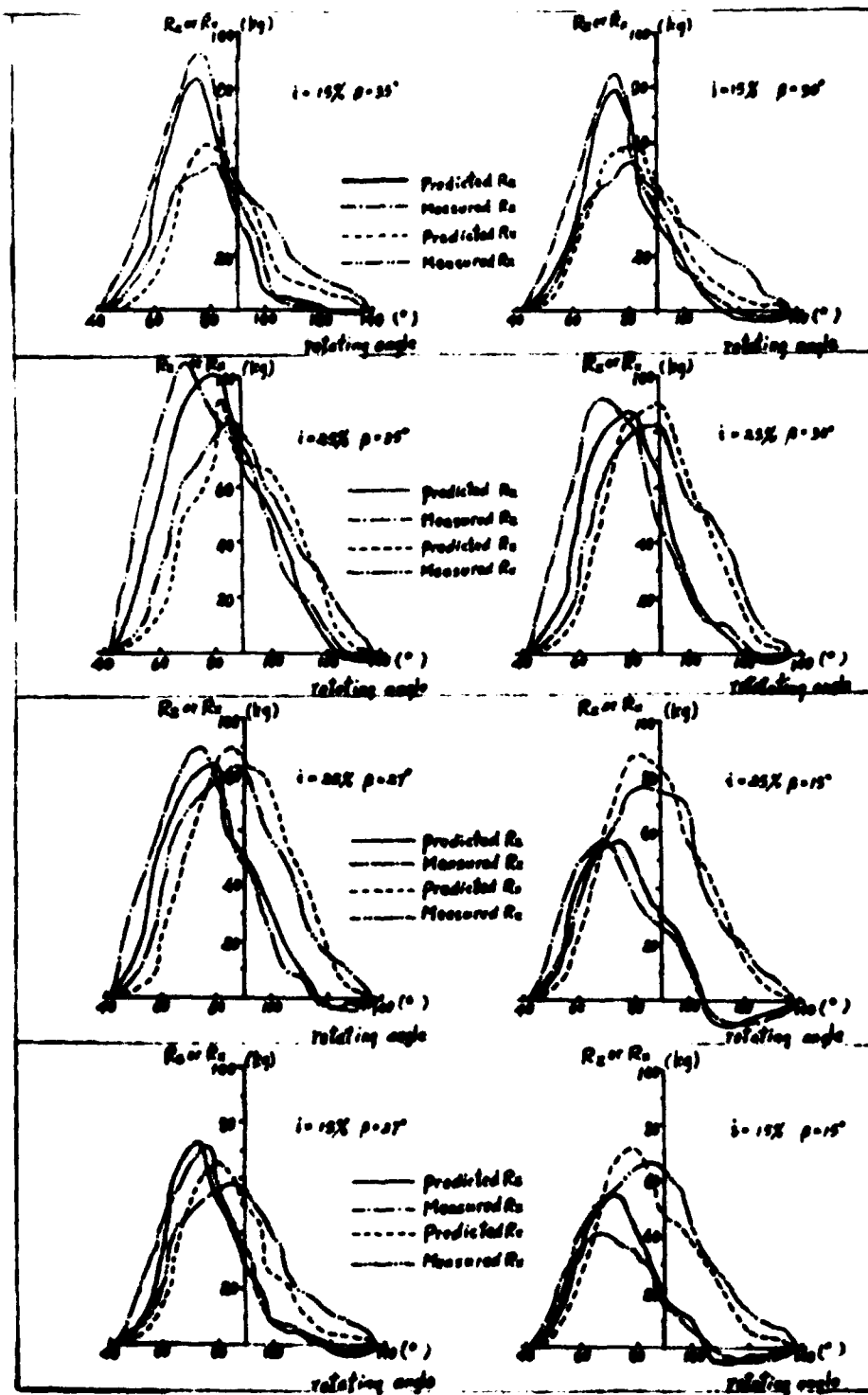
Substitute the following values ($AC = 30\text{mm}$, $BC = 60\text{mm}$, $\angle ABC = 26.57^\circ$, $AB = 67.11\text{mm}$, $r = 425\text{mm}$) into equation (2 - 2) and obtain the angle β under various inclined angle of lug as in the following table:

β	15°	27°	30°	35°
β	-2.15°	0.08°	0.64°	1.57°

From the above table, it is shown that the angle β is very small so that the measured R_t, R_r forces may be considered as the dynamic radial force and tangential force of the wheel at lug tip, and a resolution of these forces into vertical components R_z and horizontal components R_x can be calculated.

The measured values of R_z and R_x beneath single lug with $15^\circ, 27^\circ, 30^\circ, 35^\circ$ inclined angle at $15\%, 25\%$ slip under the same controlled sinkage 138mm are shown in the figures of Fig. 7. It is observed from the curves that all the soil reactions R_z, R_x at 25% slip are larger than those at 15% slip, and that the vertical components R_z obviously increase with inclined angles but the horizontal components R_x only have slight variation. It is noted that the R_z and R_x reach maximum before the lug arrives at its lowest position ($\theta = 90^\circ$), that the $R_{z\text{max}}$ always earlier than $R_{x\text{max}}$ by about 10° , that is, the maximum R_z exhibits at $\theta = 70^\circ - 80^\circ$ and maximum R_x at $80^\circ - 90^\circ$. It is interesting to note that a negative R_z ($-R_z$) is presented while the lug leaves the soil with scooping action, and that the lug with less inclined angle will have larger negative R_z , and the more the slip, the larger the negative R_z .

Fig. 7(next page) The measured and predicted soil reaction R_z and R_x



III. THE PREDICTION OF SOIL REACTION R_1

A calculating method of the soil reaction of a single lug based on the equation of passive pressure in two dimensions soil failure proposed by Hittiaratchi and Reese (9) is true for this prediction. The general passive soil resistance of the lug interface in unit width can be written in terms of the symbols defined in Notation by the following expression:

$$R_1 = f(c, \phi, \gamma, \delta, a, s, \alpha, q) \quad (3-1)$$

The soil reaction R_1 may be broken down into two parts, the adhesive component acting along the interface ($A = az \cos \alpha \sec \alpha$), and P the frictional component acting at an angle with the normal to the interface. The magnitude of P may be expressed in the following equation in which symbols defined in Notation.

$$P = \gamma z^2 K_1 + cz K_{c1} + qz K_q - \gamma z^2 K_2 e^{-\alpha z} \quad (3-2)$$

The angle between vector of P and normal to interface is δ as shown in Fig. 8.

The soil reaction R_1 to interface in unit width may be written as:

$$\bar{R}_1 = \bar{P} + \bar{A} \quad (3-3)$$

That is:

$$R_1 = (P^2 + A^2 + 2PA \sin \delta)^{1/2} \quad (3-4)$$

The angle δ_1 between R_1 and normal of interface is given by the following expression:

$$\delta_1 = \delta + \sin^{-1}(A \cos \delta / R_1) \quad (3-5)$$

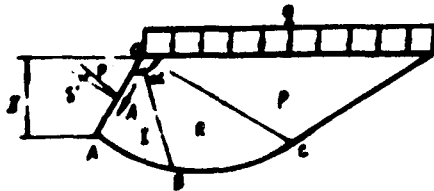


Fig. 8 Passive soil failure



Fig. 9 Horizontal shear displacement

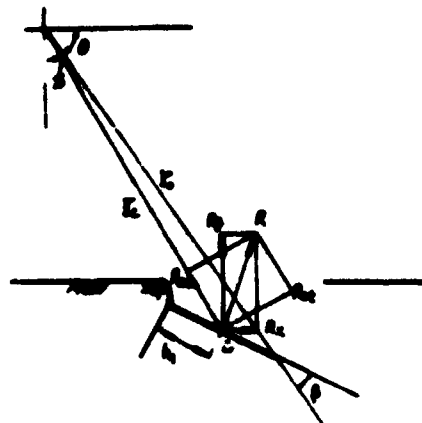


Fig. 10 Analysis of predicted forces

$$\text{Let } P_1 = czK_c + qzK_0$$

$$P_2 = \gamma z^2 (K_1 - K_2 n^{-3})$$

and the distance h_1 from the acting point of R_1 to the upper end of the interface is given by :

$$h_1 = z \operatorname{cosec} \alpha \operatorname{cosec} \delta \sec \delta \gamma [(3P_1 + 4P_2) / 6R_1] \quad (3 - 6)$$

The above expression is adaptable at the following range of values:

$$(a) \quad 5^\circ < \alpha < 170^\circ$$

(δ is the angle between the direction of motion of interface at upper end and horizontal line)

$$(b) \quad 0^\circ \leq \phi \leq 45^\circ$$

$$(c) \quad S: 0 \rightarrow \infty$$

According to a preliminary calculation, the value of P_2 is only about 1% of the friction component P . In order to simplify the calculation, the last term of P_2 may be neglected, and (3 - 2) may be simplified and expressed as:

$$P = \gamma z^2 K_1 + czK_{ca} + qzK_0 \quad (3 - 2)$$

where K_{ca} and K_0 are given by the following expressions:

$$K_{ca} = (N^2 - 1) \sec \delta \operatorname{cosec} \alpha \cot \phi \quad (3 - 7)$$

$$K_0 = N^2 \sec \delta \operatorname{cosec} \alpha \quad (3 - 8)$$

and according to (15), K_1 is approximately equal to $0.5 K_0$, we take,

$$K_1 = 0.5 K_0 \quad (3 - 9)$$

The N^2 in (3 - 7) and (3 - 8) may be calculate according to the following table.

α	δ	N^2
$\geq \alpha$	$\leq \phi$	N_1, N_2
$\leq \alpha$	$< \phi$	N_1, N_3

and in above table,

$$N_1 = \left\{ \operatorname{cosec} \delta \left[\operatorname{cosec} \delta (\sin^2 \phi - \sin^2 \delta) \right]^{\frac{1}{2}} \right\} / (1 - \sin \phi) \quad (3 - 10)$$

$$N_2 = \exp \left[(2\alpha + 2\mu - \pi) \tan \phi \right] \quad (3 - 11)$$

$$N_3 = \left\{ [1 - \sin^2 \phi \sin^2 (\alpha + \mu)]^{\frac{1}{2}} - \sin \phi \cos (\alpha + \mu) \right\}^2 / \cos^2 \phi \quad (3 - 12)$$

$$\alpha = \frac{\pi}{2} - \frac{1}{2}(\alpha + \delta)$$

$$\mu = \frac{\pi}{2} - \frac{\phi}{2}$$

In paddy field soil it seems to be important that the sideway shear resistance of soil for the tested lug with larger L/B ratio may not be neglected in calculating soil reactions beneath lug. According to (10), the equation of sideway shear resistance proposed by A.R. Reece was adaptable for soft paddy field soil. The lateral shear resistance may be expressed as:

where
$$\zeta_s = \begin{cases} 0 & \text{for } (z > B/2) \\ 2\sin(\frac{\pi}{4} + \frac{\phi}{2}) & \text{for } (z \leq B/2) \end{cases} \quad (3-13)$$

B -- the width of lug.

The lateral force S may be taken as:

$$S = S_1 + S_2 \quad (3-14)$$

where
$$S_1 = 0.25 L_1^2 \cot \phi \left\{ \exp[2(\alpha + \frac{\phi}{2} - \frac{\pi}{4}) \tan \phi] - 1 \right\}$$

$$S_2 = 0.5 L_1^2 \exp[2(\alpha + \frac{\phi}{2} - \frac{\pi}{4}) \tan \phi] \cos \phi$$

L_1 -- the contact length of lateral interface.
The lateral shear resistance P_s may be expressed as:

$$P_s = 2S \cdot \zeta_s \quad (3-15)$$

It is considered that the lateral shear resistance depends on c , so P_s is taken as a part of P_1 .

Then the rest is to determine the value of j according to the slip line, as shown in Fig.9. Take O at upper end of lug as the center (pole) of logarithmic spiral, and then draw the logarithmic spiral from lug tip. The spiral intersects the interface of lug at point A_1' . The horizontal distance from A_1 to A_1' represents a part of horizontal shear displacement j_1 . The horizontal shear displacement j for lug position A_1 may be expressed by the sum of partial displacements from A_1 to A_1' as:

$$j = \sum j_1 \quad (3-16)$$

The lug force R can be summed up by the following expression.

$$R = \left[(P_1^2 + (BA)^2 + 2P_1 BA \sin \delta \right]^{1/2} (1 - e^{-\sqrt{k}}) \quad (3-17)$$

where
$$P_1 = B(P_1 + \sqrt{\gamma} K_1) + P_s$$

Thus the vertical component R_z and horizontal component R_x of the soil reaction R on the single lug as shown in Fig.10 may be expressed as follow:

$$R_x = R \sin(\theta - \delta - \beta) \quad (3-18)$$

$$R_z = R \cos(\theta - \delta - \beta) \quad (3-19)$$

All the above equation was programmed and the R_x and R_z may be computed on a computer without using curves from chart. The computed values and curves are shown in Fig.7 in comparison with measured curves. It may be seen from these curves that there is good agreement between the predicted curves and measured curves.

IV. A THEORETICAL ANALYSIS INTO THE
DYNAMIC PERFORMANCE OF A SINGLE LUG

The dynamic performance of a single lug is analysed based on the Law of Conservation of Energy and according to the distribution of energy.

Suppose a single lug turns uniformly an angle of $d\theta$ under the torque $M(\theta)$, the input energy of the lug is $M(\theta)d\theta$, and a part of the energy will transform into available energy of pull $R_x(\theta)r d\theta$, and the other part of energy E consumed on overcoming the motion resistance, slip and soil deformation. The equation of energy equilibrium of a single lug may be expressed as follow:

$$\int_{\theta_1}^{\theta_2} M(\theta) d\theta = \int_{\theta_1}^{\theta_2} R_x(\theta) r d\theta + E \quad (4-1)$$

where θ_1, θ_2 -- the rotating angle of wheel as the lug enters the soil and leaves the soil,
 r -- the rolling radius of lug, $r = r_0(1 - i)$.

In order to evaluate the dynamic performance of a single lug based on the distribution of energy, the efficiency of the lug is defined as the ratio of output energy to input energy in the process of lug-soil interaction, that is:

$$\eta_{\text{lug}} = \frac{\int_{\theta_1}^{\theta_2} R_x(\theta) r d\theta}{\int_{\theta_1}^{\theta_2} M(\theta) d\theta} \quad (4-2)$$

Suppose the axle of wheel travels a distance of S_r while the lug moves from a position of entering the soil to other position of leaving the soil.

$$S_r = r_0(1 - i)(\theta_2 - \theta_1) = r_0(1 - i)\theta_r \quad (4-3)$$

dividing (4-2) by (4-3),

$$\frac{\int_{\theta_1}^{\theta_2} M(\theta) d\theta}{S_r} = \frac{\int_{\theta_1}^{\theta_2} R_x(\theta) r d\theta}{S_r} + \frac{E}{S_r} \quad (4-4)$$

Each term of the above expression (4-4) does have the dimensional quantity of force, so the average thrust H_{ave} , average pull P_{ave} and average motion resistance f_{ave} may be defined by the following expressions:

$$H_{\text{ave}} = \frac{1}{S_r} \int_{\theta_1}^{\theta_2} M(\theta) d\theta \quad (4-5)$$

$$P_{\text{ave}} = \frac{1}{S_r} \int_{\theta_1}^{\theta_2} R_x(\theta) r d\theta \quad (4-6)$$

$$f_{\text{ave}} = E / S_r \quad (4-7)$$

and $H_{\text{ave}} = P_{\text{ave}} + f_{\text{ave}}$

From (4-2),

$$P_{ave} = \frac{1}{S_T} \int_{\theta_1}^{\theta_2} R_x(\theta) r d\theta = \frac{1}{\theta_T} \int_{\theta_1}^{\theta_2} R_x(\theta) d\theta$$

The average bearing reaction W_{ave} may be expressed as:

$$W_{ave} = \frac{1}{\theta_T} \int_{\theta_1}^{\theta_2} R_z(\theta) d\theta \quad (4-8)$$

According to expressions (4-2), (4-6), (4-8) and the measured soil reaction, the relationship between P_{ave} , W_{ave} , η_{lug} and β can be plotted as shown in Fig. 11. From this figure, it is noted that all the W_{ave} and P_{ave} of single lug at various inclined angle increase with slip, and that at a given slip the W_{ave} increases but P_{ave} decreases with inclined angle. It is noted that the efficiency of lug at a given slip decreases with its inclined angle within the range of 15 - 35°.

The powered wheel always works with a definite load on axle. Suppose that an average bearing reaction of 30kg is needed to assure a sinkage of 138mm for the experimental lug.

In Fig. 11, draw a straight line ABCD parallel to axis from the point $W_{ave} = 30\text{kg}$. It is seen that at $W_{ave} = 30\text{kg}$ and at the same sinkage of 138mm the corresponding slips are 32%, 17%, 13% and 10% for inclined angles of 15°, 27°, 30°, 35° respectively. From point ABCD draw vertical lines upward and intersect the $\eta_{lug} - \beta$ curves of various slips at A'B'C'D' respectively. Curve A'B'C'D' is the curve of $\beta - \eta_{lug}$ relationship. From this curve it is noted that theoretical efficiency of lug reaches maximum at an inclined angle of 28° with a respective slip of 11%.

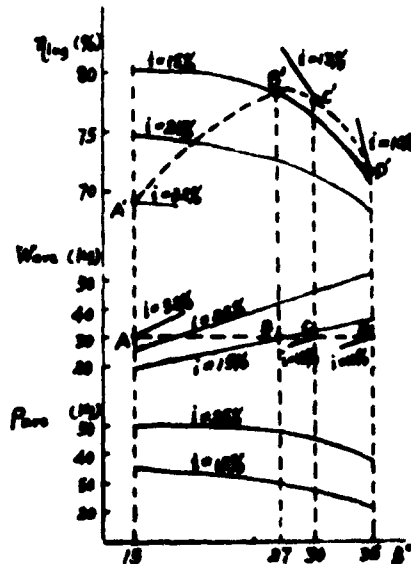


Fig. 11 The $\beta - \eta_{lug}$ curve A'B'C'D'

According to the above method of calculation of soil reaction and the analysis of dynamic performance of lug, the following procedure to predict the performance of single lug is recommended:

1. The following input data should be known:
 - (a) the soil parameters: $c, \phi, a, \delta, \gamma$,
 - (b) the geometrical parameters of lug: L, B, T_0, β ,
 - (c) the average bearing reaction and adoptable sinkage: W_{avg}, S .
2. To predict R at various slip, calculate $R_g(\theta)$ and the W_{avg} by means of Simpson's integral method.
3. To predict average pull P_{avg} according to R obtained from 2nd step and the correspondent slip i .
4. To predict the efficiency of lug by means of Simpson's integral method according to expression (4 - 2).
5. Repeat the above procedure of calculation at various inclined angle β , compare to obtain the maximum efficiency and the correspondent β .

A flow chart of computer program for the above predictions is shown in Fig.12.

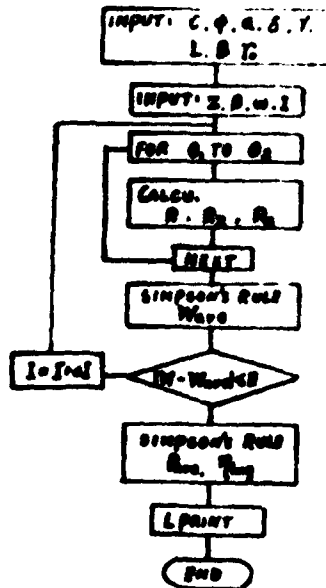


Fig.12 A flow chart of computer program to predict performance of lug

V. THE VERTICAL VIBRATION OF WHEEL AXLE AND
THE UNSTEADINESS OF SPEED AT DIFFERENT SLIPPAGE

From the experiment it was noted that the soil reaction on single lug was fluctuating and that the axle of the rigid wheel with limited quantity of lugs vibrated in the vertical direction and its speed and slip varied in travel direction, as shown in Fig.13.

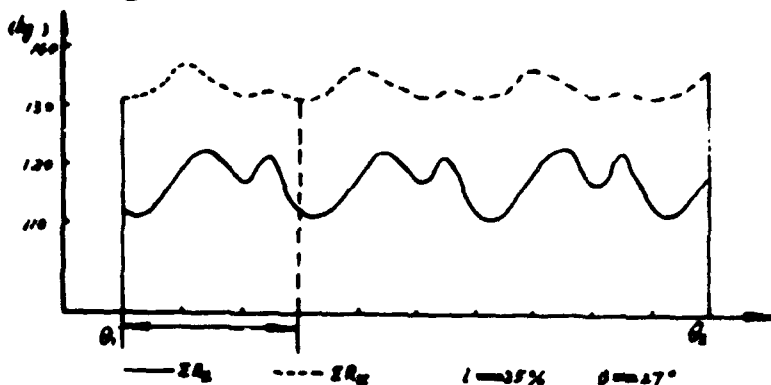


Fig.13 The soil reactions on the wheel with twelve lugs

Suppose that the motion of a rigid lugged wheel is a plane motion system of rigid body. In Fig. 14, point O' is the origin of the motional coordinate system, and o coincides with the center (axle) of the wheel. The angular speed of the wheel is expected as constant and the motion of wheel axle may be expressed by the following differential equations.

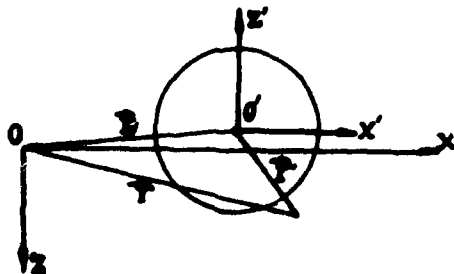


Fig.14 The coordinate system

$$\begin{cases} m \ddot{x} = \sum_i R_x^i - T_1 \\ m \ddot{z} = G - \sum_i R_z^i \end{cases}$$

where $\sum_i R_x^i$ - the sum of soil reaction on the lugs in X direction
 $\sum_i R_z^i$ - the sum of soil reaction on the lugs in Z direction
 T_1 - the motional resistance in X direction
 G - the load on the wheel axle
 m - the mass of wheel.

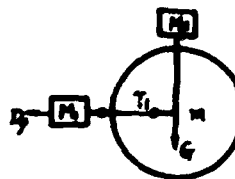


Fig.15 The analogous force system

(5 - 1)

DAI A148 635

PROCEEDINGS OF THE INTERNATIONAL CONFERENCE ON THE
PERFORMANCE OF OFF-ROAD (VI) INTERNATIONAL SOCIETY FOR
TERRAIN-VEHICLE SYSTEMS M J DWYER AUG 84

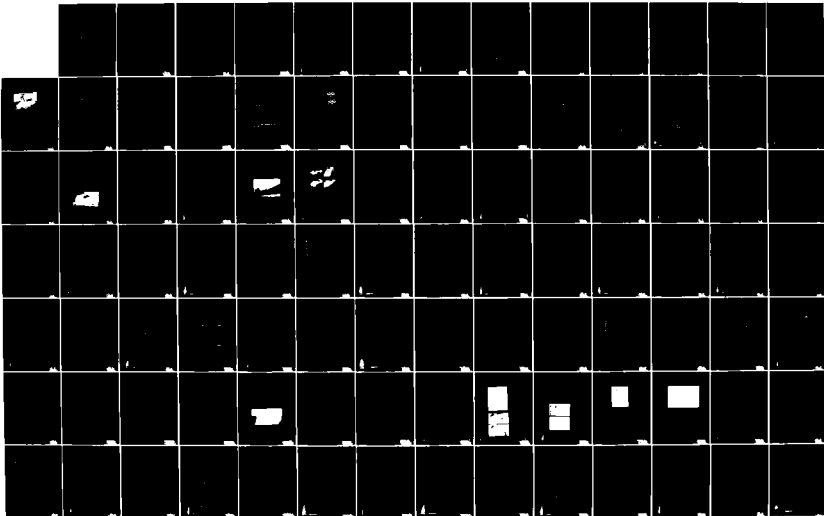
215

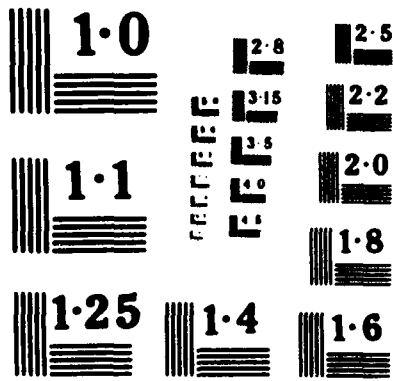
UNCLASSIFIED

DAJA45-84-M-0251

F/G 13/6

NL





Based on the analogous force system as shown in Fig.15, then we have:

$$\begin{cases} T = D + M\ddot{x} \\ G = (M_2 + m)g - M\ddot{z} \end{cases}$$

where D — constant towed resistance
 M — the mass of the towed tester
 M_2 — the disposal mass on the wheel axle

Consequently, the equation (5 - 1) may be rewritten as:

$$\begin{cases} (M_1 + M_2 + m)\ddot{x} = \sum R_x^i - D \\ (M_2 + m)\ddot{z} = (M_2 + m)g - \sum R_z^i \end{cases} \quad (5 - 2)$$

To solve the equation (5 - 2), the $\sum R_x, \sum R_z$ curve in the range between the entry angle into soil and outgoing angle of soil with respect to a specific lug as shown in Fig.15 may be expressed in Fourier series.

Let $\theta = \frac{\theta_T}{2n} i \quad (i = 0, 1, 2, \dots, 2n-1)$.

then $R_x(\theta_i) = \frac{a_0}{2} + \sum_{k=1}^{n-1} [a_k \cos(\frac{k\pi}{n} i) + b_k \sin(\frac{k\pi}{n} i)] + \frac{a_n}{2} \cos(in) \quad (5 - 3)$

where $a_k = \frac{1}{n} \sum_{i=0}^{2n-1} R_x(\theta_i) \cos(\frac{k\pi}{n} i), \quad (k = 0, 1, 2, \dots, n)$

the same as above $b_k = \frac{1}{n} \sum_{i=0}^{2n-1} R_x(\theta_i) \sin(\frac{k\pi}{n} i), \quad (k = 1, 2, \dots, n-1)$

where $R_x(\theta_i) = \frac{C_0}{2} + \sum_{k=1}^{n-1} [C_k \cos(\frac{k\pi}{n} i) + d_k \sin(\frac{k\pi}{n} i)] + \frac{C_n}{2} \cos(in) \quad (5 - 4)$

$C_k = \frac{1}{n} \sum_{i=0}^{2n-1} R_x(\theta_i) \cos(\frac{k\pi}{n} i), \quad (k = 0, 1, 2, \dots, n)$

$d_k = \frac{1}{n} \sum_{i=0}^{2n-1} R_x(\theta_i) \sin(\frac{k\pi}{n} i), \quad (k = 1, 2, \dots, n-1)$

Substitute equations (5-3), (5-4) into equation (5-2), and let $\dot{x} = V_{in}, x = 0, \dot{z} = V_{oz}, z = 0$ at $\theta_i = 0$. The solutions of the equation (5-2) may be expressed as follow:

$$\begin{cases} \dot{x}(\theta_i) = \left\{ \frac{1}{(M_1 + M_2 + m)\omega} \sum_{k=1}^{n-1} D_k + V_{in} \right\} + \frac{1}{(M_1 + M_2 + m)\omega} \left\{ \frac{C_0}{2} \theta_i + \sum_{k=1}^{n-1} [C_k \sin(\frac{k\pi}{n} i) - D_k \cos(\frac{k\pi}{n} i)] - D_1 \theta_i \right\} \end{cases} \quad (5 - 5)$$

$$\begin{cases} x(\theta_i) = \frac{1}{(M_1 + M_2 + m)\omega^2} \left[\sum_{k=1}^{n-1} \frac{C_k^2}{C_k} - \frac{C_n^2}{2C_n} \right] + \frac{1}{(M_1 + M_2 + m)\omega^2} \left\{ \frac{C_0}{2} \theta_i^2 - \sum_{k=1}^{n-1} \left[\frac{C_k^2}{C_k} \cos(\frac{k\pi}{n} i) + \frac{D_k^2}{D_k} \sin(\frac{k\pi}{n} i) - D_k \theta_i \right] - \frac{C_n}{2C_n} \cos(in) - \frac{D_1}{2} \theta_i^2 \right\} + \frac{V_{in}}{\omega} \theta_i \end{cases} \quad (5 - 6)$$

where $C_k = a_k \frac{\theta_T}{2n}, \quad D_k = d_k \frac{\theta_T}{2n}, \quad C_n = a_n \frac{\theta_T}{2n}$

$$\begin{cases} \dot{z}(\theta_i) = \left[V_{oz} - \frac{1}{(M_2 + m)\omega} \sum_{k=1}^{n-1} B_k \right] + \frac{g}{\omega} \theta_i - \frac{1}{(M_2 + m)\omega} \left\{ \frac{a_0}{2} \theta_i + \sum_{k=1}^{n-1} [A_k \sin(\frac{k\pi}{n} i) - B_k \cos(\frac{k\pi}{n} i)] \right\} \\ z(\theta_i) = \frac{1}{(M_2 + m)\omega^2} \left[\sum_{k=1}^{n-1} \frac{A_k^2}{A_k} + \frac{B_n^2}{2B_n} \right] + \frac{g}{2\omega^2} \theta_i^2 - \frac{1}{(M_2 + m)\omega^2} \left\{ \frac{a_0}{2} \theta_i^2 - \right. \end{cases} \quad (5 - 7)$$

$$-\sum_{k=1}^{n-1} \left[\frac{A_k^2}{a_k} \cos\left(\frac{k\pi}{n} t\right) + \frac{B_k^2}{b_k} \sin\left(\frac{k\pi}{n} t\right) - B_k \theta_i \right] - \frac{A_n^2}{2a_n} \cos(\pi t) + \frac{V_{ax}}{\omega} \theta_i$$

where $A_k = a_0 \frac{\partial^2}{\partial t^2}$, $B_k = b_0 \frac{\partial}{\partial t}$, $A_n = a_0 \frac{\partial^2}{\partial t^2}$ (5-5)

It is clear from all the terms on right side of equations (5-5) to (5-8) are unvaried terms indicating the non-fluctuating value, but that the second and third terms are fluctuating with angle θ_i .

Let the speed $v_0 \omega (1-1)$ of the wheel axle equals the first term of equation (5-5) on right side, then

$$v_{ax} = v_0 \omega (1-1) = \frac{1}{(M_2 + m)\omega} \sum_{k=1}^{n-1} D_k \quad (5-6)$$

The same for the vibration of the wheel axle along the vertical direction:

$$z_{b01} = \frac{-1}{(M_2 + m)\omega} \left\{ \sum_{k=1}^{n-1} \frac{A_k^2}{a_k} + \frac{A_n^2}{2a_n} \right\} \quad (5-7)$$

If the wheel was in a steady state of uniform motion under fluctuating soil reaction, all points of identical base under cyclical external force should have the same speed and the same Z coordinate. Then we have:

$$\begin{cases} \dot{z}(\theta) = v_{ax} = \dot{z}(\theta_s) \\ z(0) = 0 = z(\theta_s) \end{cases}$$

and then

$$(M_2 + m)z = \frac{a_0}{2} + \frac{1}{\omega_s} \left\{ \sum_{k=1}^{n-1} \left[A_k \sin\left(\frac{2k\pi}{\theta_s} \theta_s\right) - B_k \cos\left(\frac{2k\pi}{\theta_s} \theta_s\right) + B_k \right] + \frac{A_n}{2} \sin\left(\frac{2n}{\theta_s} \theta_s\right) \right\} \quad (5-11)$$

$$v_{ax} = \frac{1}{2\theta_s} \theta_s + \frac{1}{(M_2 + m)\omega_s} \left\{ \frac{a_0}{2} \theta_s^2 - \sum_{k=1}^{n-1} \frac{A_k^2}{a_k} \cos\left(\frac{2k\pi}{\theta_s} \theta_s\right) + \frac{B_k^2}{b_k} \sin\left(\frac{2k\pi}{\theta_s} \theta_s\right) - B_k \theta_s - \frac{A_k^2}{a_k} - \frac{A_n^2}{2a_n} \cos\left(\frac{2n\pi}{\theta_s} \theta_s\right) + \frac{A_n^2}{2a_n} \right\} \quad (5-12)$$

the same as above,
 $\dot{x}(0) = v_{ox} = \dot{x}(\theta_s)$

then

$$D_r = \frac{c_0}{2} + \frac{1}{\theta_s} \left\{ \sum_{k=1}^{n-1} \left[C_k \sin\left(\frac{2k\pi}{\theta_s} \theta_s\right) + D_k \cos\left(\frac{2k\pi}{\theta_s} \theta_s\right) \right] + \frac{C_n}{2} \sin\left(\frac{2n\pi}{\theta_s} \theta_s\right) \right\} \quad (5-13)$$

The conditions of steady motion were defined by the equations (5-11), (5-13).

The position $X(\theta_i)$, the speed $\dot{X}(\theta_i)$ in X direction and the position $Z(\theta_i)$, the speed $\dot{Z}(\theta_i)$ in Z direction could be calculated by the equations (5-9), (5-11) to (5-13) and the equations (5-5) to (5-8). From the curve shown in Fig.16, it is shown that the slip is changed with angle θ_i in a range of about 0.3 to 0.2 ($M_2 + m = 117.3kr$, $V_0 = 135kr$, $D_0 = 1303.92$, $\beta = 27^\circ$). The locus of the wheel axle is shown in Fig.17, the fluctuation is in a magnitude of about 1.4cm.

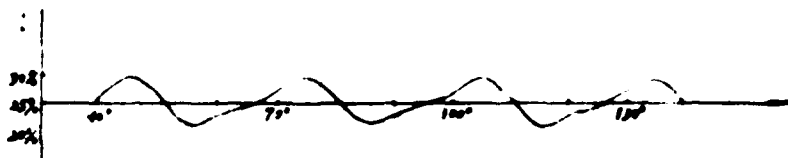


Fig. 16 The fluctuation of slip

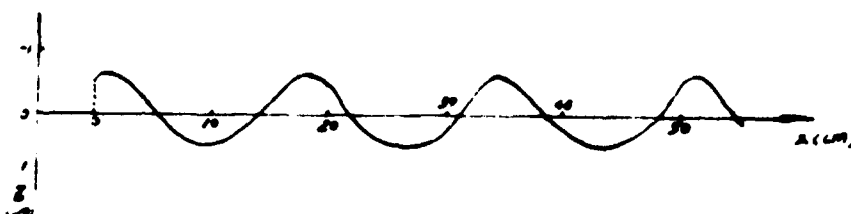


Fig. 17 The locus of a wheel axle

Based on the previous analysis, the vibration of wheel axle and the unsteadiness of speed and slip are certain and will give effect to some variation on locus of lug tip.

CONCLUSION

The lug of a rigid powered wheel is the basic element to interact with the soil. The lug angle has significant effect on the tractive performance of a rigid wheel in paddy field.

This paper describes the experiments in measuring the soil reactions on a single model lug with various inclined angle and slip in soil bin. A calculating method of the soil reactions on single lug based on the equation of passive pressure in two dimensional soil failure is presented. It is shown that there is good agreement between the measured and predicted pull and lift soil reactions on a single lug within the test range, and that the equation of passive soil resistance proposed by D.R.P. Mettiaratchi and A.R. Reece is adoptable for the tested paddy field soil in the evaluation for the soil reactions on a single lug.

A method to predict the dynamic performance of a single lug according to the energy distribution under lug-soil interaction is presented.

A preliminarily theoretical study into the vertical vibration of the wheel axle and the unsteadiness of speed and slip under fluctuating soil reaction is presented. It is shown on curves that the vibrating magnitude of the wheel axle is

1.4 cm, and the magnitude of understeer of slip is also 10%.

REFERENCES

1. Shao Y.J. Advanced analysis on the design of geometrical parameters of the blade-lug for the paddy-field wheel tractor, Proceedings 7th Int. Con. ISTVS pp1509-1551, 1981
2. Deng Z.R., You S.C. An investigation of the thrust of paddy tractor driving wheel, a paper of 1st Chinese TMSRC Con., 1982
3. Hettiaratchi D.R.P., Witney B.D., Reece A.R., The calculation of passive pressure in two dimensional soil failure, J. Agric. Engrg. Res. 1966, Vol.11
4. Gee-Clough D., Chancellor W., Pull and lift characteristics of single lug on rigid wheels in wet rice soils, Trans of the ASAE Vol.19, No.3, 1976
5. Gee-Clough D., A method for calculating the forces produced by open, lugged wheels, Proceedings 6th Int. Con, ISTVS, pp707-733, 1977
6. Gee-Clough D. etc, Recent research into vehicle performance in wetland condition, Proceedings 7th Int. Conf. ISTVS, pp 205-237, 1981
7. Wong J.Y. Theory of ground vehicle, John Wiley & Sons, 1978
8. Karafiath L.L., Nowatzki E.A., Soil mechanics for off-road vehicle engineering, Trans Tech Publications, 1978
9. Hettiarachi DRP, Reece A.R., The calculation of passive soil resistance, Geotechnique Vol.24, No.3 pp289-310, 1974

NOTATION

A, a_k	adhesive component of soil reaction	A	adhesive component of soil reaction
a	tangential adhesion	$R_x^i, R_x^i(\theta)$	X-axis component of soil reaction on ith lug
B	width of lug	$R_z^i, R_z^i(\theta)$	Z-axis component of soil reaction on ith lug
B_c, t_k	coefficient of series cohesion	R_t, R_n	tangential and normal component of soil reaction
c	coefficient of series cohesion	R_t^i, R_n^i	tangential and normal component of soil reaction on ith lug
C_k, c_k	coefficient of series cohesion	r	rolling radius
D_k, d_k	coefficient of series cohesion	r_0	radius of lug tip
D_r^i	tow resistance	r_c	acting radius of soil reaction R
E	Consumed energy	r_d	dynamic radius of soil reaction R
f	motion resistance	\bar{r}	vector of coordinate system
f_{ave}	average motion resistance	S^*	lateral shear resistance in area
g	gravitational acceleration	s_r	moving distance of axle from entry to out of soil
G	load on axle	Wave	average bearing reaction
H	thrust	α	inclined angle of interface
H_{ave}	average thrust of lug	β	inclined angle of lug
h	length of lug	γ	volumetric weight of soil
h_1	distance from point(R_s) of action to upper end of interface	δ	$= \sin^{-1}(\sin\delta/\sin\phi)$
i	slip	δ_r	external friction angle
J	horizontal shear displacement	δ_n	angle between R_1 and normal on interface
k	shear deformation module	η	angle between \bar{r}_c and \bar{r}_0
K_r	resistance coefficient for a weightless soil	η_{avg}	lug efficiency
K_s	resistance coefficient for effect of self weight	θ	rotating angle of wheel
K_q	resistance coefficient for the surcharge	θ_s	space angle of lugs
K_{ca}	resistance coefficient for both cohesion and adhesion	θ_r	rotating angle of wheel from entry of soil to leave of lug
L	length of lug or interface	μ	coefficient of lateral shear resistance
l	distance from a point to upper end of lug	ν	internal friction angle
M, m	mass	ϕ	center angle
$M(\theta)$	driving torque	ω	angular velocity
P	frictional component of soil reaction	σ	pressure stress
P_{ave}	average pull	τ	shear stress
P_s	lateral shear resistance	s	soil scale index, $s = (c-q)/\gamma_s$
q	surcharge of soil		
R	soil reaction on single lug		
R_1	soil reaction on unit width of lug		
$R_x, R_x(\theta)$	X-axis component of soil reaction		
$R_z, R_z(\theta)$	Z-axis component of soil reaction		

TOPIC 6
OPERATION ON STEEP SLOPES

STUDY OF THE MOTION OF AGRICULTURAL VEHICLES ON STEEP
GRASS-COVERED SLOPES

A. GREČENKO

AGROZET, K.VUZS, 140 03 PRAHA 4-CHODOV, CZECHOSLOVAKIA

INTRODUCTION

In large-scale farming ploughing is generally practiced up to 15° of slope, the reason of this limitation being not only the safety of operation but also the decreasing layer of tilth and erosion as well. Steeper slopes are generally covered with grass which is either harvested or grazed. The experience indicates that adapted four-wheel drive tractors with conventional tyres can harvest grass under favourable conditions on slopes up to 20°. For treatment and harvesting on slopes up to 26° special light-weight machines with low pressure tyres are used; these are able to cross some local gradients up to 33° by means of adequate manoeuvring.

The layer of soil on rocky sub-strata in mountainous regions is round 2 to 15 cm with the turf penetrating to a depth of 2 to 10 cm. The top soil is very dense so that lugs of conventional tyres with a traction tread pattern do not penetrate into such a depth to enable the beneficiary function of the tyre body. Better grip is achieved with terra-tyres having narrow and low lugs with the tread pattern STS (Goodyear).

Gradeability is considerably impaired with increasing moisture of soil which is mostly measured in 5 cm depth. Specimens contain the root system (turf). On the sandy-loam soil, "dry" specimens, i.e. very suitable for traction are those with up to 25 % moisture content. In mountainous conditions, moisture content of 30 - 40 % is considered as normal, while "wet" is the soil with more than 40 %

AD-P004 290

moisture content or more than 30 % moisture content and wet surface.

The reasons of critical situation are generally the sliding, then the overturning due to dynamic effects and also functional shortcomings of the machine.

The fundamental method of the experimental research of the travel on hillsides is the measurement in field conditions with actual vehicles. The motion of vehicles is generally investigated when they travel directly up- or downhill, along the contour line and when cornering (making a turn). Though the reproducibility is not as high as in laboratory testing, the reliability is considerably better. The results depend on the quality of the analysis and on the generalisation of the data measured. With a certain risk the acquired data are then used to predict similar properties of other vehicles. The aim of research is to maintain this risk as low as possible.

It seems that our method is similar to the methods of the Scottish Institute of Agricultural Engineering (SIAE) at Penicuik (Gilfillan 1970, Spencer-Owen 1981 and others) whose research programme includes the aspects of slope performance of tractors with respect to the safety of operation.

The investigation to the motion of machines on slopes is further bound on a more precise knowledge and understanding of kinematics and dynamics of the general plane motion of a wheel. An outline of a synthetic solution, presented by Grešenko (1975), principally complies with some newer experimental results by Krick (1971), Schwanghart (1981) and Gee Clough-Sommer (1981).

This paper is to report on some methods and results of research on the operation of vehicles on hillsides with some comments on the applicability of terramechanics.

EXPERIMENTS

Traction properties

Traction properties are generally expressed by the relation between the coefficient of gross thrust μ_x and the slip s ... a) applied to transmission of the tractive effort (e.g. the travel of a vehicle up the slope), the so-called tractive properties; b) in the transmission of the braking effort (travel of a vehicle down the slope), the so-called braking properties.

Ad a)

Tractive properties are measured by accelerated drawbar tests of vehicles in which a complete spectrum of the relation slip - drawbar force is recorded during each test run on a track of about 100 m length (Grešenko 1980). Additional measurements include e.g. the determination of the effective rolling resistance (i.e. the summary resistance of the driving and supporting devices of the vehicle which is counteracted by the total gross tractive effort). The recording, processing, analysing and plotting of the measured data is carried out by modern methods (Fig.1).

Fig.2 demonstrates the scope of differences in tractive properties of the same tyre on grass-covered surface due to the changes in soil moisture. If, for example, the slip during the travel uphill increases up to the level of s_1 , the machine will reach the limit of sliding. A similar situation threatens when the machine is travelling slewed to the contour line of a slope and assumes the angle of heading (with respect to the contour line) with the tangent equal to the slip s_1 (principle of equivalence, Grešenko 1975).

Having in mind the prediction of the vehicle performance we have been, up to the present, able to express adequately only the two-parametric curve 1 (bilinear equation, see

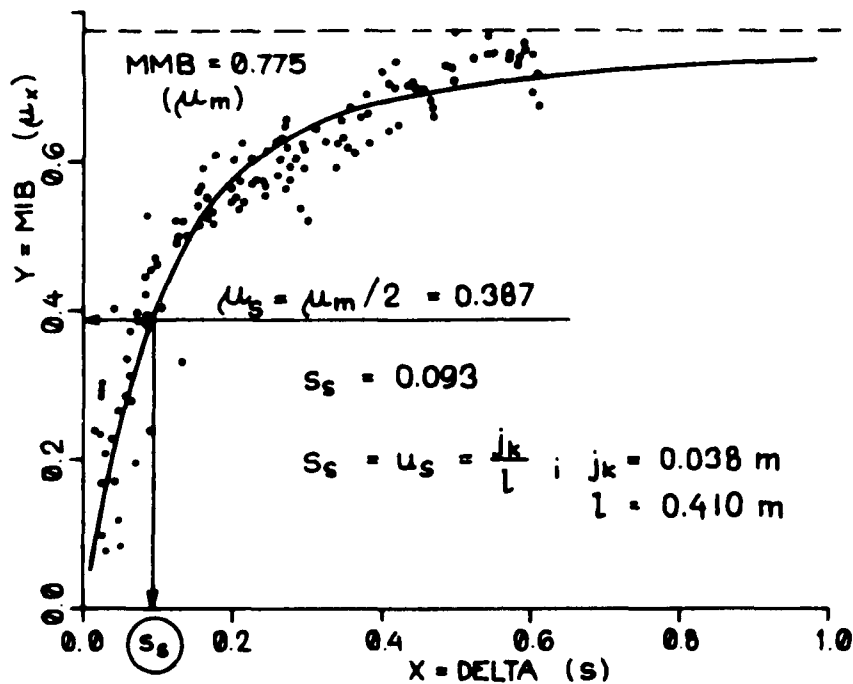


Fig.1. Record of a $\mu_x - s$ relation for driven wheels of an agricultural vehicle with 12.5/12-18 tyres on dry grass-covered ground: μ_m and s_s are parameters of the computer plotted slip curve in bilinear form.

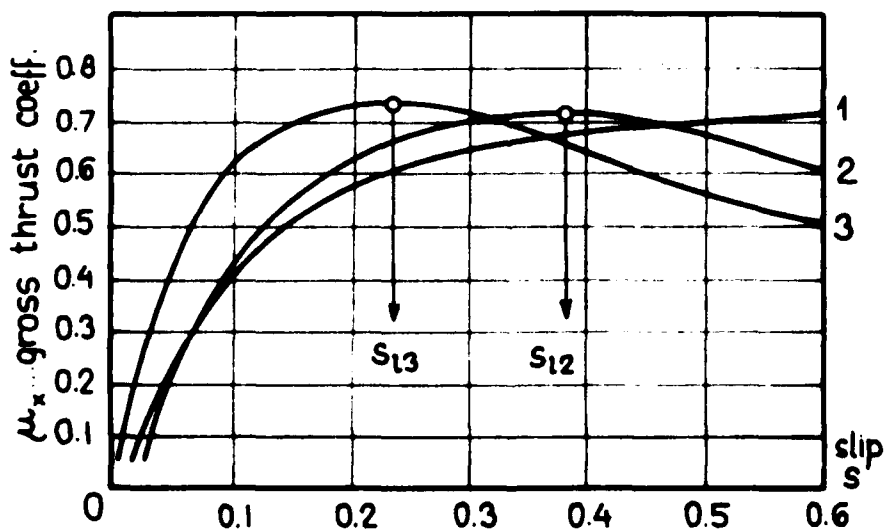


Fig.2. Thrust - slip curves of a 12.5/12-18 tyre measured on grass-covered ground change with moisture content of the soil w (1 ... $w = 15\%$; 2 ... $w = 30\%$; 3 ... $w = 50\%$).

Grešenko 1975). Exponential forms of thrust-slip curves including recent mathematical description of functions of type 2, 3 (Fig.2) by Wong-Preston-Thomas (1983) are relatively simple, but in view of the impossibility of inversion (i.e. slip-thrust), they resist more complicated practical applications (see part "Prediction of vehicle performance on slopes").

The applicability of the results of drawbar tests to the travel of vehicles up the slope is partly limited by the fact that the drawbar tests are carried out on level ground where the texture and the depth of the soil layer tend to be different.

Ad b)

Braking properties are measured on level ground by accelerated pushing tests, in which the tested vehicle is pushed forward at a steplessly increasing speed. By this method, we have achieved negative slips up to -40 % (a limit due to directional stability of the measuring set of vehicles). We have found that the braking properties in the given range of absolute slip values have been similar to the tractive properties.

The slip should be defined in both cases of traction and braking by a uniform formula containing the relation between the actual velocity v and the no-slip velocity v_t (unlike the existing ISTVS glossary of terms):

$$s = 1 - (v/v_t) \quad (1)$$

With a negative slip (skid) $s = -1$ (-100 %) the wheel is forced to travel at the velocity $v = 2 v_t$, the displacement along the contact area being $j = -s \cdot X = -X$ (i.e. in the direction of motion); the locked braking wheel marks a skid $s = -\infty$, i.e. there exists the same displacement along the contact area. The uniform formula thus complies with the fundamental rules of the terramechanics.

Higher values of skid can only be achieved by the downhill braking tests where the braking distance at the full braking effort is measured or, preferably, the maximum deceleration (Spencer - Owen - Greenhill 1983) as a function of velocity. The course of complete functions $\mu_x = f(-s)$ for braking is analogous to functions $\mu_x = f(+s)$ from Fig.2 but the maximum braking force coefficient does not attain the same high values probably due to the fact that the wheel when braking floats more on the surface (smaller slip-sinkage) and the tread may eventually be clogged with soil.

Slip (skid) of a vehicle up (down) the gradient

The slip (skid) of a vehicle on the gradient (Fig.3) is most conveniently measured in a continuous way by means of a gauge wheel. The most suitable is a slope with a variable gradient which is smallest at the foothill and increases towards the top of the slope. In this way the vehicle slip and skid were recorded as given in Fig.4.

Travel of a machine across a gradient

In order that the machine with e.g. steered front wheels could travel along the contour line of the slope, its longitudinal axis has to resume the attitude with heading γ_2 and the front wheels have to be turned by a drift (slip) angle γ_1 with respect to the contour line, i.e. by a steering angle φ in relation to the machine (Fig.5). The heading compensates the drift angles of the wheels due to the effects of lateral forces on the slope; the drift angles result from the combined lateral displacement of the soil and the deformation of the tyres. The angles γ are thus the function of the slope gradient β .

The study of this case of the travel is of importance e.g. for the designing of farm vehicles operating with a front-mounted mower (Fig.6) : in case of travel along the contour line the swath has to pass between the wheels



Fig.3. Test run of an experimental machine with an implement simulator on the gradient that is measured by means of a gyroscope ; a telemetric system transmits the data in digital form to a stationary measuring van.

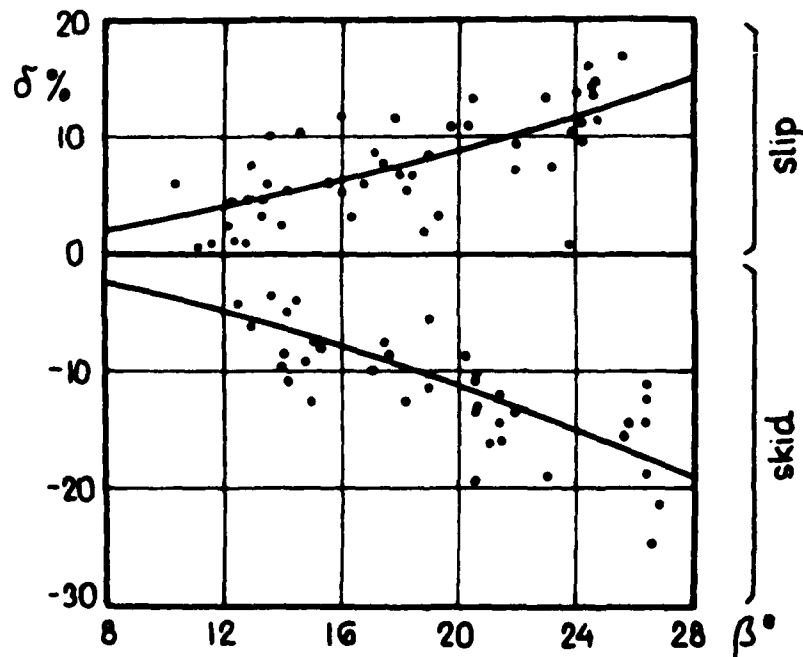


Fig.4. Measured slip and skid plotted against the gradient demonstrate similarity (four wheel-driven machine as in fig.3 with the implement simulator raised ; very moist grass-covered ground).

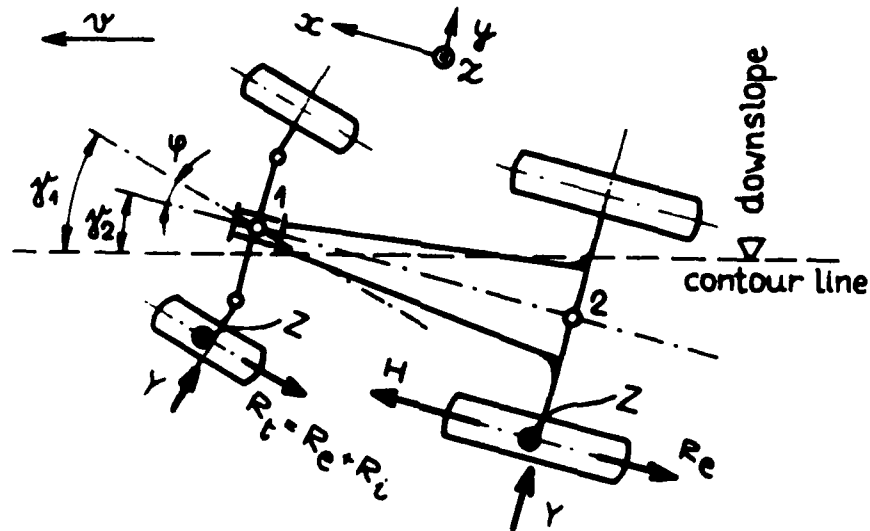


Fig.5. When crossing the hillside, a vehicle with front steering wheels assumes the attitude with heading γ_2 and steering angle φ (notation of forces acting on the wheels: H ... gross tractive effort ; Y ... lateral force ; Z ... normal reaction force ; R_e ... external rolling resistance of driving wheels ; R_i ... internal rolling resistance of free-rolling wheels ; R_t ... total rolling resistance).

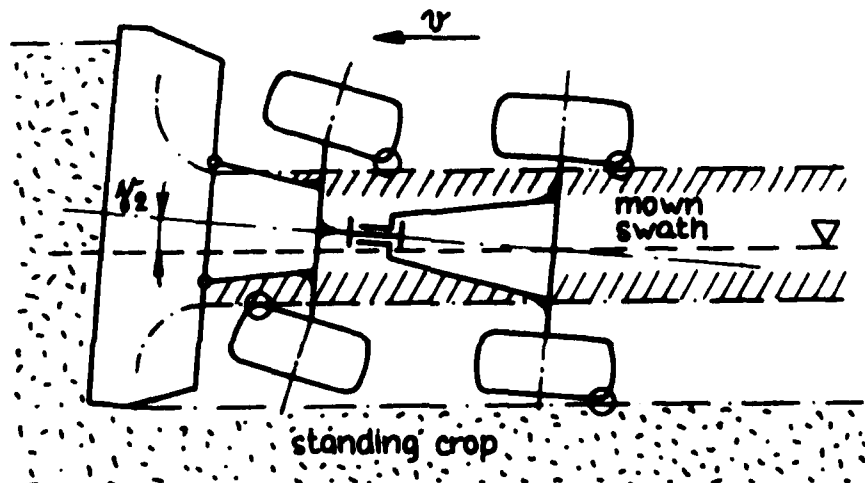


Fig.6. An agricultural machine mowing forage along the contour line of a gradient must not touch either the standing crop or the mown swath.

of the machine without being overridden and the wheels must not ride over the edge of the standing crops. If e.g. the angle $\gamma_2 = 4^\circ$ is a limiting factor, then the respective gradient β marks the maximum slope on which the vehicle can successfully operate. The relation $\gamma_2 = f(\beta)$ should be possibly flat.

The measurement of the heading of the machine is readily performed by means of two sets of sprinklers of the car electric windshield washer (Fig.7). The nozzles of the two independent sprinkler sets are fastened on two spots parallel with the axis of the machine, near to the ground. When the machine is travelling along the contour line, a washable paint is sprayed in a concentrated beam through the nozzles onto the mown surface. The angle of heading of the machine then equals :

$$\gamma_2 = \arcsin (d/s) \quad (2)$$

Generally indeed, the nozzles can be positioned in any two arbitrary spots. It is then convenient to spray two different colours of paint and the formula for the angle γ_2 becomes only a little more complicated.

The method described above was used to determine the values of headings to the contour line of a hillside machine equipped alternatively with different tyres as illustrated in Fig.8. Further examined was the influence of the speed of travel up to 12 km/h on the heading of the machine. On rough ground the heading rather tends to increase with the speed of travel (the bumps throw the machine sideways) while on smooth ground it remains unchanged or even decreases (rheology of the lateral deformations and the side slip).

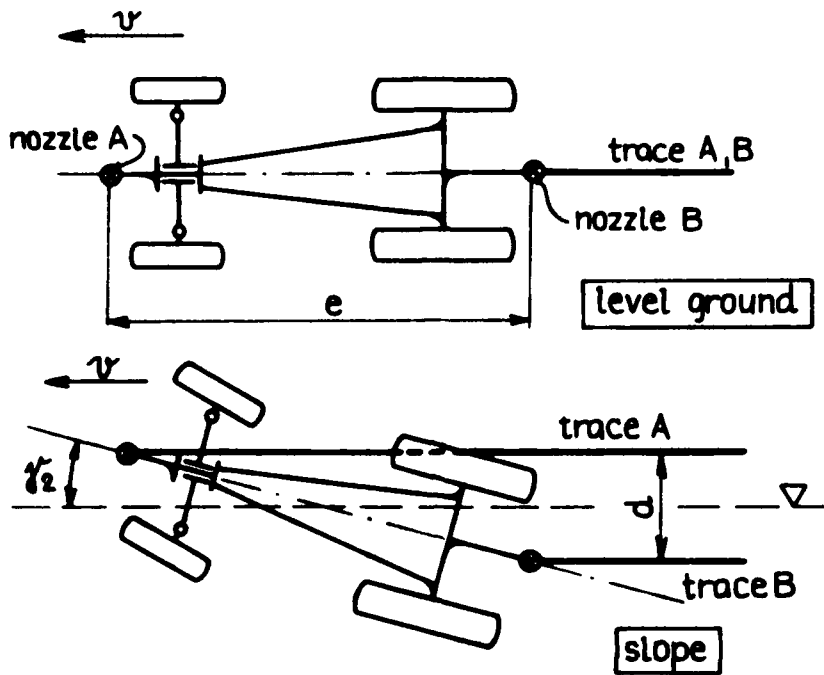


Fig.7. A method to determine the heading γ_2 of a vehicle travelling along the contour line of a gradient.

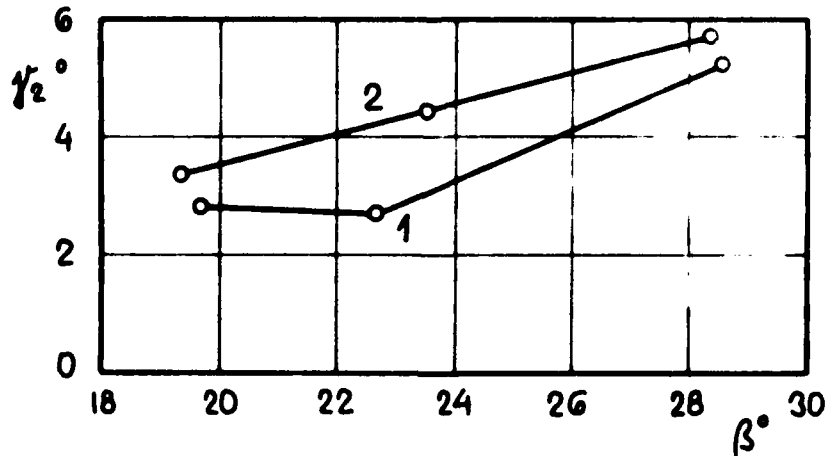


Fig.8. Measured values of heading γ_2 in relation to the gradient β (grassy slope) for a four wheel-driven vehicle equipped with terra-tyres 38x20.00-16.1 (1) or standard tyres 12.5/12-18 (2).

Manoeuvring on the slope

Characteristic manoeuvres performed and measured on the slope comprise :

- a) an ability to move out directly uphill,
- b) an ability to brake to a stop directly down the slope in function of velocity,
- c) a half circle (U) turn at the end of a downslope run in function of velocity.

The measurements are being made in connection with the assessment of the gradeability of machines.

Shape of a contact area

The contact area of a tyre varies both in shape and size when travelling along the contour line. The shape relates to the distribution of the contact pressure, which, together with the tread pattern, affect the lateral grip properties of the tyre. A scheme of a special stand enabling to take prints of a contact area up to a gradient of 30° is shown in Fig.9 together with specimens of static prints of the Barum 15,5 - 26 2S tyre.

The prints have helped to reveal that the mean contact pressure of the decisive downslope tyres of a tractor travelling along the contour line remains nearly unchanged for the variations of the gradient from 0 to 30° .

PREDICTION OF VEHICLE PERFORMANCE ON SLOPES

Travel directly uphill

The relationship of the gradient the machine can negotiate to the slip determined from earlier measurements makes a useful diagram. The computed curves in Fig.10 are based on measured data [$s = f(\mu_x)$] for the conditions as follows:

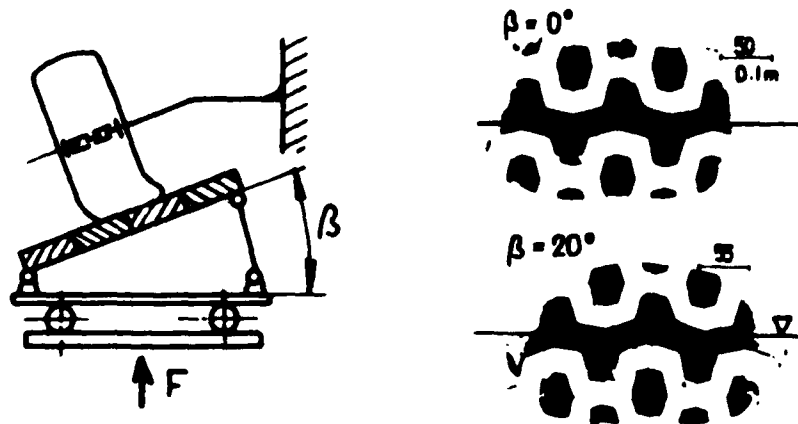


Fig.9. Schematic drawing of a stand where the geometry of tyres on an inclined plane was studied and two samples of Barum 15.5-25 28 tyre imprints.

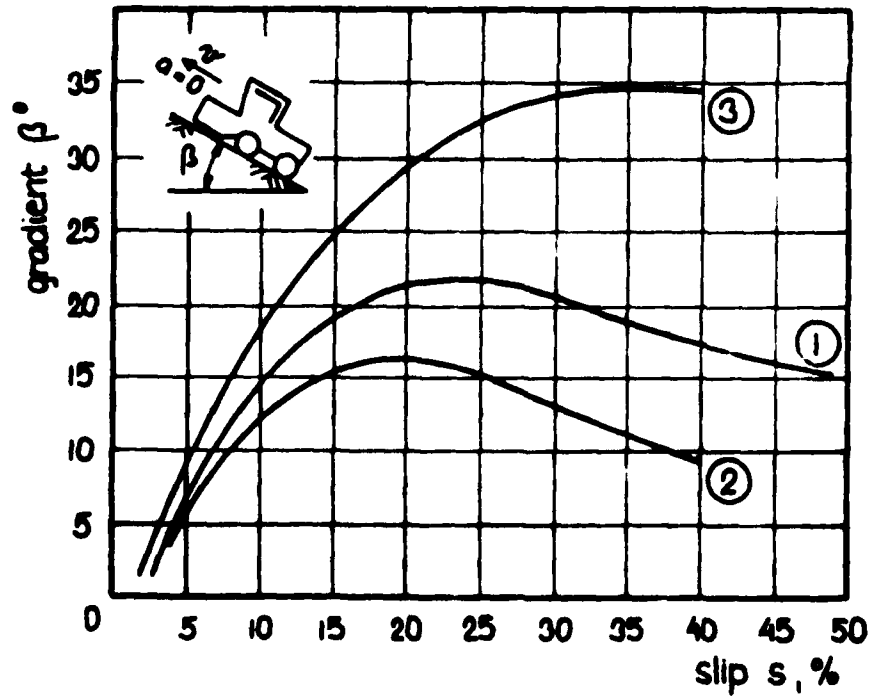


Fig.10. A computed diagram predicting the performance of an agricultural vehicle when ascending a slope for different conditions ; the top of each curve indicates the limiting ascent slope and the respective slip.

item	number of the curve		
	1	2	3
soil	loamy sand	silty loam	loamy sand
surface	meadow	meadow	meadow
condition of the surface	relatively dry	shortly after rain	dry
soil humidity, %	30	30	30
locality	Hannůvice	Jílové	Nová Ves
year	1978	1976	1976

Another alternative to the computation is the start of motion uphill with a given acceleration (usually $a = 0,05 \text{ g}$).

Travel along the contour line

The purpose is to describe the kinematic and dynamic state (situation) of a machine with respect to the angle of slope β by the following quantities at least :

kinematic :

- slip and steering angles $\gamma_1 ; \gamma_2 ; \varphi$
- speed of travel along the contour line
- revolution ratio of the upslope and downslope wheels when the axle differentials are operating

dynamic :

- normal reaction forces Z on all wheels
- gross tractive efforts H on all driving wheels
- lateral forces Y on all wheels
- rolling resistances R of all wheels.

The simplest alternative (a two-axle vehicle with a two-wheel drive and differential locked) is a three-dimensional case three times statically indeterminate which is thus described by six equilibrium equations and three deformation equations.

All deformation equations describing the interaction of the supporting mechanism of the vehicle with the ground are based on the relations between the velocities of two supporting members (e.g. the wheels) in the directions x and y (Fig.5). No-slip velocities of the wheels v_t express the kinematic ties of the drive, the actual velocities of the wheels v are bound by the condition of stiffness of the machine as a mechanical body. The relationship of the velocities should be transformed into the relationship of the slip values and also of the tangents of drift (slip) angles. These quantities can be expressed, according to the slip and drift theory of the wheel motion (Grešenko 1975), by force effects so that the result will be the relationship among the forces, in other words the wanted deformation equation.

The solution is based on the known relationships:

$$s = u \cdot \cos \xi \quad (3)$$

$$\operatorname{tg} \gamma = \frac{u \cdot \sin \xi}{1 - s} \quad (4)$$

gradient of deformation equals:

$$u = \frac{j_k \cdot J}{l} = \frac{u_s}{2} \cdot \frac{3\mu \cdot \mu_m - 2\mu^2}{\mu_m \cdot (\mu_m - \mu)} \quad (5)$$

$$u_s = j_k \cdot l \quad ; \quad \mu = \sqrt{H^2 + Y^2} / Z$$

the angles of the resultant force with the wheel plane:

$$\cos \xi = \frac{H}{\sqrt{H^2 + Y^2}} \quad ; \quad \sin \xi = \frac{Y}{\sqrt{H^2 + Y^2}} \quad (6)$$

inserting into formulae (3, 4) provides the required expression for the slip s and tangent of the drift (slip) angle γ :

$$s = \frac{m}{n} \cdot H \quad (7)$$

$$\operatorname{tg} \gamma = \frac{m \cdot Y}{n - m \cdot H} \quad (8)$$

where

$$m = u_s \cdot (3Z \cdot \mu_m - 2 \sqrt{H^2 + Y^2}) ;$$

$$n = 2Z \cdot \mu_m (Z \cdot \mu_m - \sqrt{H^2 + Y^2})$$

The rolling resistance R in the plane of the wheel remains practically constant up to the angle $\gamma = 30 + 40^\circ$ which has been again supported by the analysis of the recent measurements by Schwanghart (1981) and conclusions drawn by Gee Clough - Semner (1981).

A simple example how to formulate and apply the deformation equation is given in the Appendix.

It follows that the deformation equations can only be derived by means of relations (5) where the gradient of deformation is expressed explicitly (e.g. equation (5) with $Y = 0$ represents the relationship between the slip and the coefficient of gross traction (thrust) μ_x).

All the known equations for the gross tractive effort (or the gross traction coefficient) as a function of slip of the exponential type, i.e. comprising some numbers in the form $1/x$ and e^{-x} lack the quality to express the slip (or generally the gradient of deformation) explicitly and thus

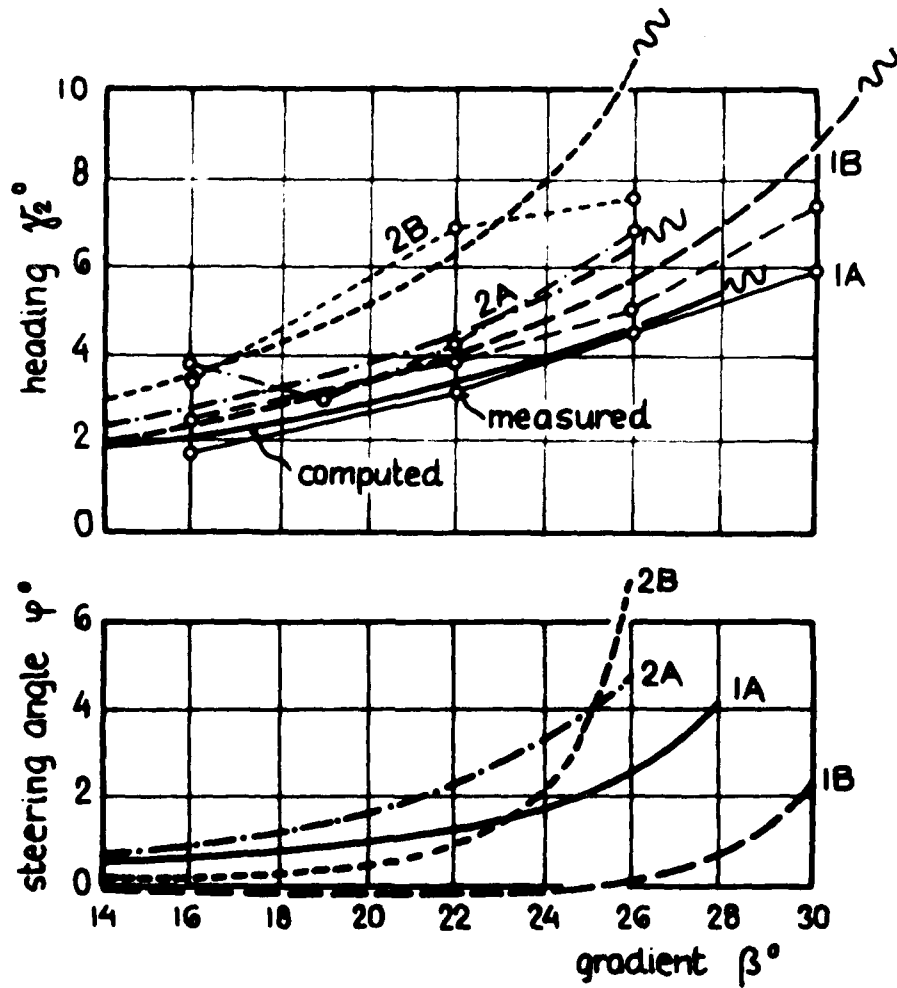


Fig.11. Computed values of heading γ_2 of an agricultural hillside machine travelling along the contour line of a dry grass-covered slope with a gradient β plotted together with experimental values ; the computed steering angle ψ of the front wheels is given in the lower section of the graph (1 ... terra-tyres 38x20.00-16.1 ; 2 ... standard 12.5/12-18 tyres ; A ... front mounted disc mower ; B ... rear mounted rake).

can hardly be used in these important applications.

By means of the slip and drift theory of the wheel motion the relevant deformation equations for different kinds of drives of two-axle vehicles were successfully formulated and the resulting sets of non-linear algebraic equations solved on a computer. Figure 11 presents, for instance, a computed interpretation of the measured angles for a hillside vehicle which is travelling along the contour line of a gradient β . The vehicle with two axles has an all wheel drive and the axle differentials in action (the case was solved as 6 times statically indefinite). In measurements, the vehicle was alternatively equipped with two kinds of tyres and an attached implement, front - or rear-mounted. The computation has again confirmed the practical value of the theory which is able to provide valuable information on the behaviour and parameters of the vehicle and of the maximum slope which the vehicle can negotiate.

CONCLUSION

The research into the hillside performance of vehicles is one of the problems of terramechanics that shift the scope of the solution into two dimensions, check up the validity and applicability of theories and offer new topics for solution.

It appears that the two-dimensional (plane) problems in the mechanics of off-the-road vehicles can successfully be solved by means of classical terramechanics in the spirit of H.G.Bekker though the sense of the old good quantities such as "cohesion" or "internal friction" may have to be reevaluated. Some of the assumptions of the academic traction theory loose their validity on grass-covered ground or on compact surface (e.g. the lugs of the tyre hardly penetrating the soil which indeed is not homogeneous)

but on the other hand without these assumptions the solution would become erratic.

The experience indicates that only such traction formulae may find use in the treatment of more complicated problems dealing with the performance of vehicles which enable to express a deformation quantity (e.g. slip) explicitly.

The slip and drift theory proves positive results in the solution of kinematic and dynamic aspects of the hill-side travel of a vehicle, the reasons being as follows:

- the theory resolves the resulting force effect on the drifting wheel in the ground plane into components in the direction of the wheel plane and wheel axis (this being by no means a formality, as in this case the gross tractive effort can be expressed in agreement with classical concepts and the rolling resistance remains nearly independent of the slip angle of the wheel),
- the theory enables to formulate the deformation equations describing statically indefinite mechanical systems by means of a bilinear formula for the gradient of deformation which has been the only one till now enabling to express the gradient explicitly.

APPENDIX

An example of deriving a deformation equation

The following problem is given: to derive formulae for the distribution of the gross tractive forces H_1 and H_2 between two similar axles 1 and 2 of a tractor with four-wheel drive (an elementary once statically indefinite case).

Three equilibrium equations can be written from which follow e.g. the normal reaction forces on the axles Z_1 and Z_2 and, furthermore, the total gross tractive effort $H = H_1 + H_2$ as a function of the drawbar force F .

The deformation equation follows from the kinematic relations :

$$v_{t1} = v_{t2} ; \quad v_1 = v_2$$

dividing these equations gives

$$v_1/v_{t1} = v_2/v_{t2}$$

or, in view of the former equation (1):

$$1 - s_1 = 1 - s_2 \quad \text{and thus:} \quad \underline{s_1 = s_2}$$

The slip of the two axles is equal. According to (3) :

$$\begin{aligned} s &= \frac{u_s \cdot (3Z\mu_m - 2H)}{2Z \cdot \mu_m \cdot (Z \cdot \mu_m - H)} \cdot H = \\ &= \frac{u_s \cdot (3\mu_m - 2H/Z)}{2\mu_m \cdot (\mu_m - H/Z)} \cdot \frac{H}{Z} = f\left(\frac{H}{Z}\right) = f(\mu_x) \end{aligned}$$

Therefore: $f(H_1/Z_1) = f(H_2/Z_2)$ resulting in :

$$\frac{H_1}{Z_1} = \frac{H_2}{Z_2} \quad \dots \quad \mu_{x1} = \mu_{x2}$$

This is the desired deformation equation which, together with the condition $H = H_1 + H_2$, results in :

$$H_1 = \frac{Z_1}{Z_1 + Z_2} \cdot H$$

$$H_2 = \frac{Z_2}{Z_1 + Z_2} \cdot H$$

REFERENCES

- Gee Clough, D. - Sommer, M.S.: Steering forces on undriven angled wheels. *Journal of Terramechanics* 1981, 18 /1/: 25-49.
- Gilfillan, G.: Tractor behaviour during motion uphill. Part I, II. *Journal Agric. Engng. Research* 1970, 15 /3/: 221-243.
- Grešenko, A.: Some applications of the slip and drift theory of the wheel. *Proceedings 5th Int. Conf. ISTVS, Detroit 1975*: 449-472.
- Grešenko, A.: Past measurements of traction properties of terrain vehicles - Measuring techniques /in czech/. *Zemědělská technika* 1980, 26 /11/ : 643-664.
- Krick, G.: Schräglaufverhalten angetriebener Reifen in nachgiebigen Boden. *ATZ* 1971, 73 /7/ : 243-246 ; /8/ : 301-306.
- Schwanghart, H.: Messungen von Kräften an gelenkten, nicht angetriebenen Reifen. *Proceedings 7th Int. Conf. ISTVS, Calgary 1981*: 335-356.
- Spencer, H.B. - Owen, G.M.: A device for assessing the safe descent slope of agricultural vehicles. *Journal Agric. Engng. Research* 1981, 26 /3/ : 277-286.
- Spencer, H.B. - Owen, G.M. - Greenhill, A.L.: A microprocessor-based safe descent slope meter. *Journal Agric. Engng. Research* 1983, 28 /3/ : 269-272.
- Wong, J.Y. - Preston-Thomas, J.: On the characterisation of the shear stress - displacement relationship of terrain. *Journal of Terramechanics* 1983, 19 /4/: 225-234.



↙
SOME STABILITY AND CONTROL PROBLEMS
WITH TRAILED FARM TANKERS ON SLOPES

A.G.M. HUNTER

SIAE, BUSH ESTATE, PENICUIK, EH26 0PH, SCOTLAND

ABSTRACT

AD-P004 291

Trailed farm tankers in Britain, which are generally used either for slurry spreading or crop spraying, have become very large in recent years. The fluid contents, which may be four times as heavy as the towing tractor, will move under gravity inside a partly full tanker and this introduces problems while driving on slopes, which have not been recognised previously. The fluid movement will affect both the stability of the tanker and the control of the tractor and trailer combination. Recent accidents where tankers overturned due to loss of stability, and where tractor and trailer combinations slid downhill due to loss of control led to extensive research on tankers. In this paper, the centre of gravity analysis of fluid in tanks and the stability analysis of tankers are both reviewed, a full treatment being given elsewhere. The control analysis of tractor and trailer combinations is presented, and this is followed by a discussion of the problems facing tractor drivers with trailed tankers. Tankers behave unpredictably because the characteristics change continuously while the contents are emptied, for example during slurry spreading. The most dangerous condition for working on slopes may be when the tanker is nearly empty, unlike other trailers which are normally safe when nearly empty.

SOME STABILITY AND CONTROL PROBLEMS
WITH TRAILED FARM TANKERS ON SLOPES

INTRODUCTION

In recent years the size and number of machines on British farms with fluid-filled tanks, mainly slurry tankers and crop sprayers, have greatly increased. Some of these tanks have a fluid capacity of up to 14,000 l (fluid weight 14 t)^{1,2} which may be four times as heavy as the weight of the towing tractor. When a farm tanker is driven onto a slope, the fluid will find its own level in the lower part of the tank unless the tank is completely full. This results in a movement of the centre of gravity of the fluid within the tank which may have a large influence on the stability of the tanker. It may also affect the weight transfer from the tanker onto the tractor, thus influencing the control of the tractor when driving on a slope. Further, when the tanker is in work its contents are discharged onto the field so that both stability and control change progressively.

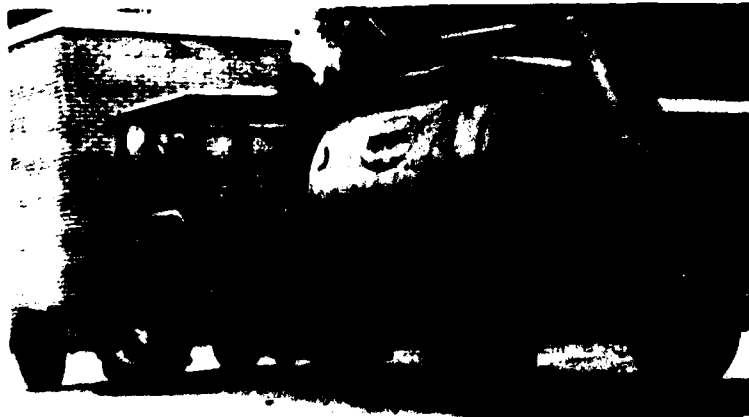


Fig. 1 Typical trailed farm slurry tanker.

When the driver is working with a tanker like that in Fig. 1 he has virtually no means of assessing these changes from his driving seat, and is unable to gauge whether it is

safe to drive the tractor and trailed tanker onto a particular slope. Two examples may be given of accidents with trailed tankers, one due to loss of stability and one due to loss of control, both in unexpected circumstances.

In the first example, a partly full slurry tanker overturned in a field of slope 24° . Using existing methods of stability analysis for a trailer with a fixed centre of gravity³, the stability limit (i.e. overturning slope) for the empty tanker was computed to be 37° , and for the full tanker 28° , both values greater than the actual overturning slope. Using an approximate estimate of the centre of gravity of the fluid in the partly full tanker on a slope, the stability limit was calculated to be 23° which was less than the stability limit for the tanker when either empty or full.

In the second example a tractor was pulling a partly full slurry tanker uphill in a grass field of slope 11° when the tractor driving wheels started to slip, and the whole outfit slid backwards to the bottom of the hill and overturned. The tractor and slurry tanker had already been driven across the same slope with no apparent safety problem. Again using an approximate estimate of the centre of gravity of the fluid in the partly full tanker on a slope, the control limit (i.e. the slope on which the outfit would start sliding) was calculated to be 11° for uphill travel, 12° for downhill travel, and 22° for travel across the slope.

The first stage in improving the estimation of tanker stability was to develop a centre of gravity analysis of fluid in inclined tanks. This is described in a separate paper⁴. The analysis was confined to fluid in tanks of circular or rectangular cross-sections because most farm tankers approximate to one or other of these shapes; in fact the tankers in the cases described above represented one of each type. The second stage was to develop a stability analysis of tankers by combining the new centre of gravity analysis of fluid in tanks with the existing stability analysis for fixed centre of gravity trailers, as described in a second paper⁵.

The purpose of the present paper is to review the work on tanker stability and to present an extension of this work which covers the control of tractors driven on slopes with

trailed tankers. The problems of assessing safety on slopes when driving tractors with trailed tankers are discussed also. The discussion may have wide application for tankers other than those for farm use, and will apply to tankers filled with liquids such as water, or granular solids such as grain, which have fluid characteristics. A related topic which is not covered is that of fluid sloshing in tanks. For example, an analysis of this problem is given by Bauer⁶ in which he demonstrates that the dynamic effects of sloshing may severely affect the stability of road tankers during manoeuvres such as braking. Only the problems related to static centre of gravity shift are covered here.

CENTRE OF GRAVITY OF FLUID IN A TANK

The standard method of calculating the centre of gravity of a body relative to fixed axes is to find the sum of the moments of mass about each axis and to divide each sum by the total mass. Where the relevant values are not already tabulated because the shape of the body is not simple or not common then integration must be used to find the sums. In many cases the method of calculation must be further extended by decomposition of the body into a number of parts each of which is easier to calculate individually than the body as a whole. It is often necessary to shift and rotate sets of axes relative to the fixed ones in order to simplify the calculations for the several parts. This approach is effective and straightforward to apply when the body is solid. With fluid contained in a tank the same approach must be applied repeatedly because the fluid assumes a shape which changes continuously as the attitude of the tank changes relative to vertical, or the tank is filled or emptied.

The photograph in Fig. 2 shows a model of a two-wheel farm tanker hitched at the front to a post in place of a tractor. The tank mounted on the trailer frame is a right circular cylinder which is transparent to show the fluid inside. The displacement of the fluid under gravity in the tank is shown clearly in this photograph. The centre of gravity of the fluid has shifted considerably from the position

at the centre of the tank which it would occupy when the tank was full. The two orthogonal reference lines on the end of the tank, which are square to the trailer frame, indicate that the fluid surface now lies at an angle to each reference line and at an angle to the longitudinal axis of the tank. It may be appreciated that although the fluid shape shown in the photograph is relatively simple it is not a shape for which one would expect to find centre of gravity data already tabulated. Even for this relatively simple case, the calculation to find the centre of gravity coordinates related to fixed axes at the centre of the tank is quite extensive.

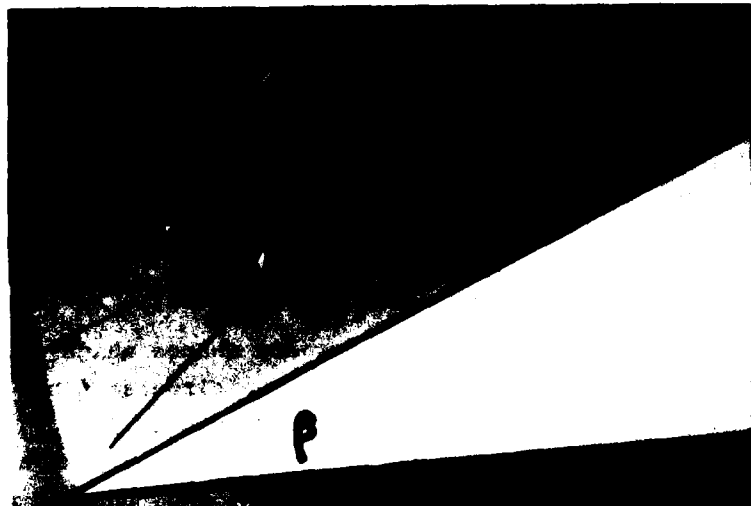


Fig. 2. Model of a farm tanker, e.g. a crop sprayer, with a transversely mounted tank, showing the fluid inside.

The particular example illustrated is for one quantity of fluid in a tanker resting at one heading angle α relative to the slope line FP , on one slope β . If any of these parameters changes then the fluid shape within the tank will change and the entire centre of gravity calculation must be repeated. For example, if the quantity of fluid shown in Fig. 2 was increased then the shape might become one that was truncated at both ends of the tank, rather than at one end as shown, while an alteration in either α or β would change the shape of the fluid. A complete centre of gravity analysis of fluid in a tanker on slopes requires the calculations to be made for

all quantities of fluid in the tank, with the tanker facing along all heading angles, on all slopes.

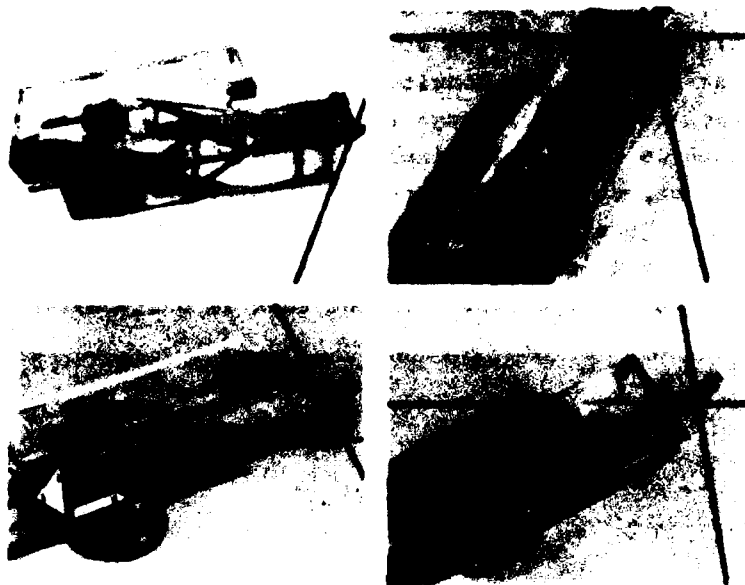


Fig. 3 $\frac{a|b}{c|d}$ Various fluid shapes in a rectangular tank. See text.

Fluid in a rectangular tank assumes shapes which are considerably more complicated than in the circular tank. A model tanker with a rectangular tank is shown in Fig. 3. In Fig. 3a the fluid is bounded by its horizontal surface and four tank faces: the bottom, the top, one end, and one side. In Fig. 3b the identical quantity of fluid assumes an entirely different shape due to moving the tanker round to an increased heading angle on the same slope. The fluid now contacts five tank faces. In Fig. 3c the slope is reduced and the tanker is returned to the original heading angle. In Fig. 3d the tanker is at the original heading angle and on the original slope but the quantity of fluid is greater and it now contacts all six faces. A complete analysis of fluid in rectangular tanks requires the entire range of possibilities to be evaluated, many more than those illustrated here.

STABILITY OF TANKERS

After determining the centre of gravity of fluid within the tank, the influence of the fluid on the overall centre of

gravity of the tanker must also be found. This is impossible to judge qualitatively; a smaller quantity of fluid which is free to move a larger distance within the tank may have greater influence than a larger quantity free to move a smaller distance, or vice versa. The process of calculating the stability of a tanker is an iterative one. First an estimate of the stability limit (i.e. the slope on which the tanker will tip over) is made; the overall centre of gravity of the tanker, including the fluid, is calculated taking account of the fluid position for this slope; then the stability limit is calculated with this overall centre of gravity. The centre of gravity must be revised for each new calculation of stability limit until the values converge. This must be done for all quantities of fluid in the tank and for all tanker heading angles.

Because of the complexity of the method described it was essential that experimental checks were used to confirm that both the stability analysis and the computer programming used to implement it were accurate. The approach was to carry out extensive checks with physical models for which slope and heading angles were easy to adjust and there were no safety problems, and to carry out limited checks with a full-scale tanker.

The models used were those illustrated in Figs 2 and 3, set on an adjustable sloping board. A protractor scale was laid out on the board to indicate heading angle. The transparent tanks were marked with a scale on the side to indicate the quantity of fluid. The stability limit for each tanker was measured by inclining the board until the tanker started to tip: either a wheel lifted from the board or the hitch lifted. The dimensions of the tankers were measured and the centre of gravity of each when empty was estimated from knife-edge measurements. The computed values of stability limit were plotted against the experimental ones and the agreement was found to be very close.

The full-scale measurements were made with the small farm slurry-tanker of circular cross-section shown in Fig. 1. The tanker and tractor were fitted sideways on three beams placed under the two sets of tractor wheels and the tanker wheels,

respectively. The load under the upper tanker wheel was measured with an electronic weighpad fitted into the appropriate beam. Clearly, if the load under the tanker wheel approached zero as the tanker was tipped, then the tanker was approaching the point of overturn. In this way the stability limit of the tanker was estimated. The experiment was repeated with four different quantities of fluid in the tank from empty, A, to completely full, D, Fig. 4. The line marked 'fluid' in the figure gives the computed results for the tanker and it is seen that the experimental values of stability limit lie close to it. These values are applicable to only one heading angle which is where the tanker lies directly across a slope. The line marked 'solid' is a plot of computed values of stability limit with the weight of fluid added to the tanker but held solid, so that no fluid movement is allowed. The difference between the two lines gives the effect due solely to fluid movement. The figure shows that for this particular tanker there is a continuous decrease in stability as the tanker is filled. The least stable condition is when the tanker is completely full.

Stability values were also computed for a different tanker of almost rectangular cross-section. In fact, the tanker was the one which overturned in the first accident mentioned in the Introduction. The plot of stability values for this tanker, Fig. 5, is entirely different from that shown above. Stability does not decrease continuously as the tanker is filled but reaches a minimum at J before rising to the value for the tanker completely full at I. At the minimum point the tanker is about 3° less stable than when completely full, and over the entire range between a fractional tank fill of 0.2 to 0.9 the stability is less than when completely full. This effect is due to the great freedom of movement of the fluid within the rectangular tank, and is highlighted by plotting the difference between the 'solid' and 'fluid' lines in the lower part of the figure. When the tank fill is only 0.2 at K, the reduction in stability limit due to fluid movement within the tank is 10° .

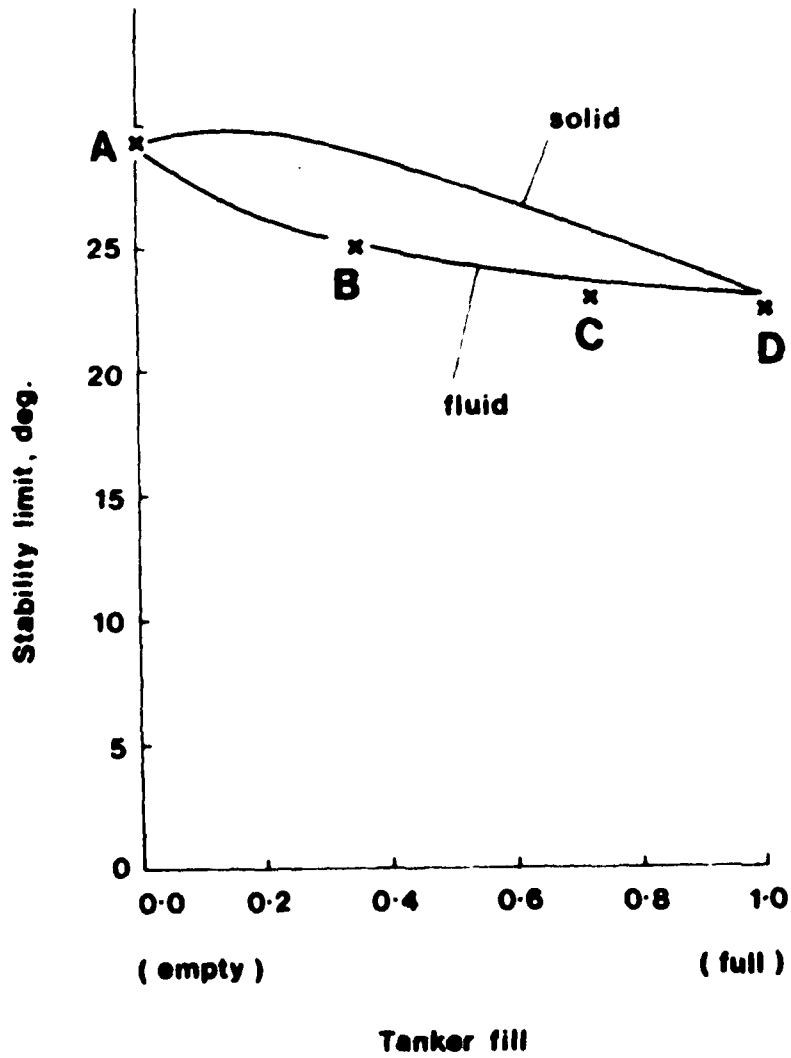


Fig 4. Experimental values of stability limit plotted against predicted curve for full-scale slurry tanker. (A,B,C,D - see text)

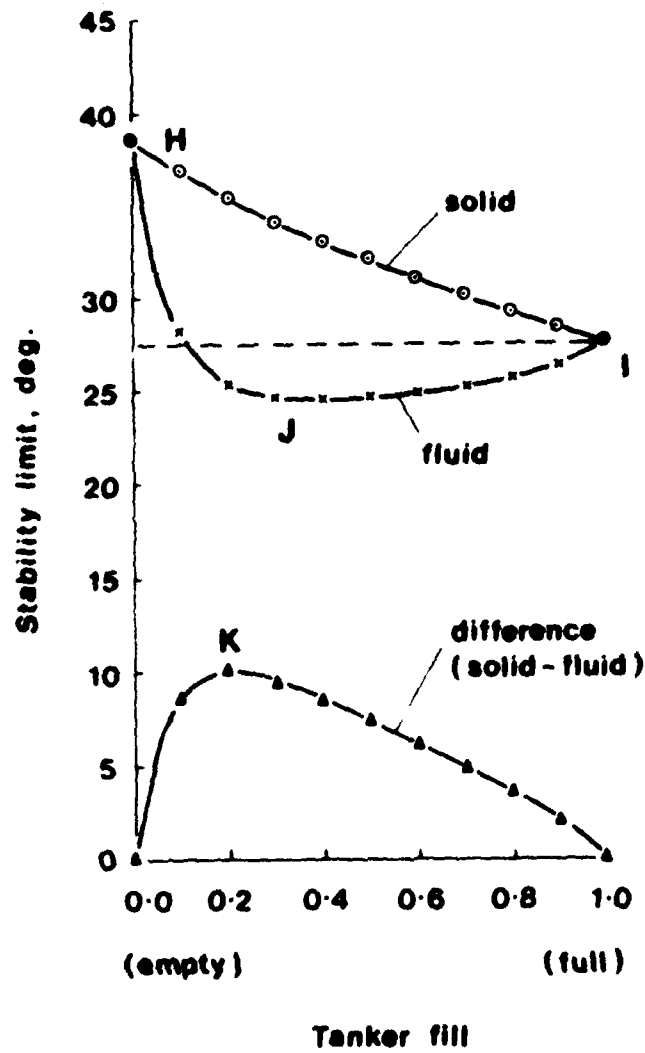


Fig. 5. Computed values of stability limit for tanker of rectangular cross-section. (H, I, J, K - see text)

CONTROL OF TANKERS ON SLOPES

Trailed equipment, especially behind a two-wheel drive tractor, is likely to push or pull the tractor out of control on a slope. After a certain critical slope is reached the tractor and trailer will slide downhill under gravity out of control. The problem is worst on hard ground covered by grass surfaces, which can be very slippery, and with heavy trailed equipment such as forage harvesting equipment⁷. Slurry tankers introduce the additional problem that the weight transfer from the tanker onto the tractor changes continuously while the tanker empties. This means that the grip which the tractor wheels are able to maintain, which is directly proportional to the weight on those wheels, will also change continuously.

Values of critical slope were calculated for a tractor and trailed tanker. The particular machines were again taken from the first accident example mentioned in the Introduction. The calculations were restricted to direct uphill and downhill travel because usually these are the directions on which the critical slopes are minima. Along these directions the only wheels to have grip on the ground are the tractor driving wheels since the others are free to roll. Along other directions all the wheels have grip sideways which increases the critical slope values. A plot of critical slopes for direct uphill and downhill travel is given in Fig. 6. This calculation was made under the assumptions that the friction coefficient between the tractor driving wheels and the ground was 0.76, and that the rolling resistance coefficient at the tractor front wheels and the tanker wheels was 0.05. The former value is the highest value measured locally⁸, chosen for these calculations in order to emphasise certain features of tractor control with tankers. The latter value is a typical one⁹.

When the tanker is full, at L, the uphill and downhill critical slopes are nearly identical, but as the tanker empties these values diverge until when the tanker is about half-full, at M, the downhill critical slope exceeds the uphill value by over 3°. As the tanker empties further the point is reached at N where the two critical slopes coincide

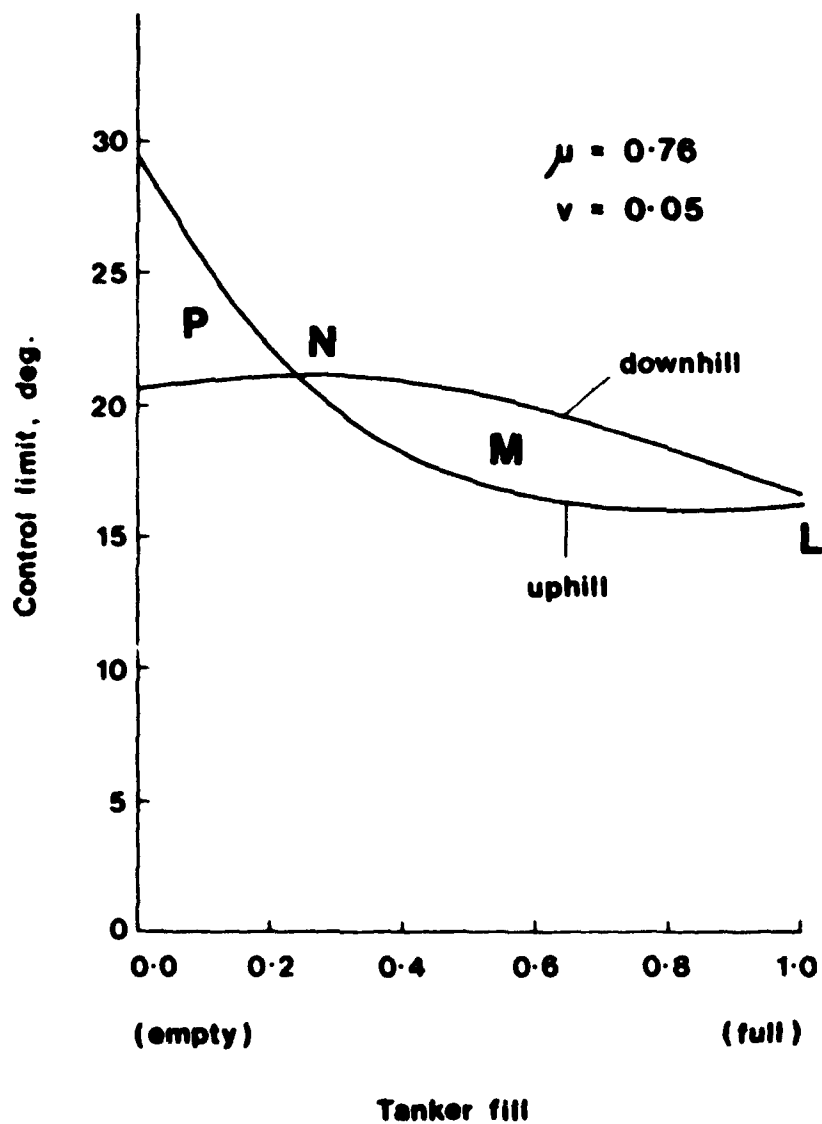


Fig. 6 Computed values of control limit for tractor and slurry tanker on ground surface with average grip. (R,S,T - see text)

again. During the period when the last fluid is emptied from the tanker, at P, the two values again diverge but this time the uphill critical slope exceeds the down-hill value. When the tanker is empty the difference in value is 9° .

These features are evident from the particular example chosen with an extreme value of friction coefficient. With an average value of friction coefficient between tractor tyres and grass of 0.4 the picture alters considerably, Fig. 7. The uphill and downhill critical slopes are no longer close when the tanker is full at R. Instead the downhill value exceeds the uphill value by about 3° over the whole period when the tanker empties, S. It is only when the tanker is almost completely empty, T, that the values converge again. These values do not necessarily cover the whole range of possibilities for movement of the values of critical slope but they do serve to indicate that there are continuous changes as the quantity of fluid in the tank changes.

DISCUSSION OF DRIVING ON SLOPES

Driving tractors with trailed tankers on slopes introduces problems of safety which have not previously been recognised. It is difficult for the driver to perceive the dangers which may arise when working with trailed tankers, and it is virtually impossible for him to assess his safety margin. The problems of working with trailed tankers may be discussed most easily in relation to the known causes of accidents with other farm machinery on slopes^{10,11,12}.

Tractors themselves are relatively stable¹³ and unlikely to overturn alone unless driven onto very steep side slopes or driven at high speed especially when cornering¹⁴. When used with trailed equipment, it is more likely that, due to its lower stability, the trailed equipment will overturn before the tractor¹⁵ and it is recognised that full trailers are generally less stable than empty ones¹⁶. If a driver was to take the slurry tanker shown in Fig. 1 onto a sloping field, most features would be similar to those of other trailed equipment. The stability limit of the tanker would at all times be lower than that of a typical tractor (35°), whether the tanker was empty, at A (29°), or full, at D (23°), Fig. 4.

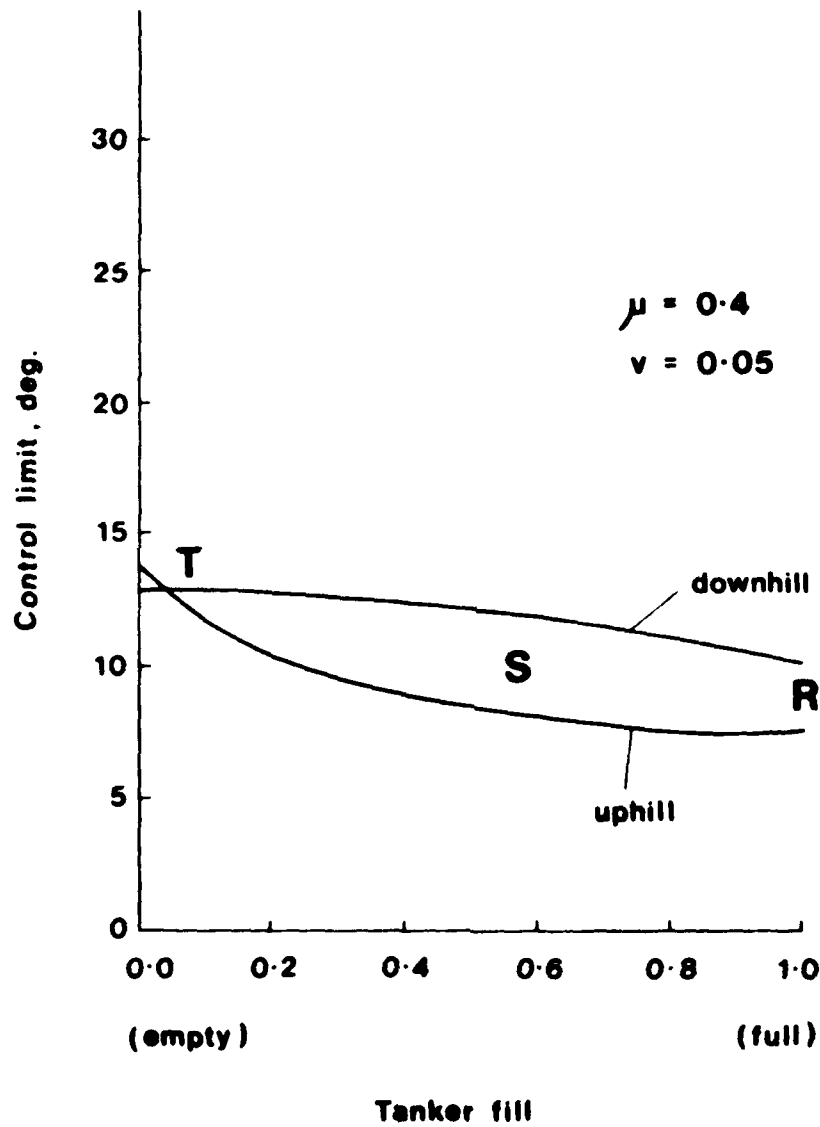


Fig. 7 Computed values of control limit for tractor and slurry tanker on ground surface with average grip. (R,S,T - see text)

The least stable condition would be when the trailer was full, but the stability would improve continuously as the tanker was emptied. There would be one new feature which was that the freedom of the fluid to move had resulted in lower values of stability limit than with a solid load, as shown by the two curves in the figure, but it is unlikely that this would be perceived by the driver.

However, with another slurry tanker, such as that which provided the basis for the stability plot in Fig. 5, the situation would be unlike that known for any other trailed equipment. The stability limit when full, at I (28°), would still be less than that when empty, at H (39°), but it would not be the minimum. From the time of starting to work in a field, with a full tanker, the stability of the tanker would be reducing progressively until the minimum was reached, at J (25°), with a tank fill of 0.3. Far from approaching the high stability limit of the empty tanker, as might have been expected with 70% of the contents discharged from the tank, the stability limit would be at its lowest. The stability limit would only start to exceed the completely full value when 90% of the contents had been discharged. The driver might well be taken unawares; he might continue to work on a slope where the tanker appeared to be stable when full only to find that the tanker was unstable when partially full; or he might move onto steeper slopes as the tanker emptied, thinking that the tanker would be more stable, only to find that it was less stable.

Tractors are known to slide downhill on grass particularly when the tractor is a two-wheel drive one¹⁷. In this case the tractor may be able to climb slopes considerably steeper than the slopes it can go down without sliding because of the greater weight on the tractor rear driving wheels when facing uphill. Trailled equipment generally reduces the value of the slope on which a tractor can be driven either uphill or downhill because of the additional weight which must be controlled by the tractor, of which only a small proportion is transferred to the driving wheels, but usually the slope which can be climbed remains steeper than the slope which can be descended. There is no safety value in this; indeed it is a feature

commonly appreciated that the driver should beware of sliding downhill even though the slope was safe for ascent.

A driver with a trailed slurry tanker has to beware of an alternative possibility, that his equipment might start sliding most easily when driven uphill, and that being able to descend a slope without sliding is no guarantee of being able to ascend. As with the stability limit, the control limit is affected by movement of fluid within the tank. When the tanker is faced uphill the fluid in the tank will run to the back, reducing the weight transfer onto the tractor, but when faced downhill the reverse will occur. The control limit curves in Fig. 6 also indicate that the behaviour of the tractor and tanker is unpredictable because the above discussion applied to the case where the tanker is about half full, at M, while the near empty case, at P, is like most other trailed equipment. When calculated for a lower friction coefficient, Fig. 7, the equipment is most likely to slide while travelling uphill regardless of the quantity of fluid in the tank, except when empty.

CONCLUSIONS

Trailed farm tankers introduce new problems to working with farm machinery on slopes because of the possibility that the fluid in the tank may move. Some of the tankers are very large, containing a total quantity of fluid which may be four times as heavy as the towing tractor, so the behaviour of the tanker on a slope may dominate the behaviour of the combination with the tractor. In order to analyse the behaviour of the tanker it was first necessary to know how the centre of gravity of the fluid moved within the tank under all conditions of tanker fill, with the tanker facing along any heading angle on any slope. The centre of gravity analysis was completed for tanks of circular and rectangular cross-sections, which included most shapes of tank used on farm tankers. The centre of gravity analysis was then used to develop a stability analysis for farm tankers in order to determine the stability limit (i.e. the overturning slope for the tanker). It was also used to develop a control analysis in order to determine

the control limit (i.e. the slope on which the tractor and trailed tanker would slide downhill).

One or two examples of tankers were then analysed and it was found that several new features emerged. Firstly, it was found that some tankers could become less stable as they were emptied rather than more stable which is the case for other farm trailers with solid not fluid loads. The least stable condition might be when 70% of the fluid had been discharged from the tanker and the stability might remain as low as when the tanker was full until 90% of the fluid had been discharged. Secondly, it was found that the weight of a trailed tanker might be most likely to cause sliding on a slope when the tractor was travelling uphill rather than downhill, which is the reverse of the case for tractors alone and tractors with other trailed equipment. Thirdly, it was found that each of the above two features was unpredictable because factors such as tank fill and the slipperiness of the ground surface might cause changes in behaviour with tankers which would not occur with other trailed equipment. Several implications of these features on driving tractors with trailed tankers on slopes were discussed.

REFERENCES

1. Slurry tankers, Power Farming, Feb. 1980, 18-25
2. Field crop sprayers, Power Farming, Oct. 1982
3. Spencer, H.B. Stability and control of two-wheel drive tractors and machinery on sloping ground. J. agric. Engng Res., 1978 23 (2) 169-188
4. Hunter, A.G.M. Centre of gravity analysis of fluid in inclined tanks. Proceedings Part C Instn Mechl Engrs, (submitted)
5. Hunter, A.G.M. Stability analysis of trailed tankers on slopes. J. agric. Engng Res. (submitted)
6. Bauer, H.F. On the destabilising effect of liquids in various vehicles. Vehicle System Dynamics, 1972 227-260
7. Hunter, A.G.M. Critical direct descent and ascent slopes of a tractor with forage harvester and trailer. Intl. J. Veh. Design, 1981 2 (3) 289-298
8. Owen, G.M. Safe working slopes for some tractors and tractor/implement combinations. Dep. Note SIN/325, Scot. Inst. agric. Engng, Penicuik, 1981 (unpubl.)
9. McKibben, E.G.; Davidson, J.B. Transport wheels for agricultural machines. Agric. Engng, 1939 20 469-473
10. Owen, G.M.; Hunter, A.G.M. A survey of tractor overturning accidents in the United Kingdom J. occupl Accidents, 1983 5

11. Hunter, A.G.M. A discussion of tractor overturning accidents on slopes due to stability or control loss. Tech. Rep. 3, Scot. Inst. agric. Engng, Penicuik, 1981
12. Hunter, A.G.M.; Owen, G.M. Tractor overturning accidents on slopes. J. occupl Accidents, 1983 5
13. Hunter, A.G.M. Tip angles for tractor sideways overturning from Norwegian test reports. Dep. Note SIN/355. Scot. Inst. agric. Engng, Penicuik, 1982 (unpubl.)
14. Owen, G.M. The effects of offset load and speed on tractor stability. Dep. Note SIN/317 Scot. Inst. agric. Engng, Penicuik, 1981 (unpubl.)
15. Owen, G.M. Trailed equipment stability : problems and solutions. Dep. Note SIN/349, Scot. Inst. agric. Engng, Penicuik, May 1982 (unpubl.)
16. Spencer, H.B. Silage crop harvesting on sloping ground - slope limits and harvesting rates (1981). Dep. Note SIN/374, Scot. Inst. agric. Engng, Penicuik, June 1983 (unpubl.)



AD-P004 292

↓
CONTROL OF TRACTORS ON SLOPING GROUND

H.B. SPENCER^{*}; D.A. CROLLA[†]

^{*} EQUIPMENT BEHAVIOUR SECTION, SIAE, PENICUIK, EH26 0PH, UK
[†] DEPARTMENT OF MECHANICAL ENGINEERING,
UNIVERSITY OF LEEDS, LEEDS LS2 9JT, UK

INTRODUCTION

Tractor and agricultural accidents on slopes fall into two categories. The most well known is a stability loss accident in which the tractor simply overturns. Much more common is the sliding control loss accident, frequently termed a 'runaway' by farmers. The 'runaway' description is apt because this is exactly how it appears to the driver - an uncontrolled speed build up when descending a slope. The accident occurs when the wheel-ground forces in the plane of the ground are no longer sufficient to maintain equilibrium on the slope. These accidents often lead to overturns of varying severity; incidents have been reported of tractors travelling up to 1.5 km from the point of control loss before coming to rest.

Means of avoiding such accidents are being studied^{(1) (2)}. However, until such techniques are adopted the drivers of agricultural machines on slopes will be faced with the possibility of sliding accidents due, for example, to a sudden reduction in tyre-ground friction following an outburst of rain.

Many of these incidents result in minor injury and many cause damage to machinery; some cause very serious injury and fatalities. Much folk lore exists amongst drivers on how best to recover from such slides, the current wisdom being "keep the tractor straight".

The problem of finding the best advice to give farmers is not easily resolved. Remote-controlled tractors have been used to study control loss⁽³⁾ but the behaviour experienced is usually representative of just one particular tractor. The effects of changing configurations, or parameters is best

studied using mathematical models of the accident process, or at least the dynamics of the control loss from which an accident may ensue.

Severity of accidents is probably highly correlated with the kinetic energy involved. It would appear therefore that during a control loss accident the driving strategy that should be aimed at is minimisation of the kinetic energy (vehicle speed). This paper describes a mathematical model of the control loss of a tractor on a slope, some confirmatory results from trials using a remotely controlled tractor, and an example of a preliminary study into driver strategy for minimising kinetic energy in an accident.

MATHEMATICAL MODEL

Notation

A	Constant in tyre/force slip angle equation
A_{max}	Maximum tyre side force coefficient when rolling
B	Constant in tyre force/slip angle equation
BR	Braking force at a wheel
f	Constant in tyre force/speed equation
fn	Function
F_L	Actual tyre force when locked and sliding
F_{LO}	Maximum tyre force when locked
g	Acceleration due to gravity
G	Gravitational force vector
k	Lateral tyre force coefficient
m	Tractor mass
p	Tyre sliding velocity
X	Longitudinal tyre force
Y	Lateral tyre force
Z	Vertical tyre load
α	Tyre slip angle
β	Slope angle
δ	Steer angle
ψ	Tractor yaw angle
μ_x	Effective coefficient of sliding friction in longitudinal direction
μ_y	Effective coefficient of sliding friction in lateral direction

The mathematical model to predict the motion of a tractor on sloping ground (Fig. 1) is based on the classical vehicle handling model with freedom in the yaw, sideslip and longitudinal directions. The well known equations⁽⁵⁾ are modified to include the effect of the inclined plane by incorporating the gravitational force vector at the vehicle mass centre,

$$\underline{G} = \begin{bmatrix} mg \cdot \sin\beta \cdot \cos\psi \\ mg \cdot \sin\beta \cdot \sin\psi \\ mg \cdot \cos\beta \end{bmatrix}$$

in the $\begin{bmatrix} x \\ y \\ z \end{bmatrix}$ direction.

The assumptions used in deriving the equations for this model are:

- (a) The inclined plane has a smooth surface, is of constant slope (β) and has consistent frictional characteristics.
- (b) The tractor body is rigid with a conventionally pivoted front axle.
- (c) Motion in the z direction (perpendicular to the inclined plane) is not included so that ride vibration motion, tyre deflections, etc are ignored.

The resulting model is non-linear because no restriction is placed on the magnitude of the tyre sideslip angles. Consequently, the entire range of the tyre side force/slip angle relationship must be included and this is non-linear for slip angles greater than say 10° . Therefore, the equations are solved by digital simulation and the results produced typically as a predicted trajectory of the tractor until it stops, overturns (zero wheel loads), etc. Alternatively, the variation of other parameters, e.g. velocity or kinetic energy, may be plotted as a time history.

The forces generated by the tyres are the sole means by which the vehicle is guided, since other external forces, e.g. aerodynamic, are trivial by comparison. An accurate representation of the way in which a tyre generates both longitudinal and lateral forces is, therefore, a key requirement of the model. More specifically, the conditions under which the wheel is locked and sliding is of particular importance in control loss studies. The force system on an individual wheel is calculated as follows:

- (a) The wheel is tested to see whether or not it is rolling.
 If $(BR + C_{RR}Z) > \mu_x Z$ wheel is rolling,
 otherwise wheel is locked.
- (b) Wheel rolling.
 $Y = kZ$,
 where $k = A(1 - e^{-B_1})$
 and $A = \text{fn}(A_{\text{max}}, X, \mu_x, Z)$.

Fig 2. shows the friction ellipse relationship used in which the actual value of X defines the shape of the side force/slip curve. From Fig. 2 it can be seen that

$$\left(\frac{A}{A_{\text{max}}}\right)^2 + \left(\frac{X}{\mu_x Z}\right)^2 = 1,$$

where A_{max} defines effectively the maximum "lateral coefficient of friction" with the wheel rolling.

- (c) Wheel locked.
 The total frictional force when sliding is
 $F_{LO} = \text{fn}(\mu_x, \mu_y, Z, \alpha, p)$.

From Fig. 3, it can be seen that if, again, the friction ellipse is used it can also be shown that,

$$F_{LO} = \left[\frac{(\mu_x \mu_y Z)^2}{\mu_y^2 \cos^2 \alpha + \mu_x^2 \sin^2 \alpha} \right]^{\frac{1}{2}}$$

and that the tyre sliding velocity,
 $p = (u^2 + v^2)^{\frac{1}{2}}$.

(d) Effect of sliding speed.

There are, apparently, no results published for the effect of sliding speed on off-road tyre forces, although work on this topic is in progress at the Scottish Institute of Agricultural Engineering (SIAE). For road vehicle tyres, however, there are several published studies, some examples of which are shown in Fig. 4. Clearly the mechanism of tyre force generation on deformable surfaces will be fundamentally different from that on road surfaces. However, in the absence of other data, it seems reasonable to take the relationship shown in Fig. 4 as a starting point.

Over the speed range of interest, i.e. 0 to 10 m/s these data approximate well to a linear relationship between tyre force and speed:

$$F_L = F_{LO} (1 - fp) ,$$

where F_L = Locked tyre force (N)

F_{LO} = Nominal locked tyre force at zero sliding speed (N)

f = Proportional constant in tyre force/speed relationship (s/m)

p = Sliding speed (m/s)

The constant, f , varies between 0.010 and 0.027 depending on conditions, with a reasonable typical value of 0.019.

(e) Wheel loads.

The technique used to calculate the wheel loads is based on the vector approach which has been described previously⁽⁴⁾. Additional terms arising from tractor acceleration components are included.

The total kinetic energy of the tractor is calculated from the standard equations using the tractor mass and inertia and the model predictions of linear and angular velocities⁽⁵⁾.

CONFIRMATORY EXPERIMENTS

The use of mathematical models in describing the behaviour of vehicles during emergency situations requires that the model predictions describe the general overall behaviour of the vehicle. On grass covered slopes the local variations of slope, friction, and ground roughness all cause perturbations which

affect the trajectory of a tractor during a control loss. The perturbations depend on the actual trajectory followed by the tractor, thus making it very difficult to make precise comparisons of the tractor behaviour with the mathematical model predictions.

For initial comparisons of measured and predicted behaviour, a radio controlled tractor was used on a site having a relatively smooth grass surface with a gradient varying slowly over a distance of 300 m from 17° to 11° ⁽⁵⁾.

Fig. 5 shows a comparison of a predicted trajectory with experimental data obtained using the radio-controlled tractor during a control loss. The trial was conducted with the steering held, nominally, at zero. The typical behaviour of a two-wheel drive tractor with the steering held at zero is a forward slide followed by a rapid rotation of the tractor until facing backwards and the slide then continuing backwards downhill. Depending on values of ground-wheel friction, slope and centre of gravity position, the tractor speeds up or slows down but always travels backwards. The model requires a steer input of a very small amount to predict the turn around. In the trial it is impossible to keep the steer angles at precisely zero and in such a condition any steer angle, or asymmetry of side forces, will cause the tractor to spin. However, as can be seen from Fig. 5, the mathematical model predicts the overall behaviour of the tractor fairly accurately.

Further trials were conducted, but on detecting a control loss full steer angles were applied and held. These trajectories and the model predictions were essentially similar. Behaviour was characterised by the tractor turning sideways on to the slope and sliding sideways down the slope but rapidly coming to rest⁽⁵⁾.

One other trial was carried out on a steeper slope of 20° . Applying full steering lock on detecting a control loss on this slope caused the tractor to overturn. The mathematical model predictions of this situation did not predict an overturn, although the up-slope wheel loads fell to quite small values (200 N). The 20° slope was relatively rough and this may have caused effective sideways wheel forces to be greater

than the model predictions. Higher side forces would promote an overturn rather than a slide on such a slope. This points to a need to obtain data on tyre forces on rough grass surfaces under the extreme conditions likely to be encountered during accident situations. Work to obtain such data is currently being carried out by SIAE.

However, the model has been shown to predict overall behaviour reasonably well and hence is suitable for use in examining possible driver strategies during a control loss on a slope.

EFFECT OF STEERING DURING A CONTROL LOSS -

A PRELIMINARY STUDY

As an example of the use of the model in the study of accidents on slopes, the effect of steering angle on different configurations of a two-wheel drive tractor during a control loss on a 20° slope is examined.

The tractor is basically a medium power two-wheel drive with a mounted hay tedder. It is assumed that a control loss occurs by driving onto a 20° slope and the driver "detects" a control loss when the tractor speed has reached 3 m/s. The driver now wishes to minimise the kinetic energy of the tractor to ensure that any resulting overturn occurs at the lowest possible energy levels.

The tractor's first configuration is characterised by a high (1.2 m), and a forward, centre of gravity position. This tends to make the tractor less stable than low and aft centre of gravity positions. The kinetic energies during the resulting tractor motion are shown in Fig. 6. Each of these steering actions resulted in a tractor overturn but the energies involved in the overturn decreased as steer angle is increased. The cab test energy for this mass of tractor is 15.835 kJ. This is much lower than the kinetic energies occurring during the accident. Fig. 6 shows that inducing an overturn early in the accident by applying maximum steer angle results in the best survival strategy. Although the kinetic energy at overturn is greater than the test energy, only a small proportion of this kinetic energy is likely to be absorbed by cab deformation⁽⁶⁾.

The effect of reducing the value of μ is shown in Fig. 7. Overturns do not occur and kinetic energy continues to increase during the control loss. In practice, ground surface roughness effects would cause overturns. Again, the strategy for minimising energy is the one of applying full steering lock and holding. The reductions in kinetic energy occur when the tractor is sliding sideways, so making use of the side forces available at the front wheels.

Reducing the centre of gravity height to 1.0 m (Fig. 8) produces detail changes in the way the kinetic energy varies but the recommendation is still to apply full steer lock and hold for minimising kinetic energy during the control loss.

The effect of increasing μ with the lowered centre of gravity height, Fig. 9, causes the tractor to come to rest. However, high energy levels persist for a large part of the time with zero steer. Application of steer and holding on this steer causes the tractor to be brought to rest relatively quickly, so reducing the potential hazard of a control loss (Fig. 9).

Moving the centre of gravity aft produces an overall lowering of kinetic energy levels during the control loss. Again, applying full steering lock minimises energy levels. However, at the low value of μ (0.377) the motion continues and the tractor does not come to rest (Fig. 10). Increasing μ (0.529) brings the tractor to rest (Fig. 11); although the energies in this case are very low, the application of steering produces the safe strategy, the tractor coming to rest quickly so avoiding higher energy levels which could be hazardous if the tractor remained in motion. Fig. 11 shows the rapid lowering of energy levels by applying the steering.

These examples show how the model can be used to analyse the consequences of a control loss accident with a particular two-wheel drive tractor on a 20° slope. They illustrate how driver behaviour can affect the outcome by applying steering, so reducing accident hazard. The machine geometry is also important, lower energy levels being associated with rearward centre of gravity positions. This accords with observations of a number of serious control loss accidents which have been associated with tractors carrying unnecessary front ballast.

CONCLUSIONS

1. A mathematical model has been developed for examining the behaviour of two-wheel drive tractor motion during accidents on slopes.
2. The model generally predicts the motion behaviour of tractors during actual accidents. In some detail aspects a need for further refinement is indicated. This would appear to be in the modelling of tyre side forces during the extreme motions occurring in accidents.
3. Application of the model to the study of minimising the hazard of a control loss accident of a two-wheel drive tractor on a 20° slope indicates that drivers should apply and hold full steer lock upon detection of a control loss.
4. The study indicates that rearward centre of gravity positions, in the situation studied, reduce the kinetic energy and hence the potential severity of a resulting accident.

REFERENCES

1. Spencer, H.B.; Owen, G.M. A device for assessing the safe descent slope of agricultural vehicles. *J. agric. Engng Res.*, 1981 26 (3) 277-286
2. Spencer, H.B.; Owen, G.M.; Greenhill, A.A. A micro-processor-based safe slope meter. *J. agric. Engng Res.*, 1983 28 (3) 269-279
3. Owen, G.M.; Spencer, H.B. Overturning and control loss experiments with a radio-controlled tractor. Dep. Note SIN/319, Scot. Inst. agric. Engng, Penicuik, 1980 (unpubl.)
4. Spencer, H.B. Stability and control of two-wheel drive tractors and machinery on sloping ground. *J. agric. Engng Res.*, 1978 23 (2) 169-188
5. Crolla, D.A.; Spencer, H.B. Tractor handling during control loss on sloping ground. *Vehicle System Dynamics* (In press)
6. Chisholm, C.J. Tractor overturning accidents and safety cab strength. *Agric. Engr.*, Vol. 36 Spring 1981 No. 1

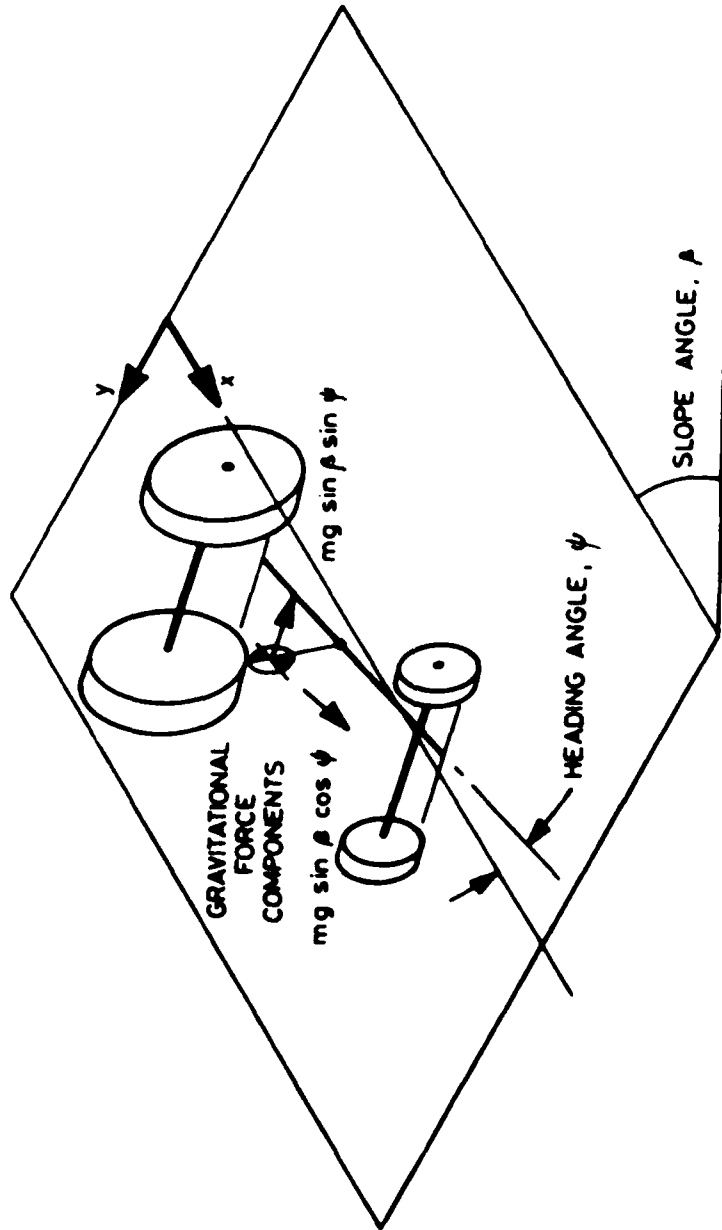


Fig. 1 Model of tractor on slope

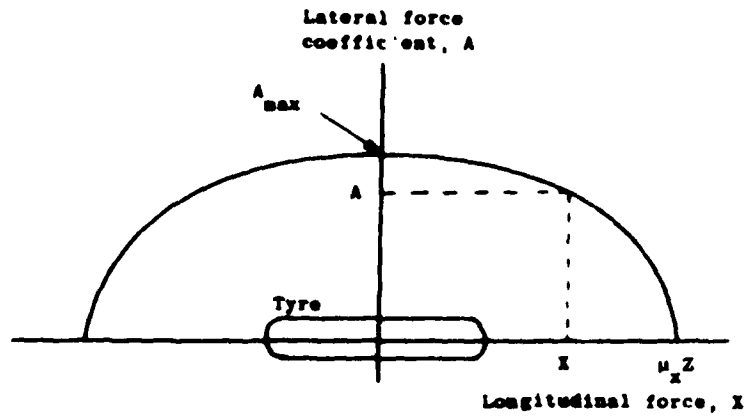


Fig. 2. Friction ellipse relationship - rolling wheel

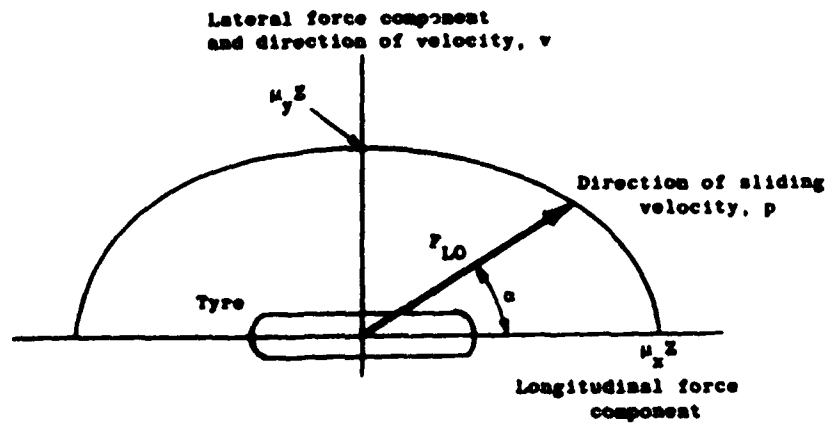


Fig. 3 Friction ellipse relationship - locked wheel

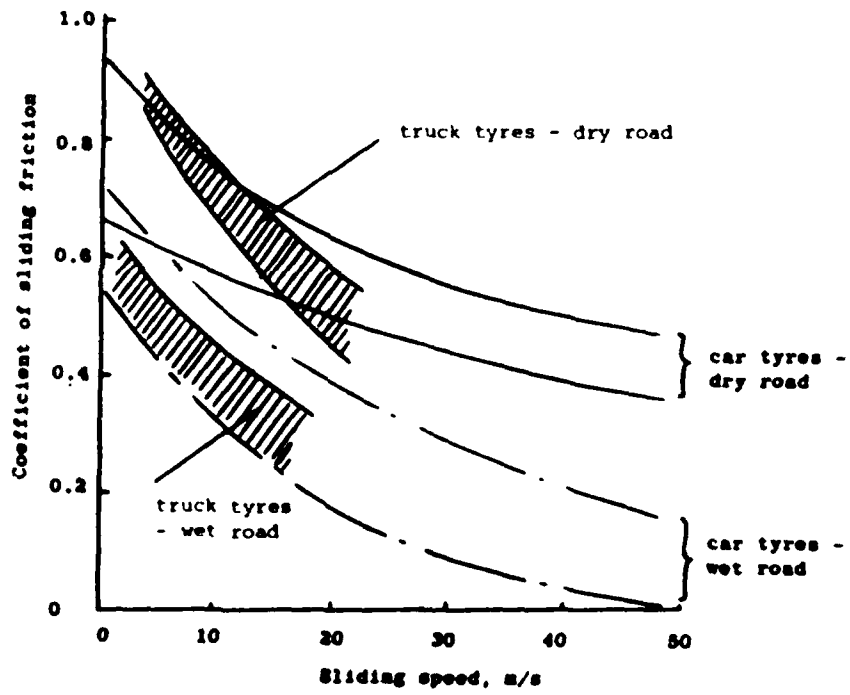


Fig. 4 Effect of sliding speed on tyre coefficient of friction

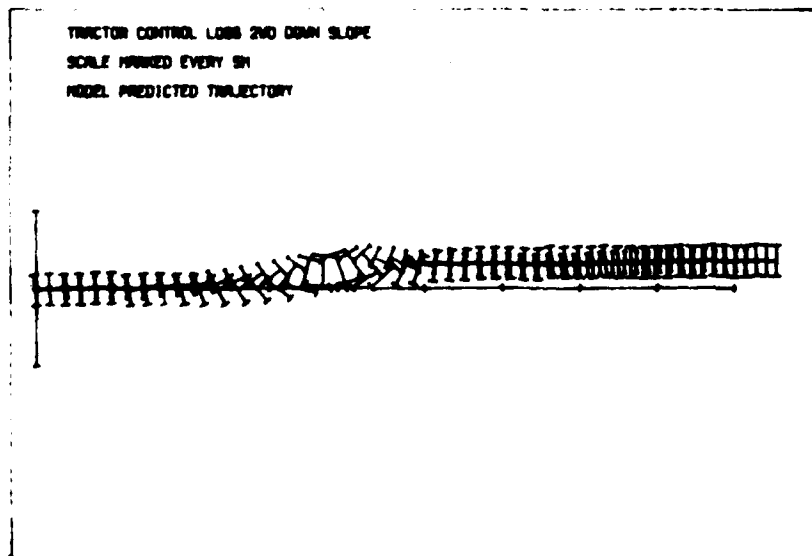
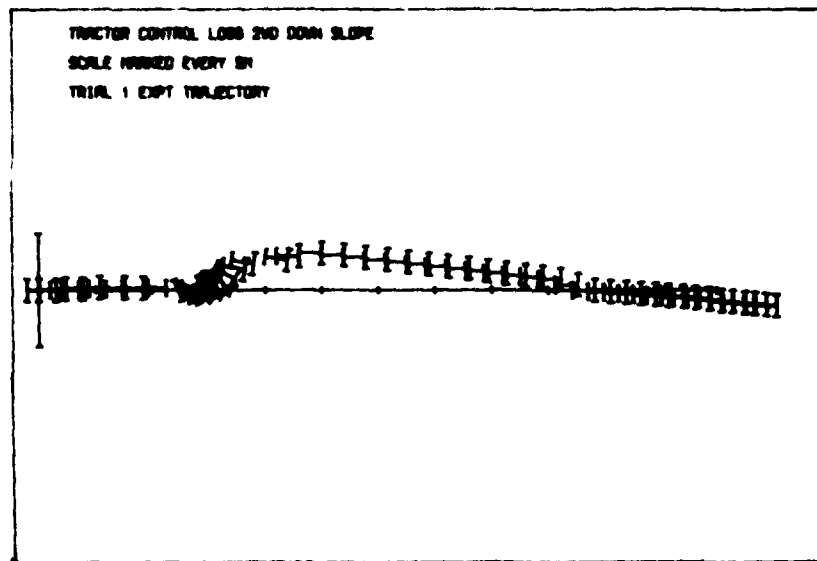


Fig. 5 Trial 1

Experimental observation (above) and mathematical model prediction of trajectory (below). Images 0.2 sec intervals. Steer angle δ nominally zero. Travel direction left to right.

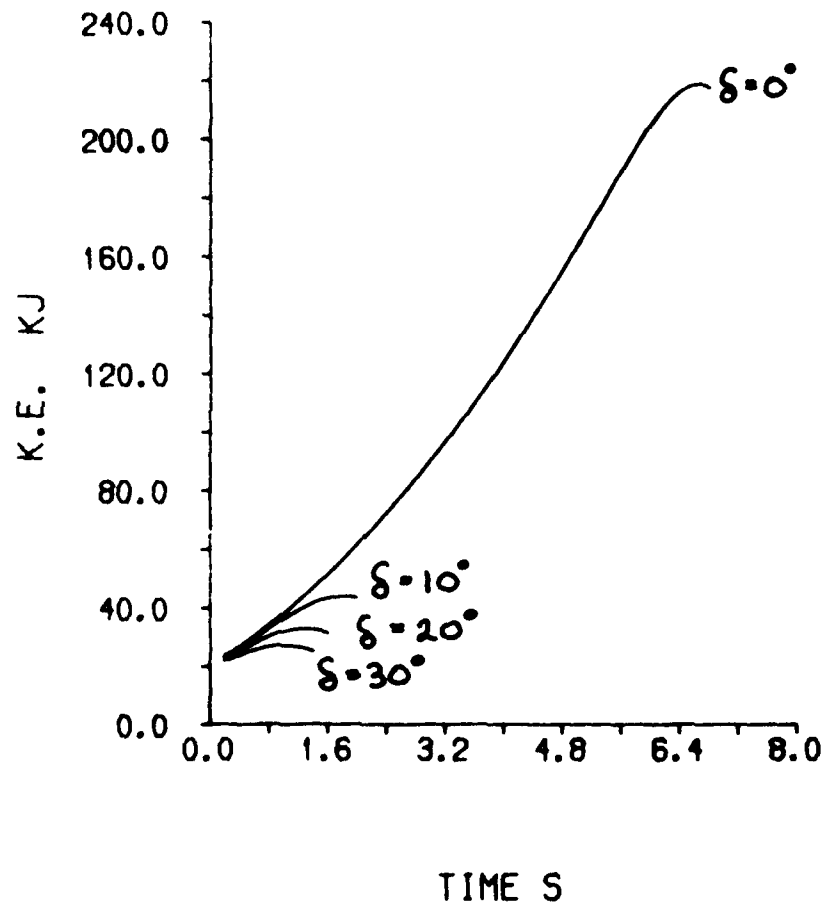


Fig. 6

Energy in a control loss for tractor with tedder.
Configuration no. 1 with high and forward centre
of gravity. $\mu = 0.529$

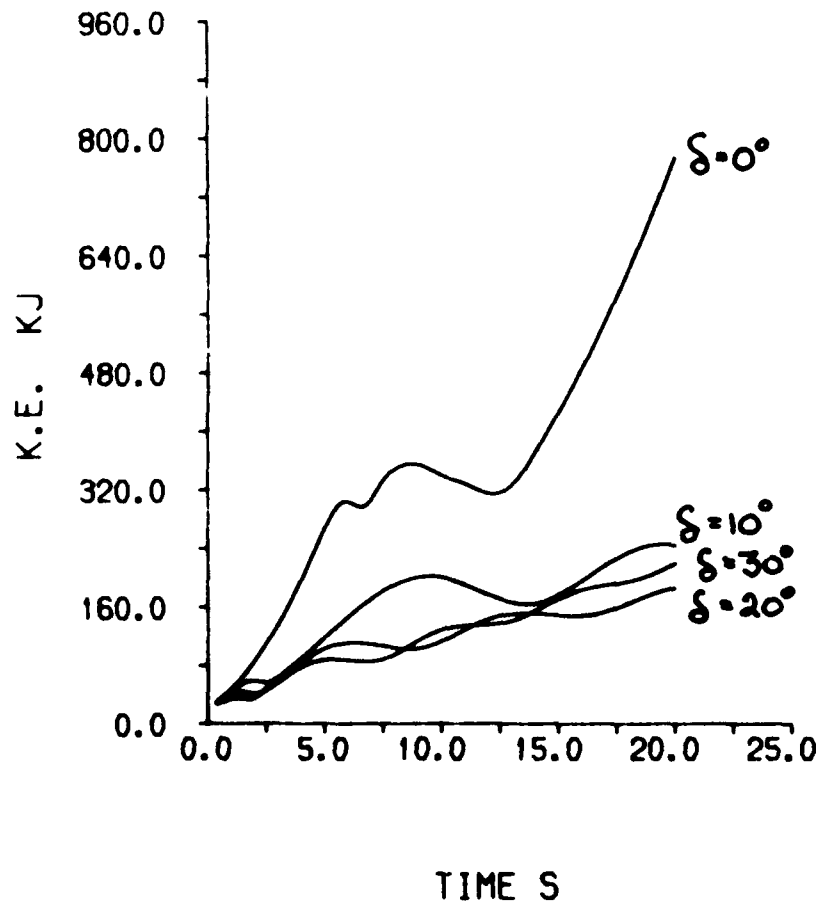


Fig. 7

Energy in a control loss for tractor with tedder.
Configuration no. 1 with high and forward centre
of gravity. $\mu = 0.377$

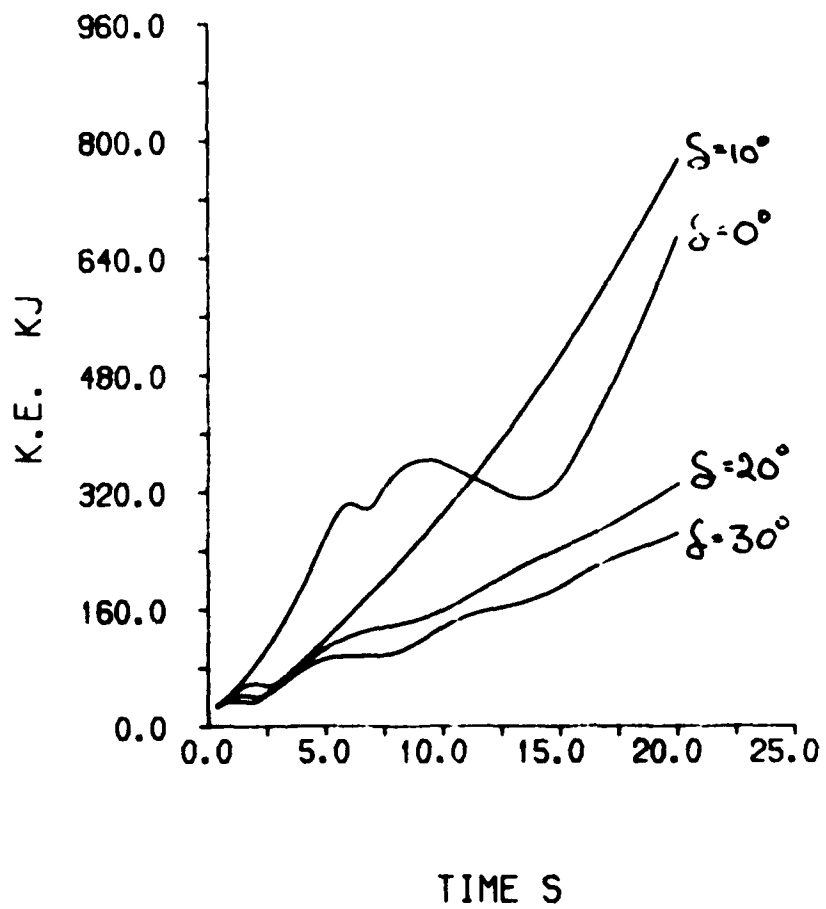


Fig. 8

Energy in a control loss for tractor with tedder.
Configuration no. 2 with low and forward centre
of gravity. $\mu = 0.377$

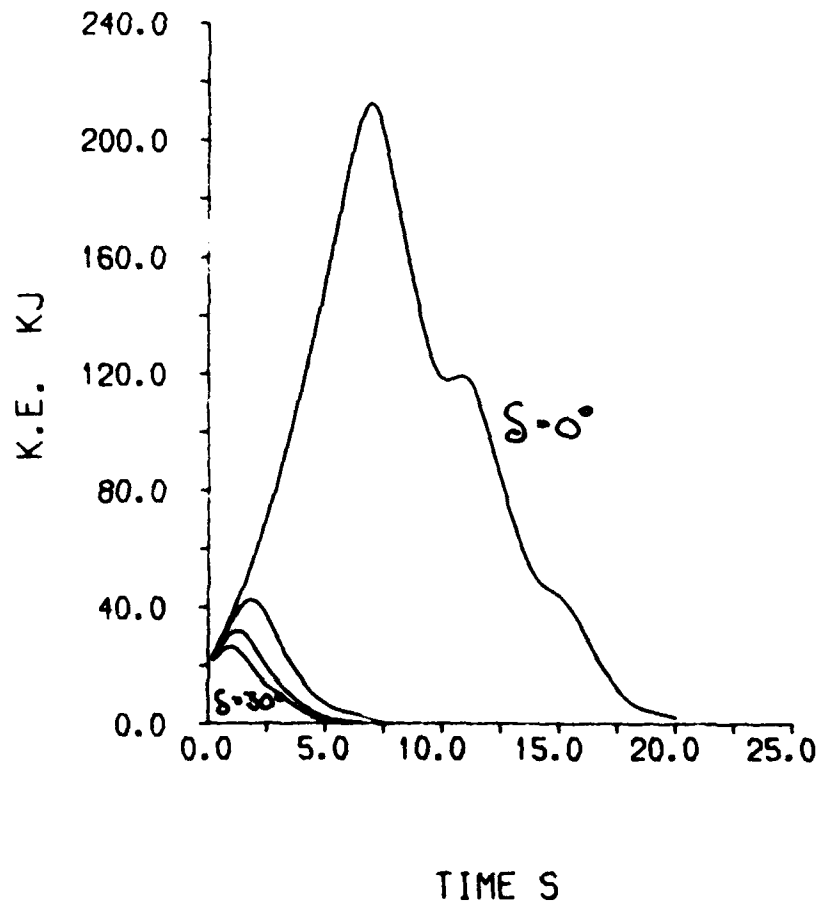


Fig. 9

Energy in a control loss for tractor with tedder.
Configuration no. 2 with low and forward centre
of gravity. $\mu = 0.529$

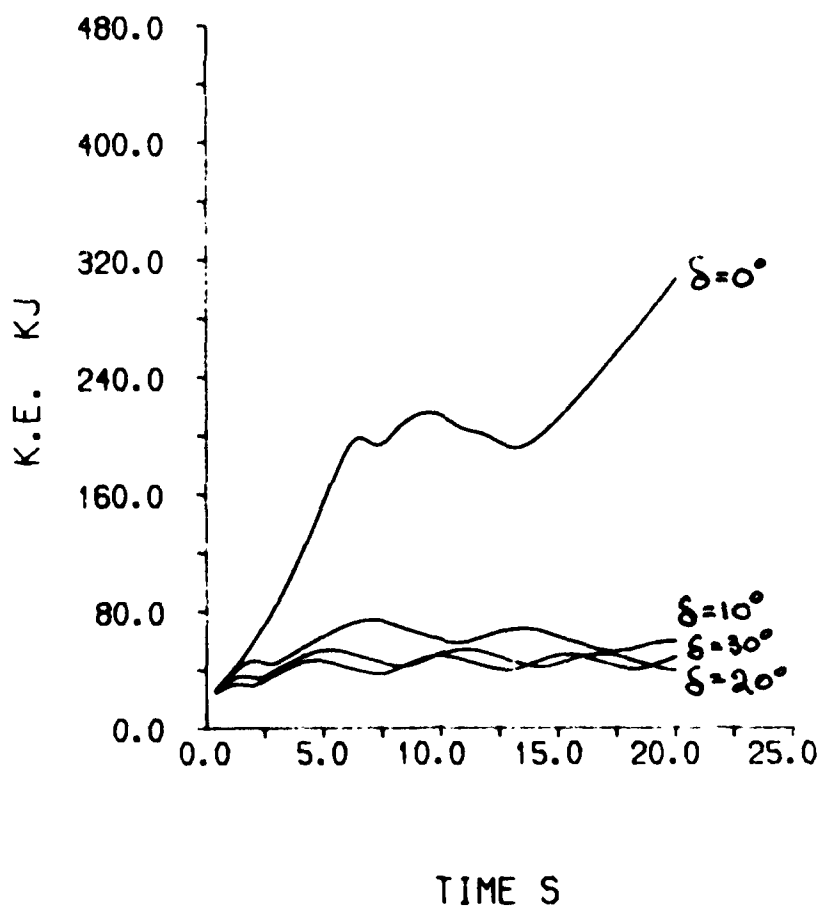


Fig. 10

Energy in a control loss for tractor with tedder.
Configuration no. 3 with low and aft centre of
gravity. $\mu = 0.377$

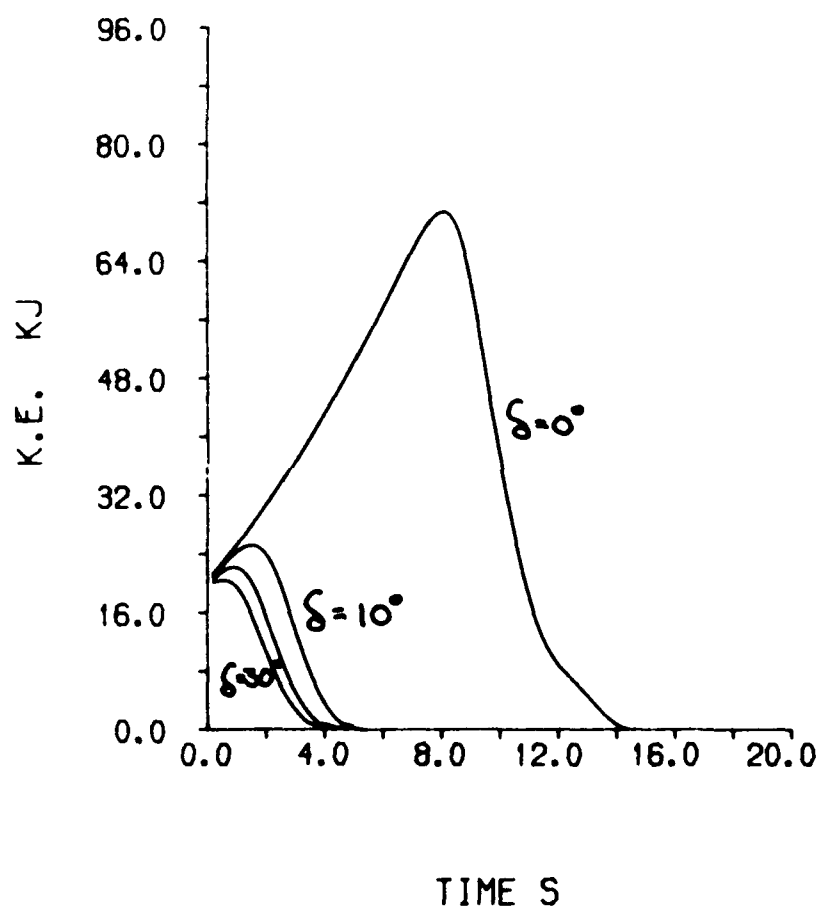


Fig. 11

Energy in a control loss for tractor with tedder.
Configuration no. 3 with low and aft centre of
gravity. $\mu = 0.529$



AD-P004 293

STABILITY INDICATORS FOR FRONT END LOADERS

G. Wray, J. Nazalewicz,* and A. J. Kwitowski**

*Stevens Institute, Hoboken, NJ; **U.S. Bureau of Mines, PA

ABSTRACT

This paper describes the development of a stability-indicating system for use in minimizing the occurrence of front-end loader (FEL) roll-overs in mining. The development proceeded in three phases: definition of FEL stability-instability characteristics; design of a 1st generation stability indicator; and design of a simplified, 2nd generation stability indicator. Goals met by the final design include confirmation of a simplified methodology for detecting machine instability; the ability to be installed on new loaders during manufacture or on older loaders on a retrofit basis; and reliable, easily interpretable operation.

INTRODUCTION

Rubber-tired FEL's, originally intended as small machines for handling loose or stockpile material, have rapidly increased in both size and number at surface mine operations over the past 15 to 20 years. Statistics bear out the fact that FEL accidents form the largest single category of machinery-related accidents in surface mining. For the years 1975 through 1981, FEL's used by the mining industry were involved in 26 fatalities and numerous less severe accidents. The vast majority of the fatalities occurred as a consequence of the FEL's rolling over and either crushing the operator within the cab or the operator being struck by the machine after jumping or being ejected from the cab.

Rollover protective structures are required on FEL's as specified in the Code of Federal Regulations, Title 30, Part 77.403a, "Mobile Equipment, Rollover Protective Structures (ROPS)." Obviously, ROPS do not prevent the vehicle from rolling over, but offer protection to the operator in the event that the vehicle does rollover. At present, FEL operators have only their own judgement against which to evaluate the stability or instability of their machines.

The Bureau of Mines, through contract with Stevens Institute of Technology, has responded to this problem with the development of a FEL stability indicator that provides the operator a reliable, easily interpreted display of the stability status of his or her machine. The stability indicator was designed to be a relatively low cost item capable of being retrofitted to older FEL's or incorporated into new loaders during their manufacture. Strain gage instrumentation is used to monitor the magnitude and rate of change of forces acting normal to the loader's wheels, with these forces being direct indicators of the machine's center of gravity relative to its stance on the terrain. The relative stability of the loader is conveyed to the operator through a display of green, amber, and red lights.

The development of the present stability indicator was undertaken in several stages; first, the stability characteristics of FEL's were analyzed and mathematically modeled; second, a 1st generation stability indicator was built that compared the calculated analog values to the measured values and issued a warning to the driver based on that difference as a safety margin; and third, the present device was produced, where the whole machine is used as the analog, and the results of the interpretation of the actual wheel loads on the ground are used to warn the driver of an impending overturn situation.

DEFINITION OF LOADER STABILITY CHARACTERISTICS

More than half of rollover accidents occur when the loaders are being trammed; that is, when they are being transported under their own power from one work area to another, when they are being moved from the working areas to maintenance shops and fueling stations, or when they are traveling over distances greater than those covered in normal loading and unloading operations. Generally, the loader operates at greater speed while tramping than it does during its normal work cycle. Eight out of ten tramping accidents occur on ungrades.

Front and side slopes contribute to an unstable operating model of the FEL. Operator-controlled factors contributing to the loss of stability are the weight of the load in the bucket, the bucket height, the yaw angle of articulation, its velocity, and the degree of braking. While any one of these parameters could be a principal contributor, it is usually a combination of these factors that produces an accident.

The first step towards alleviating the rollover problem was to define and quantify the following critical combination of factors and conditions that are most pertinent to front-end loader instability:

- o Vehicle pitch angle
- o Vehicle roll angle
- o Bucket load
- o Bucket location
- o Vehicle articulation angle
- o Inertial loads (acceleration-deceleration, centripetal forces)

A device that is to indicate to an operator just how close the machine is to an overturning condition has to account for the combined influence of all these factors on the stability characteristics of the vehicle.

MATHEMATICAL ANALYSIS OF STATIC LOAD AND INCLINATION LIMITS

The basic calculations of the static overturn limits for FEL's have to include all the variations possible in vehicle geometry. These calculations can be divided into two parts: locating the center of gravity (CG) of the loaded machine and determining whether this CG location relative to the support points induces overturn.

Most FEL's have a three-point suspension system. The rear axle is pinned to the frame at or above the axle center, creating a transverse walking beam action. This pin joint represents a single suspension point. The other two points are the ground contact point of the front tires (Fig. 1). With this type of suspension, the effective masses and CG's for pitch overturn are different from those for roll overturn. The vehicle will overturn about the front axle (nose down) if the CG of the entire mass is in front of a line connecting the front wheel ground contact points (Fig. 2).

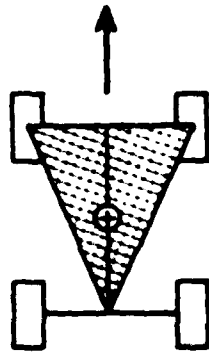


FIGURE 1: Front-end loader suspension points under normal conditions.

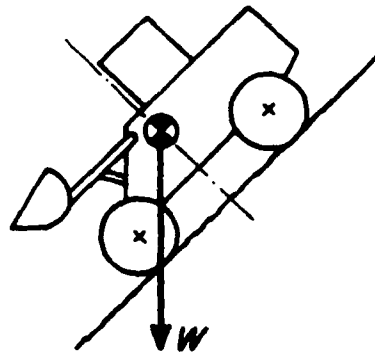


FIGURE 2: Projection of center of gravity near overturn.

Roll overturn can arise if the CG lies outside the line joining either of the front wheel ground contact points and the rear suspension pin (Fig. 1). In this latter case, the mass involved is that of the loaded vehicle less the mass of the rear axle unit. This mass is called the main mass.

There is, by design, a limit to the rotation possible about the rear axle (usually about 15°) after which the rear wheel contact point becomes the third support point (Fig. 3). A machine that has tipped enough to reach this limit will often have enough momentum to overturn completely.

Three variables affect the CG location with respect to the vehicle. The first variable is the articulation angle. To obtain the variation of CG with articulation angle, the weight and CG locations of both the front and rear units are needed. To obtain the CG of the main mass, the mass of the rear axle and its tires (plus ballast) has to be subtracted. The other two variables entering into the CG computation are the bucket load and the position of the lift arm. From this information, the location of each of the masses and the location of the CG's can be obtained in the standard manner of summing moments and dividing by the total weights. In addition, the position of the vehicle is identified by the pitch and roll angles (i.e., the angles between the gravity vector and the vehicle's x-y and x-z planes, respectively).

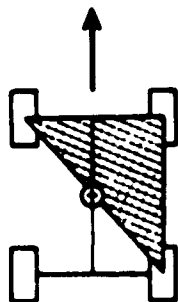


FIGURE 3: Front-end loader suspension points near overturn.

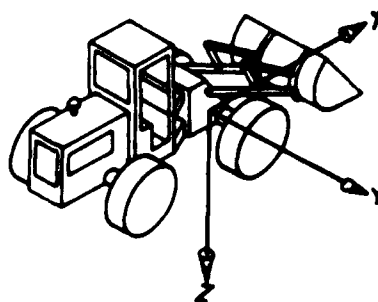


FIGURE 4: Coordinate system used in analysis.

The CG is located with respect to a vehicle coordinate system whose origin is at the center of the front axle, with the x-axis pointing forward, the y-axis to the right, and the z-axis down (Fig. 4). The mathematical procedure used is to locate the vehicle on a horizontal ground plane with a selected bucket load, lift arm position, and articulation angle. The ground plane is then inclined to a combined front and side slope, and the vertical projection of the vehicle CG is determined. If this projection falls within the stability triangle, the machine is considered statically stable; if it falls outside the triangle, it is statically unstable.

A computer program was written to solve these equations iteratively, as the most economical procedure is to establish approximate limits of the machine and to refine the results by calculating small increments of change. The final pitch-rollover points are easily determined to within 0.2°. The final solutions to the stability equations are then plotted by the computer.

STATIC OPERATING ENVELOPES

Using the above procedure, the static stability limits as functions of pitch and roll angles were generated with the bucket load, articulation angle, and lift arm position as independent parameters. Figure 5 is a plot of the pitch angle versus the roll angle with the bucket load as a parameter for 0° articulation angle and with the lift arm at the "carry" position. The FEL is stable for any combination of roll and pitch angle within the stability "triangle." Figure 6 is a similar plot except that the lift arm is in the "full-up" position. As is expected, the operating envelope is reduced in size with the lift arm in the full-up position. Figures 7 and 8 show the stability envelope when the vehicle is articulated to 35° and are directly comparable with Figures 5 and 6 (without articulation).

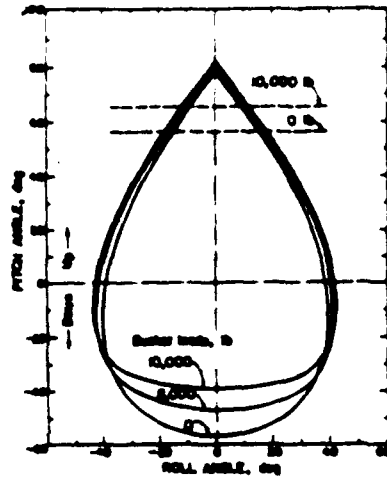


FIGURE 5: Stability envelope for arm at carry and articulation = 0°.

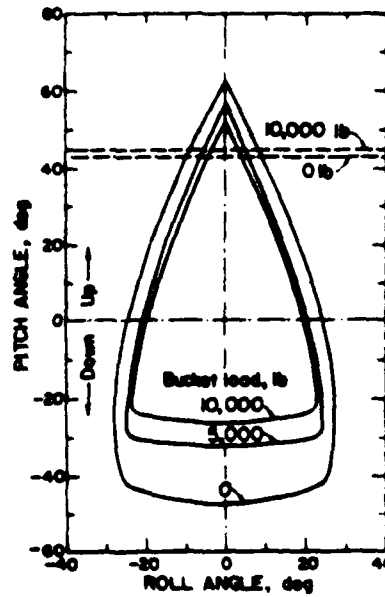


FIGURE 6: Stability envelope for arm full-up and articulation = 0°.

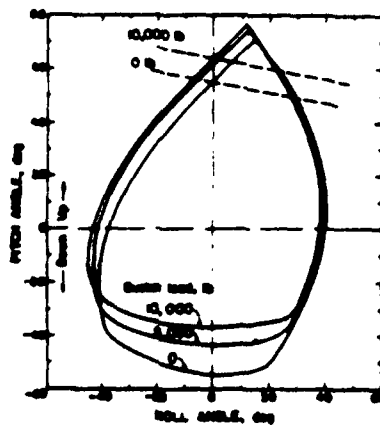


FIGURE 7: Stability envelope for arm at carry and articulation = 35°.

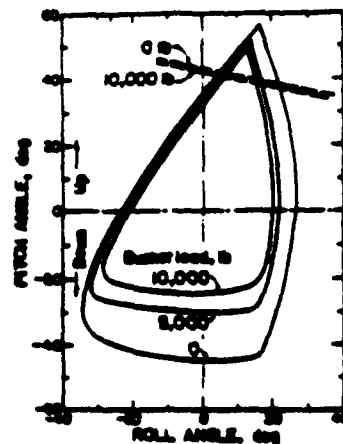


FIGURE 8: Stability envelope for arm full-up and articulation = 35°.

The articulation angle produces mirror image curves; the -35° articulation curve is inclined equally and in the opposite direction to the $+35^\circ$ articulation angle curve.

The curves readily show that it is necessary to *sense and respond* to all the parameters. To sense merely roll angle would have two opposite and unacceptable effects:

1. It could result in a warning device that is far too conservative and hence restricts the operation of the FEL to an unacceptable level and prevents its acceptance.
2. It may not give warning when it should, producing false confidence which might contribute to an accident.

These results have been compared with available experimental data from one of the manufacturers and have been found to correlate well (Tables 1 and 2).

TABLE 1: Center of gravity comparison.

	Distances from reference axis, in	
	Manufacturer's data	Calculated values
Bucket empty, arm at carry:		
Longitudinal (x).....	60.9	60.9
Lateral (y).....	0	0
Vertical (z).....	-11.2	-11.2
Bucket loaded (10,300 lb), arm full-up:		
Longitudinal (x).....	61.9	61.9
Lateral (y).....	0	0
Vertical (z).....	-29.7	-29.7

TABLE 2: Inclination limit comparison.

FEL position	Side slope angle at overturn, deg	
	Manufacturer's data	Calculated values
Bucket empty, arm at carry:		
Feeding up slope.....	36	36.4
Feeding down slope....	36	36
Parallel to slope....	36	39
Bucket loaded (10,300 lb), arm full-up:		
Feeding up slope.....	42	42.9
Feeding down slope....	22	26
Parallel to slope....	19	19

STATIC STABILITY CORRELATION EQUATION

To be able to construct the electronic logic circuitry for the 1st generation stability indicator, the stability envelope had to be mathematically defined. However, describing all the curves with one equation was quite difficult because the curves are triangular in shape and lie in all four quadrants. All attempts at generating a correlation equation by utilizing a systematic, logical, theoretical approach failed. Therefore, an alternate solution was used.

An initial decision was made that roll angles greater than 30° (about a 60% side slope) and pitch angles beyond the range of $+35^\circ$ (up) to -25° (down) would be considered outside the normal range of operation. Separate limit detectors would be employed to trigger a warning light if any of these basic limits were exceeded, regardless of any other condition. The equation of a parabola that includes the effects of

bucket load and lift arm position but not of articulation angle has the form:

$$\theta_r^2 = C_1 + C_2 W + C_3 \theta_{arm} - (C_4 \theta_p + C_5)^2,$$

where: θ_r = roll angle,
 θ_p = pitch angle,
 θ_{arm} = lift arm angle,
 W = bucket load,

and C_1, C_2, C_3, C_4, C_5 = constants.

To correct for articulation angle (θ_{art}), replace:

$$\theta_p \text{ by } \theta_p \cos .4\theta_{art} - \theta_r \sin .4\theta_{art}$$

and θ_r by $\theta_p \sin .4\theta_{art} + \theta_r \cos .4\theta_{art}$.

and the prediction equation for the critical roll angle, including articulation angle and specific constants for a specific FEL becomes:

$$\begin{aligned} |\theta_{r \text{ critical}}| &= 36.94 - 3.265 \times 10^{-4} V - 0.2239 \theta_{arm} \\ &\quad - [0.054 (\theta_p \cos .4\theta_{art} - \theta_r \sin .4\theta_{art}) \\ &\quad + 2.1577]^2. \end{aligned}$$

The absolute value of $\theta_{r \text{ critical}}$ was used since the stability curves are mirror images and the equation is valid for either positive or negative articulation angles. This absolute value of $\theta_{r \text{ critical}}$ was then compared with the corrected roll angle so that the safe operating range was represented by:

$$|\theta_p \sin .4\theta_{art} + \theta_r \cos .4\theta_{art}| < |\theta_{r \text{ critical}}|.$$

Figure 9 is a correlation plot of the critical roll angle predicted from the equation versus the roll angle calculated by the computer program. The correlation is made for a fixed articulation angle of 20° , but for three bucket loads. The individual data points represent three lift arm positions (carry, horizontal, and full-up at various combinations of pitch angle. This prediction equation thus contains all of the terms that enter into the determination of static stability.

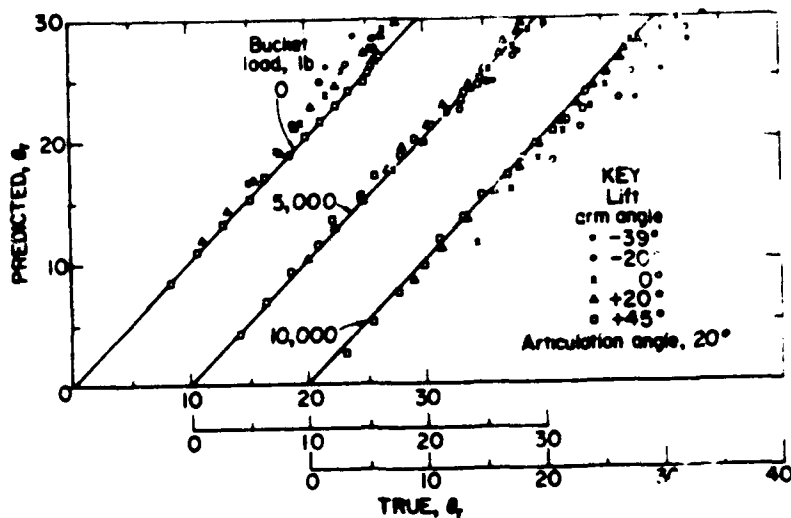


FIGURE 9: Correlation of data between predicted and actual cases.

FIRST GENERATION STABILITY INDICATOR

Analog Circuit

An analog circuit was designed to solve the prediction equation. A block diagram of this circuit is shown in Figure 10. The seven electronic circuit cards used are shown in Figure 11. This analog computer was used to solve the correlation equation from sensor inputs, and then compare the existing roll angle to the critical roll angle, and give the driver a visual warning.

Sensors and Transducers

The original approach to sense the pitch and roll angles by damped pendulum-type potentiometers was abandoned because their range of natural frequency coincides with that of FEL's, at approximately 2 Hz. Therefore, electrolytic sensors, using a semiconducting fluid in a circular tube and with a natural frequency greater than 10 Hz, were selected.

The articulation angle and lift arm position were sensed by single-turn rotary potentiometers. Special shaft bearing and seal designs made these potentiometers safe from salt spray, sand, dust, and fungus.

The bucket load was determined by sensing lift cylinder hydraulic pressure with a pressure transducer and combining it electronically with lift arm position.

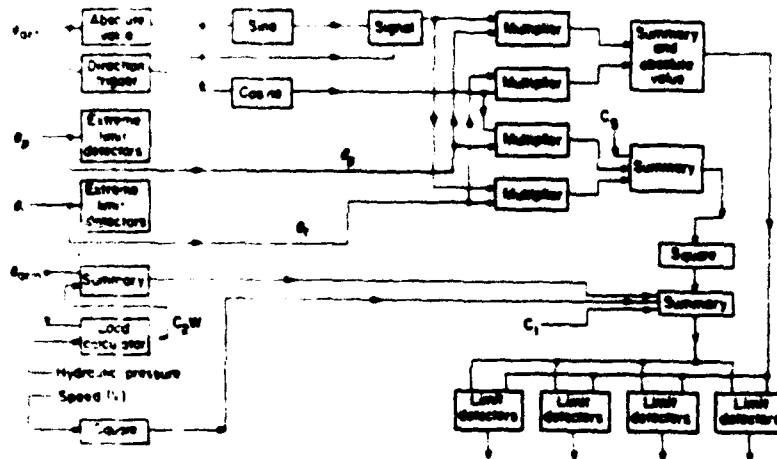


FIGURE 10: Block diagram of signal processor.

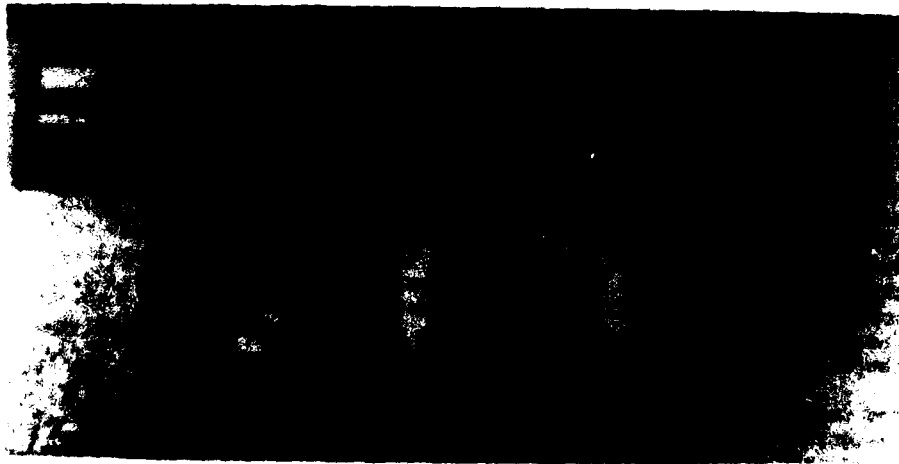


FIGURE 11: Electronic circuit boards for 1st generation stability indicator.

The speed sensor was a d/c tachometer-generator friction-coupled to the output shaft of the transmission.

Warning Indicators

The driver's warning device consisted of four indicator lights. One was green, two were amber, and one was red. The analog circuitry accepted the five sensor inputs, calculated the angle at which the machine would roll over, and compared this value to the corrected roll angle. The difference between the calculated angle and the actual roll angle was represented by a voltage that was sensed by four level detectors. Each level detector was wired to one of the lights and was adjustable for proper level and sequencing.

Evaluation

The above-described system was installed on three FEL's used in a rock quarry operation. During a 12-month test period, the units performed satisfactorily and were judged by the operators as very useful operational tools. However, these 1st generation units had several disadvantages, as follows:

1. They were costly to manufacture owing to the complexity of the electronics.
2. They were costly to install owing to the skilled labor required to install the sensors.
3. The system would not completely correct for the effects of inertia during braking, acceleration, or cornering.

THE SECOND GENERATION STABILITY INDICATOR

In an effort to reduce the complexity and cost of the system, an alternate means of obtaining a signal or measuring a parameter that would indicate rollover instability was sought. As the FEL approaches rollover instability, the CG moves towards the outside of the "stability triangle" formed by the three support points. As this happens, the normal load on the up-slope wheel decreases and the normal load on the down-slope wheel increases. At the point of rollover instability, the normal load on the up-slope wheel has been reduced to zero.

The task of designing a stability indicator has now been reduced to designing a method of sensing the normal load on each of the front wheels and using the lower value to trigger a warning system.

By utilizing strain gages, the bending stresses in the axle can be determined. To obtain the normal load from the measured axle bending stresses, it is necessary to measure, or devise a system to cancel out, the bending stresses in the axle due to the tire side forces. These tire side forces are generated to resist the downslope forces acting on the FEL; they can also be generated during steering. The tire side force acting at the ground plane creates a bending moment in the axle which is proportional to the wheel radius. By measuring the axle bending stresses at two planes, they can be subtracted, which cancels out the effects due to tire side force, leaving a measurement that is proportional to wheel normal load.

Referring to Figure 12, bending moment at plane 1 is:

$$M_1 = NL(L_1) + SF(x).$$

Bending moment at plane 2 is:

$$M_2 = NL(L_2) + SF(x)$$

$$\begin{aligned} M_2 - M_1 &= NL(L_2) - NL(L_1) \\ &= NL(L_2 - L_1) \end{aligned}$$

or
$$NL = (M_2 - M_1)/(L_2 - L_1).$$

The bending moments at planes 1 and 2 are measured using strain gages and, since the distance between the two planes is known, the normal load is determined.

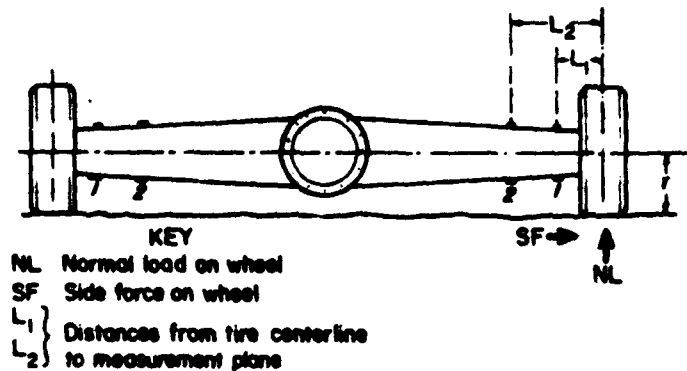


FIGURE 12: Forces acting on wheel of front-end loader.

Axle Sensors

To measure the bending strains on the FKL axle, it was decided that some form of bonded strain gage or strain transducer would have to be used. Since the output of a strain gage is represented by a voltage and the voltages obtained from the two planes must be subtracted, it was decided that a full-bridge configuration must be used in order to retain a usable signal level. A full-bridge configuration will produce four times the signal output of a quarter bridge and is inherently temperature compensated.

In an effort to find a simple, easily installed, field method of sensing the axle strains so as to reduce the overall system cost, several methods were tested and rejected or refined, as follows:

1. Strain gages bonded directly to the axle. These were field tested and rejected owing to excessive installation cost and cost of replacement or repair. Highly skilled labor was required.
2. Weldable strain gages directly spot-welded to the axle. These were field-tested and rejected owing to zero shifts caused by the lack of an extremely flat surface to mount on.
3. Strain link manufactured and strain-gaged in shop; installed by directly welding to the axle. These were field-tested and rejected owing to the difficulty of preventing gage damage due to heat conduction during welding.
4. Strain links manufactured and strain-gaged in shop. These are attached to mounting blocks which are welded to the axle using a welding fixture. This method was refined as described in the following paragraphs.

Two methods of attaching the strain links to the mounting blocks, bolting and bonding, are presently under test on a Government-owned JD-544 FEL at the Bureau of Mines facility in Bruceton, PA.

The strain link was designed so as to incorporate a mechanical gain of 3:1. This was accomplished by machining the surfaces and narrowing the cross section so that the elongation that should occur over a 1.5-in length is concentrated in a 0.5-in section where the strain gages are located. All strain gaging and intergage wiring is performed on the strain links at the time of manufacture so that the field installation consists only of attaching the strain link to the axle and connecting the output cable (Fig. 13).

The attachment method was designed so as to require a minimum of expertise and time. Three mounting blocks for each transducer are held against the axle by a simple welding fixture, and the blocks are welded to the axle. The strain link is then either bonded or bolted to the mounting blocks, and the mechanical installation is complete (Fig. 14).

At the present time, two fastening methods are being tested. The strain links on one side of the FEL axle are bolted to the mounting blocks using 3/8" socket-head cap screws. The strain links on the other side of the axle are bonded to the mounting blocks. The bonding method is quite simple, using prepackaged epoxy, and requires little skill. In addition, the strain link does not experience any zero shift, due to bolting torque, when it is bonded, thus reducing the electronic adjustments required.



FIGURE 13: View of strain links.

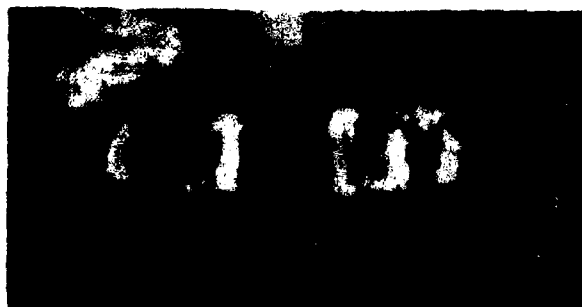
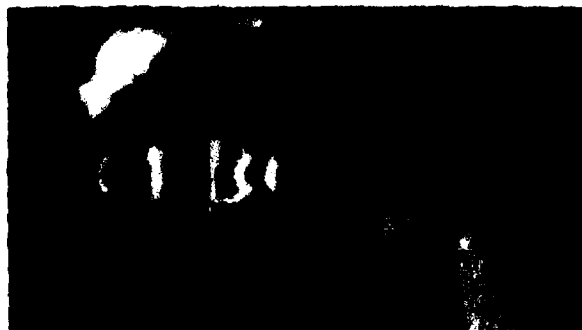


FIGURE 14: Strain links installed on front-end loader axle.



ELECTRONIC SIGNAL CONDITIONING AND DISPLAY

The electronic signal conditioning package has been considerably simplified. It is no longer necessary to perform various computations to evaluate a lengthy correlation equation as was the case with the original system. The new system consists of four integrated circuit instrumentation amplifiers to increase the signal levels from the strain links, a buffer amplifier to sum (subtract) the signals from different planes, a differentiating circuit, a quad-comparator, power darlingtons to drive the warning lights, and a power supply. The entire electronics system, including power supply, is now contained on a single 4½ x 6½" printed circuit card (Fig. 15). For simplicity and to expedite the initial field test, the single card is shown mounted in the same National Electrical Manufacturers Association enclosure previously used (Fig. 16), allowing the use of the existing wiring and connectors.

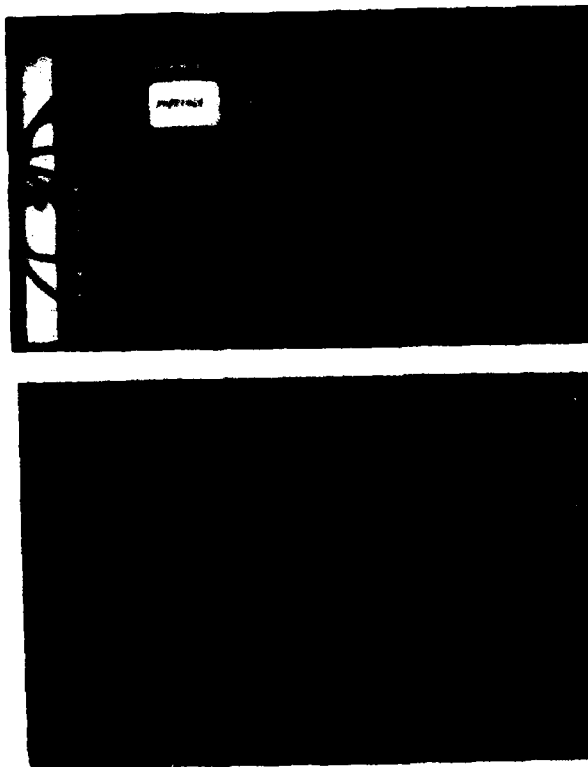


FIGURE 15: Electronic circuit board for 2nd generation indicator. (Component and foil sides of cards)



FIGURE 16: 2nd generation stability indicator mounted in original enclosure.

In an effort to take into account the effects of inertia and anticipate them, a differentiator circuit has been incorporated. This circuit accepts the normal wheel load as an input and outputs a signal proportional to the rate of change with respect to time of the normal wheel load, i.e., the first derivative. When the wheel load is positive but decreasing at some rate, the derivative will be a negative value whose magnitude depends on the rate of decrease. This negative-valued derivative is summed with the original signal to produce a new normal load signal, which is lower in value than the original, by some amount depending on the rate of decrease, and therefore turns on the warning lights earlier. By using a diode to limit the derivative to only negative values, the warning lights respond "normally" for increasing wheel loads. Figure 17 shows a representative signal for wheel load which is varying as a 1.5 Hz sine wave. Superimposed on top of the original signal is the "new" wheel load signal summed with its derivative. As can be seen, the voltage level is lower for the new signal when it is decreasing in value and is identical for increasing values.

CONCLUSIONS

Although field testing of the 2nd generation stability indicator has not yet been completed, all indications to date are positive. The design of the stability indicator:

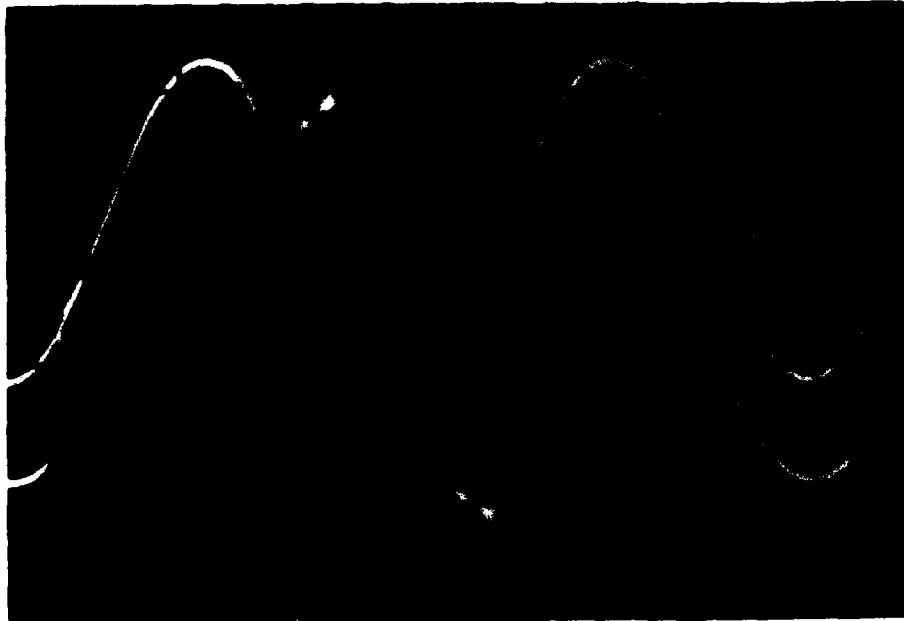


FIGURE 17: Oscilloscope trace of normal load signal and normal load signal summed with its derivative.

1. Allows for its easy incorporation on new front-end loaders during manufacture.
2. Permits its installation on older loaders on a retrofit basis.
3. Has resulted in reductions of size, complexity, and associated cost to the limit of practicality.

Extensive testing of a prototype version of the stability indicator on a Government-owned FEL has shown:

1. The methodology of sensing machine stability as a function of normal wheel loads is practical and works.
2. The strain link method of sensing the normal wheel load provides an adequate signal of wheel load and removes the influence of side forces on the wheel.
3. The strain link method allows for a quick field installation using a minimum of highly skilled personnel.

4. The exact method of attaching the strain link, bonded or bolted, is yet to be decided based on the results of tests in progress.



TOPIC 7
SOIL COMPACTION

Pressure Tests in Soil below Tires of
Agricultural Vehicles

1. Bolling

Institute for Agr.Engineering, Techn.University Munich, F.R.Germany

SUMMARY Design and measuring method of a cheap and efficient soil pressure gauge are described. Soil tank tests carried out in the laboratory demonstrate some properties of the gauge like indifference towards orientation in soil. In the soil bin the gauge measures pressures below tires rolling over and outside in the field the influence of wheel load, number of passes and vehicle speed are investigated. The results are interpreted with modified formulas of Soehne [1], which can be managed by a pocket calculator.

Introduction

Since Soehne [1], [2] and Chancellor [3] had done fundamental work on this subject in the beginning fifties, the amount of fertilization and the weight of agricultural machinery increased as well as the yield rates. Today chemical soil optimization had reached its boundaries and one looks after possibilities to improve soil structure. Von Boguslawski and Lenz [6] gave valuable advice to this problem. What did the farmer get from science to find out whether compaction is severe or not? He knows, that he has to avoid work under wet field conditions with heavy machinery and he uses the spade to estimate pore volume reduction. Perhaps it will be useful to provide him with reference values of pore volume reduction for several kinds of soils with several degrees of water content.

In view of this aim one has to get information about the range of soil stresses brought up by the actual agricultural machinery. To rise the number of data one has to select an efficient measuring procedure and the significant variables. Most common methods are bulk density and cone penetrometer measurement. Applying them, one has to concern the amount of work, the influencing parameters and the mission. The interdependence of bulk density, cone penetrometer resistance and water content together with varying kinds of soil imply a high number of experiments to get sufficient information in the field.

Measuring Method

This arguments led to the consideration to measure the pressure in soil under the tires of agricultural vehicles, which is causal responsible for soil compaction. To find out the right procedure one has to observe several criteria. The most important are:

1. The gauge should be of a bulk density close to that of the soil, in order to avoid stress concentrations, if the gauge density is higher, or to avoid stress drop at the gauge, if the gauge density is lower.
2. The gauge application should cause a minimum of disturbances in soil and it should be possible in a justifiable range of time.

two lance system

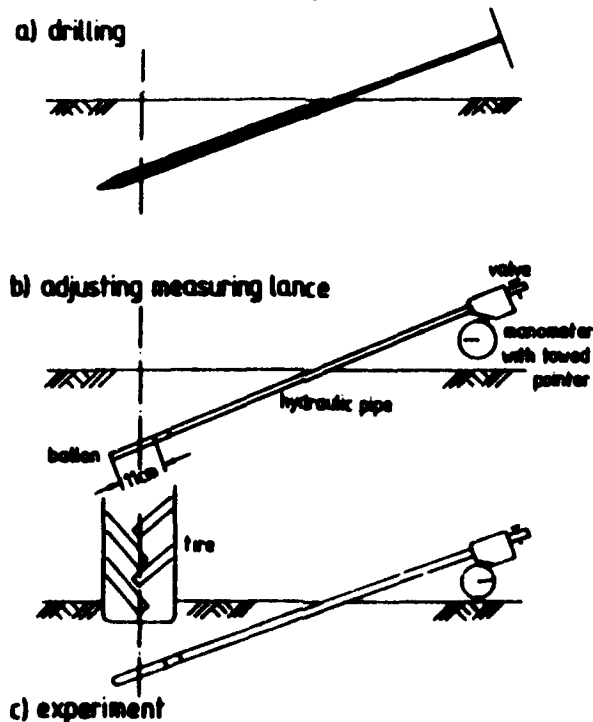


Fig. 1.: Principle and application of the pressure gauge

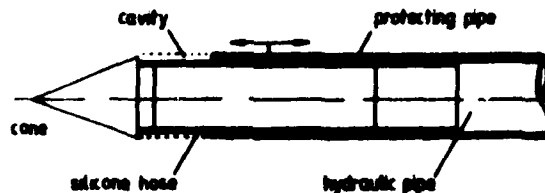
3. The gauge should measure defined stress components.
4. The gauge should be able to record the pressure during tire operation, to get information about dynamic effects.
5. Inexact gauge orientation in soil should cause minimum errors.
6. To use many gauges at the same time the costs must not be high.

Viewing the literature to this subject many valuable advices have been found for example in the works of Berdan [4], Cooper [5], Hovanessian [7], Barnes [8] and Blackwell [12]. The compromise made to observe most of the shown main criteria represents fig. 1:

A hole inclined about 15° - 20° to the surface is drilled into the soil, in which a pipe is pushed. A ballon with walls being 0,5 mm thick, a length of 11 cm and a diameter of 2 cm is turned out of the pipe by an air pump. Now the system is filled with water. This causes a gauge density of 1 g/cm^3 .

one lance systems

a) outer protecting pipe



b) inner supporting pipe

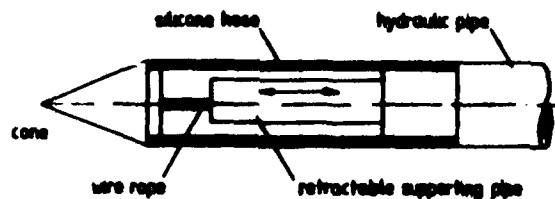


Fig. 2: Designs of one lance systems for simplified soil pressure gauge application

If a mixture of water and magnesium dichloride is used, higher densities are possible. With other fluids gauge densities between 1 and 2 g/cm³ are conceivable, to accommodate gauge and soil density. When the air bubbles are pushed out of the system, the valve is closed and the experiment starts. When the tire rolls over the gauge, the pressure in the system rises. The maximum value can be recorded by a manometer with towed pointer or one can apply a usual pressure gauge with recording system to measure dynamic processes. To improve the handling abilities of this measuring principle, it was tried to design one lance systems shown in fig. 2. Here the three steps in fig. 1 are combined: The cone forms the hole in soil and when the protecting or supporting pipes are retracted, the fluid filled silicone hose with a wall thickness of 1 mm gets flexible similar to the ballon. The most significant advantage of the one lance system is, that turning out the proper gauge and filling the system with fluid is not necessary. Later more details will be described.

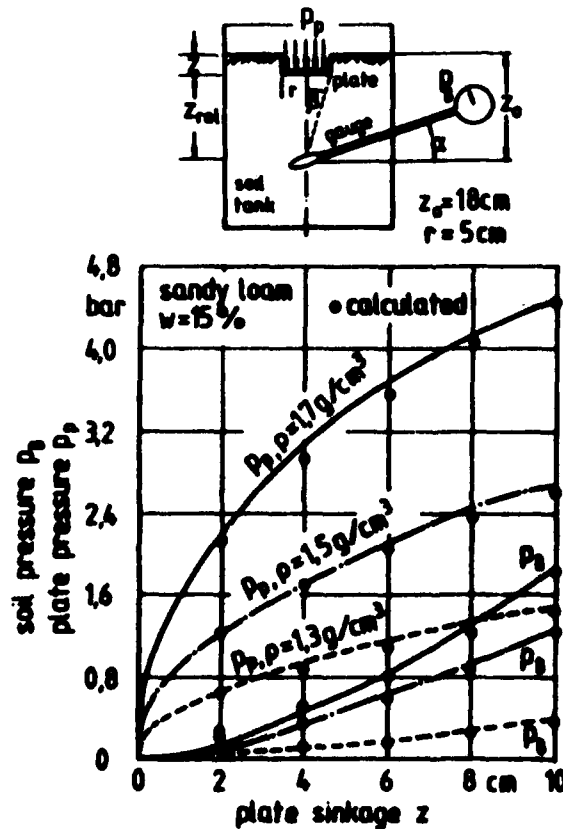


Fig. 3: Testing the pressure gauge in a soil tank with sandy loam of different dry densities

First the properties of the two lance system should be shown. In fig. 3 the curves of the soil pressure p_B in the gauge are plotted against the sinkage z of a circular plate moving into a tank with sandy loam of different densities. Increasing plate pressures p_p cause increasing gauge pressures p_B . With the bulk density the final values at $z = 10$ cm of p_p and of p_B rise, whereas the characteristics of the curves don't change. (The water content was 15 %.)

Fig. 4 gives evidence of the tests varying the inclination α of gauge and pipe. The influence is of the order of the variations caused by soil preparation. The reason may be, that the gauge is exposed to the varying

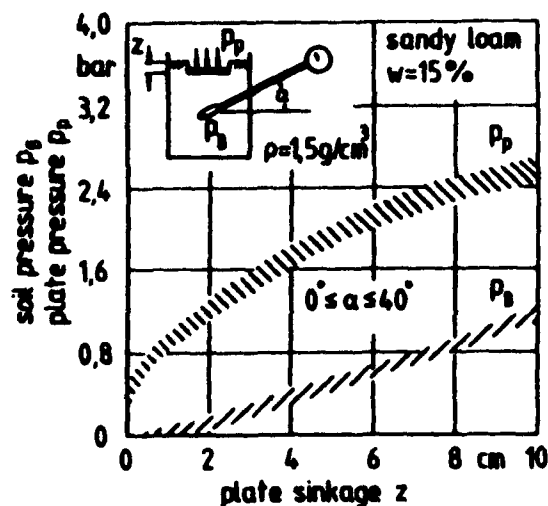


Fig. 4: Influence of gauge inclination α on the measured pressure p_B in a soil tank with sandy loam

stresses on its surface and the manometer shows the mean value of all of them. So turning the cylindric gauge body round its center of gravity is of almost no effect in the range $0^\circ \leq \alpha \leq 40^\circ$. This fact is of advantage during work in field, because the rough terrain causes considerable errors of the measurement of the angle of inclination α . Therefore one always has to excavate the gauge in field after the test to determine its real depth below the surface.

The record of the gauge pressure p_B during the roll over of a tire is plotted in fig. 5 against the position x of the tire relative to the gauge. p_B starts with zero, when the tire is half a meter away from the gauge. It reaches the maximum, when the center of the tire is over the gauge but does not decrease in the same manner. The remaining pressure of 0,25 bar at $x = 60$ cm reduces to values of about 0,1 bar after some minutes and then does not change for longer time.

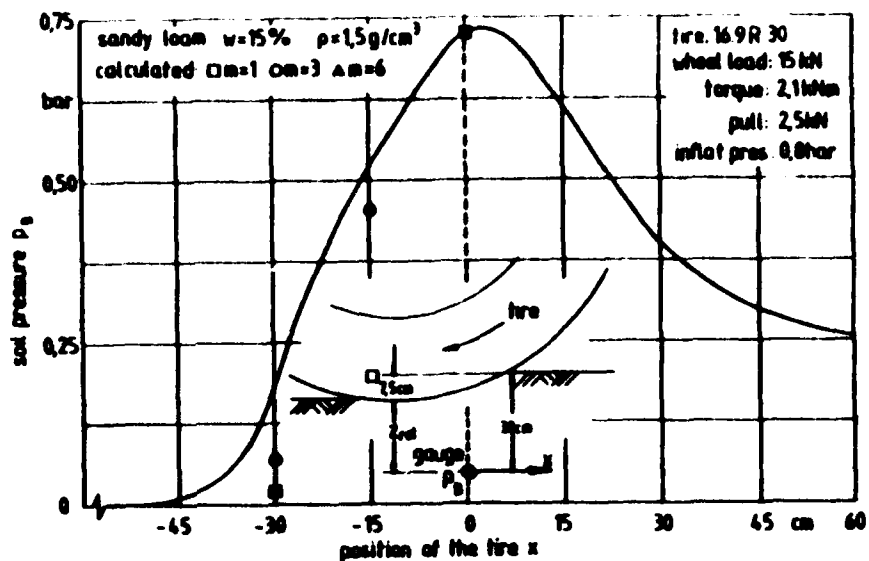


Fig. 5: Record of soil pressure p_g below a tire rolling over in the soil bin of the Institute for Agricultural Engineering of the Techn. Univ. of Munich

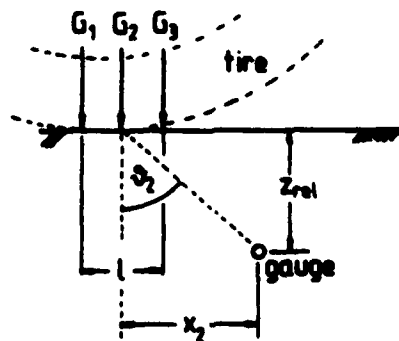


Fig. 6: Approximating the distribution of the wheel load G in the contact area of the tire by three single loads G_1, G_2, G_3

Before field tests were made, it was investigated whether the one lance system (fig. 2a) could be used. Fig. 7 shows the insufficient result: The cavity caused by retracting the protecting pipe has to be filled up with compacting soil and therefore up to a sinkage $z = 2$ cm no signal p_g is measured. Afterwards p_g is much higher than that measured with the two lance system, surely because the steel cone and the silicon tube are stiffer than the ballon and concentrate stresses on the gauge. The one lance system with supporting pipe (fig. 2b) has not yet been tested, but obviously this system avoids the problems arising with the cavity around the gauge.

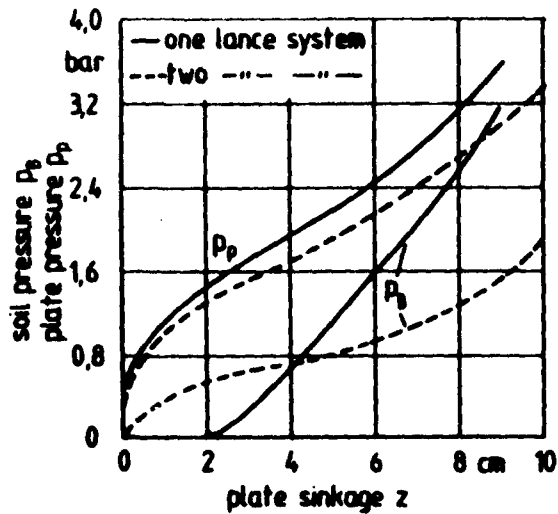


Fig. 7: Pressure p_B in sandy loam in a soil tank, measured with the one lance system (fig. 2a) and the two lance system (fig.1)

Summarizing the important properties of the two lance system in fig. 1 one can say:

1. The bulk density of the gauge can be fitted to that of the surrounding soil by using the right fluid. (For this first tests only water was used).
2. Gauge application causes disturbances in soil as far as the drilling of the hole is concerned. The amount of time for one application is less than 15 minutes.
3. The gauge does not measure defined stress components in the soil, but on the other hand
4. the gauge orientation causes minimal errors. So only the comparison of results is possible at present.
5. Using pressure gauges in spite of manometers one is able to record dynamic processes like the roll over of a tire.
6. The costs of the gauge are of an amount of about 200 - 300 DM, if a manometer is used. (The valve was built with acryl glass, to be able to observe air bubbles rising in the pipe, when the fluid is filled in.)

Field Tests

After introducing the measuring procedure now the results of field tests are described. First it was investigated whether the influence of wheel load is visible in field too. Three vehicles with a wide range of maximum rear wheel loads were tested. The maximum gauge pressure p_B occurring during one roll over correlated to the distance between the contact area of the tire and the gauge z_{rel} is plotted in fig. 8 for a smaller tractor D 4006 with 8.5 kN wheel load on the rear tire. The curve of the DX 140 tractor shows higher value of p_B . Its rear wheel load was twice as high than that of the D 4006. The front wheel of the Fahr 1300 combine harvester was loaded with 34,5 kN. One recognizes that redoubling the wheel load does not lead to redoubled values of the pressure p_B in a certain depth z_{rel} . Supposed $z_{rel} = 10$ cm, and the p_B -values are related to that of the small tractor, the heavy tractor's p_B is 143 %, that of the combine 257 %.

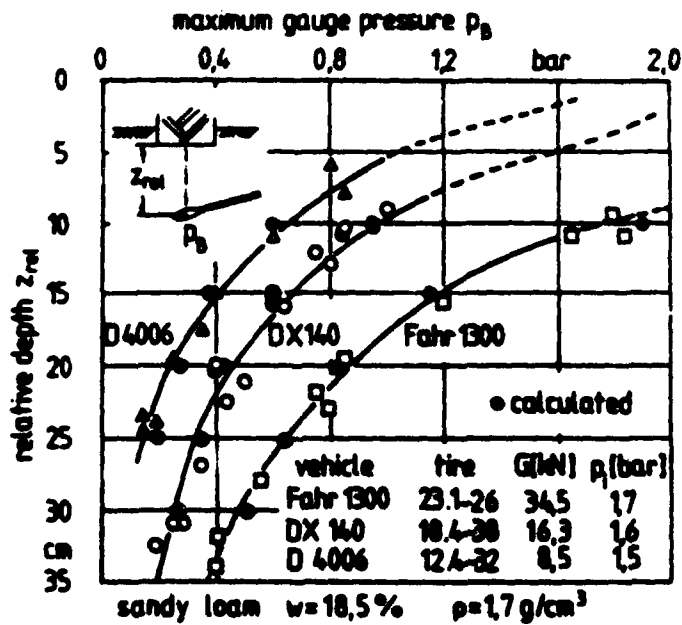


Fig. 8: Gauge pressures p_B in a sandy loam field below vehicles with fast increasing maximum rear wheel loads

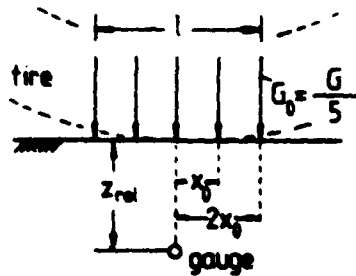


Fig. 9: Approximating the distribution of the wheel load G in the contact area of the tire length l by five uniform single loads G_0

As Raghavan [9, 10, 11, 14, 15] pointed out, besides wheel load the number of passes is of essential influence on compaction. Fig. 10 shows the sinkages z_1, z_5, z_{10} of a tractor after the 1st, 5th and 10th roll over in the same rut. The amount of the maximum gauge pressure p_B increases from the 1st to the 5th roll over more intensive than from the 5th to the 10th. This multi-pass effect on p_B is dependent on the initial pore volume P.V. of the field. Fig. 11 shows the influence of vehicle

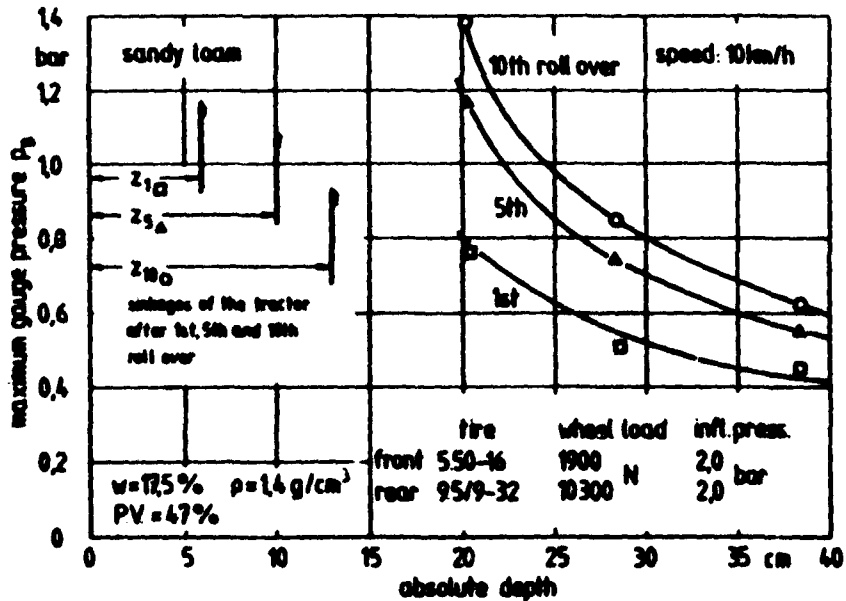


Fig. 10: Gauge pressures p_B in a field with sandy loam after one, five and ten passes

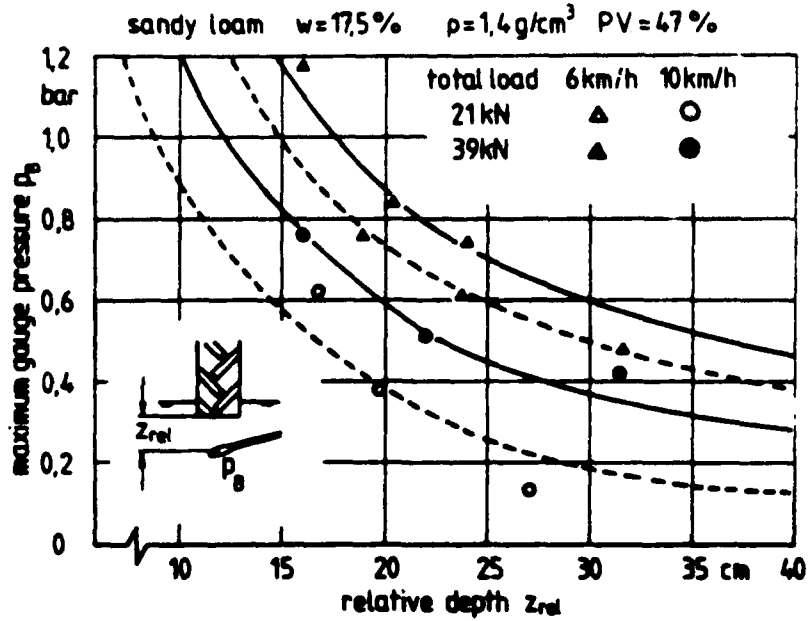


Fig. 11: Gauge pressures p_g in a soft sandy loam of high pore volume P.V. are considerably influenced by vehicle speed
 silty loam $w=17,5\%$ $\rho=1,7\text{g/cm}^3$ $PV=36\%$

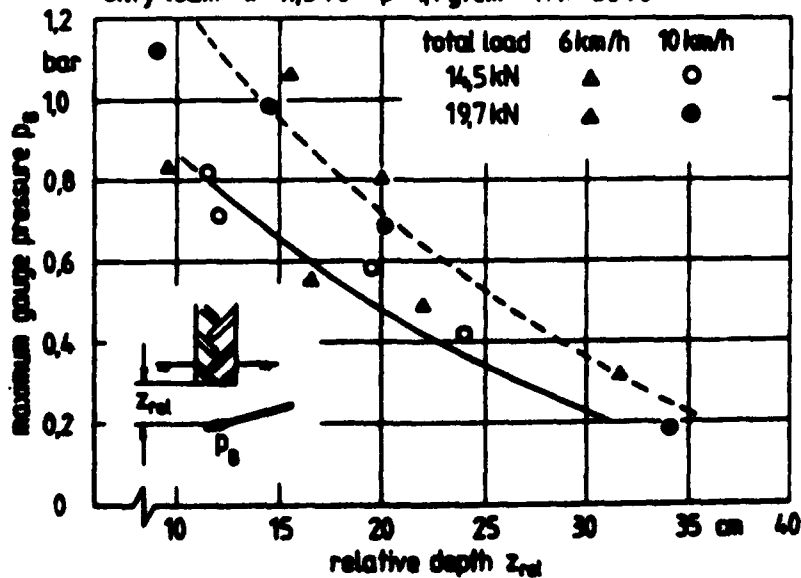


Fig. 12: Gauge pressures p_g in stiff silty loam of low pore volume P.V. are unessentially influenced by vehicle speed

speed in a soft sandy loam with high pore volume P.V. = 47 % and a dry density of $\rho = 1.4 \text{ g/cm}^3$. Increasing speed reduces the values of p_B . If one compares this results with those of a silty loam with higher initial dry density $\rho = 1.7 \text{ g/cm}^3$ and a smaller amount of initial pore volume P.V. = 36 % in fig. 12, one realizes, that only wheel load makes an effect, if the pores filled with air are of considerable smaller amount. So in the silty loam field the influence of vehicle speed is not visible. Both soils had a water content of about 17,5 %.

Soltynski [13] and Stafford [16] have found similar tendencies by investigating the increase of bulk density in soil below tires rolling over.

This view on some field tests should have demonstrated, that the introduced gauge is useful to compare the influence of different vehicle weights, speeds and numbers of passes on soil compaction.

First Simple Analytical Analysis

Now it is tried to apply the formulas stated by Soehne [1]. The vertical stress σ_z in a depth z_{rel} below the load axis of a circular plate of radius r with uniform load distribution p_p in a soil with the stress concentration factor ψ is (cf. fig. 3):

$$\sigma_z = p_p \cdot (1 - \cos^3 \beta) \quad (1)$$

$$\cos \beta = \frac{z_{rel}}{\sqrt{r^2 + z_{rel}^2}} \quad (2)$$

σ_z is not identical with the pressure measured by the gauge. But we know, that σ_z is the highest stress component appearing at the gauge. The stresses σ_z together with all other, smaller stress components acting on the fluid filled cylindrical ballon, produce a mean stress p_B in it. Therefore one can state:

$$p_B = c \cdot \sigma_z \quad 0 < c < 1 \quad (3)$$

If the plate pressure p_p is expressed by the formula describing plate sinkage tests:

$$p_p = k \cdot \left(\frac{z}{z_0}\right)^n \quad (4)$$

we can combine formulas (1) to (4):

$$p_B = c \cdot k \cdot \left(\frac{z}{z_B}\right)^n \cdot \left[1 - \left(\frac{z_{rel}}{\sqrt{r^2 + z_{rel}^2}}\right)^v\right] \quad (5)$$

The curves in fig. 3 are well approximated by (5), if the constants of table 1 are used:

table 1:

ρ (g/cm ³)	k (N/cm ²)	n (-)	c (-)	v (-)	z_B (cm)
1,3	4,8	0,46	0,43	6	1
1,5	9,0	0,46	0,85	5	1
1,7	15,5	0,46	0,85	4	1

(z_B : reference depth)

The stress concentration factors v had been chosen analogous to those Soehne [1] used in his paper. The assumption that $0 < c < 1$ came true.

To calculate the vertical stress σ_z in the distance x from the load axle of the tire in a depth of z_{rel} below its contact area, formula (6) is useful (cf. Soehne [1]):

$$\sigma_z = \frac{v \cdot G}{2\pi \cdot r_0^2} \cdot \cos^v \vartheta \quad (6)$$

$$r_0 = \sqrt{x^2 + z_{rel}^2} \quad (7)$$

$$\cos \vartheta = \frac{z_{rel}}{r_0} \quad (8)$$

(v : stress concentration factor)

To take into account, that the wheel load G is distributed over the contact area of the length l of the tire with radius R one can use the formulas (9) and (10):

$$l = \sqrt{R^2 - (R-z)^2} \quad (9)$$

$$\sigma_z = \frac{v}{2\pi} \cdot \sum_{i=1}^m \left[\frac{G_i}{(x_i^2 + z_{rel}^2)} \cdot \left(\frac{z_{rel}}{\sqrt{x_i^2 + z_{rel}^2}}\right)^v \right] \quad (10)$$

(z : tire sinkage)

Here i is the index of a proper single load G_i shown in fig. 6. m is the number of single loads.

Regarding (3) we get the term for the gauge pressure p_B :

$$p_B = c \cdot \frac{V}{2\pi} \cdot \sum_{i=1}^m \left[\frac{G_i}{(x_i^2 + z_{rel}^2)} \cdot \left(\frac{z_{rel}}{\sqrt{x_i^2 + z_{rel}^2}} \right)^V \right] \quad (11)$$

$$G = \sum_{i=1}^m G_i \quad (12)$$

In fig. 5 the results for $m=1$, $m=3$ and $m=6$ are shown for the distances $x = -30$ cm, -15 cm and $x = 0$ cm. The wheel load G was divided up into uniform single loads G_i . The constants c resulting from the calculations with a different number m of single loads shows table 2:

table 2:

m (-)	G_i (N)	c (-)	V (-)
1	15 000	0,31	5
3	5 000	0,48	5
6	2 500	0,48	5

V was set to 5, because the soil bin was filled with the same sandy loam used for the soil tank tests (fig. 3). The mean density in the bin was $\rho = 1,5$ g/cm³ and the water content (dry base) $w = 15$ %. Fig. 5 shows, that the step from $m=1$ (1 single load) to $m=3$ (3 single loads) improves the result of the calculation significantly, but not the step from $m=3$ to $m=6$. In the latter case also c does not change. Perhaps a better fit would be reached, if the wheel load G is divided up along the contact length l and along the tire width B into single loads. The lower constants c compared with those of the soil tank tests (table 1) are imaginable, if one takes into account, that in the tank with a diameter of 0,4 m soil flow in horizontal direction is more hindered by the side walls of the tank than in the soil bin where the walls have a distance of 2,5 m. So the small main stresses in the tank will be greater than in the soil bin.

At last the field tests of fig. 8 are discussed. Because tires are concerned, the formulas (6) to (12) are used for the analysis. The sandy loam had a dry density of 1,7 g/cm³ and a water content of 18,5 %. Therefore a stress concentration factor $V = 4$ was assumed. The wheel loads acting on the rear tire were divided up into five uniform single loads G_0 applying the experiences made with the evaluation of the soil bin tests. For different depths z_{rel} the pressures p_B in the load axle were calculated.

Formula (11) for this purpose becomes:

$$p_B = c \cdot \frac{v}{2\pi} \cdot \sum_{i=1}^5 \left[\frac{G_i}{(x_i^2 + z_{rel}^2)} \left(\frac{z_{rel}}{\sqrt{x_i^2 + z_{rel}^2}} \right)^v \right] \quad (13)$$

If symmetry is taken into account (cf. fig. 9), we get:

$$p_B = c \cdot \frac{v}{10\pi} \cdot G_0 \cdot \left[\frac{1}{z_{rel}^2} + \frac{2}{(x_0^2 + z_{rel}^2)} \left(\frac{z_{rel}}{\sqrt{x_0^2 + z_{rel}^2}} \right)^v + \frac{2}{(4x_0^2 + z_{rel}^2)} \left(\frac{z_{rel}}{\sqrt{4x_0^2 + z_{rel}^2}} \right)^v \right] \quad (14)$$

$$G_0 = G_i = \frac{G}{5} \quad (15)$$

Table 3 shows the constants used for the calculations and in fig. 8 the results are plotted.

table 3:

tire	rear wheel load	sinkage	tire radius	length of contact area	single load distance
	G (kN)	z (cm)	R (cm)	l (cm)	x (cm)
12.4-32	8,5	7,25	69,75	31,0	7,75
18.4-38	16,3	8,83	89,75	39,0	9,75
21.3-26	34,5	12,25	83,00	43,4	10,85

Best fit was achieved by putting $c = c_f = 0,36$ in formula (14). Compared with the value of c calculated for the soil bin test (fig. 5) $c_s = 0,48$ in the field c was lower.

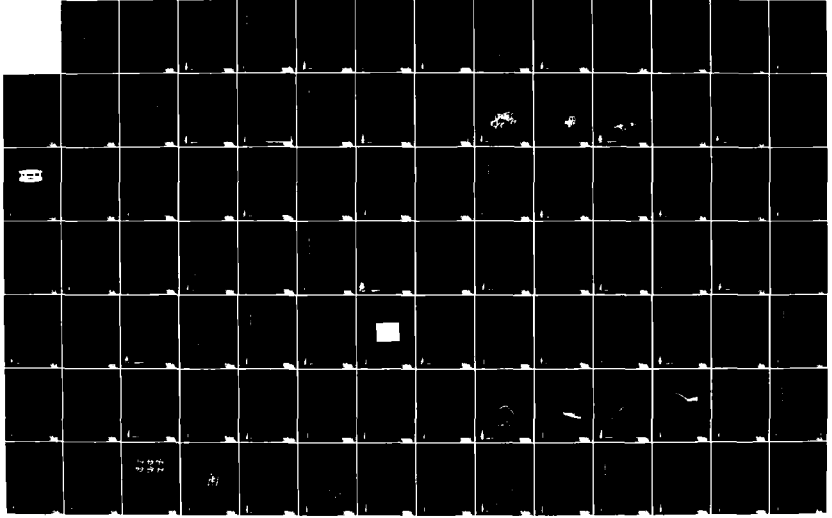
This short view on mathematical description shows, that the formulas stated by Soehne [1] need only the modification with the factor c , to regard the gauge properties. Surely this few results are not adequate to give evidence about all aspects of the constant c , but it is encouraging to see, that just simple assumptions for the calculations yield good fit. Further tests, easy to do with the described gauge, will show more about the parameters influencing c . Especially the correlation between c , stress concentration factor v , dry density ρ and the water content w should be investigated.

Conclusions

A cheap and handy gauge to measure pressures in soil below tires and pressure plates was introduced. The influence of soil density and gauge inclination on the measured pressures was shown. Tests in the soil bin proved, that the gauge can be applied in dynamic

315

AD A148 635 PROCEEDINGS OF THE INTERNATIONAL CONFERENCE ON THE
PERFORMANCE OF OFF-ROAD (U) INTERNATIONAL SOCIETY FOR
TERRAIN-VEHICLE SYSTEMS M J DWYER AUG 84
UNCLASSIFIED DAJA45-84-M-0251 T/G 13/6 NL





1.0



1.1



1.25



1.4



2.8



3.15



3.5



2.5



2.2



2.0



1.8



1.6

FFFFF



3.5

tests. The problems arising by simplifying the test mode with one large system were demonstrated. In spite of the wall thickness of 0.5 mm making the inherent stiffness of the ballon negligible, several missions in field showed, that the gauge is sturdy enough for scientific purpose. Variation of wheel load, number of passes and vehicle speed yielded well distinguishable results. Some of them could be described by the well known formulas of Soehne [1]. Modifying them by a factor c and making simple assumptions about load distribution in the contact area of the tires, led to results encouraging to further tests, yielding more details about this type of pressure gauge.

Literature:

- [1] Soehne, W.: Druckverteilung im Boden und Bodenverformung unter Schlepperreifen. Grundlagen der Landtechnik 5(1953) p. 49/63
- [2] Soehne, W.: Untersuchung der Verdichtbarkeit einiger kalifornischer Böden. detailed internal report according to [3]
- [3] Chancellor, W.J.; R.H. Schmidt, W.H. Soehne: Laboratory Measurement of Soil Compaction and Plastic Flow. Trans.ASAE (1962) p. 235/246
- [4] Berdan, D. and R.K. Bernhard: Pilot Studies of Soil Density Measurements by Means of X-Rays. Proc.Am.Soc. for Testing Mat. 50(1950) p. 1328/1342
- [5] Cooper, A.W. et.al.: Strain Gage Cell Measures Soil Pressure. Agric.Eng. April 1957, p. 232/235
- [6] von Boguslawski, F. and K.O. Lenz: Die Ertragsbildung in Abhängigkeit von Porenvolumen und Bodenwiderstand. Vorl.Mitteilg. aus dem Inst. f. Pflanzenbau und Pflanzenzüchtung der Justus-Liebig-Univ., Sept. 1959
- [7] Hovanesian, J.D. and W.F. Buchele: Development of a Recording Volumetric Transducer for Studying Effects of Soil Parameters on Compaction. Trans.ASAE (1959) p. 78/81
- [8] Barnes, K.K.: Compaction of Agricultural Soils. ASAE Monograph (1971) 2950 Miles Road, St. Joseph Michigan 49085
- [9] Raghavan, G.S.V. et.al.: Prediction of Clay Soil Compaction. Jour. of Terramech. 14(1977)1, p.31/38
- [10] Raghavan, G.S.V. et.al.: Effect of Wheel Slip on Soil Compaction. Jour. of Terramech. 22(1977)1, p. 79/83
- [11] Raghavan, G.S.V. and E. McKyes: Effect of Vehicular Traffic on Soil Moisture Content in Corn (Maize) Plots. Jour. of agric. Eng.Res. (1978)23, p.429/439

- [12] Blackwell, P.S. and B.D. Soane: Deformable Spherical Devices to measure Stresses within Field Soils.
Jour. of Terramech. 15(1978)4, p. 207/222
- [13] Soltynski, A.: The Mobility Problem in Agriculture.
Jour. of Terramech. 16(1979)3, p. 139/149
- [14] Raghavan, G.S.V. et.al.: Vehicular Traffic Effects on Development and Yield of Corn (Maize).
Jour. of Terramech. 16(1979)2, p. 69/76
- [15] Raghavan, G.S.V. et.al.: Traffic-Soil-Plant (Maize) Relations
Jour. of Terramech. 6(1979)4, p. 181/189
- [16] Stafford, J.V. and P. de Carvalho Mattos: The Effect of Forward Speed on Wheel-induced Soil Compaction: Laboratory Simulation and Field Experiments.
J.agric.Engng.Res. (1981)26, p. 333/347



↙

QUALITY CONTROL IN SOIL COMPACTION BY BEHAVIOURS OF EXCITER

By S. HATA and K. TATEYAMA

Department of Civil Engineering, Kyoto University, Japan

ABSTRACT

↖ Soil compaction is one of the most effective methods for soil stabilization and is performed in most earthworks of earth dams and road embankments, etc. However, because its quality control depends upon tests performed at only several points in the fields to estimate such factors as the dry density, water content and C.B.R., misjudgement can occur when judging the degree of soil compaction required. ←

The vibrating behaviour of an exciter is thought to be affected by the ground conditions. Then the degree of soil compaction can be judged easily throughout the fields by measuring the vibrating behaviour of the exciter.

For the proposed exciter and quality control, this study examines the experimental and analytical researches that were conducted to identify the problems that occur when applying the method to actual compaction.

1. INTRODUCTION

Quality control in soil compaction usually depends upon such parameters as the dry density, water content and C.B.R. However, the measurements of these parameters are time consuming and are taken at only several points in the fields.

Vibratory rollers for compacting soil are being employed increasingly in construction. The characteristic behaviours of vibratory rollers change with increasing ground stiffness. Thus, the degree of soil compaction required can be judged by categorizing the changing behaviours of rollers.

Though this idea was realized by some apparatus on the market for judging the quality of compacted soil through the acceleration of rollers, it has not been propagated in construction. The authors made field experiments with a vibratory roller and investigated the relationship between the acceleration of the vibratory roller and the soil compaction. These experiments showed clearly that the acceleration amplitude of the vibratory roller is affected by conditions of the roller machine, especially by changeable frequency, and that the quality control of soil compaction is difficult to obtain directly in relation to the acceleration amplitude of the vibratory roller. But the behaviour of the vibratory rollers certainly changes with increasing soil stiffness, and so the degree of soil compaction can be judged by applying the fundamental relationships between soil and machine characteristics. Thus, this research investigates the dynamic interaction between the soil vibratory-machine system and the quality control.

AD-P004 295

To simplify the analyses and experiments, analyses and experiments of the behaviour of a small exciter were conducted as follows.

(1) A mass-spring-dashpot model was employed for the analytical representation of the exciter dynamics with which the vibrating behaviours of the exciter were calculated. The results of the analyses showed that the acceleration of the exciter increased with increasing soil stiffness.

(2) Experiments to verify the analyses were performed by compacting the soil in a soil bin with a small exciter. The relationship between the vibratory properties and the soil compaction, especially the dry density of the soil, was researched by measuring the acceleration of the exciter with an attached accelerometer. The results of the experiments confirmed the same tendency as the analyses, in that the acceleration of the exciter increased with increasing dry densities.

(3) Other experiments and analyses were performed to research the adaptability of a mass-spring-dashpot model for representing prototype problems. The results from investigations of the vibrating behaviours of the exciter under various conditions of weight and dynamic force ascertained the adaptability of the model for prototype problems.

(4) A new test was conceived to determine the equivalent values of the spring constants and damping coefficients for various soils. A hammer was dropped on the soil surface and the vibrating properties of the hammer were measured with an attached accelerometer. The soil parameter values are determined from the vibrating properties of the hammer and consequently applied in analyses of the exciter dynamics.

As a result of all the investigations, a method that applies a mass-soil system was proposed for evaluating the quality control of soil compaction.

2. ANALYSES OF THE EXCITER DYNAMICS

Soils are compacted with various types of rollers in all earth dams, embankments and other soil structures. Soil stiffness increases with advancing soil compaction.

The vibrating behaviours of an exciter on soft ground are different from those on compacted ground. Then a mass-spring-dashpot model was applied to investigate the relationship between the soil stiffness and the vibrating behaviours of the exciter.

The dynamic analyses of an exciter-soil system were conducted with the one-degree-of-freedom lumped-parameter system shown in Fig. 2-1. The exciter generates the periodic dynamic force F_D , which is represented by

$$F_D = F_0 \sin \omega t$$

where F_0 : maximum dynamic force (N)
 ω : circular vibration frequency (rad/sec)
 t : time (sec)

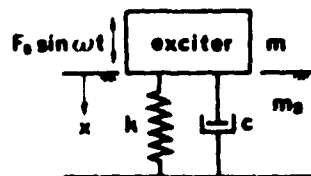


Fig. 2-1 Mass-Soil System Model for Analyses

The ground is replaced by the spring (of spring constant k) and the dashpot (of damping coefficient c), that represent the equivalent soil characteristics. The fundamental equation for dynamic equilibrium of the mass-spring-dashpot model is

$$(m + m_g) \ddot{x} + c \dot{x} + kx = F_0 \sin \omega t \quad (1)$$

where m is the mass of the exciter, m_g is the mass of soil which moves with the same phase as that of exciter, and x is the displacement of the exciter. This case occurs when the weight exceeds the dynamic force of the exciter such that the exciter doesn't leave the ground.

The solution of eq.(1) is obtained by neglecting the transient vibration and by employing only the regular vibration, and given by

$$\begin{aligned} x &= K \sin(\omega t + \theta) \\ \dot{x} &= K\omega \cos(\omega t + \theta) \\ \ddot{x} &= -K\omega^2 \sin(\omega t + \theta) \end{aligned} \quad \begin{aligned} K &= \frac{F_0 \omega^2}{c^2 \omega^2 + \{k - (m + m_g)\omega^2\}^2} \\ \tan \theta &= -\frac{c\omega}{k - (m + m_g)\omega^2} \end{aligned} \quad (2)$$

These analyses utilize a soil spring constant k and a damping coefficient c to represent equivalent soil parameters. However, these parameters change as the soil is compacted, in that the equivalent spring constant and damping coefficient of the soil are thought to increase with advancing soil compaction.

The acceleration amplitude of the exciter was calculated from eq.(2) to investigate the relationship between the soil stiffness and the behaviours of the exciter. In this calculation, the same values were applied for exciter weight, dynamic force and frequency as those of the actual exciter used in later experiments, while the soil parameters were determined using the results of past studies about stiffness and damping.1) The parameter set is shown here.

$$m = 100 \text{ kg} , \quad \omega = 125 \text{ rad/sec} , \quad k = 1500 - 3000 \text{ MN/m}$$

$$F_0 = 730 \text{ N} , \quad m_g = 150 \text{ kg} , \quad c = 0.8 - 1.2 \text{ kN sec/m}$$

The spring constant is obtained by multiplying the coefficient of the subgrade reaction, k' by the constant area of the exciter, A . In the case above, A was 900 cm². In order to compare the analytical result with the experimental result, the value of m_0 was determined such that the acceleration values obtained from the analyses were nearly equal to those values obtained from the later experiments.

The soil mass moving with the exciter is affected by the soil type, density and water content, in addition to weight, dynamic force and frequency of the exciter. The amount of soil moving with the exciter remains unclear despite many past studies. Besides, the main object of the analyses was to identify and verify the soil and exciter behavioral characteristics, not to obtain the exact solution. Considering these matters, the value of m_0 was determined as mentioned above.

The acceleration amplitudes of the exciter calculated with the above parameters ($c=1$ kN sec/m) are shown plotted against various values of the spring constant in Fig. 2-2. The soil stiffness, and thus, the soil spring constant increases as soil is compacted. Hence, the abscissa of the figure represents the degree of soil compaction. Consequently, the acceleration amplitude of the exciter increases with advancing soil compaction.

The acceleration amplitude of the exciter was calculated in the same way as the spring constant for various values of the damping coefficient, but remained almost constant, and thus, independent of the damping coefficient.

In summary, the mass-spring-dashpot model analyses demonstrate that the acceleration amplitude of the exciter increases with increasing soil stiffness.

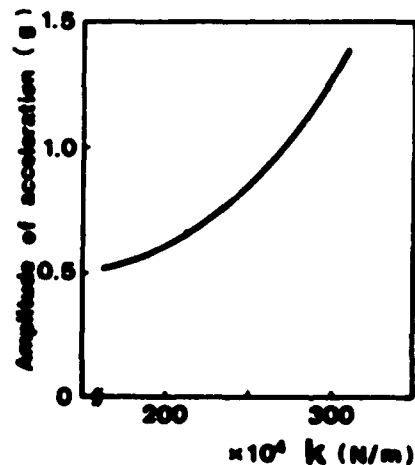


Fig. 2-2 Results of Analyses for Vibrating Behaviours of the Exciter

4. EXPERIMENTAL RESEARCHES ABOUT EXCITER BEHAVIOURS

Experiments were performed to verify the results of the above-mentioned analyses for exciter behaviours, and are described below.

a. Apparatus and Soil Sample

The apparatus used were as follows:

a small exciter with two eccentric masses rotating around two axes.

(Fig. 3-1)

equipment for measuring the acceleration of the exciter. (Fig. 3-2)

(accelerometer, amplifier and electro-magnetic oscillograph.)

a soil bin (Fig. 3-2)

Sandy soil was used in the experiments with specific gravity of 2.64, and a particle size distribution curve that is shown in Fig. 3-3.

b. Procedure of Experiments

Soil was compacted in a soil bin with a small exciter and the acceleration amplitude of the exciter was measured with the accelerometer for various degrees of soil compaction.

Result of Experiments

The measured acceleration amplitudes of the exciter are plotted against the dry densities in Fig. 3-4. The acceleration amplitudes of the exciter increased with increasing dry densities, that is, advancing soil compaction. This result is consistent with the trend predicted by the above-mentioned analyses applying a mass-spring-dashpot model. Hence, the degree of soil compaction can be judged using the acceleration amplitude of the vibrating exciter on the ground.

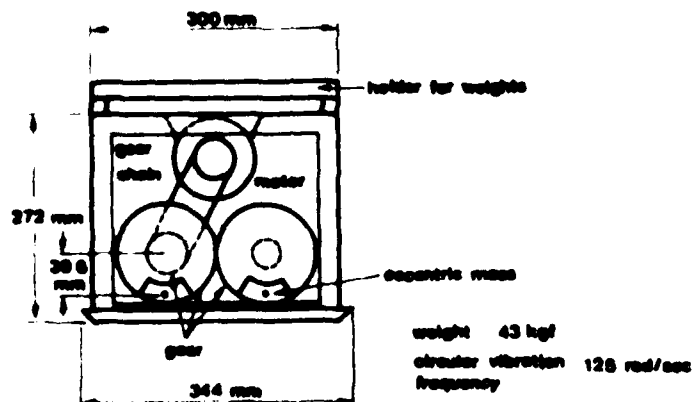
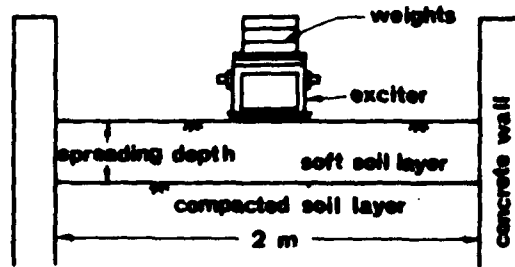
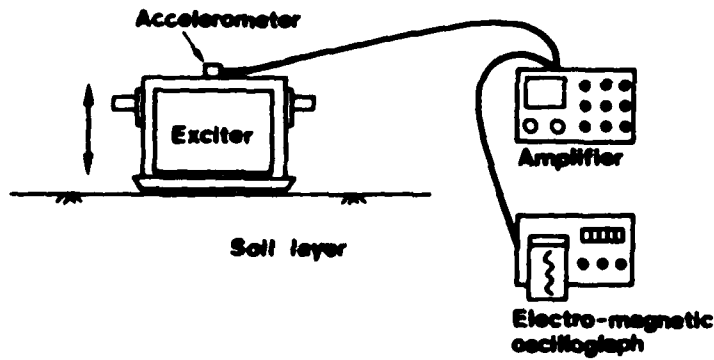


Fig. 3-1 Exciter with Two Eccentric Masses



(a) Exciter and Soil Bin



(b) Equipment for Measuring the Acceleration of the Exciter

Fig. 3-2 Apparatus for Exciter Behaviour Experiment

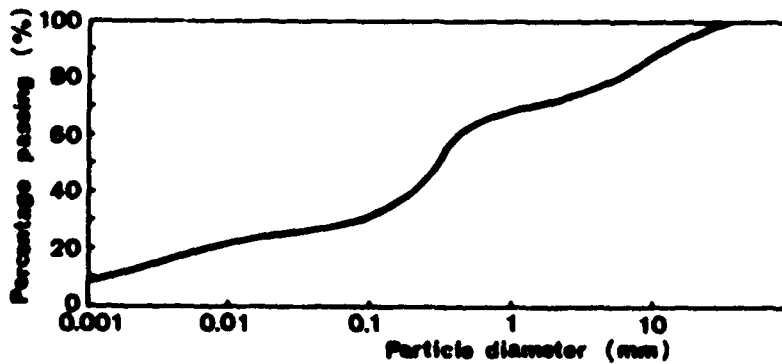


Fig. 3-3 Particle Size Distribution Curve of the Soil

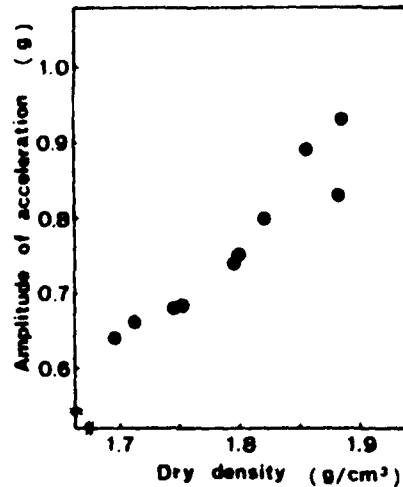


Fig. 3-4 Results of Experiments for Vibrating Behaviours of the Exciter

4. ADAPTABILITY OF A MASS-SPRING-DASHPOT MODEL

Although the mass-spring-dashpot model is easy to treat and has been applied in many past cases for the vibrations of foundations,¹⁾ the behaviours of vibratory rollers²⁾ and others, the sole use of this model for thorough analyses remains questionable. Thus, this chapter presents additional analyses and experiments that investigate the model's adaptability to actual problems in exciter dynamics.

(a) Procedures of Analyses and Experiments

The dynamic force and weight of the exciter affect its vibrating behaviour. The acceleration amplitudes of the exciter were measured for various weight and dynamic force conditions, and the results were compared to the theoretical analyses.

The apparatus of the experiments were same as those in the previous chapter, although the weight of the exciter could be changed by adding steel plates on the exciter, and the dynamic force could be changed by exchanging two eccentric masses inside the exciter.

(b) Results and Discussions

The acceleration amplitude from the results of analyses and experiments is plotted against various weights of the exciter in Fig. 4-1 and Fig. 4-2, respectively. The figures demonstrate that the results of the analyses are consistent with the trend observed in the experiments.

Fig. 4-3 and Fig. 4-4 show the results of analyses and experiments for the acceleration amplitude against various dynamic forces of the exciter, respectively. Similar to before, the same trend is observed in the analytical and experimental results, each other.

Hence, the mass-spring-dashpot model appears suitable for predicting the vibrating behaviours of the exciter, if the soil parameters are reliable. The next chapter proposes a new test to determine the equivalent spring constants and damping coefficients of the soil when applying the model.

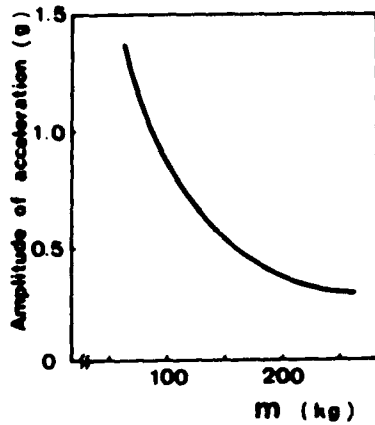


Fig. 4-1 Results of Analyses for the Effect of Weight to Acceleration of the Exciter

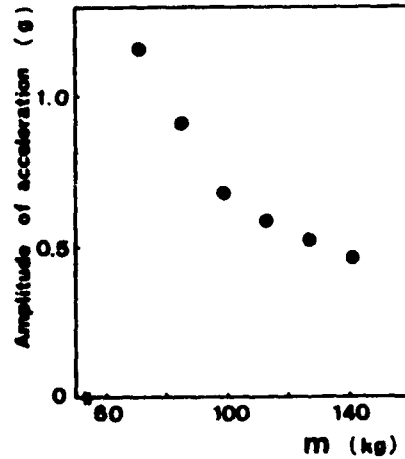


Fig. 4-2 Results of Experiments for the Effect of Weight to Acceleration of the Exciter

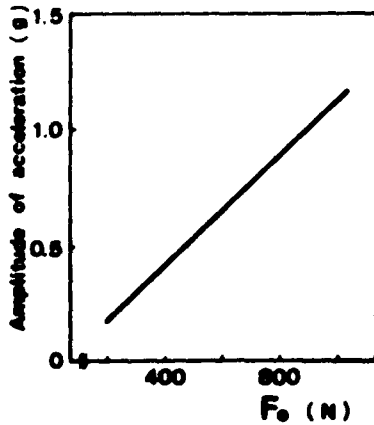


Fig. 4-3 Results of Analyses for the Effect of Dynamic Force to Acceleration of the Exciter

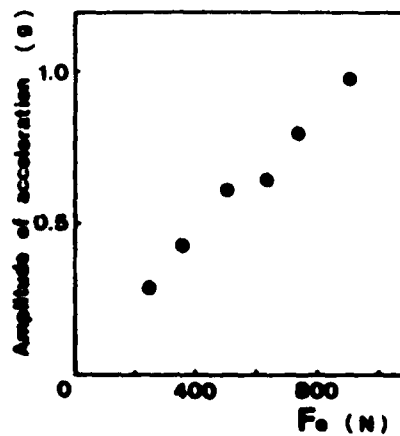


Fig. 4-4 Results of Experiments for the Effect of Dynamic Force to Acceleration of the Exciter

5. DETERMINATION OF SPRING CONSTANT AND DAMPING COEFFICIENT

The equivalent spring constant k and damping coefficient c of the soil are difficult to determine, because they depend on such ground conditions as the type, density, water content, etc. This chapter suggests a new test for measuring spring constants and damping coefficients of soils, then applies the obtained parameters to the analysis.

Since the vibrating behaviours of a hammer dropped on the ground are thought to depend on the ground conditions, the soil parameters k and c can be determined from the vibrating properties of the dropped hammer.

The equation of motion for the dropped hammer is formulated by applying a spring-dashpot model for the soil to yield:

$$m \ddot{z} + c \dot{z} + k z = 0 \quad (3)$$

where m : mass of the hammer
 k : spring constant of the soil
 c : damping coefficient of the soil
 z : displacement of the hammer

Eq.(3) expresses the behaviours only while the hammer is in contact with the ground; otherwise, the equation of motion for the hammer above the ground can be expressed as follows.

$$m \ddot{z} = m g \quad (4)$$

where g is the acceleration of gravity.

Eq.(3) can be solved with the initial condition that at $t=0$: $z=0$ and $\dot{z}=\sqrt{2gH}$:

$$z = e^{-\alpha t} A \sin \beta t \quad (5)$$

$$\ddot{z} = e^{-\alpha t} A \{ (\alpha^2 - \beta^2) \sin \beta t + 2\alpha\beta \cos \beta t \} \quad (6)$$

where $\alpha = -\frac{c}{2m}$, $\beta = \frac{\sqrt{4mk - c^2}}{2m}$, $A = \frac{2m\sqrt{2gH}}{4mk - c^2}$

H is the height of the hammer above the soil surface before being dropped.

Fig. 5-1 (a) shows the predicted displacement and acceleration waves of the hammer dropped on the soil surface from eq.(4), eq.(5), and eq.(6). Fig. 5-1 (b) shows the displacement and acceleration waves obtained in an experiment. The waves obtained by experiment are similar to those by theoretical prediction, hence, the mass-spring-dashpot model is thought to adequately express the behaviour of the hammer-soil system.

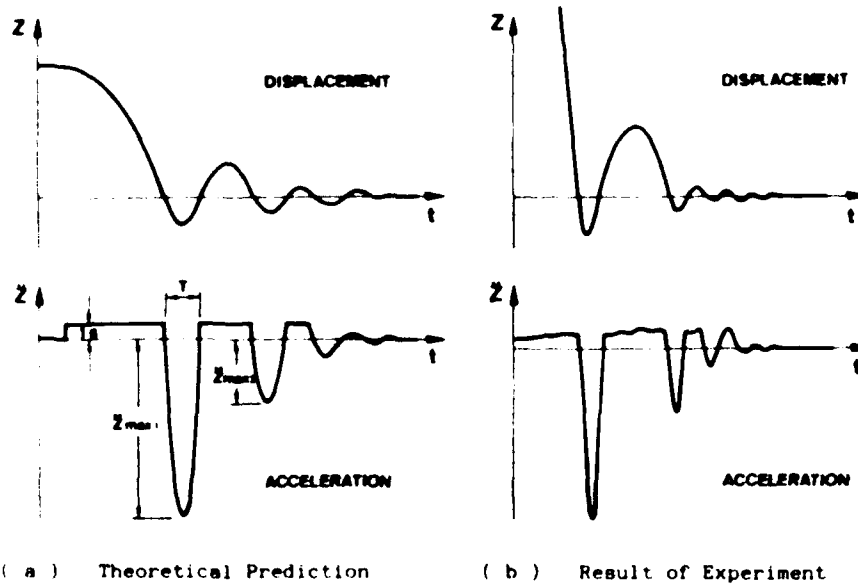


Fig. 5-1 Displacement and Acceleration Waves of Hammer

By solving eq.(6), the spring constant k and the damping coefficient c were obtained as follows.

$$k = \frac{1}{4} \frac{m}{T} \left(\left(\frac{2m\pi}{T} \right)^2 + c^2 \right) \quad (7)$$

$$c = -\frac{2}{T} \frac{m}{\ln \left(\frac{Z_{\max 2}}{Z_{\max 1}} \right)} \quad (8)$$

where $Z_{\max 1}$: the first maximum amplitude of acceleration waves.
 $Z_{\max 2}$: the second maximum amplitude of acceleration waves.
 T : the period between the time the hammer researches the soil surface to the time it jumps from the soil surface.

Thus, the spring constant k and damping coefficient c can be determined after measuring the values of $Z_{\max 1}$, $Z_{\max 2}$ and T in the hammer dropping test.

The next section presents the values of k and c that were measured in the experiments using the soil described in the above-mentioned experiment for the exciter behaviours.

The soil was compacted into a mold in those experiments that investigated the relationship between the soil parameters and soil conditions, especially dry density, and into a soil bin in those experiments that evaluated the parameters required in later analyses.

(1) Values of k and c for the Soil Compacted in a Mold

(a) Apparatus

The apparatus used in this test is shown in Fig. 5-2. The hammer was guided by a connecting rod through holes in two steel plates. The hammer was dropped on the soil surface in a mold, and its vibrating behaviours were recorded. The weight and diameter of the hammer were 2.57 kgf and 50 mm, respectively. The diameter and height of the mold were 100 mm and 127 mm, respectively. The hammer and mold are the equipments provided in JIS (Japanese Industrial Standard) A 1210.

The hammer behaviour was represented by its acceleration, which was measured by an attached accelerometer. The acceleration was transformed into an electric signal by an accelerometer, amplified by an amplifier, and read from the electro-magnetic oscillograph.

(b) Soil Sample

In these tests, the soil sample and its water content were the same as those used in the above-mentioned experiments for the exciter behaviours.

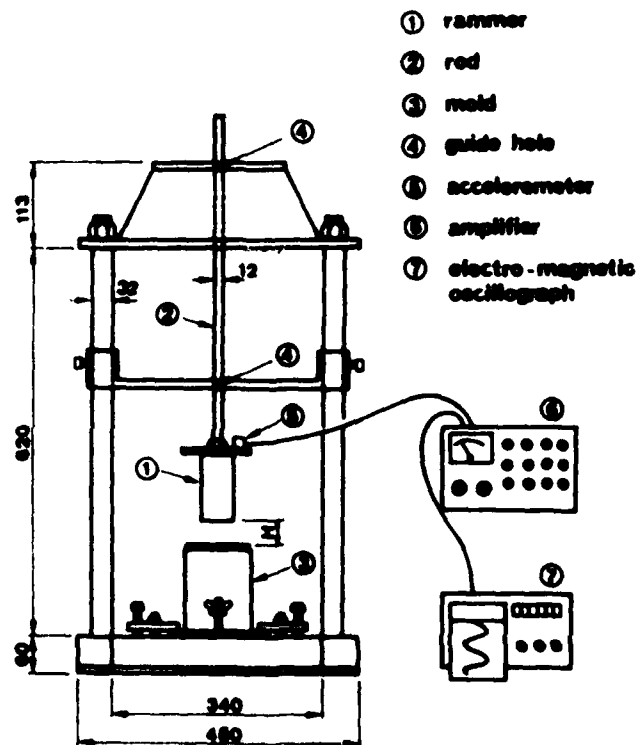


Fig. 5-2 Apparatus of Experiments for Hammer Dropping Test with a Mold

(c) Procedures of Experiments

The hammer was dropped on the compacted soil in a mold and its acceleration was measured and recorded while it was moving on the soil surface.

The values of $\ddot{z}_{\max 1}$, $\ddot{z}_{\max 2}$, and T were read from the output of the electro-magnetic oscillograph, and substituted into eq.(7) and eq.(8) to calculate the spring constant k and damping coefficient c , respectively.

The test was repeated for five different soil dry densities, which were prepared by compaction with 5, 10, 20, 30, and 45 blows of the hammer per one layer. The compaction procedure used a 2.5 kgf hammer, three soil layers, and a drop height of 30 cm.

(d) Results of Experiments

The values of k and c obtained from these experiments are plotted against the dry density in Fig. 5-3 and Fig. 5-4, respectively, which show that both k and c increase with increasing dry density.

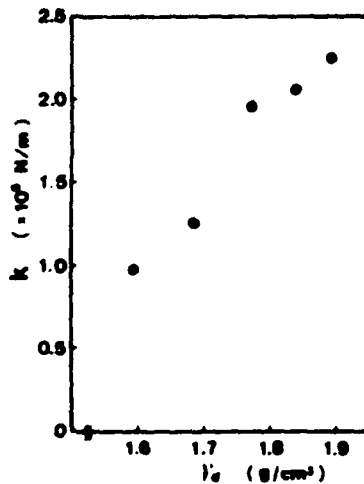


Fig. 5-3 Results of Experiments for the Relationship between k and γ_d

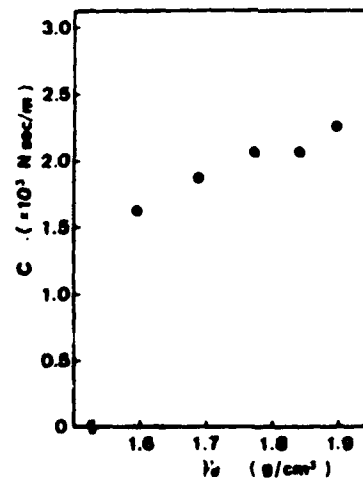


Fig. 5-4 Results of Experiments for the Relationship between c and γ_d

(2) Values of k and c for the Soil in a Soil Bin

The stiffness and damping properties of the soil are thought to be dependent on the restraint condition. For example, the stiffness of the restrained soil is larger than that of the unrestrained soil.

Consequently, the values of k and c for the compacted soil in a mold were expected to be different from those of the soil in the soil bin, and so k and c values were measured for the soil in the soil bin used in the above-mentioned experiments for the exciter behaviours.

The apparatus used in the experiments is shown in Fig. 5-5. The same mechanism was used for measurement of the hammer acceleration as in the experiments with a mold. Since the soil bin was enough large compared to the area of the hammer, the soil is considered unrestrained.

The left columns of Table 5-1 show results obtained from the experiments. The values of k and c measured for the unrestrained soil are smaller than those of the restrained soil described in Fig. 5-3 and Fig. 5-4. This reduction is thought to be affected by the soil type, density, and water content, and the size of the mold.

Later analyses on the exciter behaviours were performed using the parameters obtained from the soil in a soil bin in order to compare the results of experiments mentioned in chapter 3. Note that the parameters in a soil bin can not be determined from those of the mold-compacted soil due to the complicated influence of the restraint conditions.

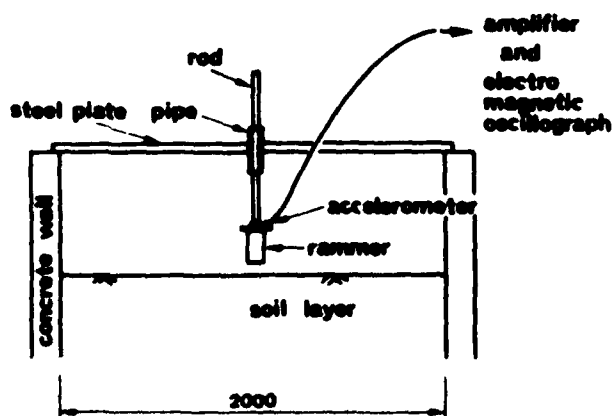


Fig. 5-5 Apparatus of Experiments for Hammer Dropping Test with a Soil Bin

Table 5-1 Results of Analyses with k and c obtained from the Hammer Dropping Test with a Soil Bin

	1	2	3	4	5	6
	γ_d (g/cm^3)	w (%)	k (kg/m)	c ($kgsec/m$)	acceleration amplitude by analysis (g)	acceleration amplitude by experiment (g)
1	1.615	1.42	0.282	0.980	0.7285	
2	1.735	1.79	0.618	0.885	0.7965	0.67
3	1.761	1.42	0.474	1.001	0.8442	0.70

(3) Analyses of the Exciter Acceleration

The acceleration amplitudes of the exciter were calculated using soil parameter values that were obtained through previously described means, and the results are compared with those of the experiments in chapter 3.

The analyses assumed that a 20 kg soil mass, which was about 25 % of the value of F_0/g , moved with the exciter³, where F_0 is the maximum dynamic force of the exciter and g is the acceleration of gravity. The other parameters used in the analyses are:

$$m = 100 \text{ kg} , F_0 = 730 \text{ N} , \omega = 125 \text{ rad/sec} , m_s = 20 \text{ kg}$$

The two right-most columns of Table 5-1 compare the results of the analyses with those of the experiments for the acceleration amplitude of the exciter. The values for the acceleration amplitude determined by analyses were slightly larger than those of the experimental results. However, this difference can be eliminated by increasing the soil mass value m_s in the analyses. More detailed research about the moving soil mass must be conducted to obtain better agreement between the analyses and the actual behaviours of the exciter.

6. CONCLUSION

The vibrating behaviours of an exciter on the soil were investigated through analyses applying a mass-spring-dashpot model and through experiments with a small exciter.

The conclusions obtained from the results are:

- 1) The vibrating behaviours of the exciter depend upon advancing soil compaction; in particular, the acceleration amplitude of the exciter increases with advancing soil compaction and increasing soil stiffness.
- 2) The vibrating behaviours of the exciter can be predicted with a mass-spring-dashpot model if the soil parameters are known.
- 3) Soil parameters for the equivalent spring constant k and damping coefficient c can be determined from the vibrating behaviours of the hammer dropped on the soil surface by applying a new test, which was described within.

The acceleration amplitude of the exciter can be calculated with the soil parameters determined from this test. However, the problem concerning the soil mass moving with the exciter remains unclear and requires further research.

In summary, the quality control for soil compaction using a new machine is as follows.

- a) The new machine should be designed using the exciter, that has a frequency more stable than that of the actual vibratory rollers, since the frequency affects significantly the acceleration amplitude of the vibratory machine.

- b) The acceleration amplitude is measured with an accelerometer attached on the new machine, and the degree of soil compaction is estimated for the construction ground through the acceleration of the machine.
- c) The compaction is admitted to be finished when the acceleration amplitude of the machine arrives at a criterion value that has been determined beforehand for each construction ground. This criterion value is determined by calculation using a mass-spring-dashpot model. The soil parameters required in this calculation are obtained from the hammer dropping test for sufficiently compacted soil. The quality control in soil compaction can be successfully carried out through these procedures.

The quality control with this new machine is favorable, but further research in field tests is suggested in order to substantiate the machine's applicability.

REFERENCES

- 1) F.E.Richert, Jr., J.R.Hall, Jr. and R.D.Woods (1970) : Vibrations of Soils and Foundations (translated from the English to the Japanese by Toshio Iwasaki and Akioshi Shimazu.) Kajima Institute Publishing Co., Ltd. pp.373-378.
- 2) Tai-Sung Yoo and Ernest T.Selig (1979) : " Dynamics of Vibratory-Roller Compaction," Journal of the Geotechnical Engineering Division, ASCE, No.GT 10, October 1979, pp.1211-1231.
- 3) Hiroaki Fujii (1972) : " Estimations of the Dynamic Properties of the Ground while Compacting by a Vibratory Roller - Experimental Studies on the Compaction of the Fill-Type Dams (VII) -," Trans. JSIDRE, October 1972, pp.47-53.



✓
SMOOTHER TERRAIN-MACHINE

Progress report from an R&D-project

B. MARKLUND

SWEDISH UNIVERSITY OF AGRICULTURAL SCIENCES (SLU), GARPENBERG, SWEDEN

AD-P004 296

BACKGROUND

Damages by terrain-vehicles on the ground and growing trees is a problem of increasing importance in forest operations, primarily in thinnings. These damages cause considerable loss of volume and quality yield in subsequent harvesting operations. The importance of this problem is expected to increase for several reasons. One is the continuously increasing area of thinning stands due to an uneven age distribution of Swedish forests. Another reason is the development towards logging systems where tops, branches etc. are utilized for energy purposes. Under such conditions the slash will not be available as a ground cover, protecting the soil for compaction and root systems for damages. Access to terrain-machines, less liable to damaging the stand, is therefore a crucial prerequisite for the successful development of future thinning systems.

The knowledge of how to design less damaging terrain vehicles is, however, very limited. A research project 'Smoother terrain-machine' was first out-lined at SLU in 1978 in order to fill this gap of basic knowledge. Following a few years of pilot studies, evaluation of alternative research approaches and development of measuring techniques, the project is now in a productive phase.

AIM OF PROJECT

The purpose of this project is to provide support for the development of smoother terrain-machines, but does not include actual machine design. Included are the analysis and quantification of interaction between machines and the forest environment. In this context, machines cannot only be looked at individually, the total harvesting systems and the methods involved must also be analyzed. Towards this background, the aim of the project has been formulated as follows:

- to evaluate the effects of changes in machine and systems design on the amount and character of stand damages.

This indicates a rather broad frame for the project. However, the emphasis so far has focused solely on damages to the ground and the root systems.

PROJECT STRUCTURE

After a few failures in trying to study and analyze overall relationships between machine parameters and damages, it was realized that the problem had to be handled as an assembly of partial and explanatory relationships fitted together in an overall structure. For this reason, including others, the project was divided into three key subprojects. This starting with the basic machine design on through to the effects on stand development, we looked at sequential cause/effect relationships.

The first subproject, named 'Chassi', deals with the relationships between machine parameters (cause) and the contact forces acting on the ground (effect), the roots or the trees.

The second subproject is named 'Damages'. It concerns the relationship between the acting contact forces (cause) and various kinds of damages incurred (effect).

The subproject 'Effects' deals with the influence of damages (cause) on the subsequent stand development (effect). See figure 1.

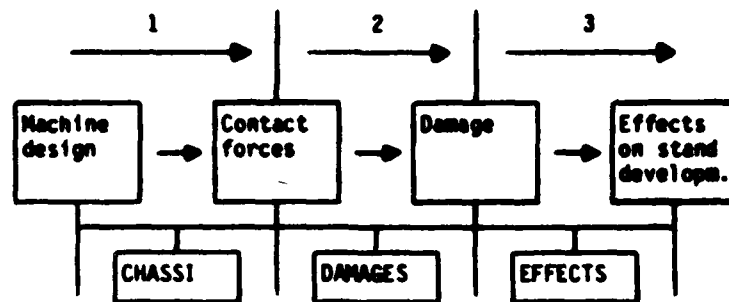


Figure 1. The division of 'Smoother terrain-machine' into subprojects.

The subproject 'Effects' is only marginally dealt with, since it mainly concerns other competences than the technical ones, such as growth and yield, soil science and mycology. The main concern of the project is to establish good cooperation between those sciences and support their research activities to evaluate damage severity.

The division into three key subprojects is basically motivated by the desire to simplify the relationship between machine or systems design and stand damages. The more complex character of the structure is better illustrated by figure 2.

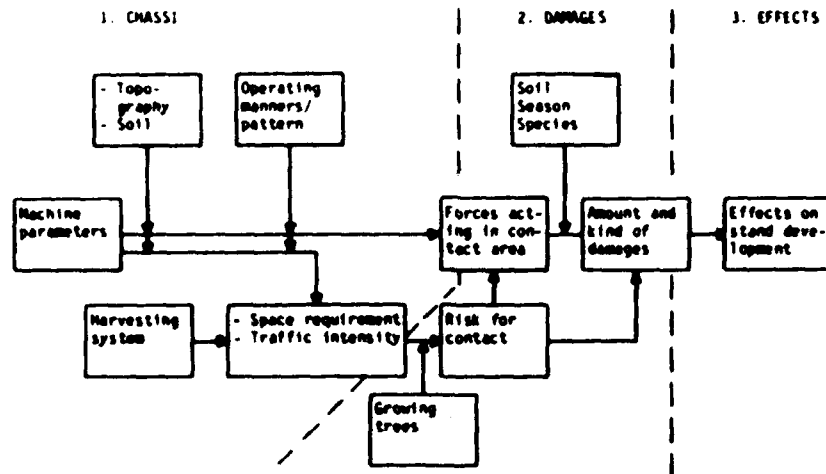


Figure 2. Schematic illustration of factor-complexes that are expected to influence relationships between machine design and stand damages.

The following brief comments are provided to help clarify figure 2. Machine parameters of primary interest are for example, vehicle weight, dimensions, design of ground contacts and transmission design. The relationship between such machine properties and the forces acting in contact areas is expected to be influenced by soil and topographical conditions as well as the manners in which the machine is operated. Another damage influencing machine property is its space requirement, which is normally connected to the vehicle steering geometry and dynamic properties. The transport capacity of machines as well as the number of different machine types involved in the harvesting system influence the traffic intensity in the stand. Increasing traffic intensity and increasing space demand are both expected to raise the risk for damaging contact with growing trees.

The extent to which the acting forces cause damage, would depend on the natural resistance of the medium that is exposed. The mediums of interest are bark and wood of tree roots and trunks as well as the soil. The resistance of these mediums will vary with season, tree species, soil types, weather conditions etc.

In what follows, one of the three subprojects, 'Chassi', will be more closely described and current achievements presented.

TEST VEHICLE

An experimental rig that allows for variation or simulation of relevant machine parameters was necessary to study the influence on forces in the contact area.

We generalized that the main demands on our experimental rig included the following:

- it should be possible to vary and study key vehicle parameters
- it should be possible to conduct various experiments, both in the laboratory and on real terrain
- the force pattern and variations in the contact area (e.g. tire to ground) must be measurable or possible to reliably estimate

Using the above criteria different possible types of research equipment were discussed, all the way from single-wheel constructions to a whole research vehicle.

We needed to continually remind ourselves that the purpose of project 'Chassi' was to find the connections between vehicle parameters and the interaction between vehicle and environment. That can mean a determination of the forces between tire and ground and study how different vehicle parameters (tires, transmission, machine weight etc.) influence these forces, or analysis of how vehicle dynamics and steering properties influence space requirements.

We concluded that a single-wheel test device would be difficult to use, because it is difficult to simulate unknown relationships. Also, since such equipment is not a real vehicle, it would be difficult to translate experimental results into meaningful vehicle characteristics. In contrast, choosing a whole vehicle could mean that the results are applicable only to that vehicle.

Our final choice was a commercial forwarder, which was stripped on the load carrier and rebuilt for our experimental purpose (fig. 3).

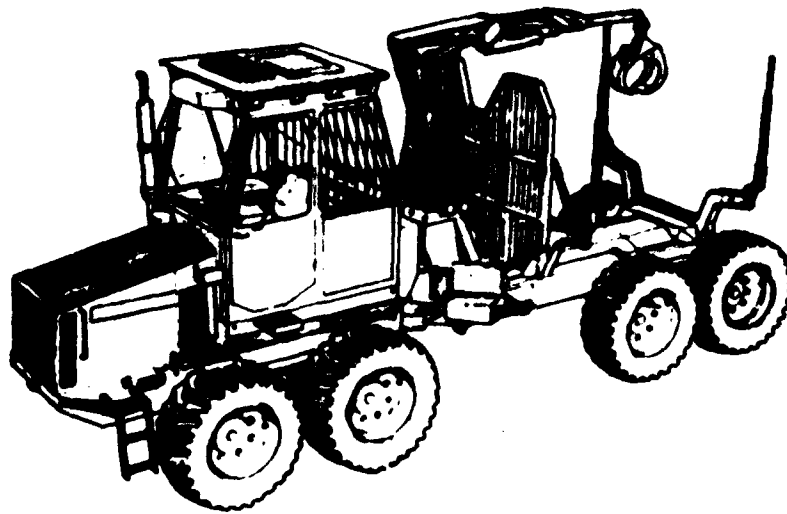


Figure 3. Kockum 83-35 forwarder.

The Kockum 83-35 is a relatively small forwarder. It has a weight of 8,500 kg, length of 8 m, width of 2.2 m and is powered by a Ford diesel engine rated at 60 kW (80 hp). It is an 8 wheel vehicle with bogie wheel suspension in the rear and front. Standard dimension on tires is 500 x 22.5/8, with possibilities to put on other types and dimensions.

The transmission is a Clark converter with 3 step power shift, a drop-box, differential (high traction) in the rear and front, chain gearing from the differential to the bogie and in the bogie.

The vehicle has articulated steering with the steering point half way between rear and front axles. The rear load carrying frame is telescopic and can be extended 0.75 m. Maximum steering angle $\pm 43^\circ$, turn radius 6.6 m/7.7 m (standard/extended).

VARIATION POSSIBILITIES

The possibility to vary different vehicle characteristics limits the use of a commercial forwarder as a research vehicle.

Concerning damage to roots, standing trees and soil one can see 4 important characteristics to vary:

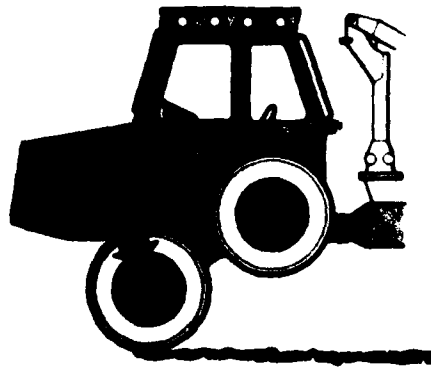
- a) ground contact
- b) geometrical behaviour (dimensions)
- c) dynamical behaviour (weight distribution)
- d) transmission

Kockum 83-35 is here quite suitable.

a) Ground contact

Although the vehicle in a standard commercial version is equipped with 500 x 22.5"/8 404 Trelleborg tires, the manufacturer allows two more possible tires: 500 x 22.5"/12 steel belt Trelleborg and the dimension 400 x 26.5". Used as a research vehicle the possibilities should be limited only by space requirements and the machine and bogie dimensions.

Figure 4. Single-wheel simulation.



It is not possible to put single-wheels on the vehicle without a reconstruction of the bogie suspension into a single-wheel suspension. However, the front bogie is equipped with a hydraulic cylinder that can raise either the front or the rear wheel. This construction is easily copied to the rear bogie. This means that 4 wheeled and 6 wheeled vehicles can be 'simulated' by raising wheel in front and rear bogie in

different combinations. The effects on weight distribution must then, of course, be concerned.

b) Geometrical behaviour, (dimensions)

The telescopic rear frame means that the geometrical behaviour in different steering designs can be studied. Raising the wheels in the bogies in different ways, gives a further possibility to vary the geometrical behaviour.

This means that the geometry and behaviour of articulated steering can be studied over a wide range of cases.

c) Dynamical behaviour (weight distribution)

As the machine is 'stripped' there is enough space to place and move around weights on the machine and study phenomena of weight and weight distribution, the telescopic rear frame is then an advantage. The limits are the vehicle service weight and the location of cab and engine.

The vehicle is not equipped with springs apart from the spring behaviour of the tires. The reconstruction of the wheel suspension into a sprung and damped suspension would be very complicated and so far we have no intentions of doing such a reconstruction. However, a similar construction could more easily be simulated in the single-wheel case as shown in figure 4, by hanging the lifted bogie-part in springs and dampers. The bogie can be fixed in a raised position, either stiff or with some kind of shock absorber.

d) Transmission

Exchange of transmission components is quite easy, due to the open module-construction. In the first place, it is very easy to change between different types of differential.

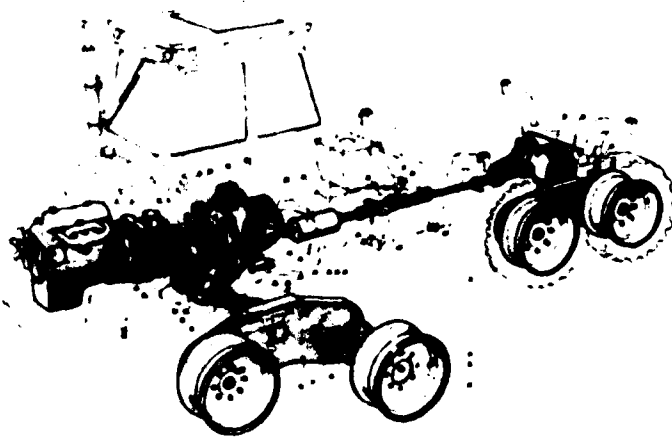


Figure 5. Transmission (Source: Kockum's part catalogue).

The converter, power shift and drop-box are all located under the cab. The space room is easily reached as one can tip the cab to the right side. On the drop-box there is a free axle-end on which a hydrostatic motor easily can be mounted. (In fact, the manufacturer has already done this for his own purpose).

The chain transmission means possibilities of changing the gearing between e.g. rear and front bogie.

This altogether gives us a large amount of options to study.

FORCE MEASUREMENT

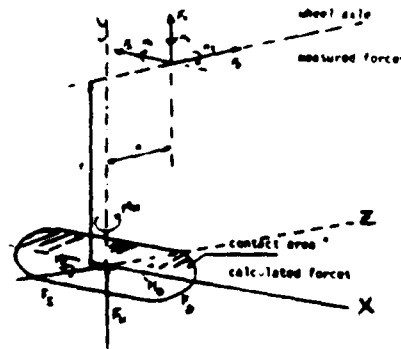
To study all these vehicle characteristics the vehicle must be equipped with transducers for force, movement, location, speed, slip etc. Thus, a system of measuring and collecting data needed to be developed.

The most interesting forces are those in the contact area between tire/track and ground. The dimensions, directions and variations patterns of these forces influence subsequent soil compaction, root damage etc.

To measure these forces directly in the contact area is extremely difficult. A suitable transducer must be used and it must not interfere with the contact pattern.

We found existing transducers to be appropriate for measuring the forces in the contact area. Thus, we decided to rely on measurements in the wheel suspension. However, efforts are continuing within the project to find transducer solutions for measurement in the contact area (fig. 6).

Figure 6. Orthogonal forces and moments on a wheel.



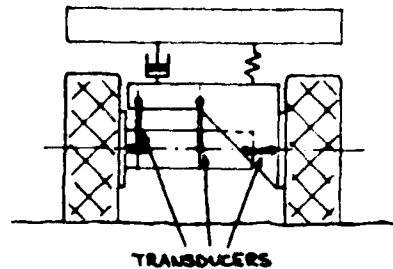
CHOICE OF MEASURING TECHNIQUE

Our current approach is to measure the three orthogonal forces (F_x , F_y , F_z) and three moments (M_x , M_y , M_z) in a single-wheel of the vehicle suspension. We saw four possible techniques:

1. Rebuild the wheel suspension so that all forces and moments can be measured directly with standard load cells.
2. Exchange the wheel suspension with a six-component loading frame consisting of standard load cells.

3. Exchange the wheel suspension with a piezo electrical wheel dynamometer.
 4. Design a single six-component force transducer for mounting in the wheel suspension.
1. Single-wheel measurements of forces and moments by method 1 is fairly common. The principal is to hang the wheel in a linkage system and to support the linkage via standard load cells (ref. 1). A transducer output signal directly corresponds to a single force. As already indicated, this way of measuring would mean that the wheel suspension would have to be considerably rebuilt (fig. 7). This means that possibilities of changing the vehicle construction or changing ground contact equipment (different wheel sizes, single-wheel, bogie, tracks etc.) will be heavily decreased. We chose not to use this method.

Figure 7. Measuring forces on wheel, method 1.



2. An alternate solution is to make a compact six-component load frame to replace part of the wheel suspension without changing the rest of the construction (fig. 8). Here the forces have to be calculated through geometry, static analysis and measured load cell forces (ref. 2).

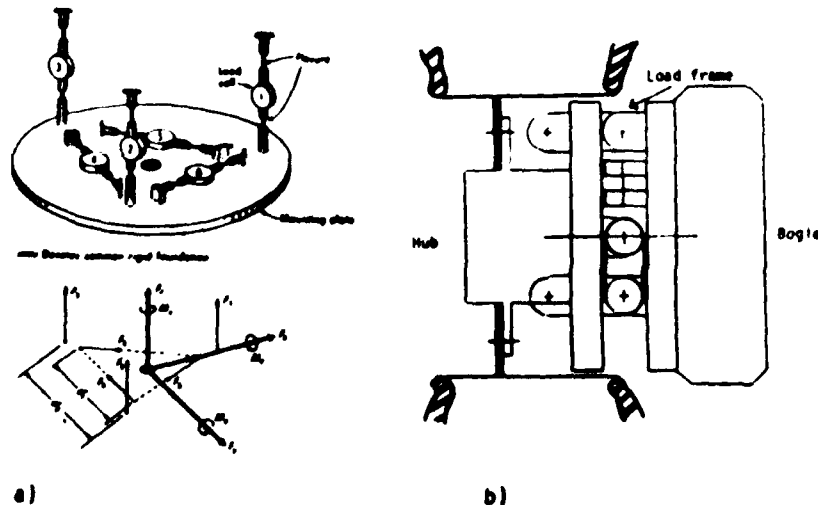


Figure 8. Method 2. a) Six-component load frame principle. b) The load frame placed in suspension.

We investigated further this way of measuring by building a non-measuring scale model. It was possible to build in such a loading frame in the available wheel suspension space. This six degree of freedom force sensor design uses various hinges, pivots or springs, such that the desired forces are decoupled and applied to pick up transducers. It is extremely difficult to make such a mechanical structure that also fits into the wheel hub or suspension. Also, this approach requires very accurate knowledge of the dimensions and stiffness. Considering these factors, the cost and complexity became too high we eliminated this method from further consideration.

3. Piezo electrical measuring.

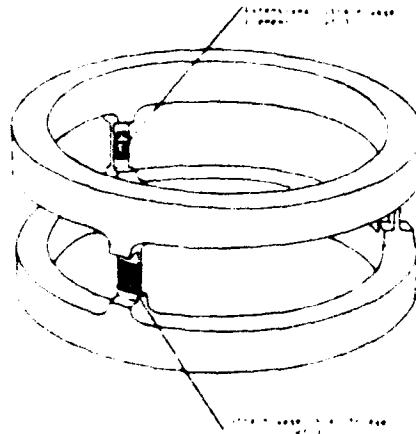
On the market there exist piezo electrical six-component dynamometers for measuring wheel force (ref. 3) mainly on cars. It would also be possible to build such a dynamometer for a terrain vehicle. After some contacts with manufacturers of this kind of equipment, we found that the dimension of our statical forces would make the construction too big and expensive. Therefore, this alternative was dropped, even though this principal has application to our problem.

4. A combination of bonded strain gauges, Wheatstone-bridge circuits, and flexible elements of various geometries have proved a versatile tool in the development of multi-component force pick-ups of both large and small size.

This approach has been used in the design of a prototype wrist force sensor for robot arms (ref. 4). The result was a single rigid body with strain gauge mounted for measuring both extension and shear. Fig. 9 shows the wrist force prototype.

This general type of solution seemed to suit our demands quite well

Figure 9. Wrist force sensor (ref. 4).



THE SIX-COMPONENT FORCE TRANSDUCER

The force transducer developed is a steel cylinder with four beams (fig. 10).

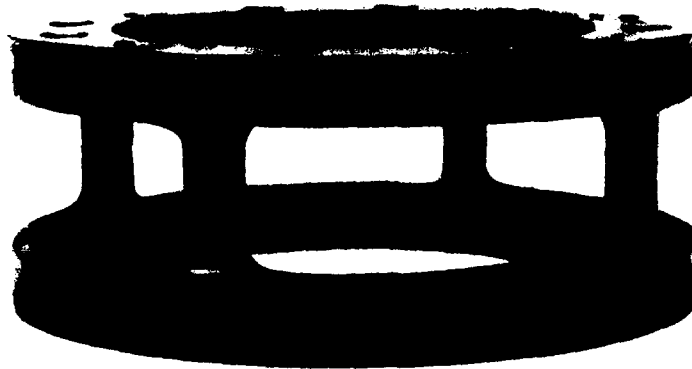
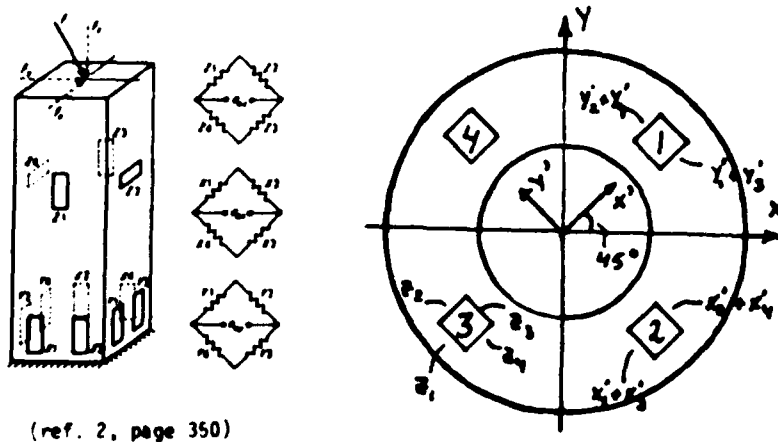


Figure 10. Six-component force transducer, body.

On each beam, two strain gauges are mounted and wired in a Wheatstone-bridge configuration, one for bending forces and one for extensional forces (fig. 11).



(ref. 2, page 350)

Figure 11. Wheatstone-bridge, arrangement of strain gauges on six-component transducer.

The method is based on the following assumptions:

1. The input member is a rigid body. The input stress can then be considered to be six forces (3 rectilinear and 3 moments) and any input stress can be reduced to the six forces at the assumed coordinate system.
2. The output voltage vector spans the space corresponding to the input, i.e. no non-zero input exists which produces no output at all.
3. Linearity and superposition apply.
4. The assembly is stable (i.e. there is no slippage).

Further, a system of calibration which uses an experimentally evaluated matrix transfer function to transform the transducer outputs into the desired force readings.

We first assume

$$\underline{V} = \underline{H} \times \underline{F} + \underline{B}$$

where \underline{V} = output voltage vector

\underline{H} = transfer matrix

\underline{F} = input force vector

\underline{B} = offset voltage vector

If \underline{B} is measured and subtracted we obtain

$$\underline{V} = \underline{H} \times \underline{F}$$

The force sensor has eight full bridges and the forces to be measured are six. Writing the matrix equation out, we obtain:

$$\begin{pmatrix} V_1 \\ V_2 \\ \cdot \\ \cdot \\ \cdot \\ V_8 \end{pmatrix} = \begin{bmatrix} h_{11} & h_{12} & \dots & h_{16} \\ & & & \\ & & & \\ & & & \\ & & & \\ h_{81} & \dots & \dots & h_{86} \end{bmatrix} \times \begin{pmatrix} f_1 \\ f_2 \\ \cdot \\ \cdot \\ \cdot \\ f_6 \end{pmatrix}$$

In order to calibrate the sensor, pure forces f_k are applied by a specially built calibration rig. This means that when f_k and V_n are known, h_{nk} can be calculated.

Once matrix \underline{H} has been found, any force \underline{F} can be determined from voltage readings \underline{V} and premeasured bias voltages \underline{B} as

$$\underline{F} = \underline{H}^* (\underline{V} - \underline{B})$$

where \underline{H}^* is a pseudo-inverse of \underline{H} given by

$$\underline{H}^* = (\underline{H}^T \underline{H})^{-1} \underline{H}^T$$

\underline{H}^* can, of course, be replaced with \underline{H}^{-1} if \underline{H} is a square matrix, i.e. $n = k$.

The scale model is presently under evaluation. It is done in the calibration rig, where separate and combined forces and moments can act on the transducer. The forces and moments are measured exactly ($\pm 1\%$ accuracy) with standard load cells. A micro computer (MY 16F, Mydata AB Sweden) is used to collect the signals from the load cells and corresponding signals from the six-component force transducer.

The matrixes H and H^* are calculated in a mini computer (MD 100, Norsk Data A/S Norway) and returned to the micro computer. In this way the standard load cell forces can be calculated from the transducer voltage output and the load cell voltage output. The calculated values can then be compared directly in the micro computer with a special calibration program. It is then possible to subtract the bias-voltage vector within the computer and to calculate accuracy and precision directly.

Testing so far shows the scale model works very well. We experienced some problems with zero drift when changing load direction. These are related to the mounting of the transducer and should be possible to reduce to an acceptable level. The voltage output from the Wheatstone-bridges are acceptably linear over the range of acting force.

The sensitivity is high for the moments, acceptable for F_x and F_y and low for F_z which one can presume. When the scale model is evaluated the decision whether to build a full-scale transducer will be taken.

The basic idea of the transducer is to estimate the ground contact forces by indirect measurement in the suspension. This means that all forces must go through the transducer and not be supported by any other chassis or transmission component. Also, there should not appear any internal forces in the wheel suspension. The problem in this connection is the driving axle, which is able to support the wheel as well as causing internal forces between suspension and axle (as in a planetary final drive). The wheel hub and bogie hub have both been reconstructed so that the axle only will transmit the driving and breaking torque (fig. 12). This means that the driving torque transmitted from the engine will go through the axle and down to the ground contact, where all forces and moments, except the driving torque, will be supported and measured by the six-component force transducer placed in the suspension. Then the driving torque must be measured in the driving axle. Therefore, all axles are equipped with transducers for measuring torque.

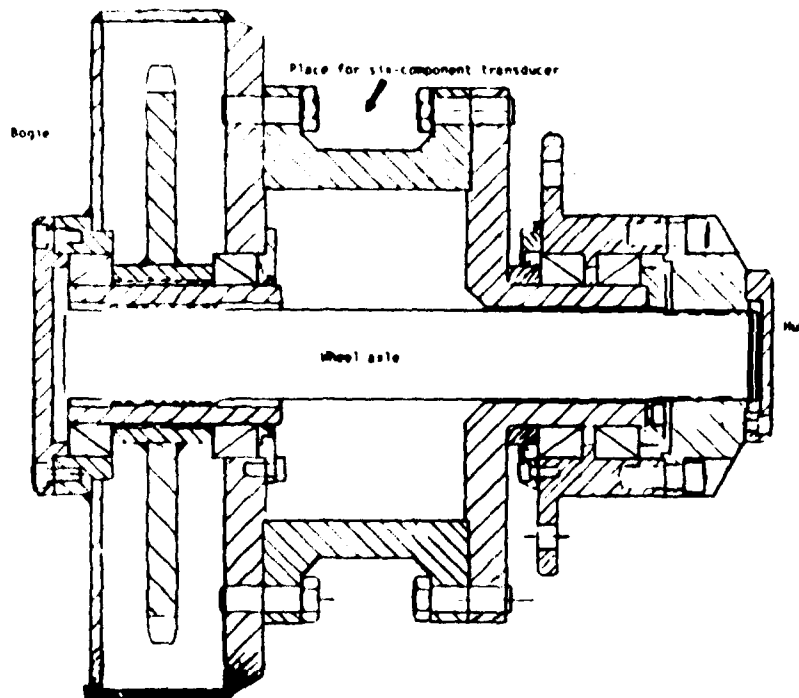


Figure 12. Drawing of the wheel suspension.

In a similar way transducers for internal forces, speed, location etc. will be developed and mounted on the vehicle. The possibilities here are limited by the system chosen to collect, transmit and save all transducer signals.

MEASUREMENT SYSTEM

The system for collecting and saving the transducer signals on the vehicle is based on micro processors.

It is a system with a hierarchy of interconnected processors, each one with its own memories and I/O. In multi processing a host 8051 micro computer (Intel SDK 51 Kit) controls a multiplicity of 8051's configured to operate simultaneously on separate portions of the overall process. This form of distributed processing is specially effective in systems where controls in a complex process are required at physically separated locations.

It is what we call a Master-Slave system. Each measuring point (transducer) has its own micro computer-slave, which takes care of and saves the transducer signals. To be able to coordinate all the measuring, one needs a superior processor, a master.

The connection between master and slaves is a serial link and consists of one transmitting and one receiving channel. All slaves are connec-

ted to the same two channels. To enlarge the system then means only to connect more slaves to the serial link. The maximum amount of slaves possible to connect to the SDK 51 Kit is 256.

The master and slave system supplies many advantages:

- extensibility
- rapidity
- replacable and interchangeable measuring points (slaves)
- insusceptible for disturbances
- an 'intelligent' system for measuring

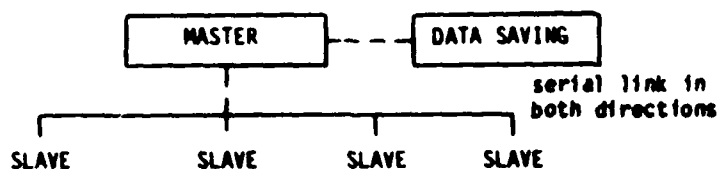


Figure 13. A system with four slaves.

The master

- coordinates the measuring
- tells the slaves what to do
- settles which slaves that should listen
- is able to send commands to all slaves at the same time
- can tell one slave to transmit status or data
- settles when a transducer signal shall be collected
- controls the slave function
- gives the alarm when a slave is out of order

The slaves

- listen to one or several names (numbers)
- listen to commands concerning them selves
- obey the command they get from the master
- are only allowed transmitting to the master one at the time
- can send information to the master influencing the data collection
- can save several series of data

Command from the master

The master has to exchange information with the slaves. This is done in the way that the master sends commands to the slaves and that data is sent to all slaves or from one slave.

Commands can be either Address-type or Data-type.

- Address command
When the master selects the slave (slaves) it wants to communicate with, it transmits an address command. Then all slaves wake up and control if they were addressed. Those who were addressed keep on listening, the others close down until next address command.

- Data command

This is used when the master has chosen to speak to one or several slaves. Only slaves addressed by a previous address command will listen to the data command.

Protocol

A protocol means the way data shall be transmitted, received and interpreted by master and slaves. A protocol can be seen as an agreement between master and slave in what way the communication shall be done and interpreted. The master always starts with transmitting a word of command, which the slave recognizes. This command tells the slave what protocol to use.

Handshake

In order to get a more safe communication between master and slave one can let the slave echo back every command or data received. The master can then check if it receives what it sent. If that is not the case, something is wrong and the master gives the alarm. An alarm is not allowed to stop the whole system.

Measuring

A slave who gets a command to make a measurement, measures and saves the value in its memory. A measuring command is usually given to several slaves at the same time. To make rapid measuring possible a high communication speed is needed (if each measuring shall be started by the master). Apart from that, it is also interesting to get information of slave status from each slave, e.g. to see if an interesting peak has been registered. This can be done quite easily; when the master transmits the word of command 'measure' (a Data-command) it also tells which slave is allowed to send back its status. This is possible as a part of the data command may be interpreted as an address. In this way the master repeats telling all the listening slaves to measure and picks back the slave status one by one. This can be done in a frequency of 1,000 words of command per second, which means that the slaves measure 1,000 times per second, but return status only when commanded.

Every slave saves its measured values. This is done in the internal memory in buffers determined by the master. A buffer has a certain page size (1 page = 256 bytes) and starts on a certain page in the memory, all this is determined by words of command from the master. In this way, the slave can save different series of measured values and the master knows where to pick them.

The slave can also process the transducer signals while measuring. Such a processing can be to compare the value with a given trigger level. If a value reaches the trigger level this can be registered by changing the status of that slave and when the master asks for that slave's status, the master will be informed that the trigger level is reached and can continue its processing (concerning that matter).

To be able to catch interesting lapse the slaves can function as a transient recorder. The slave saves measured value in a buffer starting at the first page and fills up the buffer. When the buffer is full

it will return to the first page and continues saving. In this way the buffer becomes an endless 'tape'. When one slave senses a trigger level the master records that and commands all slaves to stop measuring after a specified time interval. In this way the transient lapse can be recorded.

Signal transmission between moving parts

Driving torque is measured directly on the wheel axle. The axle is rotating. Therefore the transducer signal must be transferred from the axle to the vehicle body.

The slave connected to the driving axle will be battery-operated and rotate with the axle. The communication between master and slave will, in both directions, work over an optical connection. A transmitter (infra red light emitting diode, LED) and a receiver (photo transistor) are placed facing each other in both directions. The transmitter must transmit over an area wide enough to reach the receiver. One of the transmitters/receivers now can rotate and still be able to reach the corresponding receiver/transmitter with pulsing light (fig. 14).

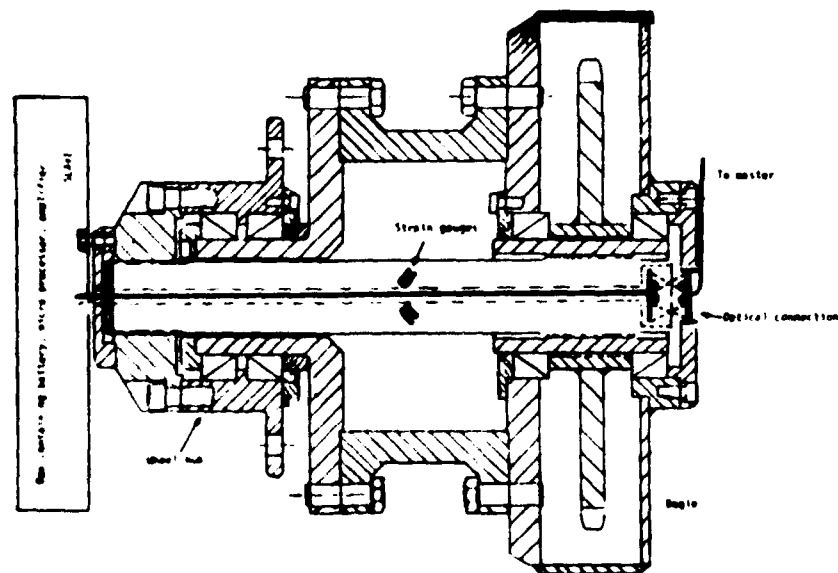


Figure 14. Signal transmission between rotation axle and vehicle body.

Concluding

Both transducer system and measurement system are being developed right now. The kind of experiments possible to make with the vehicle is very much depending on progress of this development. An overall, experimental design has been made concerning:

- wheel configuration
- steering geometry
- power distribution (between wheels)
- tires
- spring-damp system
- transmission set-ups

The forces and space requirement will be studied under controlled conditions. Apart from the conditions listed above, topography, vehicle speed, load and load distribution, acceleration etc. will be varied. It is easy to see the possibilities of making experiments and perhaps more difficult to find the adequate experiments and to limit the amount.

It is expected that these experiments will continue for a period of at least 2-3 years, of which I would like to report on a later occasion.

REFERENCES

- (1) McAllister, M. A Rig for Measuring the Forces on a Towed Wheel. Reprinted from J. agric. Engng Res. (1979) 24, 259-265.
- (2) Measurement Systems application and design. E.O. Doebelin McGraw-Hill 1975.
- (3) Piezo-Messtechnik KISTLER nr 6.052e 9.75 KIAG SWISS.
- (4) Watson, P.C. & Drake, S.H. Pedestal and wrist force sensors for automatic assembly. 5th International Symp. on Ind. Robots. III Research Institute Chicago, Illinois Sept. 1975.



✓
COMPACTION OF SAND USING ORDINARY OFF-ROAD VEHICLES

S. SHAABAN
MILITARY TECHNICAL COLLEGE, KOBRY EL KOBBA, CAIRO, EGYPT

AD-P004 297

Summary-This paper examines the possibility of compacting a sandy soil using ordinary off-road vehicles instead of compactors. Laboratory tests showed that a considerable compaction of sand can be achieved if alternative cyclic stresses are applied. Such stresses can be generated if a train of two vehicles is employed for compaction: one vehicle with all wheels driven towed another vehicle having all wheels towed. Compaction was made by making consecutive passages of the train of two vehicles. Procedure of compaction is described and test results are presented. Compacting sand by this method has increased the density up to 92% the value of optimum density obtained by modified compaction test. A considerable amelioration of soil trafficability has also been achieved, this is proved by the experimental drawbar pull-slip relationships measured before and after compaction. ✕

INTRODUCTION

The amelioration of vehicles mobility can be achieved by improving vehicles design and / or by increasing soil trafficability by compaction. Compaction is usually achieved by using compactors which need to be transported to the work sites. If compaction can be done by ordinary offroad vehicles, this would reduce costs and provide an alternative solution to the problem.

Results of triaxial experiments on sand made by FRANCO [1] showed that one can create considerable volumetric deformations in the soil by applying cycles of alternative stresses.

The intensity of these stresses should be limited so that the induced soil deformation will not be so large, otherwise soil dilatation occurs. In his study, he showed a case where soil dilatation was obtained (volume increased) when sample axial strain was large ($\pm 5\%$). He also showed another case where soil was compacted (volume decreased) when axial strain was limited to a small value ($\pm 0,75\%$).

In practice, alternative stresses are applied to the soil if a vehicle with all wheels driven tows another vehicle having all wheels towed, this is shown in Fig. 1.

Soil deformation is strongly related to wheels slip, therefore wheels slip should be kept small during compaction. Generally, slip should be lower than $30\%[2]$. This slip value corresponds in most cases to the maximum drawbar pull developed by the vehicle. Our traction tests carried out before compacting the experimental soil showed that the maximum drawbar pull is delivered at 10% slip. Thus, we tried to keep wheels slip during compaction below this value.

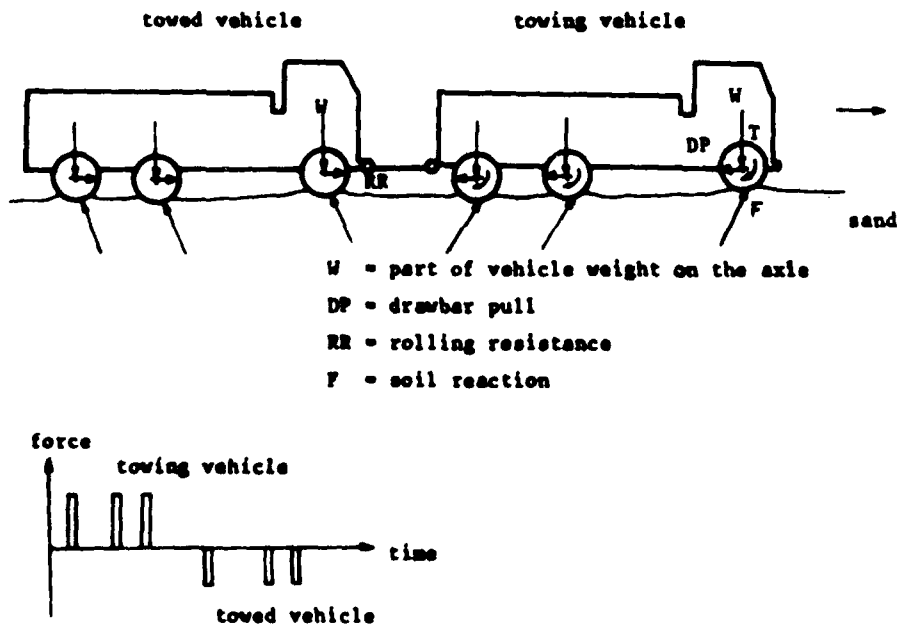


Fig. 1 Forces acting on the soil during compaction.

EXPERIMENTAL SOIL

An uniformly graded sand having a coefficient of uniformity $\frac{D_{60}}{D_{10}} = 2.1$ and a grain size distribution shown in Fig.2 was the experimental soil. Sand bin has a length of 70 m, a width of 7m and a depth of 0,8 m. Moisture content measured before compaction in the layer from 0 to 45 cm of the sand bin was nearly 4%. Laboratory standard and modified compaction tests were carried out, and the dry density-moisture relationships are shown in Fig.3. Compaction curves show that a moisture content of 3 to 5% is unfavourable for compacting such sand. Unfortunately, the existing natural content of 4% was not possible to change because of climate conditions. Surface of sand in the bin was gently levelled before compaction using a light grader.

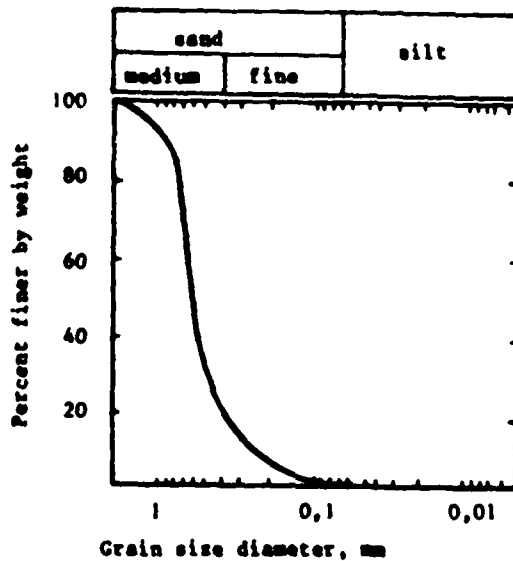


Fig.2 Particle size diameter of experimental soil.

COMPACTION PROCEDURE

Compaction was done by making consecutive passages by the train of two off-road vehicles. The towing vehicle moved with all axles driven and the lowest gear shifted (1st gear in main gear box and low gear in auxiliary gear box). The towed vehicle (connected to the towing vehicle by a steel rope) moved with engine stopped and brakes released.

To increase the resistance on the towing vehicle the top gear in the towed vehicle gear box was shifted and for further increase of resistance a lower gear was engaged.

Increased resistance caused more slip of towing vehicle wheels, thus it was possible to change the degree of slip by shifting different speeds in the towed vehicle gear box. To calculate wheels slip during compaction, the actual distance covered during ten revolutions was measured, and the theoretical distance, which would be covered if wheels purely roll, calculated. Slip value was then determined from the equation:

$$i = \frac{l_{th} - l_a}{l_{th}}$$

where:

i - wheels slip

l_{th} - theoretical distance

l_a - actual distance

First passage was situated 0,5 m from the side wall of soil bin. Followed passages were laterally shifted each by 0,3 to 0,5 m from the former, this is shown in Fig. 4.

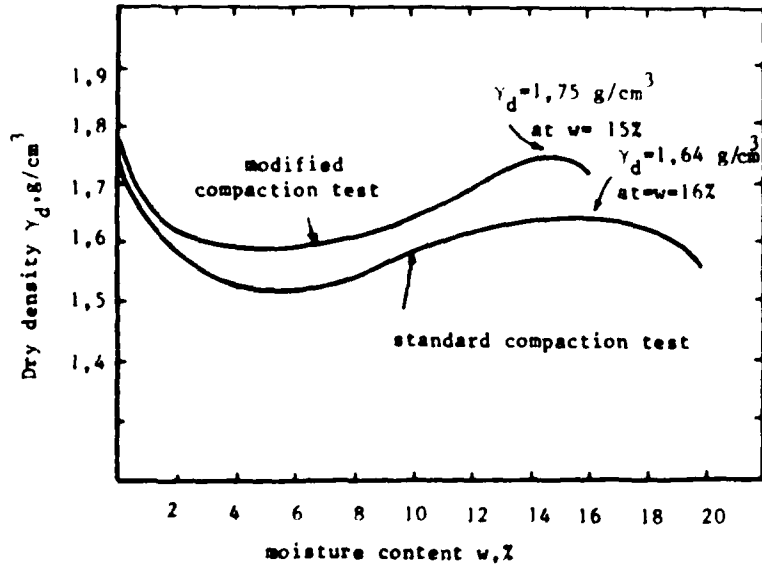


Fig.3 Experimental dry density-moisture relationships.

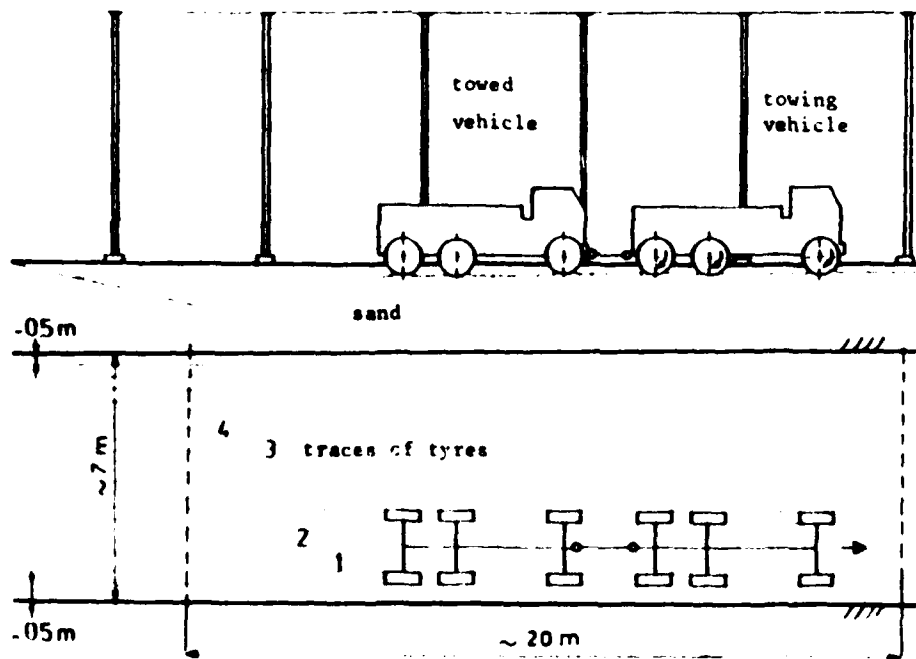


Fig.4 Compaction of the fine sand using the train of two offroad vehicles.

phases	1	2	3	4		
passages	5	4	5	5	3	2
towing	G 91200					
vehicle	p	1,5	2	2,5	3	F:3,7 R:4,0
	i	2,5	3	3,9	4,5	2,7 -
	Tyres: E 22,5 Pilote x M+S4 Michelin					
towed	G 101200					
vehicle	p	1,3	1,7	2,1	1,8	
	Tyres: 12,00-20 Michelin					

G: vehicle weight, Newtons

p: inflation pressure, bars

i: wheel slip, %

F: front wheels R: rear wheels.

Table 1. Description of compaction phases.

MEASURED VALUES

Moisture content was measured before each phase of compaction in ten points of soil bin measuring zone. This zone situated in the middle of soil bin had a length of 20 m and width of 5 m. Moisture content samples were taken at depths of 0,15,30 cm. Places of measuring the moisture content are shown in Fig. 5, and average values were as following:

before compaction	w = 4%
before 2 nd compaction phase	= 2,5 %
before 3 rd compaction phase	= 2,5 %
before 4 th compaction phase	= 3,2 %

The in situ density was measured after finishing 2nd, 3rd and 4th compaction phases using γ rays density meter in same points as for moisture content. Before measuring the density, the surface of soil bin was gently levelled. The density meter enabled to have readings of moisture content, bulk and dry densities at depths of 0 to 30 cm. For greater depth (40, 50 cm) the soil surface layers of 10, 20cm thickness were taken off (see Fig.8). The average of density values in the ten points of same layer was considered as the sand density at that depth.

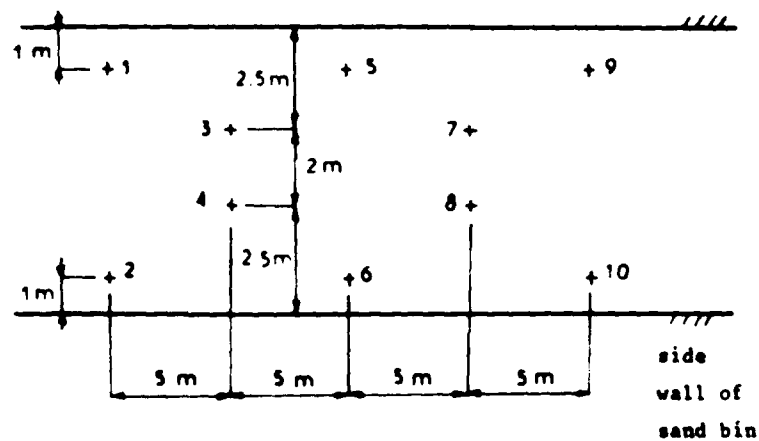


Fig.5 Points of measuring the moisture content and density.

Traction tests were carried out before and after compaction. In these tests the towing vehicle moving in the sand bin pulled a braking vehicle of adjustable braking effort. The pulling force was measured by a force dynamometer, and the speed of travel by a fifth wheel fixed to the towed vehicle. Theoretical speed of vehicle motion was measured by a pulse generator fixed to one of the towing vehicle rear wheels (Fig.9). Instantaneous values of pulling force (drawbar pull), travel and theoretical speeds were continuously recorded on a multichannel recorder, and the drawbar pull-slip relationships were traced.

RESULTS

The in situ dry density-depth relationships (Figs 6,7) are considered as a measure of degree of compaction. Fig.6 shows that after the third compaction phase the sand dry density at a depth of 20 cm increased to 93% of the optimum dry density determined by modified compaction test, at a depth of 30 cm it increased to 95% of the optimum dry density. Fig.7 shows that after the fourth compaction phase the sand dry density at a depth of 30 cm slightly decreased to 92% of the optimum value. But at 50 cm depth, it attained a high value (97% of the optimum).

The drawbar pull-slip relationships (Fig.8) measured before and after compaction are considered for evaluating the amelioration of soil trafficability by compaction. Referring to Fig.8, it is seen that the maximum drawbar pull (at 10% slip) increased by 30%, and for lower slip values it increased up to 60%. Average values of drawbar pull and the corresponding slip are given in table 2.

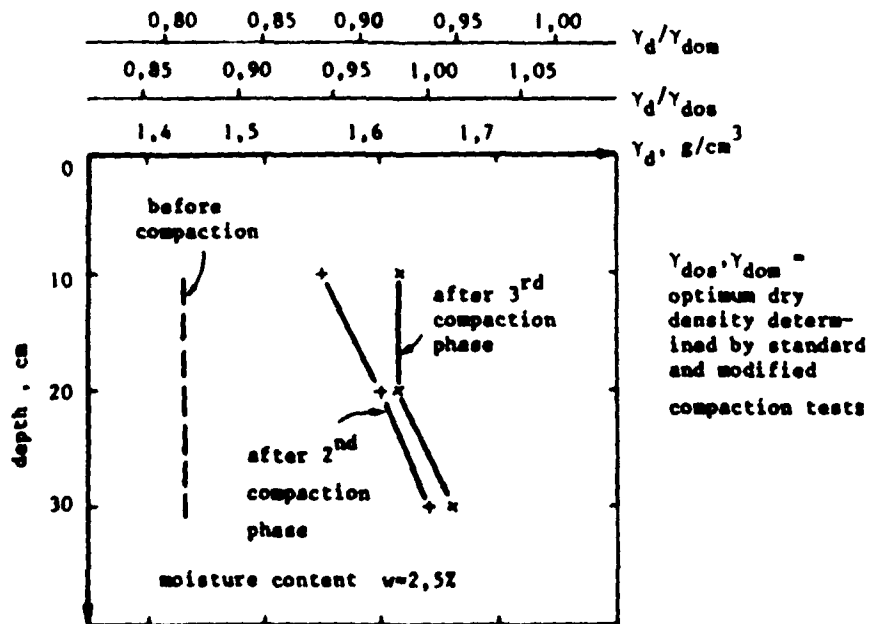


Fig.6 Dry density γ_d vs depth after 2nd and 3rd compaction phases.

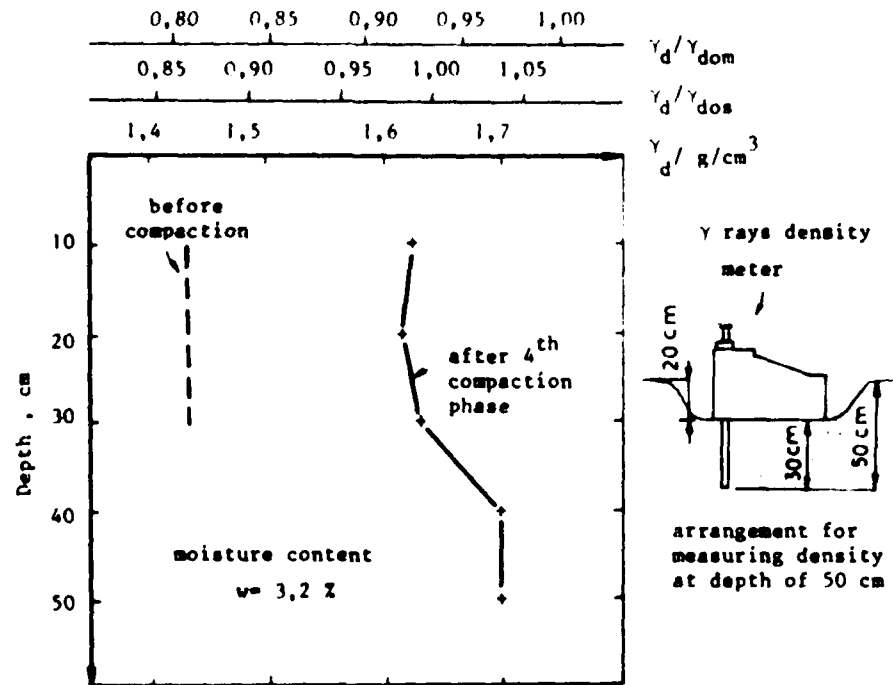


Fig.7 Dry density (γ_d) vs depth after 4th compaction phase

wheel slip%	DP before compaction	DP after compaction	% of increase
3	1360	2185	60,66
5	1625	2235	37,54
7	1785	2300	28,85
10	1830	2385	30,33
15	1825	2300	26,03
20	1690	2155	27,51
30	1560	15	17,63
40	1410	1700	20,06
60	1136	1370	20,07
80	975	1235	26,67
100	1300	2200	69,23

Table 2 Drawbar pull values before and after compaction.

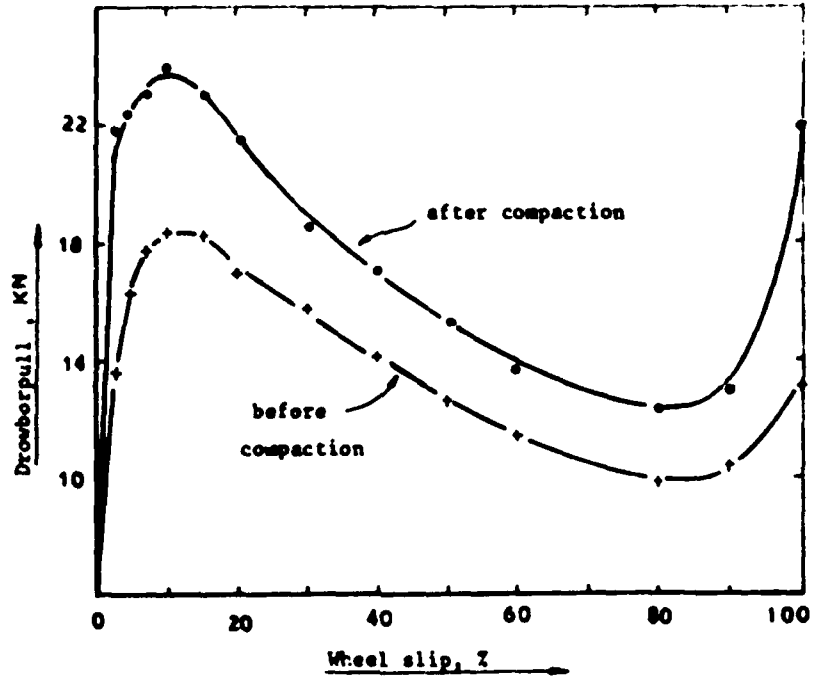


Fig.8 Drawbar pull-slip experimental curves before and after compaction.

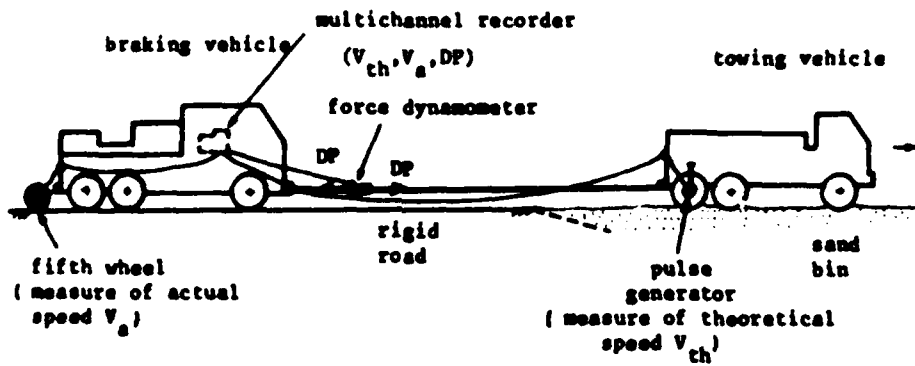



Fig.9 Traction test.

CONCLUSIONS

1. The proposed method for sand compaction in which alternative stresses are applied to the soil using a train of two off-road vehicles proved to be efficient, sand density at a depth of 30 cm increased to 92% of the optimum dry density determined by modified compaction test, and to 95% at 50 cm depth.
2. During compaction of sand, slip of wheels of compactors should be enough lower than the slip corresponding to the maximum drawbar pull determined by traction test. A slip of 5% can be considered as a limit value beyond which soil decompaction occurs.
3. Inflation pressure of vehicle tyres should be successively increased, and a pressure of 3,5 bars can be considered as a limit value. Greater inflation pressure increases the wheels slip and sinkage and leads to soil decompaction
4. A considerable degree of compaction was achieved although the sand was relatively uniform and the moisture content of 3% was unfavourable.

Acknowledgement: The author acknowledges the co-operation and assistance of the ETAS (Etablissement Technique d'Angers) in France in whose soil bin the experiments were carried out. He also wishes to express his appreciation to Professor J. Biarez, Dr Christian Grosjean, and Mr. Constantin for their support and assistance.

REFERENCES

- 1 T. Franco-Vellels, "Mesures des propriétés rhéologiques du sol en régime non permanent ou cyclique", Thesis of Dr Ing, "Ecole Centrale des Arts et Manufactures" PARIS, 1979.
 - 2 G.S.V Raghavan, E. Mekkyes, Statistical models for predicting compaction generated by off-road vehicular traffic in different soil types, Journal of Terramechanics, vol 3, No.1, 1978.
 - 3 J. Jacques Fry, "Contribution à l'étude et à la pratique du compactage", Thesis of Dr Ing, "Ecole Centrale des Arts et Manufactures, Paris, 1977.
- 

✓ A SIMPLE PREDICTION MODEL FOR SOIL COMPACTION UNDER VARIOUS
WHEEL LOADS AND GEOMETRIES AS AN AID TO VEHICLE DESIGN

D.L.O. SMITH
SIAE, PENICUIK, MIDLOTHIAN, SCOTLAND

ABSTRACT

The simple, numerical model was developed, as an aid to vehicle design, to predict changes in the dry bulk density of a soil due to the passage of a wheel, or wheels, over the soil surface. The model uses Söhne's solutions to estimate stress increases, and empirical isotropic stress-strain data to predict the resultant soil volume changes below a wheel. Accurate predictions of final dry bulk density for a layered soil require a more rigorous model and reliable data for the soil under consideration. For such a soil, the model presented here may be used effectively to examine the relative degrees of compaction caused by various wheel loads using data for an arbitrary soil. Designs for three agricultural tractor and trailer combinations and a heavy harvester are evaluated with respect to their predicted influence on soil bulk density. The importance of wheel load is revealed and is emphasised in a further sample.

INTRODUCTION

The problems associated with agricultural soil compaction, such as impaired drainage, poor soil structure and inferior crop yields, have been of concern for some time. Developments in agricultural mechanisation have led to larger and heavier vehicles and, although manufacturers and farmers have compensated to some extent by fitting more appropriate tyres, soil stresses have continued to increase. Awareness of these stress increases has led to the evaluation of potential designs as to their effect on soil compaction. The simple computer model described here was developed at SIAE as an aid to the vehicle designer and mechanisation advisor in making such evaluations.

The model requires input data on the soil physical properties, the wheel loads and the tyre/soil contact areas under consideration. The model uses stress prediction equations developed by Söhne (1953) and isotropic stress-strain data for Macmerry series soil (sandy loam) presented by Leeson and Campbell (1983)². Stress prediction in soil and isotropic stress-strain relationships are reviewed briefly as a prelude to the description of the model and examples of its use.

AD-P004 298

STRESS PREDICTION

Most methods of predicting increases in stress within a soil due to the application of a surface load are derived from the solutions of Boussinesq (1885)³. These solutions for the action of a point load on a semi-infinite, elastic mass have been applied successfully to civil engineering problems where relatively small strains occur in large volumes of dense, saturated, isotropic soil. Their application to agricultural engineering problems, where large plastic strains occur in small volumes of unsaturated, anisotropic soil, requires modification. Griffith (1929)⁴ and Froelich (1934)⁵ introduced empirical concentration factors, which tend to concentrate the stress distribution about the vertical point load axis, to account for plastic behaviour and for finite boundary conditions. Söhne, (1953, 1958)^{1,6}, having measured tyre/soil contact areas for various tyre sizes and soil strengths, developed expressions for the tyre/soil contact stress distributions for equivalent circular contact areas of soils classed as i) dense, hard, dry, cohesive; ii) fairly moist, relatively dense, sandy clay; iii) plastic flowing, wet. Söhne further derived solutions for the major and minor principal stress increases directly below the centre of a circular contact area for the three classes. Blackwell (1979)⁷ proposed a fourth class, very hard soil, for which the Boussinesq solution for a uniformly distributed load is used. Blackwell's experimental determinations of major and minor principal stresses under wheel loads confirmed the value of the solutions for the major principal stress, but led him to assume a constant major-minor principal stress ratio of 1.19. Blackwell elected to characterise the stress increases below a surface wheel load in terms of the isotropic normal stress increase alone, since deviatoric stress increases were small (approximately 8% of the isotropic normal stress increases).

To conform with critical state soil mechanics convention, the isotropic normal stress is expressed by the spherical stress, defined as:

$$p = \frac{\sigma_1 + \sigma_2 + \sigma_3}{\sqrt{3}} \quad \text{where } \sigma_1, \sigma_2 \text{ and } \sigma_3 \text{ are the principal stresses.}$$

For isotropic stress conditions the principal stresses are equal and the spherical stress is equal to the normal stress multiplied by $\sqrt{3}$

For the principal stress ratio assumed by Blackwell, and assuming that the intermediate and minor principal stresses are equal, the spherical stress increase below a wheel load is given by:

$$\Delta p = 1.548 \Delta \sigma$$

where $\Delta \sigma$, is the major principal stress increase evaluated from the appropriate Söhne solution.

ISOTROPIC STRESS-STRAIN RELATIONSHIPS

The isotropic stress-strain behaviour of loose and compacted soils is semi-logarithmic and similar to the one dimensional compression behaviour of normally consolidated and over-consolidated, saturated clays respectively.

To conform with critical state soil mechanics convention isotropic strain is expressed as a change in specific volume; specific volume is defined as:

$$v = \frac{\rho}{D_{bd}}$$

where ρ is the density of the soil particles and D_{bd} is the dry bulk density of the soil. Physically, the specific volume is the ratio of the volume of the bulk soil to the total volume of the soil particles, and is equal to one plus the void ratio.

Isotropic stress-strain relationships are commonly depicted on a $V-\ln(P)$ diagram where they appear as straight lines (Fig. 1). The virgin compression line (VCL) is the path followed by a loose soil subjected to compression for the first time. Unloading the soil allows recovery of the elastic strain and is represented by the relaxation line (RL). The unrecovered, plastic strain represents the specific volume reduction (i.e. the bulk density increase) due to the applied spherical stress. Reloading of a previously stressed soil is represented by the recompression line (RCL) which meets the VCL at a stress which is somewhat greater than the previous maximum spherical stress.

Schofield and Wroth (1968)⁸ have suggested that for saturated soils ψ , the slope of the RL, and K , the slope of the RCL, are equal.² For unsaturated soils however, Leeson and Campbell (1983)² found that they were unequal and presented data for two soils showing that K is related, by a second order polynomial, to the specific volume of the soil before recompression. Although no discernable relationship between ψ and other soil characteristics was found, they implied that ψ is less than K except at low initial specific volumes. The relationships they presented for the Macmerry series soil (sandy loam) were the more consistent of the two soils and were chosen for use in the model.

THE MODEL

The soil compaction model is based on the prediction of soil specific volume changes due to changes in spherical stress. The depth of soil to be modelled is divided into elemental layers and the spherical stress increase at the centre of each layer, directly below the wheel load, is estimated from Söhne's (1953) solutions, the soil strength class being determined by the dry bulk density of each elemental layer before compression. The thickness and

number of the elemental layers should correspond to the vertical interval between, and the number of, field measurements of dry bulk density and water content. The specific volume reduction, and hence the bulk density increase, of each elemental layer is estimated from isotropic relationships. As the soil may be initially normally consolidated or over-consolidated, the model calculates two final specific volumes for each element. The first is calculated assuming that the loading takes place, at least in part, along the virgin compression line (followed by unloading along the relaxation line). The second is calculated assuming that the loading takes place along only a recompression line, the position of which depends on the specific volume before loading. The lower of the two calculated specific volumes is selected to calculate the resultant bulk density of each elemental layer.

Multiple wheel loads may be considered, the model using the calculated elemental bulk densities after the passage of one wheel as the elemental bulk densities before loading by the subsequent wheel. The depth to the centre of each element is also adjusted after each wheel pass to account for the wheel rut which effectively moves each element closer to the wheel. To facilitate comparison between vehicles, the initial soil density profile and the predicted density profile after each pass are presented graphically. The plotting procedure takes the centre of the lowest soil element as a datum and so the depth of rut caused by each wheel can be inferred from the displacement of the centre of the uppermost element as may be seen from the examples below. For such a simple model, the predicted bulk density changes are in reasonable agreement with the limited field data (Blackwell, 1979) available. From volume change/spherical stress considerations, the field data contain anomalous changes in bulk density which may be due to measurement error near the surface. Also the model does not simulate accurately the anisotropy and non-homogeneity of field soils. Consequently the predicted bulk density changes can be at variance with the observed data.

EXAMPLES OF USE OF THE MODEL

To illustrate the use of the model, commercial designs of three large tractor/trailer combinations and a heavy harvesting machine are compared as to their effects on soil bulk density.

The following input data are required by the model:

1. Number of in-line wheel loads, number of elemental layers, thickness of elemental layers, mm

2. For each wheel: load, kN, tyre/soil contact area, m^2
3. For each elemental layer: initial dry bulk density, kq/m^3 , water content d.w.b., % w/w

For these examples 0.5 m of a uniform, sandy loam is modelled using the soil parameters presented by Leeson and Campbell (1983). A water content of 25% and an initial dry bulk density of 1000 kq/m^3 , Söhne strength class 'firm' is assumed. Although such a uniform profile is highly atypical, it allows comparison of the vehicle effects without confusion from soil irregularities. The wheel load data for these vehicles and the graphical outputs from the model are shown in Figures 2 to 5.

The overall increase in soil bulk density with depth due to the passage of a vehicle may be assessed from the depression of the ground surface indicated in the figures. The depressions predicted for the tractor and two-axle trailers (Figs. 2 and 3) are similar, approximately 130 mm, even though the total load of II is 46% greater than I. The low initial wheel load of I (Fig. 2) produces small increases in bulk density whereas the third wheel load, even though of no greater magnitude than the second wheel load, causes a large increase in bulk density, particularly near the surface, due to the high mean surface normal stress. The wheel loads and mean surface normal stresses of II (Fig. 3) are moderate for all the wheels and so the corresponding increases in soil bulk density are moderately uniform with depth. The tractor and three-axle trailer (Fig. 4) produces more compaction at the surface and at depth than the tractor and two-axle trailers because of the high wheel loads and mean surface normal stresses involved; the increase in soil bulk density due to the large third wheel load is particularly marked.

The first wheel load of the heavy harvester (Fig. 5) produces a large increase in soil bulk density, due to the high load and mean surface normal stress, but the subsequent wheel load, being only 50% of the first wheel load, produces only a small increase due to the slightly greater mean surface normal stress. The total load of the harvester is approximately equal to that of the tractor and two-axle trailer I (Fig. 2) but the harvester, having fewer wheels, produces a greater increase in soil bulk density as indicated by a 15% greater depression of the ground surface.

In all the examples above, each wheel of the vehicle contributes to the compaction process although generally, as would be expected, earlier wheels cause the greatest increases in the soil bulk density.

The model may also be used to assess the relative contribution made by a particular variable. As an example, consider the effect on soil compaction of increasing a wheel load from 5 kN to 20 kN whilst the tyre/soil contact area is increased such that the mean surface normal stress (ground pressure) is held constant at 80 kPa. It may be seen from Figure 6 that both wheel loads would cause the same degree of compaction at the surface, but that the 20 kN wheel load causes considerably more compaction especially at depth.

CONCLUDING REMARKS

The model greatly simplifies the stress applications caused by agricultural vehicles, and the response of the soil to them. It cannot be expected to achieve accurate predictions of bulk density changes even if accurate input data are used. Its usefulness lies in its ability to assess the relative contributions made by each variable to the compaction process and in its ability to compare the relative degrees of compaction caused by various wheel loads and arrangements of alternative vehicle designs.

The model is to be improved by the development of more accurate stress prediction solutions, which allow for layered soils, and by the development of triaxial stress-strain relationships to account for shear stresses.

REFERENCES

1. Söhne, W. Druckverteilung im boden und bodenverformung unter schlepperreifen. (Distribution of pressure in the soil and soil deformation under tractor tyres) Grundl. Landtech. 5, 49-63, 1953
2. Leeson, J.J. and Campbell, D.J. The variation of soil critical state parameters with water content and its relevance to the compaction of two agricultural soils. J. Soil Sci. 34(1), 33-34, 1983
3. Boussinesq, J. Application des potentiels à l'étude de l'équilibre et du mouvement des solides élastique. (Application of the study of equilibrium and displacement of elastic solids) Gauthier-Villars, Paris, 1885
4. Griffith, J.H. The pressures under substances. Engng and Contracting 68, 113-119, 1929
5. Froehlich, O.K. Druckverteilung im Baugrunde (Formulae of Boussinesq) 1934, cited in Söhne (1958)

6. Söhne, W. Fundamentals of pressure distribution and soil compaction under tractor tires. Agric. Engng 39, 276-281, 290, 1958
7. Blackwell, P.S. A method of predicting soil dry bulk density beneath agricultural wheels. Ph.D. Thesis (unpubl.) Univ. Edinburgh, 1979
8. Schofield, A.N. and Wroth, C.P. Critical state soil mechanics. McGraw-Hill Book Co., New York, 1968

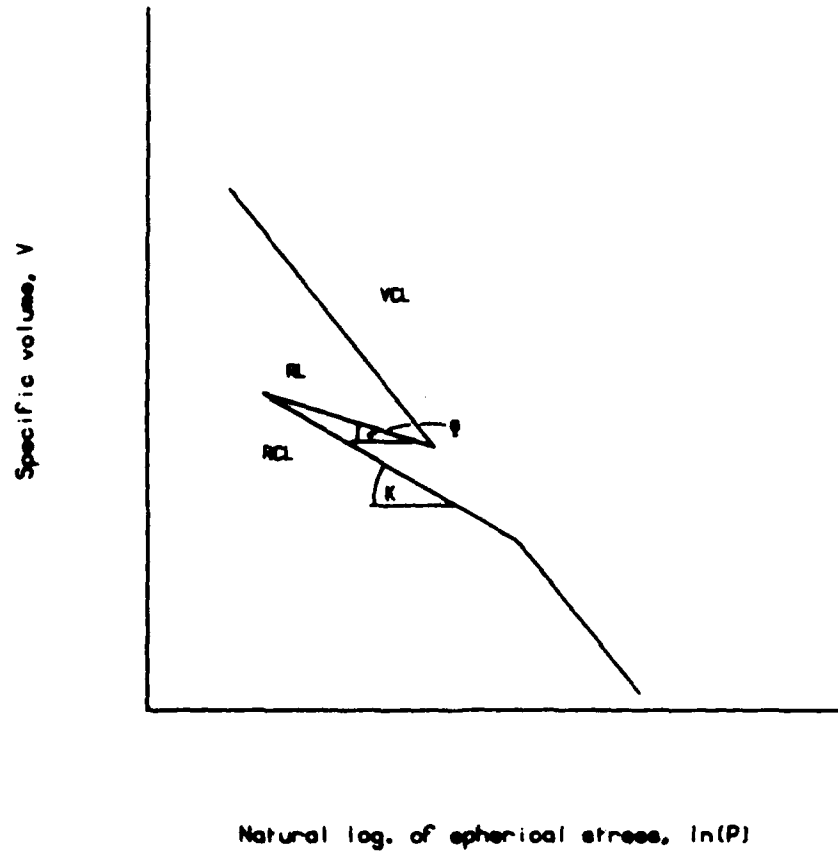
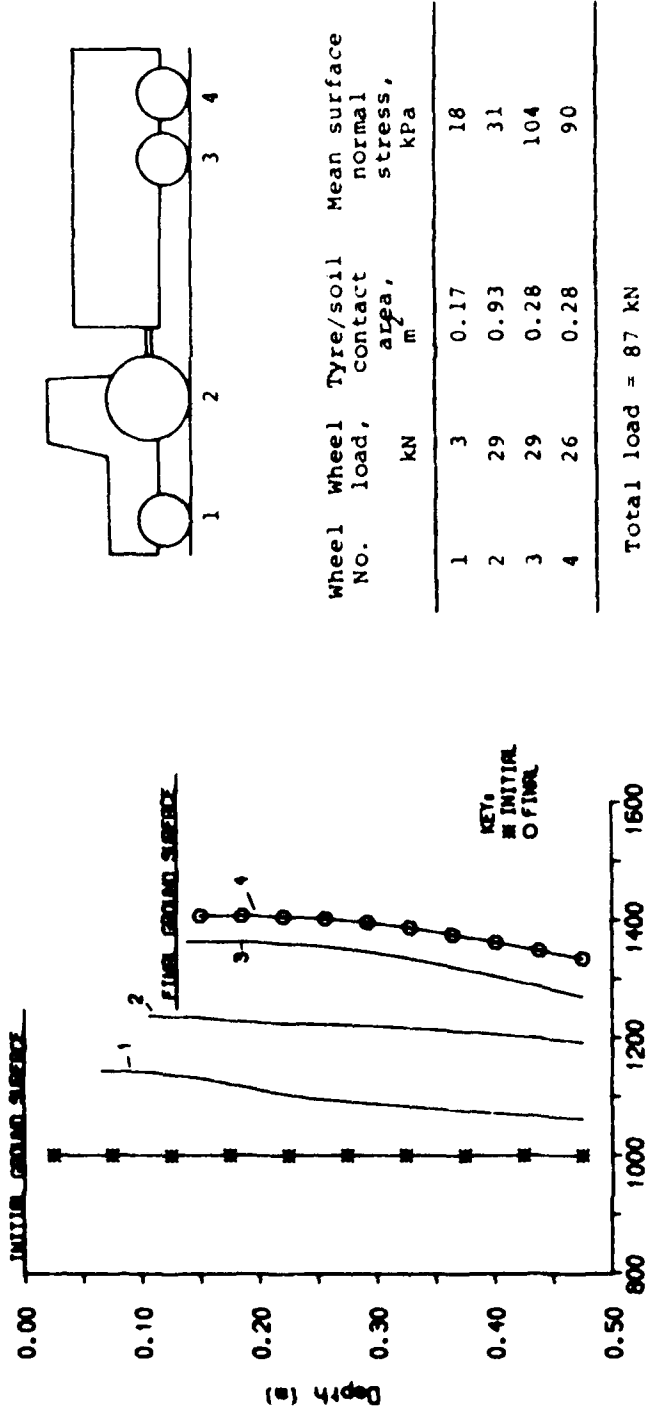


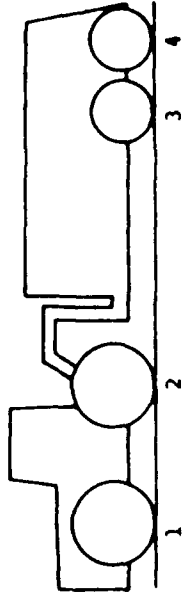
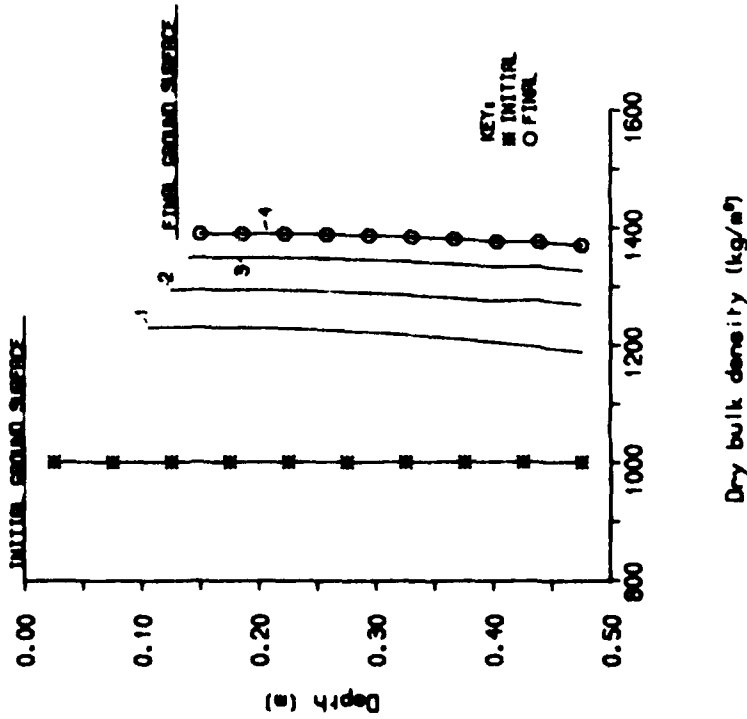
Fig. 1. Isotropic stress-strain relationships used in the model

VCL = virgin compression line,
RL = relaxation line
RCL = recompression line



Dry bulk density (kg/m³)

Fig. 2. Changes in dry bulk density due to tractor and two-axle trailer I.



Wheel NO.	Wheel load, kN	Tyre/soil contact area, m ²	Mean surface normal stress, kPa
1	30	0.93	32
2	35	0.93	38
3	32	0.60	53
4	30	0.60	50

Total load = 127 kN

Fig. 3. Changes in dry bulk density due to tractor and two-axle trailer II

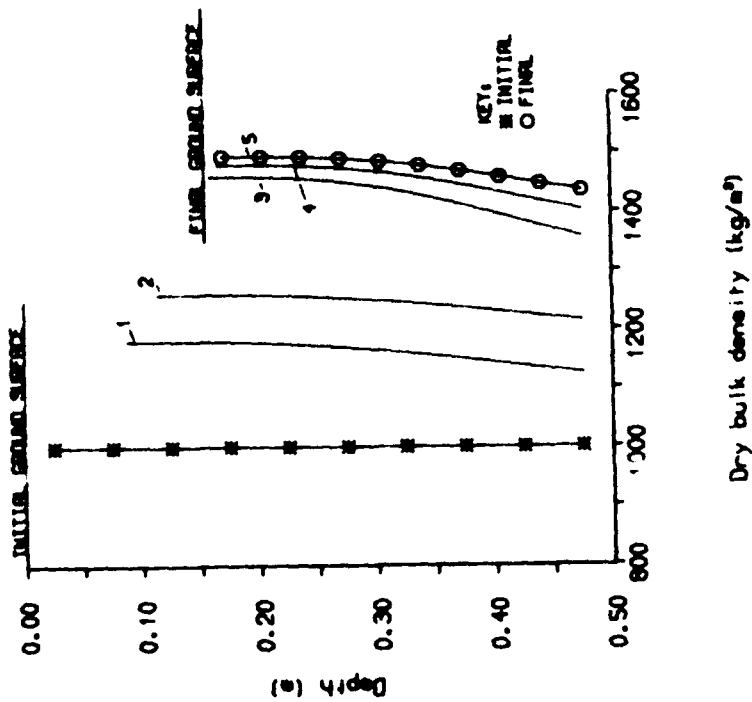
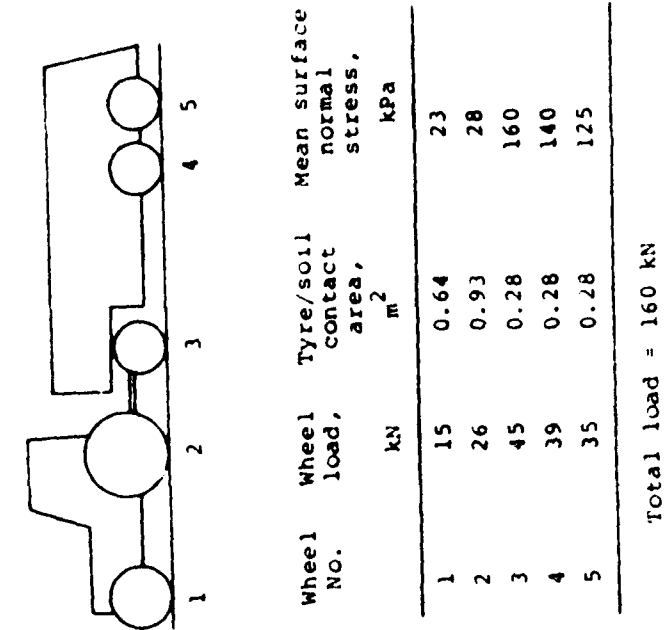


Fig. 4. Changes in dry bulk density due to tractor and three-axle trailer

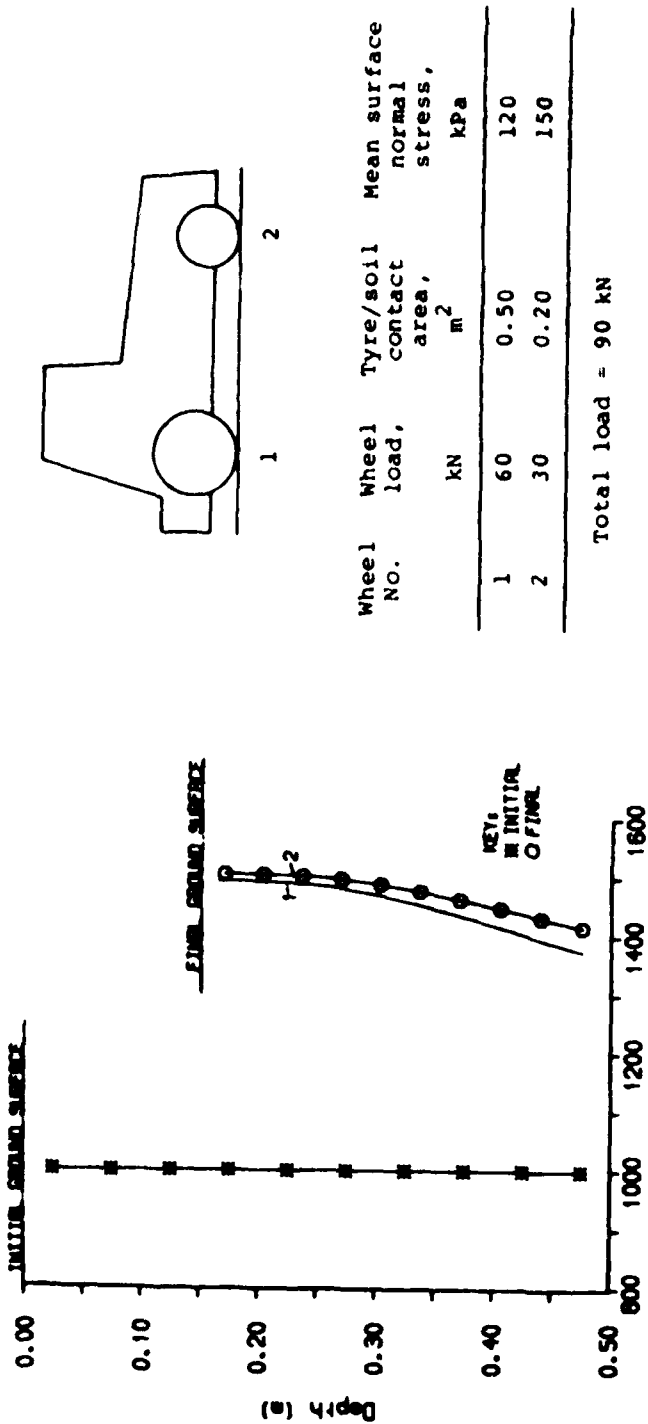


Fig. 5. Changes in dry bulk density due to heavy harvester

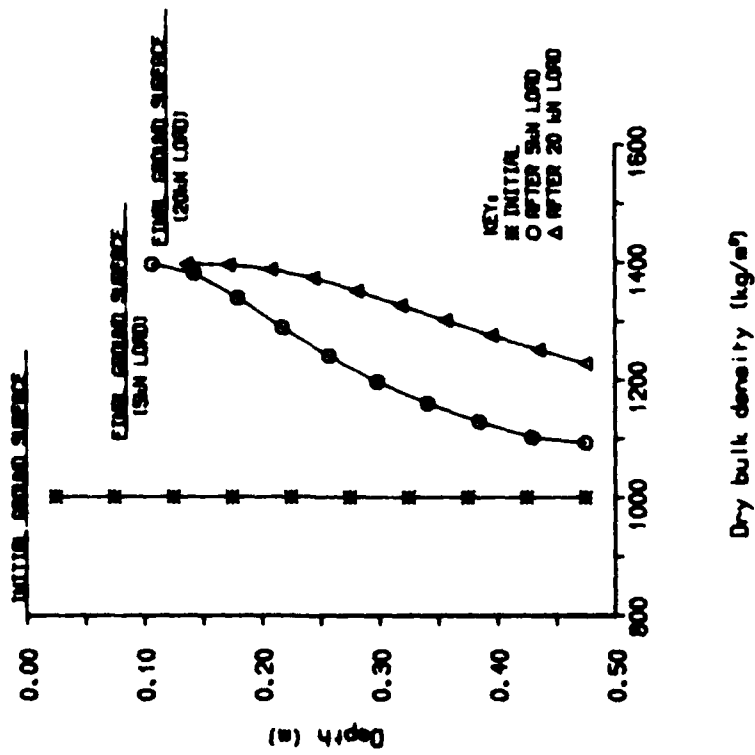


Fig. 6. Changes in dry bulk density due to a single pass of a 5 kN or a 20 kN wheel load, both imparting a mean surface normal stress of 80 kPa



✓ FLOTATION TIRES AND SUBSURFACE COMPACTION

JAMES H. TAYLOR* and EDDIE C. BURTT†

USDA-ARS, NATIONAL TILLAGE MACHINERY LABORATORY, AUBURN, AL, USA

ABSTRACT

Theoretical and applied research has shown that the pressure at a point in the subsurface soil is a function of both the surface unit pressure and the extent of the area over which it is applied (total load). Thirty years ago, most of the soil compaction from vehicle traffic was in the plow layer and was removed by normal cultural practices. As equipment has increased in size and mass, machine designers have increased tire sizes to keep the soil surface unit pressure relatively constant. However, the increase in total axle loads is believed to have caused an increase in compaction at any given depth in the soil profile, resulting in significant compaction in the subsoil.

Two tires of different sizes, a standard agricultural tire and a flotation tire were used to support equal loads. Soil pressures were measured at three depths in the soil profile directly beneath each of the tires. Two soils were used and each was prepared first in a uniform density profile, and then they were prepared with a simulated traffic pan (layer of higher density) at a depth of approximately 30 cm.

Results showed that the presence of a traffic pan in the soil profile caused higher soil pressures above the pan and lower pressures below it than was the case for a uniform soil profile. The soil contact surface of the flotation tire was approximately 22% greater than the agricultural tire. The greater contact surface did reduce soil pressures at the soil surface, of course, but the total axle load was still the dominant factor in the 18-50 cm depth range used in this study.

INTRODUCTION

The average mass of tractors and other farm machinery has increased rapidly in the past 30 years. Tire size has been increased as the mass of the machinery has increased so that the unit load applied to the soil surface has changed very little. It has been commonly believed that maintaining a relatively constant soil surface pressure beneath the tires would keep soil compaction relatively constant also. However, evidence of greater soil compaction has been reported from many countries using heavy equipment in recent years.

* Research Leader-Traction, and National Technical Advisor-Traction and Controlled Traffic Research

† Agricultural Engineer

AD-P004 299

The use of vehicles with three or four wide (flotation) tires for distribution of fertilizer or other chemicals has become a common practice in mechanized agriculture. The configurations of these vehicles provide sufficient mobility for travel over almost any agricultural soil condition. The flotation tires cover most of the soil surface. Does spreading the total load over such a large area eliminate the danger of subsurface compaction? The objective of the research reported here was to measure and compare subsurface soil pressures beneath a conventional agricultural tire and a wider, flotation type tire when the tires were carrying equal loads.

PREVIOUS RESEARCH

Compaction of soils under heavy equipment could have been predicted from Froehlich's [1] work of 50 years ago. That work showed that pressure in the subsurface soil was a function of both surface unit pressure and the total load applied. The following formula from the Boussinesq equations was adapted to describe the pressures in the soil beneath a loaded circular plate:

$$\sigma_z = P_m(1 - \cos \gamma) \quad (1)$$

where σ_z = pressure at a point beneath the load on the load axis;
 P_m = surface unit pressure;
 γ = concentration factor, dependent on soil conditions;
 α = one-half the aperture angle between the point in question and the edge of the plate.

Soehne [2] concluded that when surface pressures are equal, the pressure bulbs will be larger and will reach deeper as the total load increases. Soehne [3] stated that "The pressure in the upper soil layer is determined by the specific pressure at the surface, which depends upon the inflation pressure and the soil deformation. The pressure in deeper soil layers is determined by the amount of the load."

Reaves and Cooper [4] compared stress distribution measurements under pneumatic tires and crawler tracks carrying the same total dynamic load and pulling the same drawbar load. Bulk density was measured, but the results were erratic and were not reported.

Bailey and Vanden Berg [5], using a modified triaxial shear apparatus, found that the bulk density-soil pressure relationship involved both the mean normal stress and the maximum shearing stress. An equation containing three soil parameters was proposed to describe the relationship.

Taylor et al. [6] examined the effects of total axle load on subsurface soil compaction. They used two different size tires and adjusted the total load to give equal pressures at the soil-tire interface. The larger tire produced higher soil pressures at all depths measured. That work, which used unequal total loads but equal unit pressure under the tires, is complementary to the work being reported in this paper which used equal total loads and unequal unit pressures. Further discussion of this earlier work will follow later in this paper.

Hakansson and Danfors [7] reported on 20 years of compaction research in Sweden. Early concern was with vehicle compaction of the plow layer, but the steady increase in farm machinery mass brought subsoil compaction problems. They reported that "Axle loads exceeding 6 tons (8-10

tons on a tandem axle) may result in compaction at depths below 40 cm." Also, they found the persistence of subsoil compaction increasing with depth and sometimes lasting for decades.

PROCEDURES AND EQUIPMENT

This study was conducted in the soil bins at the National Tillage Machinery Laboratory (NTML) using the single wheel tire test machine. The flotation tire used in the study was a 67 x 34.00-30, 12-ply rating furnished to the NTML by Firestone Tire & Rubber Company*, Akron, Ohio. The tire was modified by Firestone to decrease the lugs to 1/2 the original height in order to provide clearance for operation in the NTML test machine. The standard agricultural tire was a 24.5-32, R-1 tread, 10-ply rating bias-ply supplied by Goodyear Tire and Rubber Company*, Akron, Ohio. The tires are shown in Fig. 1.



Fig. 1. A 24.5-32, 10-ply tire (left) and a 67 x 34:00-30, 12-ply tire were used in this study. (NTML Photo No. W-296)

Each of the test tires was operated at a dynamic load of 36.5 kN and at a net traction of 10 kN. Travel reduction was adjusted by computer control to the level needed for developing the 10 kN net traction. Since the forward velocity of the test machine was constant, the same level of output power was developed by each tire.

Inflation pressure values of 165 kPa and 124 kPa were used for each of three and two replications, respectively. The uneven number of replications was caused by limitations of space in the soil bins. The effective rolling radius used for each tire was determined on the test soil at 36.5 kN dynamic load and 165 kPa inflation pressure.

* Use of a company or product name by USDA does not imply approval or recommendation of that product to the exclusion of others which may also be suitable.

Pressures within the soil profile were measured by strain-gaged soil pressure cells. The cells had a diameter of 76 mm and a thickness of 16 mm. These cells were buried in the test soil in the center of the tire path prior to the tire operation. Two pressure cells were buried at depths within the soil profile of 18, 30, and 50 cm for each test run.

The two soil types used were Norfolk sandy loam and Decatur clay loam. Each soil type was prepared in two conditions: Soil fitting number one (F-1) was a loose condition tilled 46 cm deep with no compaction; soil fitting number two (F-2) was in a similar condition down to a simulated traffic pan at a depth of approximately 30 cm.

Tire performance data and soil pressure data were each acquired by a common digital data acquisition system. Pressure distributions with respect to a point directly beneath the axle were recorded and used to determine the maximum pressure from each pressure cell. Only maximum pressure values were used in subsequent data analyses.

RESULTS AND DISCUSSION

Soil pressure cells are difficult to work with because of the soil disturbance necessary to implant them. Their accuracy is questionable even when their precision is good. They are used only because alternate methods are worse. The results of the measurements of soil pressures at three depths under two tires at two inflation pressures are graphically summarized in Figs. 2-5.

In Figs. 2-5, each point on the graphs at 165 kPa tire inflation pressure represents measurements from 6 soil pressure cells while each point at 124 kPa represents 4 soil pressure cell measurements. Therefore, each of the Figs. 2-5 represents the results of 60 soil pressure cell measurements.

A statistical analysis of the data was done. However, a close look at the raw data was taken first, and some interesting trends were revealed. In Figs. 2 and 3 (F-1), the soils were tilled and left with a uniformly loose profile. The 18-cm depth on the Norfolk sandy loam (Fig. 2) shows the expected progression of soil pressures: big tire, low inflation pressure; big tire, high inflation pressure; small tire, low inflation pressure; small tire, high inflation pressure. However, the soil pressures are all between 162 kPa and 170 kPa, representing an overall variation of only about 5%. At the 30-cm depth in Fig. 2, there is a reversal between inflation pressures on the big tire which cannot be explained. The 165-kPa point appears to be low, disturbing an otherwise systematic set of data. Examination of the 6 values averaged to obtain the unexplainably low value yielded nothing unusual.

The Decatur clay loam raw data (Fig. 3) were not as predictable as the Norfolk sandy loam (Fig. 2). The soil pressure responses to inflation pressure differences on the small tire are considerable at 18 cm and 30 cm while the big tire shows little effect of inflation pressure. All values of the soil pressures under the big tire fell within the inflation pressure response range of the small tire at the 18-cm and 30-cm depths, but at the 50-cm depth, the big tire shows lower soil pressures than the small tire.

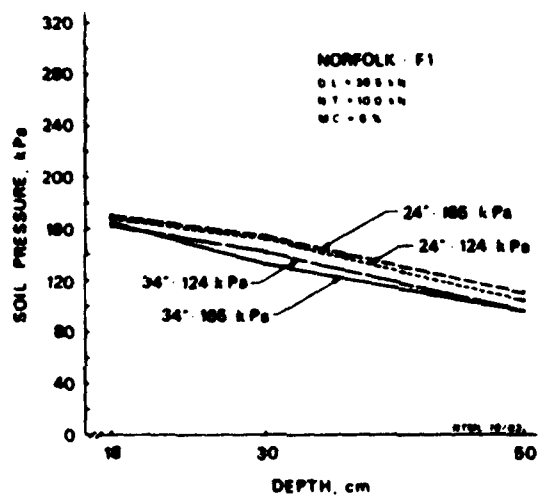


Fig. 2. Effect of total load in a uniform soil condition. (D.L. = Dynamic Load; N.T. = Net Traction; M.C. = Moisture Content). (NTNL Photo No. P10,358a)

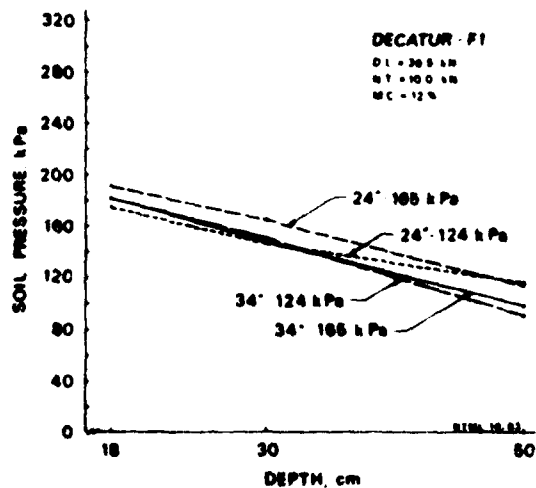


Fig. 3. Effect of total load in a uniform soil condition. (D.L. = Dynamic Load; N.T. = Net Traction; M.C. = Moisture Content). (NTNL Photo No. P10,358c)

In Figs. 4 and 5 (F-2), a traffic pan was induced in both soils at a depth of approximately 30 cm. The Norfolk sandy loam (Fig. 4) shows a relatively high soil pressure at the 18-cm depth for the big tire at 165 kPa inflation pressure. The other 11 points on the graph reveal little difference between the pressures beneath the tires at each depth. In the Decatur clay loam with a traffic pan at 30 cm (Fig. 5), there appears to be a difference in soil pressure values between tires and inflation pressures at the 18-cm depth, but the difference decreases as the depth in the soil increases.

All of the above discussion was based on graphs of the raw data. An analysis of variance was run on the data using a factorial design. The soil fitting, the measurement depth, and the fitting-depth interaction were all significant at the 1% level of confidence. Statistically, there was no difference due to tires or inflation pressure. Since total loads were equal, the analysis indicated that for the 18-50 cm depths used in this study, tire size had no significant effect on soil pressures. Only the total load mattered, not the surface unit pressure.

The larger tire footprint, or soil contact surface area, was determined to be approximately 22% greater than the smaller tire footprint for both soils using the method described in Taylor et al. [6]. Spreading the 36.5-kN load over the larger contact surface of the big tire would certainly reduce soil unit pressure at the surface. Froehlich's formula predicts that this difference in surface pressure under the two tires would gradually disappear until, at some depth, the pressures would converge reflecting the equal total loads supported.

The traffic pan, or layer of increased soil density, that was used for soil fitting (F-2), has a distinct effect on the slope of the soil pressure-depth curve. The soil pressures are much higher above the traffic pan and much lower below the traffic pan than is the case for the uniform soil condition (F-1). This was also observed in earlier (1980) work by Taylor et al. [6]. Figs. 6 and 7 show results from one soil fitted uniformly (C-1) and with a traffic pan (C-2). The 1980 tests were run at constant travel reduction. The present tests were run at constant net traction. In the earlier investigation, the soil surface unit pressure was equal under two different size tires but the total load was unequal. In the present work the total load was equal on the two different size tires, resulting in unequal soil surface unit pressures. The same change in slope is evident regardless of which loading scheme is used.

The 1980 work by Taylor et al. looked at soil pressures at three depths beneath a large tire and a small tire with total loads adjusted to give soil surface pressures that were equal for each tire (equal soil surface pressures-unequal total loads). According to Froehlich, the soil pressure-depth curves for these tires should have started at the same point for the surface pressure, but diverged with increasing soil depth.

The current work discussed in this paper used a large and a small tire carrying equal total loads which resulted in higher soil surface contact pressures under the smaller tire (equal total load-unequal soil surface pressures). According to Froehlich, the soil pressure-depth curves for these tires should have started with quite different values at the soil surface, but converged toward a single value at some depth.

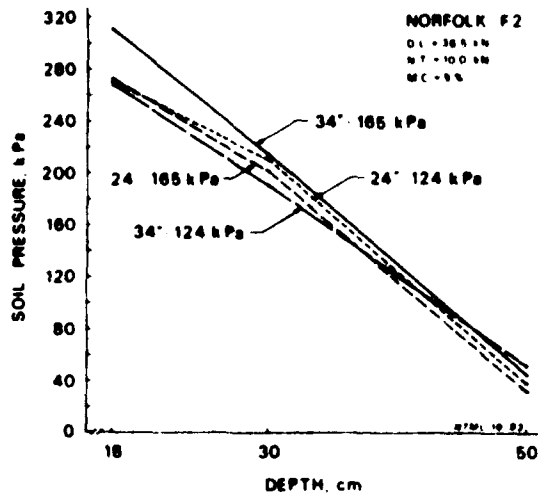


Fig. 4. Effect of total load in a soil with a hardpan at a depth of 30 cm. (D.L. = Dynamic Load; N.T. = Net Traction; M.C. = Moisture Content). (NTNL Photo No. P10,358b)

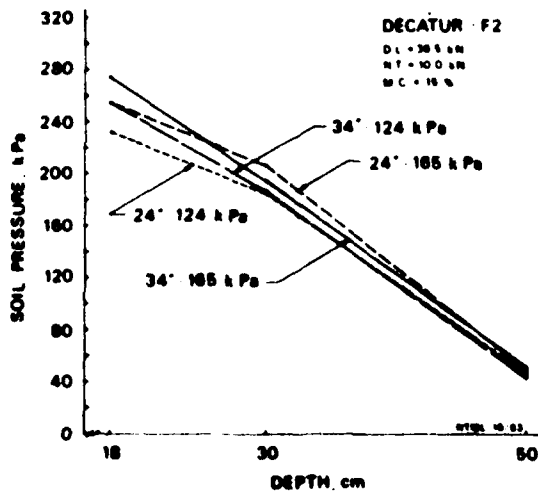


Fig. 5. Effect of total load in a soil with a hardpan at a depth of 30 cm. (D.L. = Dynamic Load; N.T. = Net Traction; M.C. = Moisture Content). (NTNL Photo No. P10,358d)

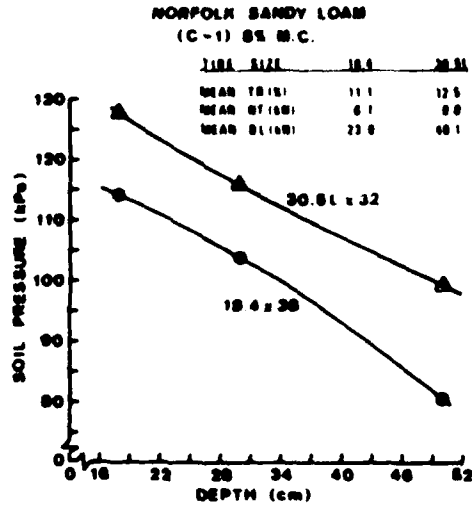


Fig. 6. Effect of total load in a uniform soft condition. (T.R. = Travel Reduction; N.T. = Net Traction; D.L. = Dynamic Load). (NTNL Photo No. P10,338b)

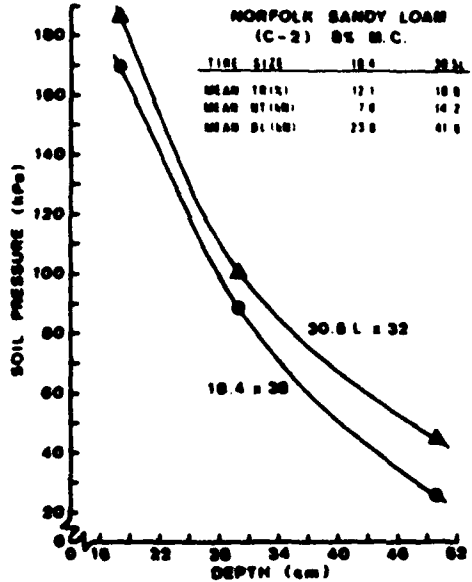


Fig. 7. Effect of total load in a soil with a hardpan at a depth of 20 cm. (T.R. = Travel Reduction; N.T. = Net Traction; D.L. = Dynamic Load). (NTNL Photo No. P10,338d1)

While the current work discussed here used two different inflation pressures, the differences were small and based on rated load for each of the tires. It is not surprising that the statistical analysis showed that the effect of inflation pressure on the subsurface soil pressures was not significant. The 67 x 34-30 tire was a flotation tire, but it was not really a low-ground-pressure tire. Future investigations are needed to determine soil pressures at several depths beneath a conventional tire and a low-ground-pressure tire carrying equal loads.

CONCLUSIONS

The presence of a traffic pan or compacted layer in the soil profile concentrated the soil reaction to traffic forces above the compacted layer. Pressures above the compacted layer were higher and pressures below the compacted layer were lower than they were for the same soil with a uniform density profile.

For the soil conditions in this study and within the range of tire size, inflation pressures, and depth of pressure measurements used, only the total load significantly affected the intensity of soil pressure at a given depth. There was no significant difference between soil pressures measured beneath the two tires.

Based on this study and an earlier study [6], the soil pressures at 18-50 cm are dependent upon total load and not significantly affected by the unit pressure under the tires at the soil surface.

REFERENCES

- [1] Froehlich, O. K. Druckverteilung in Baugrunde (Pressure distribution in the soil). Wien, 1934.
- [2] Soehne, Walter. Druckverteilung in Boden und Bodenverformung unter schlepperreifen (Distribution of pressure in the soil and soil deformation under tractor tires). Grundlagen der Landtechnik, Heft 4:49-63, 1953.
- [3] Soehne, Walter. Fundamentals of pressure distribution and soil compaction under tractor tires. Agricultural Engineering 39:276-281, 290, 1958.
- [4] Reeves, C. A. and A. W. Cooper. Stress distribution in soils under tractor loads. Agricultural Engineering 41:20-21, 1960.
- [5] Bailey, A. C. and G. E. Vanden Berg. Yielding by compaction and shear in unsaturated soil. Trans. Am. Soc. Agric. Engrs. 11(3):307-317, 1968.
- [6] Taylor, J. H., E. C. Burt, and A. C. Bailey. Effect of total load on subsurface soil compaction. Trans. Am. Soc. Agric. Engrs. 23(3):568-570, 1980.
- [7] Hakansson, Inge and Birger Danfors. Effects of heavy traffic on soil conditions and crop growth. Proc. 7th Internat. Conf. of ISTVS, Vol. 1, 239-253, Calgary, Alberta, Canada, Aug. 1981.


 TRACTOR POWER SELECTION WITH COMPACTION CONSTRAINTS

B.D. WITNEY, E.B. ELBANNA, K. ERADAT OSKOU
 EDINBURGH SCHOOL OF AGRICULTURE, WEST MAINS RD, EDINBURGH, U.K.

AD-P004 300

ABSTRACT

In the absence of a practical monitor of soil compaction, the increasing size of agricultural tractors is largely dominated by the upward trend in labour charges. The object of this study is to assess the feasibility of developing a compaction penalty index as a function of the penetration resistance of the soil and soil type.

Tractor power for primary tillage is dependent on soil strength; both traction and plough draught can be predicted by means of soil penetration resistance as the quantitative parameter. As the soil penetration resistance is a function of soil moisture content and density, it can be determined directly from soil and weather data. Soil texture, in the form of the ratio of clay to sand and silt, is also shown to be an important parameter in the prediction of penetration resistance. Combining these factors, an empirical equation for the soil penetration resistance is developed and tested under a wide range of soil conditions.

Arbitrary crop losses from soil damage are used to demonstrate the relative significance of compaction penalty costs on results from a simulation model for tractor power selection. On the basis of this simple sensitivity exercise, it is concluded that further work is justified to develop a compaction penalty index based on the penetration resistance equation.

1. INTRODUCTION

On arable farms the peak drawbar power requirement is determined by primary tillage operations. If the total tractor power is inadequate, delays incur severe financial penalties through loss of potential crop yield. In order to avoid these penalties, power and machinery replacement policy has been directed consistently towards surplus capacity. This, in itself, is simply a form of insurance cover against the risk of bad weather and machine breakdowns. Simultaneously, however, escalating labour charges have stimulated the trend towards a smaller tractor fleet size comprising fewer, but more powerful, individual units. The implication of machine size on soil damage are conveniently ignored.

Gross vehicle weight must increase in direct proportion to engine power output for efficient draught operations. Whilst every effort is made to maintain constant ground contact pressure despite the heavier machines, the net effect of using larger and wider tyres to increase the contact area is to create higher stresses at deeper levels in the soil profile. At the simplest level, the economic penalty of deep compaction is the cost of subsoiling. The repetitive frequency of this operation is in direct proportion to both the increasing size of the tractor causing the soil damage and the increasing availability of that tractor for the remedial work.

Alternatively, the economic penalty must be linked to crop responses. Compaction of the soil increases the mechanical resistance experienced by penetrating roots. Whilst the limiting mechanical resistance varies widely for different plant species, the level of mechanical resistance which reduced rates of seedling root elongation to 20% of their maximum has been estimated to lie within the narrower range of 24-35 bar for three plant species, (Gooderham, 1977). Differences between soils were found to be larger than between plant species (fig 1), as would be expected from an understanding of the mechanics of root growth (Abdalla *et al.*, 1969). Thus, it appears entirely feasible to link the rate of root elongation to cone penetration resistance, provided account is taken of soil type. It still remains to link root elongation with plant yield.

Eriksson *et al.*, (1974) have shown that the effect of top soil compaction on relative cereal yield is significantly influenced by the soil moisture content (fig 2). They adopted the term "Degree of Compactness" to indicate the change in thickness of the top soil layer. A measure of the degree of compactness can be obtained by calculating the actual bulk density of the soil as a percentage of the bulk density at a standard compacted condition induced by a static pressure of 200 kPa. The degree of compactness that is common after autumn ploughing, in the early spring and after normal spring tillage is given in the diagram. During wet years, the optimum degree of compactness is less than in average and dry years. Furthermore, the clay content of the soil also affects the yield response curve.

The object of this study is to develop an empirical equation for the cone penetration resistance of soil which incorporates soil mechanics theory in a form which is readily assimilated in agricultural applications related to the draught of tillage equipment, traction and compaction.

2. CONE PENETRATION RESISTANCE

From an earlier investigation (Eradat Oskoui and Witney, 1982), it was proposed that the cone penetration resistance of the soil was a function of soil moisture content and soil specific weight which jointly represent the cohesive and frictional components, such that:

$$C_i = f(c) + f(\gamma) \quad \dots\dots\dots(1)$$

where: C_i = cone index, MPa
 c = soil cohesion, kPa
 γ = soil specific weight, kN/m³

It was argued that the cohesive strength of the soil is substantially influenced by soil moisture content whilst both the specific weight and the angle of internal shearing resistance are affected to a lesser extent. From regression analysis of test data from three soils, ranging from sandy loam through to clay loam, the empirical equation for the soil cone index at median plough depth was:

$$C_i = 450.5 \theta^{-2} + 0.019 \gamma \quad \dots\dots\dots(2)$$

where: θ = soil moisture content, %.

This equation, however, is appropriate for only a limited soil moisture range but one, fortunately, covering the optimum soil workability conditions of agricultural operations. There is considerable experimental evidence of a much greater divergence of cone penetration resistance values at both the drier and wetter extremes of the soil moisture spectrum for different types of soils. On sandy soils, Harrison and Chang (1966) found that soil strength changed little with moisture content, in contrast with heavier soils where both cohesion and angle of internal shearing resistance decreased dramatically above the liquid limit. Voorhees and Walker (1977) quoted high cone penetration resistance values in clay soils below 25% moisture content and exceptionally high cone penetration resistances were obtained in reconstituted laboratory silt loam soil under dry conditions (Wells and Treeswan, 1977).

2.1 Clay ratio

The mechanical analysis of particle size is a simple, widely available and readily understood classification method which can account for the local variability of agricultural soils. As the clay fraction has cohesive properties by virtue of its chemical bonds, it is proposed that the ratio of clay to silt and sand, C_s , is a practical monitor of soil texture which can be included in the cone penetration resistance equation. Thus, the cohesive component of the cone penetration resistance becomes not only an inverse exponential function of the soil moisture content but also directly proportional to the clay ratio. At high clay ratios and low moisture contents, therefore, very high cone penetration resistances are predicted by this cohesive component, decreasing virtually to zero above the liquid limit when heavy soils turn into a fluid mud (fig 3a).

2.2 Pressure bulb

When a circular probe is pushed into a particulate soil, it develops a pressure bulb around its base. The frictional component of the penetration resistance depends on the weight of the soil within this failure zone, the extent of which being related to the angle of internal shearing resistance of the soil (fig 3b). From elementary soil mechanics, if the sloping face of the cone is taken as the initial radius of a logarithmic spiral, r_0 , then the final radius of the spiral, r_1 , acts as the boundary with the passive earth pressure zone which breaks into the unsupported vertical face surrounding the penetrometer shaft. For a completely formed pressure bulb, the included angle for the spiral is, approximately, π radians and the equation for the logarithmic spiral becomes:

$$r_1 = r_0 e^{\pi \tan \phi}$$

In general terms, a high value of 45° is realistic for the angle of internal shearing resistance of compact dry sands, declining to zero for heavy wet clays. For the tangent of the friction angle, the limiting values of 1 and 0 bound a range which can be related to the clay ratio by a simplistic empiricism (table 1).

Table 1. Relation between the tangent of the friction angle values of the clay ratio

Friction angle (ϕ), deg	$\tan \phi = \sqrt{1 + C_r}$	Clay ratio (C_r)
45	1	0
40	0.84	0.19
35	0.70	0.43
30	0.58	0.72
25	0.47	1.13
20	0.36	1.78
15	0.27	2.70
10	0.18	4.56
5	0.09	10.11

The frictional component of the cone penetration resistance is then directly proportional to the specific weight of the soil and to an exponential function for the logarithmic spiral effect, with the clay ratio being utilised in a form which represents the influence of friction.

In a purely frictional sand, the clay ratio is zero. Consequently, soil moisture content has no effect on the cone penetration resistance but variation in specific soil weight has a considerable effect (fig 3a). As the clay ratio increases, the effect of density diminishes and the cohesive forces predominate. Whilst, in theory, the logarithmic spiral effect should qualify the cohesive component as well as the frictional component, the inclusion of a very high clay ratio is only acceptable at high moisture contents. As the soil dries out, strong clays in the massive state also exhibit a high angle of internal shearing resistance. For simplicity, this phenomenon can only be accommodated within the empirical equation by eliminating the action of the logarithmic spiral effect on the cohesive component.

2.3 Experimental evaluation

Combining the two components, the cone penetration resistance equation takes the form:

$$CI = K_C C_r e^{-n\theta} + K_\phi \gamma e^{\Pi/(1 + C_r)} \quad \dots\dots(3)$$

where:

CI = penetration resistance, MPa
 C_r = clay ratio
 K_C, K_ϕ = coefficients
 n = exponent
 γ = soil specific weight, kN/m³
 θ = soil moisture content, %

Experimental data for four soils (Eradat Oskoui and Witney, 1982; Stafford, 1984) was analysed for each soil and in total to determine the values of the regression coefficients for equation 3 (table 2). The optimum value of the exponent, n , was found to be 0.08.

Table 2. Values of the clay ratio, cone penetration resistance coefficients, their standard errors and percentage explanation of the penetration resistance results.

Soil series	Clay ratio	Coefficients		Standard errors		Explanation %
		K_c	K_ϕ	K_c	K_ϕ	
Darvel	0.17	28.43	0.00146	3.742	0.00035	99.0
Macmerry	0.23	21.60	0.00175	4.518	0.00046	98.6
Winton	0.33	13.95	0.00317	3.453	0.00097	99.1
Silsoe	1.57	11.98	0.0123	2.330	0.0052	90.8
All soils		15.92	0.00263	0.666	0.00042	91.3

The prediction of the cone penetration resistance by means of individual equations for Darvel, Macmerry and Winton soils is very accurate with 99% of the data explained. This exhibits a minor improvement compared with the results which were obtained by means of equation 2. Although the percentage explanation of the experimental data falls when the cone penetration resistances of all the soils are determined from a single equation, it must be noted that the inclusion of the Silsoe soil series increases the range of the clay ratio five fold and the spread of the cone penetration resistance data from three times the lowest value to ten times the lowest value (table 3 and fig 4).

The fact that the values of the coefficients for the individual soils still exhibit a trend linked to the changes in the clay ratio is an indication that additional refinements are feasible. Two possibilities are, firstly, to use the deviation moisture content from a standard value, such as at the plastic limit, in place of the absolute moisture content and, secondly, to include an additional soil specific weight term equivalent to the surcharge effect of foundation bearing capacity theories. Whilst both these alternatives have credibility, it is important to balance the potential benefit which would accrue from the additional complexity of the equation.

3. APPLICATION OF THE CONE PENETRATION RESISTANCE EQUATION

By means of the cone penetration resistance equation, both the traction of a two wheel drive tractor and the draught of a plough are linked to soil texture as well as to both soil moisture content and soil specific weight. In turn, soil moisture content can be simulated from soil and weather data (Witney *et al.*, 1982), and the resultant data analysed to identify suitable work days when the soil workability meets specified criteria. Thus, it is possible to establish the operational costs for different sizes of tractors ploughing a fixed area of land in a prescribed period and for maximum acceptable soil moisture content (Witney and Eradat Oskoul, 1982). When the available power is inadequate, completion of the work is delayed and incurs a crop yield penalty (fig 5). From this example, it is evident that the penalty for an underpowered tractor is very high, whereas the extra cost of oversizing the tractor is very small.

If, however, an arbitrary value is placed on the soil damage from heavier, more powerful tractors, the optimum size of tractor becomes more specific. Consider, for example, only a 1% loss of potential yield by using a 50 kW tractor in the crop establishment operations following ploughing and that the loss doubles for every 25 kW increase in tractor power above that

Table 3. Measured and predicted cone penetration resistances from four soils, together with soil data.

Clay ratio	Soil specific weight, kN/m ³	Soil moisture content, % w/w	Cone penetration resistance, MPa	
			Measured	Predicted
0.17	12.24	25.2	0.779	0.828
		28.9	0.869	0.738
		30.8	0.586	0.701
		34.5	0.531	0.643
	12.25	25.1	0.889	0.832
		27.1	0.807	0.779
		31.1	0.586	0.696
		33.0	0.517	0.664
		34.0	0.572	0.651
		36.5	0.524	0.618
	12.27	25.6	0.827	0.819
		25.7	1.000	0.817
		35.5	0.676	0.631
	12.29	24.2	0.978	0.860
26.3		0.862	0.800	
30.7		0.676	0.704	
34.1		0.565	0.650	
0.23	11.67	31.2	0.634	0.695
		31.3	0.765	0.692
		35.3	0.599	0.612
		41.0	0.537	0.533
	11.79	29.7	0.710	0.738
		31.9	0.627	0.682
		34.5	0.572	0.629
		38.9	0.489	0.561
	12.15	29.1	0.772	0.766
		32.1	0.703	0.691
		32.5	0.703	0.682
	12.19	33.1	0.407	0.670
		41.4	0.351	0.546
	12.43	29.6	0.731	0.762
		29.9	0.699	0.752
		34.0	0.641	0.660
		38.2	0.545	0.592
	0.33	12.44	26.7	1.116
27.2			1.041	0.947
27.9			0.889	0.916
29.0			0.827	0.866
12.54		25.0	0.965	1.066
		27.3	0.905	0.945
		28.5	0.972	0.893
		28.8	0.954	0.864
		29.1	0.854	0.877
		29.8	0.813	0.837

Table 3 (Continued)

Clay ratio	Soil specific weight, kN/m ³	Soil moisture content, % w/w	Cone penetration resistance, MPa		
			Measured	Predicted	
0.33 (contd)	12.80	24.2	1.034	1.123	
		28.6	0.965	0.892	
		28.8	0.751	0.885	
	12.91	30.3	0.848	0.826	
		26.1	1.199	1.018	
		26.1	0.882	1.018	
		26.8	1.061	0.982	
		30.3	0.730	0.828	
	12.93	31.3	0.841	0.793	
		24.6	1.061	1.100	
		25.1	0.910	1.071	
		29.2	0.834	0.870	
	1.57	12.16	33.7	1.900	1.796
13.93		33.2	2.600	1.888	
14.22		31.3	2.900	2.180	
14.61		32.2	2.100	2.033	
14.81		44.1	0.900	0.869	
15.22		31.6	2.700	2.140	
15.30		32.1	3.000	2.054	
15.35		34.0	1.800	1.784	
15.49		33.1	2.000	1.909	
15.79		30.8	1.500	2.278	
16.05		41.1	1.700	1.080	
16.18		27.2	3.400	2.994	
		31.2	1.400	2.206	
		31.7	2.700	2.133	
		40.0	1.300	1.168	
		31.3	3.500	2.189	
		16.38	29.0	1.100	2.614
		16.45	32.3	2.700	2.041
		16.48	28.3	2.800	2.746
			39.6	1.600	1.204
		16.50	39.6	1.600	1.204
39.6			1.300	1.204	
16.52			43.2	1.500	0.937
16.72			28.0	4.500	2.822
16.87			25.2	2.100	3.495
16.97			27.4	2.500	2.945
17.06			41.3	1.300	1.075
			47.9	0.600	0.696
17.16			32.8	1.400	1.974
			36.7	1.800	1.481
17.26		27.9	1.400	2.849	
	32.0	1.400	2.087		
17.36	23.4	3.800	4.018		
17.47	44.3	1.500	0.881		
17.75	46.0	1.100	0.789		
17.85	32.0	2.100	2.100		

level. This 4 fold increase is not unrealistic with reference to the 100 kW tractor which requires dual tyres to retain the same ground contact pressure as the 50 kW tractor and in addition generates compaction at a deeper level. Over the total cropping area, the value of the soil damage penalty for the larger tractors mirrors the timeliness penalties for the smaller tractors and identifies, more clearly, that the extra cost of overpowered tractors is significant.

4. CONCLUSIONS AND FURTHER WORK

A two part equation is developed to predict the penetration resistance of a cone penetrometer from soil moisture content, soil specific weight and soil texture. The correlation between theoretical and experimental values of the cone penetration resistance is improved for a wide range of conditions.

It is considered that this form of equation is more appropriate for inclusion in a compaction penalty index. Further work is in progress to relate the change in cone penetration resistance from the passage of a wheel to the loss of crop yield.

ACKNOWLEDGEMENT

The authors gratefully acknowledge the cone penetration results made available by J Stafford, National Institute of Agricultural Engineering, Silsoe, Bedford.

REFERENCES

- Abdalla, A.M.; Hettiaratchi, D.R.P. and Reece, A.R. 1969. The mechanics of root growth in granular media. *J. agric. Engng. Res.* 14: 236-248.
- Eradat Oskoui, K. and Witney, B.D. 1982. The determination of plough draught. 1 - Prediction from soil and meteorological data with cone index as the soil strength parameter. *J. Terramechanics* 19: 97-106.
- Eriksson, J.; Hakansson, I. and Danfors, B. 1974. The effect of soil compaction on soil structure and crop yields. *Swedish Inst. agric. Engng. Bull.* 354. *Trans. J.K. Aase, U.S.D.A.-Agric. Res. Service.*
- Gooderham, P.T. 1977. Some aspects of soil compaction, root growth and crop yield. *Agric. Progress* 52: 33-44.
- Harrison, W.L. and Chang, B. 1966. Soil strength prediction by the use of soil analogs. *U.S.A.T.A.C. Tech. Rep. No. 9560, Warren, Michigan.*
- Stafford, J. 1984. Personal communication. *Natn. Inst. Agric. Engng., Silsoe, Bedford.*
- Wells, L.G. and Treesuwan, O. 1978. The response of various soil strength indices to changing water content and bulk density. *Trans. Amer. Soc. agric. Engrs.* 21: 854-861.
- Witney, B.D.; Eradat Oskoui, K. and Speirs, R.B. 1982. A simulation model for predicting soil moisture status. *Soil & Tillage Res.* 2: 67-80.

Witney, B.D. and Eradat Oskoul, K. 1982. The basis of tractor power selection on arable farms. *J. agric. Engng. Res.* 27: 513-527.

Voorhees, M.L. and Walker, P.M. 1977. Tractionability as a function of soil moisture. *Trans. Amer. Soc. agric. Engrs.* 20: 806-809.

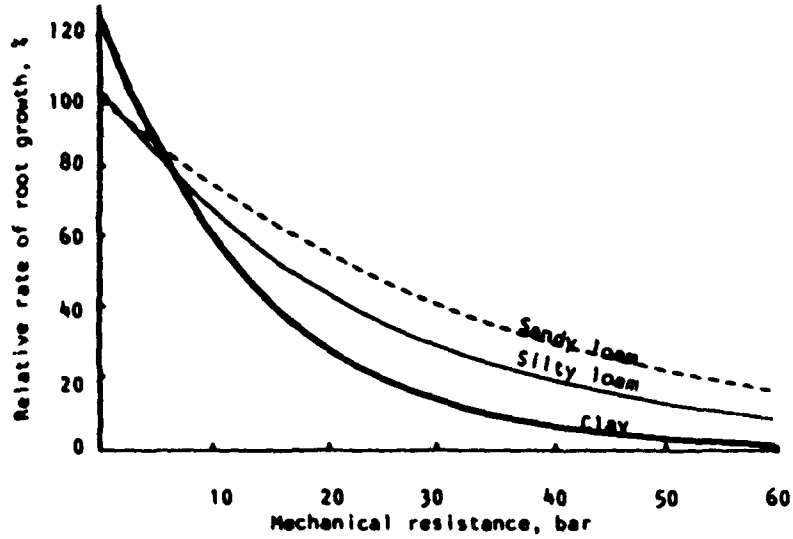


Figure 1. Effect of resistance on root growth rate for three soils (After Gooderham)

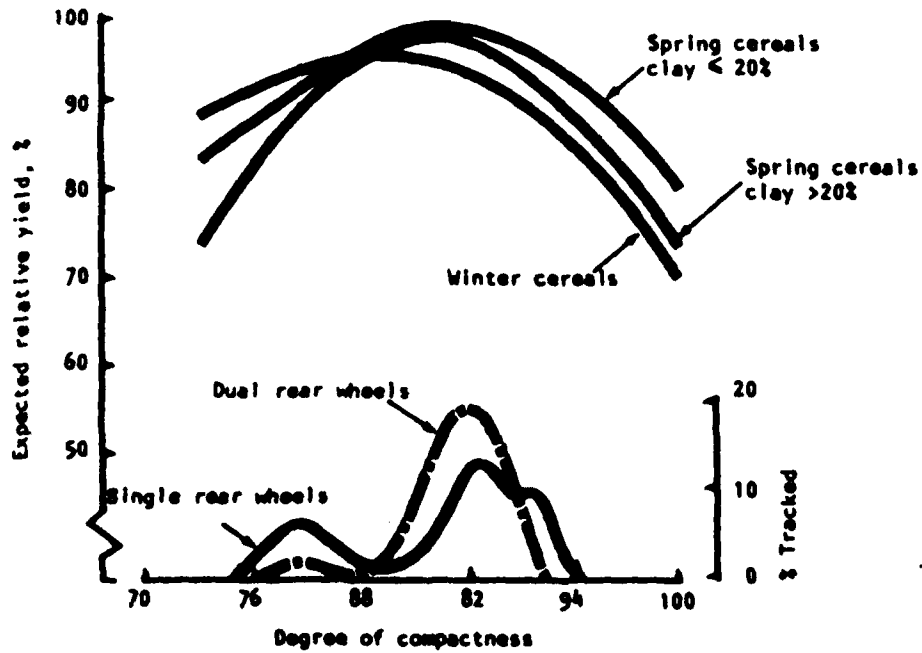


Figure 2. Top: Expected relative yield at different degrees of soil compaction

Bottom: Distribution of compaction on spring sown field for single and dual wheels. (After Eriksson et al)

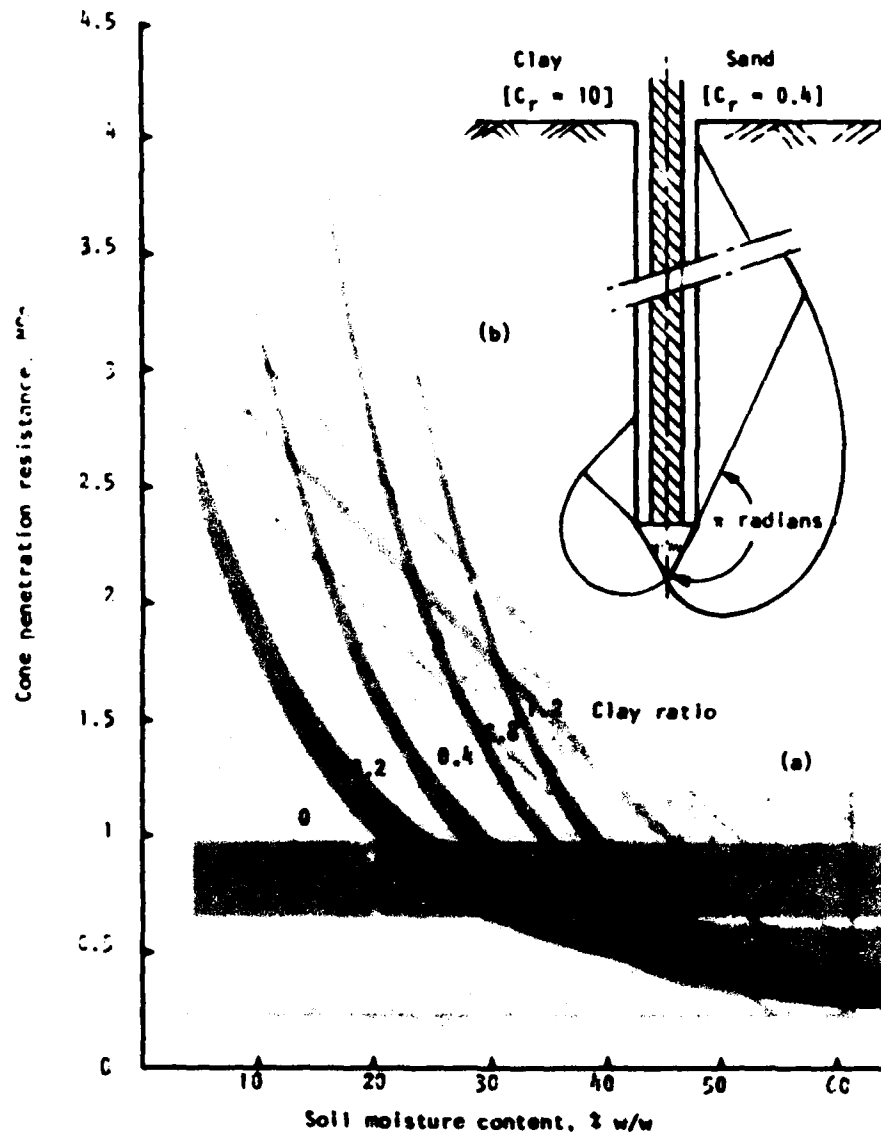


Figure 3. (a) The effect of soil moisture content, and clay ratio on the cone penetration resistance for a band of soil specific weights from 18 - 16 kN/m³.

(b) The relative size of the pressure bulb formed round the base of a cone penetrometer for clay (LHS) and sand (RHS).

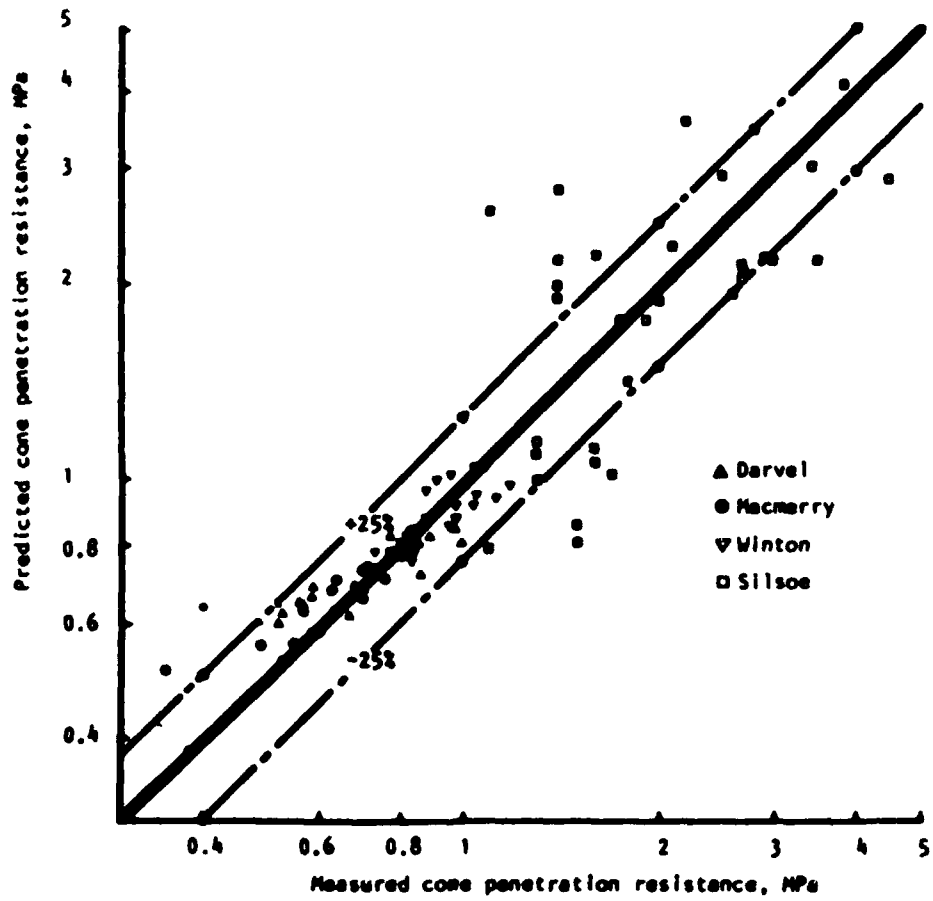


Figure 4. Measured and predicted values of the cone penetration resistance for four soils.

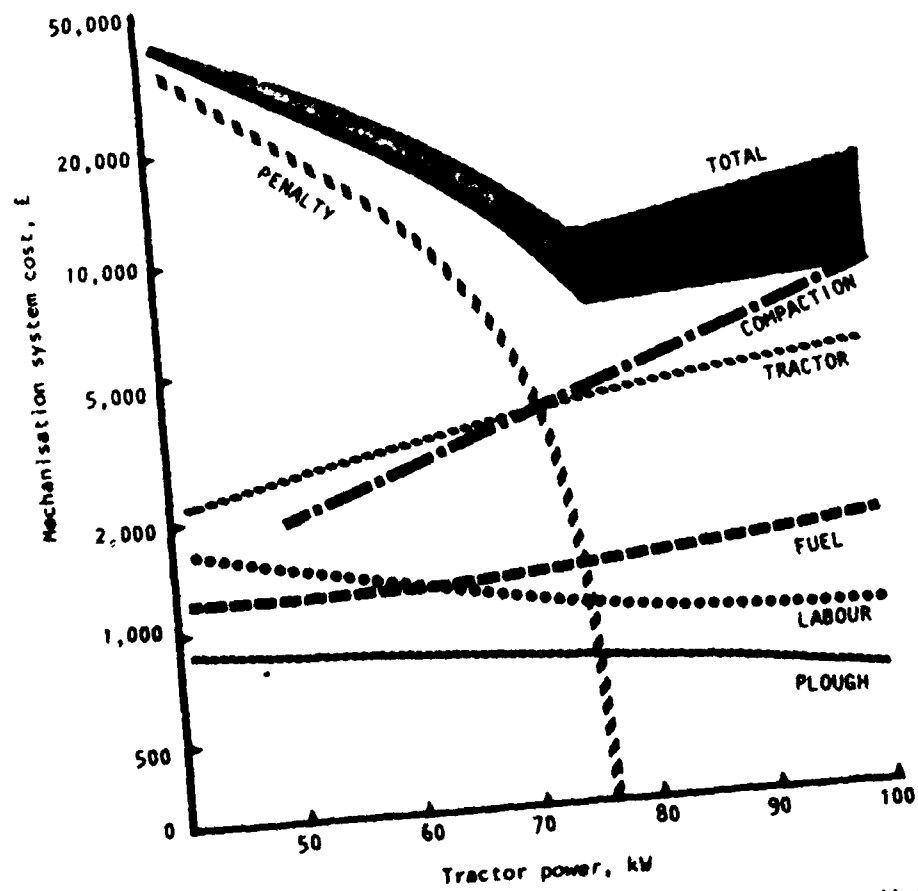


Figure 5. The cost of ploughing 400 ha of clay loam soil for winter wheat, together with timeliness penalties and an arbitrary compaction penalty, related to tractor size.



TOPIC 8

STEERING

THE GUIDELINES TO DESIGN THE TURNING GEARS OF ARTICULATED VEHICLES

P. DOZIAŃSKI, A. HANDEL
 TECHNICAL UNIVERSITY, WROCLAW, POLAND

AD-P004 301

INTRODUCTION

The landmark in machine development, particularly in loading and earth moving machines was the introduction of an articulated chassis. It considerably increased their manoeuvrability and turning abilities and improved other performance parameters in relation to the machines with steered wheels. The idea of an articulated vehicle dates back to as early as 19th century. Later years brought about the solutions of articulated vehicles suggested by a number of firms like Pavosi-Poloti (Italy), Pavosi-Wilson (England), Leturmo (France), Krupp (Germany), Lockheed (USA). For many years, however, the designers did not utilize this way of steering. The effective application of articulated machines was accelerated only by the development of drive systems, particularly of hydraulic ones.

One of the essential tasks on the design stage is the problem of selecting such a structure and geometry of a mechanism, that the obtained solution can be optimum in terms of the machine's performance requirements. The authors present the guidelines for designing turning gears in articulated machines worked out in the Institute of Machine Design and Performance, Wrocław Technical University. The details may be found in the publications [1], [3], [5], [6], [3].

RESEARCH AREA

The turning gears, in actual performance conditions, should provide the indispensable turning velocity and the indispensable twisting moment of the machine's members. The computation methods, conditions and results of studies on these quantities are presented in work [1].

Characteristics of the moment and turning velocities are determined by the design scheme of the steering system. The efforts to increase the reliability of turning gears, and first of all, to obtain the desired characteristics of power parameters, resulted in the diversity of gear's design solutions [2] and in a large number of patents. Table 1 presents the suggestion of systematising the existing design solutions of turning gears.

Table 1. Classification of turning gears of articulated vehicles

		Exemplary patents	
Turning gears	Lever		GB No 1.047.670 USA No 2.426.652 USA No 2.638.998 USA No 2.885.021 USA No 2.614.644 PL No 1.124.689
	Toothed	Cylindrical mesh	USA No 2.532.786
		Conic mesh	USA No 2.400.368 USA No 2.461.596
		Form	USA No 3.083.783
		Combined	
	with Elastic connector	Chain	USA No 2.676.664
		Rope	
	Combined	Lever-Tooth	
		Lever-Chain	

In up-to-date articulated vehicles, the most frequently used gear is, however, the lever one with hydraulic cylinders of varying length. The common application of that solution has been determined by its obvious advantages, such as: capability of carrying considerable load, high durability, infinitely variable drive system, self-lubrication and small inertia, which determines the so called steerability of a machine. The commonly used lever turning gear consists of two double action hydraulic cylinders [1]. There are also turning gears with a greater number of hydraulic cylinders or with two single action cylinders [3].

The analysis of the turning gears known from literature indicates that they do not exhaust all possible solutions and can not be approached as the solid basis for selecting the optimum solution.

STRUCTURAL SYNTHESIS OF TURNING GEAR

Prior to defining all possible structural solutions of turning gear with double action hydraulic cylinders, it was assumed that the gear consisted of two symmetrical mechanisms, working parallelly, which eliminated the favoured direction of turning [3]. On the stage of structural synthesis, the lever gear was assumed to be flat, though, in fact, it is a slightly spatial mechanism. Also on this stage, the non-plausible systems would be eliminated [4]. For example, due to manufacturing expenses and heavy performance conditions of articulated vehicles, all versions of turning gears solutions including kinematic pairs of higher order than I were excluded from considerations. With the assumption above, the gear is sought; the so called intermediary chain (T) joining the front (p) and the rear (t) member of an articulated vehicle and performing the turning of a vehicle by the assigned angle φ , Fig. 1.

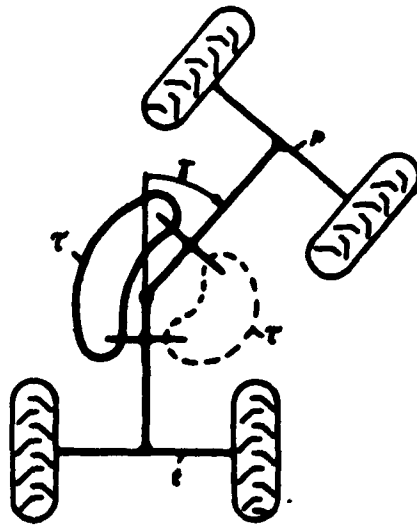


Fig. 1. Articulated vehicle with the so called intermediary chain

With the use of computer method of structural synthesis and with the above assumption, all possible solutions of the turning gears with double action cylinders were obtained [3]. They are compared in Fig. 2. There are two versions (a) and (c) from among the obtained solutions which are known to the authors, the other ones, which were new, have been patented [5].

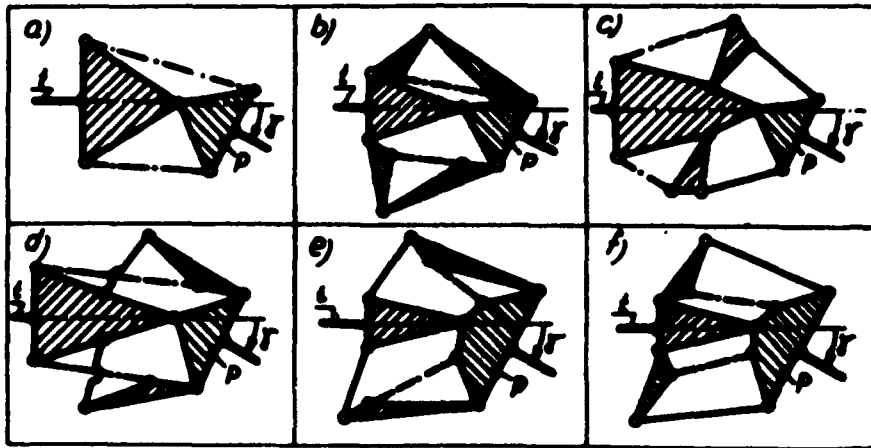


Fig. 2. Structural scheme of turning gears

PERFORMANCE REQUIREMENTS OF TURNING GEARS

The proper performance of turning gear, in the given conditions is the basis for evaluating the performance qualities of an articulated vehicle. In view of the above, the turning gear should meet a number of requirements, and, first of all it should:

a) provide the so called disposable moment $M_d(r)$ on such a level that its value over the range of turning angles of a machine should be higher than the total turning resistances $M_{or}(r)$ [1], [6] of an articulated machine, that is, according to denotations in Fig. 3 the following condition must be fulfilled:

$$M_d(r) = \eta \frac{\pi D^2}{4} (p_{\max} - p_0) \left[h_z(x, r) + \frac{D-d_t}{2} \cdot h_y(x, r) \right] =$$

$$= s_{zd} \cdot h_0(x, D, d_t, r) > M_{or}(r) \quad (1)$$

where:

- η - total efficiency of turning cylinders,
- p_{\max} - maximum pressure possible to be generated in the hydraulic turning gear,
- p_0 - run-off pressure,
- $h_z(x, r)$, $h_y(x, r)$ - outer and inner arm of forces generated in the turning cylinders,
- $x = [a, b, c, d]^T$ - vector of parameters denoting the location of turning cylinders,

d, d_c - the diameter of piston and piston rod of the cylinder -

$M_c(x, \beta, r)$ - the so called equivalent pair of turning forces,

$M_{\text{or}}(r)$ - the total moment of turning resistances.

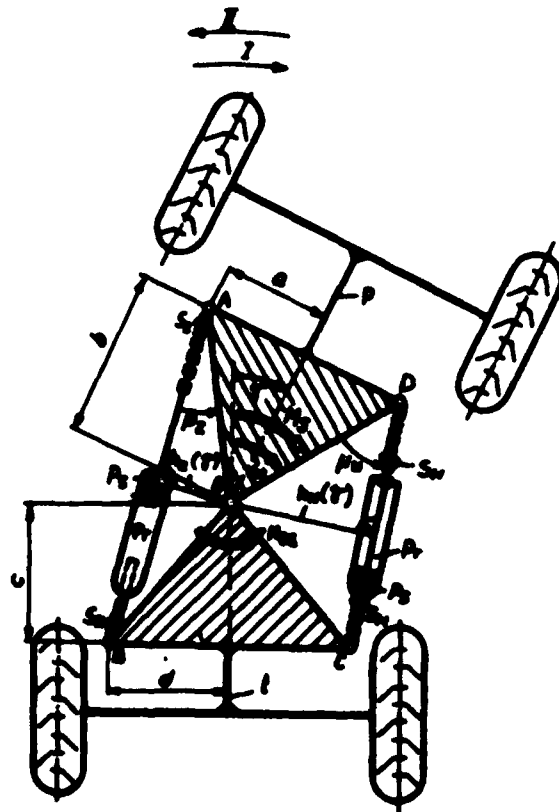


Fig.3 The turning gear commonly used, for ex. bucket loaders

The example of the effect of turning cylinders's location upon the course of disposable moment in the function of the turning angle has been presented in Fig.4 .

- b) provide the indispensable turning velocity ω_s of a vehicle, determining the machine's performance quality, e.g., such as, for instance, manoeuvrability. according to [1] $\omega_s = \omega_s(x, \beta, d, q, r)$ with q being the absorbing capacity of turning cylinders;

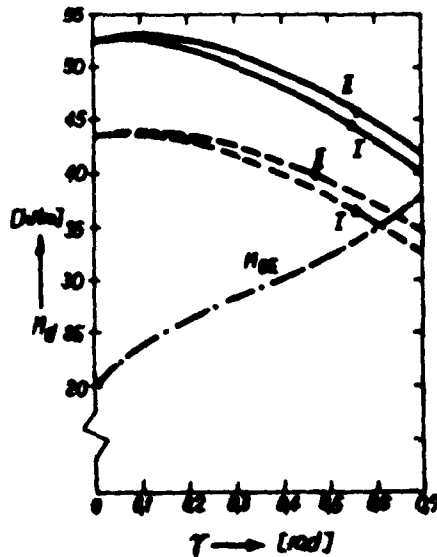


Fig.4 Relationship of articulated vehicle turning disposable moment according to Fig.3 for the following data:

$D=0,1$ m; $d_t = 0,05$ m,
 $p=100.10$ kN/m², $p_s = 0$,
 — $a=0,09$ m; $b=1,4$ m;
 $c=0$; $d=0,4$ m
 ---- $a=0,14$ m; $b=0,3$ m;
 $c=0,25$ m; $d=1,15$ m
 (does not satisfy condition (1))

- c) provide the uniformity of turning velocity which prevents the harmful dynamic load. The problem is partially solved, for example, by applying certain solutions in the hydraulic system of turning gear [7],
- d) provide possibly great angles of purchase M_2 and M_n correctness of turning gear solution in terms of, among others, manufacturing inaccuracies, effectiveness of active forces, occurrence of circulating power, and the ensuing load increase on kinematic pairs,
- e) provide the minimum power consumption during the turning.

SELECTION OF STRUCTURAL SOLUTIONS OF TURNING GEARS

In order to satisfy the requirements of engineering practice the obtained set of acceptable solutions Fig.2 was subjected to another selection in view of structural evaluation and performance requirements of turning gear.

The structural evaluation was made on the grounds of the following criteria: the degree of reliability, relative manufacturing cost, the form of power flux carried by the gear, susceptibility to manufacturing inaccuracies. Including the above criteria and employing the method of structures classification, the authors made the quality evaluation of the solutions in Fig.2, the obtained preference sequence being as follows:

1. Gear (a)
2. Gear (d) and (e)
3. Gear (b), (c) and (f).

On the second stage, the adopted selection criterion for turning gears was the condition of providing indispensable disposable moment $M_d(\gamma)$ over the whole range of turning angles; the condition was considered to be the major performance requirement for turning gear. In other words, condition (1) must be satisfied. The studies demonstrated that the total moment of turning resistances in an articulated vehicle always rose with the turning angle and reached the maximum for $\gamma = \gamma_{\max}$ [1]. Moreover, in order to ensure the equal load on turning gears, the following condition should be satisfied:

$$L_d - L_u = \int_{-\gamma_{\max}}^{\gamma_{\max}} [M_d(\gamma_{\max}) - M_{Ox}(\gamma)] d\gamma \rightarrow \min \quad (2)$$

where:

L_d - disposable work,

L_u - utilizable work of turning gears,

Condition (2) will be satisfied when the characteristic of disposable moment $M_d(\gamma)$ takes the similar course the characteristic of the total moment of turning resistances $M_{Ox}(\gamma)$, with condition (1) being observed.

In view of the above criteria, the gears (b), (c) are excluded from further considerations due to their structural complexity and always a convex function of disposable moment. Gear (a) also has such course of its disposable moment function, yet, owing to this gear's simple design it is useful for practical applications.

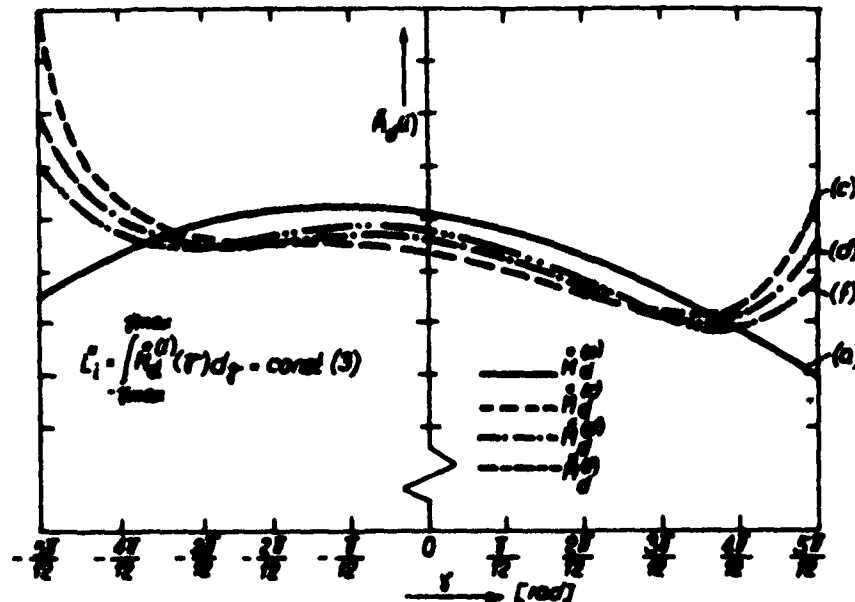


Fig. 5 The courses of the changes of disposable moments in the selected turning gears, with the condition (3) satisfied.

... of the gear is to provide the vehicle the possibility of turning within $\tau_{\min} < \tau < \tau_{\max}$

- b) each of the gears must provide the same elementary work W to be done despite the cylinders of different disposable stroke (equation 3, Fig.5).

It follows from Fig.5 that for the vehicle's turning angles $|\tau| > \frac{\pi}{3}$ the disposable moments of gears (c), (d) and (f) have, in the case of same geometric parameters, the rising character, compatible with the character of the disposable moment M_{0g} . For the angles $|\tau| < \frac{\pi}{6}$ however, the character of the changes of the disposable moments in the gears does not show essential differences.

SYNTHESIS OF GEOMETRICAL PARAMETERS OF TURNING GEARS

The selection of optimum geometry with the use of multicriteria optimization principles [3] will be proposed on the basis of the commonly used turning mechanism Fig. 2. The performance requirements of turning gears presented previously represent the purpose functions criteria possible to be considered. Two of them have been selected:

- maximization of the disposable moment $M_d(\tau)$ of a turning gear,
- maximization of the angles of purchase μ_2, μ_w .

The selection of the above criteria has been determined by the fact, that they are the major indicators affecting the performance reliability and durability of turning gears. Other criteria were carried into constraints. Maximization, thus, concerns $M_d(\tau)$; the angle of purchase μ_2 was found to satisfy the inequality $\mu_2 > \mu_{gr}$ where μ_{gr} is the arbitrary lower limit, 0,5 rad was assumed as an initial μ_2 , then increased in steps up to 1 rad. According to equation (1) the maximization of a disposable turning moment $M_d(\tau)$ is equivalent to the maximization of the, so called, equivalent arm $h_0(x, \beta, d_1, \tau)$ of turning forces. So, the solution of the following problem is sought:

$$\max_{a,b,c,d} h_0(a, b, c, d, \beta, d_1, \tau) \Big|_{\tau_{\max}}$$

over the set

$$\mu_2(a, b, c, d, \beta) \Big|_{\tau_{\max}} > \mu_{gr} \quad \mu_{gr} < 0,5 \text{ rad}; 1 \text{ rad}$$

over the set of constraints $D = [D] \cup [E]$ (Fig. 1):

1. The system of linear inequalities resulting from the design constraints

$$r_1 \leq a \leq r_2; \quad b_1 \leq b \leq b_2; \quad c_1 \leq c \leq c_2; \quad d_1 \leq d \leq d_2$$

2. The system of non-linear equations resulting from the design constraints of the turning gears and from carrying over other objective functions into constraints [1].

The non-linear programming with constraints was solved with the use of Flexiplex programme [9] (modification of the method presented in [3]).

Table 2. The results of optimizing calculation $l_{\min} = l_{\text{opt}}$

Cylinder data [m] $s=0,56; r_1=0,464,$ $r_2=0,1; d_1=0,05$	l_{\min}	μ_2	$\frac{a}{l_{\min}}$	$\frac{b}{l_{\min}}$	$\frac{c}{l_{\min}}$	$\frac{d}{l_{\min}}$	h_0	t
	[m]	[rad]					[m]	[s]
1,024		0,558	0,205	0,371	0,662	1,011	0,577	2,27
		0,611	0,185	0,371	0,566	1,091	0,574	2,27
		0,698	0,163	0,371	0,41	1,195	0,563	2,29
		0,785	0,178	0,359	0,35	1,246	0,55	2,3
		0,872	0,196	0,351	0,295	1,291	0,539	2,31
		0,959	0,226	0,339	0,27	1,328	0,528	2,33

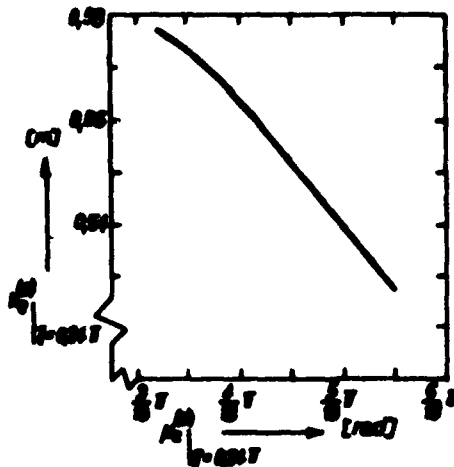


Fig. 6 Polyoptimum points of two-criterion problem: maximization of the equivalent arm h_0 and the angle of purchase μ_2 .

Table 2 demonstrates optimized computation results for the data: $r_{\max} = 0,75$ rad, $a_1 = 0,09$; $a_2 = 0,39$ m, $b_1 = 0,06$ m; $b_2 = 0,38$ m; $c_1 = 0,05$ m; $c_2 = 0,9$ m; $d_1 = 0,93$ m; $d_2 = 1,36$ m;

$M_{\text{od}} = 32 \text{ kNm}$; $\eta = 0,98$; $p_{\text{max}} = 100 \cdot 10^2 \text{ kN/m}^2$; $p_{\text{a}} = 0$;
 $Q_{\text{h}} = 0,06 \text{ m}^3/\text{s}$; the limit time of the vehicle's turning
 $t_{\text{gr}} = 3 \text{ s}$, disposable stroke of turning cylinder $S = 0,56 \text{ m}$;
 the so called dead length of turning cylinder $L_{\text{M}} = 0,464 \text{ m}$,
 $D = 0,1 \text{ m}$; $d_{\text{c}} = 0,05 \text{ m}$. Diagram 6 presents the set of polyoptimum points of two-criterion problem (maximization of the equivalent arm h_{e} and the angle of purchase μ_{z}).

It follows from the relation $h_{\text{e}}^{(0)}$ and $\mu_{\text{z}}^{(0)}$ that the lowering of the function from the maximum value results in the increase of the angle of purchase μ_{z} . Because of it, a designer may resign of the solution obtained for the maximum value of the function ($h_{\text{e}} = 0,577 \text{ m}$; $\mu_{\text{z}} = \frac{2}{18}$) for the sake of another polyoptimum solution.

CONCLUSIONS

The conducted considerations made it possible to choose four solutions from the set of the obtained structural solutions of lever turning gears. It can be stated, besides, that the simplest solution (a) is recommendable for the articulated vehicles with maximum turning angles $|\mu_{\text{max}}| < \frac{\pi}{3}$ for example, bucket loaders. One of the solutions (c), (d) or (f) however, should be applied for the machines with maximum turning angle $|\mu_{\text{max}}| > \frac{\pi}{3}$ for example, scraper, to avoid the so called dead centers.

The optimized computation results indicate that (a) quadrangle whose vertices are mounting points for turning cylinders should be a trapezoid with marked difference in the bases. The particular proportions of the trapezoid sides are dependent on machine and turning cylinder design parameters. Turning gear shaped in this way ensures considerable angles of purchase determining the correctness of operation and life. Also, with the indispensable moment twisting the machine's members ensured, it minimizes the absorbing capacity of turning cylinders necessary to provide steerability to the machine, which, consequently, leads to minimizing the power of this gear.

REFERENCES

- [1] P.A. Dudziński, The method of selecting articulated vehicle turning systems (in Polish). Doctoral thesis, Technical University of Wrocław (1977).
- [2] Patent literature.
- [3] P.A. Dudziński, Wł. Twardóg, Zur Wahl der Struktur von Stangenmechanismen. Forsch. Ing.-Wes. No 1 (1982).

- [4] B. Dzioglu, Getriebelehre B.1 -Braunschweig (1966).
- [5] P.A. Dudziński, S. Miller, Wł. Twaróg, The lever turning gears for vehicles. Polish Patent P-227659.
- [6] P.A. Dudziński, The problems of turning process in articulated terrain vehicles. 7-th ISTVS International Conference Calgary, Canada (1981) and Journal of Terramechanics, vol.19, No 4 (1982).
- [7] K. Fritzel, Eine Lenkhydraulik für Radlader mit Knick - gelenk. Fördern u. Heben, 19, No 17 (1969).
- [8] P.A. Dudziński, H. Havrylak, M. Veruus, The selection of turning gears geometry in articulated terrain vehicles using multi-criterion optimization. Int. J. of Vehicle Design, vol.1, No 4 (1980).
- [9] D.M. Himmelblau, Applied Nonlinear Programming. Mc Graw-Hill Book Company (1982).



Study on Controllability and Stability
of High Speed Tracked Vehicles

F. Eiyo and M. Kitano

Dept. of Mechanical Engineering, The National Defense Academy
Yokosuka Kanagawa, Japan

1. INTRODUCTION

Numerous studies on mobility of tracked vehicles such as bulldozer and crawler tractors have been performed. The stationary turning motions of these vehicles have been reported recently. Most of these studies have been concerned with trafficability and traction mechanics in vehicle terrain interaction because these vehicles are used mainly in off-road motion at low speeds. However, there has not been any reported studies dealing with the controllability and stability of vehicles at high speeds.

In recent years, the tracked vehicle has been widely used in the field of transportation, and in particularly, leisure and military purposes in snow covered terrain. The need for these vehicles to develop improved agility and mobility in addition to off-road crossing capabilities is indeed evident. The recent development of a military tracked vehicle which can run at a speed of 80-90km/h testifies to the importance of the proceeding issue.

With advancement of these developments, accidents have increased because of the problem of steerability such as oversteering and steering response delay of tracked vehicles. These accidents often occur when the vehicles are operated at a high speed on level ground and at a relative high speed on downward slopes.

It is essential not only to analyze soft off-road crossing capabilities, as in the past, but also to analyze the steering dynamics, controllability and stability of the vehicles at high running speeds.

In previous papers, we have presented a computer simulation model of steerability of tracked vehicles during uniform turn on firm level ground, and have experimentally verified the validity of the model with real vehicles and scale models.

This paper presents a theoretical analysis of non-stationary motion such as J-turning, for tracked vehicles on level, hard ground. The characteristics of steering motion of the tracked vehicle has been examined with respect to changes in :

- (a) position of the center of gravity (forward or backward from the centerline)
- (b) adhesion coefficient of the contact area of the tracks as influenced by the ground condition

As a result, the fundamental parameters which influence the controllability and stability of the vehicle at high speed operations can be determined.

AD-P004 302

2. EQUATIONS OF NON-STATIONARY TURNING MOTION

Fig.1 shows the two coordinate systems used to describe vehicle turning motion. The X, Y, Z coordinate system is fixed on level ground, and its origin coincides with the geometric center of the vehicle at time zero. The origin of axes for the x, y, z coordinate system is fixed on the geometric center of the tracked vehicle.

The motion of a tracked vehicle will be analyzed with the following assumptions :

- (1) The vehicle is geometrically symmetric with respect to the x-z and y-z planes.
- (2) The motion of a vehicle has 7-degrees of freedom about x and y axes, yawing, rolling, pitching, and movements in both tracks.
- (3) The vehicle has independent suspensions with identical spring rates, with n-road wheels arranged in tandem on each side of the hull (vehicle body).
- (4) Frictional forces between ground and track are isotropic in nature, and the adhesion coefficient is varied by the track slip ratio S.

The adhesion coefficient can be approximately expressed as follows :

$$\mu = \mu_0 (1 - e^{-K \cdot S})$$

where μ_0 is the maximum adhesion coefficient, and K is an experimental constant.

- (5) The distribution of the weight of the vehicle is concentrated under each wheel.
- (6) Aerodynamic forces against turning maneuvers of the vehicle are neglected.

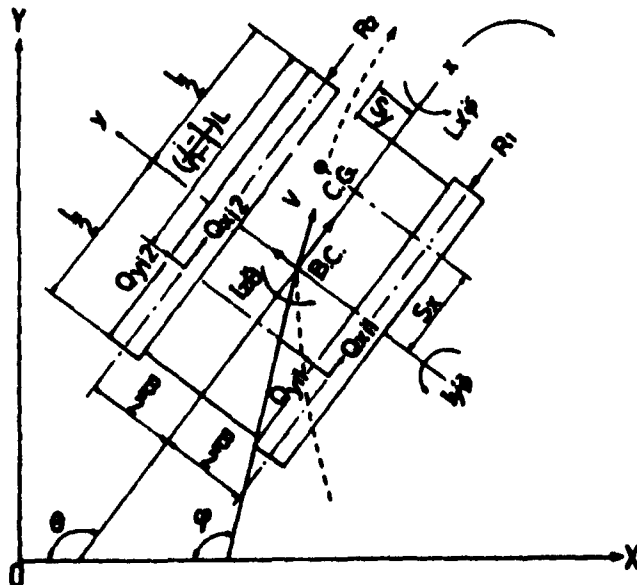


Fig.1 Coordinate Systems for Tracked Vehicle

Considering the load changes in the interface between tracks and ground due to the track tensions, the equations of motion are obtained from the equilibrium of the inertia forces acting on the geometric center of the vehicle, the frictional forces generated on each track, and the moments about x, y and z axes.

$$m\alpha_{gx} = \sum_{i=1}^n \sum_{j=1}^2 Q_{xij} - (R_1 + R_2)$$

$$m\alpha_{gy} = \sum_{i=1}^n \sum_{j=1}^2 Q_{yij}$$

$$I_y \ddot{\phi} = -m_x \alpha_{gy} (D_{hn} \cos \phi - S_y \sin \phi) - D_\phi \dot{\phi} - K_\phi \phi + \frac{B}{2} (R_1 - R_2) - m(\alpha_{gy} S_x - \alpha_{gx} S_{ym})$$

$$I_x \ddot{\phi} = m_x \alpha_{gx} (D_{hp} \cos \phi + S_x \sin \phi) - D_\phi \dot{\phi} - K_\phi \phi$$

$$I_z \ddot{\theta} = \frac{B}{2} \sum_{i=1}^n (Q_{xiz} - Q_{xii}) - \sum_{i=1}^n \sum_{j=1}^2 (Q_{yij} (\frac{1}{2} - \frac{i-1}{n-1}) L)$$

Nomenclatures are shown in Table 1.

3. RESULTS OF SIMULATION

Experience gained from previous studies on the turning motion of the tracked vehicles shows that the steering performance of vehicles depends to a large degree on the vehicle speed, terrain-vehicle interaction, and location of the center of gravity of the vehicle.

The equations of motion were numerically solved with the aid of the Runge-Kutta-Gill method, using a digital computer. From the results obtained, the fundamental parameters directly affecting the non-stationary turning motion of the vehicle such as transient response and stability were clarified.

Both track velocities as shown in Fig. 2 are used as the steering inputs (independent variables) for the calculation. The trajectories, side slip angle β and course angle rate $\dot{\psi}$ were obtained as the outputs.

The specifications of the tracked vehicle which was used for numerical analysis are shown in Table 2.

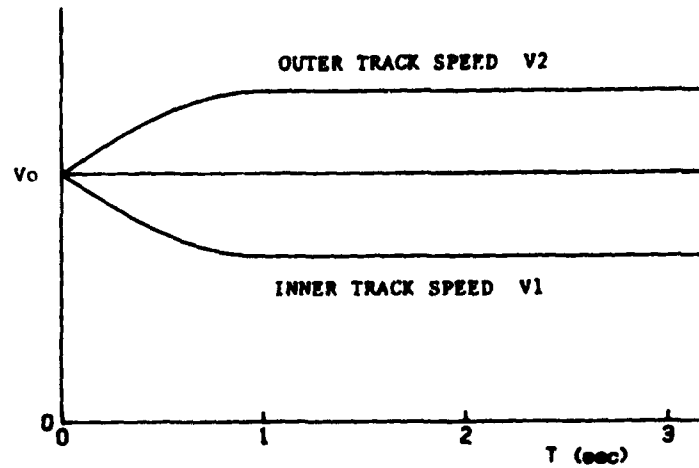


Fig.2 Change of Track Speed

Table 2 Specifications of the Tracked Vehicle

m	38000 kg	I_x	$4.57 \times 10^6 \text{ kgm}^2$
m_s	35000 kg	I_y	$1.10 \times 10^6 \text{ kgm}^2$
L	4.0 m	I_z	$1.15 \times 10^6 \text{ kgm}^2$
B	2.63 m	K_p	$1.50 \times 10^6 \text{ Nm/rad}$
H	1.09 m	D_p	$5.93 \times 10^6 \text{ Nms/rad}$
θ_r	23°	\cdot	$1.04 \times 10^6 \text{ Nm/rad}$
θ_s	26°	D_p	$7.06 \times 10^6 \text{ Nms/rad}$

AD A148 635

PROCEEDINGS OF THE INTERNATIONAL CONFERENCE ON THE
PERFORMANCE OF OFF-ROAD (U) INTERNATIONAL SOCIETY FOR
TERRAIN-VEHICLE SYSTEMS M J DWYER AUG 84

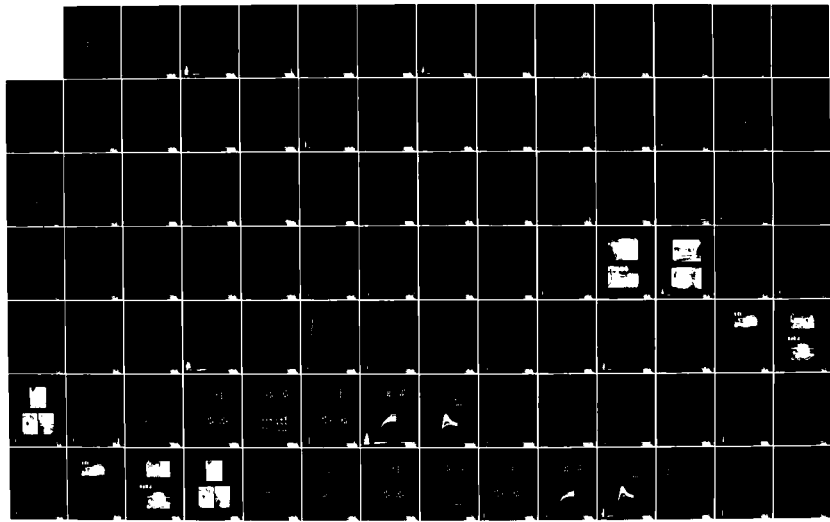
4/5

UNCLASSIFIED

DAJA45-84-M-0251

F/G 13/6

HL





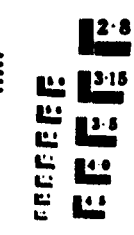
1.0



1.1



1.25



1.4



2.8



3.15



3.6



4.0



2.5



2.2



2.0



1.8



1.6

3.1 Effects of vehicle speeds on steerability

The effects of vehicle speeds on turning motion such as J-turn trajectories and side slip angle β have been investigated. In this analysis, as a general condition, the center of gravity is located at the geometric center of the hull, and the maximum adhesion coefficient of the track-ground contact area has been taken as 0.6.

Fig.3 shows the trajectories of the barycenter of the vehicle at various initial forward speeds. The arrows on the trajectory of motion indicate the posture of the longitudinal axis of the vehicle, after steering input has been given, at two-second intervals.

Fig.4 shows the side slip angle β at the center of gravity with respect to the time period under the same condition as Fig.3.

It is found from the examination of Fig.3 and Fig.4 that the stable steering characteristics of the tracked vehicle tends to become unstable rapidly at a critical forward speed. For instance, at a relative lower speed of $V_0=5\text{m/s}$ (18km/h), the vehicle is able to turn in a stable state, and the side slip angle of the center of gravity is damped to a small steady value in a period of about one second after steering. On the other hand, at a vehicle speed of 7.5m/s (27km/h), the trajectories of the vehicle spirals inwards with time, and radius of curvature decreases rapidly in about four seconds after steering. In this period, the side slip angle increases very rapidly to more than thirty degrees. This tendency is intensified as vehicle speed increases. It is clear from the theoretical simulations that a stability-instability conversion speed exists between 5m/s and 7.5m/s in this case.

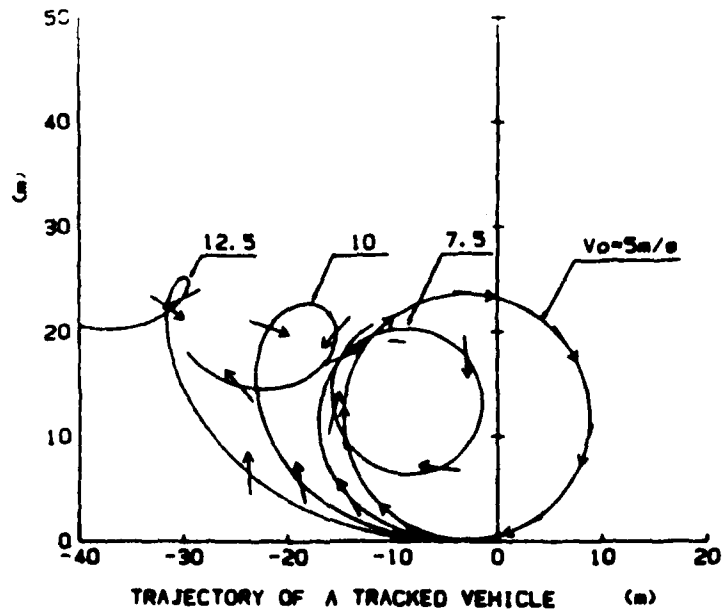
It should be noted that (a) the tracked vehicle exhibits unstable maneuver even in a relatively low vehicle speed range when the vehicle is steered transiently, and (b) the tracked vehicle is inferior to a wheeled vehicle in regard to the response to steering motion.

3.2 Influence of terrain factors of track-ground interface

Fig.5 and Fig.6 show the turning trajectories and course angle rate $\dot{\psi}$ on the geometric center of the vehicle, at a vehicle speed of 5m/s for various values of frictional force generated between the track and ground. For this case, it is considered that the center of gravity coincides with the geometric center of the hull.

The maximum adhesion coefficient μ_0 adopted in the calculations have been assumed to correspond to following ground conditions: (1) $\mu_0=0.1$; icy surface, (2) $\mu_0=0.3$; some gravel on the paved road, (3) $\mu_0=0.6$; hard soil and paved road, (4) $\mu_0=1.0$; with spikes on hard soil and pavement.

It is apparent from these results that when adhesion coefficients are large, e.g. $\mu_0=0.6$ and 1.0 , (a) the trajectories are close to each other, (b) the side slip angle of the vehicle is very small, and (c) the vehicle exhibits a stable turning maneuver.



TRAJECTORY OF A TRACKED VEHICLE (a)
 Fig.3 Effects of Vehicle Speeds on Trajectory

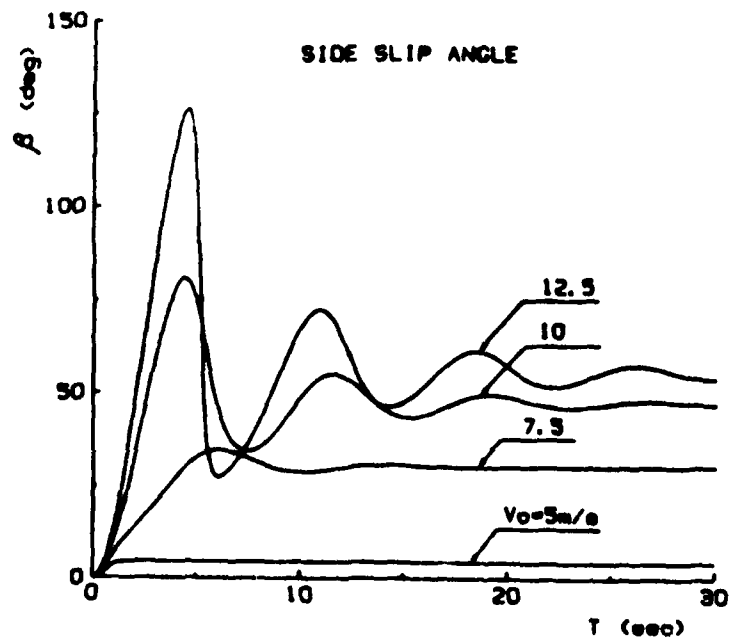


Fig.4 Effects of Vehicle Speeds on Side Slip Angle

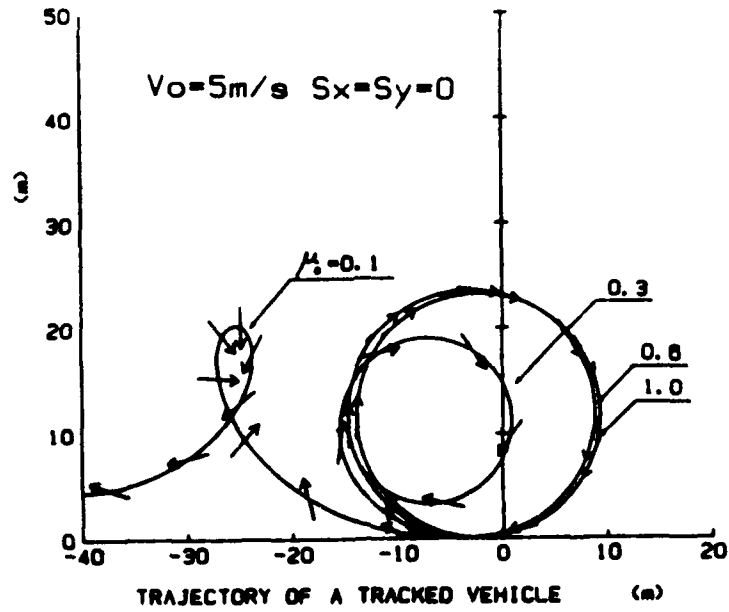


Fig.5 Influence of Adhesion Coefficient on Trajectory

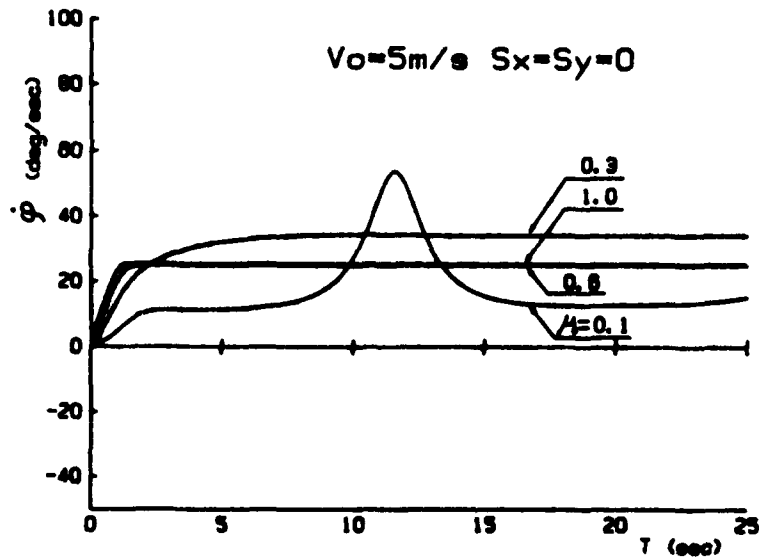


Fig.6 Influence of Adhesion Coefficient on Course Angle Rate

On the other hand, the smaller the adhesion coefficient is, the longer is the "settling time" of the course angle rate. For instance, at $\mu = 0.3$, the vehicle undergoes a spiral turning maneuver in about four seconds after steering. The vehicle exhibits a strong nose-in posture and side slip angle β increases rapidly. This tendency becomes dramatic especially when the frictional force of track contact area decreases.

It should be pointed out that the controllability and stability of the tracked vehicle are greatly affected by frictional forces at the track-ground interface and vehicle forward speed.

3.3 Influence of the position of the center of gravity

This section presents the steering performance of a tracked vehicle at high speed when the position of the center of gravity moves along the longitudinal axis. The inherent steering characteristics of a tracked vehicle are essentially different from these of a wheeled vehicle.

(1) Steering performance when center of gravity is located forward

Fig. 7 shows several steering trajectories when the center of gravity is located at 10% (of the track contact length L) forward from the geometric center of the vehicle.

Fig. 8 shows the changes of course angle rate with respect to the period after steering.

It is clearly seen on comparing Fig. 5 with Fig. 7 that the steering performance of a tracked vehicle is strongly affected by the terrain factor of the track-ground interface when the center of gravity moves to forward position. For instance, at $\mu = 1.0$, the vehicle exhibits a good response and a stable turning maneuver for transient steering inputs. However, at $\mu = 0.6$, it shows a delayed response for steering, and after a certain time, it gradually exhibits a spiral turning maneuver. For less than $\mu = 0.3$, it might be difficult to maintain the course of the tracked vehicle.

(2) Steering performance when center of gravity is located backward

Fig. 9 shows turning trajectories when the center of gravity is located at $0.1L$ backward from the geometric center of the vehicle. The course angle rate $\dot{\psi}$ in this case is shown in Fig. 10.

As is evident from both Figures, a tracked vehicle will turn stably without spinning motion even if the frictional force of the track contact area reduces to small values when the center of gravity moves backward.

A comparison of Fig. 5, 7 with Fig. 9 shows that the turning radii of the final steady states are larger than those obtained in the case of the forward barycenter. Understeer characteristics are clearly demonstrated. With decreasing adhesion force of tracks, the characteristics of the vehicle transient response becomes worse. In contrast, stable turning motions are obtained for four adhesion factors at a speed of 5m/s.

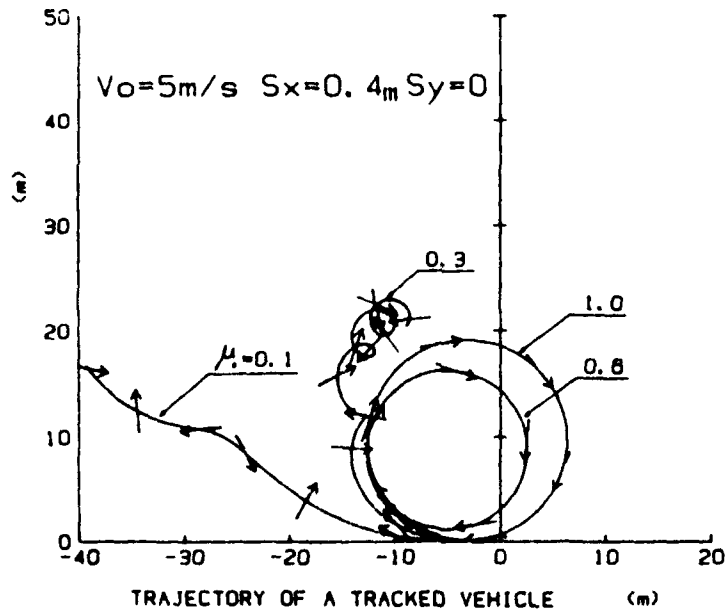


Fig.7 Trajectories in the case of Forward Barycenter

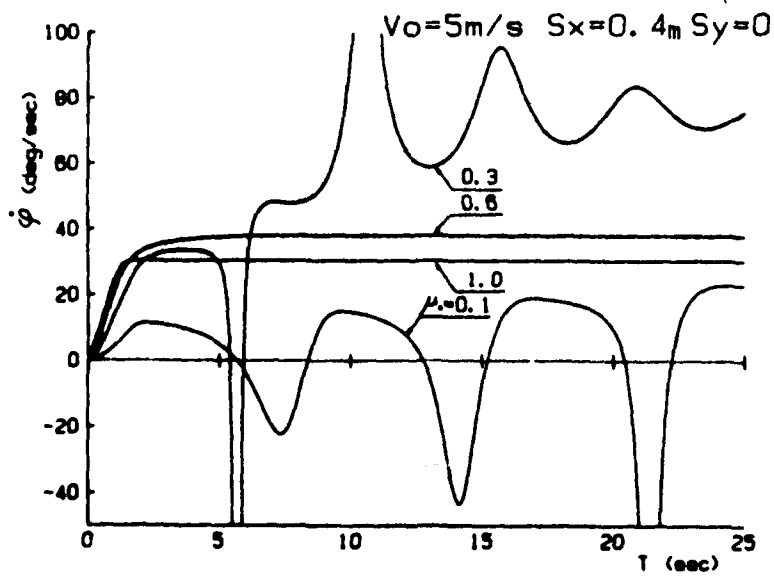


Fig.8 Course Angle Rate in the case of Forward Barycenter

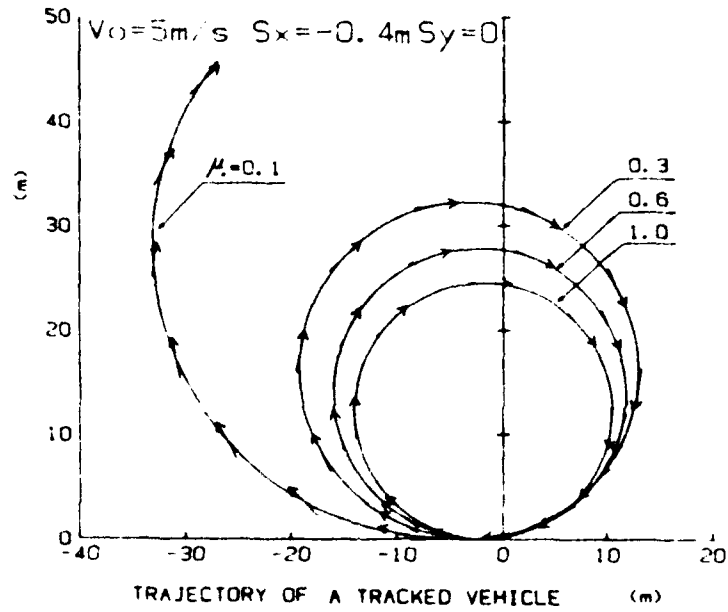


Fig. 9 Trajectories in the case of Backward Barycenter

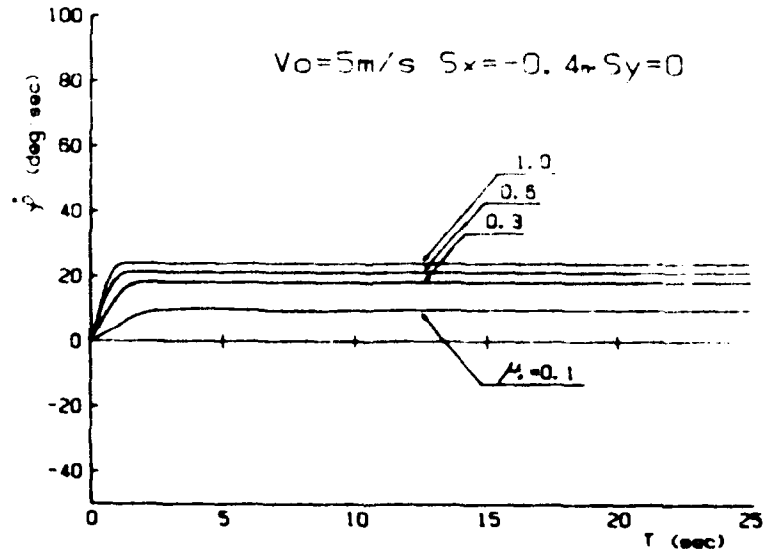


Fig. 10 Course Angle Rate in the case of Backward Barycenter

As mentioned above, it is shown that the vehicle transient response to steering inputs is essentially influenced by the position of the center of gravity. These inherent characteristics of a tracked vehicle can be explained by considering the equilibrium of the moments about the z axis.

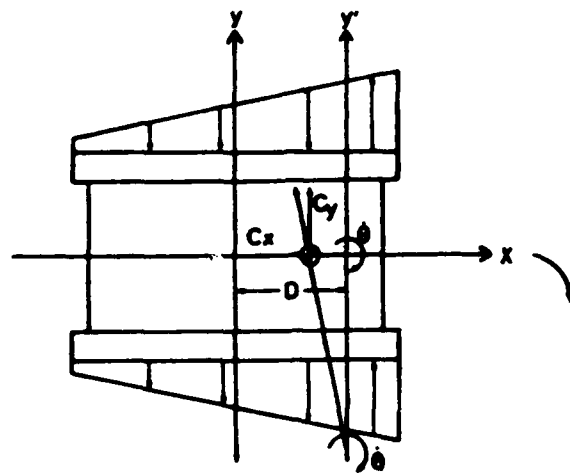
As shown in Fig. 11, in the case of the forward barycenter, the weight distribution of the track contact area becomes lighter backward position. Hence, the turning resistance moment generated by the lateral frictional force at the track ground interface will not be able to balance the turning moment applied to the vehicle by inertia forces. The vehicle can easily turn itself at small turning radii.

On the other hand, in the case of a backward barycenter, the weight distribution of the track contact area increases along the distance from the front. The turning resistance will consequently increase with respect to the turning moments from the inertia force.

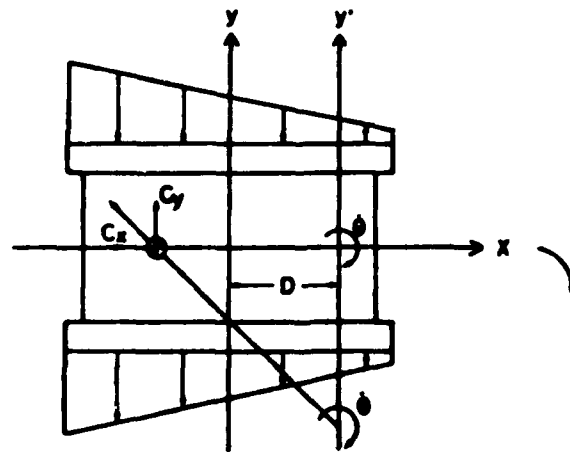
4. CONCLUSION

As a result of the theoretical analysis, the following steering characteristics of a tracked vehicle are evident :

- (1) There is a critical speed at which the turning maneuver of a tracked vehicle changes from stability to instability with transient steer inputs at high speeds.
- (2) The controllability and stability of a tracked vehicle under transient steering inputs are significantly influenced by the terrain factors at the track ground interface e.g. adhesion coefficient and load distribution.
- (3) The steerability of the vehicle is affected strongly by the locations of the center of gravity. In the case of the forward barycenter, a large improvement in steering responses is gained at higher track adhesion forces. The vehicle becomes unstable at lower adhesion forces. In the case of the backward barycenter, the vehicle exhibits understeer characteristics and stable turns for all terrain factors.



FORWARD BARYCENTER



BACKWARD BARYCENTER

Fig. 11 Weight Distribution and Turning Moments

Table 1 Nomenclature

m	kg	mass of vehicle
m_s	kg	spring mass of vehicle
L	m	track contact length
B	m	width of each track
h	m	height of center of gravity
D_{hr}	m	distance between geometric center and roll axis of a vehicle
D_{hp}	m	distance between geometric center and pitch axis of a vehicle
V_0	m/s	initial forward speed
n		number of road wheel in each side
B.C.		body center of a vehicle
C.G.		center of gravity of a vehicle
S_x	m	variation of C.G from geometric center in x axis
S_y	m	variation of C.G from geometric center in y axis
S_{ym}	m	lateral displacement of C.G by the rolling
α_{gx}	m/s ²	longitudinal component of acceleration at C.G
α_{gy}	m/s ²	lateral component of acceleration at C.G
K_ϕ	Nm/rad	spring stiffness on rolling
K_θ	Nm/rad	spring stiffness on pitching
D_ϕ	Nms/rad	damping constant on rolling
D_θ	Nms/rad	damping constant on pitching
I_x	kgm ²	moment of inertia about x axis of a vehicle
I_y	kgm ²	moment of inertia about y axis of a vehicle
I_z	kgm ²	moment of inertia about z axis of a vehicle
Q_{xij}	kg	longitudinal component of frictional force of track under (i-j) road wheel
Q_{yij}	kg	lateral component of frictional force of track under (i-j) road wheel
R_j	kg	rolling resistance

D	m	displacement of pivoting point of a vehicle
θ	rad	yaw angle
φ	rad	roll angle
ψ	rad	pitch angle
γ	rad	course angle of B.C.
θ_e	rad	entry angle of track
θ_d	rad	departure angle of track
i		subscript i-th road wheel
j		subscript inner j=1, outer j=2

REFERENCES

- (1) M.Kitano, H.Jyozaki: Study on Steerability of Tracked Vehicles(part 1) -Track Skid and Turning Radius-, Trans. JSAE(in Japanese), No.9,(1975), pp.51-57.
- (2) M.Kitano, M.Kuma, A.Kinou: Study on Steerability of Tracked Vehicles(part 2) -Effects of Center of Gravity on Steerability-, Trans. JSAE(in Japanese), No.10,(1975), pp.54-60.
- (3) M.Kitano, M.Kuma, A.Kinou: Study on Steerability of Tracked Vehicles(part 3) -On Effects of Track Friction-, Trans. JSAE(in Japanese), No.11,(1976), pp.64-70.
- (4) M.Kuma, M.Kitano: Study on Steerability of High Speed Tracked Vehicles -Effects of Load Distribution on Steerability-, Memoirs of The National Defense Academy Japan(in Japanese), Vol.14, No.1-2,(1976), pp.35-51.
- (5) M.Kitano, M.Kuma: Analysis of Non-stationary Motion of Tracked Vehicle(part 1), Trans. JSAE(in Japanese), Vol.13, (1977), pp.63-69.
- (6) H.Iida, M.Kitano, K.Sawagashira: Study on Steerability of Tracked Vehicle, Journal of The Society of Agricultural Machinery, Japan(in Japanese), Vol.41, No.1, (1979), pp.27-35.
- (7) S.Sano: Evaluation of Motor Vehicle Handling, Trans. JSAE, Vol.34, No.3,(1980), pp.211-219.
- (8) W.Lincke, B.Richter, and R.Schmidt: Simulation and Measurement of Driver Vehicle Handling Performance, SAE paper, 730489, pp.1585-1596.



FORCES ON UNDRIVEN, ANGLED WHEELS

M. McALLISTER

NIAE, SILSOE, BEDFORD, ENGLAND

SUMMARY

Rolling resistance and steering forces were measured on six tyres in a variety of field conditions. The six tyres covered the range of tread pattern and loads that are currently in use in agriculture on tractor front wheels, implements and trailers. Tractor rear tyre sizes and driven wheels were not used for this work. A correlation was found between coefficient of rolling resistance and mobility number. Exponential curves were fitted to the coefficient of side force - slip angle relationship and a correlation was found between the constants of the curves and mobility number. The use of an alternative mobility number is discussed.

The statistical analysis detected differences due to tread pattern, load and construction of the tyres, and showed a multi-ribbed implement tread patterned radial tyre to be advantageous over any other tyre tested at small steer angles.

1. INTRODUCTION

Because of increased concern for safety in agriculture, problems of stability of tractors and tractor-implement combinations, and of working on side slopes have become more important. These problems have increased because of the trend towards increased agricultural production resulting in an increase in the size and speed of agricultural machines. This has demonstrated the lack of knowledge on handling characteristics of agricultural machines and their side slope performance. This paper reports the results of work on side force measurements on tyres in field conditions and attempts to relate the forces obtained to tyre and soil parameters.

Some previous work which has been carried out on this subject, consisted mainly of simplified experiments using a limited number of tyre sizes and load variations(1,2). The first attempt to model the forces involved was performed by Taylor and Birtwistle(3) who studied the effect of angle and camber on wheels fitted to disc ploughs. They did not publish a full prediction procedure and therefore their model is of limited value. Schwanhart(4) investigated forces on angled wheels in a soil bin and developed a model to predict the lateral forces only. This has proved to be very complicated and not easy to apply in practice. This line of approach was also taken by Grecenko(5) but his analysis was also not easy to apply. A recent study into lateral forces on pneumatic tyres by Del Rosario(6) attempted a soil mechanics based analysis. He arrived at a very complicated prediction procedure which is of limited value. Spencer has been looking into stability problems on slopes for a long time(7,8) but he has been hampered by a lack of research on side forces

on agricultural wheels. He carried out some brief experiments using one size of tyre on two ground conditions in order to obtain guidelines for stability criteria⁽²⁾. A good summary of past results is given by Crolla and Hales⁽⁹⁾ who commented on the requirement for data from a wide range of conditions.

Recent work performed by Gee-Clough and Sommer⁽¹⁰⁾ included previous work by the author⁽¹¹⁾ and produced a model for all the forces on a wheel. This work was carried out under laboratory conditions and used a dimensional analysis approach. The agreement between measured and predicted values was found to be very good in the soil bin using a limited number of wheels.

This paper has attempted the same line of analysis using field results gathered over the last three years.

2. EXPERIMENTAL PROCEDURE

During the autumn and winter months, experiments to measure the forces on towed angled wheels were performed in 38 normal agricultural field conditions using the NIAE rolling resistance rig⁽¹²⁾. The experiments were planned to enable the effects of load, carcass construction and tread pattern to be established. Every experiment was not performed in every field condition. The individual experiments, which took one day each, were:

- Expt. 1 Two 7.50-16 tyres with different tread patterns at the same load and inflation pressure, and also one of the tyres at a higher load and inflation pressure.
- Expt. 2 Two tyres of size 12.0-18 and similar tread pattern, one cross-ply and one radial ply construction, at the same load and inflation pressure and also the radial tyre at a lower load and inflation pressure.
- Expt. 3 Three 12.0-18 tyres at the same load and inflation pressure. One tyre as an implement multi-ribbed tread pattern, IR2, the others a R4 traction tread pattern, one used in normal conventional traction direction (Forward tread), the other in the reverse direction (Backward tread).

Tyre dimensions, loads and inflation pressures are shown in Table 1; all tyres were inflated to manufacturers recommendations for the load carried.

All the wheels were tested at a speed of 1 m/s and at slip angles of 0, 5, 10, 15, 20, 30, 40 degrees to the direction of travel. Each test consisted of three 20 m runs at each slip angle, the results of which were averaged and gave, after analysis, all the forces on the wheel. Soil parameters were measured concurrently with each experiment so that relationships between the forces on the wheel and soil conditions could be investigated. These parameters include mechanical analysis, moisture content, plastic limit, soil bulk density, cone index and in the later fields soil/soil friction angle and cohesion.

3. LIST OF SYMBOLS

C	=	cone index, kPa
CRR _w	=	the coefficient of rolling resistance in the plane of the wheel
CRR _{w0}	=	the coefficient of rolling resistance at zero slip angle
CSP _w	=	the coefficient of side force perpendicular to the plane of the wheel
CSP _w max.	=	maximum value of coefficient of side force perpendicular to the plane of the wheel
D	=	Drag force in direction of motion, kN
EMOB	=	mobility number as defined by equation 6
M	=	$\frac{m}{CRR_{w0}}$
S	=	side force perpendicular to the direction of motion, kN
W	=	vertical load on the wheel, kN
b	=	tyre width, m
c	=	soil cohesion, kPa
d	=	tyre diameter, m
h	=	section height, m
k	=	rate constant (indicates the rate of change of CSP _w with angle)
m	=	slope of CRR _w vs slip angle relationship
n	=	exponent of friction angle
δ	=	tyre deflection under load, m
θ	=	slip angle, rads. (angle between the wheel and the direction of travel)
φ	=	soil/soil friction angle, rads.
QMOB	=	mobility number as defined by equation 7

4. ANALYSIS

In order to make comparisons between tyres the following coefficients were calculated from the results.

$$CRR_w = \frac{D}{W} \cos \theta - \frac{S}{W} \sin \theta \quad \dots (1)$$

$$CSP_w = \frac{D}{W} \sin \theta + \frac{S}{W} \cos \theta \quad \dots (2)$$

The relationship between CRR_w and slip angle resulted in the linear expression

$$CRR_w = m \cdot \theta + CRR_{w0} \quad \dots (3)$$

A large amount of scatter was present especially at the higher slip angles. As shown by Gee-Clough and Sommer⁽¹⁰⁾ the values of CRR_w at angles greater than 20° could be neglected for practical consideration and this reduces much of the scatter.

The relationship between CSP_w and slip angle was found to be accurately described by the expression:

$$CSP_w = A(1 - e^{-k\theta}) \quad \dots (4)$$

The constant A is the asymptotic value of the expression and indicates the maximum CSP_w obtained by the wheel ($CSP_w \text{ max.}$). A differentiation of the expression gives the gradient of the CSP_w vs slip angle relationship at zero slip angle and gives the result:

$$d(CSP_w) = k.CSP_w \text{ max. at } \theta = 0^\circ \quad \dots (5)$$

The results are presented in the form of CRR_w (measured), CRR_w and m (from linear regression), $CSP_w \text{ max.}$ and $k.CSP_w \text{ max.}$ from the curve fit.

In the previous report on this work⁽¹¹⁾ mobility number was used to predict the performance of the wheels. This is a non-dimensional number given by the equation:

$$MNB = \frac{Cbd}{W} \sqrt{\frac{\delta}{h}} \left(\frac{1}{1 + \frac{b}{2h}} \right) \quad \dots (6)$$

which has also been used for predicting the tractive performance of driven wheels. An alternative equation was developed by Gee-Clough and Sommer⁽¹⁰⁾ using soil frictional values instead of cone index values in an attempt to improve on the prediction procedure. Their equation is:

$$MNB = \frac{cbd}{W} \sqrt{\frac{\delta}{h}} \left(\frac{1}{1 + \frac{b}{2h}} \right) (\theta)^n \quad \dots (7)$$

where $n = 1.35$ (as used in Ref. 10).

The value of Mobility number without soil parameters is given for each of the tyres in Table 1.

5. RESULTS

Throughout the experiments we found the variation between fields caused far greater variation in the results than the variation between tyres. In the first section therefore the t-test applied to paired comparisons was used to identify differences between tyres as this test takes account of between field variability. The results in terms of CRR_w (measured), $CSP_w \text{ max.}$ and $k.CSP_w \text{ max.}$ was used to assess the tyre differences.

5.1 The effect of load, Table 2

Using the 7.50-16 tyre, with the tractor steering wheel tread pattern, no significant difference could be detected between the $CR_{\theta 0}$ at loads of 6 and 10 kN.

The 12.0-18 tyre at two loads also showed no statistically significant difference in $CR_{\theta 0}$.

The 7.50-16 tyre, gave an increased value of $k.CSP_{w \max}$ when at the lower vertical load, with no difference detected between the values of $CSP_{w \max}$.

The 12.0-18 tyre showed a significant difference in both values, with $CSP_{w \max}$ and $k.CSP_{w \max}$ being increased at the lower load.

5.2 The effect of tread pattern, Table 3

Two experiments looked into this effect by using tyres of the same size, produced by the same manufacturer, having different tread patterns.

The tractor steering wheel tyre tread, showed a significant increase in $CR_{\theta 0}$ when compared to the multi-rib implement tread. As both tyres had nominally the same dimensions this effect could only be due to tread pattern.

When comparing the 12.0-18 tyres, while no difference could be detected between the two 'M' traction treads, used in each direction, the multi-ribbed implement tread had a significantly lower $CR_{\theta 0}$ than either of them. This effect demonstrated that the direction of the traction tread made no difference to the rolling resistance of the tyre. The difference of 20% between the traction treads and the implement tread could be due to the increased penetration of the traction treads and also due to the tread bars increasing the internal resistance of the tyre.

The tractor steering wheel tyre tread pattern gave a significant increase in CSP_{\max} over the implement tyre with no significant difference in $k.CSP_{\max}$. This shows that for small angles, i.e. up to 15°, there is no difference between the tyres, the tread pattern only affecting the total side force the tyres can withstand.

In experiment 3 the side force results can be summarised as follows:

CSP_{\max} .
 Backward M tread > Implement tread
 Forward M tread > Implement tread
 No difference between forward 'M' tread and backward 'M' tread

$k.CSP_{\max}$.
 Implement tread > Forward M tread
 Implement tread > Backward M tread
 Forward M tread > Backward M tread

This demonstrates that while the M tread can withstand a greater maximum side force, at small angles its steering performance is below that of the implement tyre.

5.3 The effect of construction, Table 4

The radial ply tyre showed reductions in the order of 20% in the value of $CR_{\theta 0}$ compared to a cross-ply tyre.

The radial ply tyre had a greater value of $k.CSF_{w \max}$ than the cross-ply tyre with no difference between them in terms of $CSF_{w \max}$. As both the tyres had a similar multi-ribbed implement tread pattern and similar mobility numbers the difference between them can only be a result of the construction method used.

6. PREDICTION METHODS

6.1 The coefficient of rolling resistance ($CR_{\theta w}$)

As has been seen in section 4 tyre mobility number has been used to predict the performance of wheels. The value of $CR_{\theta 0}$ actually measured is shown plotted against $ENOB$ in Fig. 1. As can be seen the $CR_{\theta 0}$ results for the radial tyres are lower than the cross-ply results and therefore relationships between $CR_{\theta 0}$ and $ENOB$ have been calculated separately. These were found to be:

$$CR_{\theta 0} \text{ (measured)} = \frac{.2676}{ENOB} + 0.0656 \quad \dots (8)$$

significant at the 0.1% level for cross-ply tyres

$$CR_{\theta 0} \text{ (measured)} = \frac{.2009}{ENOB} + 0.0454 \quad \dots (9)$$

significant at the 1% level for radial tyres

Equation (8) is very similar to the result found previously⁽¹³⁾ where the complete spectrum of agricultural tyre sizes (including the range of tractor drive wheel tyres) was included in the analysis and gave the relationship

$$CR_{\theta 0} = \frac{0.255}{ENOB} + 0.0605 \quad \dots (10)$$

Section 4 reported that the relationship between $CR_{\theta w}$ and slip angle was found to be:

$$CR_{\theta w} = m \theta + CR_{\theta 0} \quad \dots (3)$$

No significant relationship could be found between the constant m and mobility number for any tyres.

An analysis was then attempted similar to that of Gee-Clough and Somner who produced the expression:

$$CR_{\theta w} = CR_{\theta 0} (1 + M) \quad \dots (11)$$

and found the relationship between M and $ENOB$ to be:

$$M = \frac{1.934}{ENOB} - 0.080 \quad \dots (12)$$

From our measured data the fitted curves were:

$$M = 1.984 - \frac{5.496}{E_{MOB}} \text{ significant at } 1\% \text{ level} \quad \dots (13)$$

or

$$M = 0.081 E_{MOB} + 0.550 \text{ significant at } 1\% \text{ level} \quad \dots (14)$$

for cross-ply tyres

No significant relationship could be found for radial tyres.

There is a large amount of scatter present indicating this parameter is not related as well as the others. It appears from the results that the data for some tyres lie on their own independent straight lines although this is not the case with all the tyres.

It is suggested that the scatter may be due to an accumulation of inaccuracies throughout the analysis of this data. The initial data from the rolling resistance rig are of a small magnitude and correspondingly may include some 'round-up' errors of the numbers involved. Also when performing a linear regression on the CRR_{50} vs slip angle results, the relatively few points, five, can result in a large error in the resulting value of slope. Coupled to these errors is the problem of field variability.

As reported by Gee-Clough and Sommer the value m is not, however, one of the critical parameters when studying the stability of a vehicle.

6.2 Coefficient of side force

The values of $CSF_{w \max}$ are shown plotted against E_{MOB} in Fig. 2. The relationship found is:

$$CSF_{w \max} = \frac{0.6872}{E_{MOB}} + 0.6125 \quad \dots (15)$$

significant at 5% level for cross-ply tyres

but no significant relationship could be found for radial tyres.

The graphs of $k.CSF_{w \max}$ against E_{MOB} for radial and cross-ply tyres are shown in Fig. 3. The relationships are:

$$k.CSF_{w \max} = 0.0882 E_{MOB} + 2.3401 \quad \dots (16)$$

$$\text{or } k.CSF_{w \max} = 4.0194 - \frac{6.8231}{E_{MOB}} \quad \dots (17)$$

both significant at the 0.1% level for cross-ply tyres.

$$k.CSF_{w \max} = 0.1612 E_{MOB} + 2.7915 \quad \dots (18)$$

$$\text{or } k.CSF_{w \max} = 6.7665 - \frac{19.9433}{E_{MOB}} \quad \dots (19)$$

both significant at the 0.1% level for radial tyres

Gee-Clough and Sommer reported a linear relationship between CSFw max. and EMOB which was not statistically significant, and a significant relationship between k.CSFw max. and EMOB. This relationship had an ordinate value very similar to equation 16.

The horizontal moment about a vertical axis through the centre of the contact area of the wheel-restoring moment was calculated and found to be negligibly small in all experiments.

6.3 The use of an alternative mobility number @MOB

As shown by Gee-Clough and Sommer, the mobility number @MOB can be used to model the performance of a wheel in a soil bin situation. In order to test this theory under field conditions, the frictional soil properties were measured in the last 21 fields.

The only significant relationships established were:

$$k.CSFw \text{ max.} = 3.9594 @MOB + 2.7983 \text{ significant at the } 5\% \text{ level for cross-ply tyres} \quad \dots (20)$$

$$k.CSFw \text{ max.} = 9.0952 @MOB + 3.1327 \text{ significant at the } 0.1\% \text{ level for radial tyres} \quad \dots (21)$$

$$CRF_{w0} \text{ (from regression)} = 0.1252 - 0.1496 @MOB \text{ significant at the } 1\% \text{ level for cross-ply tyres} \quad \dots (22)$$

$$CRF_{w0} \text{ (measured)} = 0.1167 - 0.1178 @MOB \text{ significant at the } 5\% \text{ level for cross-ply tyres} \quad \dots (23)$$

None of the relationships above is as statistically significant as those found previously using the mobility numbers EMOB. The reason for the poor correlation of these results compared to the findings of Gee-Clough and Sommer may be due to the method of measuring the frictional properties. In a soil bin the soil is normally homogeneous with depth as well as along the experimental run. The surface measurement of frictional properties is therefore a true value throughout the soil. In the field situation this is obviously false with the added complication that any crop residue, in terms of surface or root growth, will have an effect. More detailed measurements of frictional properties at various depths in the field are needed to establish whether @MOB will be as useful as EMOB in the prediction procedure.

7. CONCLUSIONS

In this section, the coefficient of rolling resistance in the direction of the wheel at zero slip angle (CRF_{w0}) is referred to as the 'coefficient of rolling resistance'; the maximum coefficient of side force perpendicular to the direction of the wheel (CSFw max.) is referred to as the 'maximum coefficient of side force'; the slope of the side force-slip angle curve at the origin (k.CSFw max.) is referred to as the 'slope of the side force curve'.

From the differences between tyres:

7.1 Increasing the vertical load had no effect on the 'coefficient of rolling resistance', but reduced the 'slope of the side force curve' significantly and reduced the value of the 'maximum coefficient of side force'.

7.2 A three-rib tractor front tyre tread pattern gave an increased 'coefficient of rolling resistance', and an increased 'maximum coefficient of side force' compared to a multi-rib implement tread pattern.

A multi-rib implement tread pattern had a much lower 'coefficient of rolling resistance', a lower value of 'maximum coefficient of side force', and a higher value of 'the slope of the side force curve' than the R4 traction tread used in either direction. No differences could be detected between the R4 traction treads used in either direction apart from the 'slope of the side force curve' where the tread in the normal traction direction gave a higher value than when used in the reverse direction.

7.3 Radial construction reduced the 'coefficient of the rolling resistance' and increased the 'slope of the side force curve' compared to cross-ply construction.

7.4 A linear relationship was found between the coefficient of rolling resistance in the direction of the wheel and slip angle, and an exponential relationship was found between the coefficient of side force perpendicular to the direction of the wheel and side force, which were identical to those found in previous work.

7.5 The restoring moment on the wheel was found to be negligibly small in all experiments.

7.6 Very significant relationships were found between 'the coefficient of rolling resistance', 'the slope of the side force curve', and mobility number $EMOB$ for cross-ply tyres and radial tyres independently. A very significant result was found between the gradient of the coefficient of rolling resistance-slip angle curve and $EMOB$ for the cross-ply tyres and a significant result found between the 'maximum coefficient of side force' and $EMOB$.

7.7 The mobility number $EMOB$ proved to be less useful than the mobility number MOB with all relationships having a lower statistical significance.

REFERENCES

1. PHILLIPS, J.R. Experimental determination of forces on some towed drifting wheels J. agric. Engng. Res., 1959, 4
2. GILFILLAN, G.; SPENCER, H.B.; ROWE, E.P.H. Some preliminary results from side force tests on a 7.50-16 tractor front tyre Dep. Note SSN/203, 1976, Scott. Inst. agric. Engng, Penicuik, (unpubl)
3. TAYLOR, P.A.; BIRTWISTLE, R. Experimental studies of force systems on steered agricultural tyres Proc. Inst. Mech. Eng, 1966-67, Part 2A, 181
4. SCHMANGHART, H. Lateral forces on steered tyres in loose soil J. Terramechanics 5 (1) 1968
5. GRECENIO, A. Slip and drift of the wheel with tyre in soft ground Proc. 3rd Internat. Conf., Internat. Soc. Terrain-Vehicle Systems, Essen, 1969
6. DEL ROSARIO, C.R. Lateral force investigations on steered pneumatic tyres operating under soil condition Ph.D. Thesis (unpubl) 1980, Silsoe College
7. SPENCER, H.B. Tractor and implement stability on slopes Dep. Note SIN/193, 1975, Scott. Inst. agric. Engng, Penicuik (unpubl)
8. SPENCER, H.B. Stability and control of two-wheel drive tractors and machinery on sloping ground J. agric. Engng Res., 1978, 23
9. CROLLA, D.A.; HALES, F.D. The lateral stability of tractor and trailer combinations J. Terramechanics, 1979, 16 (1)
10. GEE-CLOUGH, D.; SOMMER, M.A. Steering forces on undriven angled wheels J. Terramechanics, 18 (1) 1981
11. MCALLISTER, M.; GEE-CLOUGH, D.; EVERDEN, D.W. Preliminary results from an investigation into forces on towed angled wheels Dep. Note DN/T/916/01002 1979, natl Inst. agric. Engng, Silsoe (unpubl)
12. MCALLISTER, M. A rig for measuring the forces on a towed wheel J. agric. Engng Res., 1979, 24
13. MCALLISTER, M.; GEE-CLOUGH, D.; EVERDEN, D.W. Preliminary results obtained from an investigation into the rolling resistance of towed wheels Dep. Note DN/T/917/01002 1979, natl Inst. agric. Engng, (unpubl)

Table 1
Tyre dimensions

Tyre size	Construction	Ply rating	Tread pattern	Load kN	Inflation pressure kPa	Diameter m	Width m	Deflection/section ht $\frac{g}{s}$	Mobility no. without soil parameter	Symbol on figs
7.50-16	Cross-ply	8	3 rib tractor steering tread	6.0	212	0.812	0.208	16.91	0.01026	○
7.50-16	Cross-ply	8	3 rib tractor steering tread	10.0	406	0.812	0.208	17.16	0.00620	●
7.50-16	Cross-ply	8	Multi-rib implement	6.0	212	0.792	0.209	16.75	0.00997	△
12.0-18	Radial	-	Multi-rib implement	10.0	101	0.892	0.317	26.83	0.01244	□
12.0-18	Radial	-	Multi-rib implement	15.0	142	0.892	0.317	30.28	0.00880	■
12.0-18	Cross-ply	10	Multi-rib implement	15.0	142	0.920	0.314	27.27	0.00859	▲
12.0-18	Cross-ply	10	R4 traction tread direction	15.0	142	0.918	0.313	22.61	0.00778	▽
12.0-18	Cross-ply	10	R4 reversed traction tread direction	15.0	142	0.918	0.313	22.17	0.00771	▼

Table 2
Effect of load

Tyre	7.50-16 Tractor front		12.0-18 radial	
	6	10	10	15
Load				
CRF _w (measured)	0.123	0.121	0.069	0.069
CRF _w (from regression)	0.122	0.087	0.090	0.069
m (from regression)	0.050	0.242	0.091	0.141
CSP _w max.	0.776	0.764	0.640	0.620
K.CSP _w max.	4.071	3.285	5.049	3.747

Table 3
Effect of tread pattern

Type	7.50-16 3-rib Tractor front	7.50-16 Multi-rib implement	12.0-18 R4 Traction direction	12.0-18 R4 Reverse direction	12.0-18 Multi-rib implement
Load (kN)	6	6	15	15	15
CRho (measured)	0.114	0.095	0.100	0.100	0.079
CRho (from regression)	0.115	0.103	0.103	0.106	0.085
n (from regression)	0.053	0.086	0.106	0.103	0.099
CSFV max.	0.755	0.662	0.668	0.699	0.628
k. CSFV max.	3.746	3.950	2.624	2.475	3.250

Table 4
Effect of tyre construction

Tyre	12.0-18	12.0-18
Construction	Cross-ply	Radial
Load (kN)	15	15
CR _{Rw0} (measured)	0.077	0.067
CR _{Rw0} (from regression)	0.085	0.067
n (from regression)	0.096	0.142
CSP _w max.	0.646	0.623
k.CSP _w max.	3.316	3.796

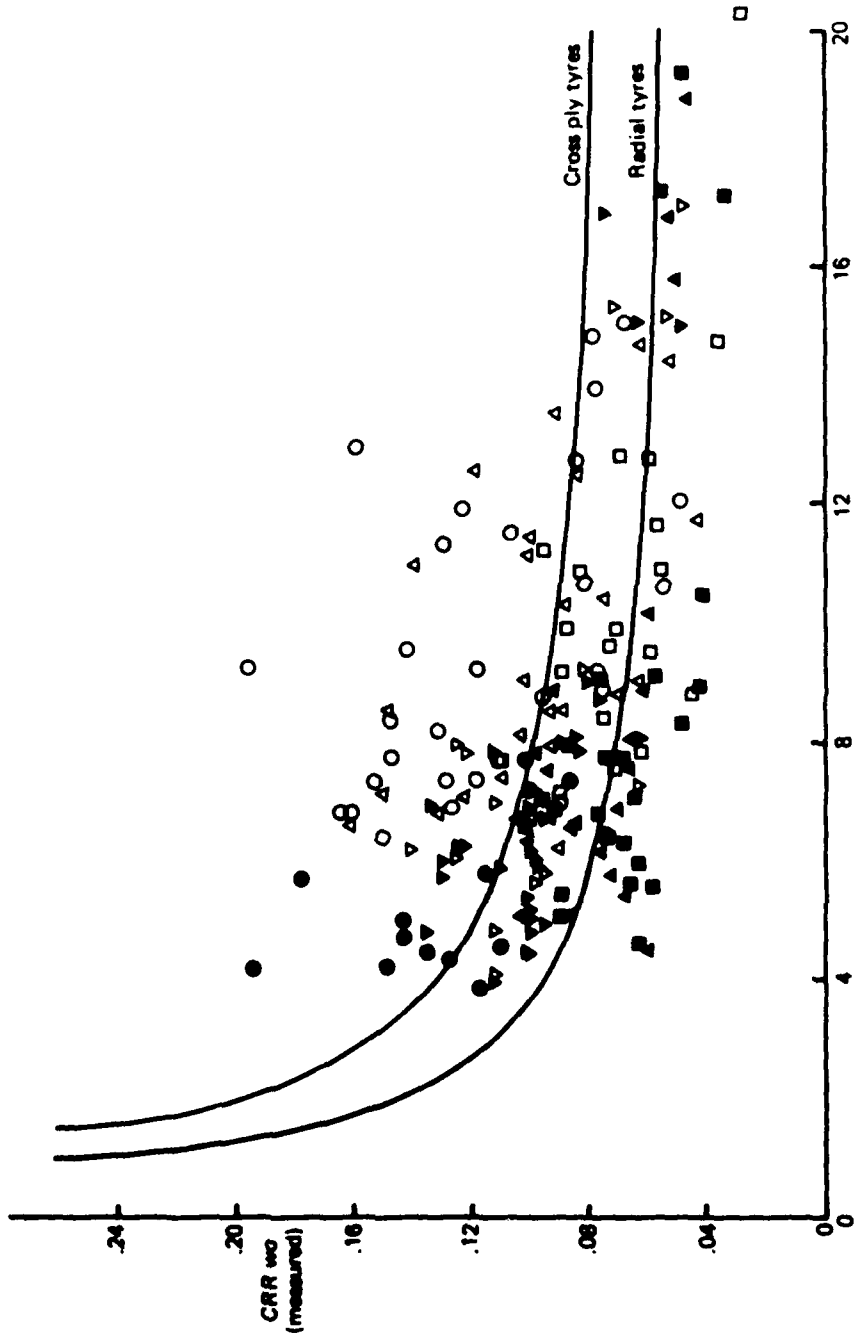


FIG. 1 CRR w/o (measured) vs mobility number EMOB (Key to symbols Table 1)

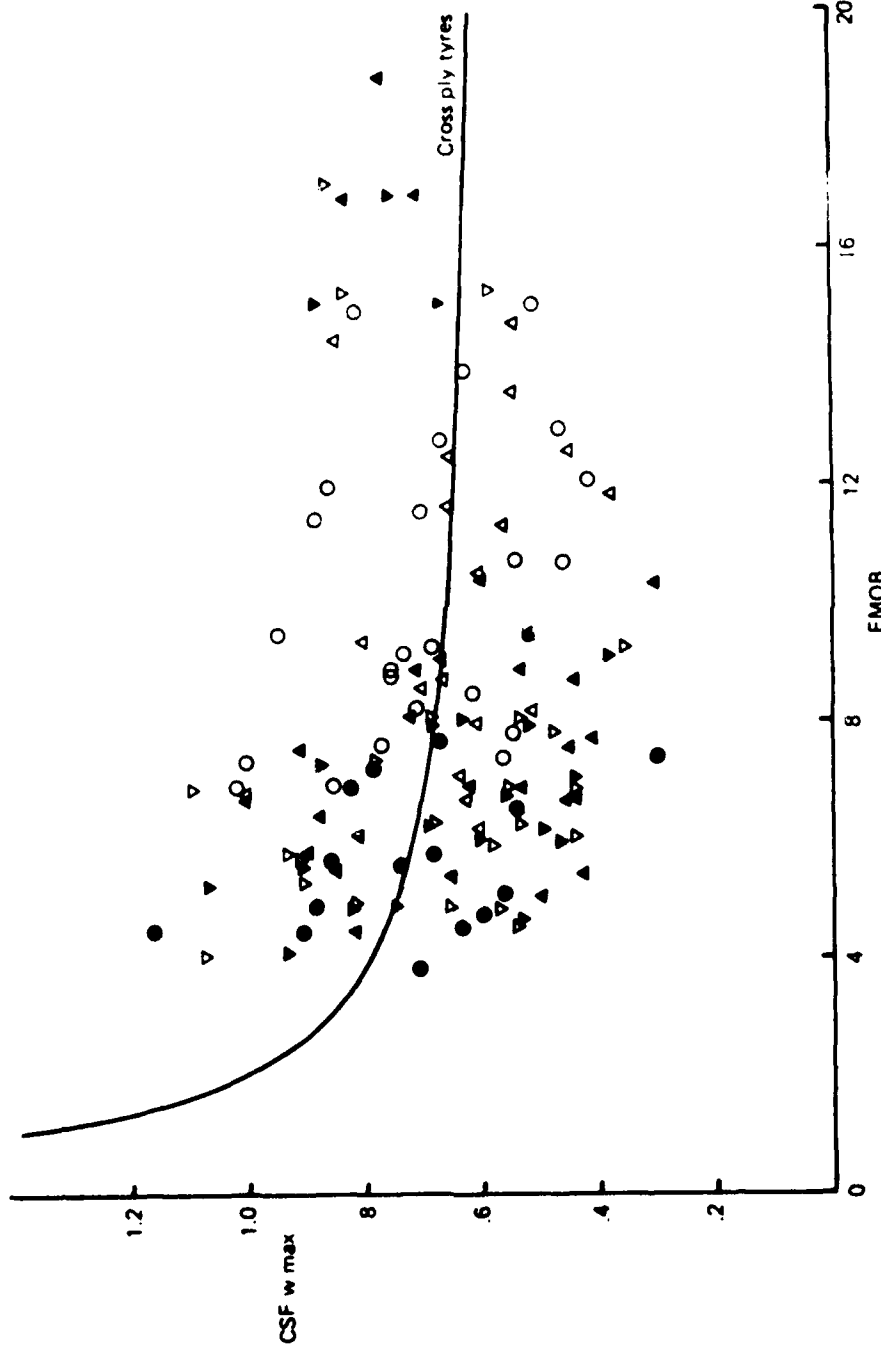


FIG. 2 CSF w max. vs mobility number EMOB for cross-ply tyres (From Table 1)

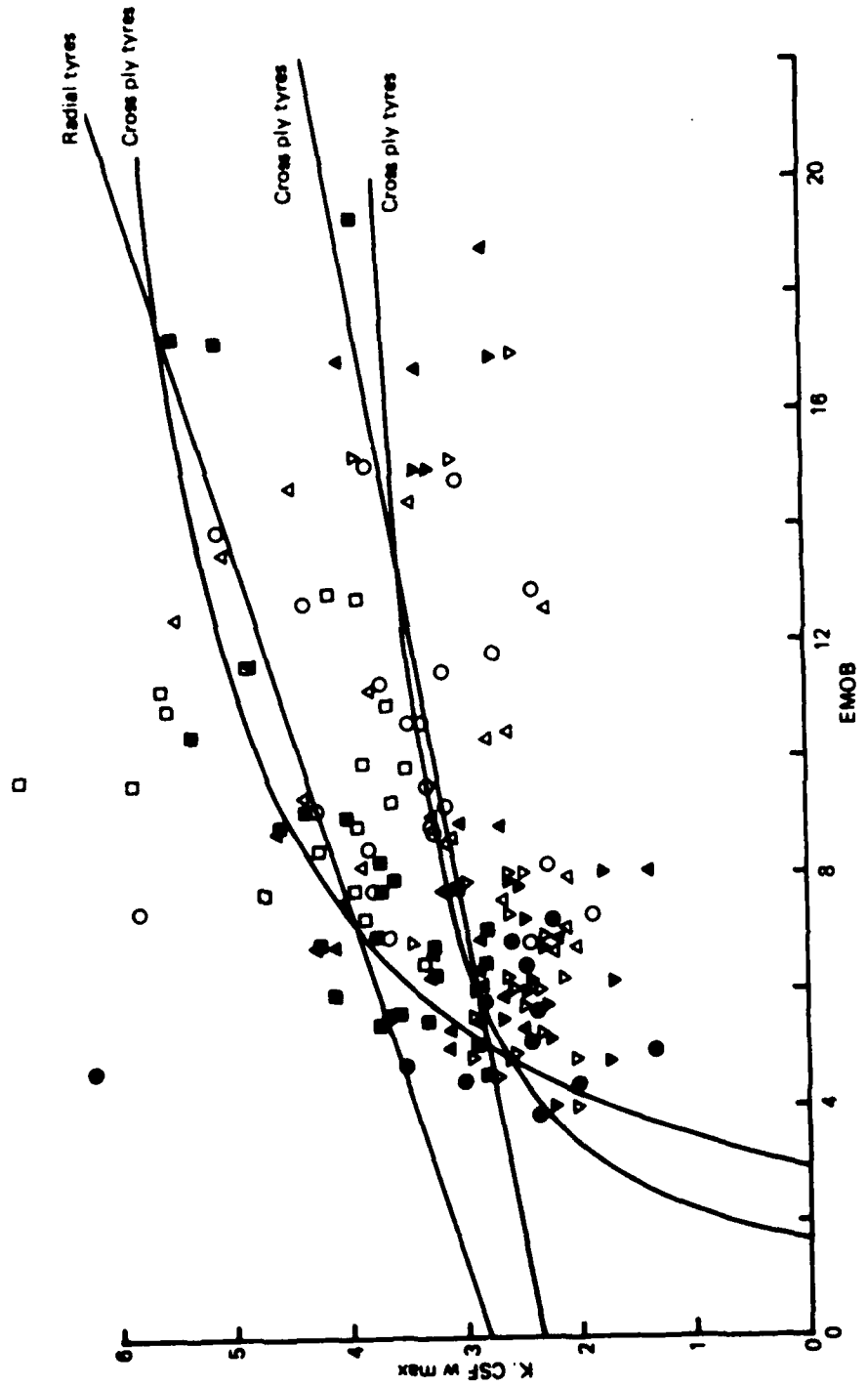


FIG. 3 k.C.S.F.W. max. vs mobility number EMOB (Key to symbols Table 1)

TURNING BEHAVIOUR OF ARTICULATED FRAME STEERING TRACTOR

A. OIDA

KYOTO UNIVERSITY, KYOTO, JAPAN

AD-P004 304

INTRODUCTION

An articulated frame steering tractor, of which construction was derived from that of a loader, consists of two parts. Those are a front part with a front axle and a rear part with a rear axle in the case of the wheeled tractor. When a steering handle rotates, the two parts bend with each other around a bending point by elongation and shortening of a hydraulic cylinder, of which both ends are respectively attached on each part. A bending angle reaches to about 38 degrees in right or left direction for a commercial articulated tractor (See reference ATT.).

In general a 4-wheel-drive articulated tractor has an engine in the front part and a transmission in the rear part, so that universal joints should be used to transmit the power from the engine to the transmission and from the transmission to a front differential gear. It has tires all of a size and the minimum tread reaches to 635 mm in a German narrow-tread tractor of 12 kW. So that it can be applied to works among narrow rows of an orchard or a wine farm. The weights of the front and the rear parts are almost equal, so that it makes an adequate contact pressure.

Generally it has been said that the articulated tractor has a small turning radius, which makes a direction change in small space easy, and it has less running resistance because the front and rear wheels move on the same ruts. However, it would not say in all cases that the front and rear wheels run in the same ruts. From the geometrical analysis of a curve running of the articulated tractor Oida has shown that the ruts of front and rear wheels were different when the bending point was not located at the center of the wheel base [1].

Dudzinski has analyzed dynamically the problems of turning process of the articulated vehicle at standstill [2]. In the actual movement of curve running there is an acceleration toward to the turning center, so that a centrifugal force acts onto the center of gravity of the tractor and each tire has a cornering force against the centrifugal force. It means that the rut of wheel varies also by this side slip caused by the centrifugal force. Oida has also analyzed this turning behaviour when the articulated tractor is suffe ed no external force such as a traction [3].

In this paper a side slip phenomenon of the articulated tractor is dynamically analyzed for the curve running in a plane with an arbitrary directed traction.

NOMENCLATURE

C : cornering force of each tire,
 F : tractive force of each tire,
 I : yaw moment of inertia of the tractor,
 K' : slippage constant of traction curve,
 P : external force (traction),
 R : rolling resistance,
 T : total thrust,
 V : running speed of the center of gravity of the tractor,

W : total weight of the tractor,
 W_f : dynamic weight of the front part,
 W_r : dynamic weight of the rear part,
 ΔW_l : longitudinal weight transfer,
 ΔW_t : transverse weight transfer,
 a : ratio of static weight of front part to W ,
 b : ratio of static weight of rear part to W ,
 d_f : distance from front tire center to y axis,
 d_h : one half of rear tread,
 d_p : distance from traction point to y axis,
 d_r : distance from rear tire center to y axis,
 d_v : one half of front tread,
 h_o : height of the center of gravity,
 h_p : height of traction point,
 i : slippage of tractor,
 i_o : initial slippage at no tractive force,
 l_e : distance from front axle center to x axis,
 l_f : distance from front axle center to bending point,
 l_{fl} : distance from front left tire center to x axis,
 l_{fr} : distance from front right tire center to x axis,
 l_h : distance from rear axle center to x axis,
 l_p : distance from traction point to x axis,
 l_r : distance from rear axle center to bending point,
 l_{rl} : distance from rear left tire center to x axis,
 l_{rr} : distance from rear right tire center to x axis,
 l' : distance between front and rear axle centers,
 m : mass of tractor including a driver,
 p_d : distance from traction point to rear axle center,
 r : yaw angular velocity around the center of gravity,
 t : time,
 α : deviating angle of rear part center line to y axis,
 β : side slip angle,
 β_o : side slip angle constant,
 γ : deviating angle of front part center line to y axis,
 δ : bending angle,
 θ : traction angle (ie. angle between the traction and the centerline of rear part),
 μ : tractive coefficient or frictional coefficient,
 ρ : coefficient of rolling resistance,
 Suffix f : front,
 Suffix l : left,
 Suffix r : rear or right,
 Suffix 1 : left,
 Suffix 2 : right.

EQUATION OF MOTION AT RUNNING ON A CURVE

Different from a standard tractor, the center of gravity of the articulated tractor moves its position according to the bending angle. In the case of tested tractor, of which detail is mentioned later, the center of gravity of the front part and that of the rear part are located closely at the centers of the axles respectively, that was confirmed experimentally, in order to reduce the vertical force onto the bending point.

Therefore a x - y coordinate system, of which origin is located on the center of gravity on a line connected both centers of axles, is attached on the tractor as a local coordinate as shown in Fig. 1.

When the center of gravity has a side slip angle β and a yaw angular velocity r , it has an acceleration of $V(\beta + r)$ toward a turning center or in

x-direction in the case of small β (3).
Each tire has also a side slip angle, which is caused by the side slip angle and the yaw angular velocity of the center of gravity.

Consequently a cornering force, which is against the side slip of each tire, acts on each tire in the perpendicular direction of the moving direction or in the perpendicular direction to the tire face when the side slip of the tire is small. Considering above conditions, the equations of motion are written as follows.

In x-direction;

$$\begin{aligned} m\dot{v}(\dot{\beta} + r) = & (C_{f1} + C_{f2})\cos\gamma \\ & + (C_{r1} + C_{r2})\cos\alpha \\ & + (F_{f1} + F_{f2})\sin\gamma \\ & - (F_{r1} + F_{r2})\sin\alpha \\ & + P\sin(\alpha + \theta) \end{aligned} \quad (1)$$

In y-direction;

$$\begin{aligned} m\dot{v} = & -(C_{f1} + C_{f2})\sin\gamma \\ & + (C_{r1} + C_{r2})\sin\alpha \\ & + (F_{f1} + F_{f2})\cos\gamma + (F_{r1} + F_{r2})\cos\alpha - P\cos(\alpha + \theta) \end{aligned} \quad (2)$$

For the yawing motion;

$$\begin{aligned} I\dot{r} = & \{d_f(F_{f1} - F_{f2}) + l_{f1}C_{f1} + l_{f2}C_{f2}\}\cos\gamma \\ & + \{-d_f(C_{f1} - C_{f2}) + l_{f1}F_{f1} + l_{f2}F_{f2}\}\sin\gamma \\ & + \{d_r(F_{r1} - F_{r2}) - (l_{r1}C_{r1} + l_{r2}C_{r2})\}\cos\alpha \\ & + \{d_r(C_{r1} - C_{r2}) + l_{r1}F_{r1} + l_{r2}F_{r2}\}\sin\alpha \\ & + P(d_p\cos(\alpha + \theta) - l_p\sin(\alpha + \theta)) \end{aligned} \quad (3)$$

First a tractive force of tire is discussed. The torques, which are applied to both left and right tires of each axle, are equal because of the differential gear. But the torque of front axle (ie. the sum of torque of front left tire and that of front right tire) is different from the torque of rear axle. Those torques vary their values, depending on the loads of axles. Representing the total thrust of four tires as T , which is also given as the total supplied torque from the engine divided by the effective radius of tire, according to the magnitude of the external force, the tractive force of each tire is written as follows.

$$F_{f1} = TW_f/(2W) - R_{f1}, \quad F_{f2} = TW_f/(2W) - R_{f2},$$

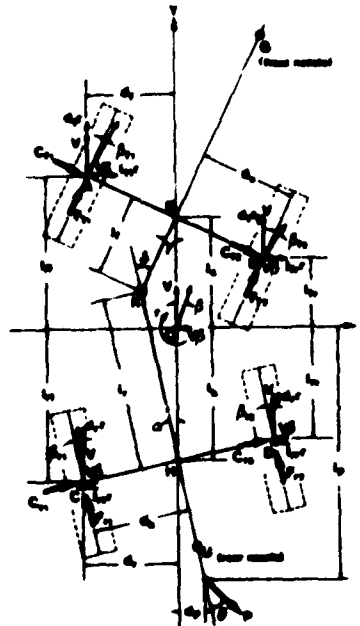


Fig. 1 Forces and angles in the case of curve running of the articulated tractor.

$$F_{r1} = TW_r/(2W) - R_{r1}, \quad F_{r2} = TW_r/(2W) - R_{r2} \quad (4)$$

The rolling resistance R of each tire would be written as follows using a coefficient of rolling resistance ρ , assuming the ground condition is uniform.

$$R_{f1} = \rho W_{f1}, \quad R_{f2} = \rho W_{f2}, \quad R_{r1} = \rho W_{r1}, \quad R_{r2} = \rho W_{r2} \quad (5)$$

In order to get the loads onto the tires it is necessary to consider the weight transfer by the traction and the inertia force dynamically. A longitudinal weight transfer is derived from the dynamic equilibrium of forces, which act to the tractor as Fig. 2.

When the tractor accelerates with \dot{V} , a inertia force $m\dot{V}$ acts on the center of gravity in the inverse direction of the acceleration V . As there is also an external force $P\cos(\alpha+\theta)$ at the traction point, a weight of front part or a reaction force to front part W_f is represented by the following equation.

$$W_f = lhW/l' - \{h_0m\dot{V} + Ph_p\cos(\alpha + \theta)\}/l' = aW - \Delta W_1 \quad (6)$$

$$\text{Then, } W_r = bW + \Delta W_1 \quad (7)$$

In order to determine a transverse weight transfer, Fig. 3 is used. In this case the transverse external forces are a centrifugal force $mV^2(\beta+r)$ and a transverse component of the traction $P\sin(\alpha+\theta)$, so that the reaction force to two left tires (ie. a force to front left tire + a force to rear left tire) W_1 is obtained as follows from the dynamic equilibrium of forces.

$$W_1 = W/2 + \{h_0mV^2(\beta + r) - Ph_p\sin(\alpha + \theta)\}/(d_f + d_r) \quad (8)$$

$$= W/2 + \Delta W_t \quad (8)$$

$$\text{Then, } W_2 = W/2 - \Delta W_t \quad (9)$$

Considering these weight transfers, the loads of tires or the reaction forces from the ground to tires are written as follows.

$$\begin{aligned} W_{f1} &= aW/2 - \Delta W_1/2 + a\Delta W_t, & W_{f2} &= aW/2 - \Delta W_1/2 - a\Delta W_t \\ W_{r1} &= bW/2 + \Delta W_1/2 + b\Delta W_t, & W_{r2} &= bW/2 + \Delta W_1/2 - b\Delta W_t \end{aligned} \quad (10)$$

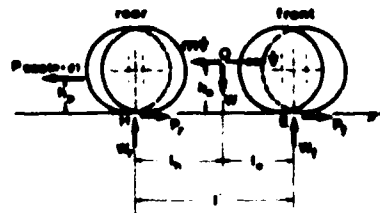


Fig. 2 Schematic figure for longitudinal weight transfer.

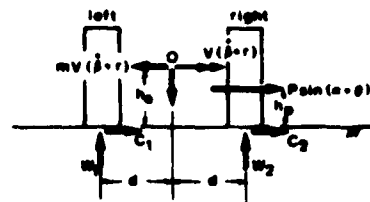


Fig. 3 Schematic figure for transverse weight transfer.

In reference [3] Gida assumed that the cornering force is proportional to the side slip angle for very small side slip angle. This assumption is valid only for very small side slip angle. However, when the traction or other external forces act on the tractor, the side slip angle of tire will be considered to have rather not small side slip angles. For this case the cornering force would be represented for example by the exponential function as follows from the consideration of test curves of cornering force to the side slip angle.

$$C = C_{max}(1 - e^{-\beta/\beta_0}) \quad (11)$$

The maximum cornering force C_{max} is restricted by the friction circle as Fig. 4. When the tire has a tractive force F , the maximum cornering force is represented as follows.

$$C_{max} = \sqrt{(\mu W)^2 - F^2} \quad (12)$$

In order to solve the dynamic motion equations (1) to (3), the cornering force C should be written as the linear function of β , r and V . So that the following approximation is taken in the relation between the maximum cornering force and the tractive force in four regions as in Fig. 5.

$$C_{max} = B_i(\mu W) - A_i F, \quad i=1 \sim 4 \quad (13)$$

Considering that the cornering force is negative when the side slip angle is positive, the cornering force C is represented as follows for all side slip angles (See Fig. 6).

$$C_{r1} = -\left(B_{r1} \mu W_{r1} - A_1 F_{r1} \right) \left(1 - e^{-\frac{|\beta_{r1}|}{\beta_0}} \right) \frac{|\beta_{r1}|}{\beta_{r1}}$$

$$C_{r2} = -\left(B_{r2} \mu W_{r2} - A_1 F_{r2} \right) \left(1 - e^{-\frac{|\beta_{r2}|}{\beta_0}} \right) \frac{|\beta_{r2}|}{\beta_{r2}}$$

$$C_{l1} = -\left(B_{l1} \mu W_{l1} - A_1 F_{l1} \right) \left(1 - e^{-\frac{|\beta_{l1}|}{\beta_0}} \right) \frac{|\beta_{l1}|}{\beta_{l1}}$$

$$C_{l2} = -\left(B_{l2} \mu W_{l2} - A_1 F_{l2} \right) \left(1 - e^{-\frac{|\beta_{l2}|}{\beta_0}} \right) \frac{|\beta_{l2}|}{\beta_{l2}} \quad (14)$$

And the side slip angles of tires are written as follows.

$$\beta_{r1} = (VB + l_{gr}r) / (V + d_{gr}) - \gamma, \quad \beta_{r2} = (VB + l_{gr}r) / (V - d_{gr}) - \gamma,$$

$$\beta_{l1} = (VB - l_{lr}r) / (V + d_{lr}) + \alpha, \quad \beta_{l2} = (VB - l_{lr}r) / (V - d_{lr}) + \alpha \quad (15)$$

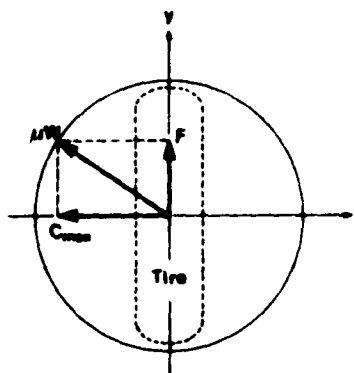


Fig. 4 Friction circle for tire.

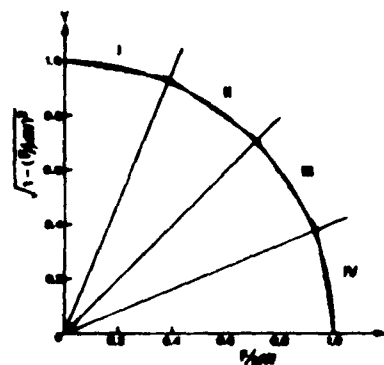


Fig. 5 Relation between the maximum cornering force and tractive force.

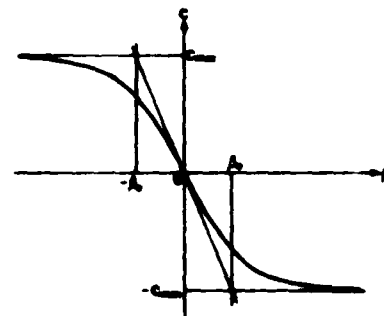


Fig. 6 Cornering force.

Representing all distances in Fig. 1 by the tractor geometry and by the bending angle and substituting all these equations into equations (1) to (3), we can get following equations.

$$\begin{aligned} a_{11}\dot{\beta} + a_{12}\dot{V} &= b_1T + c_1 = g_1(\beta, r, V, \alpha, \theta, T, P, \dots) \\ a_{21}\dot{\beta} + a_{22}\dot{V} &= b_2T + c_2 = g_2(\beta, r, V, \alpha, \theta, T, P, \dots) \\ a_{31}\dot{\beta} + a_{32}\dot{V} + a_{33}\dot{r} &= b_3T + c_3 = g_3(\beta, r, V, \alpha, \theta, T, P, \dots) \end{aligned} \quad (16)$$

$\dot{\beta}$, \dot{V} and \dot{r} are represented as follows.

$$\begin{aligned} \dot{\beta} &= (a_{22}g_1 - a_{12}g_2) / (a_{11}a_{22} - a_{12}a_{21}) \\ \dot{V} &= (a_{11}g_2 - a_{21}g_1) / (a_{11}a_{22} - a_{12}a_{21}) \\ \dot{r} &= [(a_{21}a_{32} - a_{22}a_{31})g_1 + (a_{12}a_{21} - a_{11}a_{32})g_2 + (a_{11}a_{22} - a_{12}a_{21})g_3] \\ &\quad / \{a_{33}(a_{11}a_{22} - a_{12}a_{21})\} \end{aligned} \quad (17)$$

If initial values of β , r and V are given, the time variations of three output variables β , r and V are calculated by the Runge-Kutta-Gill method for the input variables δ , θ , T , P and so on. By this method the transient phenomenon such as a starting or a braking process will be analyzed, using an arbitrary variation of the input thrust T .

As for a constant speed running, $V = 0$. So that from equation (16),

$$\begin{aligned} a_{11}\dot{\beta} &= b_1T + c_1 \\ a_{21}\dot{\beta} &= b_2T + c_2 \\ a_{31}\dot{\beta} + a_{33}\dot{r} &= b_3T + c_3 \end{aligned} \quad (18)$$

In this case a constant thrust T of the following value is supplied to the tires.

$$T = (a_{21}c_1 - a_{11}c_2) / (a_{11}b_2 - a_{21}b_1) \quad (19)$$

Then $\dot{\beta}$ and \dot{r} are written as follows.

$$\begin{aligned} \dot{\beta} &= (b_2c_1 - b_1c_2) / (a_{11}b_2 - a_{21}b_1) \\ \dot{r} &= \{b_3(a_{21}c_1 - a_{11}c_2) + c_3(a_{11}b_2 - a_{21}b_1) + a_{31}(b_1c_2 - b_2c_1)\} / \{a_{33}(a_{11}b_2 - a_{21}b_1)\} \end{aligned} \quad (20)$$

The time variations of β and r are also calculated numerically by the R-K-G method, and the effects of factors such as V , P , δ and so on on β and r would be able to discuss at the constant turning.

The initial values of β and r are obtained from the condition that there is no side slip of tire, which is represented as follows.

$$\begin{aligned} \beta + l_g r / V - \gamma &= 0 \\ \beta - l_h r / V + \alpha &= 0 \end{aligned} \quad (21)$$

Therefore,

$$\beta_{init.} = a\gamma - b\alpha, \quad r_{init.} = V\delta/l' \quad (22)$$

The initial value of V is given arbitrarily. The velocity of tractor V will vary also by the slippage of tires, which is dependent on the tractive force. From the traction-slippage curve of the test tractor in the test place the slippage is calculated as follows, corresponding to the tractive force.

$$i = K' \ln \left(\frac{F_{\max}}{F_{\max} - F} \right) + i_0 \quad (23)$$

The method of getting the running trace on the fixed general coordinate is described closely in reference [1].

METHODOLOGY OF EXPERIMENT

Experiments of constant circular turn and U-turn were conducted on the hard unpaved ground for an articulated test tractor made in Japan. The tested tractor was 4WD (4-wheel-drive) articulated tractor with the similar construction and size as those of the "Knickschlepper" of Helder Co. in BRD. It has a mass of 1400 kg, equal-size tires and a 2-cylinder diesel engine of 19 kW. When the bending angle is 0° , its wheel base is 1290 mm, the distance from the bending point to the front axle l_f is 416 mm, l_r is 874 mm, and the tread $2d_h = 2d_v$ is 990 mm.

The traction (ie. external force) P was given by braking a connected load wagon behind the tested tractor and it was measured by a load cell.

The bending angle δ and the traction angle θ were picked up electrically by rotating type variable resistors.

In order to get the running trace and to correlate it with other data signals in the corresponding time, two ink nozzles were attached at front and rear parts of the tested tractor respectively, and from the nozzles blue and red ink dropped down at one or one half second intervals, using a relay circuit. Timer signal of the circuit was also recorded by a data recorder with other data, so that the running trace could correspond with other signals such as traction and angles. The running trace was obtained by photographing the two colored ink marks.

The yaw moment of inertia of the tractor "I" was measured by a torsional spring type measuring device, which Oida designed. This method was described closely in reference [3].

THEORETICAL AND MEASURED RUNNING TRACE

When the bending angle δ , the traction angle θ and the traction P vary at curve running, the running trace of the tested tractor is calculated theoretically and numerically by assuming a constant turning in a very short time interval. Details are shown in reference [1].

On the other hand the measured running traces were got from pictures of the colored ink marks which were remained on the ground after running.

Fig. 7 shows the comparison between the theoretical calculated running trace and the measured one when the traction is small and the initial speed is 2.1 m/s. In the case of small traction the tractor moves as well as the tractor without traction and both theoretical and measured running traces are considerably well coincident.

Fig. 8 shows the running traces when the traction and the traction angle are large. In this case the tractor is forced to slip outward of the turning by the traction P . The theoretical running traces can describe well this phenomenon and agree considerably well with the measured running traces as shown in Fig. 8. It is shown from these comparisons that this simulation theory would be able to be applied to estimate the turning behaviour of the articulated frame steering tractor.



Fig. 7 Comparison between measured running trace and theoretically calculated one when traction P is small.



Fig. 8 Comparison between measured running trace and theoretically calculated one when traction P is large.

EFFECT OF GEOMETRICAL FACTORS ON TURNING BEHAVIOUR

Using the equations (1) to (3), effects of some factors on the turning behaviour will be shown in following sections including this section. Here the position of bending point and the position of the center of gravity are selected as geometrical factors. As an index to represent the position of bending point,

$$R_1 = l_g / (l_g + l_r) \tag{24}$$

is chosen. The position of the center of gravity is represented by "a", i.e.

$$a = W_g / W = l_h / l' \tag{25}$$

Fig. 9 shows the relationship between the side slip angle of the center of gravity β , the position of bending point "R₁" and the position of the center of gravity "a". The given test conditions are written in the figure. Other geometrical dimensions except "R₁" are the same as those of the test tractor. A negative β means the outward side slip of the center of gravity. The smaller "a" is (i.e. the nearer the center of gravity to the rear

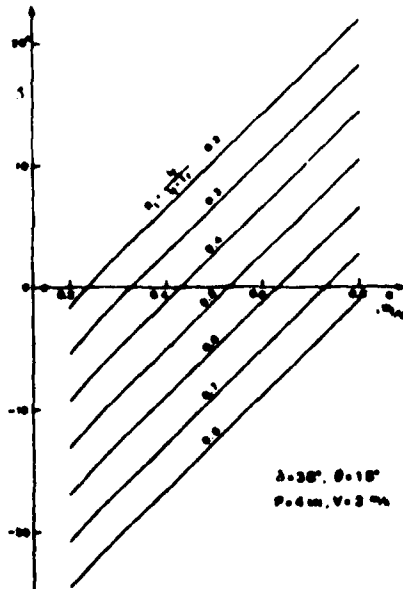


Fig. 9 Effect of positions of the CG and bending point on β .

axle is), and the larger " R_1 " is (ie. the nearer the bending point to the rear axle is), the larger the outward side slip of the center of gravity becomes. On the contrary when the center of gravity and the bending point are located near the front axle (ie. when " a " is large and " R_1 " is small), the center of gravity moves considerably inward of turning from the y direction. When the tractor running speed decreases, β approaches to zero, if the center of gravity and the bending point are located at the middle point between the front and rear axles (ie. " a " = " R_1 " = 0.5). In the case of Fig. 9 the value of β is a little negative because of the relatively higher running speed V (=3 m/s), even if " a " and " R_1 " are equal to 0.5.

Fig. 10 shows how the front and rear parts move according to the positions of the center of gravity and the bending point. In the figure β_e represents the side slip angle of the front axle center and β_h represents the side slip angle of the rear axle center. When " a " is small (ie. the center of gravity is near the rear axle), the rear axle (ie. rear tires) slips severely outward of turning. The outward slip of rear axle increases when " R_1 " decreases (ie. the bending point approaches to the front axle), especially at small " a ". On the other hand, when " a " is large (ie. the center of gravity is near the front axle) and " R_1 " is also large (ie. the bending point is near the rear axle), the front axle (ie. front tires) slips considerably inward of turning from y direction.

Fig. 11 shows the relationship between the position of turning center, " R_1 " and " a ". In the local coordinate system the origin is located on the center of gravity. However, as the origin moves according to the value of " a ", the front axle center is taken as the base point in this figure. When " R_1 " is large, the turning centers are located rather in front area from the viewpoint of tractor position. And when " R_1 " is small, the turning center moves rearward. As for " a ", the turning center approaches to the tractor when " a " is 0.5 or 0.6 and the turning radius reaches the minimum at that running condition. As a conclusion the turning radii of front and rear tires become almost equal when the bending point is located on the middle point between the front and rear axles and when the load distribution is equal or a little more onto the front part in this test condition. However this optimum condition

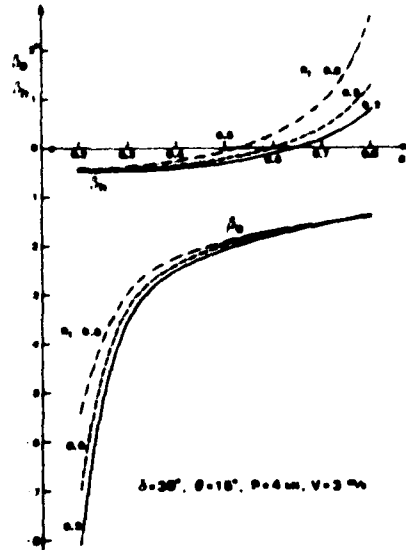


Fig. 10 Effect of positions of the CG and bending point on side slip angles of front and rear parts.

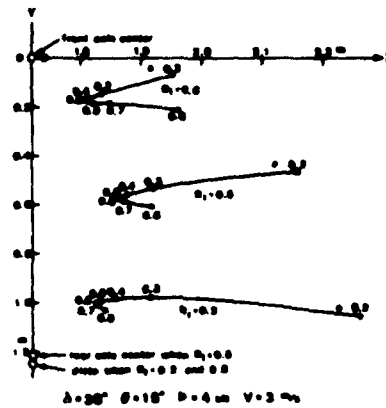


Fig. 11 Effect of positions of the CG and bending point on the position of turning center.

will change with the running speed, traction, traction angle and so on.

EFFECT OF TRACTION CONDITION ON TURNING BEHAVIOUR

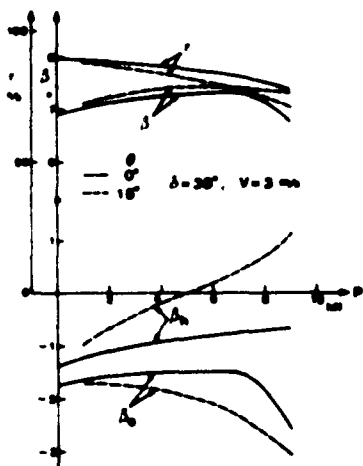


Fig. 12 Effect of traction on the side slip angles and r .

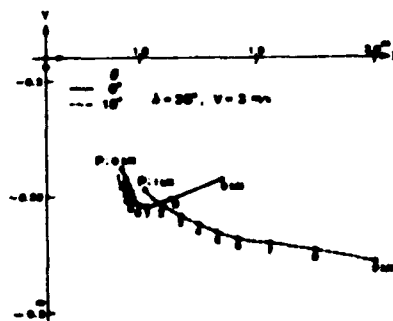


Fig. 13 Effect of traction on the position of turning center.

Fig. 12 shows the influence of traction P on the side slip angle of the center of gravity β , the yaw angular velocity of the center of gravity r , the side slip angle of the front axle center β_f and the side slip angle of the rear axle center β_h . Data of the tractor geometry, which were used in calculation, are those of the tested tractor. And these data were used in all following calculations of simulation. As the traction increases, the front part slips outward and the rear part slips inward of turning because the traction pulls the rear part of the tractor inward in this case, when

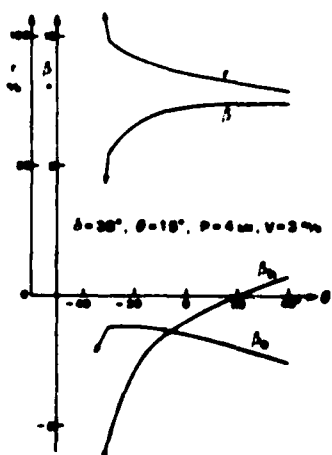


Fig. 14 Effect of traction angle on the side slip angles and r .

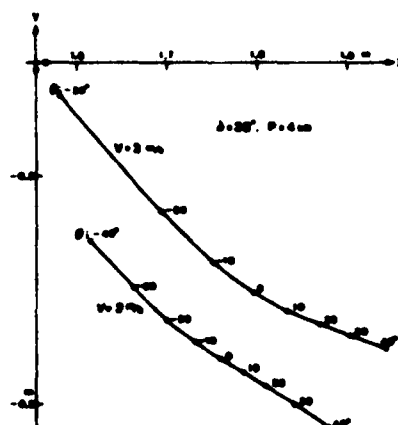


Fig. 15 Effect of traction angle on the position of the turning center.

the traction angle is not negative. The yaw angular velocity r decreases with the traction owing to the phenomenon mentioned above.

Fig. 13 represents how the position of turning center varies with the traction and it shows that the position of turning center goes away from the tractor with the increase of the traction. This trend is also explained by the variations of the side slip angles, which was shown in Fig. 12.

Fig. 14 shows the effect of the traction angle on β , r , β_e and β_h . When θ is negative, the rear part of the tractor is pulled outward, so that the rear part slips outward of turning. In this test conditions at the traction angle of -30 degrees the tractor becomes unstable. On the contrary, for the positive traction angle θ , the rear part slips inward and the front part slips outward of turning.

Fig. 15 represents that the position of turning center moves away from the origin for the larger value of the traction angle, because for the large positive traction angle the front part of the tractor slips outward of turning and the turning radius becomes larger.

EFFECT OF RUNNING VELOCITY ON TURNING BEHAVIOUR

When the running velocity V increases, the yaw angular velocity r increases also almost linearly, so that the acceleration $V(\beta + r)$ of the tractor toward the turning center increases, even if the variation of side slip angle of the center of gravity β is zero at the constant circular turning. Therefore, the larger centrifugal force acts on the center of gravity, then the side slip angles of front and rear parts become large in the outward direction of turning. Fig. 16 shows this phenomenon.

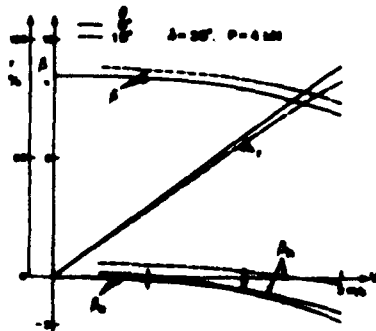


Fig. 16 Effect of running velocity on the side slip angles and r .

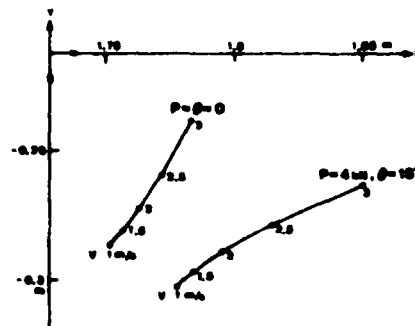


Fig. 17 Effect of running velocity on the position of turning center.

Fig. 17 shows the variation of the turning center with the value of running velocity. When $P = \theta = 0$, i.e. at the running without traction, the turning center moves toward the frontward of the tractor. It is shown as a results that the ruts of front wheels and rear wheels comes closely together when the running speed is rather high in this test condition using the test tractor. When the tractor runs with a certain traction the position of turning center moves away from the tractor. This is caused by the increase of the side slip angles due to the increase of the centrifugal force by high velocity.

EFFECT OF ROAD CONDITION ON TURNING BEHAVIOUR

The friction coefficient μ between the tire and the ground has a very important role to determine the maximum cornering force as equation (12). Therefore, when the friction coefficient μ is small, the upper limit of the cornering force becomes low, and when the traction P acts, the load of the front tires decreases due to the weight transfer. So that the front part of the tractor slips outward intensively. Fig. 18 shows this tendency. In this test condition the side slip angle of the rear axle center β_h changes hardly.

Fig. 19 shows that the position of turning center moves away from the tractor due to the reason mentioned above, when the friction coefficient μ becomes small.

The coefficient of rolling resistance ρ and the slippage constant K' have seldom effect on the side slip angles and the yaw angular velocity.

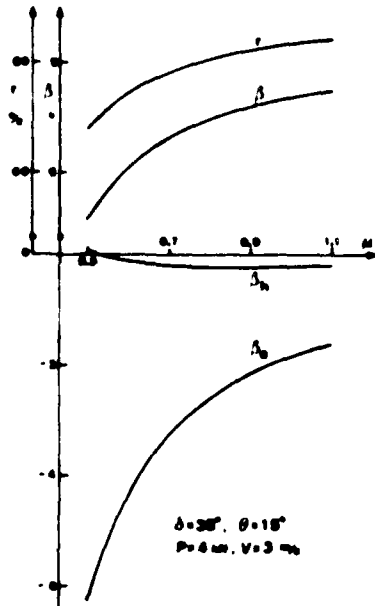


Fig. 18 Effect of frictional coefficient on the side slip angles and the yaw angular velocity.

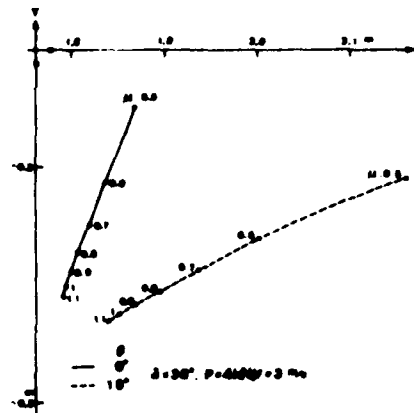


Fig. 19 Effect of frictional coefficient on the position of turning center.

SUMMARY

The turning behaviour, especially the side slips of the front and rear parts of the articulated frame steering tractor, was theoretically formulated, when it has a traction with arbitrary traction angle.

The formulated equations of motion were solved numerically by Runge-Kutta-Gill method as the initial value problem. The running trace of the tractor, which was calculated by this numerical method, was considerably well coincident with the measured running trace.

Based on this certified simulation theory, effects of some factors, for instance the position of bending point, the position of the center of gravity, traction, traction angle, running velocity and friction coefficient,

on the turning behaviour were shown graphically.

REFERENCES

- [1] A. Oida; Geometrische Spur eines Knickschleppers, *Grundlagen der Landtechnik*, Bd. 28, Nr. 5, 1920-196, 1978.
- [2] P.A. Dudzinski; Problems of turning process in articulated terrain vehicles, *J. Terramechanics*, Vol. 19, No. 4, 246-256, 1983.
- [3] A. Oida; Turning behavior of articulated frame steering tractor (Part 1) - Motion of tractor without traction -, Under contribution to *J. Terramechanics*.



A TRACKED VEHICLE TEST PLANT FOR THE SIMULATION OF DYNAMIC OPERATION

INGOBERT C. SCHMID
UNIVERSITY OF THE GERMAN ARMED FORCES, HAMBURG

ABSTRACT

In 1982, a modern test plant was taken into operation at the University of the German Armed Forces in Hamburg, which has very good dynamic properties that make it possible to simulate not only rolling resistance, but also the inertia of vehicle mass and the turning resistance of a tracked vehicle. Herewith, the dynamic loads of real vehicle action on the road and in the terrain can be run on the test stand, true to reality, as it has not been feasible on power test stands employed so far.

The test stand conception is presented and functions are explained. The fundamental principles for performance lay-out of the test stand for tracked vehicles are pointed out, referring specially to the requirements to be met for simulation of acceleration and turning conditions. The applications for testing are discussed, and several versions of control systems are presented for different modes of operation.

INTRODUCTION

In the past, many attempts were made to replace road and terrain testing of the performance of tracked vehicles by simulators. On several test stands in use, steady-state conditions can be realized (e.g. at TACOM, Detroit). However, dynamic testing, especially simulation of inertia forces and turning resistance, is not possible thereon. Dynamometer Trucks for towing and braking vehicles on the road or in the terrain were developed for the Bundeswehr Erprobungsstelle 41 and for Yuma Test Station. But with these tracked vehicles indoor tests are impossible. For indoor testing, several studies were made, for instance of roller-type dynamometers, but none of them was materialized, due to cost and technical reasons.

A most promising concept was proposed in 1976 by the University of the German Armed Forces [1] and developed by the Brown Boveri Company in close cooperation with the user. This test stand installed in Hamburg was started up in 1982. In the meantime, the test stand system has met with much approval. In the USA, it has become known under the designation of "Power and Inertia Simulator" or PAISI.

AD-P004 305

TEST STAND FACILITIES

Figure 1 shows the test stand with the tank JAGUAR of the GERMAN Armed Forces as the test vehicle. The test stand consists of two power units to which the vehicle sprockets are combined by means of cardan shafts. The tracks have been taken off. The vehicle is operated here by the driver just the same as in actual driving. That means he accelerates, he switches the gears, he brakes and he steers.

The vehicle engine drives, the two test rig power units brake, that is to say they absorb the energy. Under particular driving conditions, the power flux can be vice-versa, which means that the power units will then be driving.

Thus the test rig machines must be able to drive, as well as to brake, and furthermore, they must be able to rotate in both directions. To put this into practice, direct-current generators, so-called dc-dynamometers, are most suitable. They are thyristor controlled.

An essential part of the test rig unit is an adaptive gear box, suitable to adapt torque and speed of the generator to the test vehicle. Between the adaptive gear box and the generator, there is the torque measuring shaft.

The test hall is a sound-proof room with a 12-ton-crane, Figure 2. The vehicle is clamped on a rigid and heavy foundation. The foundation mass is approximately 1600 tons. The necessary cooling air is provided by a high-capacity blower (150 kW), via a scoop. The exhaust gases are collected at the exhaust pipe by a funnel and escape via a metal hose.

Inside the control room, the control desk consists of two identical halves, showing for each of the power units the same configuration of operating and control elements, Figure 3. From here, the condition of operation of the vehicle tested can be predetermined. The control system which is working in closed loop will then automatically provide the desired torque or the desired speed. Additionally, on the control desk, there are all instruments necessary to observe the values to insure a troublefree test run.

TEST STAND CONTROL

The control system is located in the measurement cabinets, Figure 4. For the total of 32 different modes of operation for which the plant has been designed, considerable electronics is required. For some particular cases, an external hybrid computer governs the test rig control system. Speed and torque of the power units can be controlled for each unit or for both units in combination. Thereby, different modes can be realized:

Steady-state Control

Needless to emphasize, steady-state operating conditions can be realized with the test stand. To that purpose, the torque or the speed must be kept at a constant level.

$$n_{\text{desired}} = \text{const.} \quad (1 \text{ a})$$

$$M_{\text{desired}} = \text{const.} \quad (1 \text{ b})$$

These modes are needed to measure vehicle drive characteristics. Of the two possibilities, the speed control is mostly preferable, because it allows a more stable setting of operational points than a torque control does: In view of the flat curve of the combustion engine's torque characteristics, difficulties may arise when trying to maintain with torque control a determined load point at a constant speed.

Programmed Control

Alternatively, control can be based on a desired value being variable with the course of time:

$$n_{\text{desired}} = n(t) \quad (2 a)$$

$$M_{\text{desired}} = M(t) \quad (2 b)$$

Herewith, the locomotion and load programs can be assessed, and that is where the advantages of the test stand become evident.

Motion Resistance Simulation

An even higher requirement can be met by simulating the motion resistances, and that in a way to obtain the loads as in real locomotion, dependent on any travelling condition.

The total resistance can be expressed by a function as follows:

$$T = a_0' + a_1' \cdot v + a_2' \cdot v^2 + b' \cdot \frac{dv}{dt} \pm C(R, v) \quad (3)$$

Therein $(a_0' + a_1' \cdot v + a_2' \cdot v^2)$ represent rolling resistance, slope resistance and air drag, whereas b depends on the mass inertia, and C refers to the turning resistance (v means driving speed, R is the radius of curvature).

The total resistance is split to the two sprockets. Thus the torques at the sprockets are

$$\begin{aligned} M_I &= a_0 + a_1 \cdot n_I + a_2 \cdot n_I^2 + b \cdot \frac{dn_I}{dt} + C(R, n_I, n_{II}) \\ M_{II} &= a_0 + a_1 \cdot n_{II} + a_2 \cdot n_{II}^2 + b \cdot \frac{dn_{II}}{dt} - C(R, n_I, n_{II}) \end{aligned} \quad (4)$$

(n is the rotational speed at the sprockets.)

It should be noted that the sign of $+$ or $-$ before C is opposite at the two sprockets. Simulation of rolling resistance, air drag, and slope resistance on vehicle is well known to be general state of the art. However, simulation of vehicle inertia as practised in the way reported here, and above all simulation of the turning resistance of tracked vehicles, has not been realized so far, but is single in the test stand presented here. Therefore, some considerations must be added as to simulation of the acceleration resistance as well as of the turning resistance.

SIMULATION OF TURNING RESISTANCE

As is known, tracked vehicles are steered by a higher speed at the outer track and a lower speed at the inner track, viewed from the center of curvature. Hereby, a turning resistance arises - a yawing torque - which must be overcome by an additional driving force at the outer track and by a braking force at the inner track. When simulating a curve on the test rig, the two sprockets must accordingly take up different torques at different speeds. To give an example, Figure 5 shows the torque taken up by each sprocket, depending on the rolling speed at various values of the radius of curvature. This diagram was calculated for a 43-tons tank (engine performance 610 kW, superpositioning-steering-gear box) on the road. The rolling resistance was considered to be independent from driving speed, the air drag was neglected. For calculation of the turning resistance, a relatively simple model [2] was used.

As can be seen, in circular motion with growing speed the torque at the outer sprocket increases and reaches a multiple value as compared to the torque in straight-line motion. The speed of the vehicle on a radius, however, can increase no further than to a point where the performance limit of the tank drive will be reached.

As the torque is increased at the outer sprocket, a reduced torque will arise at the inner sprocket, which will become negative when the radius drops. In that case, the inner sprocket has a braking effect.

Those torques - which are provided by the tank drive - must, in case of simulating a curve on the test stand, be counteracted by the test rig unit, as is indicated in equation (4) by the term of $\pm C$.

In the easiest case, the turning resistance can be set manually at the potentiometer of the motion resistance simulator. This is, however, not satisfactory in a driving simulation. A better possibility is the computer input of the turning resistance as a diagram of characteristics (e.g. Figure 5). This requires the availability of measured or calculated characteristics which are, however, valid only for determined vehicle data and fixed road or terrain conditions. It has, therefore, been envisaged for test stand simulation to establish the turning resistance by the aid of an analytical model of general validity, e.g. [3], [4], in on-line operation.

SIMULATION OF INERTIA OF VEHICLE MASS

In the case of battle-tank test stands, the inertia of the vehicle mass has not yet been simulated. It could for instance be realized by flywheels. Due to the substantial tank mass, however, they would have to be very large. It would then probably become necessary to provide a flywheel set with removable rotary masses to allow an adaptation by steps to the tank mass in question. But this would be quite expensive and would involve problems in simulating steering conditions. Due to changes of sprocket speed during steering, inertia forces would be induced which do not occur in reality.

Therefore, on the test stand to be considered, the mass inertia of the tank is simulated not by mechanical flywheel masses, but by the electrical generators. This involves the need of an equivalent power to be available at the test rig. This power requirement is reduced by the fact that the test rig unit has a certain basic inertia in terms of its mechanical inertia θ_{pu} so that only the difference up to total vehicle inertia

must be supplied as an electrical supplementary torque M_s on each power unit:

$$M_s = [\theta_v - \theta_{PU}] \cdot \frac{2\pi}{60} \cdot \frac{dn}{dt} \quad (5)$$

where θ_v Inertia of the vehicle simulated (50 %)
 θ_{PU} Inertia of a power unit
 related to the interface between test rig
 and unit under test

Equation (5) indicates that generation of the supplementary torque M_s involves a differentiation of the rotational speed signal n . However, in this procedure, the possible accuracy is not too good. Furthermore, feeding back the signal in a closed loop control will result in problems with regard to stability. Consequently, the control circuit is sensitive to oscillations. A certain damping could be helpful, but this would be unfavourable for obtaining a fast dynamic response, as it is necessary to simulate mass inertia.

TEST STAND DYNAMICS

The dynamic behaviour of the test stand includes the

- dynamic response to desired changes of torque or rotational speed
- the mechanical and electrical oscillations of the test stand system, which are, of course, not desirable.

When optimizing both items, problems will arise because there is a certain conflict of goals. However, the realisation of a fast control at fairly low oscillations has become possible by the development of active-damping electrical networks [5] that were harmonized with the mechanics of the test stand.

Figure 6 shows an example for the dynamic quality achieved. It can be seen that the torque follows the desired value quite well, when the desired torque increases from 30 to 50 % of its maximum within 50 ms. In the case of increasing the desired value within 20 ms, the actual value is overshooting to a certain degree. A slower increase can be followed more accurately. Considering real acceleration conditions, the behaviour demonstrated is judged to be sufficient.

Analyzing the oscillations by considering the transfer function, it could be found that the control system is capable to control the test stand up to 10 Hz. Torsional oscillations of the test stand are kept within allowable limits by adaption measures at the control system and at the mechanical system.

TORQUE MEASUREMENT

The accuracy of measurement is essential not only for the precision of the result itself but also for the test stand control in a closed circuit. While for the speed measurement at the two power units rotational speed generators are used, which do not involve any problem, the measurement of the torques is carried out by means of torque measuring shafts (Hottinger F 30 TN 10 kNm) arranged between dc-generator and adaption gear box.

Insertion at that place has the advantage that, when supposing equal test powers, the torques will be of the same order of magnitude for all test stand versions. (The test stand has been designed as a system of modules, allowing by various combinations of the testing components different additional test stand versions, such as test stands for engine, gear box, torque converter, vehicle brakes). It is, therefore, not necessary to exchange the measuring shaft for adapting the measuring range to the requirements of each case. One accepts, however, that the losses of the test stand gear box must be eliminated by a compensating circuit. There is no problem as the losses show regularity, Figure 7. Thus an accuracy of the torque measurement of at least 0,5 %, referred to the final value, will be achieved, Figure 8.

PERFORMANCE LAY-OUT

The performance requirement of the tank test stand results from the power of the vehicle drive train to be tested. It must be considered that the engine power is split to the two sprockets. Figure 9 shows torque versus speed characteristics at each sprocket, depending on the gear box steps, for a tank LEOPARD I (engine power 610 kW). Gearing losses ($\approx 20\%$) are hereby neglected, and the increase of torque due to the hydrodynamic torque converter is not recorded.

Each of the two test stand power units has to counteract the power at the sprockets. Therefore, the characteristics of a power unit must cover the torque and speed range. In the present case, this is fulfilled by dc-generators of a nominal power of 400 kW each, in combination with the test stand gear boxes. Gear box step A 1 allows high torque, gear box step A 2 high speed.

The torque versus speed characteristics considered so far are true for even power split to the sprockets. However, in a curve, the load distribution will become asymmetrical. As it was indicated in Figure 5, the torque at the outer sprocket, viewed from the center of curvature, can increase to high values and exceed the power unit margin.

For this reason, simulation of the turning resistance of the vehicle LEOPARD I would need 600 kW at each sprocket. Due to the fact that the turning resistance will occur for short periods only, it is not necessary to install dc-generators for 600 kW, because the 400 kW units may be overloaded to 600 kW for a limited time. The decisive limiting factor is the temperature of the armature winding, which then must be measured and observed, Figure 10.

Overloading makes also possible an increase of the driving torque by means of the torque converter, because its action is of short time as well. The same applies to braking of the vehicle. Therefore, braking tests are also possible on the test stand, up to a power of 600 kW at each sprocket.

The considerations above should line out that for a new test stand for tracked vehicles, the maximum engine power is not the absolute dimensioning factor. There shall be emphasized that, in spite of substantial gearing losses ($\approx 20\%$), the peak power transmitted at the outer sprocket in a curve can exceed even the drive performance gross value. At this sprocket, there can be transmitted more than the engine power, which is only possible because at the inside track of the curvature, power is taken in from the ground, and this power is transmitted by the steering gear to the outside of curvature. The test stand units must meet these performance requirements.

The performance rating of any new test rig must be based on the power requirements with the special data of vehicles to be tested and under consideration of the duty conditions to be simulated.

The user must, therefore, define the vehicles to be tested, as well as the terrain conditions and the missions to be simulated, thus enabling the manufacturer of the test rig to take care of an adequate dimensioning of performance. In view of the dynamic control of the test rig, a certain power reserve should be included, which will be required to provide dynamic behaviour of the test stand.

MODES OF OPERATION

The test stand with its multiple control versions allows several possibilities of testing and simulation, which are indicated in the following:

Steady-state Control

The easiest mode of operation is a steady-state test run with constant control. In this version, the operator at the control desk sets the desired values of the rotational speeds at the sprockets by means of potentiometers, whereas the driver provides the load, i.e. the desired torques. The test rig control system regulates the sprocket speeds in a closed loop, Figure 11.

This kind of operation is suitable for reaching step-by-step various operational conditions, in order to measure in steady state the data of torque, performance, fuel consumption, exhaust gas, noise emission, and so on. In this way, the characteristic curves can be developed. Although this is possible with conventional test stands, the advantage of the power test plant in question is a quicker and more accurate assessment of the operational points due to the control electronics. The diagrams of characteristics which have to be established point by point can thus be rapidly compiled.

Programmed Control

A larger scope of possibilities is offered by speed and torque control based on preset desired values changing as a function of time, e.g. according to the load conditions of a real locomotion. This means a repetition of load programs.

To obtain such a program, the torques at the two sprockets and the rotational speeds must be measured in the field during the fulfillment of the vehicle mission. The signals recorded on a tape represent the desired values which are preset to the test stand control system, Figure 12. The test rig power units are torque-controlled. Contrary to the previously considered cases, the driver is, however, replaced here by a driving actuator, an autopilot, which operates the vehicle. This driving actuator has the function of controlling in closed loop the speed at the two sprockets in such a way that the measured speed from the tape will be maintained.

Of course, with this kind of test rig controlling it is also possible to carry out any desired program of load and speed. For example, a test program for checking the various functions of engine, gear box, and steering gear may be carried out. Therein the selection of the desired points of operation or the passing through of determined courses of load, is controlled automatically. Therefore, the test program will be carried out in

a minimum of time resulting in a minimum period of utilization of the test rig and, consequently, in greater testing capacity of the test plant.

For time-consuming endurance tests, as is, for example, the 400 hours NATO test or the 24 hours battle-day, it seems hardly advisable to use tape recordings requiring many hours of run. Here, the use of statistical programs will be more suitable.

Such programs can be obtained by measuring torque and speed to be evaluated as a histogram. To that purpose, the range of speed and the range of torque are subdivided into different classes, Figure 13. Every operational state being characterized by a torque and a rotational speed belongs to a determined cross-square of speed and torque. Every point on the histogram marks that 1% of the time of operation is attributed to the square in question. From that kind of histogram you will be able to see at once how often and how long the different operational states occur. This depends, of course, on the terrain and on the tactical task. The example given here is the histogram for engine load during a driving test, but, of course, you can record in the same way the histograms at the two sprockets during a military maneuver.

From such histograms obtained from actual field practice, programs for operation of the test rig can be generated, Figure 14. The statistical data are reconverted to values of torques and speeds as a function of time, which are used as desired values for controlling the test rig. The desired values do not correspond to the recorded course exactly; however, from the statistic point of view, they are equivalent to reality. From the programs for different vehicle missions, a representative total program for a long range mission can be derived. It is replayable over an unlimited test period on the test rig, without repetition of uniform phases of load and speed. This mode of operation has not been executed so far, but it is feasible.

Driving Resistance Simulation

In the case of driving resistance simulation, the operator at the control desk is replaced by a driving resistance simulator, Figure 15. The latter computes the desired torques corresponding to the resistances, dependent on speed, acceleration and - if applicable - radius of curvature.

The driver in the vehicle actuates the accelerator, the gear stick, the brake; then the driving resistance as the external load occurs automatically just like under driving conditions on the road. Of course, the factors of a_0 , a_1 , a_2 and b must be preset at the driving resistance simulator, according to the vehicle and terrain data. These parameters can, however, be changed during the test run, for example to simulate the changing inclination of the road. This can be commanded to the test stand control system from outside by an additional driving program.

As has been discussed before, in an easy case, the turning resistance is controlled by hand. For circular motion, a fixed value is then preset; only the influence of speed and acceleration on driving resistance is simulated. By presetting turning resistance characteristics according to characteristic curves, such as in Figure 5, for instance by means of digital function generators, it is possible to simulate the turning resistance for a given vehicle that operates on a given road or on homogenous terrain.

In a complete driving resistance simulation which comprises in particular the turning resistance as a complex analytical model, the driving resist-

ance simulator of the test rig is overburdened. Then it will be useful to replace the driving resistance simulator by an adequate program in an external computer, Figure 16. For the reason of accuracy, it will then be necessary to work with digital output. Therefore, signal converters D/A and A/D are to be used between the analog control systems of the test stand and the digital computer. The computer treats the speed data and calculates in an on-line process the desired values for the torques at the two sprockets. Those desired values are in general not constant but are subject to permanent changes, and the test rig control system in a closed loop makes sure that on the test rig, the real values of the torques follow the desired values as accurately as possible.

In this mode of operation, the dynamic behavior of locomotion with accelerations and circular path can be simulated. The driver can freely choose the speed. The only restriction is that he must follow a given course providing a fixed dependence of the rolling resistance parameters on the distance travelled. This does not meet the requirements of cross-country locomotion, in which the course may be chosen in any direction of the whole area.

The final goal of development for the test stand controls is, therefore, locomotion with free choice of speed and free choice of course in the terrain. To that purpose, the driver must be able to see the terrain: This is shown on a monitor either by the visual scene from the vehicle or by a map of terrain on which the driver sees his own vehicle. Selection of speed and driving direction is up to the driver. The computer determines the coordinates of the tank on the map, calculates the driving resistance, and considers at the same time the terrain parameters changing with the coordinates, such as inclination or solidity of the ground. Those parameters of terrain must have been stored in the computer as a map of terrain. This kind of simulation of a freely selectable cross-country course offers possibilities of investigating the dynamic behavior of the tank also from the tactical point of view.

In driving simulation, it is a particular advantage that determined vehicle parameters can be changed, thus allowing a clear demonstration of their influence. As an example, it is possible to modify the vehicle mass by potentiometer settings and to investigate in this manner the influence of the specific performance (kW/tons) on mobility.

It should be noted that the development of the possibilities of simulating the turning resistance on the test stand has not come to a close so far.

Testing Possibilities

The spectrum of possibilities for test and simulation with steady-state control, programmed control, and driving resistance simulation has been compiled in key points, in Figure 17. In view of its high flexibility and the good simulation of dynamic loads of operation, the test stand system PAISI is adequate for a large scale of tasks in research, in the development of drive trains, in trial work as well as for inspections of acceptance after a repair.

ACKNOWLEDGEMENTS

The development of the test plant has been carried out by the Brown Boveri Company (BBC), Mannheim, West Germany, in close contact with the Automotive Institute at the University of the German Armed Forces, Hamburg. The author thanks his assistants, Dipl.-Ing. W. Ehlert and Dipl.-Ing. G. Fietz, and is very grateful to the chief of the BBC test stand division, Dipl.-Ing. H.W. Weyland and his staff for their good and engaged cooperation.

REFERENCES

- [1] Schmid, Ingobert: Das neue Laboratorium für Kraftfahrwesen der Hochschule der Bundeswehr Hamburg, ATZ 84. Jg. Nr. 1/1982
- [2] Weissbeck, H.: Simulation der Triebwerksbeanspruchungen eines Gleiskettenfahrzeugs auf der Leistungsprüfanlage, Diplomarbeit HSBw Hamburg 1981
- [3] Kitano, M., Jyozaki, H., Kuma, M.: An Analysis of Steerability of Tracked Vehicles, ISTVS 6th International Conference, Vienna 1978
- [4] Baladi, G.Y., Rohani, B.: A Mathematical Model for Terrain-Vehicle Interaction for Prediction of the Steering Performance of Track-laying Vehicles, ISTVS 6th International Conference, Vienna 1978
- [5] von Thun, H.-J.: Dynamic Improvements of Controlled Multi-Machine Test Stands, 4th International Symposium of Engine Testing Automation (ISATA), Naples 1975

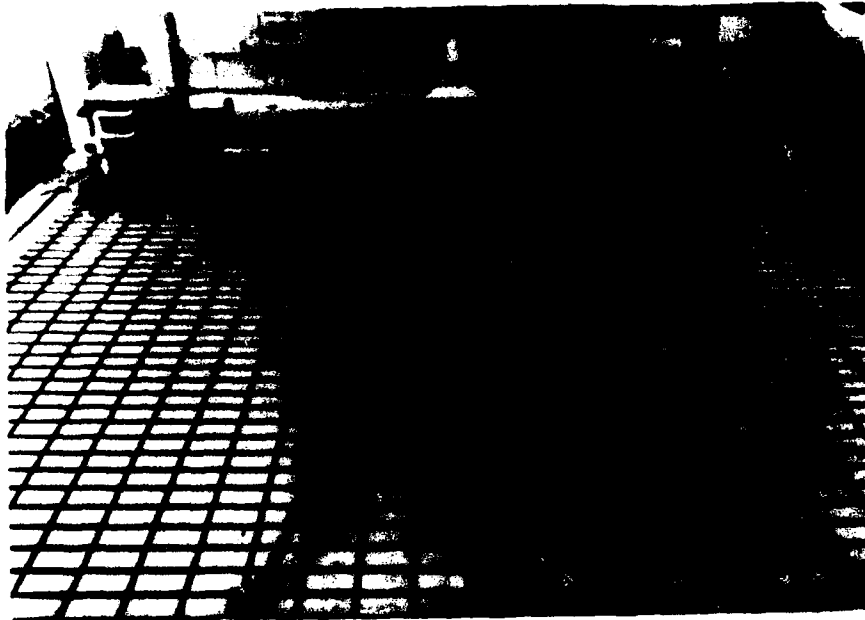


Fig. 1: Power and Inertia Simulator (PAISI)
with a test vehicle

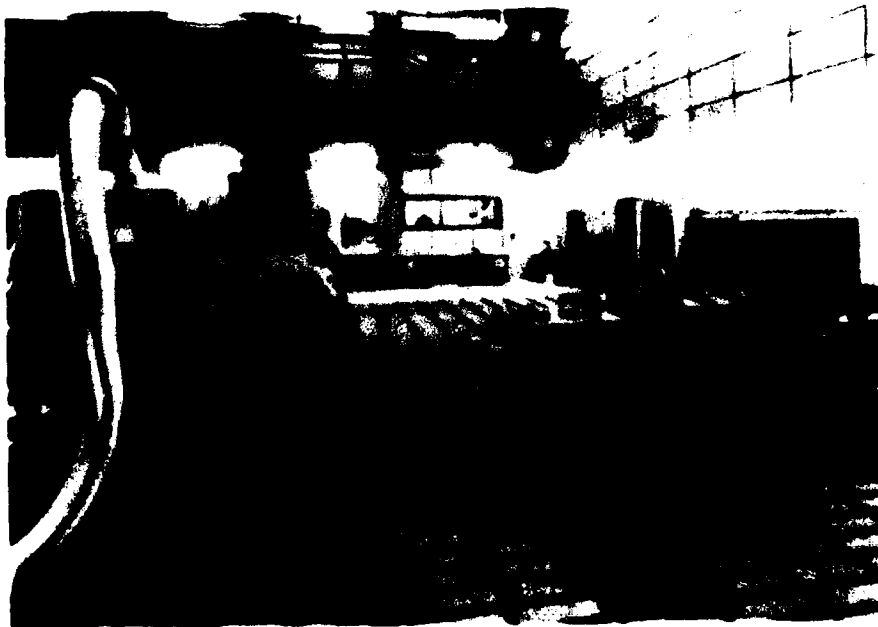


Fig. 2: Operating hall of the test stand



Fig. 3: Control desk and view to the test stand



Fig. 4: Control room with the electronics of the test stand

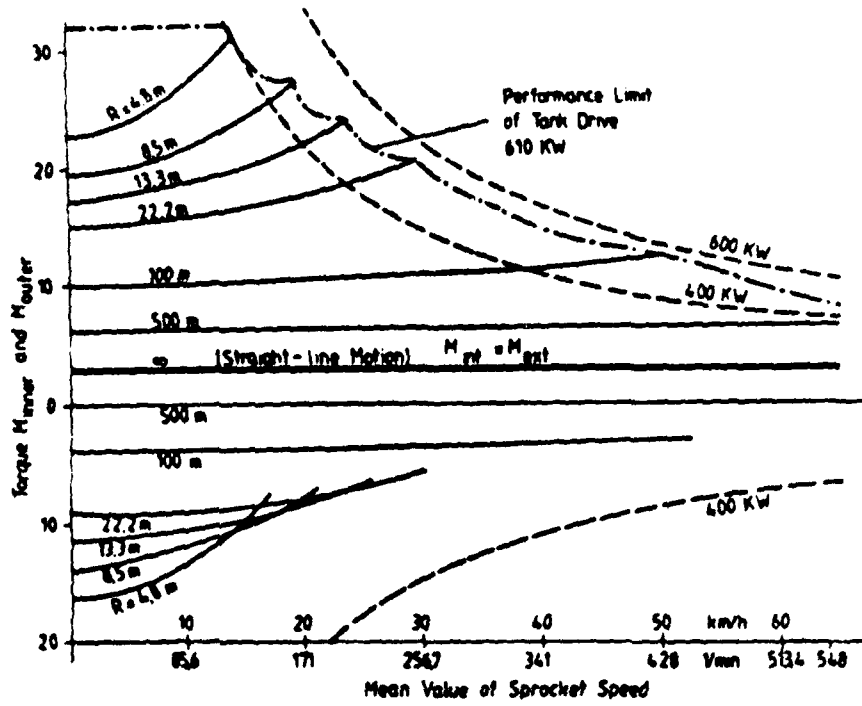


Fig. 5: Torques at the sprockets of Battle Tank LEOPARD I in circular motion (radius R) on the road

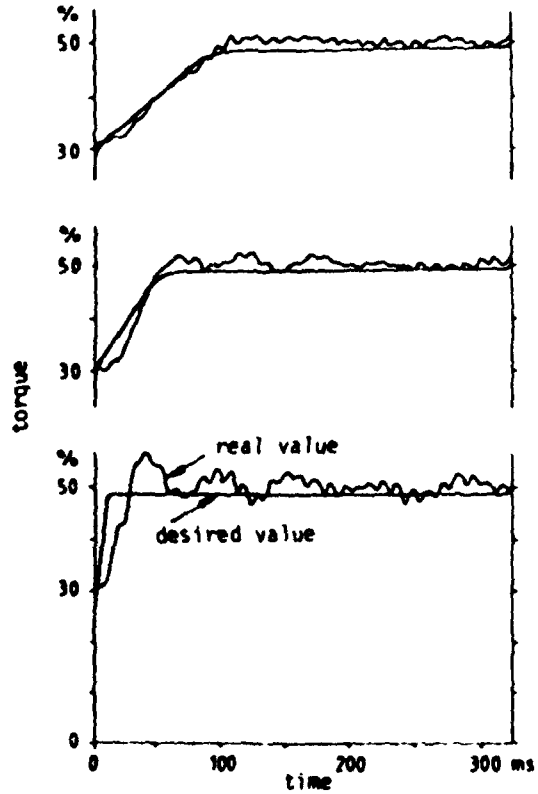


Fig. 6: Course of torque (desired and actual value) at a sudden increase of the desired value

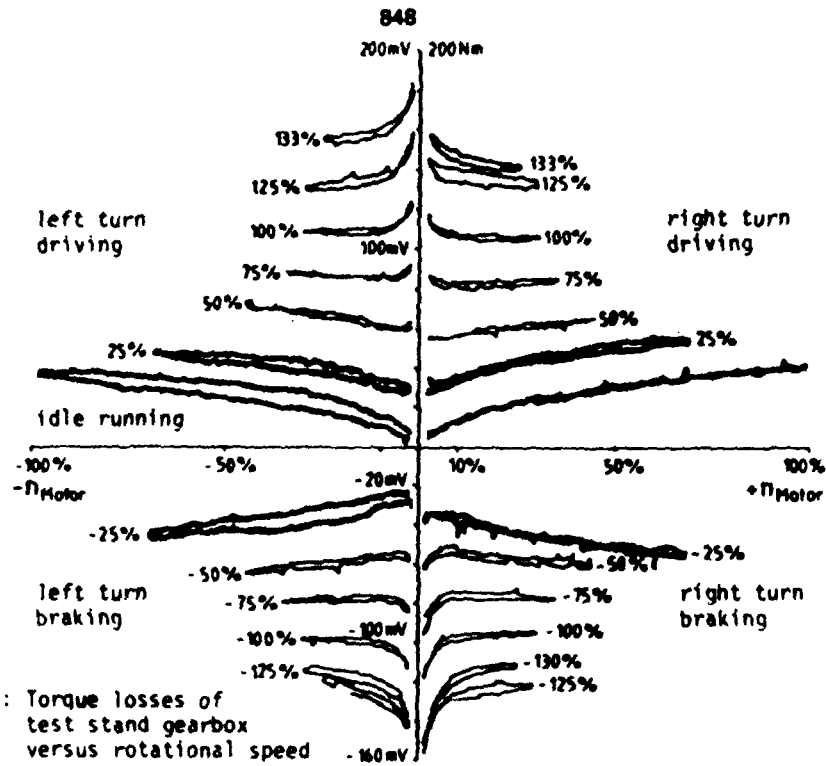


Fig. 7: Torque losses of test stand gearbox versus rotational speed

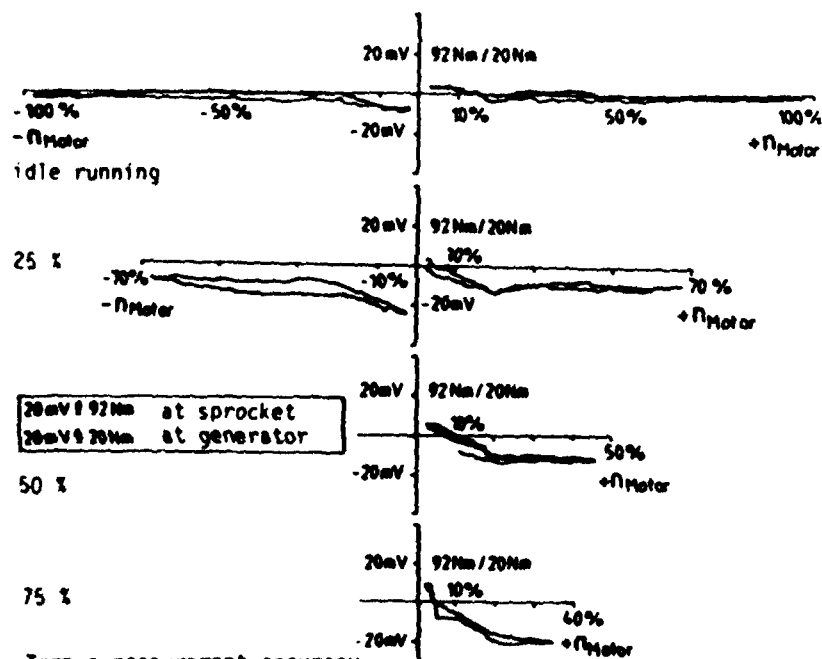


Fig. 8: Torque measurement accuracy considering losses of the test stand gearbox after compensation for different steps of load

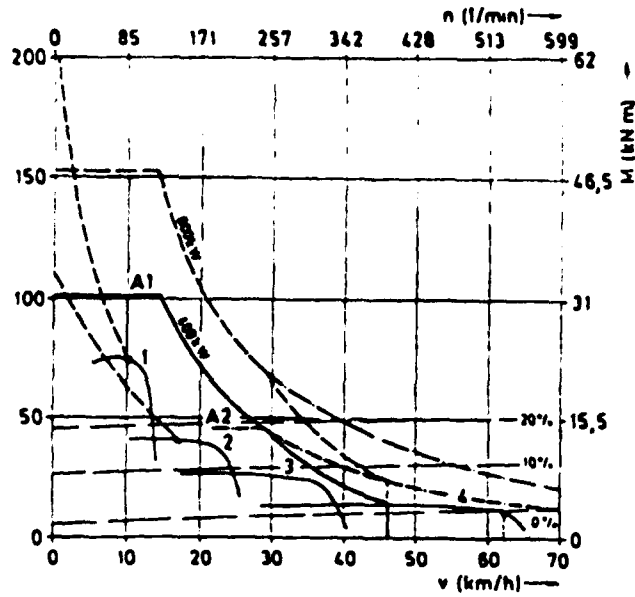


Fig. 9: Drawbar pull/torque - speed characteristics at each sprocket of a Tank LEOPARD I

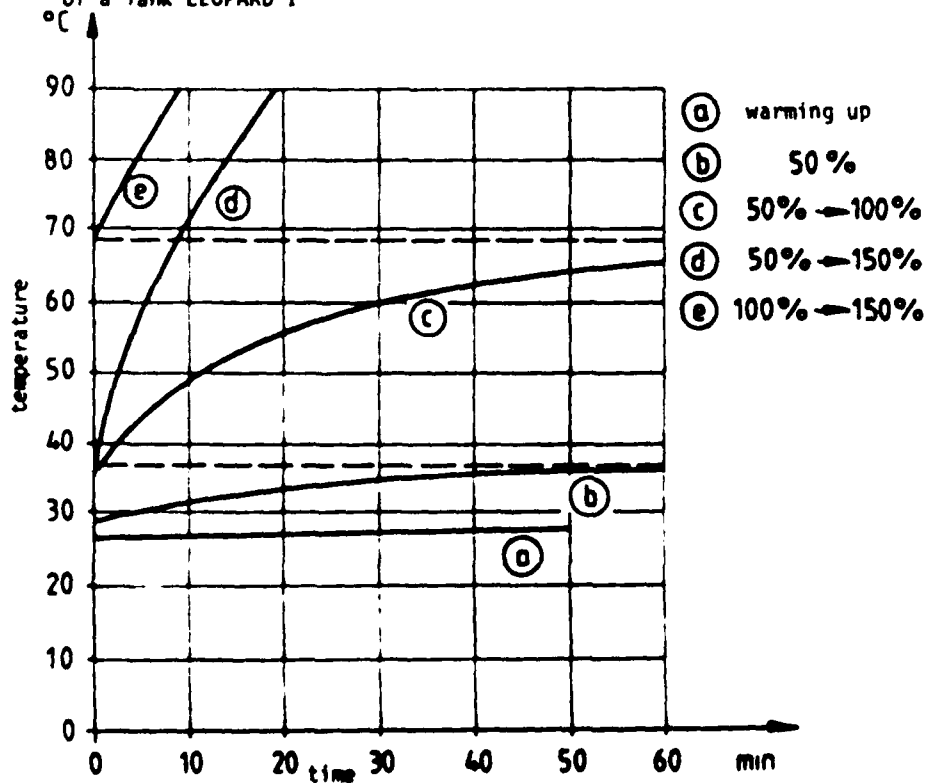


Fig. 10: Temperature versus operation time of the dc-generator during overloading

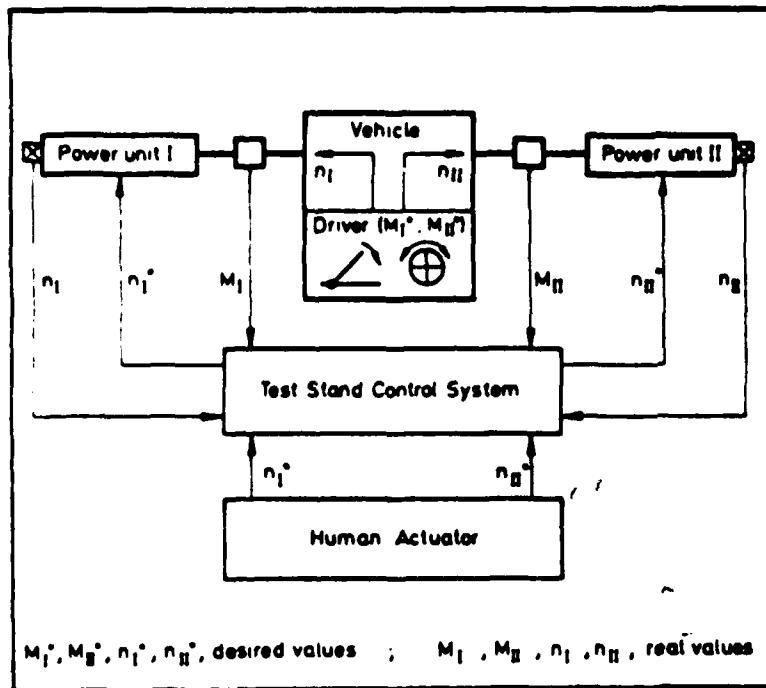


Fig. 11: Steady-state control of test stand

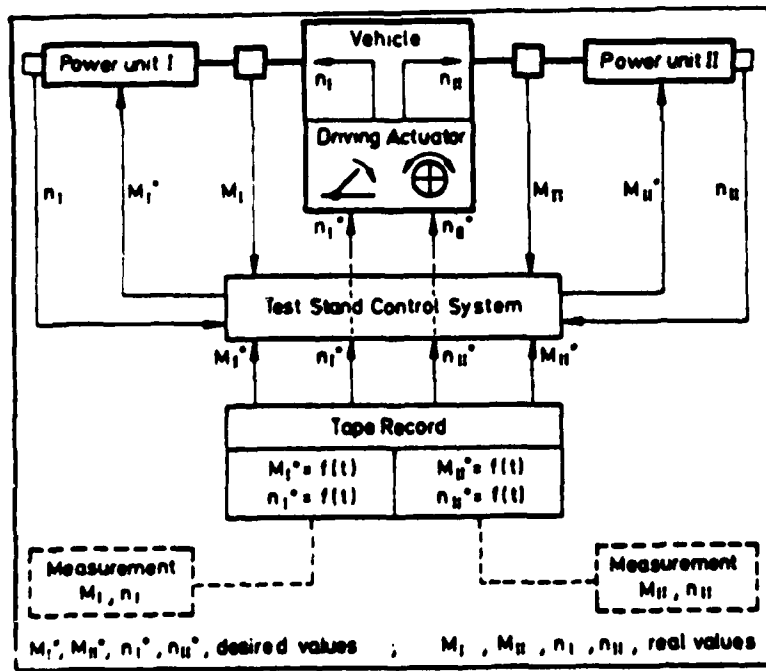


Fig. 12: Programmed control of test stand

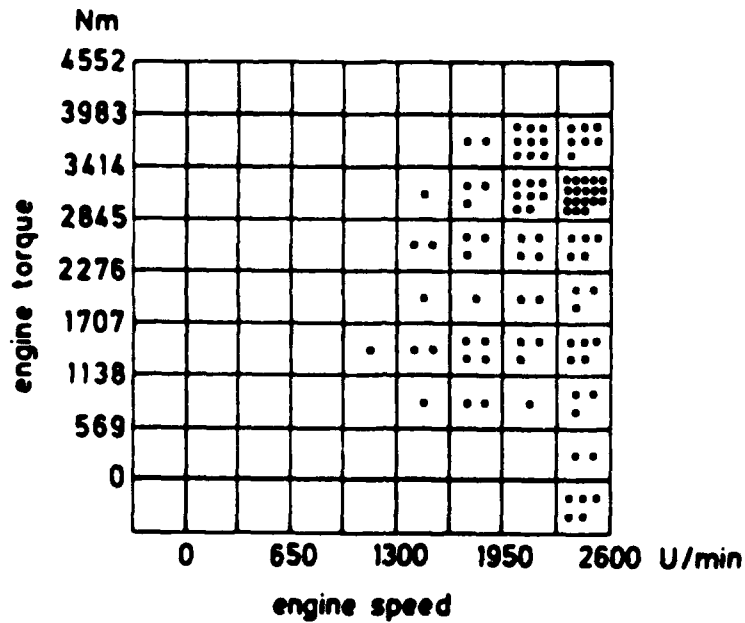


Fig. 13: Example of a load - speed collective (histogram)

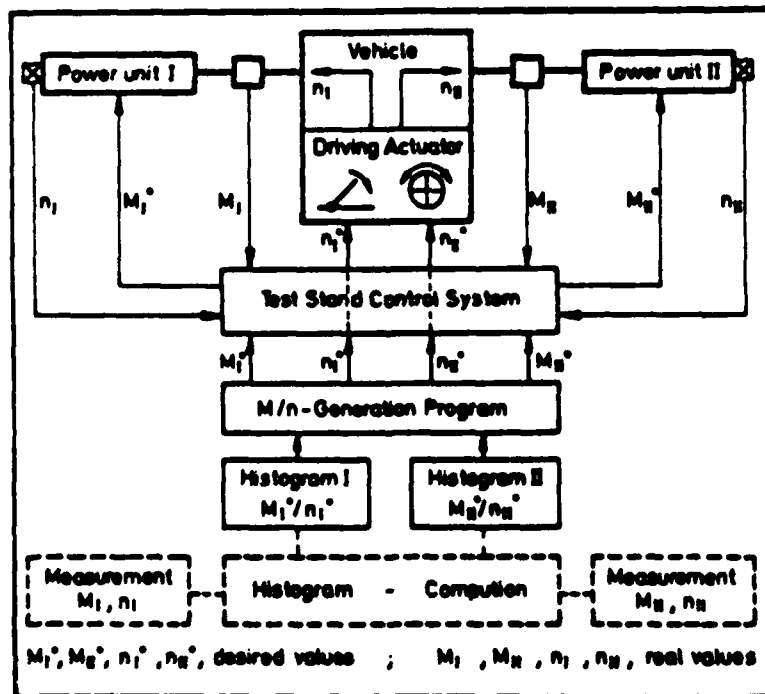


Fig. 14: Generation of stochastic load and speed program (histogram)

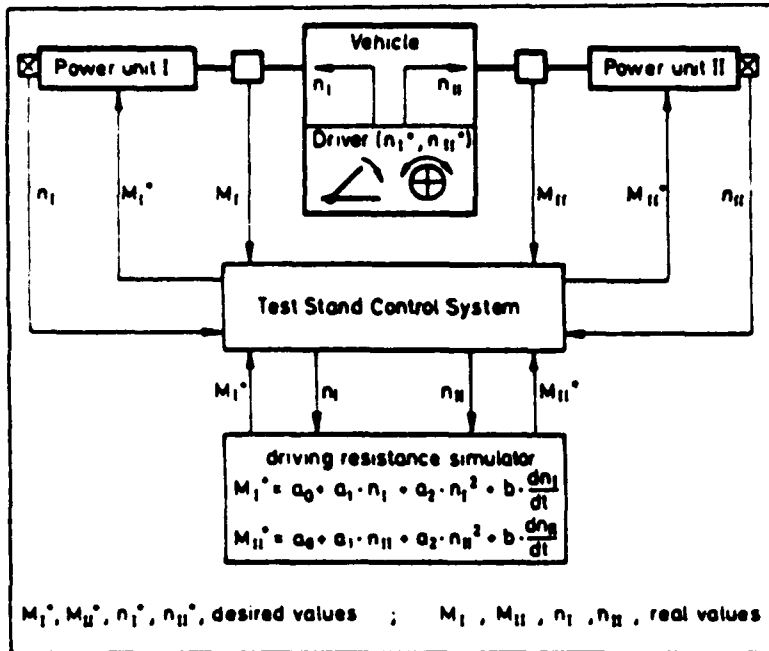


Fig. 15: Driving resistance simulation (without turning resistance)

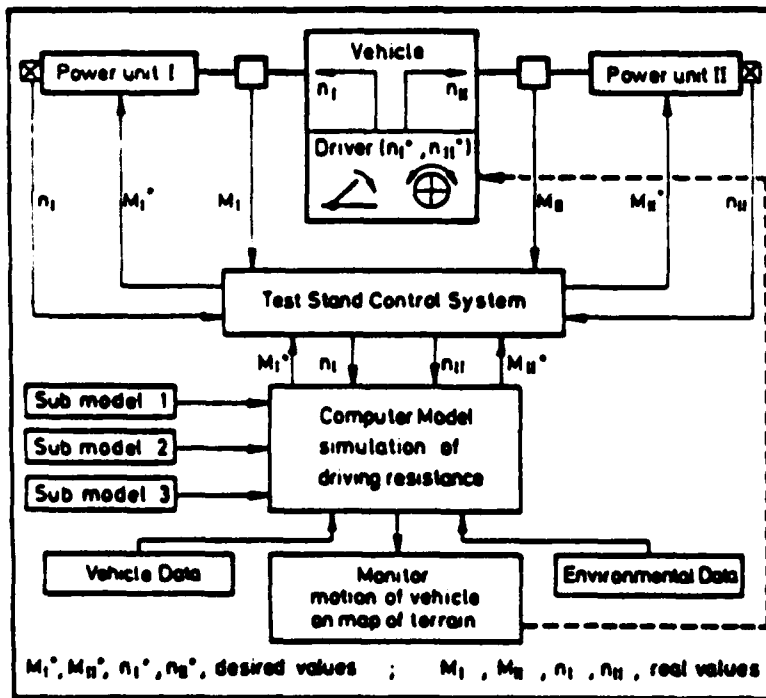


Fig. 16: Complete driving resistance simulation

TESTING AND SIMULATING POSSIBILITIES OF THE
POWER AND INERTIA TEST STAND
(TANK TEST STAND "PAISI")

<p>CONSTANT CONTROL</p> <p>$n = \text{const} (M = \text{const})$</p>	<p>PROGRAMMED CONTROL</p> <p>$M = f(t), n = f(t)$</p>	<p>DRIVING SIMULATION</p> <p>$M = a_0 + a_1 \cdot n + a_2 \cdot n^2 + b \cdot \frac{dn}{dt} + c$</p>
<p>OPERATIONAL POINTS</p>	<p>LOAD CHARACTERISTICS</p>	<p>SIMULATION OF MISSION</p>
<p>CHARACTERISTICS OF PERFORMANCE</p> <p>CHARACTERICS OF TRACTION</p> <p>VERSUS SPEED</p> <p>CHARACTERISTICS OF FUEL CONSUMPTION</p> <p>CHARACTERISTICS OF EXHAUST GAS MEASUREMENT OF EFFICIENCY</p> <p>NOISE</p> <p>DRIVE TRAINS OSCILLATION</p> <p>STARTING BEHAVIOUR</p>	<p>FUNCTIONING TESTS</p> <p>ENDURANCE TESTS</p> <p>MECHANICAL AND THERMICAL LOADS ON ENGINE, CONVERTER, GEAR BOX, STEERING GEAR, AIR AND OIL HEAT EXCHANGER</p>	<p>DYNAMIC DRIVING</p> <p>TACTICAL DRIVING</p> <p>OPTIMIZING OF SYSTEM</p> <p>MAXIMUM SPEED</p> <p>ACCELERATING CAPACITY</p> <p>SLOPE CLIMBING CAPACITY</p> <p>BRAKE TEST</p> <p>FUEL CONSUMPTION VERSUS DISTANCE TRAVELLED</p> <p>EXHAUST GAS EMISSIONS</p>

Fig 17: Spectrum of testing possibilities



PROFILING INFLUENCE ON RESISTANCE AND STEERING FORCES OF FREE ROLLING TYRES
(INFLUENCE OF TYRE TREAD ON RESISTANCE - AND STEERING FORCES OF TYRES)

1. SCHWANGHART UND K. ROTT

INSTITUT FÜR LANDMASCHINEN, TECHN. UNIVERSITÄT MÜNCHEN, F.R. DEUTSCHLAND

Summary

There are numerous publications about forces on tyres acting in or against travel direction, drawbar pull and rolling resistance, but only a few about lateral forces on steered tyres.

A test equipment, which provided a wealth of information of lateral- and travel resistance of front wheels in recent years, has been further developed for testing implement tyres. This setup is mounted rigid on a tractor Unimog and provides measurements of longitudinal and lateral forces on tyre at steering angles from 0° to 30° with different load up to 1,3 t.

To determine the influence of tread on lateral forces of steered tyres there have been made experiments with implement tyres 12,5/80-18 8 PR and a terra-tyre with the same diameter but greater width (figure 4). With five different loads and steering angles from 0° to 30° we measured the lateral force and rolling resistance on following soils: stubble field, cultivated field, meadows, gravel and cornfield after harvest. Every result curve is plotted as a polynomial regression curve (3. degree) using 35 test points for different drift angles and loads (figure 11).

The tyre tread influences the lateral force coefficient especially on meadow and stubble field. The increase is between 25 % to 70 % for profiled tyres compared with unprofiled tyres at 30° drift angle. The deep ribbed tyre generates only small lateral forces at small drift angles but supports the highest forces at greater drift angles. The traction profile running forward mounted gives more lateral forces than reversed mounted. The terra-tyre has more effect on plant covered surfaces than on smooth ones.

The rolling resistance coefficient is with profiled tyres on average 15 % until 40 % higher than with unprofiled tyres. With a drift angle of 15° the coefficient of rolling resistance is 0,15 - 0,22 at gravel, 0,18 - 0,27 at meadow and stubble field and 0,25 - 0,32 at cultivated field.

The results of these investigations enable the designer of off road vehicles to determine:

1. Required front axle loadings for the steering behaviour of tractors (with excentric drawbar pull).
2. Material forces of wheels, axles and tyres.
3. Energy loss by rolling resistance.
4. Steerability and stability of tractors on slope operation.
5. General ride behaviour of tractor (computer simulation).

AD-P004 306

1. Einleitung

In der Geländefahrt und besonders bei landwirtschaftlichen Traktoren und Anhängern gewinnen die abstützbaren Seitenkräfte an gelenkten Reifen eine immer größere Bedeutung [1 - 12]. Beim Traktor werden nicht nur hinten, sondern in zunehmendem Maße auch vorne Geräte angebaut, die erhöhte Anforderungen an die seitliche Abstützfähigkeit der Vorderräder stellen. Ein Beispiel dafür sind frontangebaute Pflüge. Sowohl bei Anhängern am Hang als auch bei angehängten, exzentrisch belasteten Landmaschinen, wie z.B. Rübenroder in der Ebene, müssen große Seitenkräfte übertragen werden. Der Rollwiderstand in Fahrtrichtung soll in allen Fällen klein sein.

Um für die Konzeption neuer Maschinen Anhaltswerte für Seiten- und Rollwiderstandskräfte zu schaffen, wurden diese an Implement-Reifen mit unterschiedlichen Profilen auf verschiedenen Böden bzw. Bodenzuständen gemessen.

2. Versuchsgerät

Bild 1 zeigt die Einzelrad-Versuchsapparatur [2], die in einem starren, hinten an einem Unimog angebauten Rahmen gelagert ist. Das lenkbare Rad ist über eine Halbachse kugelig aufgehängt (Bild 2), so daß es sich frei der Bodenoberfläche anpassen und ungestört einsinken kann. Die Querachse (2), auf der die Belastungsgewichte (14) aufgebracht werden, ist über zwei Membranen (4) im Gehäuse (3) gelagert. Die Seitenkraft quer zur Fahrtrichtung kann mit einer Kraftmeßdose (10) aufgenommen werden. Die Längskraft bzw. der Zugwiderstand wird ebenfalls über eine Kraftmeßdose (11) ermittelt, welche in dem Zugseil (7) zwischen Meßapparatur und Zugfahrzeug eingebaut ist.

Mit dem Gerät können nach Bild 3 bei gegebener Belastung der Rollwiderstand R in Fahrtrichtung und die Seitenkraft S senkrecht zur Fahrtrichtung gemessen werden. Die Kräfte werden über Trägerfrequenz-Meßverstärker und einen UV-Oszillographen aufgezeichnet und auf einem Rechner weiterverarbeitet. Dadurch, daß die gesamte Meßapparatur mit dem Versuchsreifen über den starren Anbau an die Zugmaschine in eine geradlinige Fahrtrichtung gezwungen wird, ist der geometrische Lenkwinkel gleich dem Schräglaufwinkel.

3. Versuche

Die Widerstands- und Seitenkräfte wurden an den vier in Bild 4 gezeigten Implement-Reifen 12.5/80-18 8 PR*) bei einem Luftdruck von 1 bar mit folgenden Profilen ermittelt:

- | | |
|------------------------------|---------------------------|
| a) mit Treibradprofil | (traction profil) |
| b) Profil mit 3 hohen Rippen | (deep ribbed) |
| c) ohne Profil | (nearly ribless) |
| d) Terra-Reifen (breiter) | (terra-tyre) |
| e) Treibradprofil rückwärts | (traction profil reverse) |

*) Die Reifen sind dankenswerterweise von der Firma Continental, die Felgen von der Firma Lemmerz-Werke zur Verfügung gestellt worden.

Der Außendurchmesser der Reifen betrug 987 mm. Die Belastung variierte in fünf Stufen von 1500 bis 8500 N, das ergibt für eine maximale Reifennennlast von 13000 N eine Gewichtsauslastung von 11 % bis 65 %. Der Schräglaufwinkel wurde in Schritten von 5° von 0° bis maximal 30° eingestellt. Die Fahrgeschwindigkeit während des Versuchs lag bei 1,4 km/h.

Die folgenden Bilder zeigen die verschiedenen Versuchsfelder:

Bild 5: Wiese, Bild 6: Stoppelfeld, Bild 7: Acker (gegrubbert) und Bild 8: Kiesboden. Das abgeerntete Maisfeld (ohne Bild) hatte eine glatte, feste Oberfläche.

4. Versuchsauswertung

In Bild 9 sind die Seitenkräfte des Reifens mit Treibrad-Profil in Abhängigkeit vom Schräglaufwinkel aufgetragen. Boden: abgeerntetes Maisfeld. Mit steigender Radlast N wird auch die abstützbare Seitenkraft größer. Die Meßpunkte wurden durch Regressionskurven mit Polynome zweiten Grades verbunden.

Bezieht man die Seitenkräfte auf die jeweilige Radlast, so ergeben sich die Kurven in Bild 10. Hier wurden für den Kurvenverlauf Polynome dritten Grades als Regressionskurven verwendet, da der gemessene Verlauf für bestimmte Böden ein Maximum und ein Minimum aufweist und ein Polynom dritten Grades hierbei eine bessere Annäherung aufweist.

Läßt man eine gewisse, bei Feldversuchen unvermeidliche Streuung der Werte zu, so kann man eine Regressionskurve durch alle Meßpunkte von S/W in Abhängigkeit vom Schräglaufwinkel ermitteln und in ein Diagramm eintragen (Bild 11). Hierbei ist das Ergebnis von 35 Einzelversuchen mit einem Reifenprofil bei fünf unterschiedlichen Belastungen aufgezeigt.

In derselben Weise wurden die Rollwiderstandsmessungen ausgewertet. Bild 12 zeigt den Rollwiderstand in Fahrtrichtung in Abhängigkeit vom Schräglaufwinkel bei verschiedenen Radlasten. Noch enger als bei den Seitenkräften fallen diese Kurven zusammen, wenn man den Widerstand auf die Radlast bezieht (Bild 13). Die Regressionskurve für alle Meßpunkte für ein Reifenprofil auf einem Boden, in diesem Beispiel Maisfeld, zeigt Bild 14.

5. Ergebnisse

Die Bilder 15 bis 19 zeigen den Rollwiderstandsbeiwert der verschiedenen profilierten Reifen auf Stoppelfeld, Wiese, Acker, Kiesboden und Maisfeld. Hiermit läßt sich z.B. der Rollwiderstand der hinteren Lenkräder eines Mähreschers bestimmen. Bild 15 gilt für das Stoppelfeld. Der profillose Reifen hat bei größeren Schräglaufwinkeln den geringsten Widerstand, der umgekehrt montierte Farmerreifen einen größeren Widerstand als der richtig montierte, beide ähnlich dem breiteren Terra-Reifen und der Treibradreifen mit den hohen Stollen weist den größten Widerstand auf. Ähnliches zeigen die Bilder 16 und 17 für Wiese und Acker. Für die Wiese liegt der Rollwiderstandsbeiwert bei Geradeausfahrt ($\alpha = 0^\circ$) unter 10 %, beim Acker höher, bis nahe 20 %. Der profillose Reifen hat wieder den niedrigsten Wert. Entsprechend sind die Rollwiderstandsbeiwerte für Kiesboden und Maisfeld in den Bildern 18 und 19 aufgetragen.

Da in diesen Darstellungen die Kurven nahe zusammen liegen und Unterschiede bezüglich Profilform schwer zu erkennen sind, ist in Bild 20 der Unterschied des Rollwiderstandsbeiwertes der einzelnen Profilreifen zum profillosen Reifen für die fünf Bodenarten in % aufgetragen. Die Werte gelten für 10° , 20° und 30° Schräglauf.

Wiese, Stoppel- und Maisfeld bringen die größeren Widerstandserhöhungen gegenüber dem glatten Reifen, der sehr trockene, gegrubberte Acker und der Kiesboden wirkt vielleicht wie eine mit "Kugeln" bedeckte Ebene, über die sowohl glatte als auch profilierte Reifen leichter hinweg gleiten. In den meisten Fällen weist der breitere Terrareifen den niedrigsten Rollwiderstand unter den Profilreifen auf.

Die seitliche Abstützfähigkeit verschiedener Profile zeigt Bild 21 für das Stoppelfeld. Bei kleinen Einschlagwinkeln sind meist nur geringe Unterschiede zwischen den einzelnen Profilreifen. Bei einem Schräglaufwinkel über 20° kann der glatte Reifen am wenigsten Seitenkräfte abstützen, er "rutscht" über die Stoppeln, das Stollenprofil normal und umgekehrt montiert, verhakt sich mehr in den Stoppeln und der Hochprofil-Reifen erzeugt die größten Seitenkräfte. Sehr hoch sind die Seitenkraftbeiwerte auch auf der Wiese (Bild 22). Dieser Boden "Wiese" ist in diesem Fall ein mit Gras bepflanzter Acker, auf dem das Gras zum Unterpflügen angesät wurde. Das Treibrad-Profil erreichte Werte über 1. Das kann nur so erklärt werden, daß sich das Profil gewissermaßen formschlüssig zwischen den Grasbüscheln verankert. Aber auch der Terrareifen erreicht hohe Seitenkraftbeiwerte. Diese bleiben jedoch konstant, wenn, wie auch beim profillosen Reifen, die gesamte Aufstandsfläche "abgeschert" ist. Anders zeigt sich das Verhalten des Reifens mit den drei hohen Ringprofilen (deep ribbed). In den meisten Fällen entwickelt dieses Profil bei kleinen Schräglstellungen zunächst geringere Seitenkräfte, bei großen Schräglaufwinkeln jedoch immer noch ansteigende Seitenkräfte. Das Profil ist gut für extreme Beanspruchungen.

Fast nur halb so groß wie auf der Wiese sind die Seitenkraftbeiwerte auf dem trockenen, gegrubberten Acker (Bild 23).

Ähnlich ist das Seitenkraftbeiwerts-Diagramm für Kiesboden (Bild 24) und Maisfeld (Bild 25) auszuwerten. Wenn die gesamte Fläche auf Kies bzw. feuchtem glatten Boden zwischen den Maispflanzen abschert, steigt die Seitenkraft auch bei größeren Schräglaufwinkeln nicht mehr an.

Die Bereiche, in die die Kurven der Seitenkraftbeiwerte aller untersuchten Reifen ohne Rücksicht auf Profil für eine bestimmte Bodenart fallen, sind in Bild 26 eingetragen. Die Seitenkraftbeiwerte sind bei Wiese und Stoppelfeld am höchsten und steigen auch bei größeren Schräglaufwinkeln noch leicht an. Für gegrubberten, trockenen Ackerboden sind die abstützbaren Seitenkräfte am geringsten, aber immer noch ca. 50 % der Radlast bei großen Einschlagwinkeln. Auf Kiesboden und Maisfeld steigt der Seitenkraftbeiwert rasch auf 0,4 bis 0,5 bei 10° Schräglaufwinkel an, ändert sich aber dann bei größeren Einschlagwinkeln kaum mehr.

Die Ergebnisse bezüglich der Profilunterschiede sind in Bild 27 zusammengefaßt. Die Balkendiagramme zeigen für die verschiedenen Böden und für Schräglaufwinkel von 10 bis 30° die prozentuale Veränderung des Seitenkraftbeiwertes S/W der einzelnen Profilreifen gegenüber dem unprofilierten Reifen.

Deutlich ist zu erkennen, daß die profilierten Reifen nur auf der Wiese und auf dem Stoppelfeld wesentlich mehr Seitenkräfte aufbringen können als ein glatter Reifen. Ursache dafür könnte eine gewisse "form-

schlussige Verzahnung" zwischen Pflanzen und Reifenprofil sein. Auch hier wird wieder deutlich, daß der Hochstollenreifen bei geringen Schräglaufwinkeln kleine Seitenkräfte, aber mit wachsendem Winkel immer größere Seitenkräfte abstützen kann.

In allen Fällen, mit Ausnahme vom feuchten Maisfeld, ist das Treibradprofil mit vorgeschriebener Laufrichtung montiert (Spur besteht aus rückwärts gerichteten Pfeilen) vorteilhafter als im gegen die Laufrichtung montierten Zustand.

Der Terra-Reifen schneidet bei pflanzenbedeckter Oberfläche gut ab, bringt aber keine nennenswerten Vorteile auf glatter, krümeliger bzw. kiesbedeckter Bodenoberfläche.

Im feuchten Maisfeld sind sämtliche Profilreifen bei kleinen Schräglaufwinkeln ungünstiger als der glatte Reifen. Vermutlich überwiegt dabei die Adhäsion der großen, glatten Fläche des unprofilierten Reifens, bis bei größeren Schräglaufwinkeln die Profile durch ihre Kanten mehr in den Boden eindringen und dadurch größere Kräfte abstützen können.

Bezieht man die Seitenkraft auf den Rollwiderstand, so ergibt dies eine Art Wirkungsgrad, d.h. ein hoher Quotient aus S/R zeigt eine gute Ausnutzung des Reifens für die "Seitenabstützung" an. Dieser Quotient ist in Bild 28 für alle Reifen und Böden in Abhängigkeit vom Schräglaufwinkel aufgetragen. Da bei $\alpha = 0^\circ$ keine Seitenkraft wohl aber ein Rollwiderstand vorhanden ist, beginnen alle Kurven im Ursprung. Zwischen 5° und 10° tritt in allen Fällen das Maximum auf, welches beim Acker bei S/R = 1,5 und bei den anderen Böden bei S/R = 2,5 bis 4,5 liegt. Dies zeigt an, daß im Verhältnis zur aufgewandten Widerstandskraft in Fahrtrichtung alle Reifen zwischen 5° und 10° Schräglauf den größten Seitenkrafteffekt, also den besten "Ausnutzungsgrad bzw. Wirkungsgrad" bezüglich seitlicher Abstützfähigkeit haben.

6. Zusammenfassung

Während es zahlreiche Veröffentlichungen über Kräfte am Reifen in nachgiebigem Boden in Fahrtrichtung, also über Triebkräfte und Rollwiderstände gibt, finden sich noch wenige Arbeiten, die die Kräfte senkrecht zur Fahrtrichtung, also Seitenkräfte, behandeln.

Eine in früheren Untersuchungen bewährte Einzelrad-Versuchseinrichtung wurde für Messungen an nichtangetriebenen Implement-Reifen für Ackerwagen und landwirtschaftliche Arbeitsmaschinen und Geräte weiterentwickelt. Diese Versuchseinrichtung wird an einem Traktor Typ Unimog hinten starr angebaut. Es können bei Lenkeinschlägen von 0 bis 30° und Radlasten bis zu 1,3 t die auf den Versuchsreifen wirkenden Längs- und Seitenkräfte gemessen werden.

Zur Ermittlung des Profileinflusses auf die übertragbare Seitenkraft im gelenkten Zustand wurden Reifen 12,5/80-18 8 PR und ein Terra-Reifen gleichen Durchmessers jedoch größerer Breite mit den Profilen nach Bild 4 verwendet. An jedem Reifen wurden bei fünf unterschiedlichen Belastungen und Einschlagwinkeln von 0 bis 30° die Widerstandskräfte in Fahrtrichtung und die Seitenkräfte auf folgenden Böden gemessen: Stoppelfeld, gegrubberter Acker, Wiese, Kiesboden und abgeerntetes Maisfeld. Die Widerstandskraft- und Seitenkraftbeiwerte wurden dadurch ermittelt, daß durch 35 Meßpunkte für verschiedene Schräglaufwinkel und unterschiedliche Radlasten eine Regressionskurve mit einem Polynom dritten Grades gezogen wurde.

Das Reifenprofil beeinflusst die Seitenkraftbeiwerte (Seitenkraft/Radlast) vornehmlich bei den Böden Wiese und Stoppelfeld. Die abstützbaren Seitenkräfte sind bei den profilierten Reifen gegenüber dem glatten Reifen bei einem Einschlagwinkel von 30° um 25 bis 70 % höher. Das typische Lenkreifenprofil mit zwei tiefen Rundum-Rillen (deep ribbed) erzeugt bei geringen Schräglaufwinkeln zwar kleinere Seitenkräfte, kann aber bei großen Schräglaufwinkeln die größten Seitenkräfte abstützen. Das Treibradprofil ist in fast allen Fällen in Laufrichtung richtig montiert vorteilhafter als rückwärtslaufend montiert. Der Terra-Reifen schneidet bei pflanzenbedeckter Oberfläche gut ab, bringt aber keine nennenswerten Vorteile auf glatter Bodenoberfläche. Die Fahrwiderstandsbeiwerte (Längskraft/Radlast) sind in fast allen Fällen für profilierte Reifen im Mittel um 15 bis 40 % höher als bei dem unprofilierten Reifen. Sie sind bei 15° Schräglaufwinkel für Kies 0,15 bis 0,22, für Wiese und Stoppelfeld 0,18 bis 0,27 und für gegrubberten Acker 0,25 - 0,32.

Die Ergebnisse dieser Seitenkraft- und Rollwiderstandsmessungen an Implement-Reifen mit unterschiedlichen Profilen sind nützlich für die Berechnung von:

1. notwendiger Vorderachslast für das Lenkverhalten von Traktoren (schräger Zug);
2. Materialbelastungen von Rädern, Achsen und Reifen;
3. notwendiger Leistung zur Überwindung des Rollwiderstandes der Schleppervorderachse bzw. der Hinterachse beim Mähdrescher;
4. Lenkfähigkeit und Stabilität von Traktoren und Anhängern am Hang;
5. allgemeinem Fahrverhalten des Traktors (Computer-Simulation).

Literatur:

- [1] Taylor, A. u. R. Birtwistle: Experimental studies of force systems on steered agricultural tyres.
Proc. Inst.Mech.Engineers 181 (1967) 2A, S. 1/14
- [2] Schwanghart, H.: Seitenkräfte an gelenkten Luftreifen in lockerem Boden.
Grundl.Landt. 17(1967) 5, S. 105/114
- [3] Schwanghart, H.: Lateral forces on steered tyres in loose soil.
J.Terramech. 5(1968) 1, S. 9/29
- [4] Greckenko, A.: Slip and drift of the wheel with tyre on soft ground.
Proc. 3rd Int.Conf., ISTVS, Essen (1969) Vol. II, S. 76/95
- [5] Baker, C.J. u. R.M. Collins: A comparison of tractor rear tyres in their resistance to side slip.
J.agric.Engng.Res. 17(1972) 1, S. 64/70
- [6] Krick, G.: Behaviour of tyres driven in soft ground with side slip.
J.Terramech. 9(1973) 4, S. 9/30
- [7] Greckenko, A.: Some applications of the slip and drift theory of the wheel.
Proc. 5th Int.Conf., ISTVS, Detroit (1975) Vol. II, S. 449/472
- [8] Kraft, D. u. N.S. Phillips: Turning forces developed by a pneumatic tire operation in soils, with application to vehicle design criteria.
Proc. 5th Int.Conf., ISTVS, Detroit (1975) Vol. II, S. 473/492
- [9] Crolla, D.A. u. F.D. Hales: The lateral stability of tractor and trailer combinations.
J.Terramech. 16(1979) 1, S. 1/22
- [10] McAllister, M.: A rig for measuring the forces on a towed wheel.
J.agric.Engng.Res. 24(1979) S. 259/265
- [11] Rosario, Carlos R. del: Lateral force investigations on steered pneumatic tyres operating under soil condition.
Diss. Silsoe, Cranfield Inst.of Techn. (1980)
- [12] Gee Clough, D. u. M.S. Sommer: Steering forces on undriven angled wheels.
J.Terramech. 18(1981) 1, S. 25/49

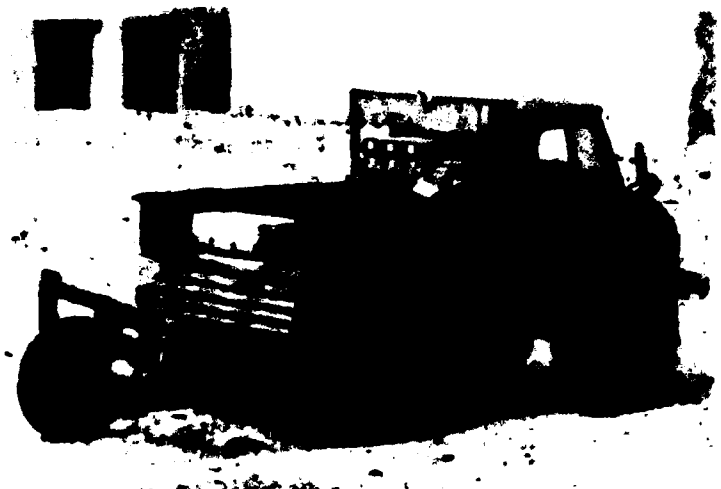


Bild 1: Gesamtansicht des Traktors Unimog mit angebaurem Seitenkraft-Meßgerät.

Total view of the tractor Unimog with mounted lateral force-test setup.

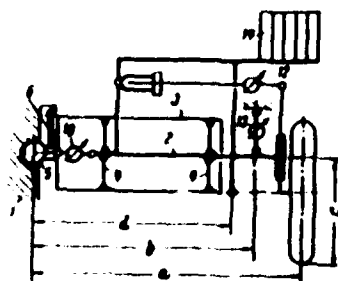
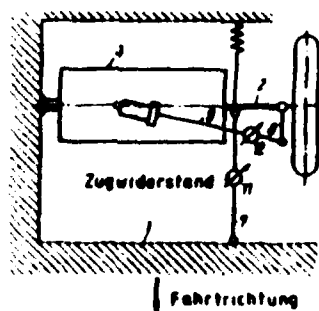


Bild 2: Schematische Darstellung der Versuchseinrichtung zur Messung der Seitenkraft und des Rollwiderstandes eines Reifens.

Test setup (schematic) for measurement of lateral force and rolling resistance of a tyre.



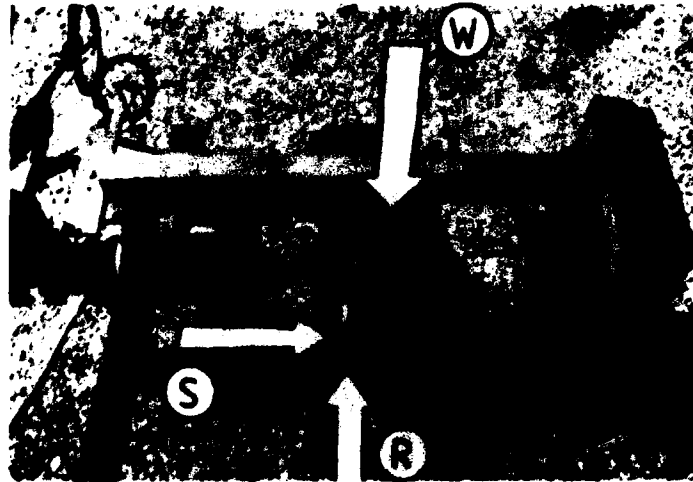


Bild 3: Einzelrad-Meßeinrichtung für gelenkte Reifen. Meßgrößen: Radlast W, Seitenkraft S und Rollwiderstand R in Fahrtrichtung.
Single wheel tester for steered tyres.



Bild 4: Versuchsreifen: Treibradreifen, Hochstollenreifen, nahezu profilloser Reifen und Terra-Reifen.

Test tyres: traction profile, deep ribbed, nearly ribless and Terra-tyre.



Bild 5: Ansicht des Stoppelfeldes.
View on stubble field.



Bild 6: Ansicht des Reifens auf der Wiese.

Tyre on meadow.

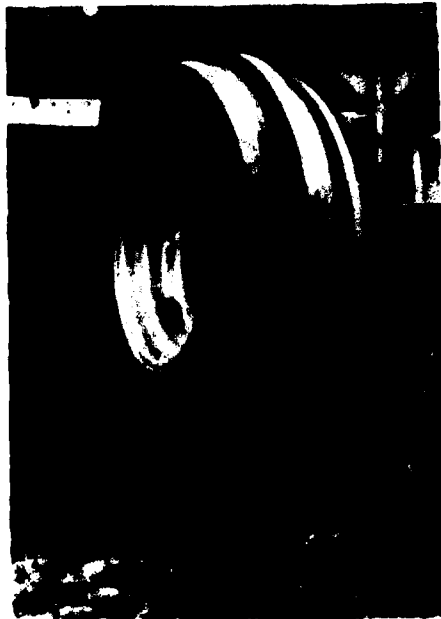


Bild 7: Ansicht des Hochstollenprofilreifens auf dem Acker.

Deep ribbed tyre on field.



Bild 8: Ansicht des Terra-Reifens auf dem Kiesboden.

Terra-tyre on gravel ground

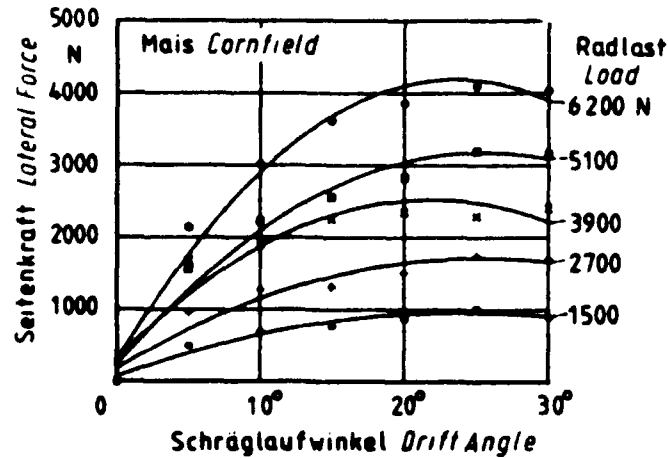


Bild 9: Seitenkräfte in Abhängigkeit vom Schräglaufwinkel am Treibradreifen bei verschiedenen Radlasten.

Relationship between lateral forces and drift angle of traction tyre at different load.

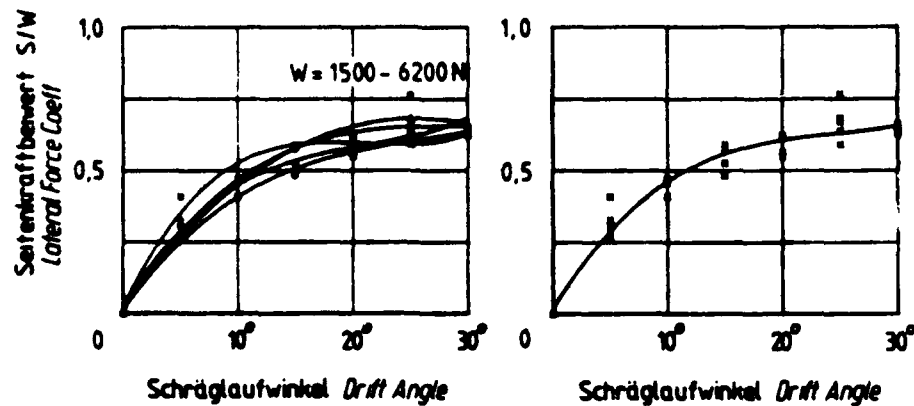


Bild 10: Die auf das Gewicht W bezogene Seitenkraft S in Abhängigkeit vom Schräglaufwinkel für die Kurven aus Bild 9.

Lateral force S referred to load W in relationship to drift angle for the curves in figure 9.

Bild 11: Mittlerer Seitenkraftbeiwert S/W in Abhängigkeit vom Schräglaufwinkel nach Punkten und Kurven in Bild 10.

Mean lateral force coefficient S/W as a function of drift angle using the points and curves of figure 10.

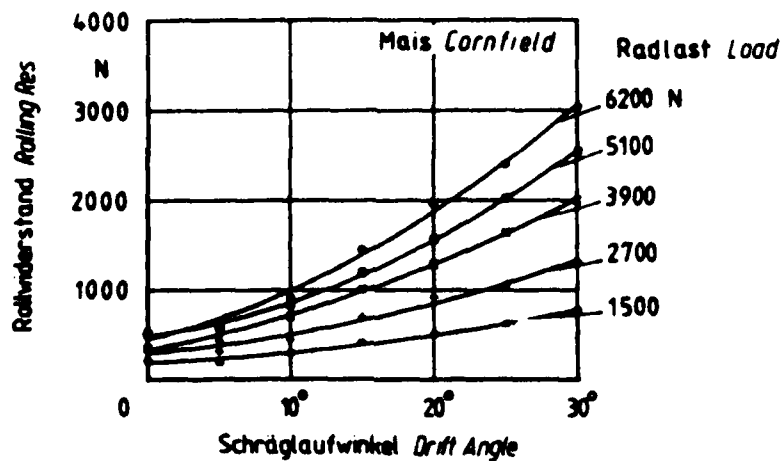


Bild 12: Rollwiderstand des Treibradreifens in Abhängigkeit vom Schräglaufwinkel bei verschiedenen Radlasten.

Relationship between rolling resistance and drift angle of traction tyre at different load.

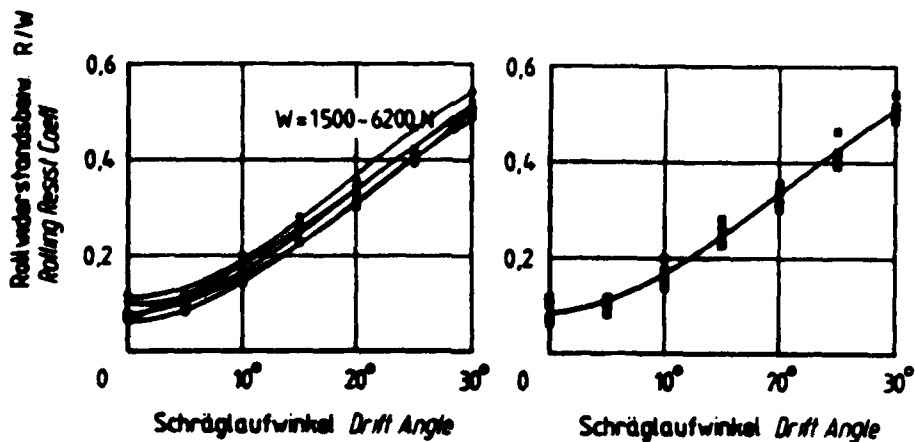


Bild 13: Rollwiderstand R nach Bild 12, bezogen auf die Radlast W in Abhängigkeit vom Schräglaufwinkel.

Relationship between rolling resistance coeff. of traction tyre and drift angle at different load from figure 12.

Bild 14: Mittlerer Rollwiderstandsbeiwert R/W in Abhängigkeit vom Schräglaufwinkel nach Punkten und Kurven aus Bild 13.

Mean rolling resistance coeff. as a function of drift angle using points and curves of figure 13.

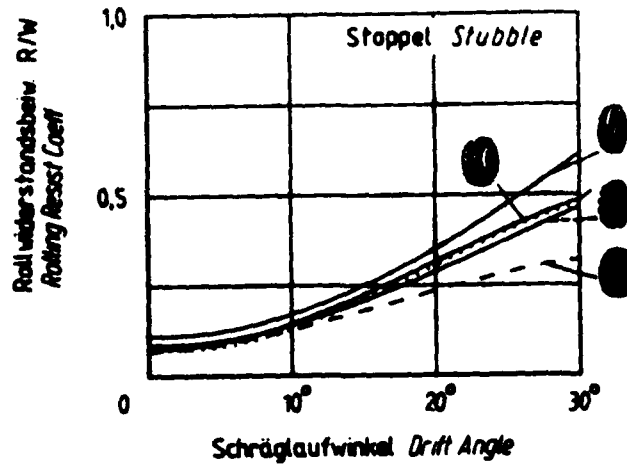


Bild 15: Rollwiderstandsbeiwert verschiedener Reifen in Abhängigkeit vom Schräglaufwinkel auf dem Stoppelfeld.

Rolling resistance coeff. in relation to drift angle.

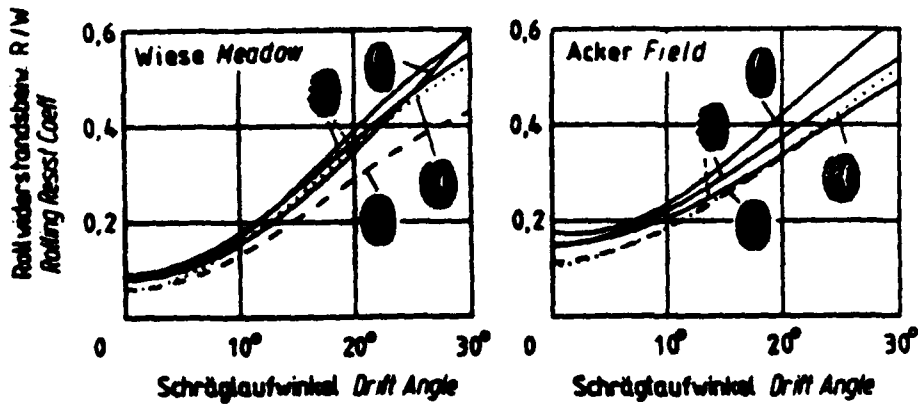


Bild 16: Rollwiderstandsbeiwert verschiedener Reifen in Abhängigkeit vom Schräglaufwinkel auf der Wiese.

Rolling resistance coeff. in relation to drift angle.

Bild 17: Rollwiderstandsbeiwert verschiedener Reifen in Abhängigkeit vom Schräglaufwinkel auf gegrubbertem Acker.

Rolling resistance coeff. in relation to drift angle.

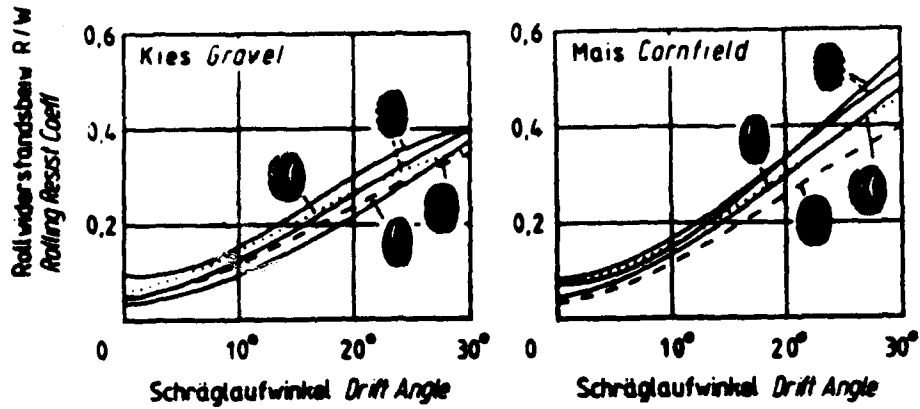


Bild 18: Rollwiderstandsbeiwert verschiedener Reifen in Abhängigkeit vom Schräglaufwinkel auf Kiesboden.

Rolling resistance coeff. in relation to drift angle.

Bild 19: Rollwiderstandsbeiwert in Abhängigkeit vom Schräglaufwinkel auf abgeerntetem, feuchten Maisfeld.

Rolling resistance coeff. in relation to drift angle.

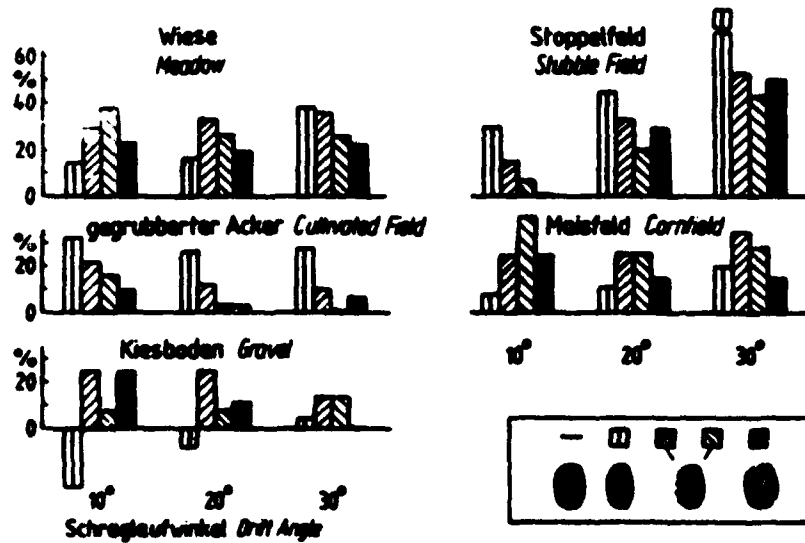


Bild 20: Prozentuale Änderung des Rollwiderstandsbeiwertes R/W von profilierten Reifen gegenüber dem profillosen Reifen auf verschiedenen Böden bei unterschiedlichen Schräglaufwinkeln.

Percentage increase of rolling resistance coefficient of profiled tyres compared with ribless tyre.

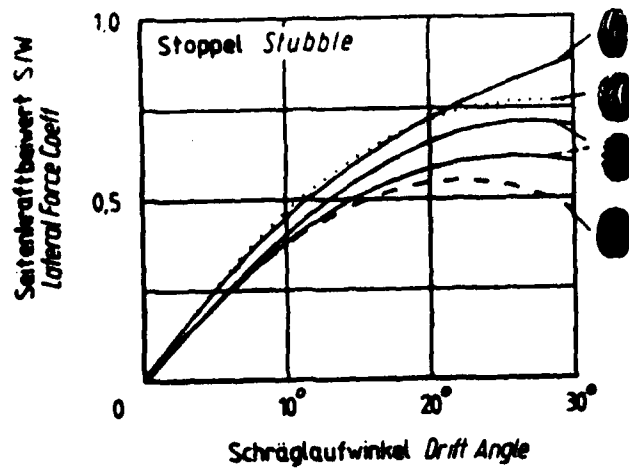


Bild 21: Seitenkraftbeiwert S/W verschiedener Reifen in Abhängigkeit vom Schräglaufwinkel auf einem Stoppelfeld.

Lateral force coeff. in relation to drift angle.

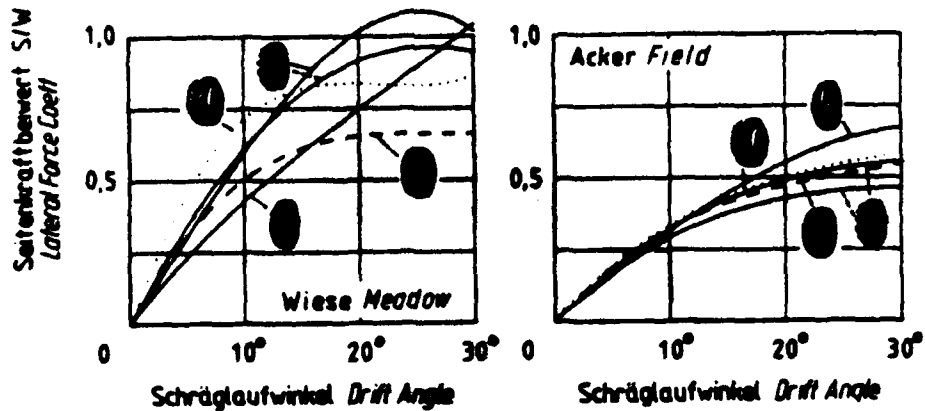


Bild 22: Seitenkraftbeiwert verschiedener Reifen in Abhängigkeit vom Schräglaufwinkel auf einer Wiese.

Lateral force coeff. in relation to drift angle.

Bild 23: Seitenkraftbeiwert verschiedener Reifen in Abhängigkeit vom Schräglaufwinkel auf einem gegrubberten Acker.

Lateral force coeff. in relation to drift angle.

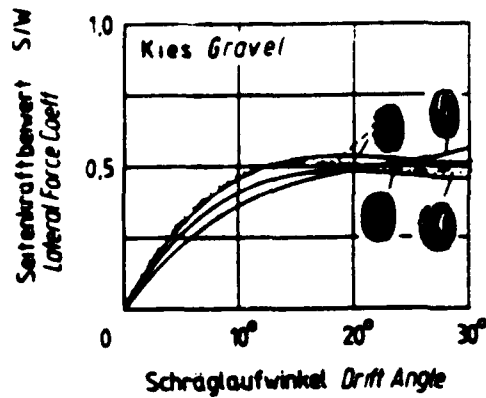


Bild 24: Seitenkraftbeiwert verschiedener Reifen in Abhängigkeit vom Schräglaufwinkel auf Kiesboden.

Lateral force coeff. in relation to drift angle.

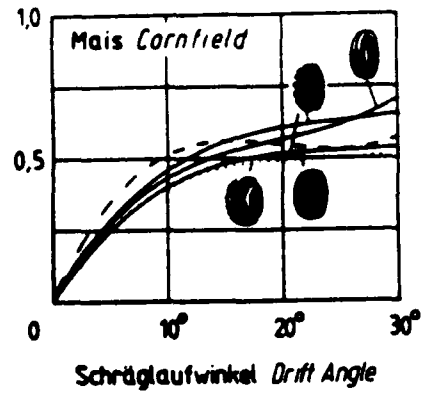


Bild 25: Seitenkraftbeiwert verschiedener Reifen in Abhängigkeit vom Schräglaufwinkel auf einem abgeernteten, feuchten Maisfeld.

Lateral force coeff. in relation to drift angle.

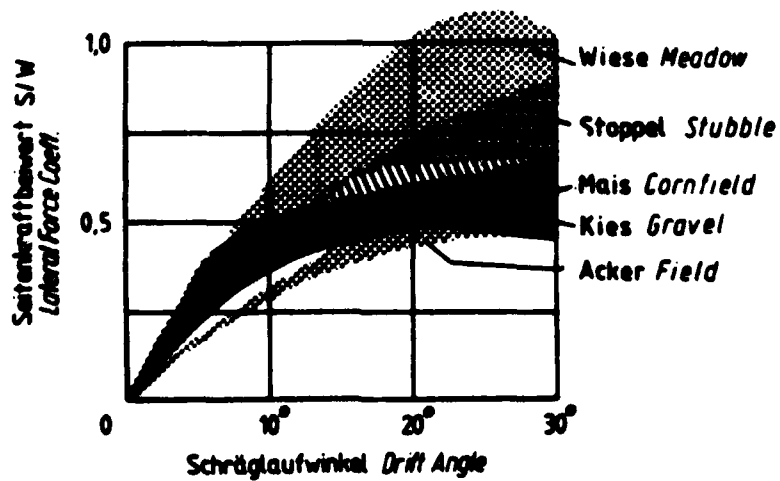


Bild 26: Seitenkraftbeiwert S/W aller hier getesteten profilierten Reifen und des profillosen Reifens in Abhängigkeit vom Schräglaufwinkel auf verschiedenen Böden.

Lateral force coeff. of all tested tyres in relation to drift angle at different soils.

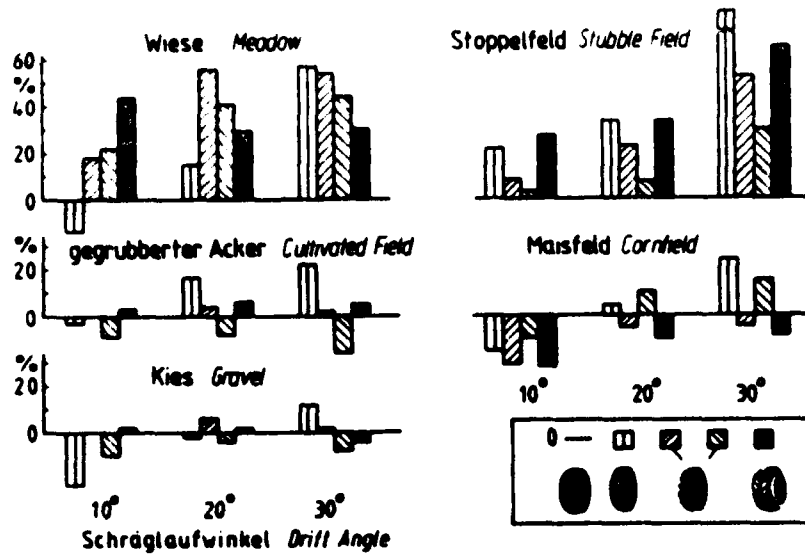


Bild 27: Prozentuale Änderung des Seitenkraftbeiwertes S/W von profilierter Reifen gegenüber dem profillosen Reifen auf verschiedenen Böden bei unterschiedlichen Schräglaufwinkeln.

Percentage increase of lateral-force coefficient of profiled tyres compared with ribless tyre.

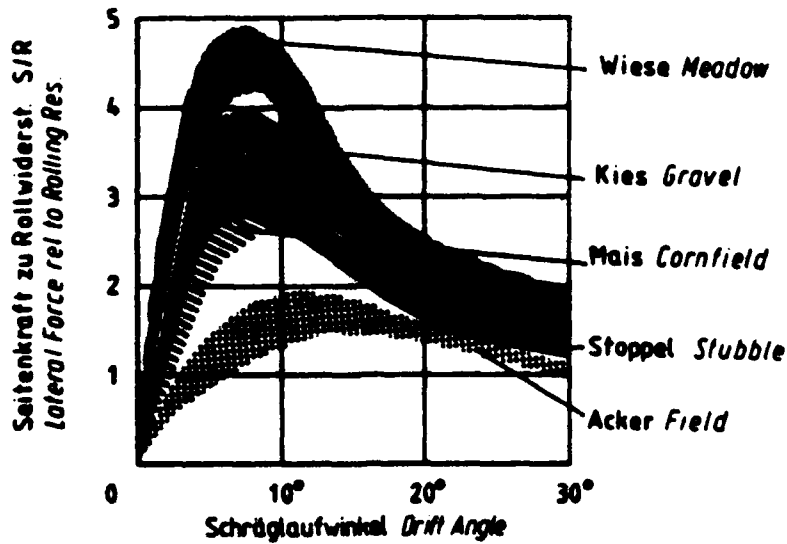


Bild 28: Verhältnis der Seitenkraft zu Rollwiderstand S/R aller getesteten Reifen in Abhängigkeit vom Schräglaufwinkel auf verschiedenen Böden. Die Werte stellen eine Art "seitliche Abstützung bzw. seitlicher Ausnutzungsgrad" der Reifen dar.

Ratio of lateral force to rolling resistance of tested tyres in relation to drift angle.



THE INFLUENCE OF THE TYRE TREAD ON THE ROLLING RESISTANCE AND STEERING FORCES ON UNDRIVEN WHEELS

H. SCHMIDT and K. ROTT

INSTITUT FÜR LANDMASCHINEN, TECHN. UNIVERSITÄT MÜNCHEN, F.R. DEUTSCHLAND

(Translated by Miss G. Bateman, NIAE, Silsoe, England)

SUMMARY

There are numerous publications about forces on tyres acting in or against travel direction, drawbar pull and rolling resistance, but only a few about lateral forces on steered tyres.

A test equipment, which provided a wealth of information of lateral and travel resistance of front wheels in recent years, has been further developed for testing implement tyres. This setup is mounted rigid on a tractor Unimog and provides measurements of longitudinal and lateral forces on tyre at steering angles from 0° to 30° with different load up to 1.3 t.

To determine the influence of tread on lateral forces of steered tyres there have been made experiments with implement tyres 12.5/80-18 8 PR and a terra-tyre with the same diameter but greater width (Fig. 4). With five different loads and steering angles from 0° to 30° we measured the lateral force and rolling resistance on the following soils: stubble field, cultivated field, meadows, gravel and cornfield after harvest. Every result curve is plotted as a polynomial regression curve (3 degree) using 35 test points for different drift angles and loads (Fig. 11).

The tyre tread influences the lateral force coefficient especially on meadow and stubble field. The increase is between 25% to 70% for profiled tyres compared with unprofiled tyres at 30° drift angle. The deep ribbed tyre generates only small lateral forces at small drift angles but supports the highest forces at greater drift angles. The traction profile running forward mounted gives more lateral forces than reversed mounted. The terra-tyre has more effect on plant covered surfaces than on smooth ones.

The rolling resistance coefficient is with profiled tyres on average 15% until 40% higher than with unprofiled tyres. With a drift angle of 15° the coefficient of rolling resistance is 0.15-0.22 at gravel, 0.18-0.27 at meadow and stubble field and 0.25-0.32 at cultivated field.

The results of these investigations enable the designer of off road vehicles to determine:

1. Required front axle loadings for the steering behaviour of tractors (with eccentric drawbar pull).
2. Material forces of wheels, axles and tyres.
3. Energy loss by rolling resistance.
4. Steerability and stability of tractors on slope operation.
5. General ride behaviour of tractor (computer simulation).

1. Introduction

The lateral forces which can be supported on steered tyres are of increasing importance in cross country transport and especially in the use of agricultural tractors and trailed implements(1-12). Increasingly implements are being mounted on tractors not only behind but also in front, which increases the demands on the lateral support capacity of the front wheels. Front mounted ploughs are an example of this. Large lateral forces must be transmitted for trailed implements operating on a slope and also for eccentrically loaded trailed agricultural machines, e.g. beet lifters operating on flat land. The rolling resistance in the direction of travel should be kept small in all cases.

In order to provide reference values for lateral and rolling resistance forces which may be used in the design of new machines, forces were measured on implement tyres with various treads on different soils or ground conditions.

2. Test rig

Fig. 1 shows the single wheel tester (2) which is positioned in a frame mounted rigidly behind a Unisoy tractor. The steerable wheel is suspended in a ball joint above a half-shaft (Fig. 2) so that it can adapt to the soil surface and sink in freely. The transverse axis (2), onto which the ballast weights (14) are attached, is positioned above two diaphragms (4) in the casing (3). The lateral force perpendicular to the direction of travel can be measured with a load cell (10). The horizontal force or rolling resistance is also determined with a load cell (11), which is set in the towing cable (7) between the measuring apparatus and the towing vehicle.

The tester, as shown in Fig. 3, can be used to measure the rolling resistance R in the direction of travel and the lateral force S perpendicular to the direction of travel for a given load. The forces are recorded via carrier-frequency - test amplifiers and a UV-oscillogram and processed further by computer. The geometric steering angle is equal to the drift angle because the whole test rig with the test tyres is forced to travel in a straight line because of its rigid attachment to the towing vehicle.

3. Tests

The resistance and lateral forces were determined on the four implement tyres shown in Fig. 4, 12.5/80-18 8 PR² at an air pressure of 1 bar with the following treads:

- a) traction tread
- b) tread with three deep ribs
- c) untreaded
- d) Terra-tire (wider)
- e) reversed traction tread

*The tyres were kindly made available by the Continental Company, and the tyre rims by the Lemmerz-Werke Company.

The external diameter of the tyres was 987 mm. The loading varied in five steps between 1500 and 8500 N, which gives a weight loading of between 118 and 658 for a maximum tyre nominal load of 13 000 N. The drift angle was adjusted in stages of 5° from 0° up to a maximum of 30°. The forward speed during the test was 1.4 km/h.

The following figures show the various test fields:

Fig. 5: meadow, Fig. 6: stubble, Fig. 7: arable (cultivated) and Fig. 8: gravel. The harvested maize field (no Fig.) had a smooth firm surface.

4. Test evaluation

Fig. 9 shows the lateral forces of the tyre with the traction tread in relation to the drift angle. Ground conditions: harvested maize field. The lateral force to be supported also becomes greater with increasing wheel load W . The measuring points were linked by regression curves with polynomials of the second degree.

If the lateral forces are related to the respective wheel load, then the curves shown in Fig. 10 are obtained. Here polynomials of the third degree were used as the regression curves, as the measured curve shows a maximum and a minimum for specific soils; a polynomial of the third degree thus gives a better approximation. If a certain deviation of the values - as is unavoidable in field tests - is permitted, then a regression curve can be determined through all the measured points from S/W in relation to the drift angle and incorporated in a diagram (Fig. 11). This shows the results of 35 individual tests for a tyre tread with five different loads.

The rolling resistance measurements were evaluated in the same way. Fig. 12 shows the rolling resistance in the direction of travel in relation to the drift angle with different wheel loads. These curves coincide more closely than those for the lateral forces, if the resistance is related to the wheel load (Fig. 13). Fig. 14 shows the regression curve for all the measuring points for a tyre tread on a soil, in this example, a maize field.

5. Results

Figs. 15 to 19 show the rolling resistance coefficient of tyres with various treads on stubble, meadow, cultivated field, gravel and maize field. Using these one can determine, for example, the rolling resistance of the rear steered wheels of a combine harvester. Fig. 15 is valid for the stubble field. The untreaded tyre has the lowest resistance with increasing drift angle, and the traction tread tyre mounted reversely has a greater resistance than the tyre correctly mounted; both of these tyres are similar to the wider Terra-Tires. The traction tread tyres with the deep cleats show the greatest resistance. Figs. 16 and 17 show the same for the meadow and cultivated land. When driving straight ahead ($\alpha = 0^\circ$) the rolling resistance coefficient for the meadow is less than 10%, and higher for the cultivated land up to almost 20%. The untreaded tyres again have the lowest value. The corresponding rolling resistance coefficients for gravel and maize field are given in Figs. 18 and 19.

As in these figures the curves are almost together and differences in the tread form are difficult to distinguish, the difference in % of rolling

resistance coefficient of individual tread tyres compared with the untreaded tyres is given in Fig. 20 for the five soil types. The values are valid for drift angles of 10°, 20° and 30°.

Meadow, stubble and maize fields give the greater resistance increases in comparison with the smooth tyre. The very dry, cultivated field and gravel surface act in the same way perhaps as a flat surface covered with "spheres", over which both smooth and treaded tyres pass more easily. In the majority of cases the wider Terra-Tires have the lowest rolling resistance after the treaded tyres.

Fig. 21 shows the lateral support capacity of various treads on the stubble field. There are generally only small differences between the individual treaded tyres with small steering angles. With a drift angle of more than 20°, the smooth tyre has the least ability to support lateral forces because it "slides" over the stubble; with the traction tread mounted normally and reversely, tread penetration in the stubble is greater and the deep treaded tyre produces the greatest lateral forces. The lateral force coefficients are also very high on the meadow (Fig. 22). The soil type labelled "meadow" is in this instance arable land planted with grass which is to be ploughed in. The traction tread obtained values of more than 1. This can only be explained by the fact that the tread becomes caught in the grass tufts, giving a binding effect with the surface. But even the Terra-Tires have high lateral force coefficients. These, however, remain constant when the total contact area is "sheared off", which also occurs with untreaded tyres. The behaviour of the tyre with the three deep ring profiles (deep ribbed) is different to this.

In most cases this tread first develops smaller lateral forces with small drift angles; with large drift angles, however, the lateral forces still increase. The tread is optimum for extreme conditions.

The lateral force coefficients on the dry, cultivated soil are less than half as great as on the meadow (Fig. 23).

The lateral force coefficient diagram for gravel (Fig. 24) and the maize field (Fig. 25) can be evaluated similarly. If the total surface on the gravel or deep smooth soil shears off between the maize plants, the lateral force no longer increases even with increasing drift angles. Fig. 26 shows the areas in which the curves of the lateral force coefficients of all the tyres tested fall for a certain type of soil without regard to the tread. The lateral force coefficients are highest for the meadow and stubble field and are easily increased even with greater drift angles. The lateral forces to be supported are least for the cultivated, dry soil, but still approximately 50% of the load with large drift angles. The lateral force coefficient increases quickly from 0.4 to 0.5 at a 10° drift angle on gravel soil and maize field, but then hardly changes with larger drift angles.

The results with regard to tread differences are summarised in Fig. 27. The bar graphs show the percentage change of the lateral force coefficient S/W of the individual treaded tyres in comparison with the untreaded tyres for the various soils and for drift angles from 10 to 30°.

It can clearly be seen that the treaded tyres can only produce significantly more lateral forces than the smooth tyre on the meadow and on the stubble field. One cause of this may be a certain binding of the plants

and tyre tread. It also becomes clear here once more that the deep cleat tyres can support limited lateral forces with small oblique angles, but with increasing angle can support increasing lateral forces. In all cases, with the exception of the damp maize field, the traction tread mounted in the recommended direction of travel (track consists of arrows directed backwards) is more favourable than the condition mounted against the direction of travel.

The Terra-Tire penetrates a plant covered surface well, but has no noticeable advantages on smooth, crumbly or gravel covered surfaces. All treaded tyres with small drift angles are less favourable than smooth tyres on the damp maize field. Presumably here the adhesion of the large smooth surface of the untreaded tyre predominates, until with greater drift angles the edges of the tread penetrate more into the soil and thus can support larger forces.

If the lateral force is related to the rolling resistance, then a sort of efficiency is produced, i.e. a high quotient from S/R indicates good tyre efficiency for the "lateral support". This quotient is given in Fig. 28 for all tyres and soils in relation to drift angle. As there is no lateral force or rolling resistance available for $\alpha = 0^\circ$, all curves start at the origin. In all cases the maximum occurs between 5° and 10° , which is $S/R = 1.5$ for cultivated land and $S/R = 2.5$ to 4.5 for the other soils. This shows that in relationship to the resistance force exerted in the direction of travel, all tyres have the greatest lateral force effect between drift angles of 5° and 10° and thus the greatest "utilisation coefficient or efficiency" with regard to lateral support capacity.

6. Summary

Although there are numerous publications dealing with the forces acting on tyres in soft ground in the direction of travel, also on drawbar pull and rolling resistance, there is still little work on the forces acting perpendicular to the direction of travel and on lateral forces.

A single wheel tester used in earlier investigations was further developed for measurements on the non-driven implement tyres of field vehicles, agricultural work machines and equipment. This test rig is mounted rigidly behind a Unimog tractor. With steering angles of 0 to 30° and wheel loads of up to 1.3 t the longitudinal and lateral forces acting on the test tyres can be measured.

To determine the influence of tread on the transferable lateral force on steered tyres, a $12.5/80-18$ 8 PR tyre and a Terra-Tire with the same diameter, but with a greater width and with the treads according to Fig. 4, were used. The resistance forces in the direction of travel and the lateral forces were measured on each tyre for five different loads and steering angles ranging from 0 to 30° on the following soils: stubble, cultivated, meadow, gravel and harvested maize field. The rolling resistance force and lateral force coefficients were determined by this method, so that a regression curve with a polynomial of the third degree could be drawn through 35 measuring points for various drift angles and loads.

The tyre profile influences the lateral force coefficients (lateral force/wheel load) in particular on the meadow and stubble field.

The supportable lateral forces are between 25 and 70% higher for treaded tyres compared with smooth tyres with a drift angle of 30°. The standard steered tyre with a deep ribbed tread produces smaller lateral forces with small drift angles, but can support the greatest lateral forces with large drift angles. The traction tread is in almost all cases more favourably mounted correctly in the direction of travel than reversely mounted. The Terra-Tire penetrates plant covered surface well, but has no particular advantage on smooth soil surfaces. The rolling resistance coefficients (horizontal force/wheel load) are in almost all cases on average between 15 to 40% higher for treaded tyres than for untreaded tyres. With a drift angle of 15° these are 0.15 to 0.22 for gravel, 0.18 to 0.27 for meadow and stubble field and 0.25 to 0.32 for cultivated land.

The results of these measurements of lateral forces and rolling resistance on implement tyres with various treads are useful for the calculation of:

1. required front axle loading for the steering behaviour of tractors (eccentric drawbar pull);
2. material loading of wheels, axles and tyres;
3. required output to overcome rolling resistance of tractor front axle or rear axle of combine harvester;
4. steerability and stability of tractors and implements during operation on slopes;
5. general drive behaviour of the tractor (computer simulation).

References

- [1] Taylor, A. & R. Birtwistle: Experimental studies of force systems on steered agricultural tyres. Proc. Inst.Mech.Engineers 181 (1967) 2A, 1/14
- [2] Schwanghart, H.: Lateral forces on steered pneumatic tyres in loose soil. Grundl.Landt. 17(1967) 5, p, 105/114
- [3] Schwanghart, H.: Lateral forces on steered tyres in loose soil. J.Terramech. 5(1968) 1, p, 9/29
- [4] Grecenko, A.: Slip and drift of the wheel with tyre on soft ground. Proc. 3rd Int.Conf., ISTVS, Essen (1969) Vol. II, p, 76/95
- [5] Baker, C.J. & R.M. Collins: A comparison of tractor rear tyres in their resistance to side slip. J.agric.Engng.Res. 17(1972) 1,p, 64/70
- [6] Krick, G.: Behaviour of tyres driven in soft ground with side slip. J.Terramech. 9(1973) 4, p, 9/30
- [7] Grecenko, A.: Some applications of the slip and drift theory of the wheel. Proc. 5th Int.Conf., ISTVS, Detroit (1975) Vol. II, p, 449/472
- [8] Kraft, D. & N.S. Phillips: Turning forces developed by a pneumatic tire operation in soils, with application to vehicle design criteria. Proc. 5th Int.Conf., ISTVS, Detroit (1975) Vol. II, p, 473/492
- [9] Crolla, D.A. & F.D. Hales: The lateral stability of tractor and trailer combinations. J.Terramech. 16(1979) 1, p, 1/22
- [10] McAllister, M.: A rig for measuring the forces on a towed wheel. J.agric.Engng.Res. 24(1979) p, 259/265
- [11] Rosario, Carlos R. del: Lateral force investigations on steered pneumatic tyres operating under soil condition. Diss. Silsoe, Cranfield Inst.of Techn. (1980)
- [12] Gee Clough, D. & M.S. Sommer: Steering forces on undriven angled wheels. J.Terramech. 18(1981) 1, p, 25/49



Fig. 1 Overall view of the Unimog tractor with mounted lateral force test rig.

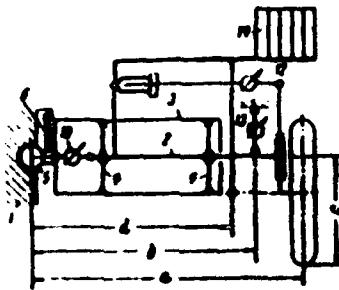
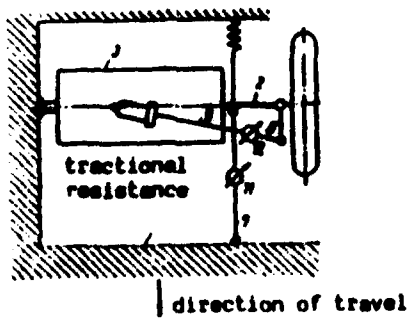


Fig. 2 Test rig (Schematic) for measurement of lateral force and rolling resistance of a tyre.



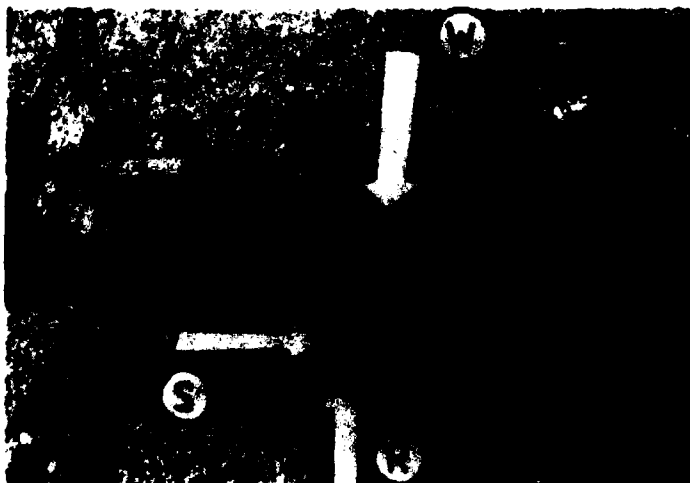


Fig. 3 Single wheel tester for steered tyres. Measuring variables: wheel loading W , lateral force S and rolling resistance R in the direction of travel.



Fig. 4 Test tyres: traction tread, deep ribbed, nearly ribless and terra-tire.



Fig. 5 Stubble field



Fig. 6 Tyre on meadow



Fig. 7 Deep ribbed tyre on cultivated field.



Fig. 8 Terre-Tire on gravel surface.

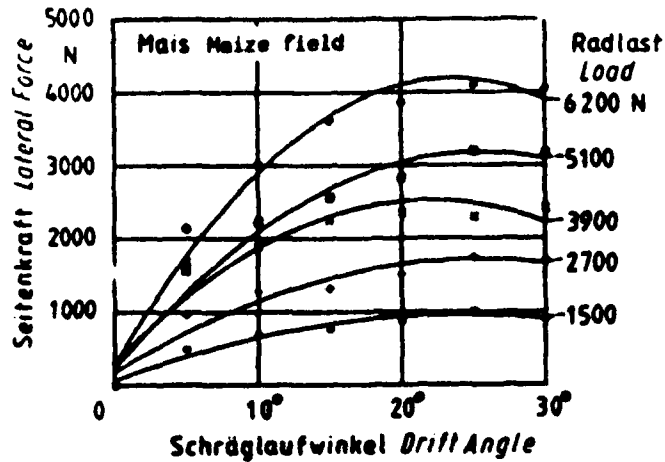


Fig. 9 Relationship between lateral forces and drift angle on traction tyre with different loads.

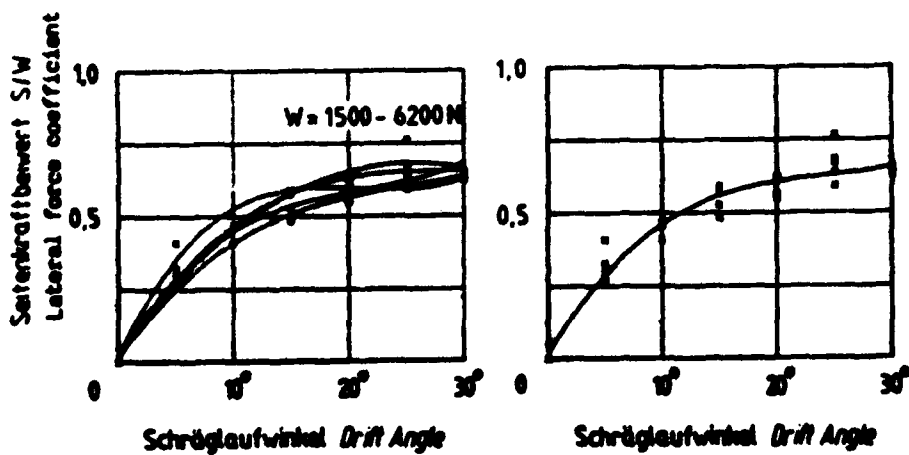


Fig. 10 Lateral force S referred to load W in relationship to drift angle for the curves in Fig. 9.

Fig. 11 Mean lateral force coefficient S/W as a function of drift angle using the points and curves from Fig. 10.

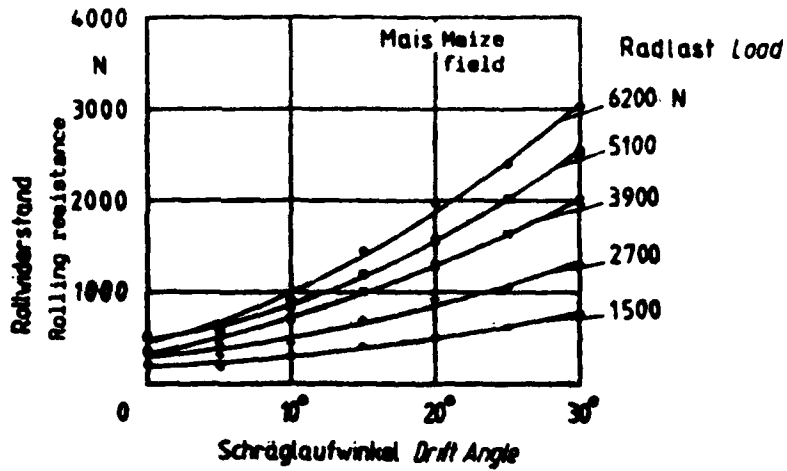


Fig. 12 Relationship between rolling resistance and drift angle of traction tyre using different loads

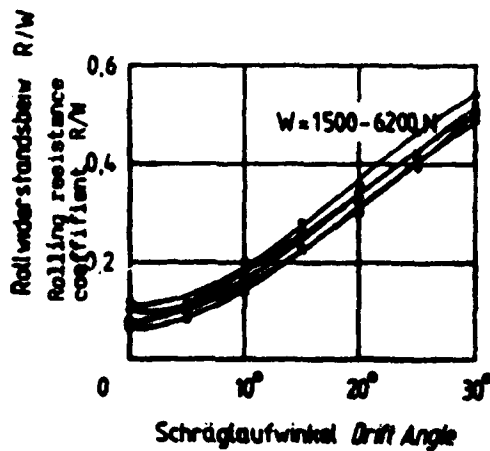


Fig. 13 Rolling resistance R according to Fig. 12 as a function of load W in relation to drift angle.

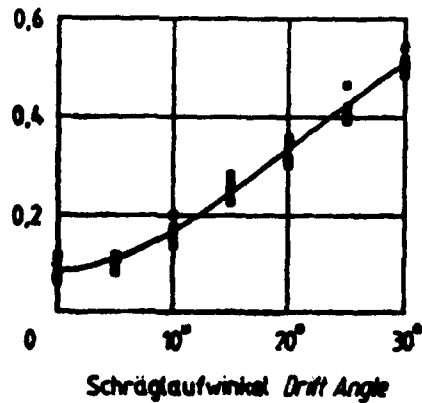


Fig. 14 Mean rolling resistance coefficient R/W as a function of drift angle using points and curves from Fig. 13.

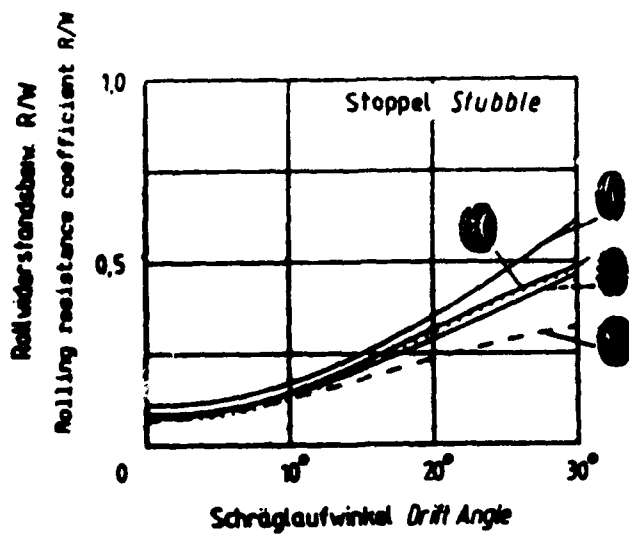


Fig. 15 Rolling resistance coefficient of various tyres in relation to drift angle on a stubble field.

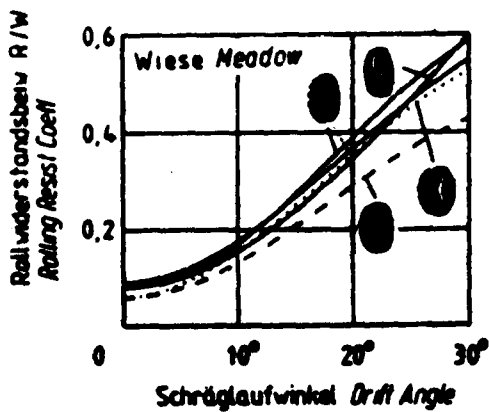


Fig. 16 Rolling resistance coefficient of various tyres in relation to drift angle on a meadow

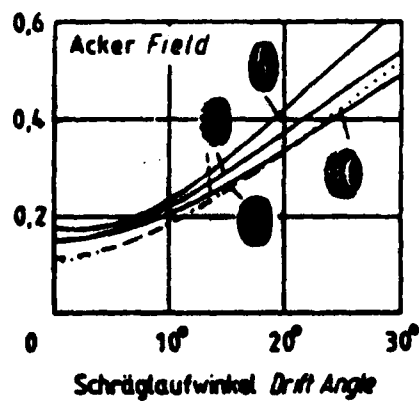


Fig. 17 Rolling resistance coefficient of various tyres in relation to drift angle on a cultivated field.

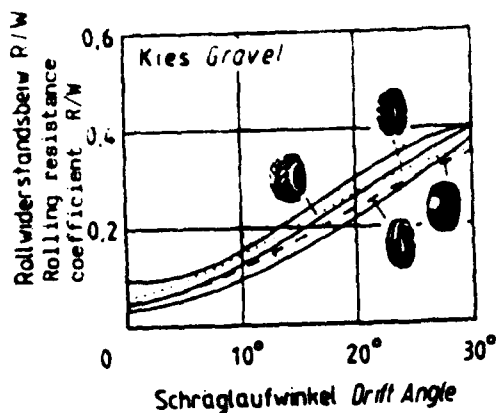


Fig. 18 Rolling resistance coefficient of various tyres in relation to drift angle on gravel.

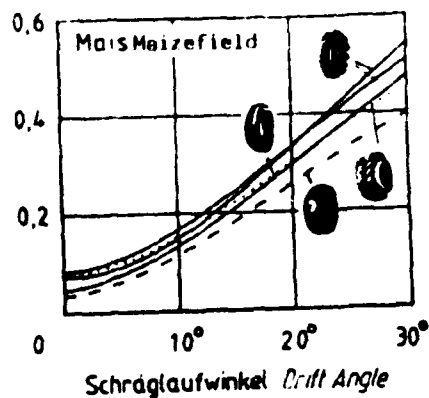


Fig. 19 Rolling resistance coefficient in relation to drift angle on harvested damp maize field.

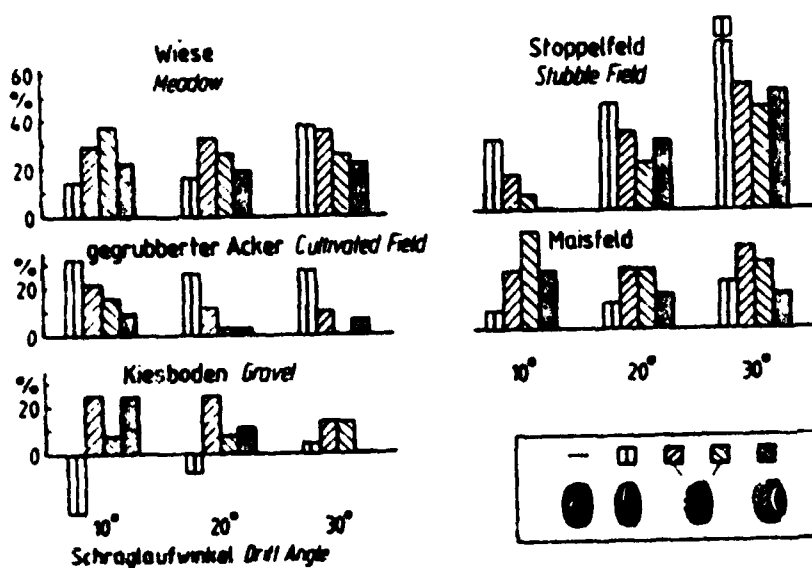


Fig. 20 Percentage increase of rolling resistance coefficient R/W of treaded tyres compared with untreaded tyre on various soils with different drift angles.

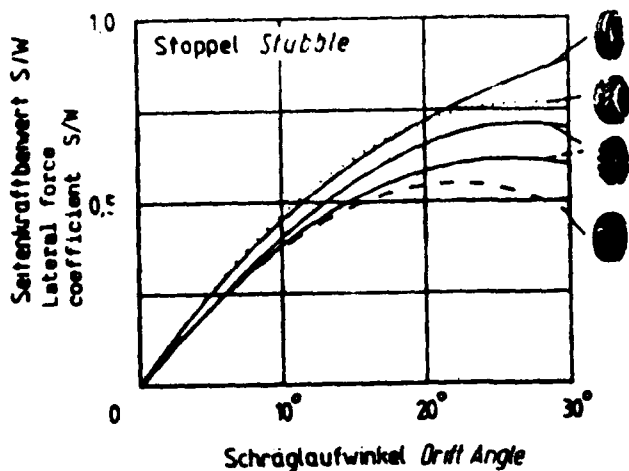


Fig. 21 Lateral force coefficient S/M of various tyres in relation to drift angle on a stubble field.

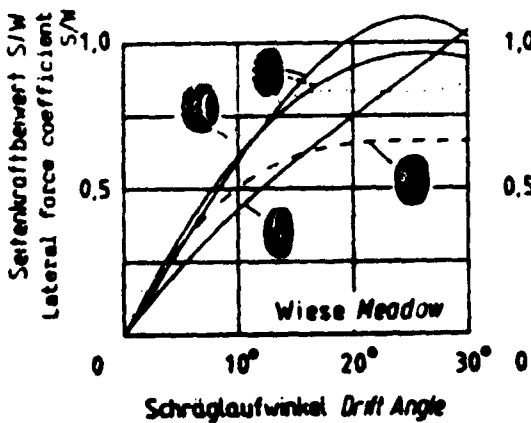


Fig. 22 Lateral force coefficient of various tyres in relation to drift angle on a meadow.

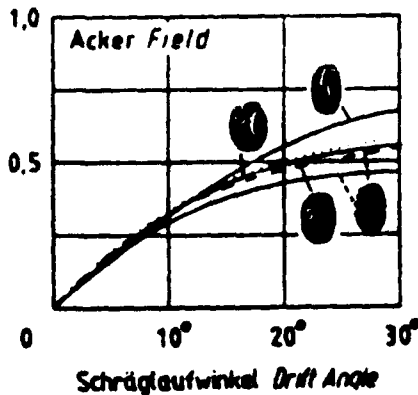


Fig. 23 Lateral force coefficient of various tyres in relation to drift angle on a cultivated field.

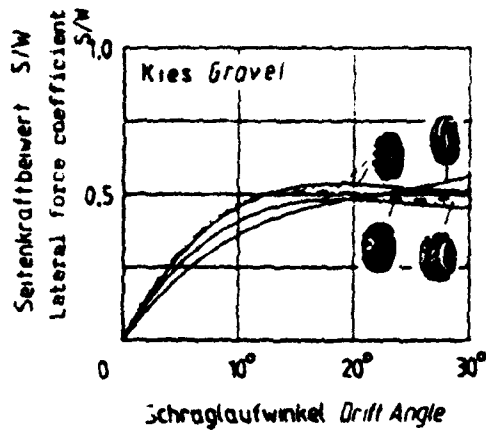


Fig. 24 Lateral force coefficient of various tyres in relation to drift angle on gravel.

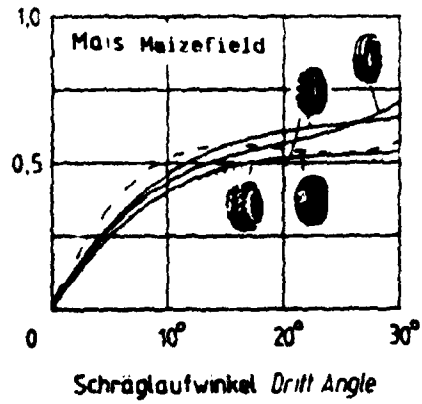


Fig. 25 Lateral force coefficient of various tyres in relation to drift angle on a harvested, damp maize field.

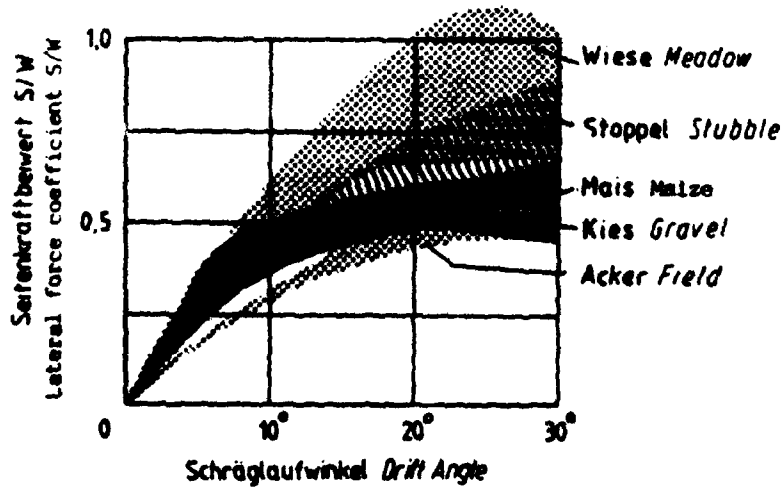


Fig. 26 Lateral force coefficient S/W of all treaded and untreaded tyres tested in relation to drift angle on different soils.

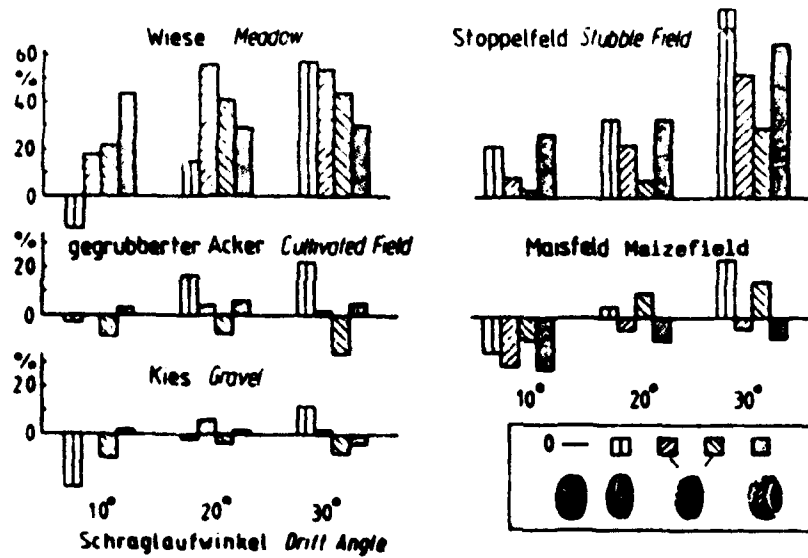


Fig. 27 Percentage increase of lateral-force coefficient S/N treaded tyres compared with untreaded tyre on various soils at different drift angles.

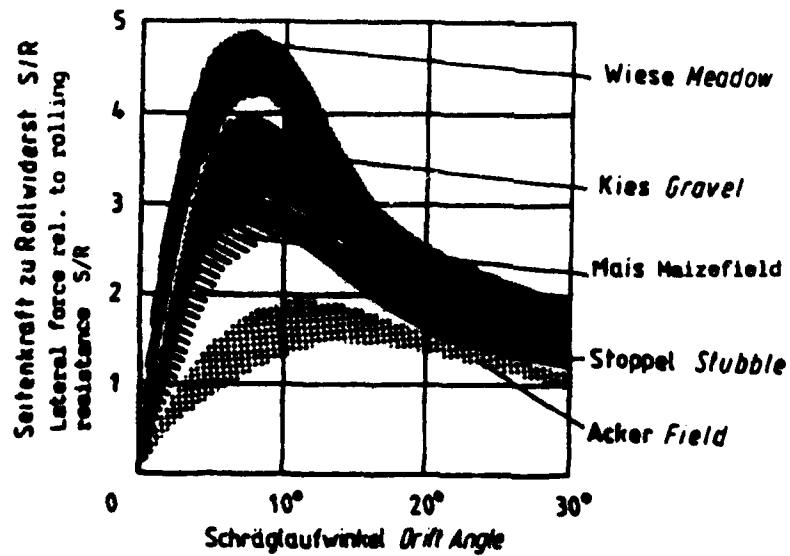


Fig. 28 Ratio of lateral force to rolling resistance of all tested tyres in relation to drift angle on various soils. The values represent a sort of "lateral support or lateral utilisation coefficient" of the tyres.

AD-P004 307

4

BASIC STUDY ON THE TURNING RESISTANCE OF TRACK

NOBORU SUGIYAMA and HIROSHI KONDO

TOKAI UNIVERSITY, KANAGAWA, JAPAN

1. INTRODUCTION

In recent years, the construction equipments have been used even on the soft ground. The vehicles of crawler type, such as bulldozer, are superior in the trafficability of off the road. On the contrary, the turning resistance may be several times larger than that of straight travelling. Therefore the turning performance of tracked vehicles gives a serious problem. Formerly, the turning resistance was calculated by using the adhesion coefficient or coefficient of slip resistance between soil and under side of the track. But the turning resistance of the track should consist of the slip resistance of its bottom and the bulldozing resistance due to the passive earth pressure produced by side face of the track.

On the hard ground, the torque of the bulldozing resistance is small and not noticed, but on the soft ground, in case of the track turns with its sinkage, it increases so much that it can no more be disregarded.

Consequently, to solve those problems basically, the experimental study was conducted by using models of several types of rigid tracks. And this thesis reports that the moment of turning resistance of the inner track when the tracked vehicle makes spin turn which produces the largest turning resistance would be predicted by the proposed formulae.

2. EXPERIMENTAL APPARATUS AND METHOD

2.1 Characteristic of used soil

The experiment was conducted with Toyoura standard sand and its moisture content was kept at about 7.8 percents to increase bearing capacity. At this time, the characteristic of the standard sand was as follows, unit weight $\gamma = 1.35 \text{ gf/cm}^3$, angle of shearing resistance $\phi = 27^\circ$, apparent cohesion $c = 17 \text{ gf/cm}^2$ and ultimate bearing capacity of the experimental surface $P_{max} = 1 \text{ kgf/cm}^2$. The apparent cohesion mentioned above was so small amount that could not obtain by the common shear test. So it was obtained by the equation of the critical height : $h_{cr} = 4c/\gamma \cdot \tan(45^\circ + \phi/2)$.

2.2 Test apparatus

Fig.1 illustrates the outline of the experimental apparatus. The turning handle was rotated manually and the turning torque worked to the track's model, the sinkage and turning angle were measured respectively. Fig.2 illustrates the shape and dimensions of the models. The models were prepared seven kinds.

2.3 Experimental method

(1) The prescribed amount of the standard sand was put into the soil bin (length : 150cm, width : 60cm, depth : 60cm) and stired, compacted to make it constant density.

(2) The surface was smoothed to make the depth from the bottom of the soil bin 20cm.

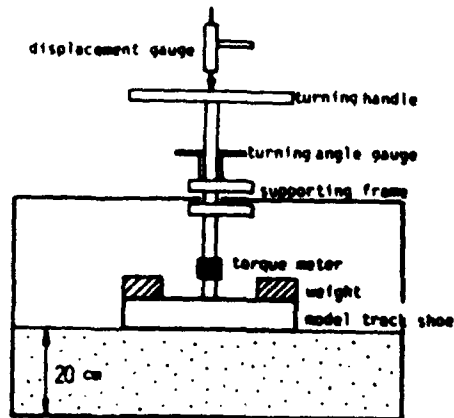


Fig.1. Schematic diagram of test apparatus

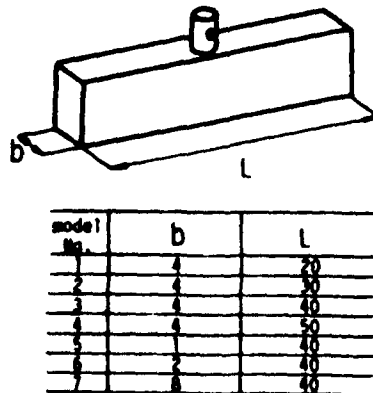


Fig.2. Model of track shoe

- (3) Put the model at the center of the soil bin and fit the displacement gauge to measure the sinkage.
- (4) Load the weight to make it required contact pressure (0.2, 0.4 kgf/cm²) or two kinds of weight (16, 32 kgf) and measure the static sinkage Z_s .
- (5) Turn the model until 90 degrees at a uniform velocity, self-record the turning angle, turning torque and slip sinkage.
- (6) Observe the state of bulldozing soil and so on.

3. EXPERIMENTAL RESULT AND CONSIDERATION

3.1 Effect of the track's shape on the slip sinkage

Fig.3 shows the relation between slip sinkage Z_s and track width b , using different width models No.3, No.5, No.6 and No.7 with a constant contact pressure and 90 degrees turning. From this results it can be considered that the slip sinkage Z_s is almost independent of track width b and maintains constant values.

Next Fig.4 shows the relation mentioned above also, using different length models No.1, No.2, No.3 and No.4 with the same conditions. From those results, when the contact pressure p is 0.4 kgf/cm², the slip sinkage Z_s increases as the track length L becomes wider. The slip sinkage to $L=50$ cm is about double as large as that to $L=20$ cm. But when the constant pressure p is 0.2 kgf/cm², those relations are not so clear.

Fig.5 shows the relation between the slip sinkage Z_s and track width b with the weight W (16, 32 kgf) and the track length L (40cm) are constant respectively. Fig.6 shows likewise the relation between the slip sinkage and track length with the weight mentioned above and the track width b (4cm) are constant respectively. From those figures, it is considered that next matters will be evident.

If the contact pressure becomes small amount, the slip sinkage decreases.

but its rate of decrease of the track made its width wider to decrease the contact pressure is larger than that of the track made its length longer. The contact area of the model No.1 and No.6 is same, but the slip sinkage of the model No.6 (length is longer, and width is smaller) indicates from one and half times to double as large as that of the model No.1.

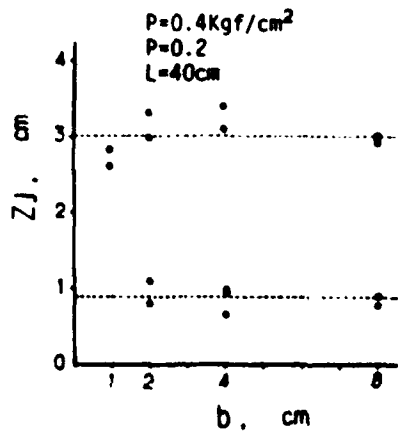


Fig. 3. Relationship between slip sinkage and track width with equal contact pressure

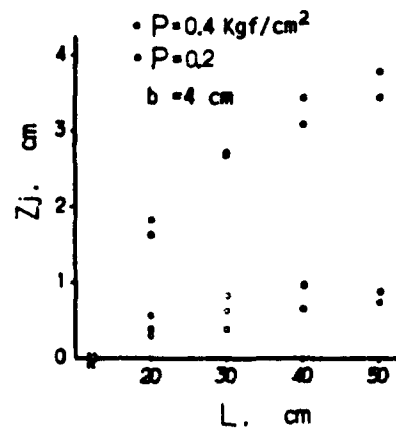


Fig. 4. Relationship between slip sinkage and track length with equal contact pressure

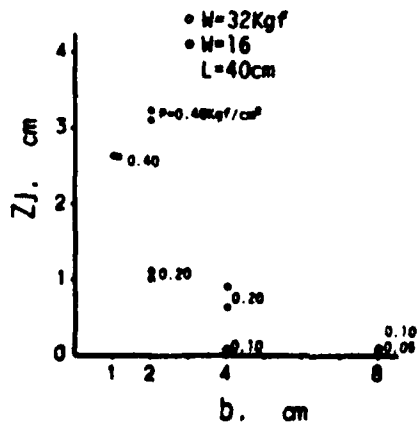


Fig. 5. Relationship between slip sinkage and track width with equal model weights

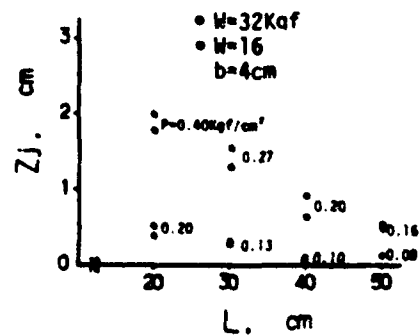


Fig. 6. Relationship between slip sinkage and track length with equal model weights

515

AD A148 635

PROCEEDINGS OF THE INTERNATIONAL CONFERENCE ON THE
PERFORMANCE OF OFF-ROAD (U) INTERNATIONAL SOCIETY FOR
TERRAIN-VEHICLE SYSTEMS M J DWYER AUG 84

UNCLASSIFIED

DAJA45-84-M-0251

F/G 13/6

NL



END
DATE
FILMED
85



1.0



1.1



1.25

EEEEEE

2.8

3.15

3.5

4.0

4.5

5.0

5.6

6.3

2.5

2.2

2.0

1.8

1.6



1.4



1.6

To get the slip sinkage Z , as the criterion variables, with three factors as the predictor variables, contact pressure p , track width b , and track length L , the multiple regression equation is obtained as follows.

$$Z_i = 94.5p + 0.352L - 23.0 \quad (1)$$

(partial correlation coefficient $R=0.969$)

3.2 Effect of the track's shape on the turning resistance

Fig.7 shows the relation between the moment of turning resistance M_t and the turning angle α , with variation of the track width b , under the contact pressure $p=0.4 \text{ Kg/cm}^2$ and the track length $L=40 \text{ cm}$. The rate of increase of the moment of turning resistance becomes larger as the track width is wider. At this time, as the slip sinkage is constant approximately (see Fig.3), it's understood that the more the track is wide, the more amount of bulldozing soil. This fact is confirmed by observation of the test.

Fig.8 shows the relation between the moment of turning resistance and track length and it corresponds to Fig.6. If the track length is made longer to decrease the contact pressure, the moment of turning resistance shows a tendency to increase, but there is upper limit on this tendency.

Fig.9 shows the relation between the moment of turning resistance and turning angle with models of different width No.3, No.6 and No.7, using 32 Kg weight. The test result of the model No.7 shows a constant moment approximately in the range of more than 30° in spite of its continuous sinkage. This is considered that the moment of slip resistance decreases according to the increase of turning angle.

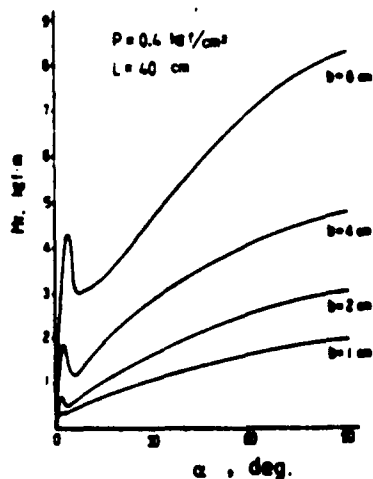


Fig.7. Relationship between moment of turning resistance and turning angle with equal track length

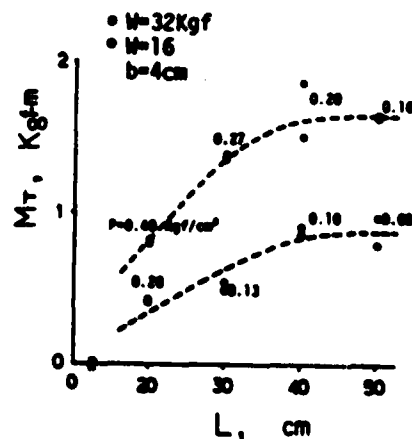


Fig.8. Relationship between moment of turning resistance and track length with equal model weights

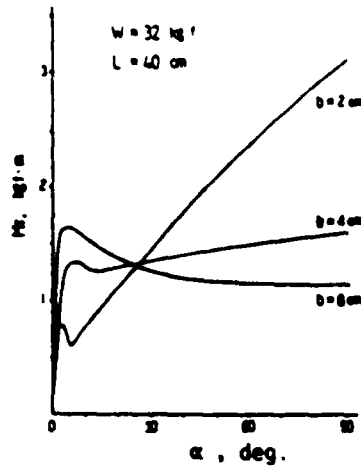


Fig.9. Relationship between moment of turning resistance and turning angle with equal track length

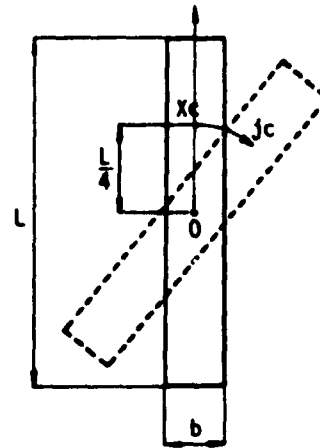


Fig.10. Coordinate system and symbols for track's model in turning

In the same way of a clause 3.1, to get the moment of turning resistance M_t as the criterion variables, with five factors as the predictor variables, contact pressure p , track width b , track length L , weight W and sinkage Z , the multiple regression equation is obtained as follows.

$$M_t = 0.0534L + 0.0521W + 0.0606Z - 0.246 \quad (2)$$

(partial correlation coefficient $R = 0.967$)

4. TURNING RESISTANCE CONSIDERED THE SLIP SINKAGE

Fig.10 shows the coordinates and the relation between the symbols and acting forces while the track turns. The turning center of the track is the origin O , x axis is the longitudinal direction of the track, the symbol j_c is the mean turning amount at the point of X_c (a quarter length L from the center of the track).

4.1 Bulldozing resistance

When the tracked vehicles make spin turn on the soft ground, the inside tracks turn with each sinking. The relation between the slip sinkage Z_s and the mean turning amount j_c is expressed by next equation

$$Z_s = u \cdot j_c^v \quad (3)$$

where

u, v : constants obtained by test result

the relation between the slip sinkage Z_s and the turning amount j_c at a distance x from the track's center is expressed from equation (3) as follows.

$$Z_{1n} = u_n \cdot j_n \quad (4)$$

where

$$u_n = u(x/x_n), \quad j_n = j_0(x/x_n)$$

As the slip sinkage Z_1 is small amount relatively to the ground contact length of the track, the soil amount scattered from the edge of the track to the ground might be able to neglect. And it's able to consider that the soil amount dug up by the track equals that heaped up on the ground (Fig.11(b)). Then, as mentioned already and showed in Fig.7, in spite of nearly constant of the slip sinkage, the rate of increase of the turning resistance becomes large as the track width is wider. Namely it'll be able to consider that the soil amount of bulldozing will become much more according to the track width becomes wider. So the weight of the heaped soil (δBx) on a small part of the track's sidefacs (dx) is expressed as follows.

$$\begin{aligned} \delta Bx &= \gamma \left\{ \int_0^{x_n} (Zjx + Z_1) djx + \frac{b}{2} \cdot Zjx \right\} dx \\ &= \gamma \left(\frac{u_n}{v+1} \cdot j_n^{v+1} + Z_1 \cdot j_n + \frac{b}{2} \cdot u_n \cdot j_n^v \right) dx \end{aligned} \quad (5)$$

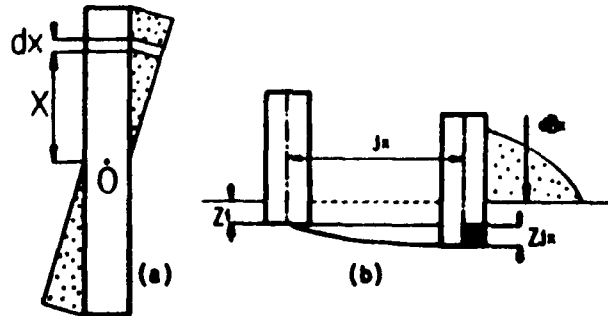


Fig.11. Schematic diagram of filling on side edge of track shoe

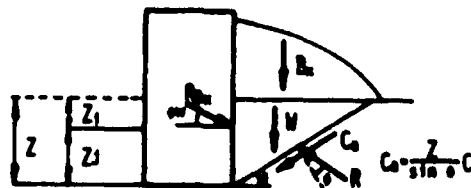


Fig.12. Forces acting around of track shoe

where

Z_1 : the initial sinkage

b : the track width

In the equation (5), the third term indicates the heaped soil becomes much more amount according to the wider track. (Fig.11(b) part of hatching) And it's assumed that the shape of the heaped soil will disregard and its weight will act on the surface of soil wedge uniformly. The state of acting forces around track is illustrated by Fig.12 and the bulldozing resistance R_{bx} is obtained from the balance of those forces as follows.

$$R_{bx} = \frac{Bx + \int (Z_1 + Z_2)^2 + (Z_1 + Z_2) \cdot c \cdot (1 + \cot \theta \cot(\theta + \phi))}{\cos \phi_w \cot(\theta + \phi) - \sin \phi_w} \quad (6)$$

where

θ : angle of failure surface

ϕ : angle of shearing resistance

ϕ_w : wall friction angle

c : cohesion

The value of R_{bx} becomes minimum against a certain value of θ , and at this value of θ , the earth is regarded as break. Then the moment of bulldozing resistance M_b is expressed as follows.

$$M_b = 2 \int_0^t R_{bx_{min}} \cos \phi_w x dx \quad (7)$$

4.2 Moment of slip resistance

To obtain the slip resistance, the contact pressure acted under the track must be given first. In case of spin turn, the center part of the inside track sinks at that place with compression of soil, but a part of its end sinks with removal of soil. So the distribution of the contact pressure increases at the center and decreases at the end of the track according to its turning. Consequently the moment of the slip resistance decreases according to increase of the turning amount.

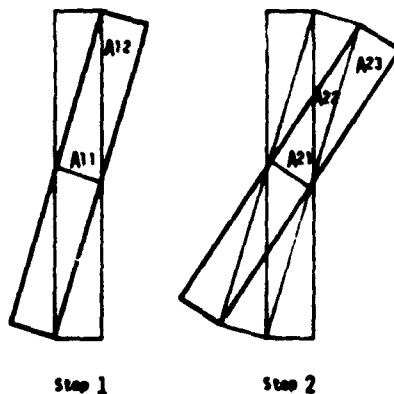


Fig.13. Movement of track shoe for step unit

Now, as Fig.13 shows the changing state of the under face of the track with its contact pressure, each step is divided to the unit ($j = L/2 \tan^{-1}(b/L)$) to consider the contact pressure. At the step 1, beneath the area A_{11} , the contact pressure increases with more compression than initial state. On the contrary, beneath the area A_{12} , the contact pressure decreases with the reason mentioned above. At the step 2, beneath the area A_{21} , the contact pressure increase more than that of beneath the area A_{11} . By application of this method to the step 3,4,..., the contact pressure of each step will be possible to predict.

At the step 1, each symbols put respectively as follows.

A_{1m} : subdivided area

P_{1m} : contact pressure of subdivided area

X_{01m} : distance from point O the center of A_{1m}

And the moment of the slip resistance is obtained by next equation.

$$M_s = 2 \sum_{m=1}^{n-1} \mu \cdot P_{1m} \cdot A_{1m} \cdot X_{01m} \quad (8)$$

where

μ : coefficient of the slip resistance

l : number of the step

m : appointed number of subdivided area

Next, the predicting method of the contact pressure P_{1m} will be mentioned. Fig.14 shows the relation between the mean turning amount j_c and the slip sinkage Z_j . In the figure, $j_c(1)$ is the slip amount of each step unit, $j_c(1)$ is a half amount of slip $j_c(1)$, $Z_j(1)$ and $Z_j'(1)$ are the sinkage, correspond to each $j_c(1)$ and $j_c'(1)$ respectively. An amount of compression ΔZ which is produced by the track, while it turns on the uncompressed, new ground, is assumed as follows.

$$\Delta Z = Z_j(1) - Z_j'(1) \quad (9)$$

And the relation between the contact pressure and sinkage for the loading test will be expressed by the exponential function.

$$P = P_{max} \cdot (1 - e^{-kZ}) \quad (10)$$

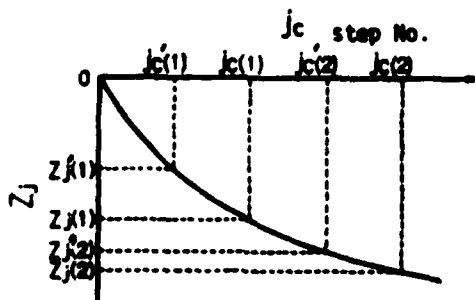


Fig.14. Typical variation of slip sinkage and turning amount

where

p: contact pressure
 Pmax: ultimate bearing capacity
 S: sinkage
 λ: shape factor

This method has the advantage of expression of the curve of loading test with a simple type.

Then, the contact pressure at the step 1 is obtained by next equation.

$$P_{1i} = P_{max} \left\{ 1 - \exp\left(-\frac{Z_1 + Z_1(1)}{\lambda}\right) \right\} \quad (11)$$

$$P_{1m} = P_{max} \left[1 - \exp\left\{-\frac{Z_1(1) - Z_1(m-1)}{\lambda}\right\} \right] \quad m \geq 2 \quad (12)$$

By above result, the moment of turning resistance Mt is expressed as follows.

$$M_t = M_D + M_S = 2 \int_0^L R_{Bx} \cdot \cos\phi_s \cdot x dx + 2\mu \sum_{m=1}^{i+1} P_{1m} \cdot A_{1m} \cdot X_{G1m} \quad (13)$$

5. AN EXAMPLE OF CALCULATED RESULTS

Table.1 shows each data used calculation.

Fig.15(a) shows the distribution of the bulldozing resistance R_B , calculated by the method of a clause 4.1, at the turning angle $30^\circ, 60^\circ$ and 90° . At the turning angle 30° , it distributes approximately uniformly, but at the turning angle 90° , the bulldozing resistance of a part of the track's end shows the value of about 1.25 time as large as that of around center of the track.

Tab.1 Parameter used for calculation

track width	b=4cm
track length	L=50cm
static sinkage	$Z_1=0.1cm$
coefficient of the slip resistance	$\mu=0.5$
slip sinkage - turning amount curve	$Z_j=0.0554j_c^{0.800}$
P - S curve	$P=1.01(1-e^{-\frac{S}{1.01}})$

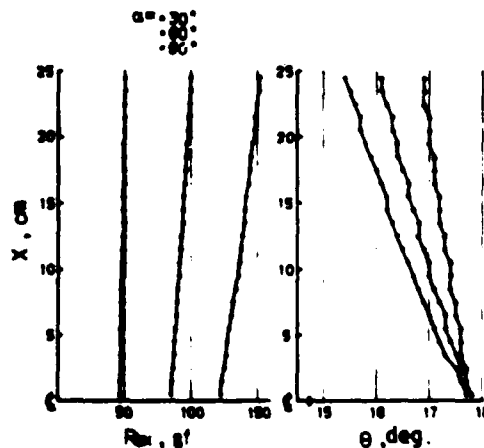


Fig.15. Change of bulldozing resistance and failure surface angle with turning angles

Fig.15(b) shows the changing state of the failure angle θ in case of Fig.15(a). The failure angle θ of a part of the track's end shows the tendency of decrease as the turning angle increases. But that of around center of the track shows nearly constant value. The failure angle increase linearly forward the center from the end of the track, and at the turning angle is 90° , the difference between both is about 2.3° . In Fig.17 the mark Δ shows the moment of the bulldozing resistance calculated from the bulldozing resistance obtained by the turning amount of each step of the unit. M_b increases linearly as the turning amount increases.

Fig.16 shows the distribution of the contact pressure calculated by the method of clause 4.2 and the changing state of its mean value along the vertical direction to x axis (direction of the track width) at each step

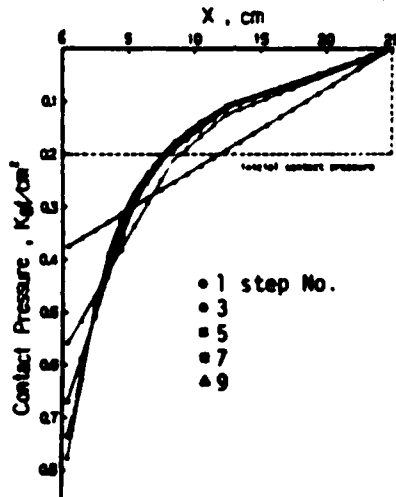


Fig.16. Change of contact pressure with each steps

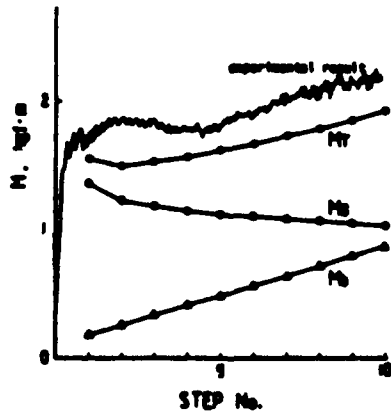


Fig.17. Comparison of the experimental results with calculated results

respectively. The contact pressure of a part of the track's end decreases as the turning amount increases, but that of around center of track shows rapid increase. (checked by earth pressure gauges buried)

Therefore, the moment of the slip resistance M_s decreases as the turning angle increases. This calculated results are illustrated by mark \odot in Fig.17.

Then the moment of the turning resistance M_t is obtained by the sum of M_b and M_s and those results are illustrated by mark \bullet in Fig.17. The calculated results are about ten percents smaller than the experimental results but the tendency is very similar each other.

6. CONCLUSION

When the tracked vehicles make a spin turn, characteristics of inner track's turning resistance, which is considered as the fundamental to solve the problems as the moment of the turning resistance, were studied by a series of model experiments and then semi-theoretical formulae were proposed to predict the moment of the slip resistance M_s and moment of the bulldozing resistance M_b .

Those results were verified by the experiments and could be concluded as follows:

- (1) When the contact pressure is identical, the sinkage Z , increases in proportion to the track length L , but it is independent from the track width b .
- (2) Under the same condition above mentioned, the rate of increase of the moment of the turning resistance becomes larger in accordance with the width of track in spite of the identical slip sinkage Z .
- (3) When the track length L is increased to decrease the contact pressure under the constant weight, the moment of the turning resistance increases with a certain possible upper limit.
- (4) For the spin turn of the actual vehicle, a new turning method which is considered to be the characteristics of the low turning resistance will be developed.
- (5) The semi-theoretical formulae were derived from the relation between the experimental slip sinkage Z , and the mean turning angle. Then calculation were compared with the experimental results and found to be in fairly good agreement.

In case of spin turn, characteristics of the turning resistance of the inner track were clarified to a certain extent.

Further studies will be continued mainly to suggest relating equations between the slip sinkage and the turning angle. Some problems in case of ordinary turn by a certain radius would also be pursued.



Study on Steerability of Articulated Tracked Vehicles

K. Watanabe and M. Kitano

Dept. of Mechanical Engineering, The National Defense Academy
Yokosuka Kanagawa, Japan

AD-P004 308

ABSTRACT

In previous paper, we have presented available equations of motion for analyzing the plane motion of the coupled (non-articulated) tracked vehicles with tow-pins.

In this paper, a mathematical analog for predicting the steerability of articulated tracked vehicles has been developed and computerized for numerical application. The analog contains all the basic parameters such as the vehicle characteristics and terrain factors related to steering problems of the vehicle. The accuracy of the analog in application has been verified by scale model tests and predictions proved quite satisfactory. Furthermore, the analog has been applied in a parametric study concerning the steering performance of the vehicles under various environmental conditions ranging from hard surface to soft soils.

As a result of the simulation, it was found that steerability (such as steering response), required sprocket torques for steering, track slippage and sinkage were significantly improved in articulated tracked vehicles when compared with a single and coupled tracked vehicle.

INTRODUCTION

A tracked vehicle exhibits excellent trafficability because of its low ground pressure on off road. They are normally steered by slipping the tracks with some form of steering device. This means the sprocket require considerable power. Track slippage and sinkage increase power requirements when steering on soft ground. Articulated tracked vehicles with articulate steering systems have been recently developed in order to improve steering performance of skid-steered tracked vehicles. For example, the BV206¹⁾ is an articulated tracked vehicle with a hydrostatic articulate steering system.

The steering dynamics and mechanism of these vehicles are complicated, so a theoretical analysis of steering motion has never been presented.

In previous paper, we have presented available mathematical models of a single vehicle²⁾ and coupled (non-articulated) tracked vehicles³⁾ for predicting the steering performance in stationary and non-stationary turning motion. The equation of plane motion of the coupled tracked units was established and numerically solved on a computer for steering characteristics. The model was experimentally verified on actual vehicles and scale models. It was found that the velocities of the vehicles, their coupled joints, steering time lag and mass ratio have an important influence on the steering performance.

We also found a coupled tracked vehicle is inferior in steerability when compared to a single vehicle.

In this paper, a mathematical model for predicting the plane turning motion of articulated tracked vehicles has been developed and compared with turning characteristics of a single and coupled tracked vehicles. In order to validate the actual application of a mathematical model, scale models were used in the turning maneuver test upon hard surface and as well as in dry loose sand. The turning radius, sprocket torques, track slippage and sinkage were measured.

As a result, it was found that mobility, required sprocket power, track slippage and sinkage in steering on soft ground were significantly better in articulated vehicles when compared with single and coupled tracked vehicles, and the steerability of articulated tracked vehicles was excellent at high speed.

THEORETICAL ANALYSIS OF THE MATHEMATICAL MODEL

1 Theoretical analysis

(1) Coordinate system and Kinematic of vehicle:

Fig.1 shows coordinate systems and the motion of articulated tracked vehicles on level ground. The X-Y coordinate system is fixed on the ground and its origin of axes coincides with the center of gravity of the front unit at time zero. The origins O, O' of body centered axis systems $x-y, x'-y'$ are fixed the center of gravity of each vehicle respectively.

Coupled tracked vehicles as in the previous paper⁴⁾ are steered by controlling track speeds of front vehicle, while, articulated vehicles are steered by articulate mechanism by changing the position of the front and rear units with respect to each other. The driving power of each vehicle is transmitted to each track through differentials.

The slip motion of tracks and load distribution of road wheels in a turning maneuver can be defined in the same form for coupled vehicles⁴⁾. The load distribution in the interface between tracks and ground is concentrated under the road wheels. The frictional coefficient between track and ground is given by $\mu = \mu_0(1 - e^{-KS})$, where, the parameters μ, μ_0, S and K denote the frictional coefficient, the maximum friction coefficient, track slip ratio and a positive constant respectively.

(2) Condition of constraint

As mentioned above, steering of articulated vehicle is accomplished by relative turns in front-rear plane. therefore, from the kinematic diagram in Fig.1, the articulate angle ζ , yaw angle θ and velocity components V_x, V_y of the articulate point can be written as follows;

$$\left. \begin{aligned} \dot{\theta}' &= \dot{\theta} - \dot{\zeta} \\ V_x' &= V_x \cos \zeta + (V_x + \dot{\zeta}) \sin \zeta \\ V_y' &= \dot{\zeta}' - V_x \sin \zeta + (V_y + \dot{\zeta}) \cos \zeta \end{aligned} \right\} \quad (1)$$

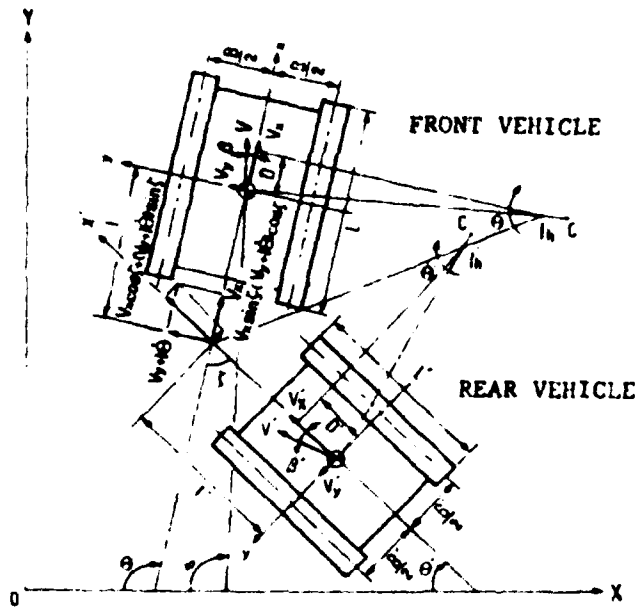


Fig. 1 Coordinate system of articulated vehicles in turning motion

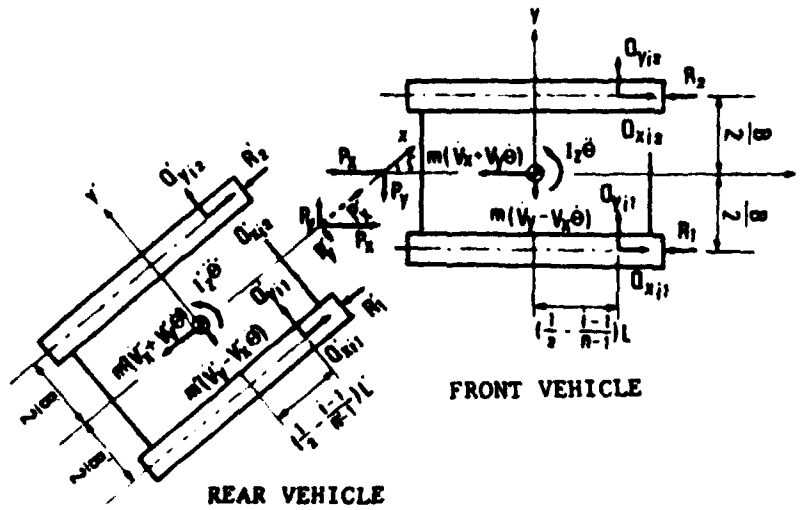


Fig. 2 Forces and moments being exerted on articulated vehicles

(3) Balance of forces of differential system:

As the driving power is transmitted through differential systems to the driving sprockets, it is considered that output torques of both sprockets are equal. But internal friction forces are developed in the differential gears and sprocket because of sprocket gear and track tension. If F_{f1} and F_{f2} are internal friction forces of both driving power train, the circumference forces of sprockets F_1, F_2 can be written as follows.

$$\left. \begin{aligned} F_1 &= F_{f1} + \sum_{i=1}^n Q_{x11} \\ F_2 &= F_{f2} + \sum_{i=1}^n Q_{x12} \end{aligned} \right\} \quad (2)$$

hence

$$F_{f1} + \sum_{i=1}^n Q_{x11} = F_{f2} + \sum_{i=1}^n Q_{x12} \quad (3)$$

It is generally considered that the internal friction forces F_{f1}, F_{f2} for both sprockets are the same values. Therefore, total friction forces of both tracks under road wheels can be written respectively as follows:

$$\left. \begin{aligned} \sum_{i=1}^n Q_{x11} &= \sum_{i=1}^n Q_{x12} \\ \sum_{i=1}^n Q_{y11} &= \sum_{i=1}^n Q_{y12} \end{aligned} \right\} \quad (4)$$

where Q_{xij}, Q_{yij} are x, y components of friction forces of tracks under (i, j) road wheel, i indicates the order of road wheel from the front vehicle, j indicates the inner track when j=1 and the outer track when j=2.

(4) Equation of motion:

Fig. 2 shows the forces being exerted on the articulated tracked vehicles in turning maneuvers. The equation of motion of articulated units can be expressed by the following equation from the dynamic balance between all forces and moments about the z axis acting on two articulated units.

For the front vehicle;

$$\left. \begin{aligned} m(\dot{V}_x + V_y \dot{\theta}) &= \sum_{i=1}^n \sum_{j=1}^2 Q_{xij} - P_x - (R_1 + R_2) \\ m(\dot{V}_y - V_x \dot{\theta}) &= \sum_{i=1}^n \sum_{j=1}^2 Q_{yij} - P_y \\ I_z \dot{\theta} &= \frac{B}{2} \sum_{i=1}^n (Q_{x12} - Q_{x11}) - \sum_{i=1}^n \sum_{j=1}^2 Q_{yij} \left(\frac{1}{2} - \frac{l-1}{n-1} \right) L - P_y L + \frac{B}{2} (R_1 - R_2) \end{aligned} \right\} \quad (5)$$

For the rear vehicle:

$$\left. \begin{aligned} m(\dot{V}_x + V_y \dot{\theta}) &= \sum_{i=1}^n \sum_{j=1}^2 Q'_{21j} + P_x - (R_x + R_z) \\ m(\dot{V}_y - V_x \dot{\theta}) &= \sum_{i=1}^n \sum_{j=1}^2 Q'_{71j} - P_y \\ I_x \dot{\theta} &= \frac{B}{2} \sum_{i=1}^n (Q'_{212} - Q'_{211}) - \sum_{i=1}^n \sum_{j=1}^2 Q'_{71j} \left(\frac{1}{2} - \frac{l-1}{n-1} \right) L + P_z L + \frac{B}{2} (R_x - R_z) \end{aligned} \right\} (6)$$

By substituting equation (1)~(4) into equations(5) (6), the equation of motion of an articulated tracked vehicle may be represented directly in the terms of unknown quantities V_x, V_y, θ and V_{tj} .

2 Numerical analysis

In order to compare steerability of articulated vehicles with coupled vehicles, a numerical analysis has been carried out on actual identical vehicle systems. These main parameters are listed in Table 1.

Fig3 shows an example for numerically computed results of trajectories for the front vehicle of articulated and coupled vehicles.

Solid line shows the trajectories of articulated units. Steering input to articulated units is given by

$$\delta = kt \quad (7)$$

where, k is angular velocity of articulation, t is time.

Numerical analysis has been performed for various steering rates of $k=2,4,6$ degree/sec. It is clearly seen from these trajectories that, in the case of articulated units(solid line), the trajectories depend upon steering rate k . Yawing velocity increases with respect to steering rate. In contrast with the articulated units, steering response of the coupled units is not dependent upon the steering period, but it is influenced by the final steering ratio. It should be pointed out here that steerability of an articulated vehicle is significantly superior to a coupled vehicle.

On the other hand, dotted lines show the trajectories of coupled units. In the case of coupled vehicles, the steering input is given by varying the track velocity V_{tj} of the front vehicle as follows;

$$V_{tj} = V_0 + V_e \sin\left(\frac{\pi}{2} t/T_s\right) \quad (8)$$

where V_{tj} : velocity of inner or outer track, $j=1,2$
 V_0 : track velocity in straight line direction
 V_e : track velocity variation for final steering ratio
 T_s : steering period
 t : times

where, the final steering ratio of the front vehicle becomes $\xi=1.18$ at three various steering period $T_s=1,2,3$ sec.

Table 1 Parameters of the Actual Vehicle

Ground contact length	$L=L'$	3.12 m
Vehicle width	$B=B'$	1.68 m
Weight	$G=G'$	5450 kg
Height of C.G	$H=H'$	0.88 m
Numbers of wheel	$n=n'$	5
Distances from articulate joint to C.G	$l=l'$	3.12 m

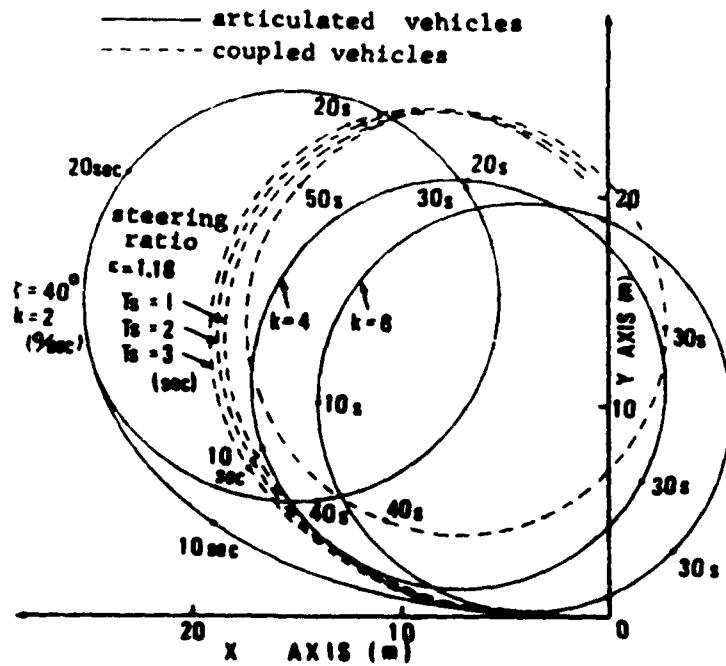


Fig.3 Theoretical turning paths of articulated vehicles and coupled vehicles

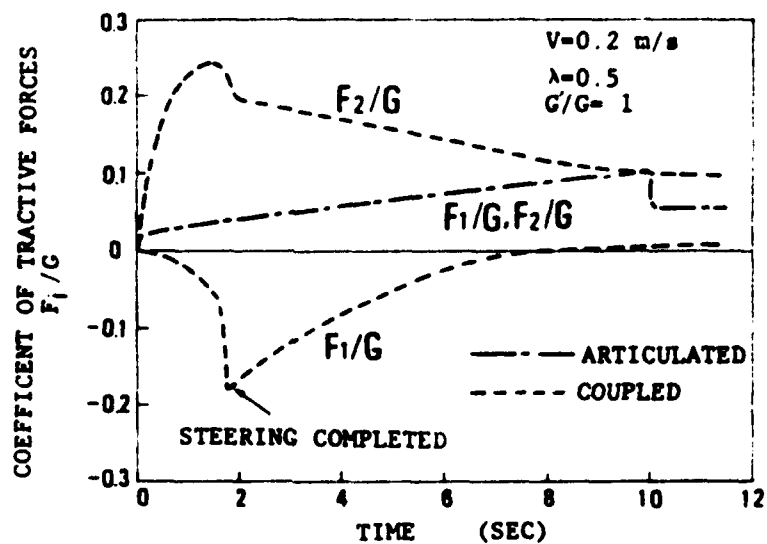


Fig. 4 Tractive forces of articulated units and coupled units

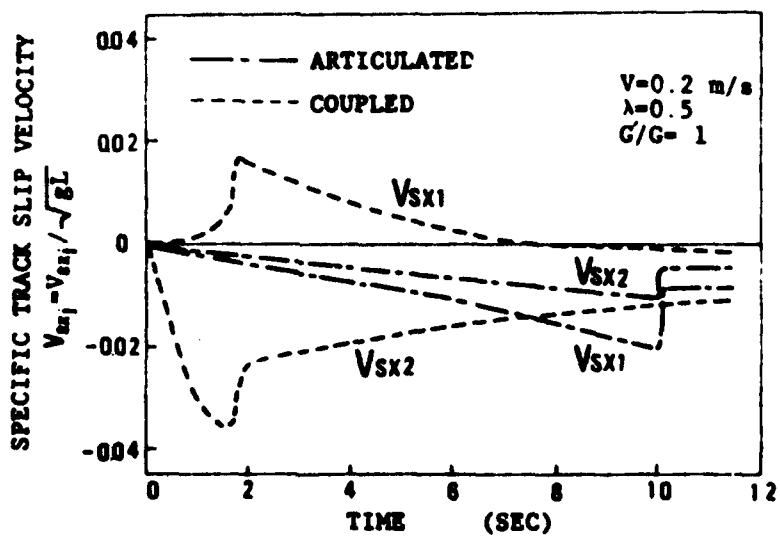


Fig. 5 Slip velocities of articulated units and coupled units

It is found from Fig.3 that the steering performance of the coupled vehicles is influenced by the final steering ratio and that turning is independent of steering times. However, it takes a longer time to reach a stationary turning circle. Consequently, steering response is considered to be inferior to the articulated vehicle.

Fig.4 and Fig.5 show the tractive forces and track slip velocities of the articulated vehicle, in comparison with those of the coupled unit, when the steering maneuvers of each vehicle have been set so each vehicle will on the same path.

As mentioned above, in the turning motion of track vehicles, tractive forces are closely connected with track slip velocities. The tractive forces and track slip velocities of the articulated unit are very small, especially in the first stage of steering, as compared with those of the coupled unit. The coupled unit exhibited approximately ten times the tractive forces and the slip velocities of articulated one. It was found that required sprocket power of an articulated tracked vehicle for steering is very small when compared with a single and coupled unit.

EXPERIMENTAL EXAMINATION BY USING THE SCALE MODEL

1 experimental devices

(1) Chassis and driveline:

So as to evaluate the steerability and mobility of the articulated tracked vehicle, scale models were used in maneuver tests. The overall view of the scale model is shown on Fig.6. Table 2 shows the parameters of the scale models. The center of gravity is located on the body center. The five road wheels on each side of each unit have an independent spring suspension. The engine and transmission are synchronized by propeller shaft are transmitted through the differentials gear to sprocket axes and both sprocket torques are balanced.

(2) Steering system:

In the case of stationary turning motion tests, it is possible for the vehicle to circle by using the connecting plate in which articulate angle can be selected arbitrarily.

In the case of non-stationary maneuver motion tests, the vehicle is handled by the controlled articulation joint with a stepping motor. The steering input is a linear function, such as $f=kt$, operated by a stepping motor.

(3) Test ground:

Turning test were carried out first on hard level ground and then on flat dry loose and using the scale model. The surface of the hard level ground was formed by a wooden plate covered with a synthetic resin film about 0.3 mm thick. A sand bin with standard sand 15 cm thick was used as the soft surface. The vehicle tracks were covered with rubber pads about 2 mm thick in order to generate the usual friction performance and ground pressure of tracks.

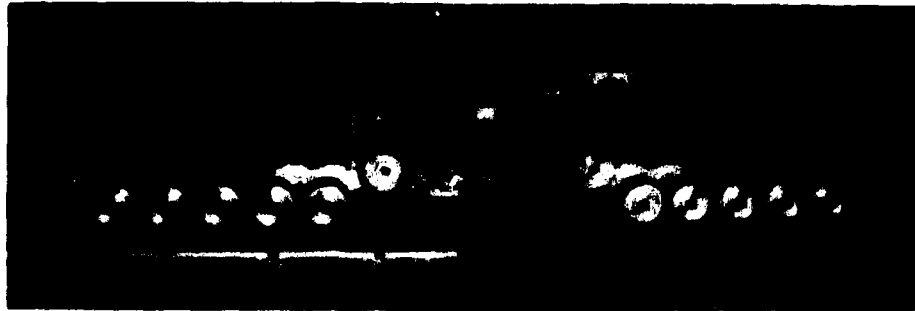


Fig. 6 The overall view of the scale model

Table 2 Parameters of the scale model

Ground contact length	$L=L'$	0.43 m
Vehicle width	$B=B'$	0.29 m
Weight	$G=G'$	55.5 kg
Height	$h=H'$	0.11 m
Numbers of wheel	$n=n'$	5
Distances of from articulate joint to C.G	$l=l'$	0.54 m



(a) A single vehicle



(b) An articulated vehicle

Fig. 7 The photographs of track sinkage measured by the optical method

2 Experimental method

(1) On hard level ground:

Stationary turning motion and non-stationary maneuvering tests were conducted with the articulate point equidistant from the center of gravity of each vehicle. In order to measure the turning radius and the trajectories of the centers of gravity, marker lamps were attached over the center of gravity of each unit. The required sprocket torques for steering were measured by using sprocket axes with strain gages.

(2) On dry loose sand:

Stationary tests were carried out on dry loose sand in order to measure the damage to ground surfaces and tractive forces of units. Track slippage and sinkage were measured from the ruts left in the surfaces.

Fig. 7 shows the photographs of track sinkage, measured by the optical method, when a single and an articulated vehicle were turned at stationary motion on the sand.

EXPERIMENTAL RESULTS

1 Turning tests on hard ground

(1) Stationary turning motion:

Fig. 8 shows the comparison between the experimental results and numerical prediction of tractive forces of articulated, coupled units and a single unit during stationary turning motion. It is clearly seen that for a single and coupled units, large driving forces and braking forces are developed in the outer and the inner track, respectively, because of the skid-steering. In the case of articulated tracked vehicles, driving forces of both tracks were balanced by differential gears and required sprocket torques for steering were considerable smaller than those of single and coupled units.

(2) Non-stationary turning motion:

Fig. 9 shows an example for numerically computed results of the path curve of the center of gravity of the unit compared with the experimental trajectory when the vehicles are steered at an articulate steering angular velocity of $k=3.6^\circ/s$ and steering time $t=15$ s. The marker lamp is installed on the right side of the center of gravity as a clue to elucidate the steering behavior. The white dots mark on the experimental trajectory trace show the starting and ending position in steering. The good agreement between the experimental and theoretical results, as shown in Fig. 9, suggests that the mathematical model is capable of analyzing the steering of articulated units.

Fig. 10 shows the comparison between the tractive forces of the front and rear units during non-stationary turning motion when the angular velocities of the articulation joint are $k=1.8$ and $3.6^\circ/s$, respectively. In contrast with smaller tractive forces of the rear unit, the tractive forces of the front unit increase with time after the steering maneuver has

been initiated. The largest cause for the difference between the tractive forces of the two units is the off-tracking of each trajectory. In other words, the front unit pulls the rear one causing it to turn in a larger radius. This means that slippage and sinkage of tracks of the front unit increases on the soft ground.

Consequently, by designing the differentials to equalize tractive forces of two units, the mobility and steerability of an articulated vehicle might be improved.

2 Turning tests on the dry loose sand

From the results of numerical analysis, it is conceivable that steerability, mobility, track slippage and sinkage on the soft ground will be improved in an articulated vehicle when compared with a single or coupled units. In order to compare the steering performance of each vehicle, stationary turning tests were run on the dry loose sand, and sinkage, slip ratio and required tractive forces of tracks were measured.

Fig.11 shows relationships between turning radius and track sinkage in comparison with single and articulated vehicles. It was found that the sinkage of the inner track of a single vehicle rapidly increases with decreasing turning radius, while, the sinkage of the outer track increases gradually. On the other hand, in the case of articulated vehicles, there is little difference between sinkage of the inner and outer track. Track sinkage of an articulated unit is significantly small in comparison with that of skid-steering vehicles. This is due to the fact that articulated vehicles are not steered by slipping the tracks, but by track velocities controlled by differential systems.

Fig.12 shows relationships between turning radius and slip ratio S_j of track, where S_j is defined as;

$$S_j = \frac{V_j - V_a}{V_j} \quad \begin{array}{l} V_j : \text{track velocities} \\ V_a : \text{body velocity} \end{array} \quad (9)$$

It was also found that the slip ratio S_j of the articulated vehicle exhibit approximately the same value, because the driving forces of both tracks are balanced by the differentials. The slip ratio values are very small in comparison with that of a single unit. It should be pointed out here that the articulated steering systems for tracked vehicle should be of advantage.

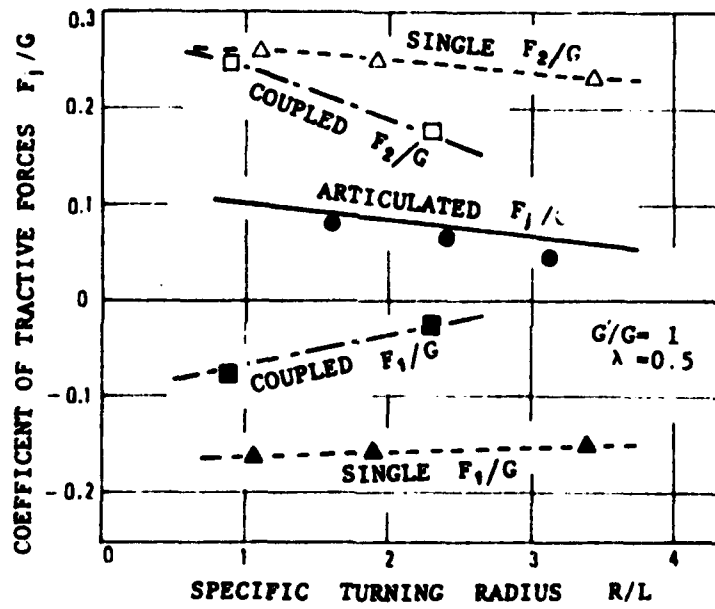


Fig. 8 Relationships between tractive forces and turning radius

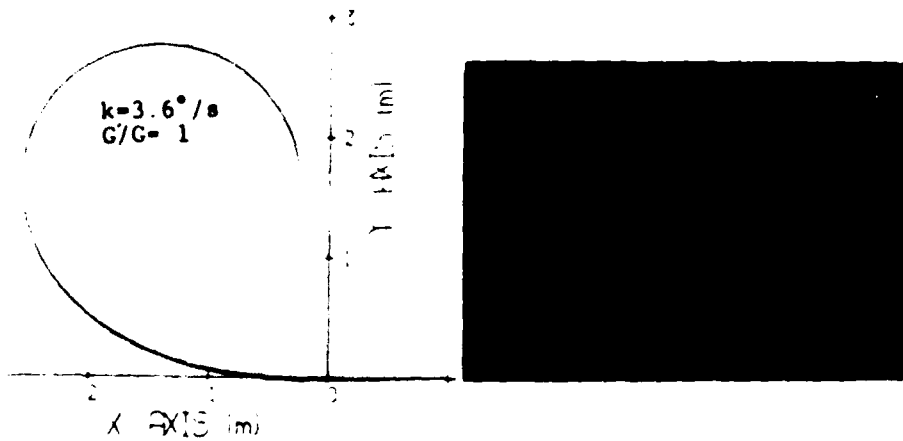


Fig. 9 Trajectories of non-stationary turning motion (experimental and theoretical results)

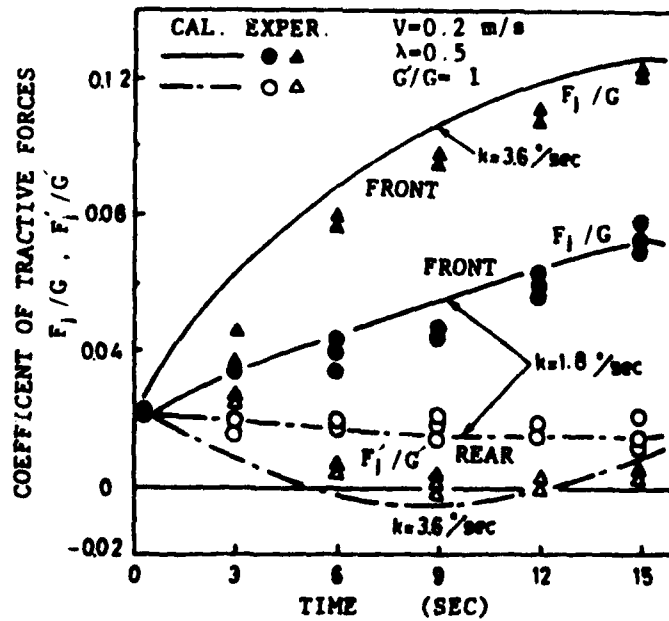


Fig. 10 Tractive forces of both sprockets during a non-stationary turn

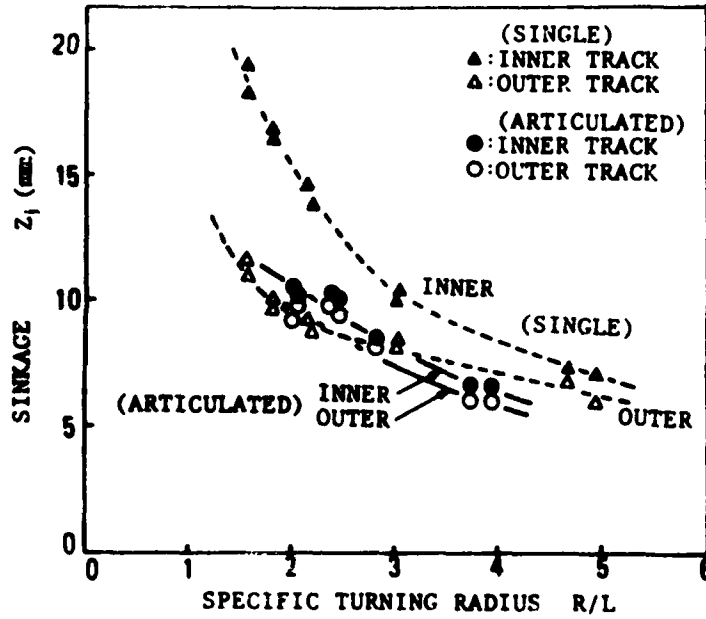


Fig. 11 Relationships between turning radius and track sinkages

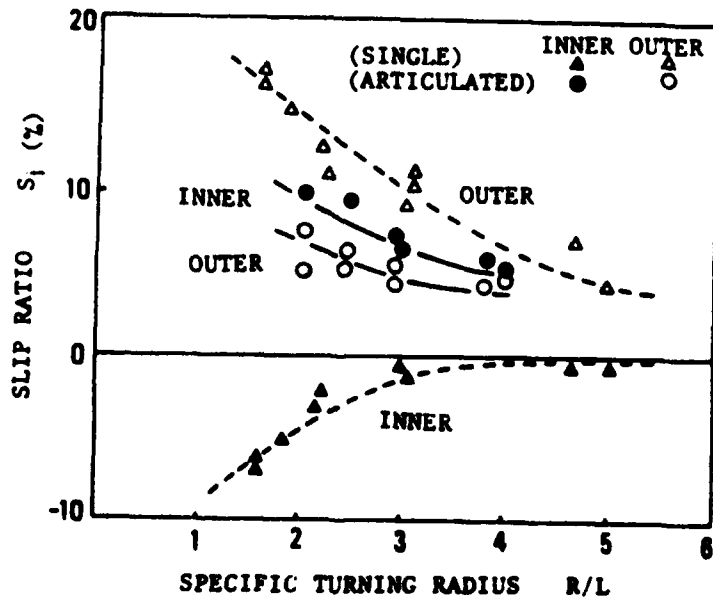


Fig. 12 Relationships between turning radius and slip ratio

CONCLUSIONS

In this paper, a mathematical model of plane motion for predicting the steerability and mobility of articulated vehicles has been developed and computerized for numerical applications. The validity of the model has been experimentally verified by use of a scale model. The experimental results obtained by utilizing the scale model agreed with the theoretical results.

The following results are obtained;

1. In comparison with a single frame vehicle and tow-pin coupled units, required driving forces of sprockets and slippage and sinkage of tracks of articulated vehicles for steering are significantly small. Consequently articulated steering systems produce a significant gain in mobility and steerability on soft terrain which would be impassable to a single unit.
2. A significant improvement in the steering response in transient motion and in high speed operation can be made by articulation.
3. The mathematical model will enable us to obtain numerous data indispensable in designing articulated vehicles.

REFERENCES

- 1) J. Ljunggren; BV 206 A New Swedish All Terrain Vehicle, Proceedings of ISTVS 7th International Conference, Vol. I (1981) PP. 677-689.
- 2) M. Kitano, H. Jyozaki; A Theoretical Analysis of Steerability of Tracked Vehicles, Journal of Terramechanics, Vol. 13, No. 4 (1976) PP. 241-258.
- 3) M. Kitano, M. Kuma; An Analysis of Horizontal Plane Motion of Tracked Vehicles, Journal of Terramechanics, Vol. 14, No. 4 (1978) PP. 11-24.
- 4) M. Kitano, K. Watanabe, K. Swagashira, A. Kinou; An Analysis of Plane Motion of Articulated Tracked Vehicles, Proceeding of ISTVS 7th International Conference, Vol. II (1981) PP. 1413-1447.

